Development of an opto-microfluidic assay, to probe kidney glomerulus function and signaling on-chip

Maxime Mauviel

INSTITUT POLYTECHNIQUE DE PARIS

ÉCOLE POLYTECHNIQUE

IP PARIS

NNT : 2023IPPAX135

Thèse de doctorat

Development of an opto-microfluidic assay to probe kidney glomerulus function and signaling on-chip

Thèse de doctorat de l'Institut Polytechnique de Paris
préparée au Laboratoire d'Optique et Biosciences à l'École Polytechnique

École doctorale n°626 : École Doctorale de l'Institut Polytechnique de Paris (ED IP Paris)
Spécialité de doctorat: Biologie

Thèse présentée et soutenue à Palaiseau, le 1/12/2023, par

Maxime Mauviel

Composition du Jury :

Charles BAROUD Professeur, Institut Pasteur/École Polytechnique (– LadHyX)	Président
Benoit LADOUX Directeur de recherche, Institut Jacques Monod (– UMR CNRS 7592)	Rapporteur
Isabelle BONNET Maîtresse de Conférence, Institut Curie/Sorbonne Université (– UMR 168)	Rapporteure
Olivia LENOIR Chargée de recherche, PARCC (– U INSERM 970)	Examinatrice
Cédric BOUZIGUES Professeur assistant, École Polytechnique (– U INSERM 1182/ UMR CNRS 7645)	Directeur de thèse
Antigoni ALEXANDROU Directrice de recherche, École Polytechnique (– U INSERM 1182/ UMR CNRS 7645)	Co-directrice de thèse

Acknowledgement

First and foremost, I extend my sincere gratitude to the president and to the members of my jury for dedicating their time and expertise to reviewing my work. Special appreciations are due to my reporters, Isabelle Bonnet and Benoit Ladoux, for their insightful comments and valuable feedback on my manuscript.

I am particularly thankful to my thesis supervisors, Cédric Bouzigues and Antigoni Alexandrou. Your mentorship has been a cornerstone of my journey. The quality time spent under your guidance, coupled with your human qualities and exceptional scientific insights, has been instrumental in shaping both my work and my personal growth.

I express my heartfelt appreciation to my interns, Ghadi and Joanna, for their exceptional work and dedication to this project. Their contributions have been remarkable and will leave a lasting impact. Additionally, I am excited to acknowledge Aichata, who will be continuing this work in the future, and I look forward to seeing the advancements she will bring.

A special thank you goes to the entire nanoimaging team - Nicolas, Thuy, Rivo, Fanny, Robin, Christophe, Valia, Alessia, Dorian, Kate, and the others. Your camaraderie, our shared moments, and your precious advices have enriched my experience and daily routine immeasurably.

I am grateful to our collaborators from LOB: Pierre, Gaël, Marie-Claire, Martin, and others, for their assistance in various aspects of this project. Your collaborative spirit and expertise have been critical in the success of this work.

My appreciation extends to all the other members of the LOB, especially Laure and Christelle, who have been incredibly helpful with the administrative aspects of the lab bureaucracy. Your support in navigating these complexities has been a great relief.

I would also like to express my gratitude to our collaborators from PARCC, Olivia Lenoir and Pierre-Louis Tharaux, for their dedication to providing me the outmost needed cells for this project, and their kind support and advices. Thanks also to Thierry, Raphael and Rabeï from PMC for their assistance with the nanoparticles, and Eric Rubinstein from the André Lwoff Institute for the CD9 antibody.

Acknowledgment is also due to the engineers from the various platforms that have been pivotal to this project: Claire Boulogne and Cynthia Dupas from Imagerie-Gif for their training in TEM, Joni Frederick from the Leduc microfabrication facility, and Gareth and Aline from the Polytechnique Fab-Lab. Your expertise and willingness to share your knowledge have been critical to my research.

Many thanks to my family - my parents, my grandparents and my brother - and my friends - from Antony and Villejuif to Granville - for their unfailing support. Your encouragement and presence over the years have been a great source of strength and motivation.

Finally, my most profound thanks are reserved for my partner, Joëlle. Your support through every high and low, your unwavering belief in me, and your encouragement to pursue this thesis until the end are gifts of immeasurable value. Your role in this journey has been fundamental, and for that, I am eternally grateful.

Remerciements

Tout d'abord, je tiens à exprimer ma sincère gratitude au président et aux membres de mon jury pour avoir consacré leur temps et leur expertise à l'examen de mon travail. Je tiens à remercier tout particulièrement mes rapporteurs, Isabelle Bonnet et Benoit Ladoux, pour leurs commentaires et leurs remarques précieuses sur mon manuscrit.

Je suis particulièrement reconnaissant à mes directeurs de thèse, Cédric Bouzigues et Antigoni Alexandrou. Votre mentorat a été la pierre angulaire de mon parcours. Le temps de qualité passé sous votre direction, associé à vos qualités humaines et à vos perspectives scientifiques exceptionnelles, a joué un rôle déterminant dans l'élaboration de mon travail et dans mon développement personnel.

J'exprime ma sincère reconnaissance à mes stagiaires, Ghadi et Joanna, pour leur travail exceptionnel et leur dévouement à ce projet. Leurs contributions ont été remarquables et laisseront un impact durable. En outre, je suis heureux de saluer Aichata, qui poursuivra ce travail à l'avenir, et j'ai hâte de voir les progrès qu'elle apportera.

Je remercie tout particulièrement l'ensemble de l'équipe nanoimagerie du LOB - Nicolas, Thuy, Rivo, Fanny, Robin, Christophe, Valia, Alessia, Dorian, Kate et les autres. Votre camaraderie, nos moments partagés et vos précieux conseils ont enrichi mon expérience et mon quotidien de manière incommensurable.

Je remercie nos collaborateurs du LOB : Pierre, Gaël, Marie-Claire, Martin, pour leur aide dans divers aspects de ce projet. Votre esprit de collaboration et votre expertise ont été déterminants pour la réussite de ce travail.

Ma reconnaissance s'étend à tous les autres membres du LOB, en particulier Laure et Christelle, qui ont été d'une aide précieuse pour les aspects administratifs du laboratoire. Votre soutien dans la gestion de ces complexités a été un grand soulagement.

J'aimerais également exprimer ma gratitude à nos collaborateurs du PARCC, Olivia Lenoir et Pierre-Louis Tharaux, pour leur dévouement à me fournir les cellules nécessaires à ce projet, ainsi que pour leur soutien et leurs conseils bienveillants. Merci également à Thierry, Raphael et Rabeï du PMC pour leur aide avec les nanoparticules, et à Eric Rubinstein de l'Institut André Lwoff pour l'anticorps CD9.

Je souhaite remercier également les ingénieurs des différentes plateformes techniques qui ont joué un rôle essentiel dans ce projet : Claire Boulogne et Cynthia Dupas de la plateforme Imagerie-Gif pour leur formation en MET, Joni Frederick de la plateforme de microfabrication Leduc, Gareth et Aline du Fab-Lab de l'Ecole Polytechnique. Votre expertise et votre volonté de partager vos connaissances ont été essentielles à ma recherche.

Un grand merci à ma famille – mes parents, mes grands-parents et mon frère – et à mes amis – de Antony et Villejuif à Granville –, pour leur soutien indéfectible. Vos encouragements et votre présence durant ces années ont été une grande source de force et de motivation.

Enfin, mes remerciements les plus profonds sont réservés à ma compagne, Joëlle. Ton soutien dans tous les moments forts et difficiles, ta confiance inébranlable en moi et ton encouragement à poursuivre ma thèse jusqu'au bout sont des cadeaux sans commune valeur. Ton rôle dans cette aventure a été fondamental et je t'en serai éternellement reconnaissant.

Content

List of abbreviations

ADAM: Disintegrin and Metalloproteinase domain-containing protein
ANCA vasculitis: Anti Neutrophil Cytoplasmic Antibody-associated vasculitis
BS: Bowman Space
CD9: cell surface glycoprotein 9 (tetraspanin)
CGN: Crescentic GlomeruloNephritis
CTGF: Connective Tissue Growth Factor
DBSCAN: Density-Based Algorithm for Discovering Clusters in Large Spatial Databases with Noise
DCF: DihydrodiChloroFluorescein
dSTORM: direct Stochastic Optical Reconstruction Microscopy
DT: Distal Tubule
ECM: Extra Cellular Matrix
EGF: Epidermal Growth Factor
EGFR: Epidermal Growth Factor Receptor
EM-CCD: Electron-Multiplying Charge Coupled Device
EMT: Epithelial-to-Mesenchymal Transition
ER: Endoplasmic Reticulum
ESCKD: End-Stage Chronic Kidney Disease
ESL: Endothelial Surface Layer
ET-1: EdoThelin-1
F-actin: Filamentous actin
FITC: Fluorescein IsoThioCyanate
FP: Foot Proccess
FRET: Förster Resonance Energy Transfer
FSGS: Focal Segmental GolmeruloSclerosis
FWHM: Full Width at Half Maximum
GAG: GlycosAminoGlycan
GBM: Glomerular Basement Membrane
GECs or GEnCs: Glomerular Endothelial Cells, CiGEnCs Conditionnaly immortalized human Glomerular Endothelial Cells
GFB: Glomerular Filtration Barrier
GFP: Green Fluorescent Protein
GSC: Glomerular Sieving Coefficient
GSH: reduced glutathione
GSSG: glutathione disulfide
HB-EGF: Heparin-Binding Epidermal Growth Factor
hEGF: human recombinant Epidermal Growth Factor
HSPGs: Heparan Sulfate ProteoGlycans
HUVECs: Human Umbilical Vein Endothelial Cells
iPSCs: human induced Pluripotent Stem Cells
LC-OCT: Line-field Confocal Optical Coherence Tomography
MAPK: Mitogen-Activated Protein Kinase
MCs: Mesangial Cells

MPS: MicroPhysiological Systems
N.A.: Numerical Aperture
NAMs: New Approach Methodologies
NOX: NADPH oxidase
NPHS1 and NPHS2: genes responsible for coding nephrin and podocin
OCT: Optical Coherence Tomography
OoC: Organ-on-Chip
PA-FP: PhotoActivable-Fluorescent Proteins
PALM: PhotoActivated Localization Microscopy
PAM: PolyAcrylaMide
PDGF: Platelet-Derived Growth Factor
PDGFR: Platelet-Derived Growth Factor Receptor
PDMS: PolyDiMethylSiloxane
PECs: Parietal Epithelial Cells (iPECs intermediary, cPECs cuboidal, fPECs flat, mPECs mouse primary, CirPECs/CihPECs conditionnaly immortalized rat/human PECs)
PET: PolyEthylene Terephthalate
PFTE: PolytetraFluoroeThylEn
PI3K: PhosphoInositide 3-kinase
PL: PhotoLuminescence
Pod/podo: Podocytes, CiPodocytes conditionnaly immortalized human Podocytes (CiPococytes)
PSF: Point Spread Function
PT: Proximal Tubule
ROS: Reactive Oxygen Species
RPGN: Rapidly Progressive GlomeurloNephritis
SD: Slits Diaphragms
SEM: Scanning Electron Microscopy
SIM: Structured-Illumination Microscopy
SMLM: Single Molecule Localization Microscopy
SNR: Signal to Noise Ratio
SPT: Single Particle Tracking
Src: Proto-oncogene tyrosine-protein kinase
STED: STimulated Emission Depletion
dSTORM: direct Stochastic Optical Reconstruction Microscopy
TEER: TransEpithelial/transEndothelial Electrical Resistance
TEM: Transmission Electron Microscopy
TEMs: Tetraspanin-Enriched Microdomains
TGF: Transforming Growth Factor
TIRFm: Total Internal Reflection Fluorescence microscopy
VE-cadherin: Vascular Endothelial-cadherin
VEGF-A: Vascular Endothelial Growth Factor-A
VEGFR: Vascular Endothelial Growth Factor Receptor
WLI: White Light Interferometry
WT1: Wilms Tumor protein 1
ZO-1: Zonula Occludens 1

General introduction

The identification of signaling pathways is the basis of understanding physio-pathological processes to design efficient pharmacological treatments. This can be based on the detection and/or characterization of interactions *in vitro* or *in vivo*. However, in complex diseases, such as some inflammation-related conditions, this approach is often insufficient both to understand the pathology mechanisms, and to design targeted treatments. It may be necessary to identify *in situ* the loci, the timing, and the quantity of the production or activation of the involved molecules resulting from their complex interplay with the environment. It is thus essential to develop technologies (i) to design assayable physiologically relevant systems adapted for quantitative analysis and (ii) to quantitatively probe biological processes from the molecular to the organism scale, at high temporal and spatial resolutions.

This is notably true for Rapidly Progressive GlomeurloNephritis (RPGN) and Focal Segmental GolmeruloSclerosis (FSGS), causing terminal kidney failure, due to major disorganization of the glomerulus, the filtering unit of the kidney. This is characterized by an uncontrolled de-differentiation and migration of specialized cells relying on a complex molecular interplay between different local cues, whose action can be mediated by the production of Reactive Oxygen Species (ROS). Among multiple putative local cues, HB-EGF (Heparin-Binding Epidermal Growth Factor), PDGF (Platelet-Derived Growth Factor), and the transmembrane protein tetraspanin CD9 have been identified as key regulators of RPGN progression and PDGF inhibition has beneficial effects in RPGN (Lazareth et al., 2019). EGF and PDGF pathways are known to involve intracellular ROS production. Since ROS is a key second messenger in EGF and PDGF signaling, it is assumed that ROS is a central regulator for RPGN.

The lack of efficient quantitative assays, both for cell response in a multicellular environment and for ROS detection, has so far hindered the understanding of its mechanisms. The integration of molecular mechanisms leading to this pathological phenotype at the organ scale is thus the key problem to tackle. In this context, we used innovative technologies to measure cell responses (intracellular ROS concentration, membrane protein activation/organization,…), in systems of controlled complexity to identify critical mechanisms that could be the basis for *in vivo* methods of RPGN/FSGS treatment or management.

We have developed an opto-microfluidic biomimetic assay, combining a thorough glomerulus reconstitution on-chip to decipher complex migration processes, and advanced quantitative imaging methods, notably using lanthanide-based luminescent nanoparticles to achieve fast ROS detection in cell microsystems. This framework allows to quantitatively assay cell responses and the associated ROS production under various controlled HB-EGF/PDGF stimuli. This systematic approach will be the basis for the understanding of complex pathophysiological mechanisms controlling RPGN/FSGS. This device aims at filling the gap between the *in vitro* and *in vivo* scales, at which multiple concomitant effects often blur results, in order to further identify critical targetable pathways and to screen putative drugs to contribute to an efficient molecular therapeutic strategy design.

Altogether, this work aims at contributing to the elaboration of powerful tools to accurately understand molecular signaling in a normal and pathological situations and to elaborate strategies to

non-invasively and quantitatively profile complex pathologies (tumor, auto-immune diseases,…), which are essential for the further conception of personalized treatments.

Outline

Chapter 1 briefly introduce the anatomy and function of the kidney, introduces inflammatory kidney diseases (RPGN and FSGS), and discusses the significance of glomerular Endothelial, Parietal Epithelial Cells (PECs) and Podocytes behavior in upholding kidney function and their contribution to inflammatory kidney disorders.

Chapter 2 describes the design of an optically accessible microsystem that accurately mimics the human glomerulus using the “Organ-on-chip” technique. By replicating the glomerular filtration barrier in this system, we ensured the system functions similarly to a real human glomerulus. We then sought to understand the cellular and organ-level processes in pathophysiological responses induced by EGF stimulations.

Chapter 3 develops tools for molecular and cellular assays to study the EGFR behavior and their interactions with CD9 upon HB-EGF stimulation. Using single molecule based imaging techniques, the goal is to provide a clearer understanding of EGFR interaction with CD9-rich domains. One of the potential outcomes of such interactions is a modulated EGFR signaling. The chapter then explores the use of Europium-doped nanoparticles to quantitatively measure ROS concentrations mediated by EGFR activation/transactivation in PECs, and CD9-KO PECs, post HB-EGF/PDGF stimulations. The last part explores to integration of ROS sensitive surfaces in “Organ-on-chip”.

Chapter 1. Glomerular pathophysiology: Glomerulonephritis and Glomerulosclerosis

1.1 The kidneys and the glomerulus

1.1.1 Physiology and cellular organization

The kidneys are paired organs located in a retroperitoneal position, whose primary role is to filter blood and concentrate waste into urine. The kidneys also plays a crucial role in removing metabolic wastes from the blood, which is essential for fluid balance, osmoregulation, blood pressure regulation, vitamin D synthesis, bone mineralization, and red blood cell development (Lote, 1994). Although relatively small in size (comparable to a human fist), the kidney is densely vascularized. Both kidneys process a significant volume of blood, roughly 20% of the total heart output (Stein & Fadem, 1978). Humans typically produce about 1 liter of urine daily due to kidney filtration. This urine generation and concentration happens along the nephron's length, the kidney's foundational unit.

Anatomically, they consist of an outer cortical zone, or cortex, which contains all the glomeruli, proximal and distal tubules, and an inner medullary zone, or medulla, where the Henle's loop and collecting ducts are located (Figure 1, A).

1.1.1.1 Functional unit of the kidneys: the Nephron

A nephron is divided functionally into a filtering segment named the renal corpuscle, or glomerulus, and a segmented tubular absorption section (series of interconnected epithelial tubules) starting with the proximal tubules, the loop of Henle, the distal tubules, and a final collecting duct (Figure 1, A & B). An adult human kidney houses around 1 to 2.5 million nephrons (Bertram et al., 2011; Puelles et al., 2011). The term glomerulus refers to its complex inner capillary tuft, echoing the Latin word for a ball of yarn. The first microscopic description of the glomerulus is credited to the Italian anatomist Marcello Malpighi in 1666 (Fogazzi, 1997), in a work called *De renibus*. Malpighi named the glomerulus, which in Latin he defined as *minimae glandulae* (literally, tiny glands), and provided a comprehensive description (Malpighi, 1687):

> *"... and also the other claim that all this portion of the kidneys is fibrous and contains nothing but blood vessels is difficult to be accepted. In fact, in all the kidneys of whatever animal and of man himself I have happened to have in my hands so far, I have always noticed the presence of tiny corpuscles. To see these corpuscles the artery of the kidney has to be injected with a black liquid mixed with the spirit of wine until the whole kidney swells and the most external part of it turns black. Once the capsule of the kidney is removed, even by the naked eye one can see ... the small corpuscles which have turned black, hanging from the black vessels; by sectioning the kidney longitudinally, one can see among the tubules and the interstitium a large number of these corpuscles, hanging like apples, from the blood vessels which, swollen with the black liquid, look like a beautiful tree."*

The glomerulus is a specialized tangle of capillaries located between two arterioles: one afferent that carries blood and an efferent arteriole from which the latter leaves (Figure 1, C). This vascular network is bounded externally by the Bowman's capsule. This structure is composed of 4 distinct cell types:

- glomerular *endothelial cells* (GECs or GEnCs) forming a fenestrated endothelium which participates in the selective filtration of plasma in the primitive urine,

- *podocytes* which are terminally differentiated pericytes appended to the capillary on the urinary side. Podocytes are named for their detailed projections or "foot processes," which are closely wrapped around glomerular capillaries,
- *parietal epithelial cells* (PECs) create a watertight enclosure known as the Bowman's capsule,
- *mesangial cells* (MCs) that provides structural support to the glomerular vessels.

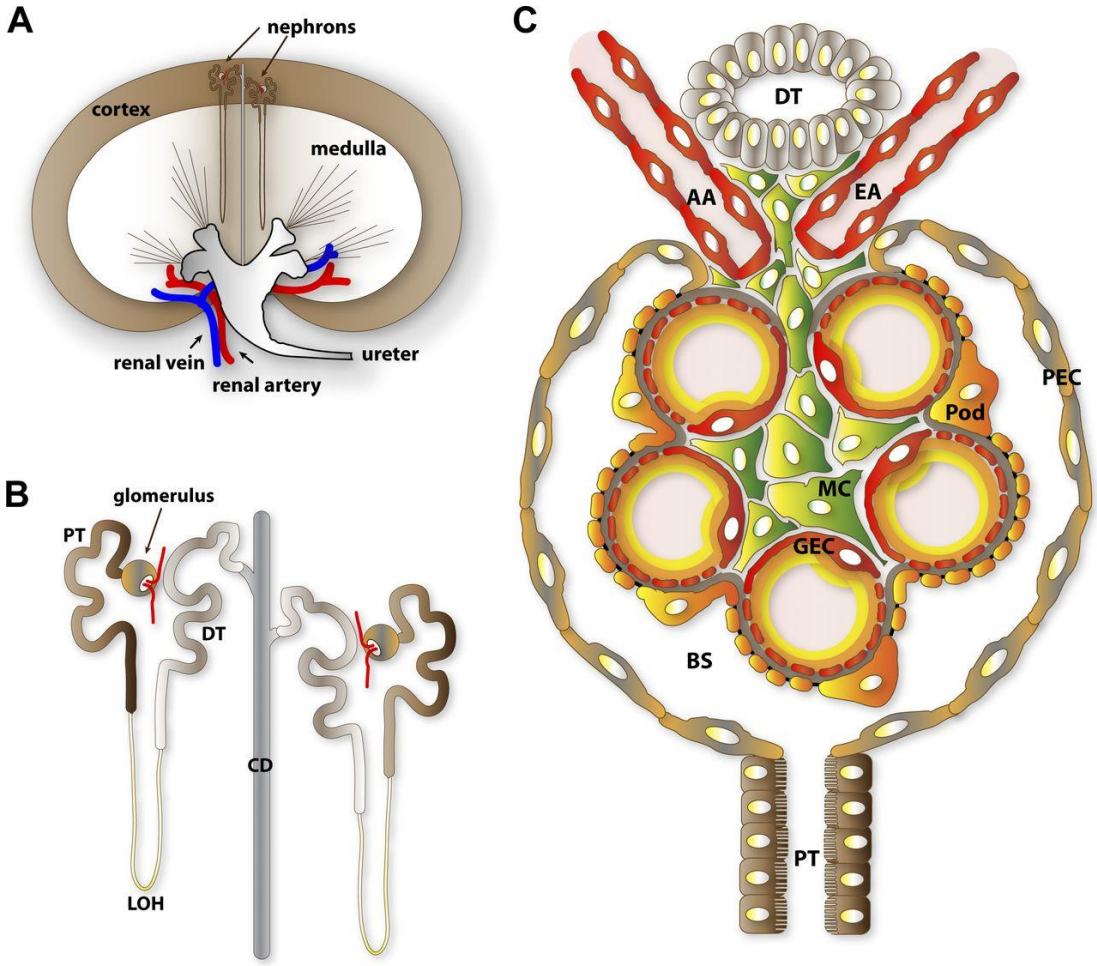

Figure 1: Anatomical breakdown of kidney filtration processes, A) schematic depiction of the nephron arrangement within the kidney, the glomeruli, which serve as the nephron's filtration units, are located in the renal cortex, B) detailed segmentation of the nephron, the vascular glomerulus is situated at the starting point and leads to an array of renal tubules where the makeup of the urinary filtrate is modified via reabsorption and secretion, C) the intricate cell structure of the glomeruli. Legend: GEC, glomerular endothelial cell (or GEnC); AA, afferent arteriole; EA, efferent arteriole; Pod, podocyte; MC, mesangial cell; PEC, parietal epithelial cell; PT, proximal tubule; DT, distal tubule; LOH, Henle's loop; CD, collecting duct; BS, Bowman's space. Image from (Scott & Quaggin, 2015).

Both GEnCs and podocytes share a common extracellular matrix called the glomerular basement membrane (GBM, Figure 2, E). Together, the GEnCs, podocytes, and the GBM form the glomerular filtration barrier (GFB), a precise sieve that selectively filters blood to produce a primary urinary filtrate mainly devoid of proteins. Primary urinary filtrate accumulates in the Bowman's capsule and flows through connected proximal and distal tubules, the Henle's loop and collecting ducts (Figure 1, B), crucial for fluid balance and electrolyte regulation.

1.1.1.2 The Glomerulus and the Glomerular Filtration Barrier (GFB)

The glomerular capillaries, formed by GEnCs, are replete with transcellular pores and lack a surrounding layer of smooth muscles. These pores on the glomerular capillary, termed fenestrae, span 60–100 nm in width and account for roughly 20% of the endothelial surface (Hjalmarsson et al., 2004; Levick & Smaje, 1987; Rostgaard & Qvortrup, 2001; Satchell & Braet, 2009). Such a design makes these capillaries channels efficient for the swift flow of large fluid volumes, a hallmark of renal filtration (Figure 2, D, based on, Levick & Smaje, 1987). The glomerular capillaries inner surface and the fenestrae surfaces are adorned with a negatively charged glycoprotein matrix known as the glycocalyx (Singh et al., 2007) (Figure 2, E, based on Curry & Adamson, 2012; Rostgaard & Qvortrup, 2001). Moreover, plasma components absorbed into the glycocalyx form a thicker layer exceeding 200 nm, termed the endothelial surface layer (ESL, Hjalmarsson et al., 2004). The intricate structure and potent negative charge of the ESL essentially constrict and regulate the fenestrae and filtration.

Situated between the endothelium and the epithelial podocytes, the glomerular basement membrane (GBM) serves as the intermediate layer (Figure 2, E). This GBM is a distinct extracellular matrix made up of components like laminin, type IV collagen, nidogen, and heparan sulfate proteoglycan (Byron et al., 2014; Miner, 2012). In humans, its thickness is around 400 nm and it possesses a negative charge (Suleiman et al., 2013) also responsible for filtration properties.

The glomerular capillary epithelial layer is made up of unique renal cells called podocytes (Figure 2, A). These podocytes envelop the glomerular basement membrane using cytoplasmic extensions known as foot processes (FPs) (Figure 2, B). These processes create gaps or Slits Diaphragms (SDs) approximately 35 nm wide between them (Figure 2, E) (Shirato et al., 1991). The Podocytes provide the last filtration properties of the GFB.

Altogether these 3 components form the Glomerular Filtration Barrier (GFB) (Figure 2, E). To enclose the glomerulus, the Bowman's space houses a single layer of parietal epithelial cells (PECs). Both PECs and podocytes originate from the same mesenchymal lineage during glomerulogenesis (Shankland et al., 2014). While endothelial cells and podocytes are composing the glomerulus filtration barrier, PECs form the Bowman’s capsule, a tight epithelium leading to the formation of the proximal tubule.

We further detail in the following sections, the role of the glomerular endothelium, the basement matrix, the podocytes and the parietal epithelial cells composing the glomerulus in physiological, as well as in pathological contexts.

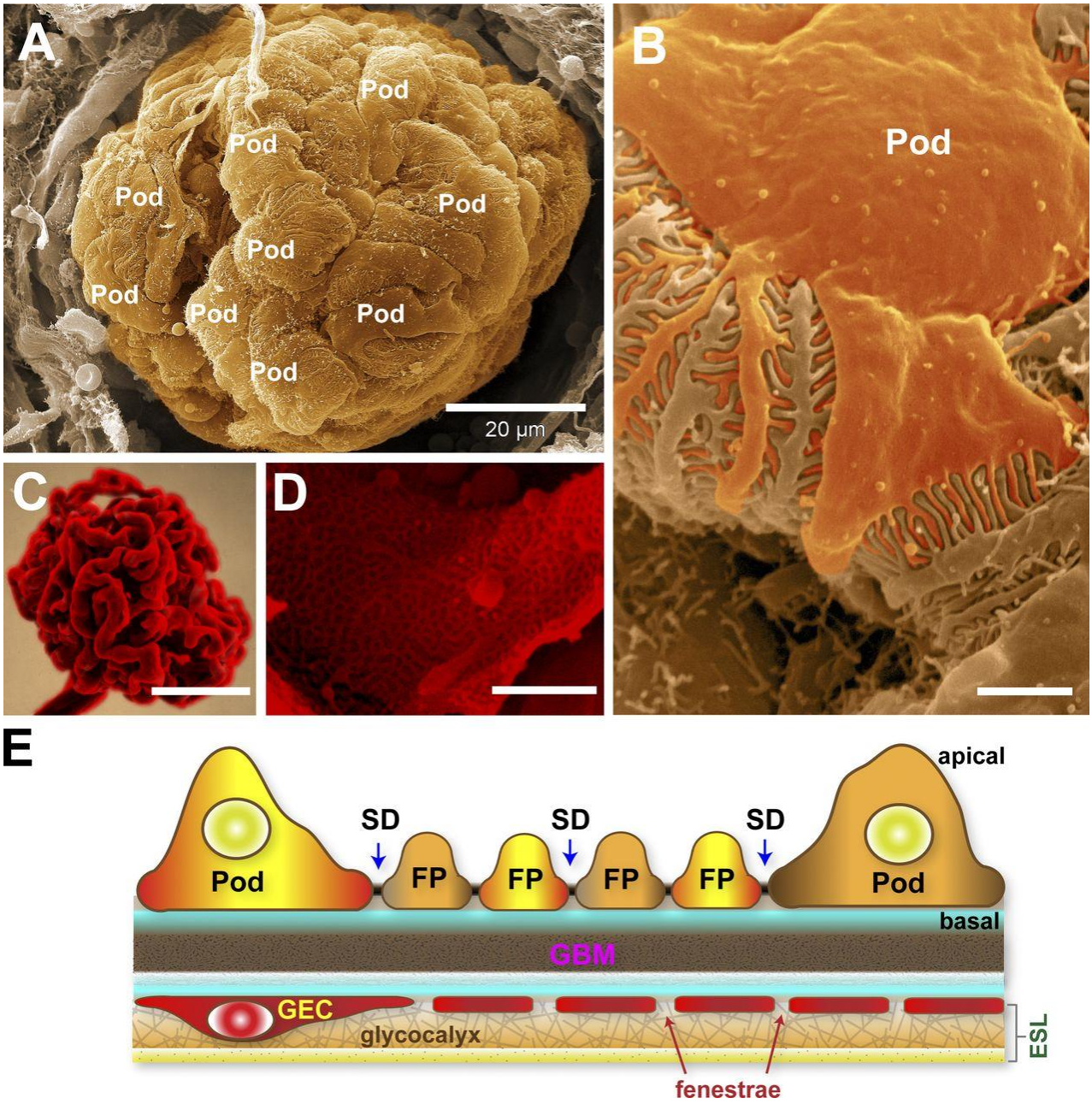

Figure 2: Detailed examination of podocytes and the glomerular endothelial structure, A) electron microscopy image showing a glomerulus, in this colored micrograph, the Bowman's capsule has been ruptured, allowing a clear visualization of the podocytes (Pod) wrapped around the glomerular capillaries entirely. B) A closer look at a podocyte inside the glomerulus, displaying the interdigitated foot-processes (FPs). C) A resin cast of the glomerular capillary tuft, with corroded cells highlighting its intricate, coiled structure. D) Electron microscopy view of an unveiled glomerular capillary, showing its abundant fenestrations. E) A basic illustration of the Glomerular Filtration barrier (GFB), the GEC (or GEnC) and its fenestrae are covered by a fibrous glycocalyx rich in negatively charged proteoglycans, this glycocalyx, combined with the attached plasma elements, creates the denser Endothelial Surface Layer (ESL). The GBM acts as a layered Extra Cellular Matrix (ECM) nestled between podocytes and GECs. Podocytes constitute the GFB's concluding layer. The interdigitating Foot Processes (FPs) of the podocytes are connected through permeable Slit Diaphragm (SD), facilitating the passage of the primary urinary filtrate. Scale bars: A) 20 µm; B and D) 1 µm; C) 50 µm, image from (Scott & Quaggin, 2015).

1.1.1.3 Glomerular ENdothelial Cells (GEnCs) and the glomerular capillaries

There have been debates regarding the effectiveness of the glomerular capillary as a genuine filtering section because of the dimensions of its fenestrae (60–100 nm) (Satchell & Braet, 2009).

These fenestrae appear broad enough to accommodate albumin, which has a molecular size of 8 × 8 × 3 nm (Sugio et al., 1999). Yet, biophysical evaluations have shown that both fenestrated and non-fenestrated capillaries display similar permeabilities to macromolecules (Hemant, 2010). More recent research emphasizes the proactive role of the glomerular endothelium in renal filtration, largely attributed to its glycocalyx negatively charged surface (Curry & Adamson, 2012; Rostgaard & Qvortrup, 2001) and heparanase levels (Singh et al., 2007). ROS have been identified to break down the glycosaminoglycan (GAG) chains in proteoglycans, essential for the protective function of the GEnCs glycocalyx. When hydrogen peroxide was externally added, there was a noticeable reduction in lectin and heparan sulphate markings on the GEnC surface, resulting in an elevated movement of albumin across the endothelium (Singh et al., 2013).

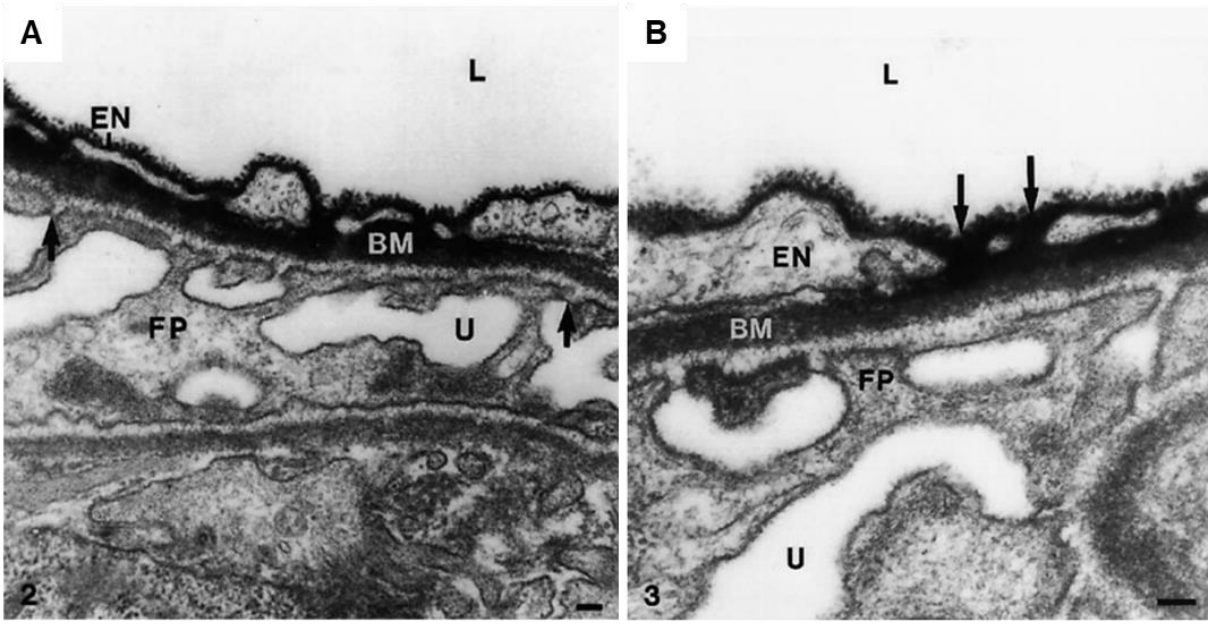

Figure 3: An electron micrograph of the structure of the glomerular capillary wall. The endothelium is bordered by a noticeable, thread-like protective layer, roughly 60 nm in thickness, visible on the inner face of the endothelium. This layer fills the fenestrae (indicated by arrows in B) and extends over the spaces between them. In the image, the three components of the GFB are distinguishable: the fenestrated endothelium (EN), the basement membrane (BM), and the podocyte characterized by its foot processes (FP) and the gaps marked by filtration slit diaphragms (indicated by arrows in A). L represents the capillary chamber, while U signifies the urinary area. The depicted magnifications are A) 33,500 and B) 60,000. Scale bars are set at A) 0.5 and B) 0.1 µm respectively. Image from (Rostgaard & Qvortrup, 2001).

Moreover, plasma components absorbed into the glycocalyx form a thicker layer exceeding 200 nm, termed the endothelial surface layer (ESL, (Hjalmarsson et al., 2004). The intricate structure and potent negative charge of the ESL essentially constrict and regulate the fenestrae. Enzymatic degradation of ESL components or salt perfusion (Fridén et al., 2011) led to an increase in albumin excretion, a reduction in ESL depth, and a decrease in anionic sites on the endothelial surface (Jeansson & Haraldsson, 2003, 2006; Meuwese et al., 2010).

The ESL role in glomerular filtration has been scrutinized in disease models related to proteinuria. For instance, renal perfusion with adriamycin, a drug used to trigger proteinuria in mice, led to a significant reduction of the glomerular ESL, which adversely affected the size selectivity and charge density of the GFB (Jeansson et al., 2009). Additionally, in rats, age-related proteinuria was linked to a decrease in the glomerular ESL (A. H. J. Salmon et al., 2012). Similar observations were made in both animal models and human subjects where diabetes-induced proteinuria showed a strong

association with injuries to the ESL (A. H. Salmon & Satchell, 2012). Some suggest the ESL may act as a mechanosensor to fluid movement, which aligns with the observed loss of vasodilation upon ESL removal (Curry & Adamson, 2012; Fu & Tarbell, 2013). Collectively, these insights support the idea that the ESL is an indispensable aspect of the glomerular endothelium, playing a pivotal role in controlling glomerular permeability.

1.1.1.3.1 Signaling

To form a functioning GFB, the correct development of the glomerular endothelium is crucial. Early-stage podocytes release Vascular Endothelial Growth Factor-A (VEGF-A), a powerful attractant and growth factor for migrating angioblasts that eventually form the glomerular endothelium (Bertuccio et al., 2011; Hakroush et al., 2009). VEGF-A binds to receptors like VEGFR1, VEGFR2, and neuropilin-1, found on these angioblasts (Robert et al., 2000). Deleting both copies of the Vegfa gene from podocytes hampers glomerular growth and the formation of a GFB. A partial deletion, $Vegfa^{+/-}$, results in abnormal growth of GEnCs and a subsequent loss of fenestrae, termed endotheliosis (Eremina et al., 2003, 2006). This deterioration of the glomerular endothelium was also observed when Vegfa was removed from adult mouse podocytes or when its receptor was missing in GEnCs, highlighting that VEGF-A operates through VEGFR2 in a paracrine manner (Eremina et al., 2008; Sison et al., 2010). Effects of VEGF-A and VEGF-C on production and charge characteristics of the endothelial glycocalyx were also characterized. VEGF-C promotes hyaluronic acid (HA) synthesis and increased the charge density of synthesized GAGs. In contrast, VEGF-A induced shedding of charged GAGs (R. R. Foster et al., 2013).

Nephrin-VEGFR2 complex is modulated by tyrosine phosphorylation of both cytoplasmic domains and acts as a key mediator to transduce local VEGF-A signals to the podocyte actin cytoskeleton by involving Nck and actin, and regulating the foot process structure and glomerular filter integrity (Bertuccio et al., 2011). Notably, excessive $VEGF\text{-}A_{164}$ (the primary VEGF-A form in the kidney) in podocytes results in a total collapse of the glomerular tuft, swift GEnC depletion, and significant proteinuria (Eremina et al., 2003). In Vegfa-null mutant mice endothelial detachment has been observed (Eremina et al., 2003). Since diabetic individuals typically exhibit increased circulating VEGF-A levels, these overproduction experiments hint that excessive VEGF-A signaling may further diabetic nephropathy progression (Chiarelli et al., 2000; Hovind et al., 2000). Such findings emphasize the need for a finely-tuned VEGF-A level to guide the development and maintenance of the glomerular endothelium and podocytes.

1.1.1.4 The glomerular basement membrane (GBM)

Originating from the amalgamation of the respective basement membranes of both podocytes and GEnCs (Abrahamson, 2012; Miner, 2012), the GBM showcases a stratified lattice replete with diverse pores when viewed under ultrastructure imaging *via* electron microscopy (Figure 5). Studies centered on proteomics have discerned 144 unique proteins within the purified human glomerular ECM, inclusive of the GBM (Byron et al., 2014; Lennon et al., 2014). Predominant amongst these are collagens (including subunits of types IV, VI, and XVIIII), laminins (α5, β2, and γ1), nidogen-1, and heparan sulfate proteoglycans (HSPGs, such as agrin and perlecan).

Acting as a pivotal sieving matrix, the GBM is crucial to the GFB. Beyond this, it may act as a reservoir for pro-angiogenic ligands and secreted mediators which foster cellular dialogues between podocytes and GEnCs. Importantly, by facilitating cell–ECM adhesive interactions, the GBM ensures the stability of the GFB (Farquhar, 2006). Among its components, type IV collagens and laminins are essential (Figure 4).

The GBM integrity is impaired by conditions like Alport syndrome, a hereditary disease which primarily affects the GBM. This condition traces back to anomalies in the genes responsible for encoding the type IV collagen subunits (Miner & Sanes, 1994). This disease begins with mild proteinuria in youth and can culminate in end-stage renal failure. Disruptions in this process, as seen in Alport syndrome, compromise the structural integrity of the GBM, leading to prominent abnormalities. Diseases such as Goodpasture's and Pierson syndrome further underscore the significance of the GBM's composition. Goodpasture's, an autoimmune condition, targets the α3 subunit of collagen IV, causing glomerulonephritis (Cui & Zhao, 2011). In contrast, Pierson syndrome is an autosomal recessive disorder connected to mutations in the LAMB2 gene, which codes for laminin β2.

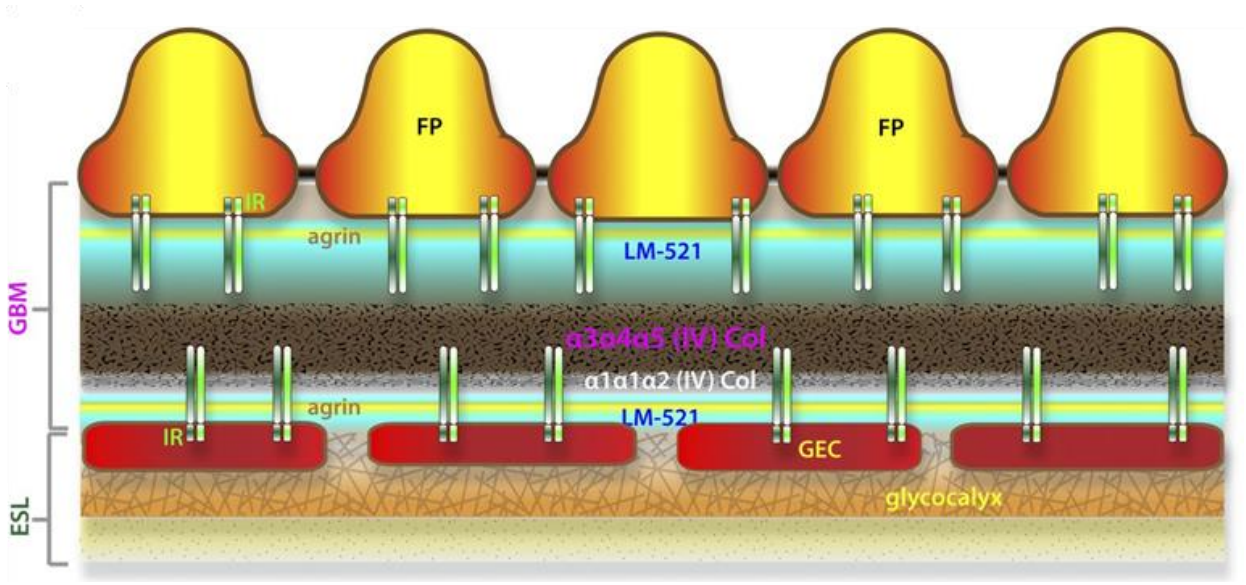

Figure 4: Molecular arrangement of the Glomerular Basement Membrane (GBM). Stratified layering of GBM elements: laminin LM-521 and agrin exhibit a dual distribution, while collagen IV structures are predominantly centered within the GBM. The minor α1α1α2 collagen (Col) is predominantly inclined towards the glomerular endothelium. Both the dominant α3α4α5 and the rarer α1α1α2 type IV collagens are usually out of reach from β1–integrin receptor (IR) assemblies on the side of the podocyte. This hints that while LM-521 and agrin are typical physiological bindings of IR assemblies expressed by podocytes, type IV collagens are not. Image from (Scott & Quaggin, 2015).

Detailed analyses *via* scanning electron microscopy unveil that the GBM is a highly structured network of interconnected fibrils. The width of these fibrils can fluctuate between 4 to 10 nm (Kubosawa & Kondo, 1985). Within this structure, the fibrils are densely aggregated at the center, featuring pores that average around 10 nm in diameter. Advanced imaging methods such as correlative Stochastic Optical Reconstruction Microscopy (STORM) and electron microscopy (STORM-EM) revealed insights into the GBM's layered arrangement (Suleiman et al., 2013, Figure 5), pinpointing the positions of its key components in relation to others. For instance, while collagen IV and nidogen-1 predominantly occupy the GBM's central region, laminin-α5, agrin, and integrin-β1 are distinctly bifurcated into two separate layers. Interestingly, the collagen IV networks are situated closer to the endothelial side, further from the podocyte surface.

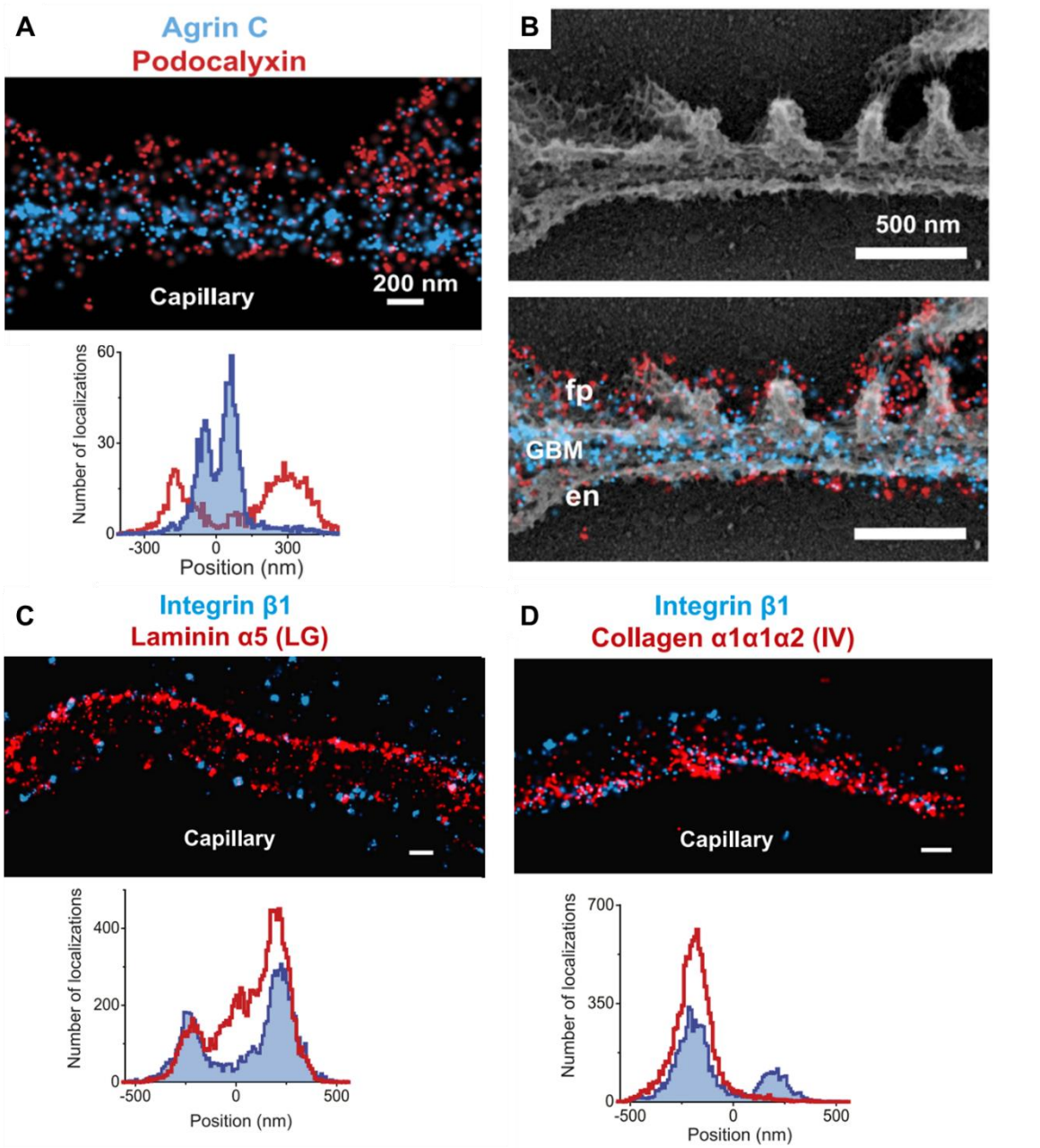

Figure 5: Super resolution image (STORM) and correlative image correlation (STORM-EM) of the mouse GBM. A) A 2-color STORM image details the distribution of agrin C and podocaylxin along a capillary area, accompanied by quantitative analysis. B) The top image shows a platinum deep etch replica derived from the section in A) viewed through electron microscopy (EM). The bottom image is a composite of STORM and EM images, revealing ultrastructural details like podocyte foot processes (fp), endothelial cells (en), and the GBM. The periphery of the foot processes is marked by podocalyxin, while agrin is located within the GBM. Human kidney sections were stained for STORM using antibodies against integrin β1 ectodomain C), laminin α5 (LG), D), and collagen α1α1α2 (IV), Scale bar: 200 nm. Image adapted from (Suleiman et al., 2013).

By imaging of Alport mice kidneys, profound alterations in the arrangement of agrin and α1α1α2 (IV) collagen across the GBM's breadth were observed (Suleiman et al., 2013). This realignment may lead to the podocytes abnormal exposure to type IV collagens, a scenario that could mirror the pathological transformations seen in Alport disease. These imaging assessments highlight that the GBM ultrafine pore structure is important in normal filtration and any disruption in its molecular and structural organization can precipitate proteinuria.

The GBM rich content of HSPGs, such as agrin, perlecan, endows it with a pronounced negative charge. This led to assumptions linking the GBM's charge profile to the charge selectivity of the GFB (Goldberg et al., 2010; Harvey et al., 2007; Rennke et al., 1975; Rennke & Venkatachalam, 1977; Van Den Hoven et al., 2008). Yet, genetic studies aiming to attenuate the GBM's negative charge have contrarily shown no evident proteinuria (Goldberg et al., 2010; Hamano et al., 2010; Harvey et al., 2007; Rossi et al., 2003). Consequently, it is speculated that the primary charge repulsion mechanism operates within the glomerular compartment, rather than within the GBM itself.

1.1.1.5 Podocytes, their foot processes (FPs), and Slit Diaphragms (SDs)

Podocytes are post-mitotic specialized epithelial cells that are unable to finalize cytokinesis (Kriz et al., 1995; Lasagni et al., 2013), with a limited ability to regenerate (Puelles & Moeller, 2018).

Normal and fully differentiated podocytes boast a complex ‘octopus-like” star shaped cytoarchitecture. This includes a branched cell body with multiple outgrowths that break down into major processes and more intricate pedicels or foot processes (FPs) (Figure 2, A and B). Microtubules and intermediate filaments fortify the major processes, while the FPs are rich in actin and connect to the GBM through focal adhesions (Ichimura et al., 2003). These podocyte cell bodies and FPs encase the glomerular capillaries in a complex interlocking pattern. Neighboring podocytes are interconnected *via* their FPs through specialized intercellular junctions known as the slit diaphragms (SDs, Figure 6).

This SD is distinct from tight junctions as it does not contain E-cadherin and is structurally permeable to water and small solutes (Tassin et al., 1994). Its primary function is to act as the exit for primary urinary filtrate, playing a crucial role in retaining plasma molecules. The discovery of nephrin and podocin as core components of the SD emphasized the importance of podocyte structure in establishing and preserving the GFB (Boute et al., 2000; Holzman et al., 1999; Huber et al., 2003; Kestila et al., 1998; Ruotsalainen et al., 1999; Schwarz et al., 2001). Dysfunctional mutations in NPHS1 and NPHS2 genes, responsible for coding nephrin and podocin, lead to a specific nephropathy that sees the collapse of FPs and absence of SDs (Boute et al., 2000; Kestila et al., 1998). This transformation in podocytes, also known as FP effacement, indicates podocyte damage and proteinuria.

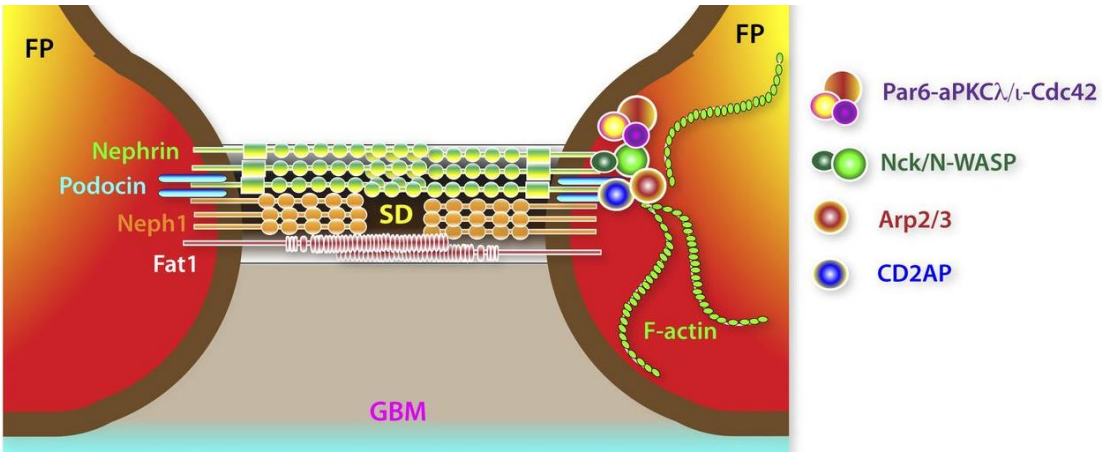

Figure 6: Molecular arrangement of the Glomerular Basement Membrane (GBM) and the Slit Diaphragm (SD).B) Streamlined depiction of key adhesion receptors (nephrin, Neph1, and Fat1) present in the SD. The position of the SD within lipid-rafts hinges on cholesterol-binding podocin. The SD is linked with both F-actin regulatory (Nck–N-WASP–Arp2/3 and CD2AP–Arp2/3) and cellular alignment (Par6–aPKCλ/ι–Cdc42) assemblies. Image from (Scott & Quaggin, 2015).

Although many SD components have been identified, the understanding of the mechanism forming a functional unit remains limited. Adhesion receptors in the SD, particularly nephrin and Fat1, are thought to connect opposing FPs (Ciani et al., 2003; Gerke et al., 2003; Heikkila et al., 2011; Inoue et al., 2001; Khoshnoodi et al., 2003; Wartiovaara et al., 2004). Reflecting its function as a junction between differentiated podocytes, other SD elements are essential molecules often found in adherent and tight junctions, including ZO-1, spectrins, α-actinin, CASK, MAGI-2, cingulin, and occludin (Fukasawa et al., 2009; Lehtonen et al., 2005). ZO-1, a scaffold protein, is notably crucial for regular FP interlocking and SD formation (Itoh et al., 2014). Lack of ZO-1 can lead to early-stage proteinuria, effacement of podocytes, and glomerular scarring. Additionally, ZO-1 is responsible for maintaining the position and expression of nephrin and podocin and has been observed to be reduced in diabetic nephropathy (Garg et al., 2010).

The distinct structure of podocytes underscores the importance of cell polarity in their biology. The SD creates a clear separation between the apical and basolateral membrane regions of podocytes (Huber et al., 2003). Nephrin and Neph1 exhibit interactions with specific polarity proteins (Huber et al., 2003). The loss of these proteins leads to proteinuria and irregular junctions (Hirose et al., 2009).

Actin filaments are the backbone of FPs, and their disruption results in FP effacement and the breakdown of the SD (Jones et al., 2006). The Nck adaptors, for example, link the SDs to the actin cytoskeleton and play an essential role in podocyte development and the maintenance of FPs (Jones et al., 2006). Since Nck proteins are also known to bind to other complexes, they might also have a role in anchoring podocytes to the GBM. Additionally, various proteins and complexes contribute to connecting the actin skeleton and the SDs. The structure of the actin meshwork is crucial for podocyte function, and multiple proteins and signaling pathways, including calcium signaling and endocytosis, are involved in its regulation and the broader function of podocytes (Blaine & Dylewski, 2020).

Flattening of podocyte FPs suggest alterations in cell-cell connections, or SDs, but also indicate a faulty response aimed at restoring deteriorating focal contacts on the GBM. Indeed, the detachment of podocytes and exposed GBM are frequently observed in the advanced diabetic nephropathies and chronic kidney diseases (Kriz & Lemley, 2015; Toyoda et al., 2007; Weil et al., 2012). The actin-related protein, palladin, is known to be present in high levels in podocytes (Endlich et al., 2009). By generating a mouse model with a podocyte-specific palladin knockout, and using super resolution imaging, changes in the shape and structure of the podocyte's foot processes were observed (Artelt et al., 2018). This effacement of FPs is illustrated in Figure 7. Thus the structure of the podocytes FPs play a major role in the filtration function.

1.1.1.5.1 Signaling

Aside from the formation of the SD, podocytes have other critical functions, such as supporting endothelial cell growth and participating in the creation of the GBM. VEGF-A, Angpt1, and SDF1 are compounds secreted by podocytes and play a crucial role in the normal development of the glomerular endothelium (Eremina et al., 2003; Sison et al., 2010). Furthermore, podocytes interact with the glomerular endothelium to structure the GBM (Abrahamson et al., 2009), as VEGF-A is a required growth factor for GEnCs, and is produced and secreted by podocytes. Nephrin signaling complex transduces extracellular cues to the podocyte cytoskeleton and regulates podocyte shape and function. Nephrin-VEGFR2 complex is modulated by tyrosine phosphorylation of both cytoplasmic domains and acts as a key mediator to transduce local VEGF-A signals to the podocyte actin cytoskeleton by involving Nck and actin, and regulating the foot process structure and glomerular filter integrity (Bertuccio et al., 2011).

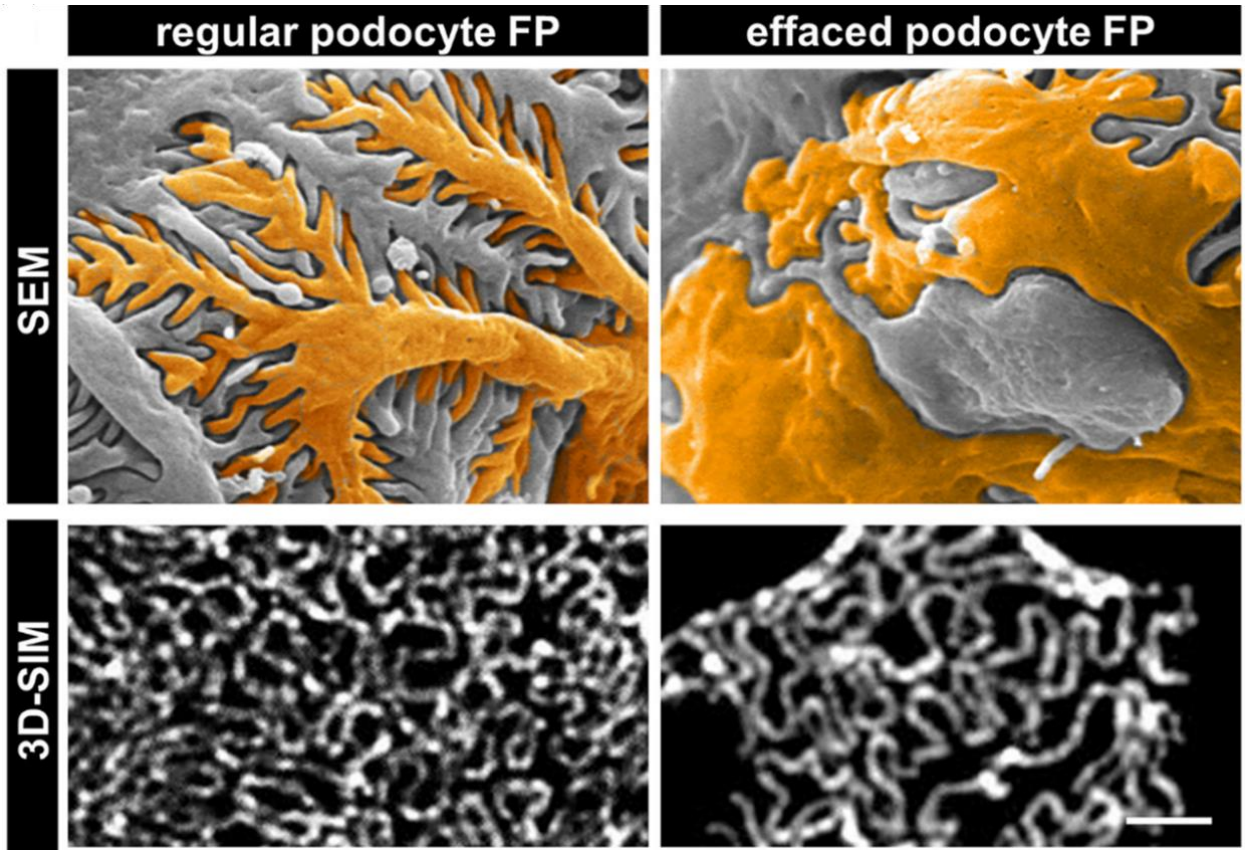

Figure 7: Illustration of regular and effaced podocyte foot processes (FP) of 6 month old control and podocyte-specific palladin-knockout mice (Podocytes palladin−/−). Upper panels display images taken by scanning electron microscopy (SEM), Images below display kidney sections stained for the slit diaphragm protein nephrin imaged by 3D-SIM. Scale bar represents 1 µm. Image from (Artelt et al., 2018).

1.1.1.6 Parietal Epithelial Cells (PECs) and the Bowman capsule

The urinary space of the glomerulus is externally bordered by the Bowman's capsule (Figure 1), which is a basal membrane supporting a monolayer of polygonal epithelial cells called parietal epithelial cells (PEC). While these glomerular cells were first identified in the 1800s (Bowman, 1842), it is only in more recent times that a possible PEC role in postnatal podocyte augmentation and their involvement in the formation of glomerular lesions has been demonstrated (Wong et al., 2021). The expression of proteins ZO-1 and claudin-1, which physiologically forms the tight junctions between PECs, would act as a barrier to prevent the leakage of the urinary ultrafiltrate outside the Bowman capsule (Ohse, Pippin, et al., 2009).

Morphologically, PECs are squamous epithelial cells, with a small cell body. Electron microscopy studies have shown that there are cilia and microvilli of varying number on the surface of PECs with on average 0 to 2 cilia per cell (Arakawa & Tokunaga, 1977, Figure 8, A).

The proportion of parietal cells remains a minority in the composition of the glomerulus. In rats, the number of parietal cells within a normal glomerulus represents 14.8% of the total number of glomerular cells (Bertram et al., 1992). Despite a thin cell body, the parietal cells form junctions between adjacent cells, thus constituting a complex and structured formation called "labyrinthine" (Figure 8, B). Electron microscopy studies highlight the tight junctions near the apical surface of the PECs (Ohse, Pippin, et al., 2009).

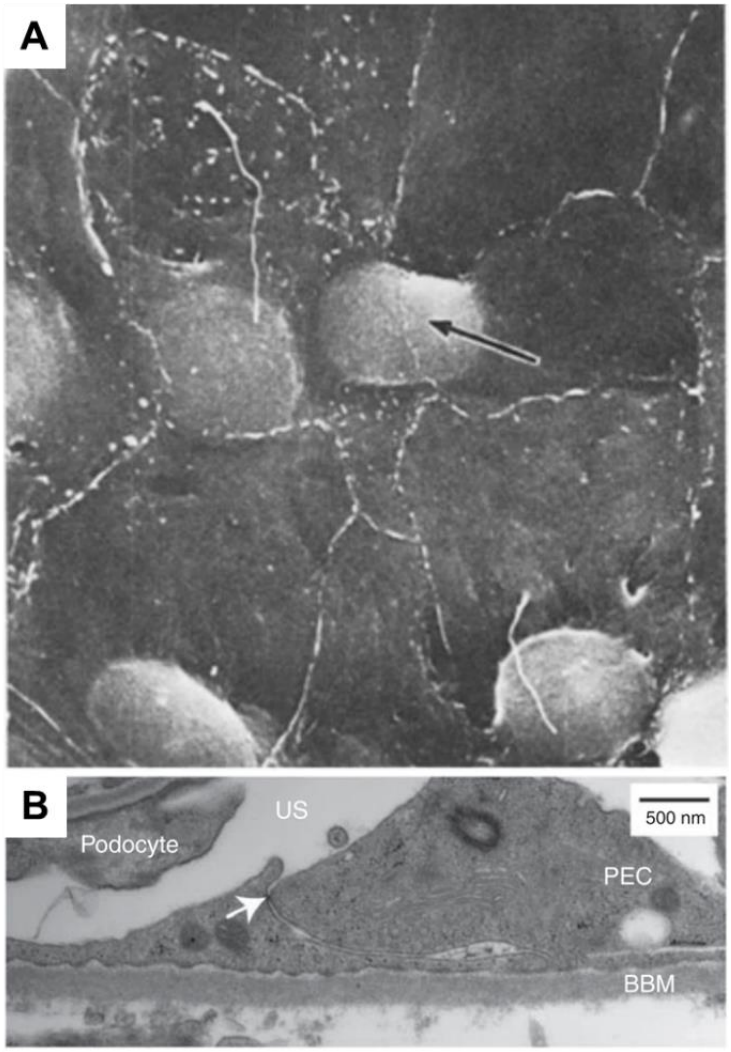

Figure 8: A) Scanning Electron Microscopy (SEM) image of a portion of the Bowman's capsule, showing parietal epithelial cells (PECs) with polygonal shapes and occasionally seen one or two long cilia, image from (Arakawa & Tokunaga, 1977) *B) Transmission Electron Microscopy (TEM) image showing the interface between adjacent parietal epithelial cells (PECs) and a tight junction near the top (indicated by the arrow), US: Urinary Space, BBM: Bowman's Basement Membrane, image from (Ohse, Pippin, et al., 2009).*

Sagrinati and colleagues identified the presence of CD24 and CD133 in PECs, leading to the theory that PECs might have stem cell-like attributes (Sagrinati et al., 2006). Later research by Ronconi et al., (2009) postulated that these cells could act as precursors to podocytes. In a separate study, Appel et al., (2009) demonstrated through genetic lineage tracing that a minority of PECs in young mice migrated to the glomerular tuft and simultaneously exhibited podocyte indicators, such as nephrin and WT-1. The simultaneous expression of podocyte and PEC markers in glomerular cells (Ohse, Pippin, et al., 2009), and the manifestation of podocyte indicators in PECs during aging (Puelles et al., 2016) was further noticed.

In addition to the flat parietal epithelial cells (fPECs), there are proximal tubular epithelial-like cells, a subset of PECs (cuboidal or cPECs), that constitute the foremost section of the proximal tubule and might also line portions of the Bowman's capsule. Moreover, a third intermediary PECs (iPECs) subset has been recognized at the intersection between the flat and cuboidal PEC groups at the tubular opening as illustrated in Figure 9 (Kuppe et al., 2019).

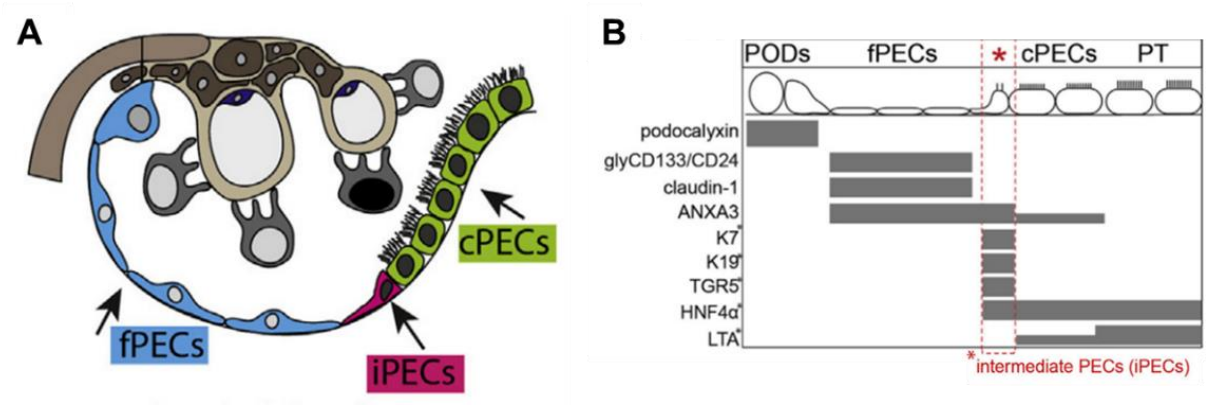

Figure 9: A) Parietal epithelial cells (PECs) subgroups are highlighted in color. Red, intermediate PECs (iPECs) at the epithelial interface between Bowman's capsule, delimited by flat PECs, and proximal tubule cells known as cuboidal PECs (cPECs). B) Markers identifying specific subgroups of cells within the glomerulus. ANXA3, annexin A3; glyCD133/CD24, glycosylated CD133 and CD24; HNF4a, hepatocyte nuclear factor-4; K7, keratin 7; LTA, lotus tetragonolobus agglutinin; PODs, podocytes; PT, proximal tubule; TGR5, G protein-coupled bile acid receptor 1. Image adapted from (Kuppe et al., 2019).

Because of their localization, PECs are constantly exposed to low levels of filtered albumin. Thus, under physiological conditions, PECs have the ability to internalize albumin (Chang et al., 2012). In all pathological situations associated with significant proteinuria, albumin internalization drastically increases and leads to the apoptosis of PECs (Chang et al., 2012).

1.1.2 Renal filtration

The glomerulus is the initial site of blood ultrafiltration. A properly functioning glomerulus ensures cells and vital macromolecular components of plasma are retained in the blood, resulting in a protein depleted urine. Several models can explain these filtration properties (Hausmann et al., 2012; Moeller & Tenten, 2013). We discuss here the 2 most commonly accepted mechanism.

1.1.2.1 The selective size barrier model

Albumin movement across the filter is determined by two flows: convection and diffusion. Both of these processes push albumin outwards, leading it from the filter into the urine. The sole factor limiting albumin passage is the filter meshwork or pores defined by the Glomerular Filtration Barrier (GFB).

According to this hypothesis, the GFB acts as an ultrafiltration membrane that sorts macromolecules on the basis of molecular size. In the context of the glomerulus, the sieving coefficient is typically described as the concentration of species within Bowman's space compared to the concentration in arterial plasma (Haraldsson et al., 2008). As such, it describes the transport of a solute across the GFB in relation to that of a freely filtered solute (for example, inulin, which behaves similarly to water, has a coefficient of 1). As the size of macromolecules increases, their sieving coefficient decreases progressively (Figure 10). In the case of neutral solutes, such as Ficoll, this size selectivity becomes especially noticeable (Blouch et al., 1997; Lund et al., 2003). For most plasma proteins, the glomerular sieving coefficient (GSC) is very low, indicating that they are largely restricted from passing into the filtrate. For example, albumin, the major plasma protein, has a GSC that is has been reported at around 0.02 using 2-photon microscopy intravital imaging on rats (Russo et al., 2007), and 0.0006 with the micropuncture technique (Tojo & Endou, 1992). In contrast, the albumin urinary excretion is ~20 mg/day, giving a global sieving coefficients of 10^{-5}, thus reflecting

the extensive albumin tubular reabsorption (Haraldsson et al., 2008).

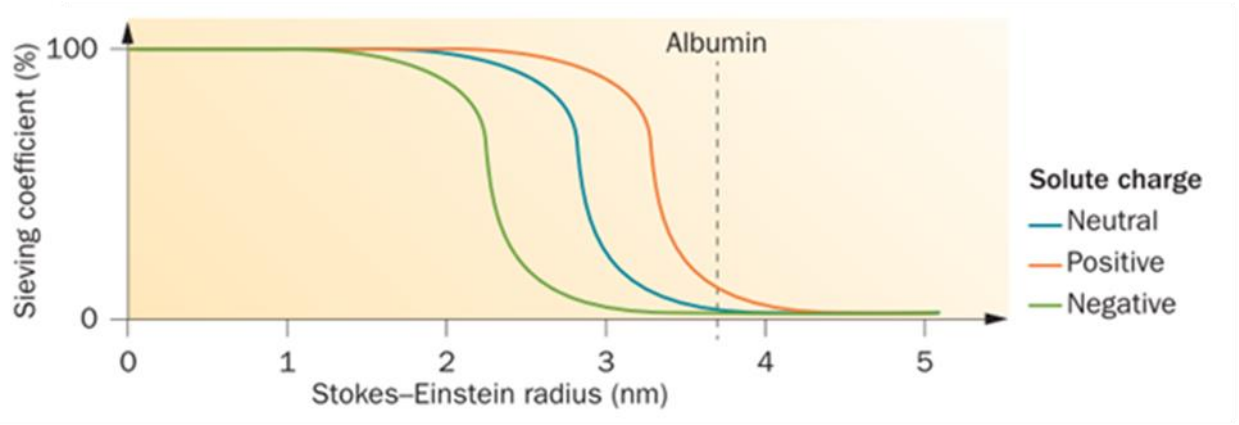

Figure 10: Diagram illustrating the sieving coefficients for macromolecules, whether neutral, negatively charged, or positively charged, in relation to their molecular dimensions. The Stokes–Einstein radius for albumin, at 3.6 nm, is highlighted. Image from (Moeller & Tenten, 2013).

The fenestrated endothelium, the glomerular basement membrane (GBM), and the epithelial filtration slits create an organized structure (Figure 11). The flow spreads out as it moves from the fenestrae into the GBM and then narrows down again when it reaches the filtration slits. Since the hydraulic resistances of both the cellular layers and the GBM combine, the overall sieving coefficient for a macromolecule is determined by multiplying the sieving coefficients of the individual layers (Deen et al., 2001). In such models, the spatial frequency of filtration slits is anticipated to play a pivotal role in determining the total permeability, a finding that aligns with histological observations in various human glomerular diseases presenting filtration impairment (Gagliardini et al., 2010; Ichimura et al., 2019; Kriz et al., 2013).

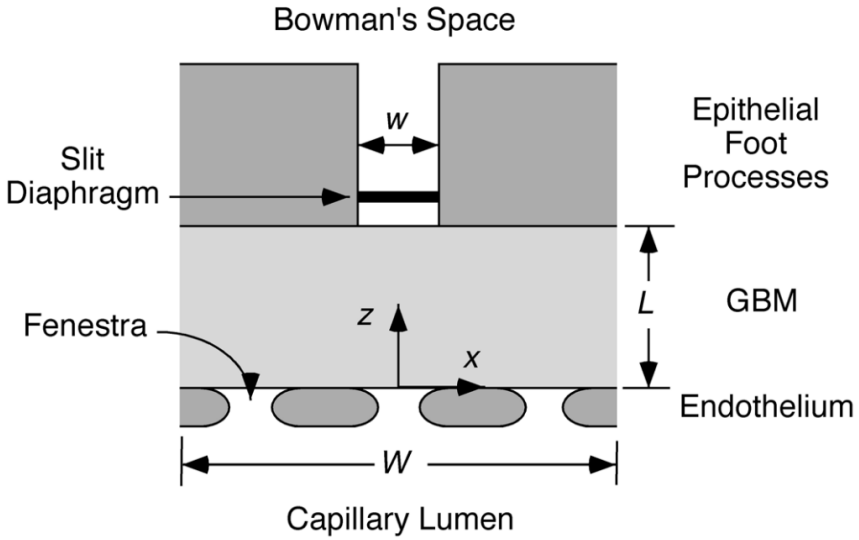

Figure 11: Simplified structural representation of a segment of the glomerular capillary wall, aligned with one filtration slit. W represents the width of the segment; L denotes the thickness of the glomerular basement membrane (GBM); w indicates the width of the filtration slit. Image from (Deen et al., 2001).

However, these models do not take into account the charged nature of the ESL nor the effect of the glycocalyx filling the endothelial pores (Figure 2).

1.1.2.2 The electrokinetic model

The pore theory posits that proteins cross the filter solely through convection and diffusion. In contrast, the electrokinetic model suggests that the streaming potential applies an added electrophoretic force, pushing negatively charged macromolecules towards the bloodstream.

The role of electrokinetics in determining the selective nature of renal filtration has been proposed, particularly in explaining the charge selectivity observed. An experiment involving micropuncture measurements on the glomeruli of salamanders (*Necturus maculosus*) revealed that the filtration pressure creates a distinct streaming potential or charge difference across the Glomerular Filtration Barrier (GFB). Specifically, the Bowman's space is more negatively charged compared to the endothelial lumen (Hausmann et al., 2010).

A streaming potential (electrical field or 'filtration-dependent potential') is observed when electrolytes are driven by a pressure difference across a channel or porous medium that possesses a permanent charge. The electric field has been experimentally confirmed to be around –0.045 mV for every 10 cm H_2O effective filtration pressure in *Necturus* (Hausmann et al., 2010). The proposed electrokinetic model suggests that when small cations pass through the GFB, they bind to the negatively charged surfaces inside the GFB (Figure 12). Once a threshold is reached, the movement of these small cations is slower than that of small anions, leading to a separation of charges and creating an electric field across the GFB (Hausmann et al., 2012; Moeller & Tenten, 2013).

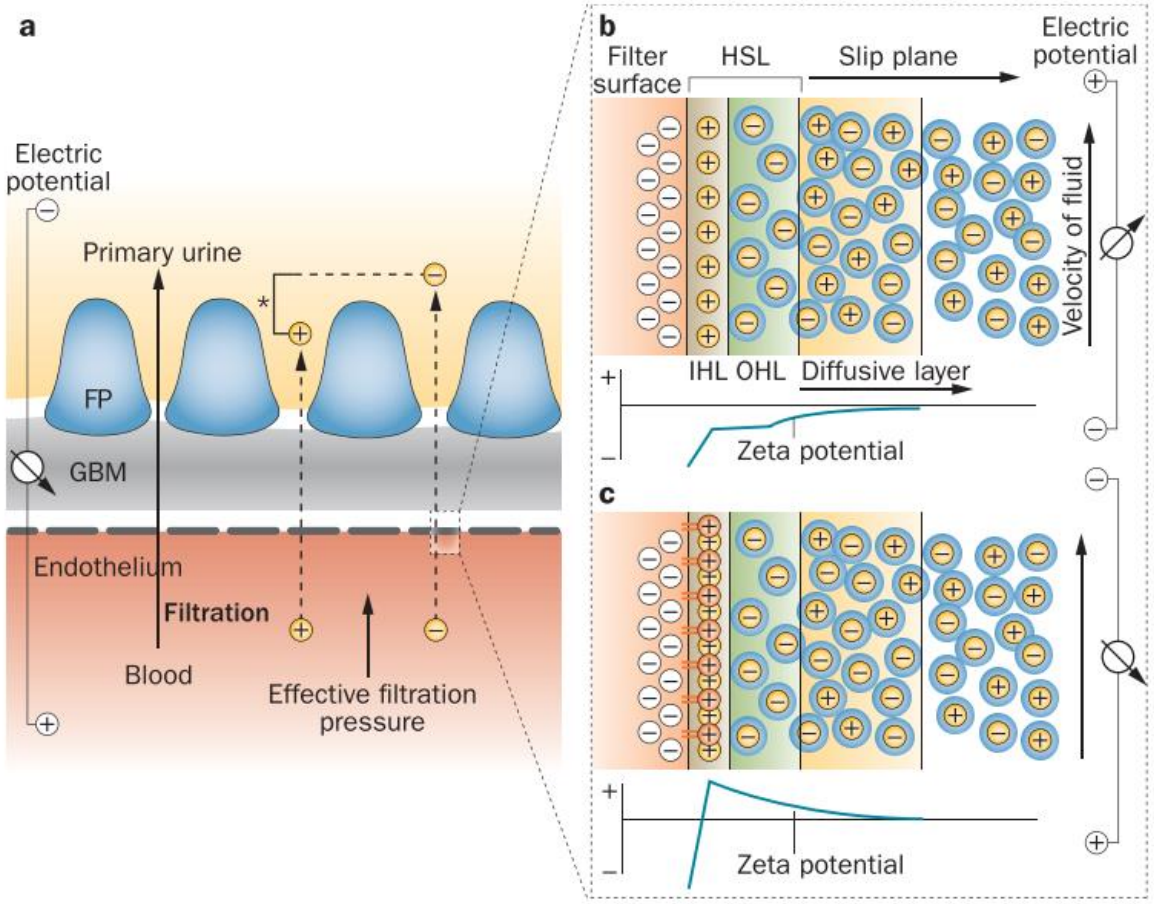

Figure 12: The electrokinetic theory. a) When ionic plasma is filtered, small anions tend to move slightly quicker than small cations due to their interaction with the filter's surface. This speed discrepancy leads to a voltage difference (streaming potential) across the GFB, which correlates with the effective filtration pressure. b) Concept of Electrical Bilayer Creation. The ionic liquid

flows alongside the filter surface. Layers of counter ions (IHL: Inner Helmholtz Layer and OHL: Outer Helmholtz Layer) adhere to the charged filter, partially neutralizing it (local potential). As we move away from the surface, the electrostatic bond weakens and ions become surrounded by water (depicted as 'blue halos'). The boundary where distinct ion layers no longer appear marks the beginning of the diffusion plane. In the given illustration, the local potential remains negative, causing cations to cluster within the yellow zone, which influences the filter's electrokinetic characteristics. The growing hydrodynamic viscosity restricts the sideways fluid movement from the filter surface up to the slip plane, where the fluid starts to flow. c) Charge reversal, also known as overcharging, can take place when extra counter ions (depicted in orange) are attached within the IHL. This leads to an inverted potential within the electrically active segment of the diffusive layer (highlighted in yellow), causing small anions to move more swiftly through the filter. Image from (Moeller & Tenten, 2013).

This model then implies that larger anions, such as native albumin, would face an electrophoretic field that opposes the direction of the hydraulic flow. Since the Glomerular Basement Membrane (GBM) does not have many negative charges, it is inferred that the streaming potential mainly originates from the highly charged Endothelial Surface Layer (ESL). Indeed, when mice were given intravenous injections of GAG-degrading enzymes, effectively degrading the glycocalyx, an increase in the fractional clearance for albumin, was observed, suggesting that the endothelial cell glycocalyx is indeed an important component of the glomerular barrier through ESL elements (Jeansson & Haraldsson, 2006).

Some evidence supporting this model is found in observations that neutral albumin can pass through the GFB without being influenced by the glomerular filtration rate. However, the passage of native anionic albumin becomes more restricted as glomerular pressure increases, aligning with the electrokinetic model (Lund et al., 2003). Another observation supporting this theory is the ease with which albumin diffuses across the GFB when plasma flow stops (Ryan & Karnovsky, 1976).

This model predicts that any disruption to the podocyte foot processes (FPs), such as their effacement, can impede the creation of a streaming potential. When small anions encounter the widened FPs, they are deflected back, effectively disrupting the electrical field across the GFB (Hausmann et al., 2010, 2012). This implies the importance of maintaining the intricate structure of podocytes and their network of FPs and slit diaphragms (SDs) for consistent filtration across the GFB.

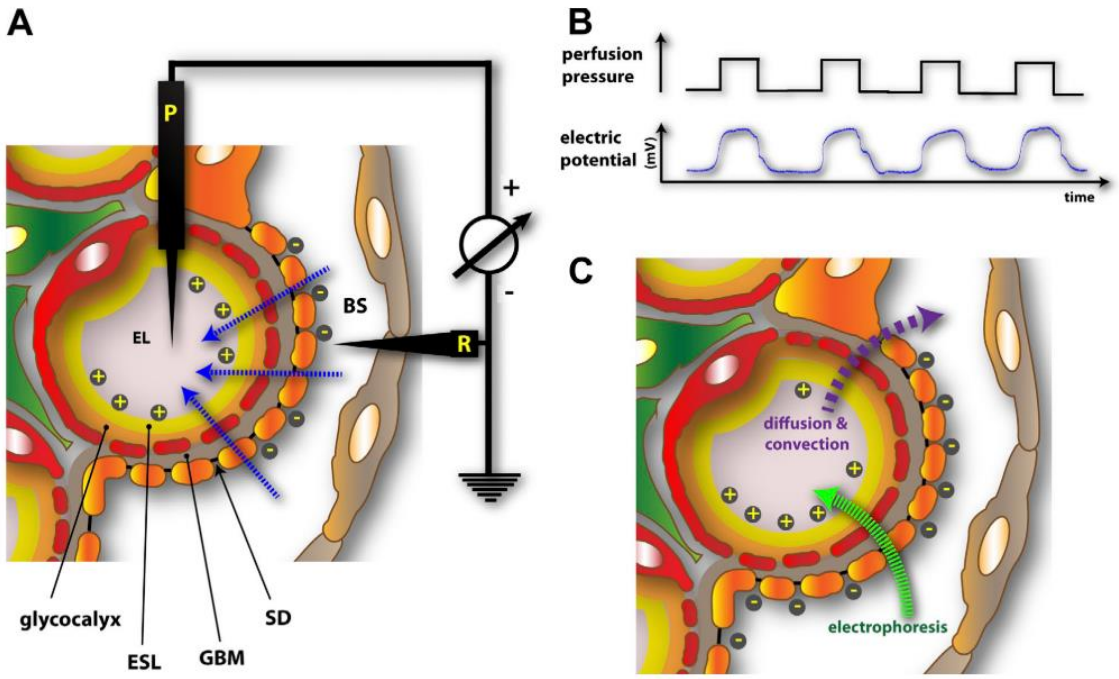

Figure 13: Electrokinetic Perspective on Kidney Filtration: A) An experimental configuration, leveraging the glomeruli of the salamander (N. maculosus), was designed to identify a flow-induced electrical potential (streaming potential) across the GFB. Here, "P" stands for the potential electrode, while "R" denotes the reference electrode. Due to varying interactions with the negatively charged GFB, small ions produce a charge gradient, recognized as a streaming potential. This results in the endothelial lumen (EL) having a more positive charge than Bowman's space (BS). B) The glomerular streaming potential is dependent on filtration pressure. C) Streaming potentials give rise to a reverse electrophoretic field. As a result, macromolecules face a shifting electrophoretic field (indicated by the green arrow) which runs counter to the flow of diffusive and convective currents (indicated by the purple arrow). Consequently, albumin, being a negatively charged macromolecule, faces not just size-based restrictions by the GFB, but is also pushed away from the GFB during active filtration due to electrophoretic forces. Image from (Scott & Quaggin, 2015).

M.G. Farquhar (Farquhar et al., 1960; Farquhar & Palade, 1961) observed that the sizeable negatively-charged molecule, ferritin, was prevented from entering the glomerular filter, particularly at the endothelial and GBM layers. Given the relatively permeable nature of the glycocalyx on the endothelium, it suggests a mechanical hindrance is not the primary deterrent. This points to the probable impact of the streaming potential, across the barrier. In salamander glomeruli, the presence of streaming potentials was inhibited by protamine, a protein known for neutralizing the GFB's negative charge leading to proteinuria (Hausmann et al., 2010).

Consistently, Rennke (Rennke et al., 1975) isolated and perfused mouse kidneys and found that negatively charged ferritin largely stayed out of the filter (Figure 14, Farquhar et al., 1960; Farquhar & Palade, 1961). A substantial amount of neutrally charged ferritin (pI 6–8) infiltrated the glomerular filter and lodged at the GBM level, positively charged ferritin (pI > 8.8) sticked to the negatively charged endothelial glycocalyx, and was moreover trapped within the filter, including beneath the filtration slits.

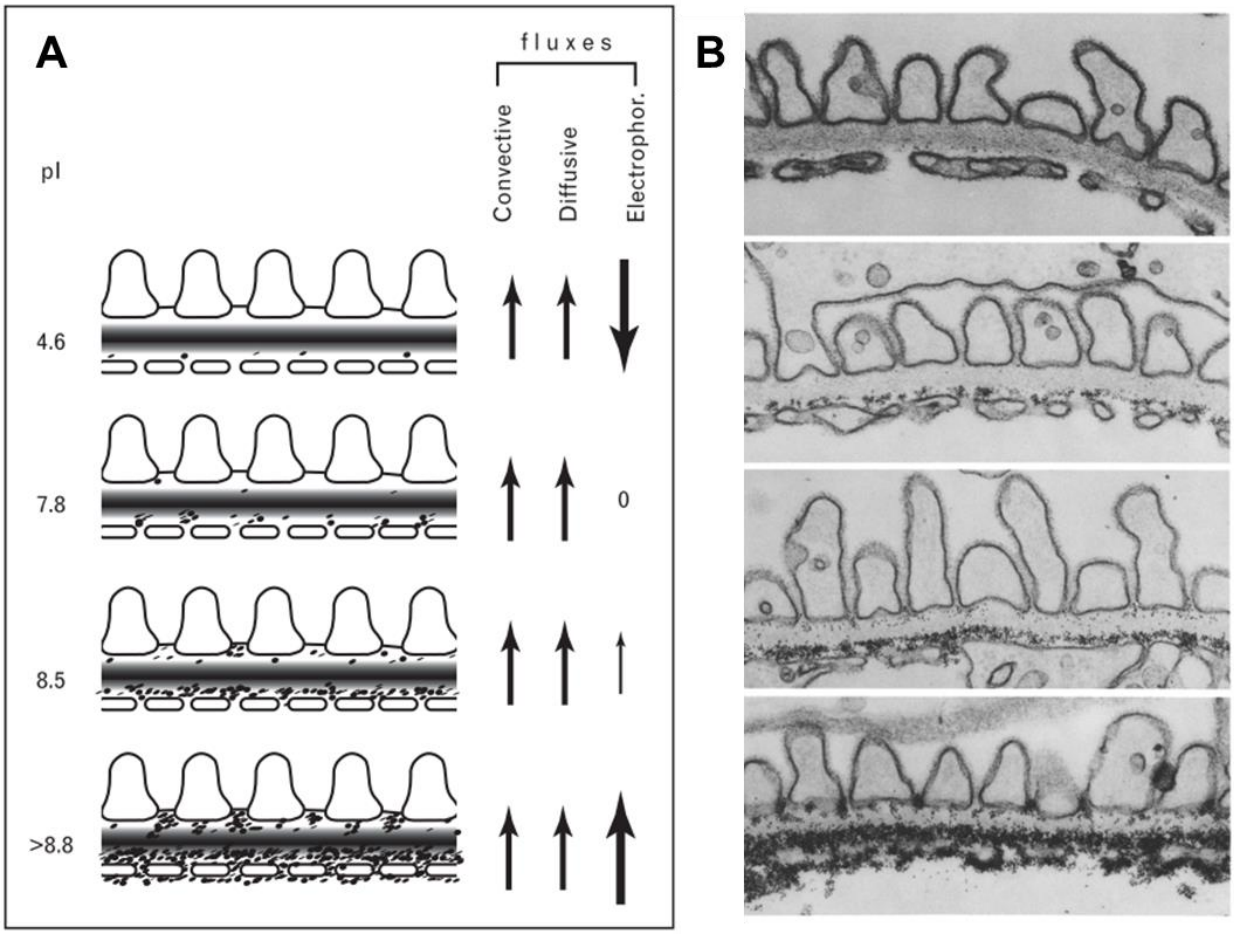

Figure 14: In a tracer study, isolated kidneys were infused with varying preparations of cationized ferritin, differentiated by their isoelectric point (pI) from top to bottom. Ferritin with a negative charge (pI=4.6) barely penetrated the glomerular filter. This was because the electrophoretic flow was dominant over the combined convective and diffusive flows, preventing much of the ferritin from entering the filter. With near-neutral ferritin (pI ranges from 7.8 to 8.5), an increasing amount of ferritin got trapped by the GBM and, to a lesser extent, by the slit diaphragm. In this scenario, the strength of the electrophoretic flow wasn't enough to oppose the combined forces of the convective and diffusive flows, allowing more ferritin to enter the filter. When cationic ferritin was used (pI>8.8), the maximum quantity of ferritin was captured within the filter. This is because the direction of the electrophoretic flow was reversed, pushing even more ferritin into the filter, leading to clogging. Additionally, this cationic ferritin stuck to the endothelial glycocalyx due to electrostatic attraction. Image A) from (Hausmann et al., 2012), and B) from (Rennke et al., 1975) scale bars absent.

From these experiments, several insights emerge: an electrical field contributes barring ferritin from the filter. In the absence of electrical influences, the GBM and slit diaphragm function essentially as size-selective filters, evidenced by neutral ferritin behavior. Under regular conditions, minimal plasma proteins interact with these structures. Positively charged ferritin pronounced retention cannot be simply attributed to 'charge selectivity', as cationic ferritin should face reduced retention. Instead, it congested the filter, pointing again to a notable electrical field influence. The intensified influx of cationic ferritin burdens the intricate framework of the GBM and slit diaphragm, leading to eventual clogging.

It has been hypothesized that active cellular processes play a role in preventing filter clogging (Akilesh et al., 2008). Indeed, podocytes are cells with a high endocytic activity. When proteins block the filter, they are quickly taken up by not just podocytes, but also by endothelial and mesangial cells

(Akilesh et al., 2008; Haraldsson et al., 2008; Hausmann et al., 2010; Lewis et al., 1978). Although this streaming potential hypothesis provides a fair explanation for the mechanics of renal filtration and is compatible with the size exclusion filtration hypothesis, more complex models such as the gel hypothesis were imagined (see Moeller & Tenten, 2013).

1.2 Glomerulonephritis and Glomerulosclerosis

End-stage chronic kidney disease (ESCKD), previously termed uremia or Bright's disease after Dr. Richard Bright's early 1830's description, is a critical condition where kidney filtration deteriorates, causing toxin build-up, notably urea. Dr. Bright's research findings were initially published in 1827 (Bright & London, 1827). Here, he identified edema and proteinuria (albumin presence in urine) as the primary symptoms of the severe kidney condition.

In France, 2016 saw 84,693 ESCKD diagnoses, equating to 1,262 cases per million people, with a 10% mortality rate among treated cases. The main contributors to ESCKD in France are hypertension, diabetes, and, in third, glomerulonephritis, responsible for 11.9% of such diagnoses. Of these, the most prevalent is focal segmental glomerulosclerosis (FSGS), with 3.2 cases per million, trailed by membranous and extracapillary glomerulonephritis, with 1.3 cases per million (Lazareth, 2020).

Glomerulonephritis and glomerulosclerosis denote glomerulus damage, either acute or chronic, in the kidney filtration system. They commonly involve glomerular cells activation (podocytes and parietal epithelial cells), resulting in changes like proliferation and migration, eventually leading to glomerular damage and kidney failure, though the precise molecular mechanism of cell activation are yet to be fully comprehended (Eymael et al., 2018; Lazareth et al., 2019; Miesen et al., 2022; Moeller & Smeets, 2014; Wong et al., 2021).

1.2.1 Rapidly Progressive GlomeruloNephritis (RPGN) and Focal Segmental GlomeruloSclerosis (FSGS)

1.2.1.1 Rapidly Progressive GlomeruloNephritis (RPGN)

Extracapillary glomerulonephritis is characterized histologically by a crescent extracapillary proliferation. Cells invade the urinary chamber and adopting a crescent shape (Figure 15). This crescent is a multilayer of epithelial cells present within the urinary space. Therefore, extracapillary glomerulonephritis is also called crescent glomerulonephritis or rapidly progressive glomerulonephritis, which is a glomerular syndrome, characterized by a doubling of creatinine levels within 3 months (kidney impairment).

Extracapillary glomerulonephritis are rare but serious conditions. Their incidence and prevalence differ based on the underlying disease. The overall incidence of a Anti Neutrophil Cytoplasmic Antibody (ANCA)-associated vasculitis is around 13 to 20 cases per million inhabitants in Europe (Moiseev et al., 2017), and has been increasing since the 1980s (Lazareth, 2020). The incidence of Goodpasture's disease is lower, between 1 and 2 cases per million inhabitants (McAdoo & Pusey, 2017). The morbidity and mortality linked to these conditions are significant. Before the availability of immunosuppressants, life expectancy was approximately one year after diagnosis for ANCA-associated vasculitis, and it now stands at around 5 years, though a quarter of ANCA vasculitis patients progress to end-stage renal failure within 3 to 4 years (Booth et al., 2003; Moiseev et al., 2017).

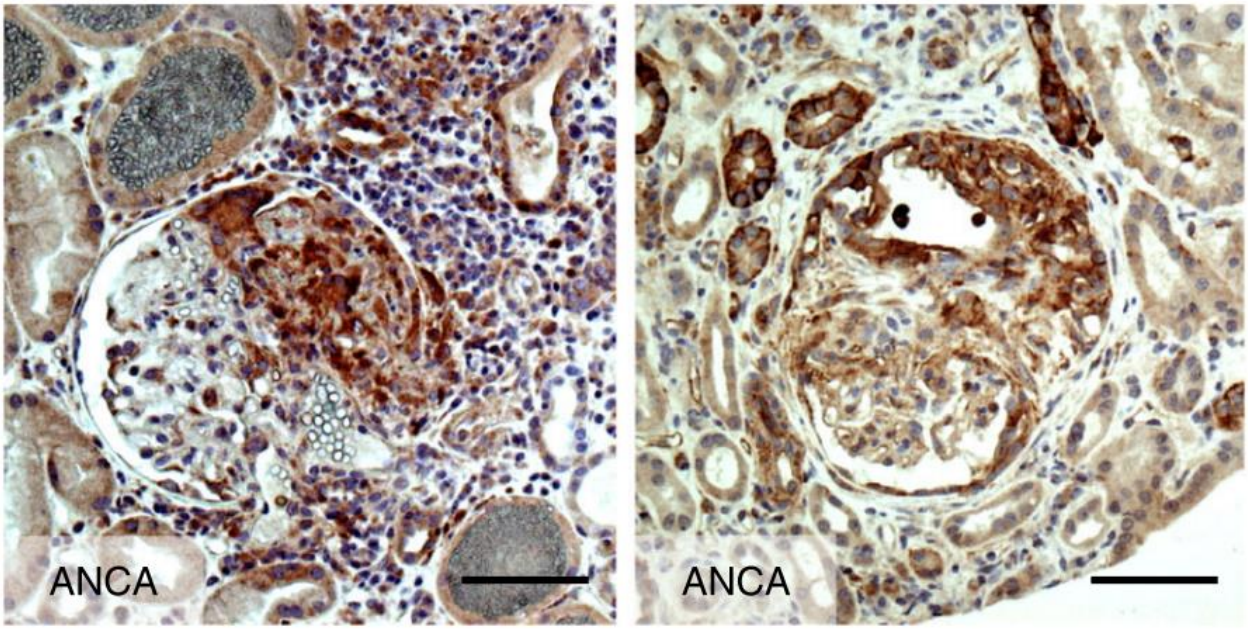

Figure 15: Representative images showing immunohistochemical CD9 staining (brown) marking the crescents, from pathological human kidneys harboring ANCA vasculitis. Scale bar: 50 µm, image from (Lazareth et al., 2019).

Three major types of crescentic glomerulonephritis are described based on their immunopathological characteristics:

- Pauci-immune Glomerulonephritis (or **ANCA-associated vasculitis**): These account for 60% of extracapillary glomerulonephritis cases (Couser, 1988; Jennette et al., 2003). They are systemic vasculitis caused by circulating antibodies targeting neutrophil cytoplasm (ANCA), proteinase 3 (ANCA anti-PR3), or myeloperoxidase (ANCA anti-MPO). It has been widely demonstrated that ANCA are pathogenic antibodies responsible for the observed vascular lesions (Hilhorst et al., 2015; Jennette & Falk, 1997; Van Der Woude et al., 1985).
- **Goodpasture's Disease** (anti-glomerular basement membrane antibodies disease): Its incidence is low, making Goodpasture's disease rare (McAdoo & Pusey, 2017). It represents 10 to 20% of crescentic Glomerulonephritis (CGN) cases (Andrassy et al., 2008; Couser, 1988). It typically presents as a lung-kidney syndrome, combining intra-alveolar hemorrhage with rapidly progressive glomerulonephritis. First described by Goodpasture in 1919 (Collins, 2010; Goodpasture, 2009), the causative anti-GBM antibodies were identified by Lerner et al. in 1964 (Lerner et al., 1967). These antibodies are mainly IgG1 autoantibodies targeting the α3 chain of collagen IV found in the glomerular basement membrane and lung alveoli. Exposure of the epitope on the GBM leads to antibody binding, activating the complement cascade, resulting in endothelial injury (Phelps & Turner, 2010). PECs proliferate in response and form a crescent shape (Lazareth et al., 2019).

  The treatment of the disease involves frequent and immediate dialysis, along with intense immunosuppression, and it's not uncommon for the renal insufficiency to progress to end-stage renal disease (Phelps & Turner, 2010).
- **Immune Complex-Mediated Glomerulonephritis**: This is the least common of the three. Causative conditions include IgA nephropathy, mixed cryoglobulinemia, lupus nephropathy, and post-streptococcal glomerulonephritis (Jennette, 2013).

1.2.1.2 Focal Segmental GolmeruloSclerosis (FSGS)

The diagnosis of focal segmental glomerulosclerosis (FSGS) is made histologically. First described by Fahr in 1925 (Fahr, 1925), the term FSGS refers to a non-specific histological lesion marked by the collapse of the glomerular capillary combined with sclerosis made of extracellular matrix deposits (Figure 16, D'Agati, 1994).

It reflects damages to, and loss of podocytes, leading it to also be referred to as podocytopathy (D'Agati et al., 2011). The injury to podocytes results in the flattening of podocyte foot processes, causing albuminuria and nephrotic syndrome. FSGS is classified based on various pathophysiological, histological, or genetic factors. It was suggested that FSGS could be divided into primary (idiopathic) FSGS and secondary FSGS (D'Agati et al., 2011; V. D. D'Agati et al., 2004). A histological classification has been developed which includes several FSGS variants (Barisoni et al., 2007; V. D. D'Agati et al., 2004). Lesions are anatomically classified by their location, the presence of glomerular hypercellularity, or flocculus collapse (D'Agati et al., 2011). Therefore, different histological forms of FSGS can be identified, applicable to both primary and secondary forms.

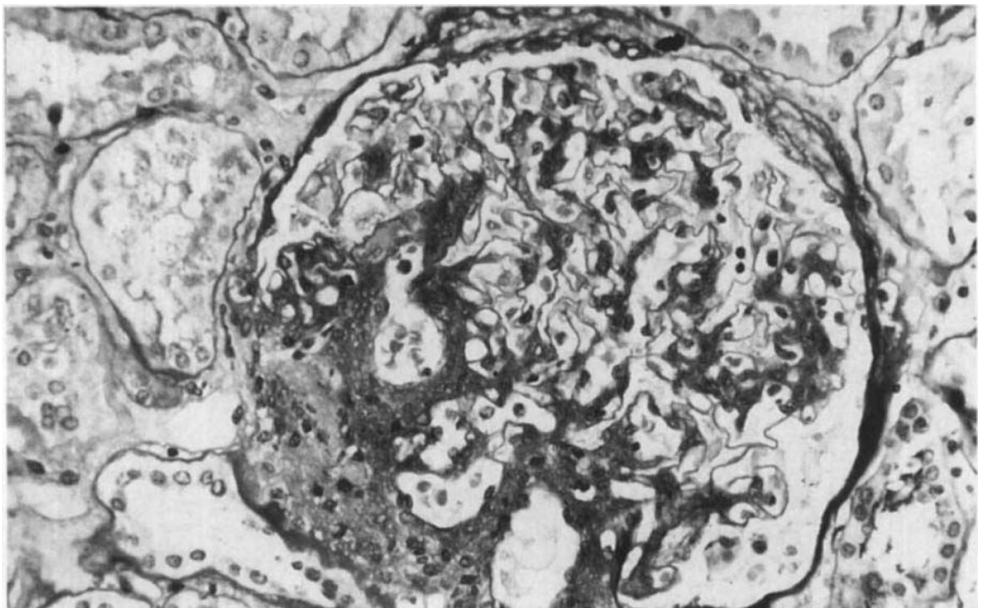

Figure 16: Discrete lesion, located at the vascular pole, of segmental sclerosis. Image from (V. D'Agati, 1994), *magnification 250 X.*

FSGS is a major cause of chronic kidney disease. Compared to other glomerulopathies, its global prevalence appears to be increasing, making it one of the main causes of end-stage renal disease. However, the exact prevalence and incidence of the condition are challenging to estimate due to the indications and accessibility to kidney biopsy worldwide. The reported annual incidence rate ranges from 0.2 to 1.8 cases/100,000 people, translating to between 130 and 1,200 new cases annually in France (McGrogan et al., 2011). Thus, FSGS accounts for 20% of nephrotic syndromes in children and 40% in adults. In the United States, FSGS is the leading cause of primary glomerulopathy leading to end-stage renal disease with a prevalence of 4% (Saran et al., 2019). Although there are various factors that may explain the occurrence of FSGS, primary forms remain the most common, with 80% of FSGS cases.

1.2.2 PECs role in RPGN and FSGS

Despite sharing a common cellular lineage, parietal epithelial cells (PECs) exhibit limited proliferation under normal physiological conditions in contrast with podocytes. The daily turnover rate of PECs in rats is estimated at 1%, similar to the rates of glomerular endothelial cells and mesangial cells (Pabst & Sterzel, 1983). Podocytes, on the contrary, are not able to self-renew (Kriz, 2020; Nadasdy et al., 1994).

Cellular crescents, which form in the urinary space in RPGN and FSGS, arise from cellular proliferation. The origin of the cells constituting the crescent has long been debated. However, recent research indicates that the crescent results from leukocyte infiltration (Jennette & Hipp, 1986) and the proliferation of both podocytes and PECs (Moeller et al., 2004; Smeets et al., 2009).

PEC indeed proliferate during focal segmental glomerulosclerosis (FSGS, Figure 17, Kuppe et al., 2015). In patients with FSGS, cells forming the tip lesions expressed markers of intermediate PECs (Kuppe et al., 2019). Instances of podocyte detachment have been reported, with areas of the glomerular basement membrane getting covered by a new basement membrane and epithelial cells (Figure 17, Kuppe et al., 2015). These regions contained desmosomes and intercellular junctions, suggesting a possible reparative role of PECs in response to podocyte injury (Kihara et al., 1997). Another study, revealed that cells involved in cellular lesions during human FSGS co-expressed proliferation markers (like Ki-67 and Cyclin-A) and specific PEC cytokeratins, but did not express podocyte markers. Electron microscopy studies confirmed that these proliferating cells exhibited features unique to PECs (Nagata et al., 2000). Similarly, proliferating cells in human FSGS expressed parietal markers rather than podocyte markers (Dijkman et al., 2005).

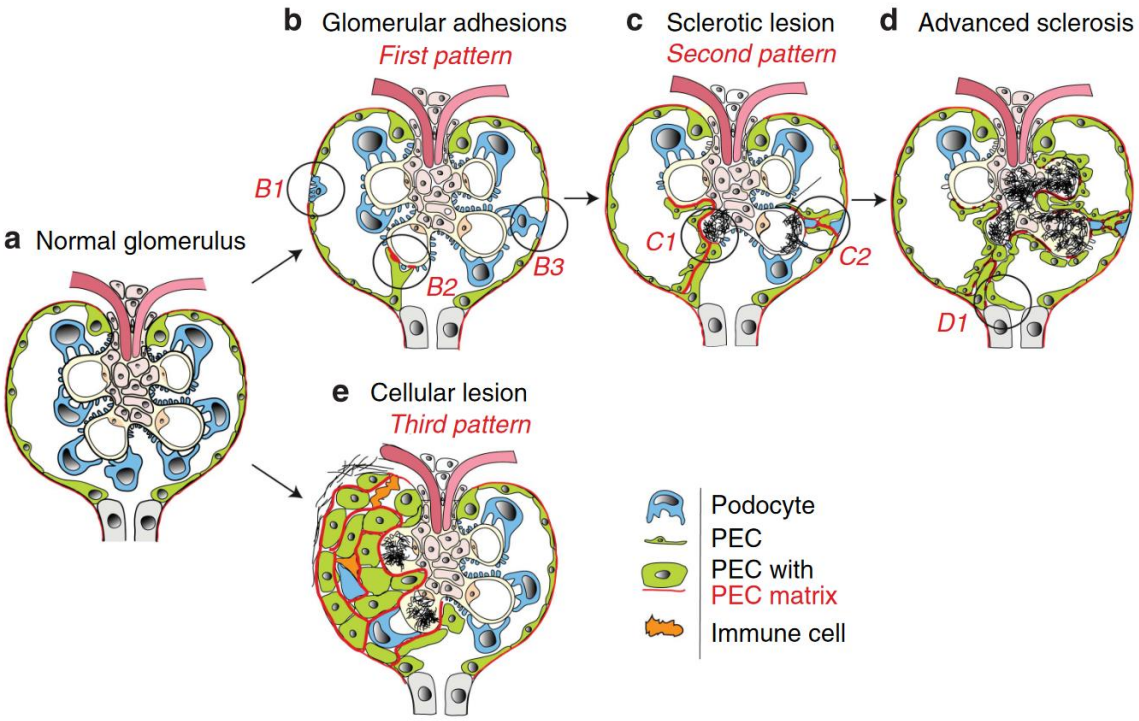

Figure 17: Histological patterns show the involvement of PECs in the lesions of FSGS: a) healthy glomerulus. b) Glomerular adhesions or synechiae are formed either by podocytes (B1) and/or PECs (B2), c) migration of PECs onto the GBM also coincides with sclerosis forming in the adjacent endocapillary space (C1), podocytes can still be observed within these adhesions (C2), d)

With advanced sclerosis, potential PECs cover the entirety of the sclerotic tuft sections, leading to the tubuloglomerular outlet being blocked (D1), e) cellular lesions are largely made up of cells that express PEC markers. A higher number of these presumed PECs display activation markers when compared to the sclerotic lesions. Image from (Kuppe et al., 2015).

The balance between the proliferation and loss of PECs is crucial for maintaining the structure and function of the glomerulus. Apoptosis of PECs and infiltrating cells is often observed within cellular crescents (Lan et al., 1997). Proliferation of PECs, podocytes (contributing 25%), and infiltrating inflammatory cells all contribute to crescent formation (Tipping & Timoshanko, 2005). These studies suggest that the transition from cellular crescents to fibrous crescents is linked to PEC apoptosis, which reduces cell numbers, eventually leading to their replacement by fibrous tissue that damages the glomerulus (A. Shimizu et al., 1996). Parietal epithelial cells have been detected in the urine of patients with various glomerular diseases, such as FSGS, and membranoproliferative glomerulonephritis (Achenbach et al., 2008). Therefore, apoptosis and detachment contribute to the reduction in PEC numbers, although the adaptiveness of these mechanisms remains uncertain.

Epithelial-to-mesenchymal transition (EMT) occurs within PECs, with increased expression of α-SMA (alpha-Smooth Muscle Actin) observed in two crescentic glomerulonephritis models (Fujigaki et al., 2001; Ng et al., 1999). EMT describes a process where epithelial cells lose their characteristics and gain a more mobile "mesenchymal" phenotype (Thiery & Sleeman, 2006). The role of Ilk (Integrin-linked kinase) in promoting PECs EMT and crescent formation was further emphasized (M. Shimizu et al., 2006). Since α-SMA is detected in PECs during toxic nephritis and TGF-ß is associated with a transition of PECs towards a myofibroblast phenotype, it is plausible that blocking TGF-ß leads to reduced EMT in PECs, thus reducing crescent numbers (A. Zhou et al., 2003). Exposing PECs to TGF-ß in culture increases Snail transcription factor levels and results in the loss of claudins and occludins (Ikenouchi et al., 2003; Ohse, Pippin, et al., 2009), that could possibly indicate a dedifferentiation. It was further demonstrated *in vitro* EMT transition of PECs into cells expressing EMT markers (TGF-ß, Snail, vimentin, and nestin) (Swetha et al., 2011).

PEC migration is a significant phenotypic change in extracapillary glomerulonephritis (Kuppe et al., 2017) and in segmental and focal sclerosis (Dijkman et al., 2005; Kuppe et al., 2019; Smeets et al., 2009). It was demonstrated that PECs and the Bowman capsule act as barriers against urinary flow (Kriz et al., 2001). In two spontaneous FSGS models and one anti-GBM glomerulonephritis model, the PECs monolayer detaches from the basement membrane, urine flow becomes misdirected, leading to urine leakage into the periglomerular space (Kriz et al., 2001). Contrarily, after PEC injury, even with an intact cell monolayer, the expression of junctional proteins decreased, leading to urine leakage into the periglomerular space (Ohse, Chang, et al., 2009). In summary, glomerular lesions develop when the PEC-formed urine permeability barrier is compromised, which underlines their essential role in maintaining the glomerular homeostasis.

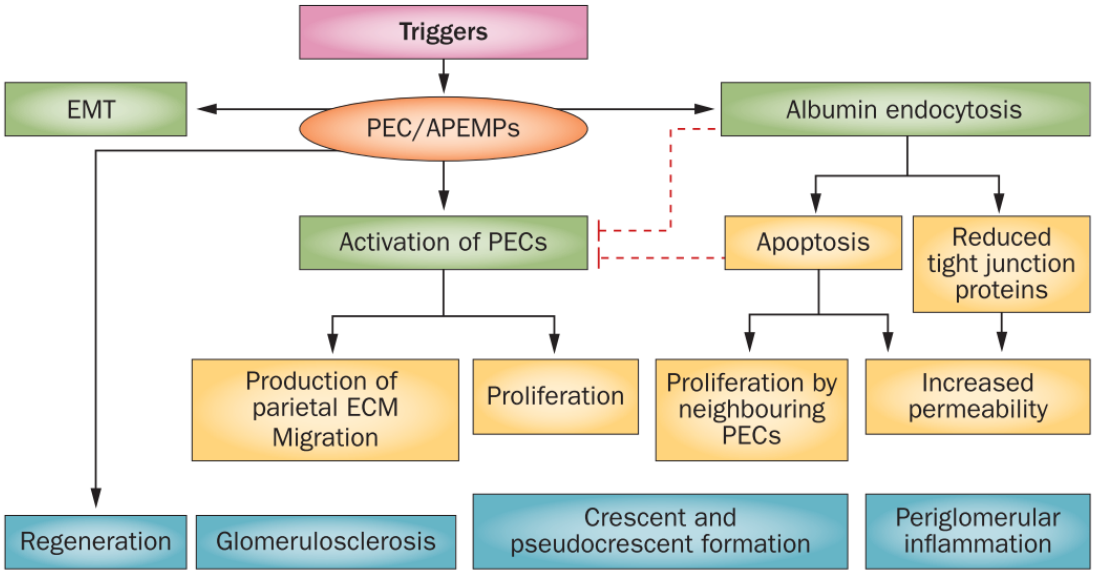

Figure 18: Potential of PECs in kidney diseases. Image from (Shankland et al., 2014).

Crucially, in experimental CGNs, podocyte loss has been pinpointed through lineage tracing and optical clearing techniques (Puelles et al., 2019). Additionally, in human biopsy samples from ANCA-CGN patients, this was observed using deep learning methods (Siegerist et al., 2022; Zimmermann et al., 2021). This phenomenon might be due to the rupturing of the basement membrane, resulting in direct interaction among PECs, podocytes, and immune cells. Furthermore, it could indicate the inability of PECs to effectively replace the podocytes lost during CGN.

In FSGS, glomeruli exhibit segmental scarring due to the infiltration of the glomerular tuft by activated PECs. This intrusion causes the segmental scars to disrupt the continuous epithelial layer. Yet, even in glomeruli with progressive lesions, non-sclerotic segments appear to remain intact. PECs are responsible for creating matrix layers that act as a barrier between the unaffected and the sclerotic glomerular segments (Miesen et al., 2022).

In conclusion, parietal epithelial cells play a significant role in maintaining glomerular function and homeostasis. They undergo phenotypic changes in response to various injuries, often resulting in glomerular disease progression (Figure 18). Understanding the molecular and cellular mechanisms underlying these alterations is crucial for the development of therapeutic interventions targeting glomerular diseases.

1.3 Local factors of RPGN and FSGS

Several growth factors, including CTGF, PDGF, and EGF, play roles in PECs response to injuries (Ohse, Pippin, et al., 2009). CTGF, a pro-fibrotic factor, is expressed in crescents in human glomerulonephritis (Ito et al., 1998). In a model of rapidly progressive glomerulonephritis, CTGF mRNA levels increased in PECs before fibroblast numbers did. CTGF mRNA was expressed in crescents without any macrophage markers, suggesting that PECs produce CTGF, thereby contributing to glomerular damage (Kanemoto et al., 2003). Rat PECs under physiological conditions, have a low expression of PDGF-BB and its receptor PDGFR-ß. In a toxic nephritis model simulating crescentic glomerulonephritis, it was noted an early increase in PDGF-BB and PDGFR-ß levels in crescent-forming cells (Fujigaki et al., 2001). EGF and its receptor EGFR are involved in cell growth,

proliferation, and differentiation. EGFR expression is more commonly found in cellular crescents, suggesting its role in extracellular matrix production and renal fibrosis progression (Nakopoulou et al., 1994). The pathological role of the HB-EGF/EGFR pathway was demonstrated in mouse and human extracapillary glomerulonephritis (Bollée et al., 2011). The involvement of the TGF-a/EGFR pathway, promoting renal fibrosis, is shown in PECs from glomeruli in crescentic glomerulonephritis (Laouari et al., 2011).

More recently, CD44-positive activated PECs have been identified in FSGS and CGN models. For cd44-/- mice, albuminuria was significantly lower compared to wild type mice. The number of glomerular Ki67-positive proliferating cells was significantly reduced and was associated with a reduced number of glomerular lesions in crescentic glomerulonephritis (Eymael et al., 2018). Antibodies against CD44 also inhibited human PEC migration.

The tetraspanin CD9 expression noticeably elevates in PECs in mouse models of CGN and FSGS, as well as in kidneys from people with these conditions. Targeting the Cd9 gene specifically in PECs prevents glomerular damage in mouse models of CGN and FSGS. At the cellular level, the absence of CD9 stops the directional movement of PECs into the glomerular tuft and blocks their increase of CD44 and β1 integrin expression (Lazareth et al., 2019).

1.3.1 HB-EGF, PDGF, and the tetraspanin CD9

1.3.1.1 Heparin-Binding EGF-like Growth Factor (HB-EGF) pathway

Heparin-Binding EGF-like Growth Factor (HB-EGF), is a growth factor belonging to the Epidermal Growth Factor (EGF) family. Its initial description traces back to 1990 when Besner et al. identified a new heparin-binding growth factor produced by cultured human macrophages (Besner et al., 1990). This discovered factor was characterized as heat-resistant, cationic, with a molecular weight ranging between 14 and 25 kDa. The protein was later isolated (Higashiyama et al., 1990).

Pro-HB-EGF is produced as a transmembrane precursor protein, undergoing significant proteolysis to yield mature HB-EGF. Initially, pro-HB-EGF is cleaved by a furin-like enzyme (Nakagawa et al., 1996). Subsequently, ADAM proteins (Disintegrin and metalloproteinase domain-containing protein), a disintegrin and metalloproteinase domain protein, further cleaves pro-HB-EGF, releasing the soluble mature HB-EGF. This proteolytic event is commonly termed ectodomain shedding (Asakura et al., 2002; Izumi et al., 1998; Sunnarborg et al., 2002; Yan et al., 2002).

The release of soluble HB-EGF through ectodomain shedding modifies the remaining intracellular domain of HB-EGF to form a carboxy-terminal domain named HB-EGF-CTF (Carboxy Terminal Fragment) (Nanba et al., 2003; Z. Zhou & Harding, 2007). Both HB-EGF and HB-EGF-CTF are potential stimulants of proliferation through EGFR-dependent and independent mechanisms (Besner et al., 1990; Nanba et al., 2003; Z. Zhou & Harding, 2007). This process is illustrated in Figure 19.

Mature soluble HB-EGF contains six highly-conserved cysteine residues corresponding to the EGF-like domain. This domain, shared among all EGF family members, is crucial for binding and activating the EGF receptor (EGFR) (Thompson et al., 1994).

Like other EGF family members, HB-EGF biological activity is mediated by binding and activating tyrosine kinase receptors. Ligand binding induces receptor dimerization, autophosphorylation, phosphorylation of various intracellular substrates, and the recruitment of signaling molecules containing SH2 (Src homology 2) domains to phosphorylated tyrosine residues in the receptor's intracytoplasmic tails (Davis-Fleischer & Besner, 1998). Among the four known EGF receptor isoforms, HB-EGF specifically binds to EGFR (ErbB1/HER1) and ErbB4 (HER4) (Yarden & Shilo, 2007).

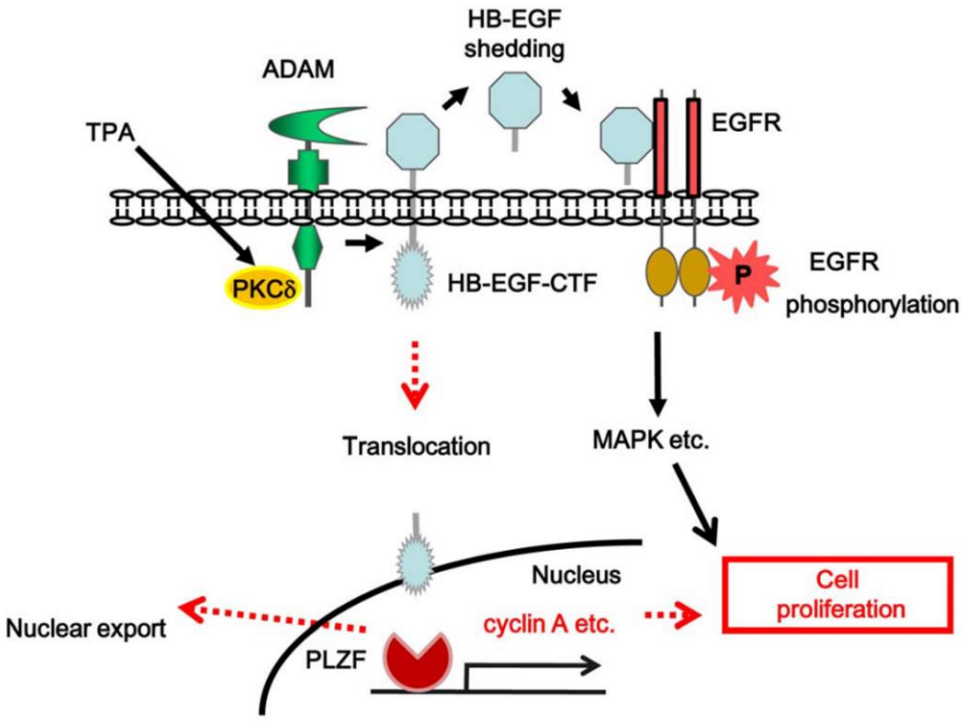

Figure 19: The coexistence of two signaling pathways involves EGFR phosphorylation and the nuclear relocation of the HB-EGF C-terminal fragment during cell growth. Cleavage in proHB-EGF through ADAM, leads to the release of its N-terminal portion and the creation of an intracellular C-terminal segment (CTF). The freed HB-EGF connects with the EGFR, prompting a brief and immediate phosphorylation of EGFR. This phosphorylation subsequently activates the transcription of multiple genes. At the same time, the HB-EGF-CTF shifts into the cell nucleus, where it prompts the outward movement of PLZF, thus propelling the cell's growth cycle forward. 'P' is phosphorylation, PKCδ is protein kinase Cδ, MAPK is mitogen-activated protein kinase, and PLZF stands for promyelocytic leukemia zinc finger. Image adapted from (Ozeki et al., 2013).

EGFR transactivation by GPCR (G Protein-Coupled Receptor) signaling is a common mechanism in various cells such as astrocytes, fibroblasts, keratinocytes, and smooth muscle cells (Sahin et al., 2004; Taylor et al., 2014), and involves the release of soluble mature HB-EGF, which binds to heparan sulfate proteoglycans (HSPG) and the EGF receptors, leading to the activation of MAPK (is mitogen-activated protein kinase) and the cyclin-D/Cdk (cyclin-dependent kinase) complex, promoting cell cycle progression. HB-EGF-CTF translocate to the nucleus, either exporting the transcriptional repressor PLZF (promyelocytic leukemia zinc finger), which triggers the cyclin-A/Cdk DNA replication initiation complex (Nanba et al., 2003), activating DNA replication. HB-EGF thus plays a major role in cell survival and proliferation.

1.3.1.2 Platelet-Derived Growth Factor (PDGF) pathway

The Platelet-Derived Growth Factor (PDGF) was first described in 1974 by Ross et al. as a factor in plasma that depends on platelets to stimulate the growth of arterial smooth muscle cells in vitro (Ross et al., 1974). That same year, another research work, by Koehler and Lipton, observed a growth factor originating from platelets that promoted the proliferation of murine fibroblasts (Kohler & Lipton, 1974).

The human PDGF was initially characterized as a dimer formed by two polypeptide chains connected through a disulfide bridge and could be separated *via* reverse phase chromatography (Johnsson et al., 1982). Mammals have two classes of PDGF isoforms, distinguished by the presence of basic retention motifs for Class I (PDGF-A and PDGF-B) or CUB domains for Class II (PDGF-C and PDGF-D) (Reigstad et al., 2005). While Class I isoforms are secreted in their active form, Class II isoforms get activated post-secretion by the cleavage of their CUB domain (Andrae et al., 2008).

PDGF functions as dimers, and they are secreted and linked by disulfide bridges. Collectively, the four isoforms can come together to form five dimers, primarily four homodimers: PDGF-AA, PDGF-BB, PDGF-CC, and PDGF-DD, and one heterodimer, PDGF-AB (Figure 20) (Reigstad et al., 2005).There are three receptor types for PDGF: PDGFR-αα, PDGFR-ββ, and PDGFR-αβ. These receptors are specific in their associations with different PDGF isoforms (Figure 20).

After ligand binding, the PDGFR units dimerize, activating their tyrosine kinase domain, leading to a cascade of intracellular signaling (Andrae et al., 2008; Hoch & Soriano, 2003). PDGF are naturally expressed in various tissues. For instance, PDGF-A is found in podocytes and mesangial cells, PDGF-B specifically in mesangial cells, and PDGF-C only within proximal and distal tubes (Heldin & Westermark, 1999).

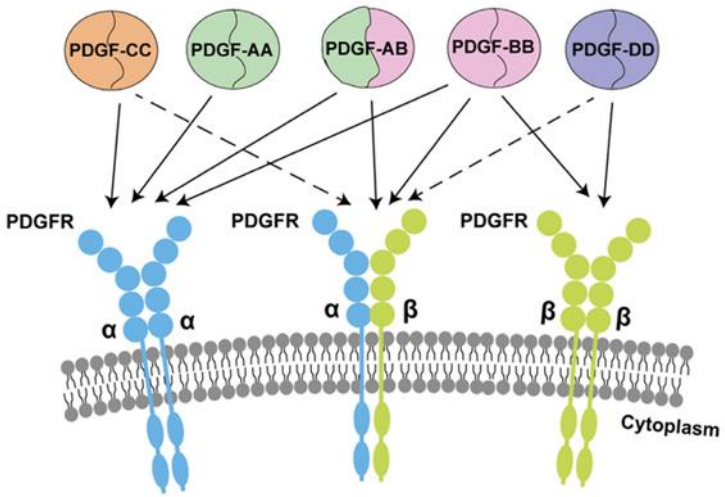

Figure 20: PDGF association with PDGFR, the PDGF dimer associates with the PDGFR, where each segment of the PDGF dimer connects to a single receptor component. Interactions demonstrated are solid arrows, interactions that are either faint or have mixed findings are shown as dotted lines. Image from (Evrova & Buschmann, 2017).

As discussed before, PDGF receptors are tyrosine kinase receptors. When they bind to their ligand, they dimerize and undergo autophosphorylation of their cytoplasmic tyrosine residues. These

phosphorylated residues become docking sites, anchoring adapter proteins and signaling molecules, initiating signal transduction (Figure 21) (K. C.-W. Chen et al., 2007). Specific molecules can be recruited to these sites, like Src, PI3K, p120, RasGAP, SHP-2, and PLC-g. Both the α and ß receptors activate similar signaling pathways, but they have slight differences in their interactions, resulting in functional differences between PDGFR-α and PDGFR-ß (*in vivo*) (Klinghoffer et al., 2001; Rosenkranz & Kazlauskas, 1998). Activation of PDGFR (α and ß) triggers several intracellular signaling pathways, including PI3K, PLC-γ, and Ras-MAPK. MAPK stimulates the transcription of genes related to cell growth, differentiation, and migration (Seger & Krebs, 1995). PDGF activation of the PI3K pathway results in actin reorganization, cellular growth stimulation, and apoptosis inhibition (Hu et al., 1995). PLC-γ activation causes an increase in intracellular calcium and PKC activation, promoting cell growth and mobility (Kundra et al., 1994). Additionally, PDGF receptors also interact with integrins, stimulating cell proliferation, migration, and survival (Assoian, 1997; Frisch & Ruoslahtit, 1997). The interaction between PDGFR and integrins facilitates their localization at focal contacts, initiation sites for numerous signaling pathways and cross-talks (Clark & Brugget, 1995).

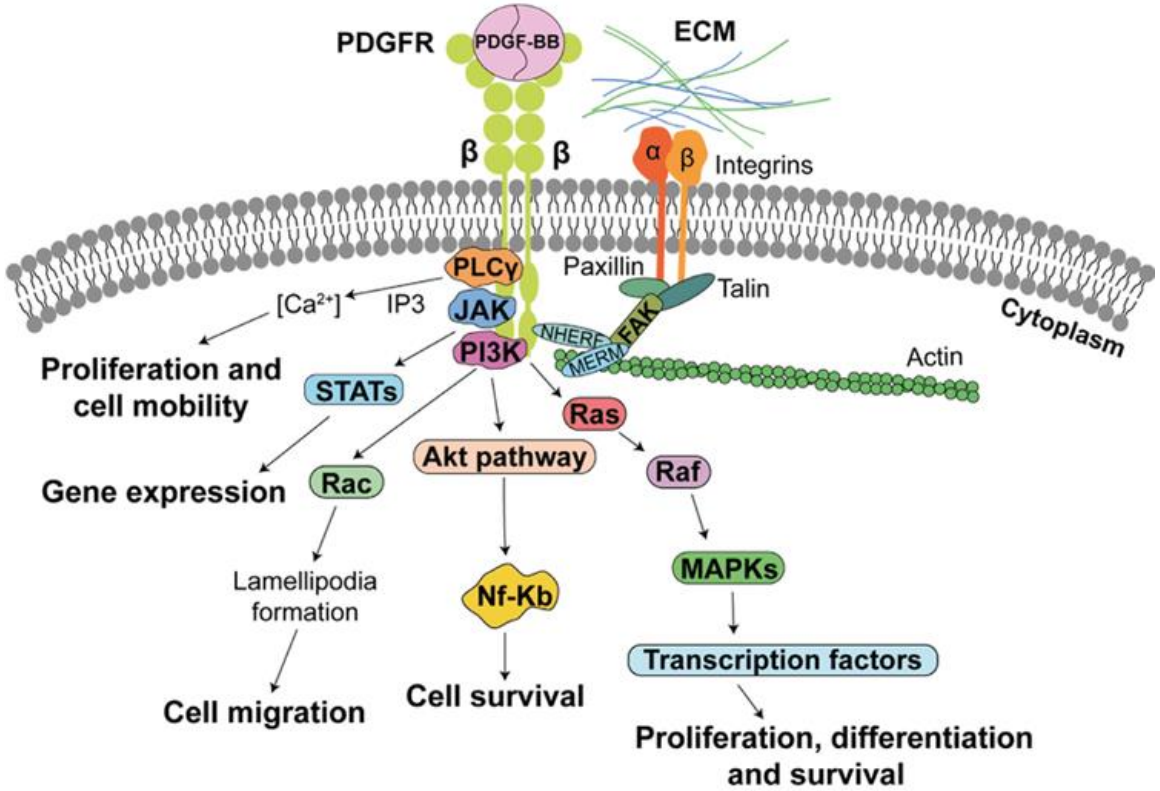

Figure 21: PDGF signal transduction mechanisms following the PDGF-BB attachment and its engagement with the cytoskeleton and integrins. This is a streamlined depiction of the primary actors and functions, with several components and processes, notably feedback systems, left out. Image from (Evrova & Buschmann, 2017).

Altogether, PDGF regulates processes at the cellular and tissue levels, including proliferation, differentiation, and migration.

1.3.1.3 CD9

Tetraspanins are molecules that have been highly conserved throughout eukaryotic evolution. The tetraspanin family consists of 32 member in mammals. They are widely distributed and are

located on the cell membrane as well as within various organelles and granules, protruding only about 4 to 5 nm (Hemler, 2005). At the single cell scale, a cell typically expresses between 30,000 to 100,000 copies of each given tetraspanin (Hemler, 2003). The typical conformational structure of tetraspanins is illustrated in Figure 22.

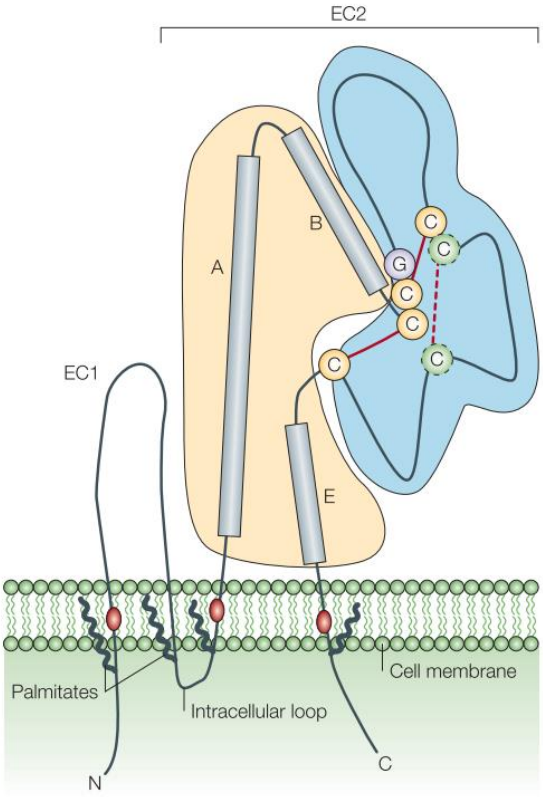

Figure 22: Tetraspanins exhibit distinctive structural components, including: four membrane-spanning domains, an external short loop (EC1), a particularly brief internal loop (usually composed of 4 amino acids), and an extended external loop (EC2), short N-terminal and C-terminal tails in the cytoplasm (8–21 amino acids). Image from (Hemler, 2005).

The EC2 loop houses α-helices, A, B, and E domains, and a flexible domain (blue) that offers multiple sites for protein-to-protein interactions (Kitadokoro et al., 2001; Stipp et al., 2003). While the majority of interaction sites are found in EC2, the structure or purpose of EC1 remains largely unknown.

CD9 is a surface glycoprotein that belongs to the tetraspanin family. Historically, CD9 (or p24) was identified as a 24 kDa antigen found on the surface of B lymphocytes from acute lymphoblastic leukemia (Boucheix et al., 1983). The human protein has been crystalized recently (Figure 23) in complex with its single membrane-spanning partner protein, EWI-2 (Umeda et al., 2020).

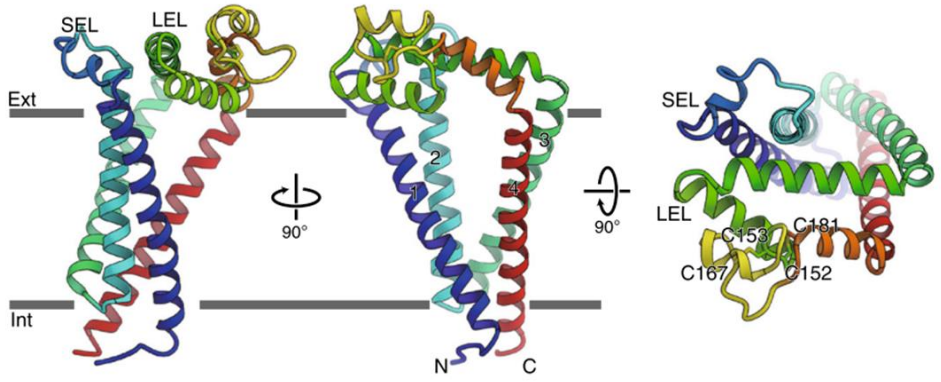

Figure 23: The structure of human CD9, observed from two perspectives: from the plane of the membrane and from the external cellular viewpoint (right). The four spanning helices within the membrane and the two extracellular loops, known as SEL and LEL, are distinctly marked. The formation of disulfide bonds occurs between Cys152 and Cys181, as well as between Cys153 and Cys167, image from (Umeda et al., 2020).

When CD9 molecules are present within a lipid environment, they induce curvature in lipid membranes. There is substantial evidence suggesting the presence of tetraspanin proteins in particularly curved sections of cell membranes (Umeda et al., 2020). For example, both CD9 and its associated tetraspanin, CD81, are found at the emerging tips of virus buds, playing a role in the viral infection cycle and directly contributing to membrane curvature (Dahmane et al., 2019; X. A. Zhang & Huang, 2012). The uneven shape of CD9, and the resulting curvature observed, might explain its concentration in specific areas with a small curvature radius. Additionally, many studies have posited that tetraspanins forms clusters in biological membranes (Hemler, 2005). Such clusters could produce localized membrane curvature, potentially leading to the restructuring of cell membranes, as hinted at earlier (Bari et al., 2011).

CD9 regulates growth factors from the EGF family, notably HB-EGF (Higashiyama et al., 1995; Iwamoto et al., 1994; Lagaudriere-Gesbert et al., 1997; Takemura et al., 1999). It interacts with TGF- α, reducing the proteolytic conversion of TGF-α to its soluble form, thereby increasing EGFR activation, leading to enhanced cell proliferation. However, the co-expression of CD9 and TGF-α reduces the autocrine activity of TGF-α on epithelial cell growth (Shi et al., 2000). CD9 also associates with pro-HB-EGF, a precursor of HB-EGF and a member of the EGF family. CD9 enhances the availability of pro-HB-EGF and the cell sensitivity to them (Iwamoto et al., 1991, 1994; Mitamura et al., 1992), subsequently amplifying the juxtacrine activity of HB-EGF (Higashiyama et al., 1995; Lagaudriere-Gesbert et al., 1997).

CD9 associates with growth factor receptors, notably EGFR and PDGFR. CD9 forms a complex with EGFR (and integrin β1) in gastric tumor cells, leading to EGFR internalization, thereby reducing EGF/EGFR signals responsible for tumor cell proliferation and survival (Murayama et al., 2007). CD9 also binds to PDGFR (α and β) and regulates signaling induced by PDGF-BB (Jeibmann et al., 2015).

CD9 interacts with the integrin family, especially integrins ß1. Integrins are heterodimeric transmembrane receptors involved in cellular adherence to the extracellular matrix (Hynes, 2002). The interaction between CD9 and integrin β1 in epithelial cells increases the expression of integrin β1 and cell migration (Kotha et al., 2008). CD9 also interacts with claudin-1, a tight junction protein. The deletion of CD9 does not change paracellular permeability but destabilizes the membrane expression of newly synthesized claudin-1 molecules, suggesting an interaction between CD9 and

claudin-1 in tetraspanin-rich domains (Kovalenko et al., 2007). Lastly, CD9 collaborates with other tetraspanins (like CD63, CD81, CD82, or CD151) to form tetraspanin-enriched microdomains (TEM) or "tetraspanin web". Tetraspanins might act as organizers of multimolecular complexes on cell surfaces. These TEMs would be key molecular signaling areas on the cell surface (See section: 3.1.4).

These evidences indicate that CD9 is implicated in adhesion, migration and proliferation mechanism, and is localized in specialized membrane domains. The organizational role of CD9 in membrane domains might participate significantly in regulation of signaling processes.

1.3.2 Implication in kidney diseases

The involvement of CD9 in renal pathologies has been the subject of fewer studies. Under physiological conditions, CD9 is not expressed in the human glomerulus but primarily in collecting duct cells (C. Huang et al., 1997). *In vitro* studies have shown that CD9 is expressed in polarized MDCK cells, located in the apical membrane microvilli (Yáñez-mó et al., 2000). Blumenthal and colleagues found that CD9 was overexpressed in cultured podocytes subjected to mechanical stress. Functionally, CD9 expression correlated with the formation of membrane protrusions on the surface of these podocytes. The adhesive properties of these CD9-expressing podocytes were altered, and their migratory capacity increased during a scratch test (Blumenthal et al., 2015). It was hypothesized that CD9 might play a role in extracapillary glomerulonephritis and FSGS, given its close association with the EGFR receptor and pro-HB-EGF, whose pathogenic role was established (Bollée et al., 2011).

Research into HB-EGF and the EGFR pathway has provided significant insights into renal pathology (Harskamp et al., 2016). Studies focused on renal fibrosis have shown that mice with an endothelial absence of Hbegf present reduced albuminuria and decreased signs of glomerulosclerosis and renal fibrosis when compared to their wild-type counterparts, especially in the context of prolonged angiotensin II stimulation (Zeng et al., 2016).

Regarding rapidly progressive glomerulonephritis (RPGN) models, there is a novel expression of HB-EGF in glomerular epithelial cells, podocytes, and parietal epithelial cells across mice, rats, and humans (Bollée et al., 2011; Harris, 2011). Other models, such as the puromycin-induced FSGS and the extramembranous glomerulonephritis (known as Heymann nephritis), also show similar patterns (Paizis et al., 1999).

Interestingly, a lack of Hbegf gene activation correlates with a deactivated EGFR pathway in an experimental RPGN setup. This Hbegf gene absence in an anti-GBM disease resulted in a 100% survival rate for mice, contrasting the 30% mortality rate in wild-type mice over an 8-day period (Bollée et al., 2011). Further findings in mice showed that when the EGFR was specifically deleted in podocytes, the severity of RPGN was reduced (Bollée et al., 2011). The pharmacological inhibition of EGFR has been furthermore shown to positively affect the progression of both RPGN in mice (Bollée et al., 2011), and mesangioproliferative glomerulonephritis in rats (Rintala et al., 2015).

The role of PDGF in proliferative glomerulonephritis has been extensively researched. The PDGFR-β and its ligands, PDGF-BB and -DD, are key mediators of mesangial proliferation (Floege et al., 2007, 2008). Overexpression of PDGFR-β and its ligands is observed in mesangioproliferative glomerulonephritis (Floege et al., 2008), and they can induce mesangial proliferation in vitro (Floege et al., 2007, 2008; Ostendorf et al., 2003). Furthermore, systemic or podocyte overexpression of PDGF-DD in wild-type mice results in mesangioproliferative glomerulonephritis (Hudkins et al., 2004; Roeyen et al., 2011). It has been demonstrated that cells forming the crescentic structure

overexpress PDGFR-β and PDGF-BB in crescentic glomerulonephritis in humans (Waldherr et al., 1993). This is also the case in rats in an anti-MBG model (Fujigaki et al., 2001). The use of specific PDGF inhibitors, notably Trapidil and Imatinib, has been explored in crescentic glomerulonephritis models (Iyoda et al., 2009, 2013). Both compounds improved outcomes in these mouse models by reducing macrophage infiltration. Additionally, the PDGF/PDGFR signaling pathway is also involved in the proliferation and regeneration of tubular cells in cases of acute renal failure (Kok et al., 2014).

The implication of CD9 in the regulation of HB-EGF and PDGF pathways in models of CGN and FSGS was identified recently (Lazareth et al., 2019). *De novo* expression of CD9 in PECs in mouse and humans diagnosed with these diseases was observed. Cd9 gene deletion in PECs prevents glomerular damage in CGN and FSGS mouse models (Figure 24).

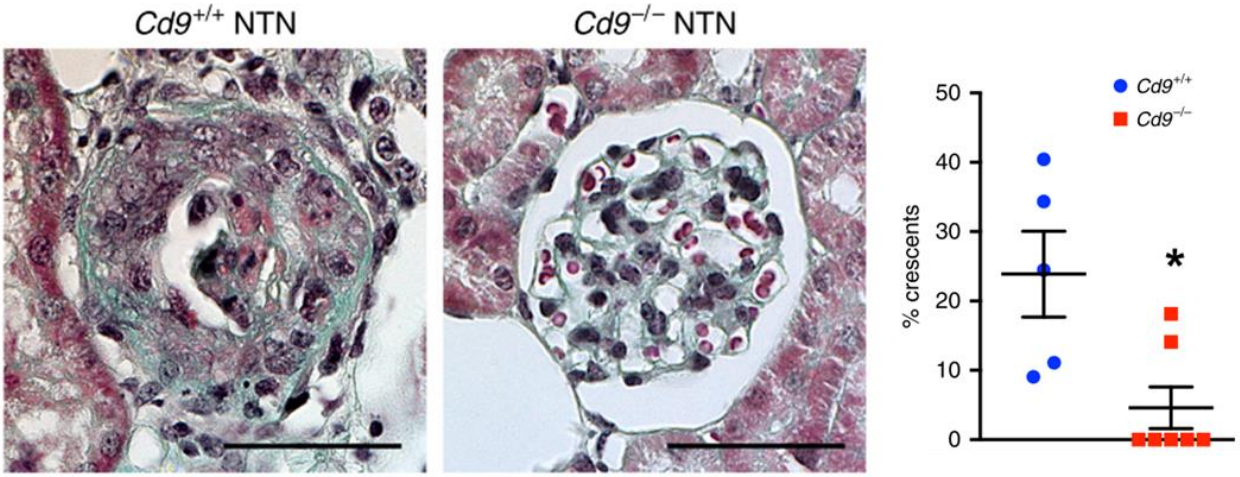

*Figure 24: Left, Mice with a complete genetic depletion of CD9 showed resistance to crescentic glomerulonephritis (CGN) induced by nephrotoxic serum. $Cd9^{-/-}$ and $Cd9^{+/+}$ mice were stained using Masson's trichrome method, 10 days post-nephrotoxic serum injection (NTN). Right, percentage of glomeruli with crescentic formation. The average percentages were derived from data on 5 mice ($Cd9^{-/-}$) and 7 mice ($Cd9^{+/+}$). *P < 0.05, scale bar = 50 µm, image from (Lazareth et al., 2019).*

It was further observed that, while PDGF-BB induced a rapid and transient PDGFR-β phosphorylation, CD9-depleted PECs showed impaired PDGFR-β phosphorylation. Similarly, HB-EGF pathway was also defective in CD9-depleted cells with a decreased level of total EGFR and its phosphorylation after HB-EGF stimulation (Figure 25) (Lazareth et al., 2019).

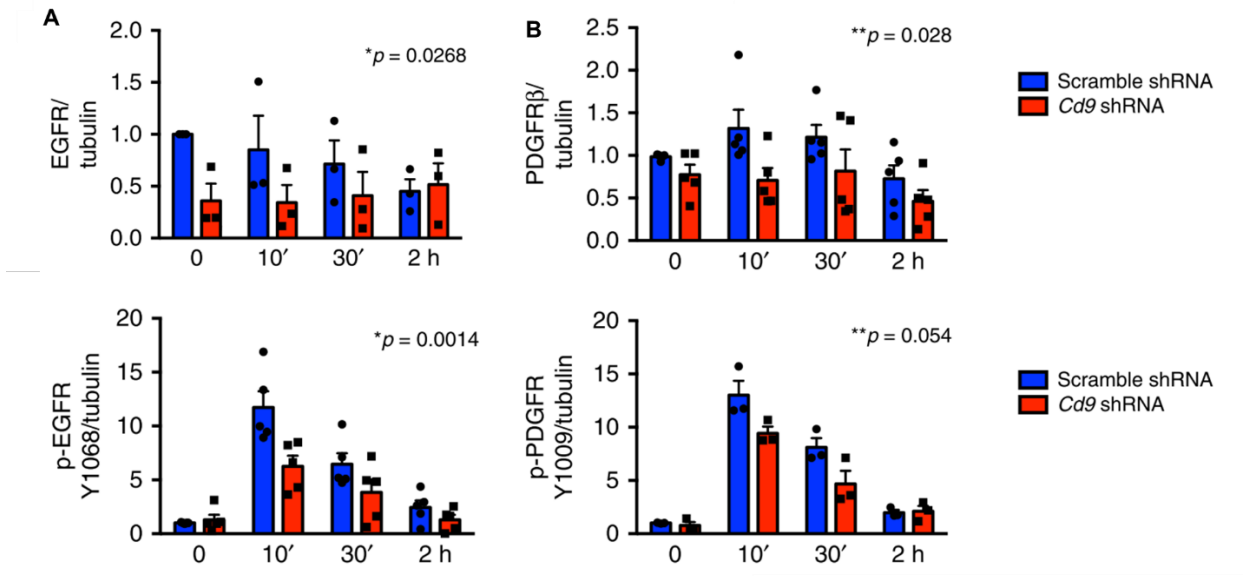

*Figure 25: Semi quantitative analysis by Western-blot (not shown) of the expression of A) phospho-EGFR Y1068 and EGFR, after time stimulation with HB-EGF (20 ng/ml) and B) of phospho-PDGFRβ Y1009 and PDGFRβ, after time stimulation with PDGF-BB (20 ng/ml), in control (scramble shRNA) and CD9-depleted (Cd9 shRNA) murine PECs, tubulin was used as a loading control, mean and SEM of n =4 experiments, *from two-way ANOVA test, images from (Lazareth et al., 2019).*

In vitro, CD9-deficient PECs displayed a strong delay in adhesion with reduced cell spreading, and a reduced migration in scratch assays when stimulated with HB-EGF or PDGF-BB. Furthermore, by creating a steep growth factor gradient in microfluidic channels (Figure 26), CD9 depletion impaired the ability of PECs to migrate towards the PDGF-BB gradient (Lazareth et al., 2019).

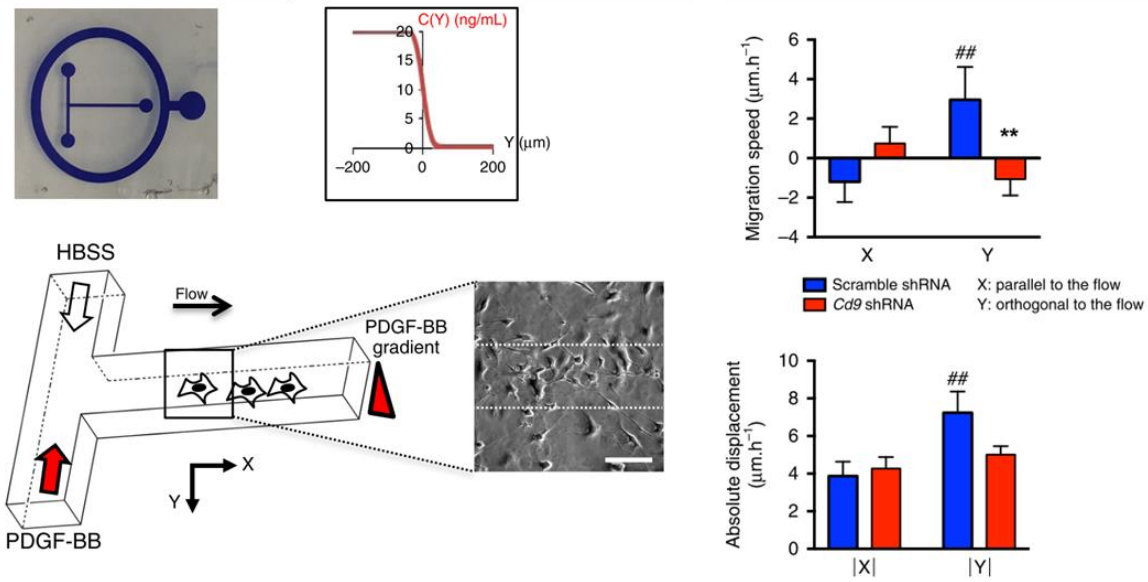

*Figure 26: Left, T shaped microfluidic device to generate gradients in a microchannel, with the profile of the gradient. Right, quantification of the oriented migration and of the absolute displacement, of control (scramble shRNA) and CD9-depleted (Cd9 shRNA) murine PECs after stimulation with a gradient of PDGF-BB (20 ng/mL during 3 h). ##P < 0.01 between X (displacement in the flow) and Y (displacement in the gradient) in basal PEC; **P < 0.01. The data are shown as the mean +/− s.e.m. of n > 30 cells in 3 or 4 T-shape microfluidic channel per condition, image from (Lazareth et al., 2019), scale bar 100 µm.*

The data point towards HB-EGF/PDGF and the activation of the EGFR/PDGFR pathway as potential regulators of pathological transition, underscoring their importance as prospective therapeutic touchpoints. Additionally, CD9 has been identified to have a potential role in controlling related signaling.

To decipher this complex interplay we performed a series of experiments detailed in the next chapters.

Chapter 2. Development of a Glomerulus-on-chip

Abstract:

The aim of this work was to develop a biomimetic microsystem that combines an organ-on-chip approach with advanced noninvasive optical measurement methods. This was done to uncover the mechanisms behind pathophysiological responses at both cellular and organ scales. The microsystems were designed to mimic the human glomerulus, with compartments representing the vascular and urinary spaces separated by a membrane. The compartments were co-cultured with specialized cells (CiGEnCs and CiPodocytes) in order to recreate the glomerular filtration barrier.

The bottom of the system was lined with a parietal epithelial cell layer (CirPECs), and offers an optical window for observation. The cells were cultured using a gravity-driven perfusion approach, allowing sustained culture (≥2 weeks). After two weeks of co-culture, specific markers of differentiated cells found in the actual glomerulus were identified. Cells formed confluent monolayers, secreted relevant amount of ECM proteins, and aligned with flow under shear stress.

Functional assays demonstrated that the systems mimicked the filtration properties of an actual glomerulus, particularly for small molecules and albumin. Further experiments stimulated the systems with EGF, resulting in reduced filtration capabilities, increased CirPECs proliferation, and destabilization of the CiPodocytes layer—markers of diseases like FSGS and RPGN. In summary, the study successfully replicated glomerular organization and function in a chip-based system using glomerular cells. The ability to induce disease-like phenotypes through signaling activations opens up possibilities for investigating complex signaling pathways and developing potential therapeutic strategies.

Graphical abstract

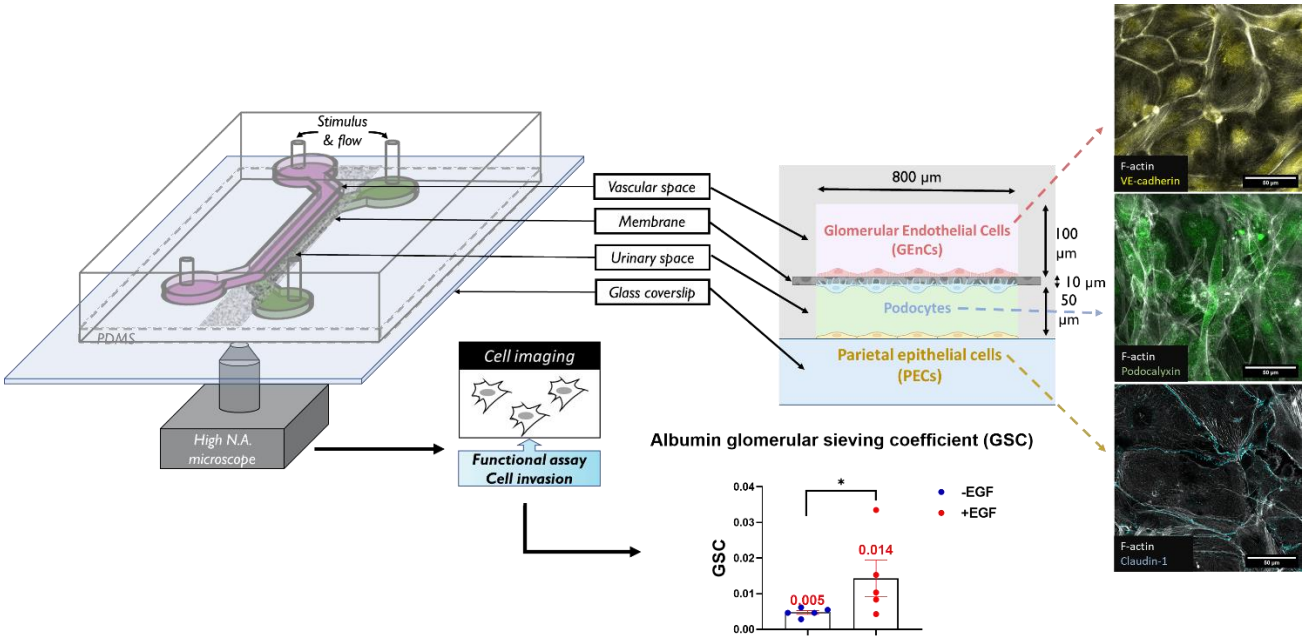

Keywords: *Glomerulus-on-chip, Podocytes, GEnCs, PECs, EGF signaling.*

2.1 From cell culture to Organs-on-a-chip

2.1.1 The drug development bottleneck

The pharmaceutical innovation landscape has led to a prolonged and costly drug development process, with an average of over 10 years required to bring a new, safe, and effective treatment to market, including biological products and drugs. Currently, drug development expenses are estimated to be around $2.6 billion per drug, with costs continuing to rise (Y. I. Wang et al., 2018). While there are no fixed requirements for the number and type of non-clinical studies, the traditional approach outlined in FDA (United States Food and Drug Administration) guidelines involves a combination of *in vitro* assays and animal testing.

Before clinical trials, non-clinical testing is conducted to assess the safety of human pharmaceuticals. However, traditional cell culture and animal models used in preclinical drug screening often lack predictive power for human response (Sneddon et al., 2017), resulting in high attrition rates during clinical trials, the most expensive phase of drug development. Roughly 90% of drug candidates that show promise in preclinical studies fail to progress in clinical development, often due to unforeseen safety issues or lack of efficacy (Evens, 2016).

To tackle this challenge, there is a growing interest in developing alternative models that use human cells to create *in vitro* biomimetics of the human body. These advanced models aim to include physiologically relevant organ interactions, providing a more accurate representation of human physiology (Edington et al., 2018). Implementing such human-based *in vitro* models has the potential to transform drug development, offering a cost-effective and efficient approach while reducing reliance on animal studies (Sneddon et al., 2017). Such recent advancements in New Approach Methodologies (NAMs) for non-clinical testing, are now being used in drug development. These innovative approaches, like MicroPhysiological Systems (MPS), encompass a range of *in vitro* techniques that enhance physiological relevance beyond traditional cell culture methods (Avila et al., 2020). These systems, of increasing complexity, are often pioneered by research laboratories, and therefore lack both standardization and accessibility (Mastrangeli et al., 2019). Such new approach methodologies often strive for the reduction of animal models (Díaz et al., 2020).

2.1.2 Early co-culture models

Biological functions rely on both heterotypic and homotypic cellular interactions. To investigate these interactions *in vitro*, co-culture models have proven to be highly versatile tools (W. Li et al., 2018; Puschhof et al., 2021; Yuan et al., 2023). A co-culture refers to a cell culture where two or more distinct cell populations are grown with some level of contact between them. This arrangement serves multiple purposes, including the study of interactions between different cell populations, enhancing the success of culturing specific cell populations (Rheinwald & Green, 1975), establishing synthetic interactions between diverse populations (Kim et al., 2022), and studying secreted factors (Casalena et al., 2020).

Early models involved co-culturing cells on a layer of irradiated feeder cells obtained from easily cultured cancer cell lines (Rheinwald & Green, 1975). When human skin cells are plated together with these 3T3 cells, the growth of human fibroblasts is significantly suppressed, while the epidermal cells develop from individual cells into colonies.

Improving the efficacy of culturing or increasing the differentiation of particular cell populations were a first step towards more complex models.

Subsequently, more complex chambered co-culture models, such as Transwell invasion or co-culture assays, were developed, enabling a more in-depth investigation of cell communication and interplay such as the influence of paracrine factors (Robinson & Craig Jordan, 1989). The spatial separation of the cells shows how these factors affect the growth of hormone-dependent cells.

2.1.3 Micropatterning and hydrogels

New strategies not only enabled the assessment of communication between different cell types but also provide a better understanding of cell interactions with their immediate environment, such as the Extra Cellular Matrix (ECM), and shed light on the effects of mechanical constraints on cells.

To explore the influence of cell-substrate contact and cell shape on the regulation of differentiation, a newly developed method that enables precise manipulation of cell-substrate contact while excluding cell-cell contact was developed (Watt et al., 1988). This technique was later called micropatterning and two mains approaches were developed, micro-contact printing (Kane et al., 1999; Théry et al., 2005), that employ stamps or channels made from elastomeric materials to facilitate the protein patterns transfer, or the use of direct photolithography to pattern ECM proteins by photoablating proteins adsorbed on a surface (Hammarback et al., 1985).

Eventhough growing cells on patterned biologically relevant 2D surfaces helped understanding the role of mechanical constrains, many components of the cell-substrate interactions are not recapitulated as their three-dimensional environment was not yet recapitulated. Some attempts to include a third dimension in these micro-tissues organization were made by casting cells directly on (Civerchia-Perez et al., 1980) or into (Hendrix et al., 1987) hydrogels mimicking the ECM or by letting cells colonize these gels from a 2D layer (L. Wang et al., 2017).

Although growing cells in/on three-dimensional extracellular matrix (ECM) gels has shown some improvement in tissue organization, it still falls short of replicating the structural and functional aspects of whole living organs, which are crucial for their proper function.

2.1.4 Organoids to mimic organs

3D cell self-organization of cells in the form of spheroids or organoids is a biological phenomenon that mimics the natural within tissues and organs. This principle capitalizes on the intrinsic ability of cells to interact and assemble into complex structures without the need for external scaffolding or manipulation.

In spheroids, cells are cultured in suspension, often in a non-adherent environment, allowing them to aggregate and form spherical clusters (Landry et al., 1981). This process resembles how cells naturally come together during embryonic development or tissue repair. Cells in the core of the spheroid may experience reduced oxygen and nutrient supply, leading to gradients of cell states from the core to the periphery (Nashimoto et al., 2017). This organization promotes cell-cell interactions, signal exchange, and differentiation, resulting in the creation of a 3D microenvironment that better reflects in vivo conditions.

Organoids take this concept further by allowing cells to self-assemble into more complex structures that resemble miniaturized organs (Lancaster et al., 2013). This is achieved by providing cells with specific biochemical cues and growth factors that mimic the developmental processes of the organ they are modeling. The cells in an organoid differentiate into distinct cell types and arrange themselves spatially, just like in the actual organ. The resulting structure contains multiple cell types and exhibits rudimentary organ-like functions. Organoids are valuable tools for studying organ development, disease modeling, and drug screening.

Recently, a team combined kidney organoids and disease-relevant cytokine stressors, analyzing single cell transcriptomics, and comparing with human data. They provided evidence for the relevance of the kidney organoid to model human kidney disease, notably FSGS, highlighting the potential for organoids to advance bio-marker development (Lassé et al., 2023)

In summary, 3D cell self-organization in the form of spheroids or organoids harnesses the innate abilities of cells to spontaneously arrange and differentiate, offering a powerful tool for advancing our understanding of complex biological processes and developing innovative approaches in fields like regenerative medicine and drug discovery. While organoids are useful tools for studying solid organs, they are inadequate for mimicking organs that heavily rely on perfusion, such as the glomerulus, as there is currently no efficient method to promote functional vessel formation in kidney organoids (Homan et al., 2019; J. H. Low et al., 2019).

2.1.5 Microfluidics and microfabrication techniques

To enhance the biological relevance of 2D culture, an alternative method involved the utilization of microfluidic chambers. Microfluidics involves the manipulation and control of tiny amounts of fluids within small-scale channels, typically at the micrometer or nanometer scale. The technology principle of microfluidics is based on the physics of fluid behavior at small scales, where factors like surface tension and viscosity become more dominant than in larger-scale systems. This has been used in various scientific and engineering disciplines, including cell biology, by providing innovative tools for studying cells, tissues, and biological processes in highly controlled and precisely monitored environments (Tabeling, 2014).

Microfabricated devices contain channels capable of generating accurate shear forces or gradients of chemotactic factors, enabling controlled delivery and removal of media or molecules directly in the cell environment.

For example, microfluidic chemotaxis chambers (MCC) were able to generate precise gradients of chemotactic factors and studied the migration behavior of human neutrophils in interleukin-8 (IL-8) gradients. The cells displayed strong directional migration towards higher IL-8 concentrations in linear gradients (Li Jeon et al., 2002). In the case of metastatic breast cancer cells (MDA-MB-231), MCC was used to investigate chemotaxis in response to epidermal growth factor (EGF) gradients. MDA-MB-231 cells exhibited increased speed and directionality when exposed nonlinear EGF gradients (S. J. Wang et al., 2004).

Some cells *in vitro* are actually sensitive to shear stress (Friedrich et al., 2006), (S. H. Yang et al., 2017), strain (Dessalles et al., 2021) or stretch (Endlich et al., 2001) and actually require shear forces to differentiate. The same is also true for tensile stress (Endlich et al., 2001), and curvature (Korolj et al., 2018). These relevant quantities are often brought to the cells using microfluidics or

microfabricated devices. An experiment employed a conditionally immortalized mouse podocyte cell line to examine the effects of fluid shear stress in a flow chamber. This setup imitated the flow of glomerular ultrafiltrate across podocyte surfaces within Bowman's space. When shear stress exceeded 0.25 dyne/cm^2, there was a significant loss of podocytes within 20 hours, while proximal tubular epithelial cells remained unaffected (Friedrich et al., 2006).

Designing and perfusing such microfluidic culture systems, even for routine culture of adherent mammalian cells, present several technical challenges. Flow rate control is a critical parameter to manage, as a pipetting error can generate enough hydrostatic pressure to induce uncontrollable flow rates within the microchips (Lochovsky et al., 2012). External flow controllers, such as syringe pumps, peristaltic pumps, or pressure-driven pumps, are commonly used to deliver flow and ensure precise fluid control at the microfluidic scale.

Accurate control of flow rate is essential for achieving laminar flow in microfluidic systems, allowing for the controlled application of shear stress. For tissue types highly perfused *in vivo*, such as the liver and kidney, microfluidic perfusion culture can more closely mimic the *in vivo* microenvironment where cells are in proximity to the microvascular network. By preserving *in vitro* models that retain the *in vivo*-like phenotypes of cells from these tissues, biologically meaningful data can be obtained during cell-based assays.

2.1.5.1 Microfabrication techniques

Photolithography is one of the most widely used techniques in microfabrication. It involves using light-sensitive materials (photoresists) and a mask to pattern a substrate (Duffy et al., 1998). UV light is shone through the mask onto the photoresist-coated substrate, creating a patterned resist. The exposed or unexposed areas can then be selectively etched, or treated, to form channels, chambers, or other structures. Photolithography is used to create the master mold for replicating the microfluidic device.

Photolithography is often used to fabricate molds for replicating channels using soft-lithography, which is a versatile technique that involves using elastomeric materials, such as PolyDiMethylSiloxane (PDMS), to create replicas of microstructures (Alvaro et al., 2005). PDMS is cast onto the mold and cured to create a flexible replica. PDMS replicas can then be bonded to glass or other substrates to form functional microfluidic devices. Soft lithography is favored for its simplicity, flexibility, and low cost. PDMS is the most commonly used material for fabricating microdevices used in cell culture and cell-based assays (Alvaro et al., 2005). PDMS offers several advantages, including high transparency, good mechanical properties in the MPa range, easy sterilization and functionalization, and biocompatibility. The dimensions of microchannels that best suit PDMS characteristics typically range from 5 µm to millimeters (Alvaro et al., 2005).

Microcontact printing is a subset of soft lithography that involves using elastomeric stamps to transfer molecules or patterns onto a surface (Flachsbart et al., 2006). This technique is often used to functionalize microfluidic devices with specific chemical or biological molecules.

Hot embossing involves pressing a heated mold into a polymer substrate to create microstructures (Gates et al., 2005). This technique is suitable for high-throughput replication of microfluidic devices and is commonly used for large-scale production. Similar to hot embossing,

injection molding uses a mold to create microstructures in a polymer substrate. It is a high-volume manufacturing technique used to create microfluidic devices in large quantities.

In addition to replication techniques, direct machining of plastics or elastomers can be achieved through methods such as laser ablation. In laser ablation, the local application of an intense laser beam causes the sublimation of plastics. UV, CO_2, and femtosecond lasers are commonly utilized in this technique (Y. Fan, 2018). It is a flexible technique that can be used for rapid prototyping and small-scale production.

Micromilling is a subtractive manufacturing technique used to create microstructures and features on various materials, including polymers, metals, and ceramics. In the context of microfluidics, micromilling involves using computer-controlled milling machines to create precise channels, chambers, and other structures in substrates, typically on the scale of micrometers to millimeters (Jiménez-Díaz et al., 2019).

Additive manufacturing techniques, such as 3D printing, are becoming more popular in microfluidics. They allow for the direct fabrication of complex 3D microfluidic structures, enabling rapid design iterations and customization. They can either be based of stereolithography or extrusion based printing methods (He et al., 2016).

The extreme application of this concept is 3D bioprinting. 3D bioprinting utilizes a 3D printer-like device equipped with specialized print heads that dispense bioinks (cell-laden materials) in a controlled manner (Lee et al., 2020). The bioinks can consist of living cells, hydrogels, polymers, and growth factors that are suitable for the target tissue or organ (Figure 27). These materials are deposited layer by layer to create a complex 3D structure. The process is often guided by computer-aided design (CAD) models to achieve specific tissue geometries.

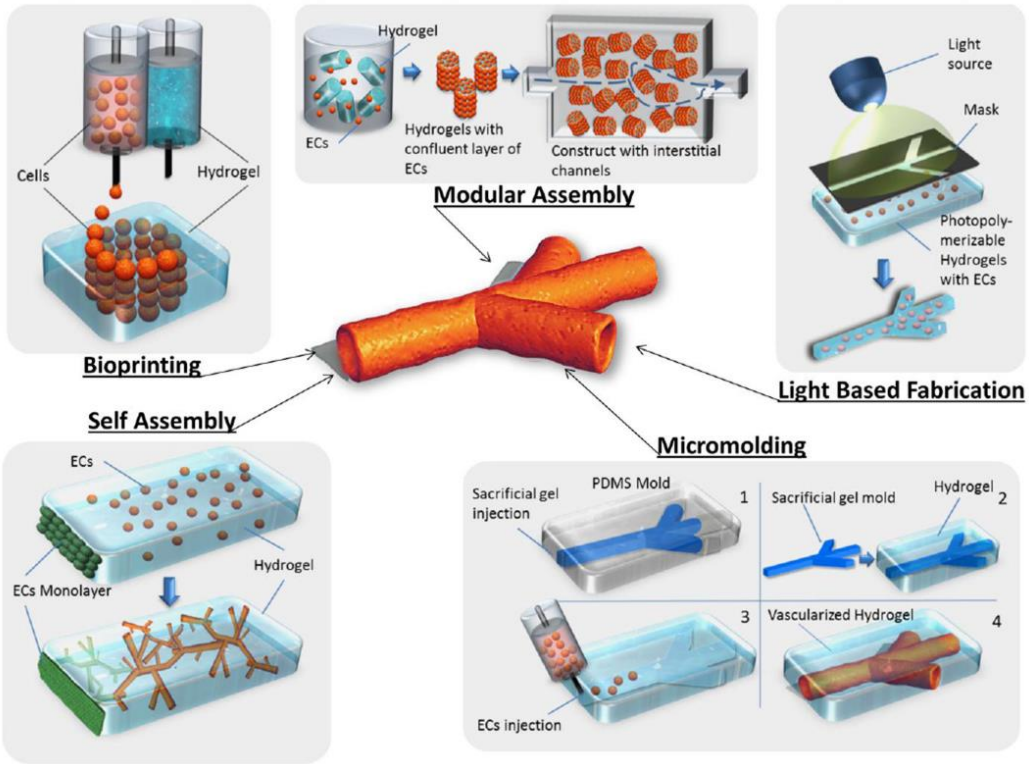

Figure 27: Some current microfabrication approaches for the generation of microvascular networks. Image from (Bersini et al., 2016).

2.1.6 Control of the structure to recapitulate organ functions (towards Organs-on-a-chip)

Organ-on-chip (OoC) technology is an innovative approach that aims to recreate the structure and functions of human organs or tissues in miniature devices, often referred to as "chips." These chips contain microfluidic channels, cells, and biomimetic environments to simulate the complexities of human physiology and disease in a controlled laboratory setting (Huh et al., 2010).

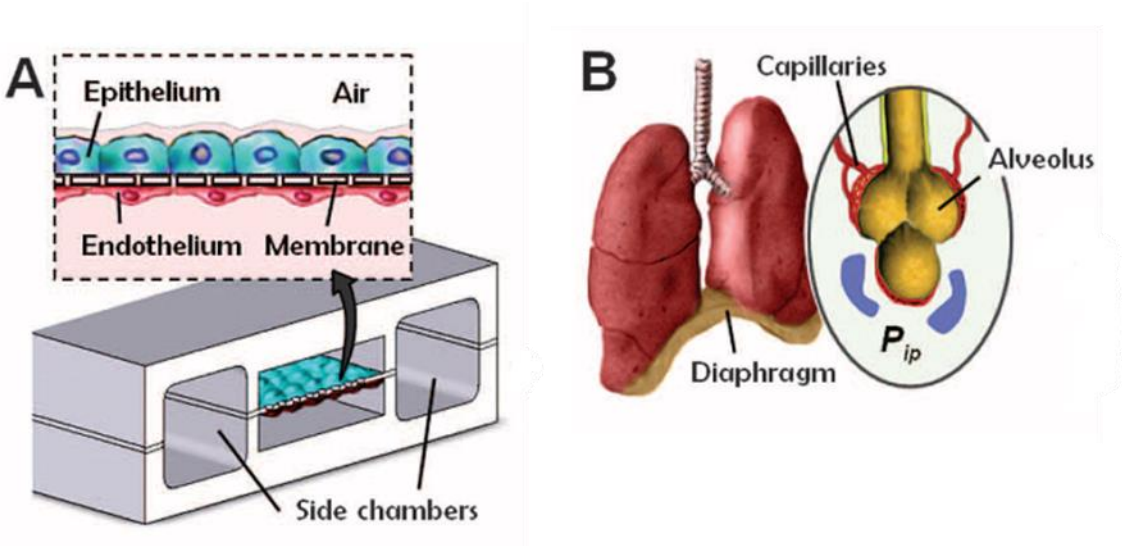

Figure 28: Biologically inspired design of a human breathing lung-on-a-chip microdevice. (A) The microfabricated lung mimic device forming the alveolar-capillary barrier (B) from (Huh et al., 2010).

These models often employ microfluidics to control the organization of co-cultured pluripotent or differentiated cells and enable the application of dynamic mechanical forces such as breathing movements, shear stress, peristalsis, and tension that are critical for the development and proper functioning of living organs (Low et al., 2021).

Organ-on-a-chip systems (or OoCs) have become valuable and powerful tools for integrating cells/microtissues and hydrogels into microfluidic devices with precise control over multiple microphysiological environments, allowing for the recreation of in vivo-like 3D microstructures and specific organ functions (Vunjak-Novakovic et al., 2021). Organ-on-chip platforms, with their higher structural complexity, have the potential to mimic tissue or organ homeostasis and functions more effectively. For example, an organ-on-chip platform mimicked the alveolar-capillary interface of the human lung (Huh et al., 2010). This device was mechanically active modeling the breathing motion of the lungs. This mechanical stress/strain enhanced cellular uptake of nanoparticulates and their transport into the pseudo vascular channel.

As an alternative to conventional 2D cell culture or animal models with species differences, organ-on-a-chip technologies offer tremendous potential in drug development, personalized medicine, and disease modeling.

2.2 Kidney-on-a-chip technology

2.2.1 State of the art

In vitro kidney multicellular systems, either in the form of spheroids (Tuffin et al., 2021) or organoids (J. H. Low et al., 2019; Raikwar et al., 2015; Takasato et al., 2015) have previously been developed. Kidney organoids have not attained an adequate level for evaluating the selectively permeable function of the glomerular filtration barrier owing to the lack of capillary loop formation in the glomerulus (Hale et al., 2018; Homan et al., 2019; J. H. Low et al., 2019).

Glomerulus-like chips, on the other hand, have demonstrated the reconstitution of key glomerulus features such as differentiation and filtration (Hart et al., 2023; Iampietro et al., 2020; Musah et al., 2017; Petrosyan et al., 2019; Roye et al., 2021; L. Wang et al., 2017; Xie et al., 2020; Zhou et al., 2016). They either use stem cells of differentiated cells derived from different origins to recapitulate the Glomerular Filtration Barrier (GFB) composed of Glomerular Endothelial Cells (GEnCs) and Podocytes separated by a membrane.

The use of co-culture of human induced Pluripotent Stem Cells (iPSCs) has notably been applied to glomerulus-like chips (Musah et al., 2017; Roye et al., 2021). In these systems, the filtration function was observed, through the co-culture of two different cell types (iPSCs derived podocytes and endothelial cells) on two sides of synthetic membranes (*e.g.* holed PDMS/PET/PFTE) in a commercial organ-on-chip system (Emulate). Other approaches rely on the use of either murine primary cells (Hart et al., 2023; L. Wang et al., 2017; Zhou et al., 2016) or human conditionally immortalized and primary cells (Iampietro et al., 2020; Petrosyan et al., 2019; Xie et al., 2020).

Though some systems can recapitulate filtering properties, they cannot mimic the actual glomerulus structure with two small (tens of microns) vascular and urinary chambers separated by a thin and specialized basement membrane. None of the models included parietal epithelial cells which adds a third layer in the microsystems (delimiting Bowman's space). Furthermore, no efficient quantitative monitoring either of cell responses (migration, proliferation) or molecular events was associated with these devices, since no microsystems are optimized for both imaging and physiological modeling of the glomerulus.

2.2.2 Limits

2.2.2.1 Accessibility

Organ-on-chip platforms aim to mimic the physiological conditions of the human body as closely as possible. This often imposes a geometry to mimic an organ, such as for membrane systems where the membrane often separates two superimposed microfluidic channels (Ingber, 2022).

Glomerular function involves intricate fluid dynamics and cellular interactions. To capture these aspects comprehensively, a combination of imaging modalities (such as fluorescence, confocal, or super-resolution microscopy) may be required. Glomeruli are tiny structures with intricate features that need high-resolution imaging techniques to capture their details accurately. Conventional imaging systems may struggle to achieve the required spatial resolution to visualize fine structures within the glomerulus. The major limiting factor up to date are the dimensions of the commercial systems with large channels (hundreds of micrometers) that both limits biomimetic mimicry of the glomerulus and imaging capabilities.

Bringing the possibility to have high numerical aperture (N.A.) microscopy, allowing high resolution imaging to be performed on a glomerulus-on-chip model with biomimetic dimensions, would allow an optimal accessibility.

2.2.2.2 Membrane versatility

Moreover, having the ability to use different types of membranes in organ-on-chip platforms is crucial for modeling barrier systems accurately. Barrier systems, such as the glomerular filtration barrier, play a fundamental role in regulating the exchange of molecules and maintaining homeostasis. Commercial systems are limited usually to one type of membranes, with defined hole size, thus limiting the versatility of organ-on-chip to model complex systems that would need tailored membranes.

By being able to incorporate various types of membranes one can better mimic the physiological conditions, since each barrier has its own selective permeability and transport mechanisms. By using membranes that mimic the properties of healthy and diseased barriers, we can accurately represent the pathophysiological conditions associated with specific diseases. Some specific aspects of barrier function, such as composition, permeability, or response to mechanical forces are critical to model membrane systems accurately.

Hence developing a microsystem allowing membrane versatility and biomimetic membranes is of critical importance.

2.2.2.3 Keeping costs and complexity to a minimum

Maintaining low costs for organ-on-chip platforms is also critical for several reasons, primarily to promote accessibility, scalability, and widespread adoption of these innovative technologies. Affordable platforms are critical in areas such as drug development, disease modeling, and toxicology testing, that often require a substantial number of replicates for statistically significant results. Reducing costs for organ-on-chip platforms can also contribute to the reduction of animal testing.

Moreover, tubing setups for perfusion can be intricate and time-consuming to assemble. Each chip may require multiple tubing, connections, and pumps, making the setup process more complex, especially when dealing with a large number of chips. Regular monitoring, troubleshooting, and recalibration may be needed, adding to the time and effort required. Allocating these resources for a large number of setups may strain laboratory capabilities. Tubing used for delivering perfusion can be a potential source of contamination, affecting experimental outcomes, especially when working with sensitive cell cultures or biological samples.

Setting up and managing a large number of tubing connections requires additional space in the laboratory. This can be especially challenging in labs with limited physical space such as cell culture labs. The costs associated with purchasing, maintaining, and replacing tubings, connectors, and pumps for a high-throughput setup can be substantial.

To address these limitations, we should strive for simple fabrication process of microsystems, and for interconnected (with few tubings) or even towards tubeless perfusion systems.

2.2.2.4 A 3-layer system

So far, all glomerular models focused of recapitulating the Glomerular Filtration Barrier (GFB), composed of Glomerular Endothelial Cells (GEnCs) and Podocytes separated by a basement membrane. None of them accounted for the presence and role of Parietal Epithelial Cells (PECs).

Adding PECs to fully model the glomerulus in an organ-on-chip platform is of critical importance for several reasons. PECs play a crucial role in the function and structure of the glomerulus *in vivo* (Kaverina et al., 2020). Including them in the organ-on-chip model helps replicate the complexity of the native glomerular environment, enabling more accurate and physiologically relevant studies. PECs contribute to the formation of the Bowman's capsule and help create a urine tight barrier between the urinary space and the glomerular capillaries (Shankland et al., 2014).

PECs are implicated in various kidney diseases, including crescentic glomerulonephritis (CGN) and focal segmental glomerulosclerosis (FSGS) (Moeller & Smeets, 2014). Integrating PEC cells allows first to study the specific role of these cells in disease progression and test potential therapeutic interventions.

PECs interact closely with other cell types in the glomerulus, such as podocytes (Wrede et al., 2020). Their presence in the model enables the study of intricate cell-cell communication, helping to uncover novel insights into cellular interactions and signaling pathways.

These limitations show a clear roadmap for the development of an organ-on-chip platform to model accurately the glomerulus in a device compatible with; several imaging modalities, the ability to use several types of membranes, keeping costs and complexity of the system to a minimum, and adding PECs to the model.

2.3 Building a microfluidic device compatible with imaging

While OoC devices provide advanced culture systems for replicating the *in vivo* condition more accurately, one of the main issues remains to monitor complex mechanisms within the newly arranged cells in their complex geometry. This issue is often addressed by the integration of sensors within the microsystem or by designing a probe compatible system from the beginning (Aydogmus et al., 2023; Kann et al., 2022; Zhang et al., 2017).

Here our objective was to design from the start a microsystems suitable for imaging to be able to observe fine changes in glomerular cells organization, differentiation, or migration, as well as imaging down to the molecular scale through super resolution techniques. For this, the difficulty was first to realize a two-layer PDMS/glass microsystem, composed of two chambers (mimicking respectively the capillary and the Bowman space) separated by either a porous synthetic membrane (polyethylene terephthalate, PET) or self-supported biomimetic membranes made of collagen and basement membrane proteins (*e.g.* laminin, collagen IV). Secondly, to realize this systems directly on a glass coverslip, providing and adequate “optical-window”, allowing virtually any type of microscopy to be performed in the device (Figure 29).

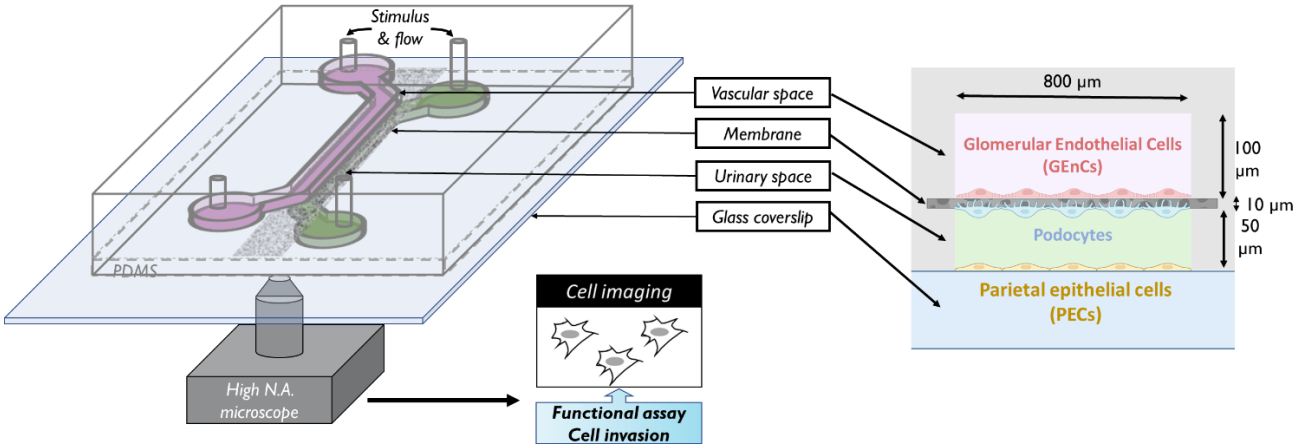

Figure 29: Imagined "optical-window" microsystem to mimic the glomerular organization.

2.3.1 Designing a microphysiological system

Efficient dimensioning of the system results in a harmonious balance between optical and biological considerations. It is crucial for the system to maintain relevance within biological orders of magnitude, such as the filtration surface, spacing separating different cell types, flow rates, and shear stress. Compatibility with imaging techniques was essential to enable effective visualization and monitoring of the cellular processes within the microsystem. Striking this balance ensured that the organ-on-chip system could accurately replicate physiological conditions while allowing for detailed observation and analysis of the biological interactions taking place.

2.3.1.1 Optical considerations

The primary focus of the design is to replicate the organization of the glomerulus while ensuring compatibility with imaging at various scales, from single molecules to the cellular and tissue levels, both in *live* and fixed conditions.

Various imaging modalities have been considered for this project, including:

- *Live* imaging to follow cell migration/proliferation with or without fluorescent reporters (contrast enhanced transmission or epi-fluorescence microscopy), at low to medium resolution (10 to 40X magnification).
- Full system volume imaging at high speed and low photo-toxicity (light-sheet (Albert-Smet et al., 2019), confocal with resonant scanners, Line-field Confocal Optical Coherence Tomography LC-OCT (Ogien et al., 2020),…), for short to long time scales to extract functional information, such as filtration, or the tissue response to stimulation (response to long term stimuli such as gradients of molecules of shear stress), at low to medium resolution (20-40X).
- High resolution imaging to assay for precise morphology and differentiation of cells using 3D imaging of the whole system (Confocal, optical sectioning in epi-fluorescence/apotome (Chasles et al., 2007) 40 to 100X).
- Super-resolution imaging (Structured or Random Illumination Microscopy (SIM (Gustafsson, 2000) or RIM (Mangeat et al., 2021)), Single Molecule Localization Microscopy (SMLM) (Betzig et al., 2006), (Rust et al., 2006)) to access unprecedented resolution in a 3D microsystem allowing characterization down to the molecular scale.

- Single molecule imaging techniques (Single Particle Tracking (SPT), single nanoparticles imaging, Fluorescence Correlation Spectroscopy (FCS),…), compatible with live imaging to have access to molecular dynamics in the device.

Most of these imaging techniques have been adapted for commercially available inverted microscopes and are being acquired by imaging platforms. Careful dimensioning of the system is crucial to avoid limitations in 3D imaging capabilities due to high magnification (and high numerical aperture, N.A.) objective's short working distances (~100 µm from the coverslip surface for a 100X objective). Furthermore, single molecule imaging requires a N.A. at least equal to 1.3. Additionally, high N.A. objectives are often corrected for chromatic and spherical aberrations in the window of the working distance, specifically designed for 170 µm glass coverslips. Going for a thinner bottom surface than 170 µm could be considered by using custom bottom surfaces like optically transparent polymers (COP/COC).

The main objective was to ensure that the height of the systems remains within the working distance of most objectives using a conventional glass surface as an "optical-window," allowing various microscopy techniques in the system. Precise control of the membrane height was achieved using microfabrication techniques. The aim was to make all three layers of cells optically accessible, with the top layer of endothelial cells situated just below this maximal working distance of 100 µm to be able to resolve them.

The membrane used in the devices also plays a major role in optical properties of the whole system as it is equivalent to introducing a strong change in refractive index in the optical path. A sudden change in refractive index can lead to abrupt changes in the path of light, causing reflections, scattering, and optical aberrations. This can result in degraded image quality, reduced resolution, and loss of contrast, or imaging artifacts, such as halo effects, glare, or shadows, which can obscure or distort the features of interest in the sample.

Specialized imaging methods, such as adaptive optics, may be employed to compensate for aberrations caused by refractive index variations and improve image quality (Saha et al., 2020). Overall, understanding and managing refractive index changes are crucial to obtaining accurate and reliable 3D microscopy results, but remain a complicated task to tackle.

Collagen I scaffold have been reported to be of interest for ophthalmological grafts applications due to their high transmittance and ability to sustain cell growth as a scaffold (Tidu et al., 2018). Previously reported collagen vitrified membranes refractive index values range from 1.33 to 1.34 (Calderón-Colón et al., 2012), which closely match that of biological tissues and water. On the other hand, PET, which is among the most commonly used membrane material to model biological barriers, has a 1.5709 refractive index at 570 nm. While PET membranes are transparent and around 10 µm thick, it can be assumed that their optical properties will significantly decrease imaging capabilities compared to biomimetic membranes.

Considering imaging speed, it is important to find a balance where the whole volume of the system can be imaged relatively quickly while remaining physiologically relevant. This will drive the lateral dimensioning of the system to limit acquisition time. With a few hundreds of micrometer width, a 20X magnification can efficiently capture most of the system (around 500 µm field of view) and a few fields of view in length (approximately 1-2 mm), making it feasible to capture the entire

system within a few tiles (around 10) on a confocal microscope. This approach ensures efficient imaging without compromising the system physiological representation.

2.3.1.2 Physiological considerations

Mimicking the complex 3D structure and close cellular proximity of the glomerulus poses significant challenges in the design of the microsystem. The glomerulus is highly perfused and has dimensions of around 100/200 µm in diameter (Vimtrup, 1928). One crucial aspect to replicate is the close proximity or vicinity of the different cell types encountered in the glomerulus, such as glomerular endothelial cells and podocytes separated by a basement membrane at the scale of a few tens of nanometers (Farquhar, 2006), and parietal epithelial cells being a few tens of micrometers away from podocytes (Appel et al., 2009). To facilitate cell contacts and exchanges, the height of the membrane defining the separation space between parietal epithelial cells and podocytes should not exceed this order of magnitude. A membrane height of around 50 µm is deemed appropriate and feasible in terms microfabrication and is also in agreement with the optical design, as illustrated in Figure 30.

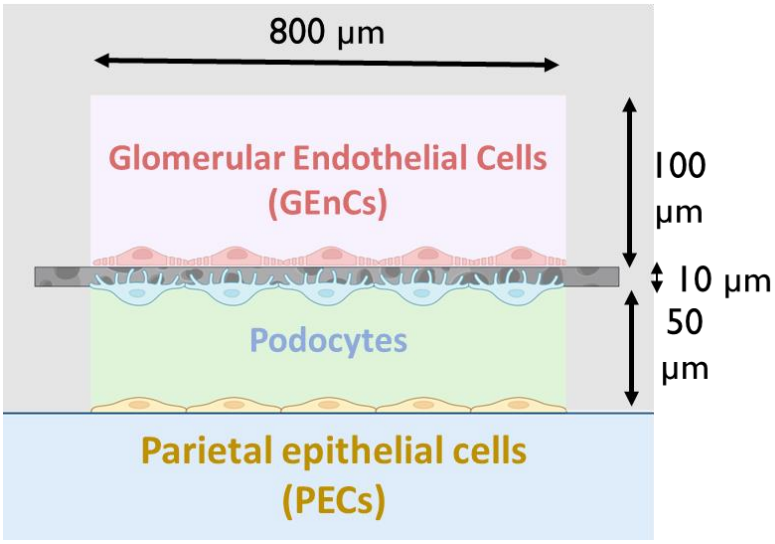

Figure 30: Dimensions of the Glomerulus-on-chip.

The choice of the membrane used in the device plays a pivotal role in mimicking physiological conditions. Biomimetic membranes in organ-on-chip platforms offer the potential to investigate the impact of the extracellular matrix (ECM) scaffold on cell differentiation, and phenotype. Furthermore, they can be employed to study ECM remodeling over time in disease contexts.

However, accurately recapitulating the basement membrane is complex as it is not made of a single fibrillar component (Miner, 2012; Shirato et al., 1991). Fibrillar collagen I, which is not normally part of the basement membrane, is often used as a fibrillar support for other biomimetic membrane and allows membranes to be manipulated to be incorporated into microdevices (Dems et al., 2020; Mondrinos et al., 2017a). Additionally, precisely tuning collagen permeability and thickness in a repeatable manner may prove to be more complicated compared to synthetic PET membranes.

In contrast, the thickness of PET membranes obtained from commercial sources is not controllable (~10 µm). However, the pore size of these membranes can be chosen, ranging from 0.4

to 8 µm. Choosing an appropriate pore size is critical for filtration experiments, as a too small pore size could artificially increase the free diffusion time of molecules across the membrane, while a too large pore size might allow cells to cross the membrane and perturb the organization of the cell layers. It is essential to strike a balance in pore density to enable efficient exchange between the urinary and vascular compartments. Table 1 summarizes characteristics of commercial Transwell inserts PET membranes, providing valuable insights for selecting an appropriate membrane for the microsystem.

Table 1: Pore size and density of commercial PET Transwell inserts membranes.

$0{,}4\ \mu m\ pores\ \approx 4.10^6\ pores/cm^2 \approx\ 0{,}5\ \%\ of\ total\ membrane\ surface$
$3\ \mu m\ pores \approx 2.10^6\ pores/cm^2 \approx\ 14\ \%\ of\ total\ membrane\ surface$
$5\ \mu m\ pores \approx 6.10^5\ pores/cm^2 \approx 12\ \%\ of\ total\ membrane\ surface$

To maximize the exchange surface for filtration experiments while preventing cell transmigration, a membrane with 3 µm pore size appears to be well-suited for the microsystems.

In designing the microsystem, one approach is to aim for relevant quantities of the actual organ being mimicked. For instance, in the case of the human glomerulus, a MPS should ideally recapitulate the filtration surface of a glomerulus. While the exact total glomerular filtration area in humans is challenging to determine precisely, estimates suggest it to be around 500 cm^2, with approximately two million glomeruli in both kidneys (Bohle et al., 1998). This would mean that the filtration surface per glomerulus is approximately 0.025 mm^2, corresponding to an area of 25 µm × 1 mm. Achieving such precise alignment when assembling compartments in the microsystem could be challenging.

The total retained dimensions of the microsystem are a 32 mm^2 total culture surface (channels and inlets/outlets) for each cell type (spread across 3 cell layers), with a channel width of 800 µm and a microchannel length of 8 mm, with 2 mm shared between the top and bottom compartments (resulting in a co-culture surface of 1.6 mm^2). This configuration would recapitulate approximately 60 times the filtration surface of a single glomerulus. This ensures that the microsystem provides a substantial representative filtration area, enhancing its functional relevance for mimicking glomerular organization and physiological processes.

Indeed, in order to mimic the glomerulus as a perfused organ, it is crucial to consider quantities related to flow in the microdevice. Flow rates and shear stress experienced in the glomerulus are important factors to replicate for functional accuracy. To achieve this, the microsystem should be designed with channels that allow for easy control and recapitulation of flow rates. Proper flow control and recapitulation of shear stress are essential to ensure the success and relevance of the microphysiological system as a model for studying glomerular function and interactions between different cell types within the glomerulus. The glomerular capillary flow rate is estimated between 5 and 15µl/min (M. Zhou et al., 2016a).

Different perfusion techniques to optimize the flow dynamics within the microdevice will be explored and discussed in the following sections (see section: 2.4.2).

2.3.2 Microfabrication and characterization

The microsystem is specifically engineered to replicate the structure and function of the glomerulus. It consists of three primary components:

Bottom optically accessible layer: this layer is designed to house the lower urinary chamber. It allows for optical access, enabling visualization and monitoring of cellular processes and interactions within the chamber. The material and design of this layer are thus carefully selected to ensure optimal imaging capabilities and compatibility with the biological components.

The membrane is a crucial component of the microsystem. We explored two alternatives, a PET membrane with a specific pore size or a self-supported collagen I-based membrane of controlled thickness. Both membrane options are designed to facilitate a co-culture environment, closely resembling the glomerular basement membrane (GBM), which is essential for mimicking the natural interactions between podocytes and endothelial cells in the glomerulus.

The top layer of the microsystem accommodates the vascular channel, as well as inlets and outlets for the microfluidic system. This configuration allows for the controlled introduction of cells and flow within the device. Precise and localized fluid flow is essential for creating physiological conditions, facilitating nutrient supply, and mimicking the microenvironment present in the glomerulus.

Each of these layers is fabricated separately before the final assembly of the microsystem. Specific techniques are employed to characterize the properties and structural features of each layer. The combination of these carefully designed components results in a functional and biomimetic glomerulus-on-chip microsystem (Figure 44, B).

2.3.2.1 Photolithography, micromilling and soft-lithography

The top layer of the system is realized through photolithography or micromilling, and PDMS soft lithography.

To realize the microchannel we fabricate a negative mold of the desired shape, this allows later replicating of the channels by casting elastomers that will give the microchannels (Figure 2). This process of replicating a structure using a mold is called soft-lithography (Rogers & Nuzzo, 2005). Then the critical part of this process is to realize accurate molds using microfabrication techniques. The aim is to obtain high aspect ratio molds that are long lasting, allowing the casting of elastomer several times from the same molds. Given the aspect ratio (800:2000 µm) of the desired shape of the microsystem many microfabrication techniques could have satisfied our needs to realize molds later used to replicate the microchannels, such as Stereolithography (SLA) 3D printing, micromilling, photolithography, Selective Laser Sintering (SLS),…

2.3.2.1.1 Photolithography

Photolithography is a fast and efficient process that enables the exploration of various geometries for rapid prototyping, all while maintaining cost-effectiveness when utilizing desktop lab equipment (Pan & Wang, 2011). Through this method, we conducted several tests to determine the optimal channel width and height that would result in the most effective microsystem assembly and cell seeding conditions.

In the typical photolithography process, an optical mask is employed to transfer a geometric design onto a light-sensitive chemical (photoresist) coated on the substrate, usually using ultraviolet light (UV). The photoresist undergoes changes where it is exposed to the light, either breaking down or hardening. Subsequently, the patterned film is formed by selectively removing the softer parts of the coating using appropriate solvents, also referred to as developers in this context (Figure 31).

Lithography masks were generated using an offset printer (Figure 32). These masks were created by employing laser flashing on a transparent plastic film. The lateral resolution of the masks is limited to the width of the laser Gaussian profile, which affects the ability to precisely resolve complex features due to the inertia of the laser scanning process.

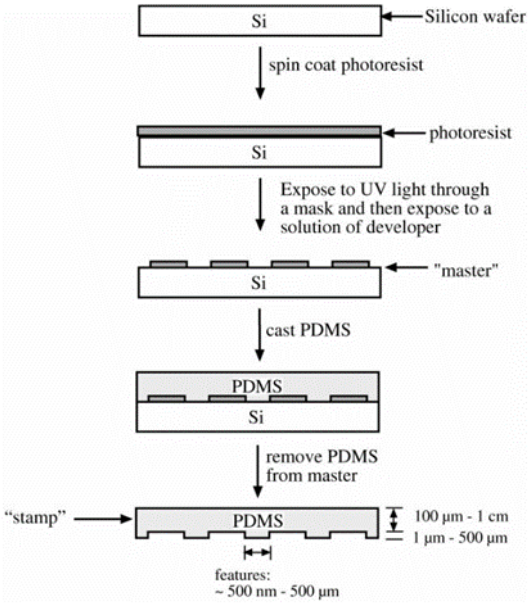

Figure 31: Scheme of photolithography and soft-lithography adapted from (Kane et al., 1999).

The mask designs were created using an open-source vectorial drawing software (Inkscape), offering flexibility and ease of design. Total dimensions of the systems are a 32 mm^2 of total culture surface for each cell type (3 layers) with a channel width of 800 µm a 8 mm long microchannel, and 2 mm of this channel is to be shared between the top and bottom compartments (or a co-culture area of 1.6 mm^2).

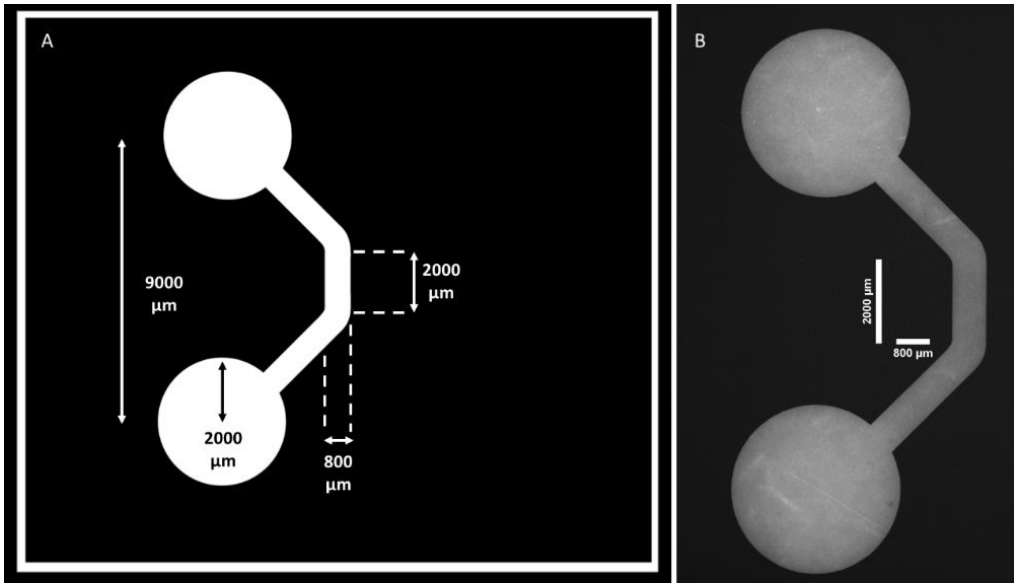

Figure 32: A) Vectorial drawing of the desired mask, B) Mask obtained by laser flashing imaged with a macroscope (7,5X magnification).

For the photolithography process, instead of using a photo-sensitive resin (SU-8) spin-coated on a wafer, readily available photoresist films of different thickness can be directly used as a substrate for photolithography (Farjana et al., 2021). The top channel molds are realized using the dry film photoresist soft lithography technique. The photoresist layers (Laminar E9200 dry negative films, 50 µm thick, Eternal Chemical) are laminated onto a clean glass slide (24 × 60 mm) using an office laminator (Peak) at 100°C. To obtain the desired thickness several layers of dry film are laminated on top of each other. To obtain a 100 µm channel height 2 layers of resists were stacked.

It was then exposed to UV light (Kloé UV Kub1, 100% power, 120 seconds of continuous exposure) through the photomask. The resist is then developed by immersion in an aqueous bath of carbonate potassium at 1% mass concentration until the glass surface is fully cleared of unexposed resist and left to dry in the dark for one day.

Obtained molds were characterized using reflection light microscopy, mechanical probing, and White Light Interferometry (WLI) to determine accurately the obtained channels height and width (aspect ratio) of the structures as well as the repeatability of the fabrication process (Figure 33).

To measure the channel molds width obtained with photolithography, molds were examined under a reflection metallurgical microscope (Kern optics) equipped with a CCD camera, and two 5X and 10X objectives. The calibration of the actual image pixel size was done using a standard step-height pattern (Filmetrics SHS-16160) with 200, 100, 50, and 20 µm lines patterns. The mean channel width obtained with photolithography was $775 \pm 5\ \mu m$ (Figure 33). This dimension was slightly smaller than the mask mean width ($798 \pm 1\ \mu m$), this is probably due to two factors, first there is a border effect when illuminating through the mask during UV curing, and secondly, the development process is controlled only with visual examination, so that we could in general over develop the resists. The dimensions remained close enough to the target width.

To have a good first appreciation of the channels height quickly after manufacturing the molds, an electronic sliding caliper was used to measure the difference in height of the channels from the mold surface. The mean channel height obtained was $95 \pm 3\ \mu m$ (Figure 33) which corresponds to laminating two 50 µm photoresists sheets (Figure 31).

The height of the microchannels was also assessed using a WLI profilometer (Profilm3D). White light interferometry is an optical technique used to non-contactly measure surface height of 3D structures. It is applicable to surface profiles ranging from tens of nanometers to a few centimeters (Pavliček & Mikeska, 2020). It functions as a Michelson interferometer utilizing a broadband light source, a CCD camera serves as a multi-detector at the interferometer's output. The object being measured replaces one of the interferometer's mirrors, while the other mirror functions as the reference. The reference mirror position defines the reference plane within the object arm, and its distance from the beam splitter mirrors the distance of the reference plane from the beam splitter (Figure 33).

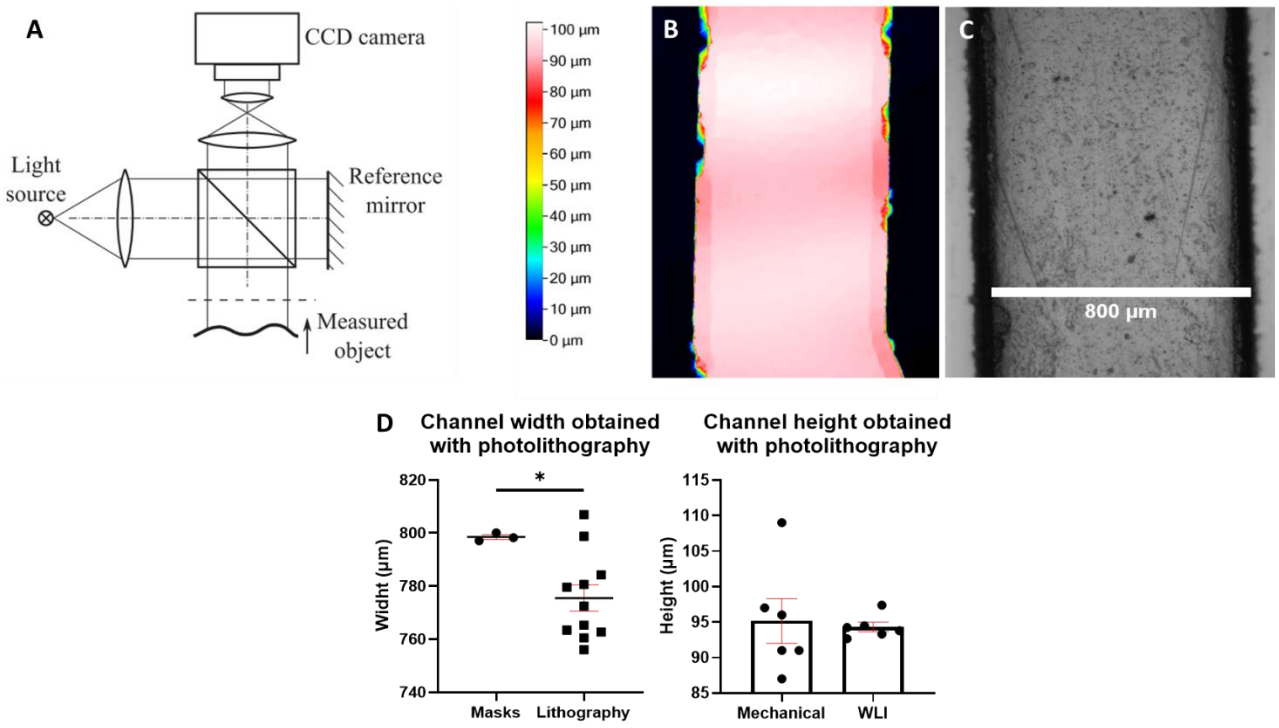

Figure 33: A) Typical setup for WLI from (Pavliček & Mikeska, 2020), B) height map obtained by WLI profilometry (10X), C) reflection image of mold obtained by dry film photoresist photolitography (10X), D) width and height distribution of molds obtained by dry film photoresist photolithography (error bars are SEM).

This profilometer uses a 10X objective with a 2 mm field of view allowing the measure of the whole channel height. An example of the height map obtained using WLI is shown Figure 33, B. For each measure on a microchannel, triplicate measures were done by the profilometer and then averaged. We obtain a $94{,}0 \pm 0{,}7\ \mu m$ mean channel height (Figure 33, D).

While allowing a rapid prototyping approach dry film photoresists molds lifespan are actually limited, hence the need to develop news molds after a few tens of elastomer casting on top of channels. Since these molds are temporary, we decided to realize permanent mold that will not be affected by the elastomer casting process over time. This was done through aluminum micromilling.

2.3.2.1.2 Micromilling

Micromilling has also been used to obtain molds usable for soft-lithography. The requirement is to obtain flat surfaces to allow similar surfaces of the replicas, needed to bond the different components of the system. A variation kept below a few microns allows bonding of the surface.

We thus designed numerical models of our molds to perform aluminum micromilling. Aluminium molds were fabricated using Computer Numerical Control (CNC) micromilling on a Datron M8Cube. The design and milling steps were programmed using Autodesk Fusion 360. Briefly, a 5 mm aluminium foil was first reduced to the desired outlined shape using a 3 mm bur, then a 1 mm bur was used to finalize the patterns removing 50 µm at each pass. 4 microchannel molds were milled from the same piece of aluminum foil and characterized individually for the channel width and height using the techniques previously described.

We obtained accurate lateral dimensions with this technique, the channel target with was 800 µm and was measured at $801 \pm 2\ \mu m$, and we obtained a $135 \pm 6\ \mu m$ height by mechanical measurement, and the height measured with WLI was $134 \pm 4\ \mu m$ (Figure 34). This 35 µm observed offset is due to a mistake in programming the CNC steps file (target 130 µm).

Regarding the surface aspect, the quite large height error measured with WLI is in fact due to small (up to 3 µm deviation from the mean height) and localized surface asperities (Figure 34). These were created as the bur passes on the surface of the channel to remove aluminum, with a 300 µm overlay in different pass directions creating these slight patterns on the metal surfaces.

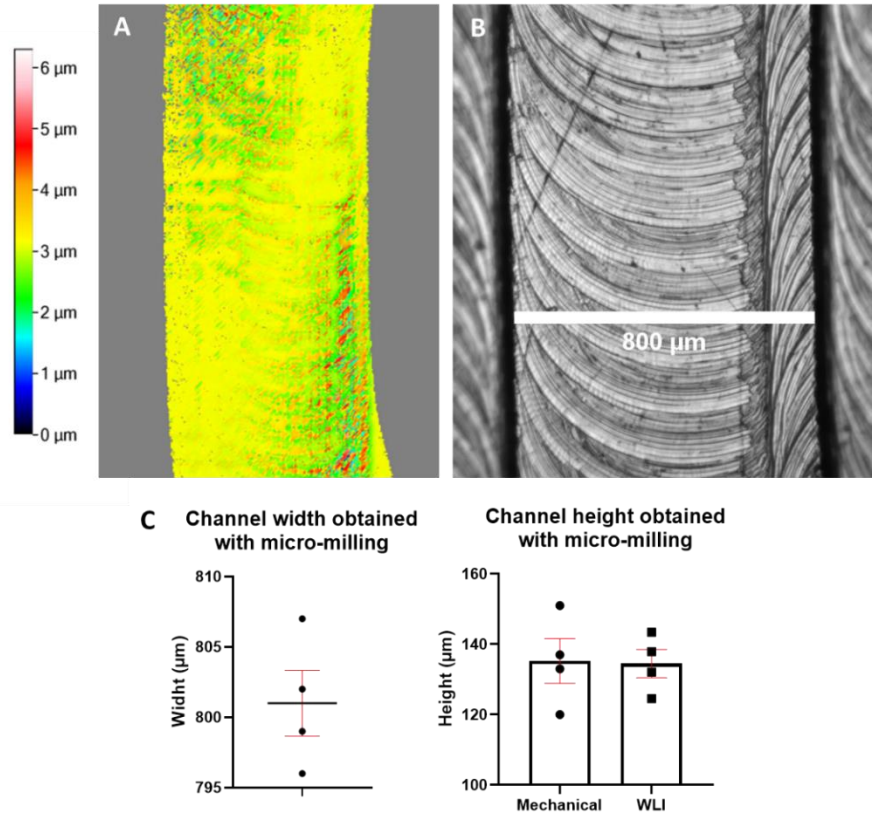

Figure 34: A) Height map obtained by WLI profilometry (10X), B) reflection image of mold, C) width and height distribution of molds obtained by micromilling (error bars are SEM) obtained by micromilling (10X).

The accuracy of CNC micromilling ensures that the aluminum molds are precisely fabricated, allowing for consistent and reproducible results in the casting process. This permanence and robustness of the molds makes them ideal for repeated use without degradation or wear, ensuring the reliability and longevity of the microfluidic devices produced.

Both techniques showed minimal deviation from the target aspect-ratio (800:100, and 800:130 for micromilling, Figure 35). Micromilling was however more precise largely due to the width reduction of the mold observed with photolithography. It is thus the more viable option for both precise, and long lasting molds manufacturing.

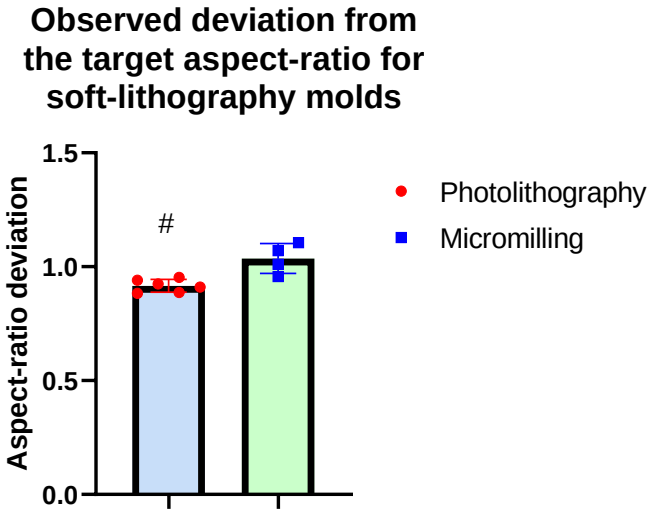

Figure 35: Deviation observed from the target aspect ratio (=1), # indicate significative difference from 1.

2.3.2.1.3 Soft-lithography

Once the fabrication process of the master molds is complete using either of previously described techniques, the soft-lithography can be performed. This consists in casting an elastomer on the molds that will replicate the negative of the molds form.

PDMS (Polydimethylsiloxane) is often the material of choice for soft lithography (Alvaro et al., 2005) due to several advantageous properties it possesses: PDMS is highly biocompatible and minimally reactive with biological molecules and cells, transparent in the visible and near-infrared range of the spectrum, flexible and elastic, which is critical for replicating microscale and nanoscale features accurately during soft lithography processes. PDMS is also gas-permeable, allowing gas exchange and the maintenance of a suitable environment for cells and tissues when used in microfluidic devices. Furthermore, PDMS is relatively inexpensive compared to other materials used in microfabrication, it can form strong bonds with glass and other materials, enabling the integration of microfluidic devices with various substrates. Due to these combined properties, PDMS is highly versatile and has become a staple material in soft lithography, enabling the creation of microdevices for a wide range of applications in biological and biomedical research.

Previously prepared and degassed PDMS (1:10 ratio of curing agent to bulk material, SYLGARD 184, Dow Corning, Midland, MI) is then poured over the master mold and cured for at least 5 hours at 75°C. After peeling off, the cured PDMS channels are cut, inlet and outlet holes punched out of PDMS at the reservoirs places, and placed facing the microchannel side for oxygen plasma treatment (High power, 60 s; PDC-002-HPCE, Harrick Plasma).

2.3.2.2 CO_2 laser cutting of the "optical window"

The bottom channel of the system, or optical window, cannot be realized through

photolithography since it requires a 50 µm thick holed PDMS sheet. The bottom channel is directly spin-coated onto a glass coverslip ($0{,}170 \pm 0{,}005\,mm$), to precisely control its thickness. This is the only alternative to minimize the channel height and allow observation of the system with any inverted microscope. The holed channel is then obtained through direct laser cutting of the PDMS sheet/glass coverslip assembly and peeling of the cut PDMS channel.

Spin-coating PDMS allows a fine-tuning of PDMS thickness. Thickness of the spin coated PDMS was assessed using WLI (described previously) after the channel PDMS layer was removed. Typically, we could obtain a 30 to 70 µm thickness range for the PDMS layer which corresponds to spinning of 1600 to 600rpm for 60 seconds at 25°C (on a Laurell WS-650MZ spin-coater, Figure 36).

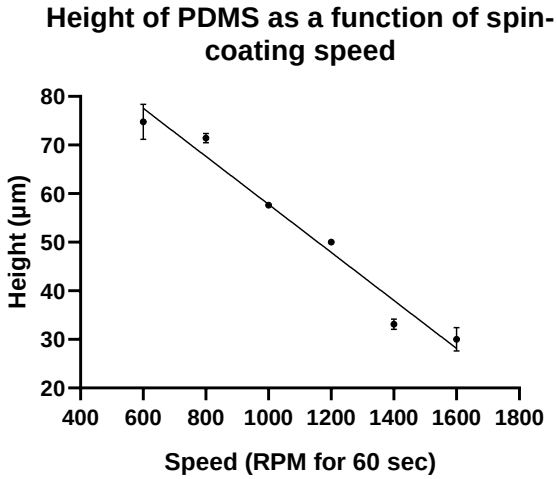

Figure 36: Height of PDMS microtrenches obtained by CO_2 laser cutting PDMS layers of controlled height (error bars are SEM, n= 3/condition).

Once the sheets were obtained, they were cut using a CO_2 laser cutter (Epilog Mini Elix 30W). PDMS is burning while cutting so the vapors were continuously extracted during the process. The flaming was kept reduced to a minimum first because the PDMS layers were thin and the actual speed of the laser and its frequency was very high. The glass coverslip is also slightly attacked by the CO_2 laser (Figure 37, B) and could become brittle if the thickness of the burn is too important.

Adjusting the speed, the power, and the frequency of the laser we could manage to actually cut the PDMS layer while keeping the glass coverslip damage to a minimum. For a 70 µm PDMS sheet the laser cutter speed was set at 100% and the laser power at 5%, and for a 50 µm an 100% speed, and 2% power was used. Frequency was best set at 2500 Hz. By fabricating 50 µm microtrenches, the repeatability of the process was confirmed as we obtained on average a $52 \pm 1\ \mu m$ layer height (Figure 37, C).

After laser cutting the microtrenches (Figure 37, A), a cleaning step was realized to remove eventual dust from PDMS burns on the surface, facilitate the removal of the trench during peeling as well as sterilizing the device lower part. Sequential ultrasonic baths of 10 min first in water then in 70 % ethanol, are conducted before peeling the trench, the peeling is realized using tweezers under a binocular, then a last ethanol bath of 10 min is done to ensure that no contaminants remain in the lower channel. Bottom channels are then dried in an oven at 50°C for 1 hour before assembling the membrane and top compartments (Figure 44, B).

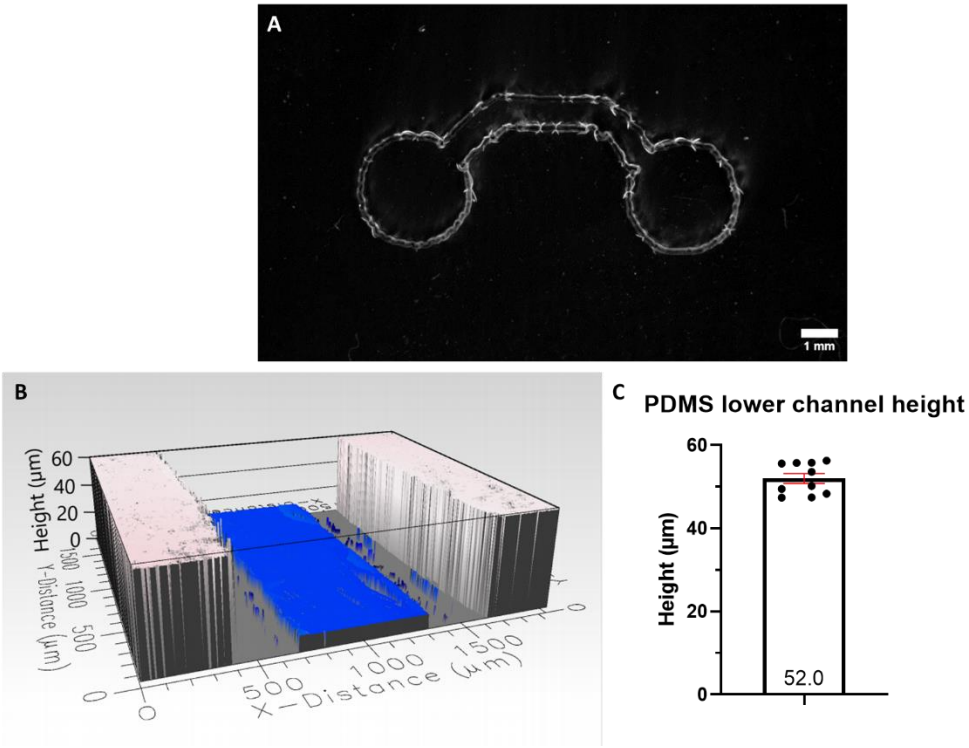

Figure 37: A) CO_2 laser cut 50 µm PDMS sheet spin-coated on a glass coverslip (image magnified 70 times) B) 3D prolife obtained with WLI (10X) after PDMS microtrench removal C) height distributioon obtained for 10 individual microtrenches obtained by spin coating of PDMS at 1200 RPM for 60s (error bars are SEM).

By using these fabrication techniques, we obtained both top and bottom compartments with precisely controlled dimensions.

2.3.3 Physiological relevance of the barrier

The third and last part of the systems, is the membrane that separates the top and bottom microchannels, thus delimiting the vascular and urinary space. For this we used two types of membranes either commercial PET membranes or Collagen based biomimetic membranes.

PET membranes are convenient for different reasons; they are rigid and in that sense easy to position while assembling the device, their porosity is well defined and can be accounted form when modeling filtration, and they allow for cell-cell communication and/or contact if the pore size is large enough. However, their mechanical properties are similar to that of conventional cell plastic culture ware, and their flat topology are not really relevant of the glomerular basement membrane environment.

In an attempt to further increase the biomimetic modeling of the glomerular filtration barrier, self-supported collagen I based membranes were tested as a replacement alternatives for PET membranes. These membranes are realized only with extra cellular matrix proteins such as collagen I through fibrillation. They thus exhibit increased biomimicry in terms of possible cell-matrix interactions, more relevant mechanical properties, gel like diffusion of small molecules…

2.3.3.1 Building biomimetic artificial collagen I based membranes

Glomerulus-on-chip approaches to model the glomerular filtration barrier have previously been developed (Musah et al., 2017; Roye et al., 2021; M. Zhou et al., 2016a). In these systems, the

filtration function was observed, through the co-culture of two different cell types on two sides of synthetic membranes (*e.g.* holed PDMS/PET/PFTE).

On the other hand, self-supported biomimetic membranes are being developed for organ-on-chip applications, and their composition can be closer to that of the actual basement membrane (collagen IV, laminin, peptidoglycans…). They are usually made, at least partially, of fibrillar proteins and can be prepared by different techniques like electrospinning (Dems et al., 2020), drop-casting (Arik, 2021) or vitrification (Mondrinos et al., 2017a). Collagen I membranes can be synthesized in absence of crosslinker or polymer support directly in buffered media by electrospinning (Dems et al., 2020). However, the collagen fibrillar structure obtained can be limited and the throughput of the technique can be argued. These biomimetic membranes seemed an interesting alternative to synthetic membranes for organ-on-chip applications. We thus have decided to develop self-supported collagen I-based membranes of controlled thickness, which can serve as a alternatives for PET membranes in our glomeruli-on-chip system.

Although type I collagen fibrils are not part of the normal glomerular basement membranes (GBM), they can be considered as a foothold for podocytes and endothelial cells. This technique also allows the incorporation of non-fibrillar basement membrane proteins directly within the collagen I mix, providing additional physical support. The protocol was adapted from Mondrinos et al., 2017 without cross-linking the membrane.

The process of preparing biomimetic membranes involves drop-casting a mixture of rat tail collagen I (2mg/ml in phosphate buffer PB pH 7.2) with or without basement membrane proteins (mouse laminin 20µg/ml and mouse collagen IV 20µg/ml) on a PDMS surface. Gelation takes place for 1 to 2 hours at 37°C, followed by drying under a laminar flow hood overnight. Collagen membranes were then rehydrated in sterile water and rinsed several times to remove impurities. Membranes then underwent another drying cycle. Subsequently, the membranes are peeled off the PDMS surface, cut, and inserted into the microsystem similar to microporous PET membranes (Figure 44 & Figure 45).

2.3.3.2 Collagen I & collagen I/IV/laminin membranes characterization

Membranes were thoroughly characterized through Scanning Electron Microscopy (SEM), to assess their biological relevance. To characterize the collagen I and collagen I&IV/laminin membranes, we assessed the collagen fibrils diameter and D-banding periodicity, fibrils orientation, their dry and hydrated thickness, as well as their final assembly in the microdevices.

After preparation, the membranes were dehydrated using ethanol baths (sequential 10 min baths in 50, 70, 95 %, and absolute ethanol) and subjected to vacuum (Harrick, $1{\sim}2.10^{-1}$ Pa) to remove excess liquid. A 7 nm platinum/palladium contrasting layer was then deposited on the membranes using a sputter coater (EMITEC K550X, 25 mA current for 1.5 min). SEM images were acquired on a Hitachi S-4800 electron microscope at varying voltage and current settings (Hitachi S-4800 operating between 5 and 10 kV at 5nA current with a Working Distance, WD, around 4 mm).

Through SEM imaging, we observed a fibrillar structure of the collagen membranes (Figure 38), with fibers longer than the field of view. While certain fibrils were bundled to form higher-order fibrillar structures, many individual fibers were also observed. We also characterized collagen I membranes in which basement membrane proteins were added to the collagen I hydrogel (collagen

IV and laminin) before gelation of the hydrogel (Figure 38), in order to incorporate non fibrillar basement membrane proteins to increase physiological relevance.

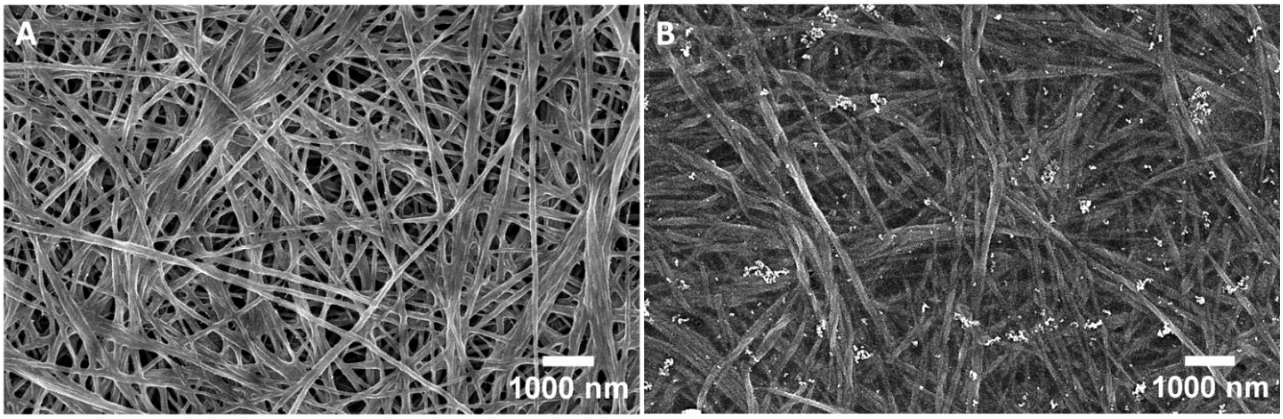

Figure 38: SEM images of A) Collagen I membrane B) Collagen I&IV/laminin membrane both prepared by drop casting.

Collagen I&IV/laminin membranes observed by SEM showed an increased staining density, as if the membranes pores between fibers were filled with basement membrane proteins. Some aggregates of a few tens of nanometers were also observed randomly distributed on the membrane. Our best guess is those are collagen IV or laminin aggregates.

We determine the diameter of individual collagen I fibrils, by performing line plots of the signal intensity along single fibrils and calculated the Full Width at Half Maximum (FWHM) using a Gaussian fitting method (FWHM = 2.355σ, Figure 39). The mean diameter of collagen individual fibrils was 64 ± 2 nm.

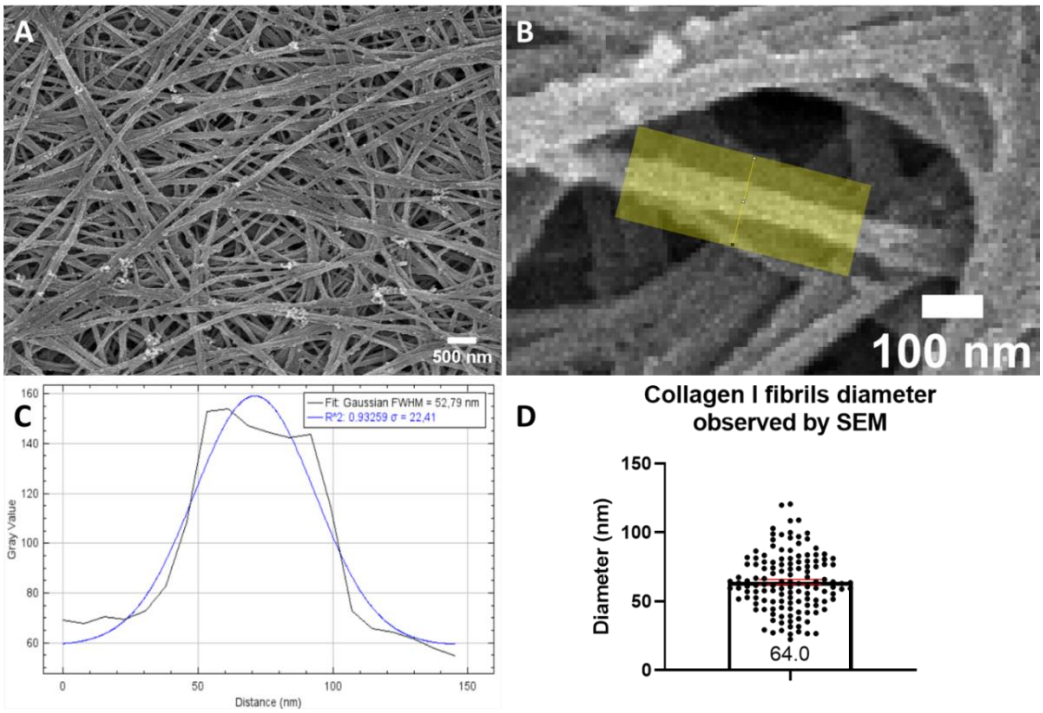

Figure 39: A) Collagen I (2 mg/ml) membrane prepared by drop casting observed by SEM B) individual collagen I fibril C) Line plot intensity of B fitted with a gaussian to extract FWHM (~fibril diameter) D) Size distribution of individual collagen fibers obtained from 5 collagen membranes (n=4, error bars are SEM).

The D-banding in native collagen type I is a structural feature seen at the quaternary level, where collagen fibrils are composed of monomers assembled end to end and aligned in a parallel and staggered manner (Blackstone et al., 2021). This arrangement gives rise to light and dark bands that are visible using Transmission Electron Microscopy (TEM) (Dems et al., 2020) and has also been reported with SEM (Mondrinos et al., 2017a). The D-banding is crucial to the mechanical properties of native collagen, as it provides strength and structural stability to the tissue (Blackstone et al., 2021).

However, when collagen is solubilized and electrospun, the process of denaturation can disrupt the native quaternary structure, leading to the loss of the D-banding pattern in the resulting electrospun collagen fibers (Blackstone et al., 2021). As a consequence, the mechanical properties of electrospun collagen scaffolds may differ from those of native collagen.

By adopting solvent-free conditions during the preparation of collagen membranes using drop casting, we were able to observe the D-banding pattern, which is a characteristic feature of fibrillar collagen I, through Scanning Electron Microscopy (SEM) analysis.

The spacing of D-bands in fibrillar collagen I can vary depending on factors such as the species, tissue source, and experimental conditions. Typically, the D-band spacing in collagen fibrils from different sources can range from around 64 nm to 67 nm. For rat tail collagen specifically, the D-band spacing is reported to be around 67 nm (Stylianou, 2022).

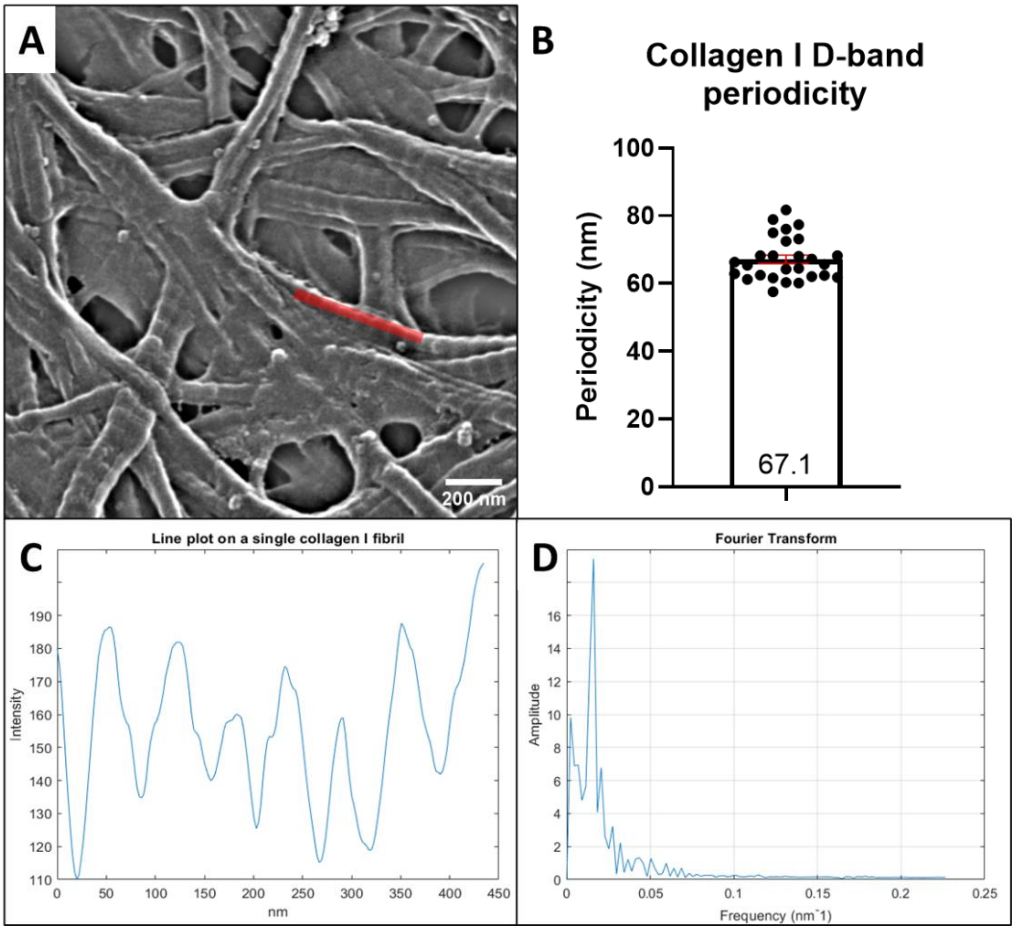

Figure 40: A) High magnification SEM image of collagen I fibrils with characteristic D-banding visible, B) Collagen D-banding periodicity determined as the highest amplitude pic of spatial frequency (error bars are SEM) (D) obtained from FFT of line plotting the signal of individual collagen fibrils (C).

To determine the periodicity of the D-banding structure, we performed line plotting of the signal intensity along the length of individual fibrils. This generated a signal representing the variation in signal intensity across the fibrils (Figure 40, A-C). We used a Fast Fourier Transform (FFT) to analyze this 1D signal and retrieve the spatial periodicity of the D-banding pattern (MATLAB analysis). This allows identifying the dominant frequency components in the signal, which corresponds to the spatial periodicity of the D-banding structure in the collagen membranes. When analyzing individual fibrils (Figure 40, B), we found the D-band spacing to be 67 ± 1 nm which is in agreement with the literature (Stylianou, 2022).

These membranes are thus made of fibrillar collagen I with a complex fibrillar structure and organization due to these long fibers and the gelation process. We quantified the level of fibrils organization to understand how the meshwork is composed.

Collagen I fibrils orientation

As adherent cells have the ability to sense their substrate and its alignment (Baker & Chen, 2012) it is important to characterize its organization level. In the following section we demonstrate how to analyze the collagen I fibrils scaffold organization and orientation using image and data processing from obtained SEM images (Figure 41).

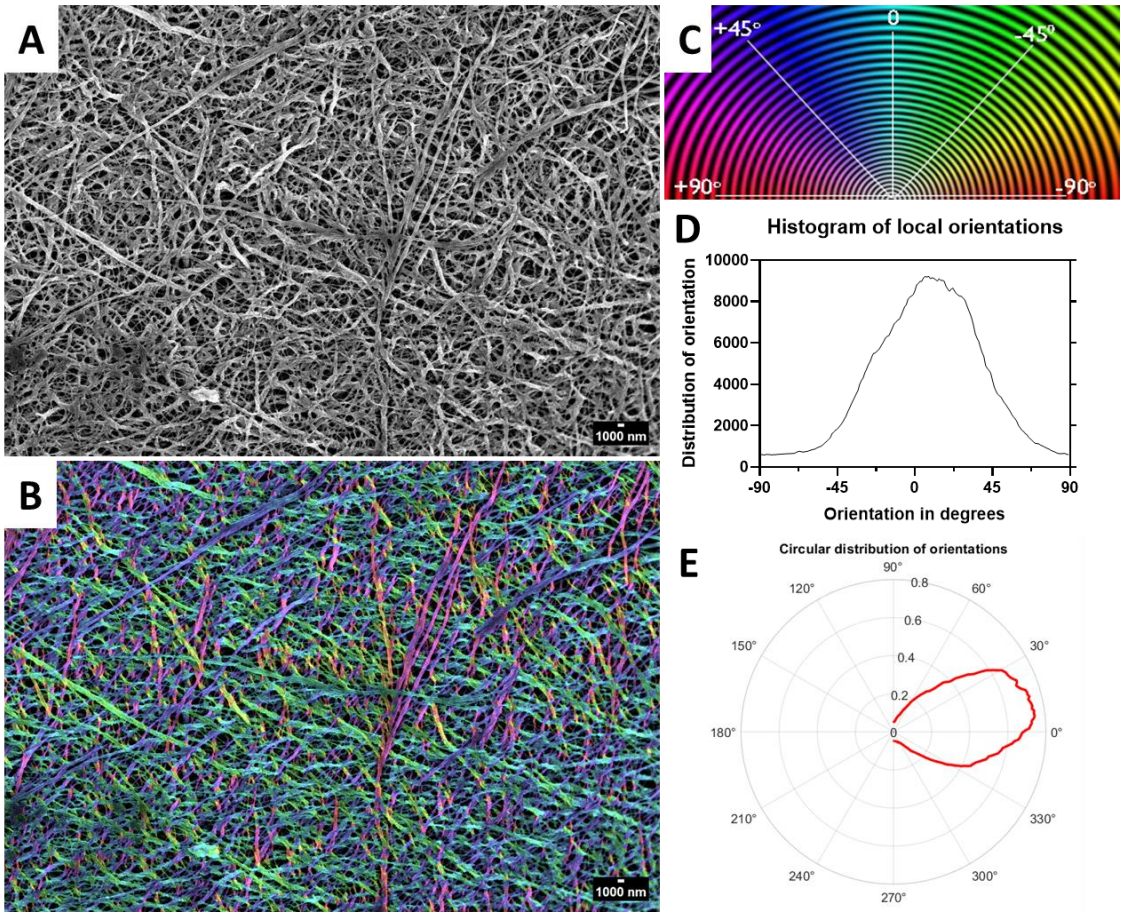

Figure 41: A) SEM image of collagen I membrane B) fibrils' orientation color coded with C) orientation LUT and D) obtained pixels' orientation distribution also plotted in E) circular coordinates (obtained with MATLAB).

In the context of orientation distributions, which are angular distributions with periodicity, a suitable fit is achieved by using a Von Mises distribution. The Von Mises distribution, also known as the circular normal distribution is a probability distribution that describes data on a circular domain.

The Von Mises distribution is a natural extension of the normal distribution to circular data.

The probability density function (PDF) of the von Mises distribution is given by:

$$f(\theta \mid \mu, \kappa) = \frac{e^{\kappa cos(\theta-\mu)}}{2\pi I_0(\kappa)}$$

where:

- θ is the circular random variable (angle) with values on the unit circle (usually measured in radians).
- κ is the concentration parameter, which is a measure of how tightly the data clusters around the mean direction, or "sharpness". It is a positive real number, where larger values indicate stronger concentration, and $\kappa = 0$ represents a uniform distribution. In essence, the parameter $1/\kappa$ serves as an analogue of variance σ^2 in a Gaussian distribution. In practical terms, κ reflects the intensity of orientation for the elements under consideration (Figure 42: A).
- μ is the mean direction parameter, or location parameter, which indicates the central tendency of the distribution or the angle of the distribution peak where most data is concentrated (Figure 42: B).
- $I_0(\kappa)$ is the modified Bessel function of the first kind and order 0, used as a normalizing constant to ensure that the distribution integrates to 1 over the unit circle.

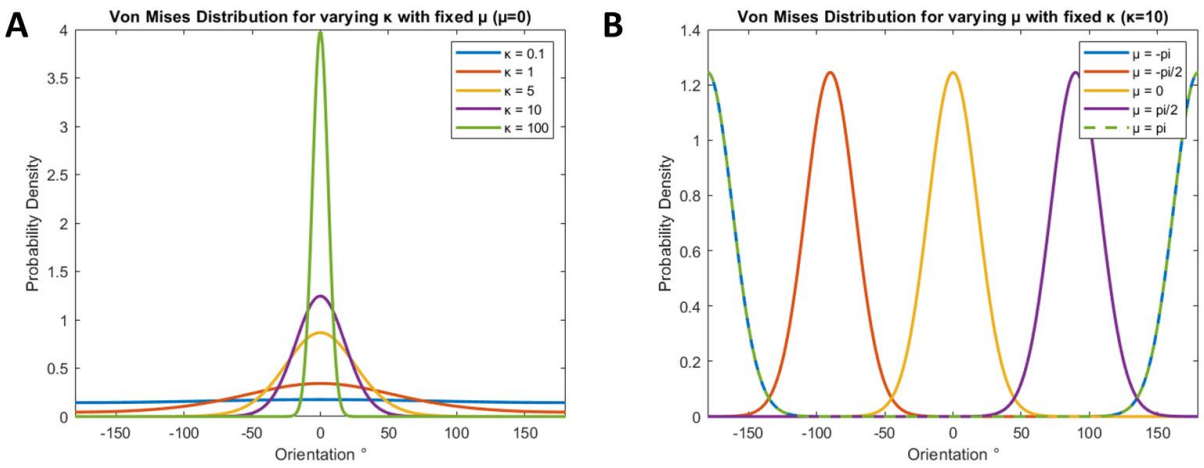

Figure 42: A) Illustration of the influence of the concentration parameter κ and B) the direction parameter μ on the PDF of the Von Mises distribution (obtained with MATLAB).

To analyze collagen fibrils orientation from SEM images we used the plugin OrientationJ (Rezakhaniha et al., 2012) in ImageJ to obtain the pixels orientation distribution (Figure 41: D). In the orientation analysis, the mean direction of a region is determined using the local gradient structure tensor. The local window size is a user-defined parameter representing the size of the elementary unit of analysis that exhibits a uniform orientation. If the window size is too large, the image is undersampled, leading to a loss of local orientation information. On the other hand, if the window size is too small, the image is oversampled, causing noise in the resulting orientation.

OrientationJ generates color-coded images showing orientations (Figure 41: B, C), and tables containing the distribution of orientations for every pixels, binned on 1° angles on a π period (Figure

41: D). The probability density function was normalized by dividing the number of elements in each bin by the total number of elements.

Von Mises distributions are defined on a 2π period, whereas the data obtained from OrientationJ is π periodic (Figure 41: E). To accommodate this periodicity difference, and due to their apolar nature, collagen I fibrils can be considered similarly oriented at either 0 or 180 degrees, so linearly stretching the data onto a 2π-long interval is possible.

The collagen I fibrils pixel orientation distributions showed a good agreement with the Von Mises distribution (Figure 43). The concentration and direction parameters are retrieved using the Von Mises fitting functions. After obtaining these parameters, the fitted von Mises distribution are plotted back on a π-long interval to properly visualize and interpret the results in the context of the original data periodicity. This transformation allowed for an appropriate comparison between the von Mises distribution and π-periodic data.

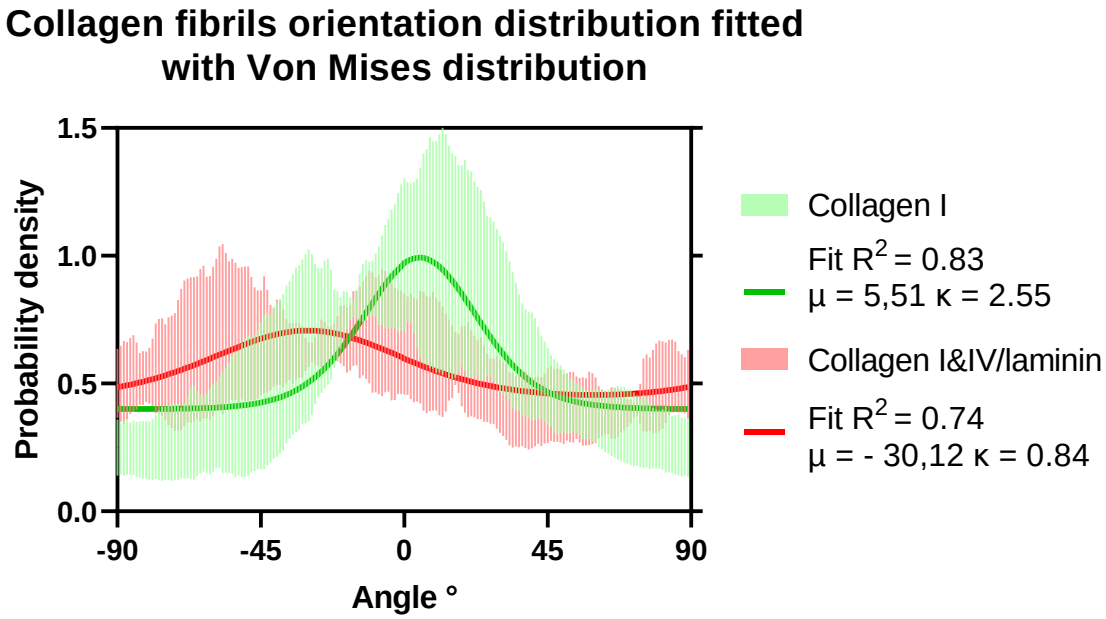

Figure 43: Plot of orientation distributions (obtained from 4 collagen I and 3 collagen I&IV/laminin SEM images using OrientationJ) normalized and fits obtained from fitting with a Von Mises distribution (MATLAB).

Collagen I membranes showed a slightly more organized orientation of fibrils than collagen I&IV/laminin membranes. This indicates that adding basement membrane proteins in the collagen hydrogel might protect the collagen I hydrogel structure from adopting a preferred orientation while drying.

These biological membranes are thus both physiologically relevant and highly anisotropic, which is an interesting property to be able to study their remodeling with the action of cells, strain or stress.

2.3.4 Assembly of the microsystem

To finalize the systems, the membrane must be placed between the top and the bottom compartments allowing efficient cell support and separation (Figure 44: B). All the compartments are

then bonded together to prevent leaks of culture media, cell dissemination, potential contaminations,…

2.3.4.1 Bonding of the membrane in the organ-on-chip

The PET membrane, with its defined pore size, regulates the passage of molecules and cells, creating a selective barrier within the microsystem. Microporous PET membranes are obtained from commercially available Transwells inserts then cut down to the desired size and placed between the two PDMS microchannels. Two types of microporous membranes were used, Millicell PET membranes with pores of 5 µm (MCMP06H48), and Falcon® transparent PET membranes (353091) with pores of 3 µm.

Collagen I or collagen I/IV/laminin membranes are obtained as previously described (section: 2.3.3.1) and peeled of their PDMS surface before assembly (under sterile conditions) with forceps.

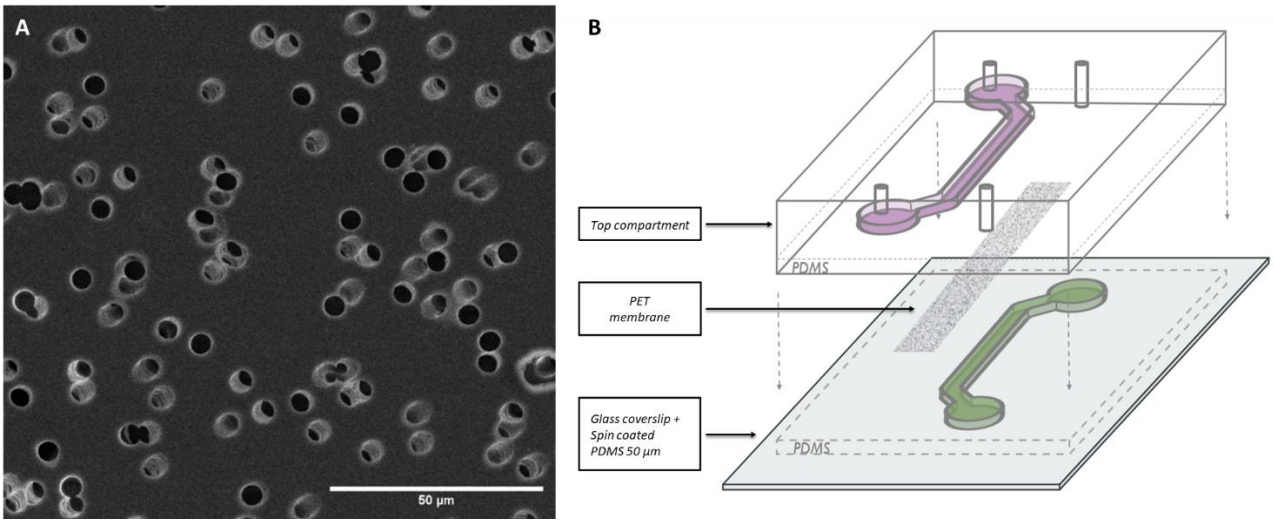

Figure 44: A) SEM image of 5 µm pore PET transwell membrane B) Scheme of microdevice assembly.

For PET, the membrane is bonded to the top component of the device by using oxygen plasma treatment followed by bonding of the top-membrane assembly to the bottom component containing the other channel. For Collagen membranes the top and bottom compartments are first plasma activated, and the membrane is then placed between both before contact is made. The large area of PDMS/PDMS contact between the top and bottom compartment securely ties the membranes in place and provides sealing. Devices are then sterilized by UV treatment for 15 minutes before use.

To assay for the proper positioning of the membranes a non-destructive imaging technique is used. Line-field Confocal Optical Coherence Tomography (LC-OCT, Damae medical), was used to characterize the final assembly of the microsystems (Figure 45). Line-field Confocal Optical Coherence Tomography (LC-OCT, Ogien et al., 2020) combines the principles of Optical Coherence Tomography (OCT) (D. Huang et al., 1991) and confocal microscopy to provide high-resolution, three-dimensional imaging of biological tissues and materials.

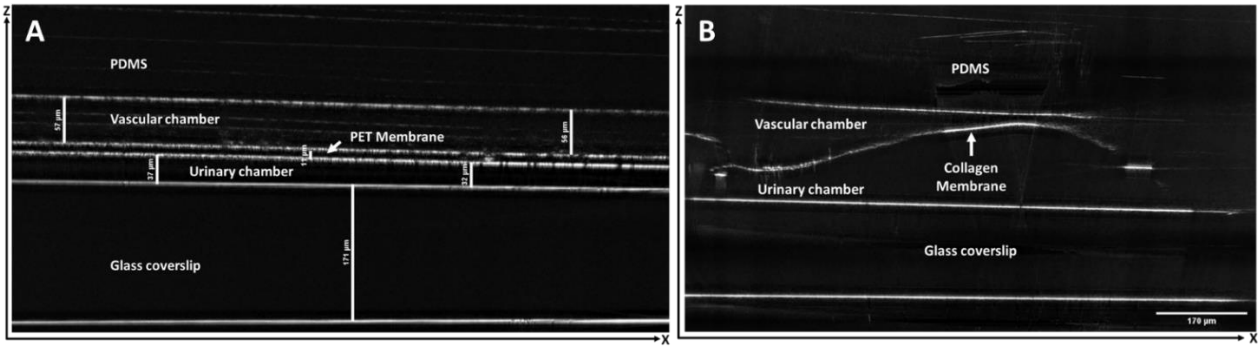

Figure 45 : LC-OCT image of microsystems with A) a PET membrane, B) a collagen I membrane.

After detachment from the PDMS surface, collagen membranes, tend to form ruffles when handled manually. Consequently, immobilizing them in the microsystems becomes more challenging. This aspect presents both advantages and inconveniences. On the one hand, the ruffled surface of the membrane can contribute to a more biomimetic support structure for Podocytes, as previous studies have demonstrated that curvature enhanced their differentiation (Korolj et al., 2018). On the other hand, the ruffling may result in blocked channel compartments, impeding flow circulation within the device (Figure 45, B).

The assembly of the microdevices using PET membranes, was however possible and showed a reproducible membrane positioning (Figure 45, A). The membrane lies suspended above the glass coverslip parallel to its surface. This is critical for proper cell seeding and flow control in the device.

LC-OCT is sensitive to changes in refractive index, that gives this contrast for each interface of the device; PDMS/air, air/PET, and air/glass coverslip (Figure 45). However, when hydrated, the collagen membrane index matches almost the water index (1.33 to 1.34 Calderón-Colón et al., 2012) and the contrast is lost. Thus limiting LC-OCT to observing and measuring biomimetic membranes thickness in their dry state.

2.3.4.2 Membranes thickness

The dry thickness of the membranes was measured using Line-field Confocal Optical Coherence Tomography (LC-OCT) and then compared to the thickness of PET membranes. To determine the thickness of the dry membranes, they were first placed onto a glass coverslip before imaging. Then, a line stack of a depth containing both the coverslip and the membrane was realized (Figure 46: A&B).

The thickness was determined with the same method, as previously described, of fitting a Gaussian on a line plot perpendicular to the dry membrane signal. The base collagen I membranes were $9 \pm 1\ \mu m$ thick while the collagen I&IV/laminin membranes were on average significantly thicker, $16 \pm 1\ \mu m$ (Figure 46: C). This thickness difference is probably due to the laminin and collagen IV network formed in these membranes.

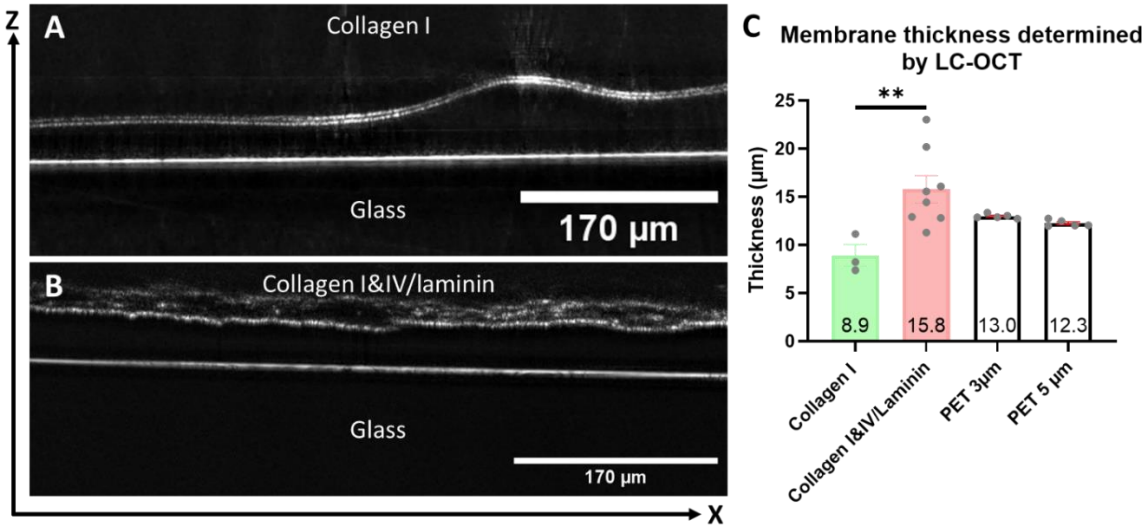

Figure 46: A) LC-OCT image of collagen I membrane B) collagen I&IV/laminin membrane, C) distributions of PET and collagen based membranes thickness determined by LC-OCT (error bars are SEM).

The membranes were also analyzed in their hydrated state after being mounted in the microsystems. Collagen membranes, like many biological tissues, exhibit natural autofluorescence when excited in the visible spectra (Sherlock et al., 2018). Leveraging this property, we characterized the thickness of the collagen I&IV/laminin membranes in the microdevice under hydrated conditions (PBS).

Following the previously described preparation method, the collagen I&IV/laminin membranes were assembled in the devices. To facilitate imaging, the systems membranes were also coated with FITC-labeled human fibronectin (20 µg/ml in HBSS) by adsorption at 37°C for 1 hour. Subsequently, the systems were subjected to confocal imaging, results are presented in Figure 47.

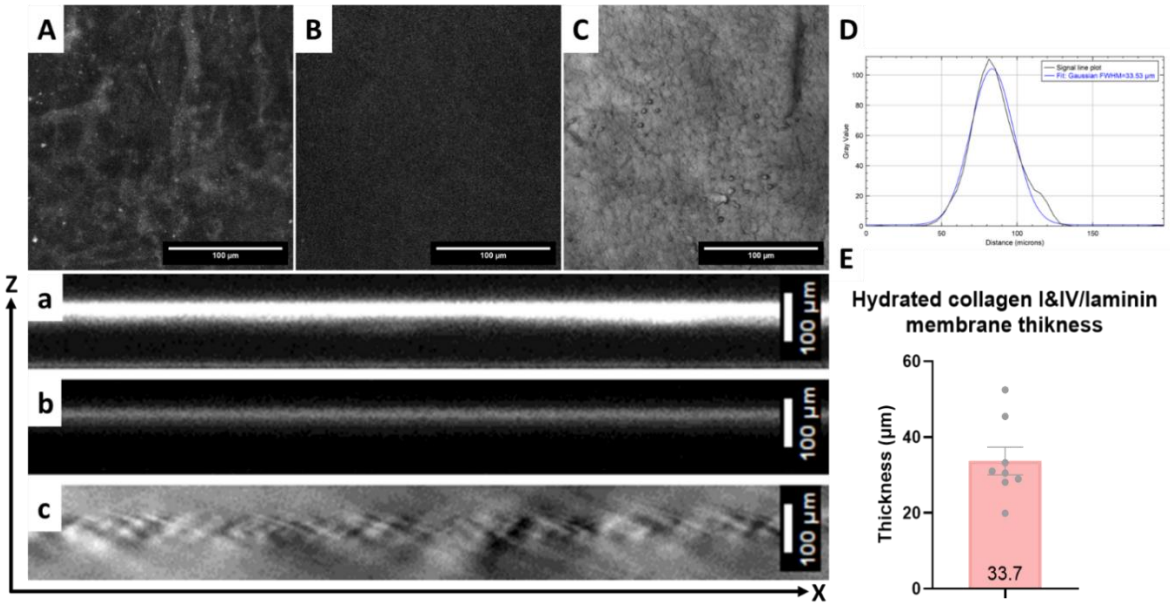

Figure 47: A&a) FITC-Fibronectin coating, B&b) collagen I&IV/laminin autofluorescence (excitation 594 nm and detection 615-750 nm), C&c) transmission images obtained from confocal imaging (20X), a,b,&c) are axial projections on the whole system height, D) thickness (FWHM) of individual membranes were obtained by gaussian fitting the signal of the Z axis profile of the collagen (b) membranes, D) Thickness distribution of membranes (error bars are SEM).

Comparing the measurements obtained with LC-OCT in dry conditions, the hydrated collagen membranes exhibited a two-fold increase in thickness ($34 \pm 4\ \mu m$), occupying around 23% of the channels height and being significantly larger than PET membranes.

Thus, despite their biomimetic potential, collagen membranes present several challenges, including difficulties in assembly within the microdevice, variations in thickness that could lead to channel blockage, and autofluorescence. We thus decided to use PET membranes for our glomerulus-on-chip.

2.3.5 Effect of the substrate on podocytes

Before incorporating these biomimetic collagen-based membranes into our organ-on-chip platform, we conducted preliminary investigations to determine if cell culture on these membranes was feasible, and whether the addition of basement membrane proteins in the collagen I fibrillar structure induced any changes in podocytes differentiation and morphology. We also compared the cell morphology to that of cells cultured on PET membranes.

Conditionally immortalized human Podocytes (CiPodocytes) (Saleem, O'Hare, et al., 2002) (kind gift from M. Saleem, University of Bristol) were used. This human podocyte cell line with conditional immortality was generated through the introduction of the temperature-sensitive SV40-T gene *via* transduction. These cells have the ability to proliferate at a permissive temperature of 33°C. When transferred to a non-permissive temperature of 37°C, they undergo growth arrest and exhibit markers of differentiated podocytes found *in vivo*.

We first compared the morphological differences between differentiated podocytes and proliferating podocytes grown on artificial collagen I membranes. Next, we examined whether CiPodocytes grown on collagen I or collagen I&IV/laminin membranes displayed any phenotypical changes. Finally, we conducted a comparison of podocytes morphology when grown on collagen membranes versus PET membranes.

2.3.5.1 Effect of podocyte differentiation on Collagen I membranes.

CiPodocytes culture medium is detailed in Appendix: 4.1. CiPodocytes were either differentiated for 2 weeks before seeding on the membrane or seeded while still proliferating on immobilized PET or collagen membranes. Cells were then grown for at least 3 days either in permissive (33°C) or non-permissive conditions (37°C).

To study CiPodocytes morphology trough SEM and confocal imaging, we fixed the membranes with 4% paraformaldehyde (PFA) and 1% glutaraldehyde for 1 hour at room temperature. After rinsing three times with 0.1 M phosphate buffer (PB), we dehydrated the membranes in sequential 10-minute baths of 50%, 70%, 95%, and absolute ethanol. Subsequently, the membranes were subjected to vacuum for 15 minutes. Electron microscopy preparation was performed similarly to collagen membranes. A platinum/palladium contrasting layer was deposited on the membranes using a sputter coater. SEM images were acquired on a scanning electron microscope at varying voltage and current settings.

CiPodocytes seeded of collagen I membranes either previously differentiated or proliferating exhibited different morphological aspects (Figure 48*)*. Proliferating podocytes remain rather flat (B&D) while previously differentiated CiPodocytes (A&C) exhibited more cytoplasmic sproutings

towards adjacent cells (Figure 48, A, white arrows). This was also confirmed with immunofluorescence imaging (Figure 49 & Figure 50). Immunofluorescence images also show a normal adherent phenotype on collagen membrane where no particular cytoskeletal arrangement is observed (Figure 49). Furthermore, differentiated CiPodocytes grown on collagen I membranes expressed differentiation markers (*e.g.* Podocin, Figure 50).

However, some differentiated podocytes showed either blebbing on their membrane that could indicate apoptosis or a roundish shape, evenly distributed amongst the whole cell population (Figure 48, A, green arrows), probable indication of apoptosis (Appendix: 4.3). This could be explained by the fact that these podocytes were cultured for 2 weeks prior seeding on the membrane hence during passaging a proportion of cells could have suffered.

Proliferating podocytes however did not show such type of round-like cells and were evenly spread on the membrane (Figure 48, Figure 49), probably indicating a morphological switch induced by differentiation. These results suggest the ability of podocytes to grow, proliferate, and differentiate on collagen membranes.

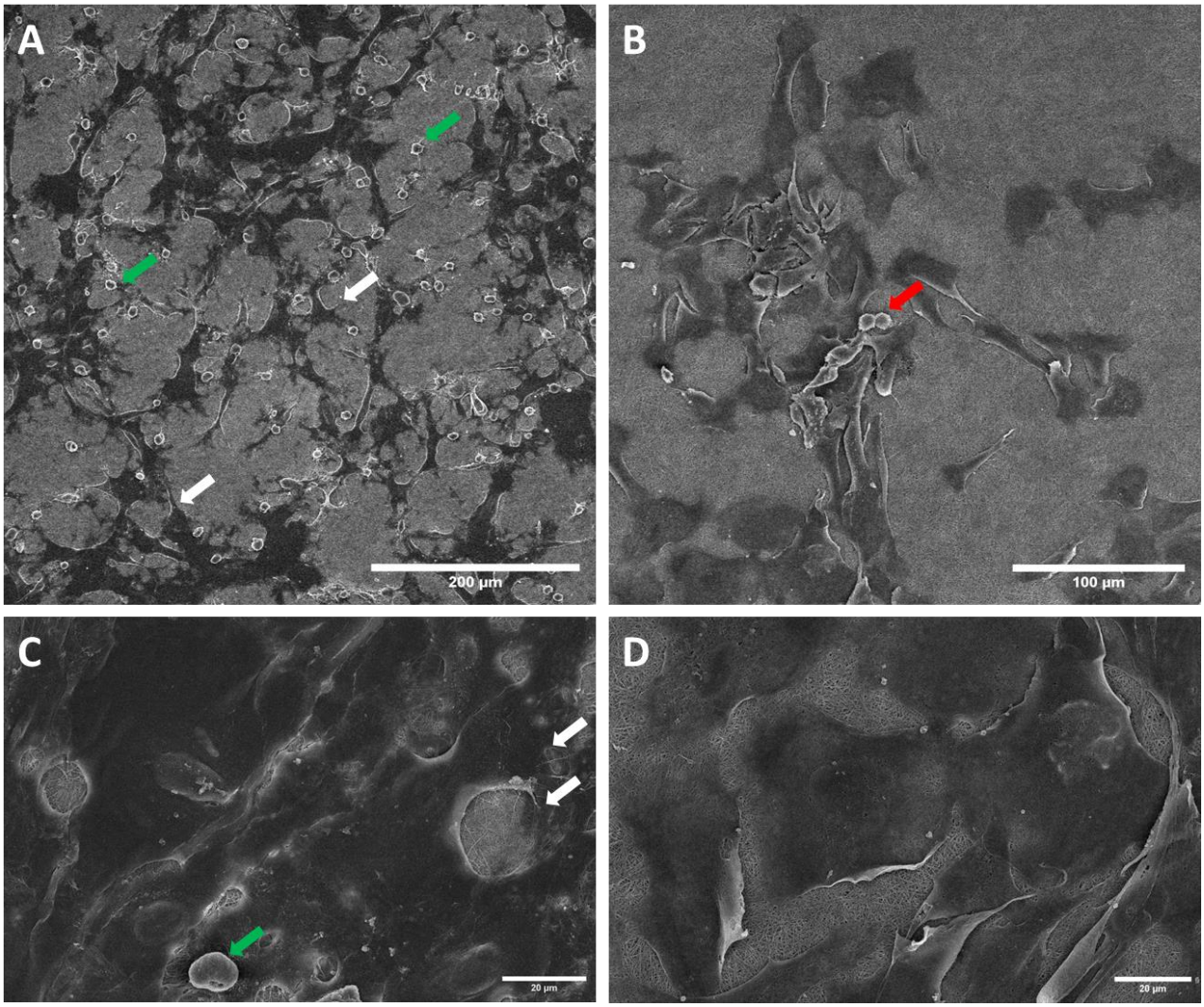

Figure 48: A&C) CiPodocytes differentiated for 2 weeks prior seeding on collagen I membrane B&D) proliferating CiPodocytes seeded on collagen I membrane observed by SEM at different magnifications. White arrows indicate cell sproutings, green arrows, dead cells, red arrows dividing cells.

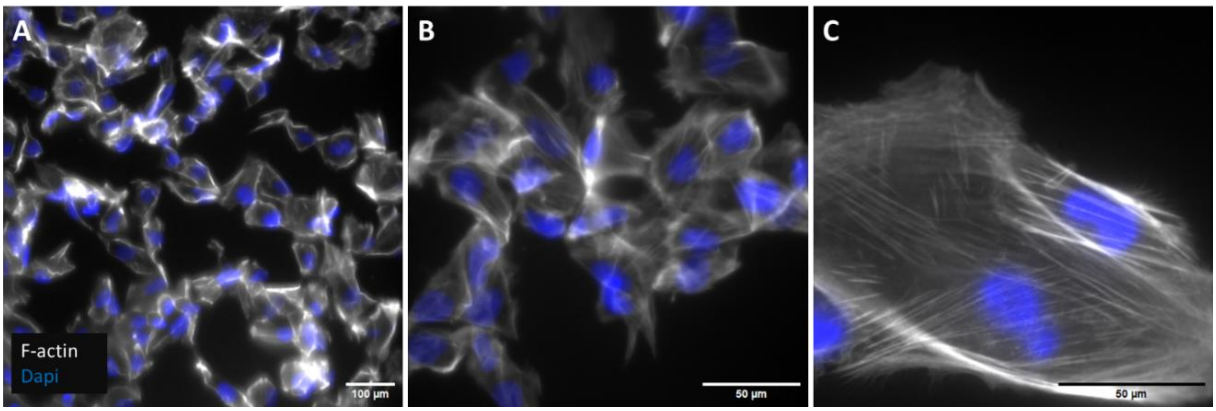

Figure 49: Images of proliferating podocytes on collagen I membranes (epi-fluorescence) at different magnifications (A) 10X, B) 40X, C) 60X) stained with DAPI and f-actin (rhodamine red phalloidin).

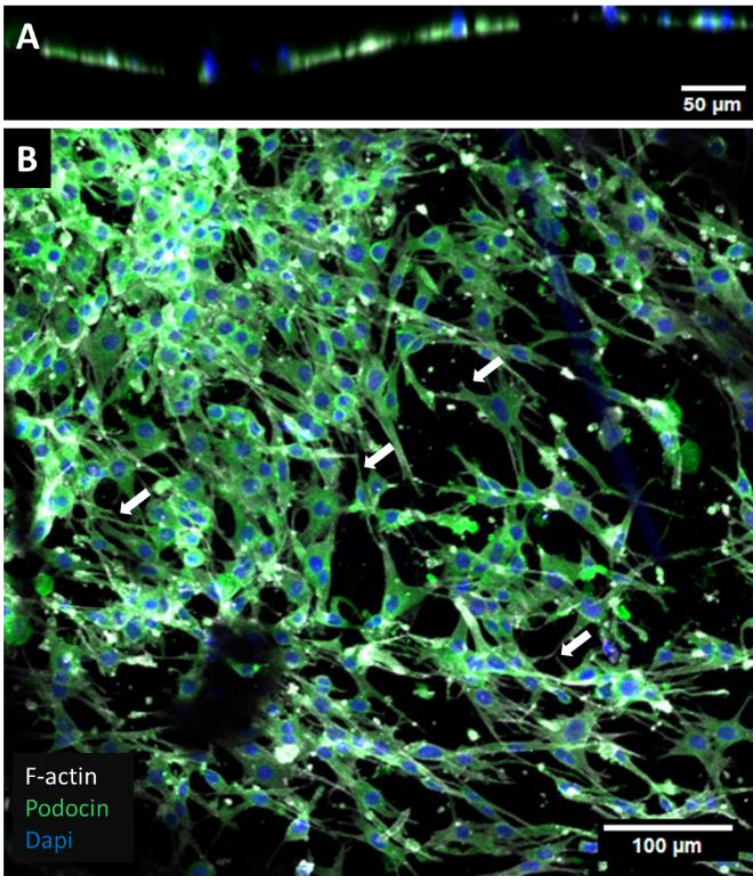

Figure 50: Confocal image of differentiated CiPodocytes seeded on collagen I membrane A) XZ view B) maximal Z projection of the stack (20X) stained for nuclear staining (DAPI), f-actin (rhodamine red phalloidin), and podocin (rabbit Alexa Fluor™ 488). White arrows indicate cell sproutings.

2.3.5.2 Effect of membrane composition on CiPodocytes

CiPodocytes seeded on collagen I&IV/laminin membranes exhibited more foot-like cytoplasmic processes compared to plain collagen I membranes and showed active but small membrane protrusion (~200 nm) covering their cellular body (Figure 51, B) indicating a good level of structure preservation during preparation for electron microscopy with a low risk of artifacts induced by dehydration of the cells.

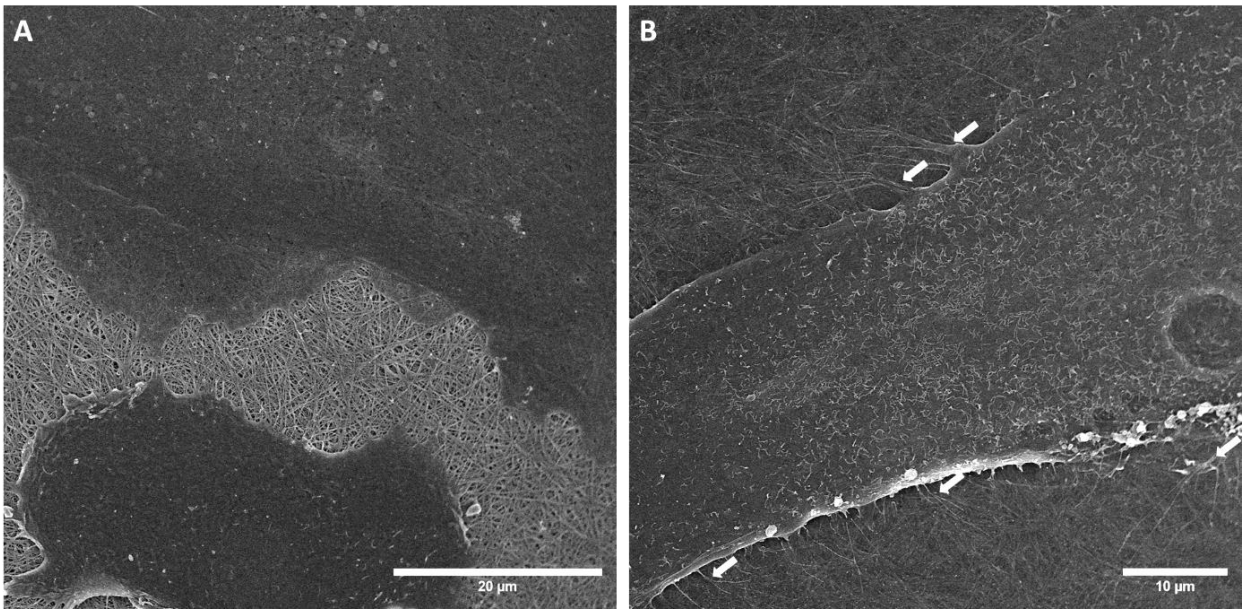

Figure 51: A) CiPodocytes seeded on collagen I membranes and B) on collagen I&IV/laminin membrane observed by SEM. White arrows indicate cell sproutings.

Such phenotypic difference were not visible with immunofluorescence and confocal imaging typically because of such feature size cannot be resolved with classical imaging methods. This shows that podocytes are more active on collagen I/IV/laminin substrates compared to plastic, probably indicating a higher differentiation level.

2.3.5.3 CiPodocytes grown on PET membranes

When growing CiPodocytes on PET membranes we first observed that CiPodocytes spread on the membrane surface blocking the membrane pores without major change of cellular structure (Figure 52: A). They also form pedicels like structures at cellular junctions (Figure 52: B).

Overall, CiPodocytes grown on PET or collagen based membranes did not show change major phenotypic differences.

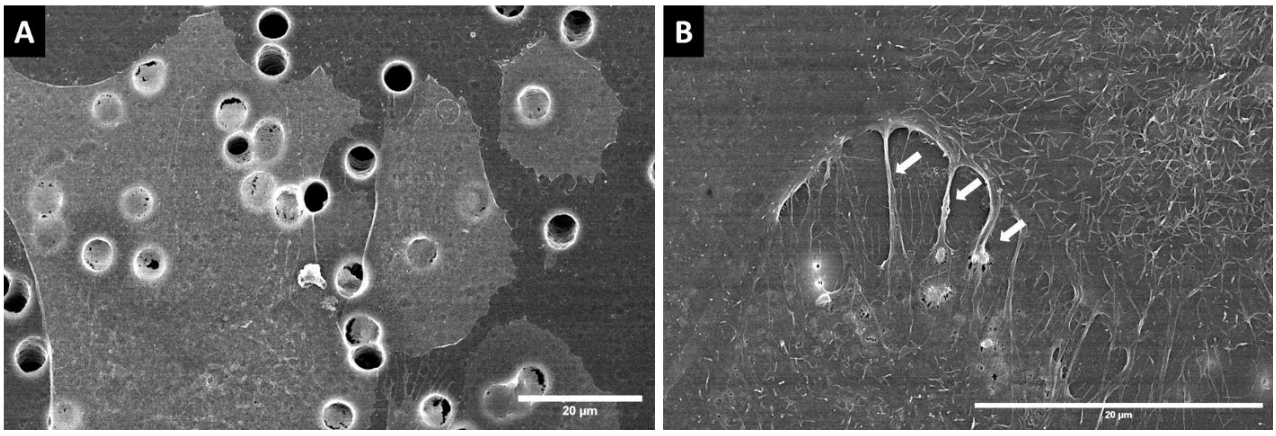

Figure 52: A&B) CiPodocytes grown on PET membranes with 5 µm pores observed by SEM. White arrows indicate pedicel like structures.

These investigations allowed to assess the suitability of the collagen-based membranes for cell culture and to gain insights into how the addition of basement membrane proteins and cell differentiation influenced CiPodocytes morphology compared to PET membranes.

SEM allows defining fine cell ultrastructural changes. We found that tuning the membrane composition can lead to phenotypical changes in differentiated podocytes. Overall PET membranes and collagen I based membranes are able to sustain podocytes culture.

Both membrane options provide distinct advantages for studying glomerular functions and pathological conditions in the glomerulus-on-chip system. The choice between PET and collagen I membranes depends on the specific research objectives and the desired level of biomimicry required to accurately investigate glomerular physiology.

In summary, while collagen-based membranes hold promise for biomimetic applications, these findings highlight the need to address practical issues such as assembly and thickness control to fully harness their potential in microsystems.

By employing these techniques, we gained valuable insights into the structural characteristics of the collagen membranes, particularly regarding their fibrillar arrangement and periodicity, which are vital aspects in the context of tissue engineering and biomimetic support for glomeruli-on-chip systems.

2.4 Long-term cell culture on a chip

2.4.1 Cell sources and seeding

2.4.1.1 Cell sources

In order to recapitulate a glomerulus-on-chip, specific kidney cells of precise lineage must be used. The glomerulus is composed of an endothelial layer (glomerular endothelial cells or GEnCs), podocytes, and a final layer of parietal epithelial cells (PECs). Since our collaborators from PARCC (Olivia Lenoir and Pierre-Louis Tharaux) previously worked with isolated glomerular cell lines, they generously provided them to recapitulate the glomerular organization, also hoping to reach functional behavior. We describe here the motivation for each cell type choice as well as their main characteristics.

The first step of the microsystem validation was to identify if it was able to sustain cell culture. This was done with HeLa (W. F. Scherer et al., 1953) epithelial cells, originally derived from cervical cancer cells. They were used principally as a tool to investigate the ability to co-culture cells confluently on 3 layers in the microsystems, and assay for cell viability in microfluidic culture conditions.

Due to their well-established characterization and availability, Human Umbilical Vein Endothelial Cells HUVECs (Maciag et al., 1982) (kind gift from O. Lenoir, PARCC) were the initial choice of endothelial cell line to replicate the endothelial barrier in microsystems. This particular cell type is a primary cell culture, meaning it has limited ability to proliferate even in serum-supplemented medium. However, its serial propagation, or consecutive passaging, can be enhanced by culturing it on a human fibronectin matrix and in the presence of Endothelial Cell Growth Factor (ECGF) (Maciag et al., 1982). Furthermore; these cells provide a good control for the Glomerular formation barrier as they do not originate primarily from the glomerulus microvasculature.

Conditionally immortalized human Podocytes (CiPodocytes) (Saleem, O'Hare, et al., 2002) (kind gift from M. Saleem, University of Bristol) were then used in co-culture with HUVECs to first try to recapitulate a glomerular filtration barrier. This human podocyte cell line with conditional immortality was generated through the introduction of the temperature-sensitive SV40-T gene *via* transduction. These cells have the ability to proliferate at a "permissive" temperature of 33°C. However, when transferred to a "non-permissive" temperature of 37°C, they undergo growth arrest and exhibit markers of differentiated podocytes found in vivo.

In subsequent phases of this study, two additional conditionally immortalized cell lines were obtained: human endothelial cells derived from glomerular microvasculature and rat parietal epithelial cells. This enabled the establishment of a co-culture system in which all cells are controlled by the same heat sensitive oncogene. Thus, by switching temperature to 37°C, the differentiation induction could be precisely synchronized and controlled for all the cell lines used. Conditionally immortalized human Glomerular Endothelial Cells (CiGEnCs) (Satchell et al., 2006) (MTA S. C. Satchell, University of Bristol) were obtained using the same transduction method as for CiPodocytes, and cultured in presence of Vascular Endothelial Growth Factor (VEGF), human recombinant Epidermal Growth Factor (hEGF), a recombinant analog of Insulin-like Growth Factor (IGF), and serum.

CirPECs (Guhr et al., 2013) (MTA C. Meyer-Schwesinger, University Medical Center Hamburg-Eppendorf) were recently derived from rats. CirPECs are cultured with Bovine Brain Extract (BBE), hEGF, Insulin-Transferrin-Selenium (ITS), and serum. A stable CirPEC-GFP expressing cell line was obtained (kind gift from O. Lenoir, PARCC) by lentiviral transduction of a scramble shRNA-GFP.

All cells culture medium compositions are detailed in Appendix: 4.1. These cells were employed at different stages of the organ-on-chip development process. A final human parietal epithelial cell line (CihPECs) was obtained after the experiment, enabling future perspective to recapitulate a fully human "glomerulus-on-chip".

2.4.1.2 Culture in the microsystems

Sterile microsystems are obtained as previously described. To boost cellular adhesion in the systems several matrix proteins coatings were used.

Systems are activated with plasma treatment and then coated, *via* passive adsorption, with extracellular matrix proteins to promote cell adhesion and differentiation. Matrix proteins were diluted in sterile Phosphate Buffered Saline (PBS) at pH 7.2 with concentrations ranging from 10 to 25 µg/ml, perfused in the microsystems and incubated for 1h at 37°C or overnight at 4°C prior to cell seeding. Coated systems can be kept in the fridge up to a week prior cell seeding.

Several matrix proteins were used in mixture or on their own:

- Mouse Laminin (Corning 354239) at 10 µg/ml,
- Human Fibronectin purified from human plasma (Corning 354008) and human FITC-Fibronectin (Sigma F2733) at 10 µg/ml,
- Rat tail Collagen I (Corning 354249) at 25 µg/ml,
- Mouse Collagen IV (Corning 354233) at 10 µg/ml,

The cell seeding in the microfluidic channels has to be done with a high concentration of cells to further promote cell adhesion. We used a concentration of 1.10^7 $cells/ml$, this allows for the cells to cover the full surface of the microsystems and to promote cell confluency (Figure 53). Cells in excess need to be removed from the microchannels after a few hours of seeding to remove excess cells and prevent asphyxiation.

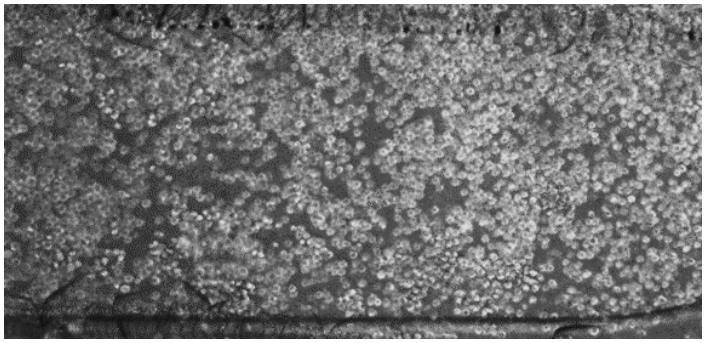

Figure 53: Example of CiGEnCs seeding density in the microdevice observed with a phase contrast microscope (10X).

When using different cell types, we must unsure that cell adhere and grow on the intended surface. For cell culture in different orientations across the membrane, cells are sequentially injected.

For the 3 cell types/layer systems, CiPodocytes are the first injected cells in the urinary compartment (bottom channel), the microdevice is then flipped so that the cell seeding occurs on the lower side of the membrane. Cells are left to adhere for 6h before rinsing with media. Then HUVECs or CiGEnCs, and PECs are injected into the top and bottom channel respectively. Systems are incubated at 33°C for 4 to 6 h before rinsing to flush excess cells with culture media. The systems inlets and outlets are then blocked with 200µl sterile filter tips filled with media to provide continuous buffering. The top channel (vascular) inlets/outlets and reservoirs are filled with GEnCs or HUVECs media while the bottom channel (urinary) inlets/outlets and reservoirs is filled with PECs medium (with is composed at 50% of the podocytes medium).

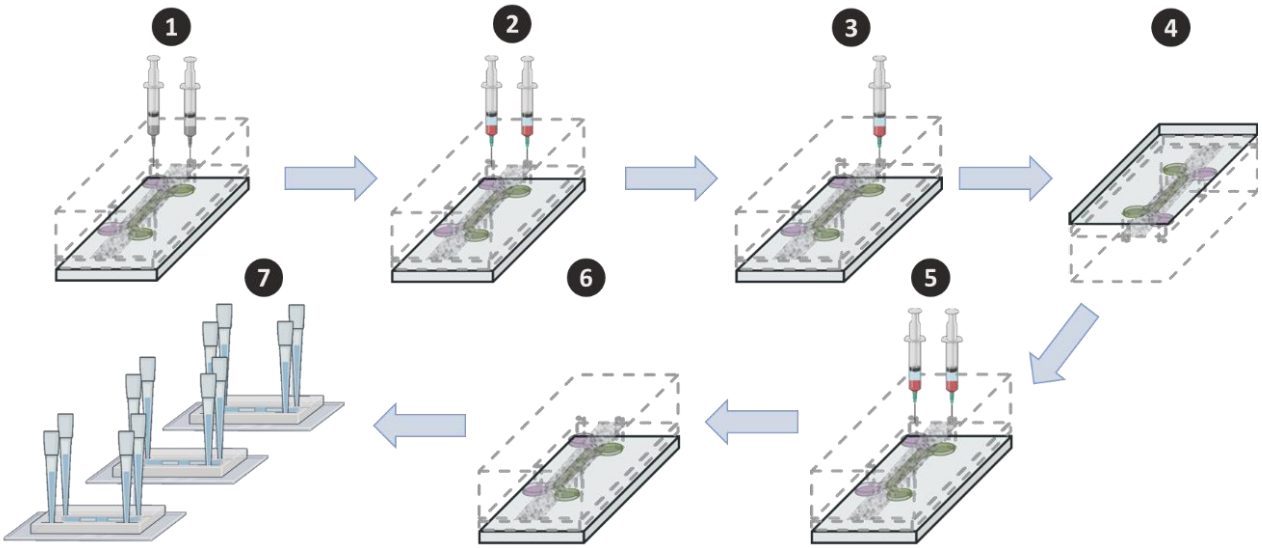

Figure 54: Illustration of cell culture protocol in the Glomerulus-on-chip. 1) System coating with ECM proteins, 2) media equilibration, 3) podocytes seeding in the lower channel and 4) gravity induced seeding on the lower side of the membrane by turning the system upside down, 5) GEnCs and PECs seeding in the top and bottom compartment respectively, 6) flush of non-adherent cells, 7) reservoir and media filling for long term culture.

Cells are left to grow under perfusion (detailed in the next section) for 2-3 days under the permissive temperature (33°C) until fully confluent monolayers are formed. Then the cells are switched to the differentiation temperature (37°C), and left to differentiate for 2 weeks under perfusion.

2.4.2 Long term perfusion (>2 weeks)

Once the cells became adherent in the microsystems a continuous media renewal and relevant shear stress has to be brought to unsure correct cell survival, differentiation,… One major issue is to determine with accuracy the glomerular capillary shear stress and mimic it by perfusing the device with the appropriate flow rate. In glomerular capillaries, wall shear stress has been estimated to be approximately 31 dynes/cm^2 in rats (Ferrell et al., 2015) using intravital imaging. In typical circumstances, the glomerulus experiences a high shear stress environment, where shear forces typically fall within the range of 5 to 20 dynes/cm^2 in most capillary loops (Ballermann et al., 1998). However, certain computational models have suggested a broader range of 1–95 dynes/cm^2 (Remuzzi et al., 1992). Some studies consider the capillary normal flow rate to be 5µl/min and the hypertensive 10-15µl/min (M. Zhou et al., 2016a). Such perfusion rates can be provided by syringe or peristaltic pumps.

Furthermore, CiPodocytes are quite sensitive to shear stress (Friedrich et al., 2006), so we need to work with extremely low shear forces (≤0.25 dyn/cm^2) in the urinary channel to limit cell stress.

However, one of the principal hurdles of microfluidic culture is to provide constant and continuous media renewal as well as other relevant cues, such as shear stress, over the whole course of the experiment. In our case primary conditionally immortalized cells need to differentiate for at least a week before expressing differentiation markers. This means that cultures should be maintained without introducing air bubbles, contaminants, shear stress variation over the course of weeks. If we summarize the requirement for a perfusion system in the context of the glomerulus-on-chip, we have:

- Long time media renewal (≥2 weeks)
- Low shear stress on podocytes (≤ 0.25 dyn/cm2) in the urinary chamber
- Sampling possibility
- Scalability

The main aspect to tackle with microfluidic cell culture is to deal with the necessary air bubbles present due to the application of the perfusion. Accumulation of unwanted bubbles in microfluidic channels can abruptly alter the microenvironment surrounding adherent cells, resulting in cell damage and death (Zheng et al., 2010). The presence of a single bubble can adversely impair biological function and often viability as it increases the wall shear stress in a liquid-perfused microchannel by at least one order of magnitude. This is particularly true for long-term culture (≥ weeks). Current methods for trapping bubbles in microfluidic systems have limitations, including the necessity to halt fluid flow or the need for an external vacuum or pressure source.

In the early stages of the project, and in order to validate cell culture protocols in fabricated systems, we first used a classical syringe driven perfusion approach ensuring that the cells could actually grow confluently in a microsystem and form monolayers of cells. This was done through

culturing HeLa cells on the 3 layers of the system for a restricted duration (1 week), since these cells proliferate quite rapidly.

2.4.2.1 Syringe driven perfusions

To be able to grow cells in microchannels, both media renewal and relevant shear stress has to be brought to the cells. This is usually done with microfluidic perfusion systems based on the use of peristaltic, syringe or membrane pumps. For perfusion exceeding a day, bubble management becomes critical. We present here the approach used to culture HeLa cells in our systems.

We used several syringe pumps in line with a custom made bubble trap (Figure 55) to supply the media flow (0.3 µl/min) allowing precise delivery of low shear-stress forces inside the channel and continuous media renewal. For this first proof of principle we used HeLa cells to validate that cells could grow confluently and survive in the systems on 3 layers when provided with continuous media renewal, low shear stress, bubble free conditions for at least a week. The cells could grow confluently using such perfusion technique for a week forming monolayers of cells on the 3 layers of the system (see section 2.6.1.1).

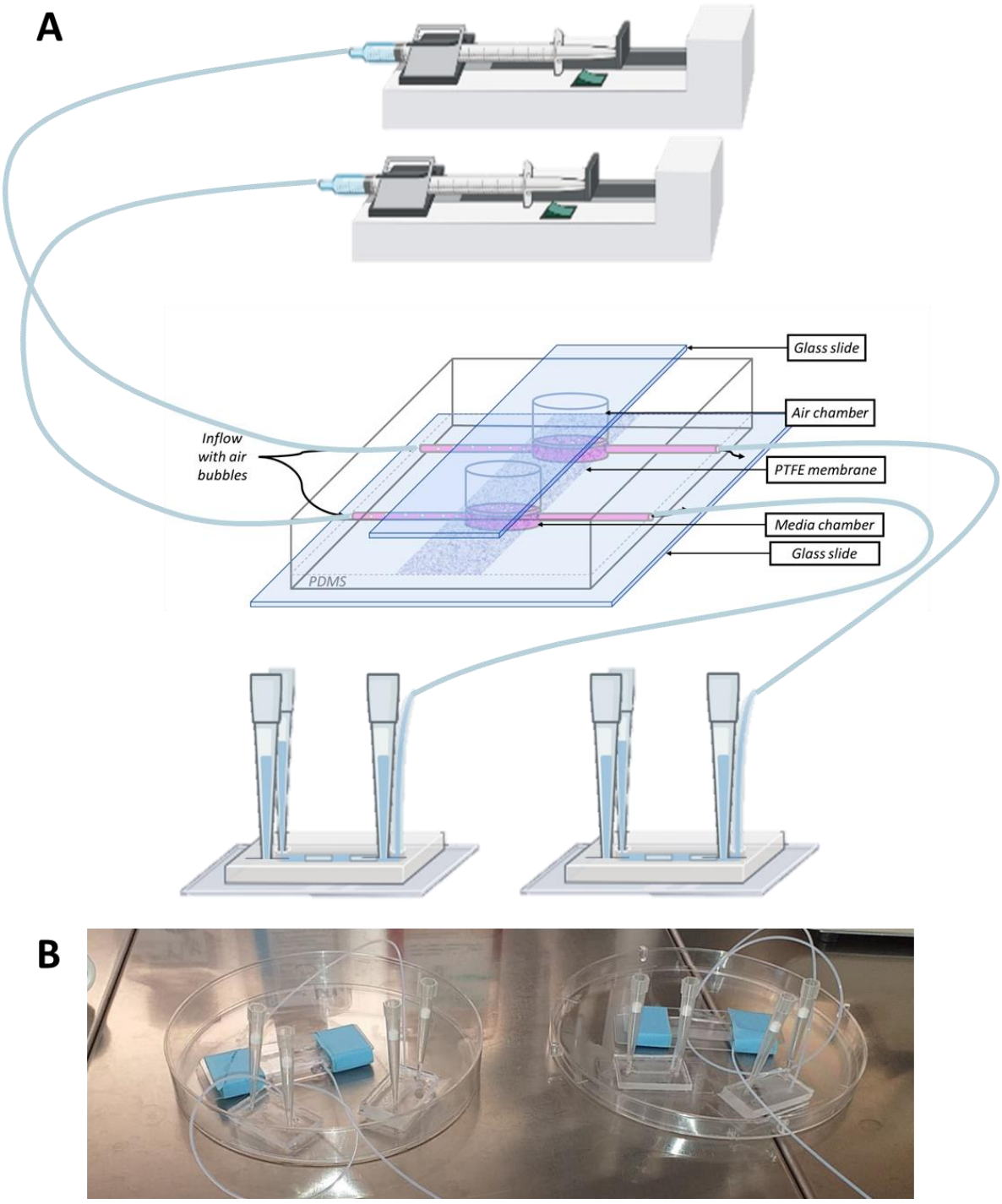

Figure 55: A) Scheme of syringe driven perfusion in line with bubble trap. When bubbles reach the trap chambers they are trap and ruptured on the PTFE membrane and reservoir. The traps are then connected to the systems. B) picture of the assembly under the hood.

The hydrodynamic properties of the microsystems were characterized through numerical simulations to notably identify the dependencies of the relevant quantities (shear stress, flow rate) with the system geometry (size, shape,…). This provides a quantitative knowledge of the stimulation parameters in the actual chips.

We used a robust simulation framework for flow profiles in the microsystems. A 3D model of the microsystem was constructed using computer-design software (Fusion 360, Autodesk). The

model is then exported to a computational fluid dynamics software that instantly finds flow trends while updating input parameters or making geometry updates.

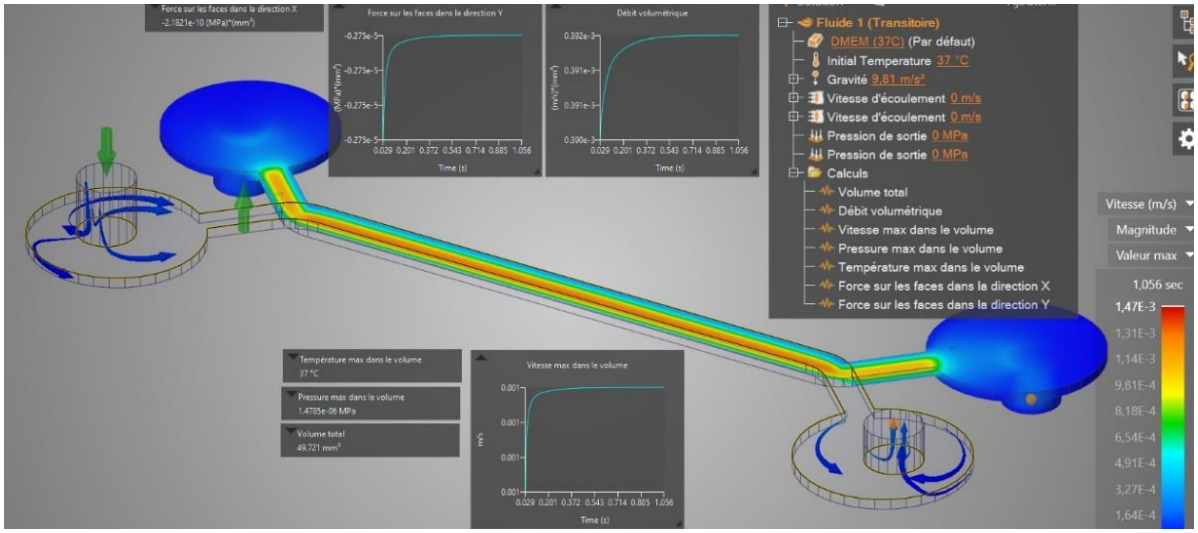

Figure 56: CFD (Computational Fluid Dynamics) simulation in Ansys Fluent solver, requires the fluid parameters such as viscosity, density, and temperature and calculates on the run the fluid flow profile from the inlet.

The wall shear stress within our channels is equal to ~ 0.053 and 0.212 dynes/cm^2 respectively in the vascular and urinary compartments for a flow rate of 0.3 µl/min, and we can operate perfusion between 0.1 and ~30µl/min easily.

While co-culture is feasible using this approach, syringe driven perfusion autonomy is limited to the syringe distribution volume (with 1 ml syringes and 0.3µl/min perfusion, 2.3 days). Microfluidic tubings, bubble traps, and interconnects are also fairly complicated to manage for long term perfusions more so if many systems are grown in parallel, were contamination became an issue due to the frequent tubing changes.

We thus decided to develop a more scalable approach using gravity driven perfusion, taking advantage of the reservoirs in our system, to provide a continuous media renewal on cells as well as relevant shear stress.

2.4.2.2 Gravity driven perfusions

Our objective it to bypass the previous limitations; tubings, contaminations, media filling, user intervention, while still providing relevant cues; minimal shear stress (on podocytes), media renewal for weeks.

This gravity-driven flow approach was developed during Ghadi Nehmé bachelor's internship, under my supervision. The objective of this project was to develop a simple, inexpensive permanent gravity driven perfusion approach to get rid of conventional microfluidic related plumbing issues and increased throughput.

The principle is that, in order to recirculate the culture medium in a permanent manner in the system, we need to perturb the hydrostatic equilibrium. By introducing reservoirs of controlled heights filled with medium at the inlets and outlets of each channels, and by rotating the system between an angle α and $-\alpha$, the difference of hydrostatic pressure can create a sufficient flow to have a full chamber media renewal (Figure 57, A).

To rotate the systems, a simple and inexpensive oscillator (Figure 57, B) was designed, allowing microdevice inclination changes of angles ranging from 1 to 30°. The oscillator initial position is of angle $-\alpha$, then after the equilibrium is reached and to initiate the flow in the device the oscillator goes to α position. This cycle is repeated automatically and the time period is user programmable in the touch control graphical user interface that is piloting the servomotor.

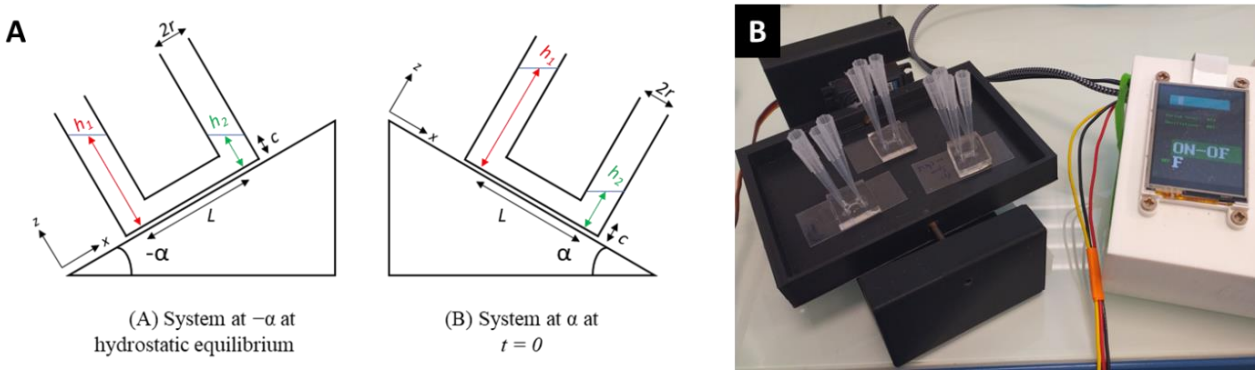

Figure 57: A) System before and after the rotation of the plate by angle 2α, B) Custom Arduino based oscillator allowing precise inclination and rocking period control, servo-motor is waterproof to be compatible with cell-culture incubators, 3 systems and reservoir are shown.

After reaching the hydrostatic equilibrium at −α, we put the system at an angle α. Here the hydraulic resistance is estimated to be of the first order for a rectangular channel of dimensions *b*, *c* and *L*. *h* and *H* represent the fluid height in the reservoirs, are geometrically reservoir centered and are measured from coverslip surface (bottom of the channels). We have initially at $t = 0$, that $h_1(0) = h_0 + L\,tan(\alpha)$ and $h_2(0) = h_0$. We define $H(t) = \big(h_1(t) + L\,tan(\alpha) - h_2(t)\big)\,cos(\alpha)$. Using the geometry of the problem, we get that: $H(0) = 2L\,sin(\alpha)$.

After a given time *T*, the system will reach a new hydrostatic equilibrium, where:

$$h_1(T) = h_0 \text{ and } h_2(T) = h_0 + L\,tan(\alpha)$$

Then, the displaced volume will be:

$$V = \pi r^2\big(h_2(T) - h_2(0)\big) = \pi r^2 L\,tan(\alpha) \approx \pi \times 2^2 \times 9\,tan(5°) = 9{,}8\,mm^3 \approx 10\,\mu L$$

$r = 2\,mm$ for 200 µL pipet tips filled with 200 µL of medium.

The total volume of media in the lower channel of the microsystem is 1,6 µL, and 3,2 µL in the upper channel, so a single equilibrium change can fully replace the media in both channels.

The difference of pressure between the first and the second reservoir drives the fluid. We have that the pressure difference is:

$$\Delta P(t) = \rho g H(t)$$

This generates a Poiseuille flow, with flow rate:

$$Q = \frac{bc^3\Delta P}{12\eta L}$$

By conservation of the flow rate, we have that the flow in the two cylinders is equal to the flow in the linking part, then:

$$Q = Q_2 = Q_1, \text{ with } Q_1 = -\pi r^2 \frac{dh_1}{dt} \text{ and } Q_2 = \pi r^2 \frac{dh_2}{dt}$$

We obtain the characteristic time τ :

$$\tau = \frac{6\pi r^2 \eta L}{bc^3 \rho g \cos(\alpha)}$$

At $T' = 5\tau$, $H(T') \approx 0$.

For the lower urinary channel, seeded with podocytes and PECs:

$r = 2mm, \eta = 10^{-3} Pa.s, L = 9mm, b = 800\mu m, c = 50\mu m, \rho = 10^3 kg.m^{-3}$, we get that:

$$T' = \frac{30\pi r^2 \eta L}{bc^3 \rho g \cos(\alpha)} \approx 3405\ s \approx 56\ min$$

For the upper vascular channel, seeded with endothelial cells:

$r = 2mm, \eta = 10^{-3} Pa.s, L = 9mm, b = 800\mu m, c = 100\mu m, \rho = 10^3 kg.m^{-3}$, we get that:

$$T' = \frac{30\pi r^2 \eta L}{bc^3 \rho g \cos(\alpha)} \approx 425\ s \approx 7\ min$$

The equilibrium is reached in the lower urinary channel after 56 and 7 minutes in the vascular channel for 200 µl reservoir and a 5° angle giving flow rates that are 0.17 and 1.42 µL/min on average. This yields a wall shear stress of 0.120 and 0.250 dynes/cm^2 respectively. This enables to have a lower shear stress on the lower compartment needed for podocytes survival.

Depending on the size of the reservoir size (height and diameter) the channels height, and the angle we can reach physiological flow rates while maintaining a flow difference between the urinary and vascular channels.

Even though the flow rate profile in the devices is not linear and unidirectional, this setups allows for minimal user intervention on the systems letting cells grow to confluence and differentiate. This system allows to culture multiple organ-on-chips simultaneously with long term culture and low stress on the cells.

We built several oscillators, allowing positioning up to 6 microsystems per oscillator in parallel in the incubator, while being fully programmable from the confined cell-culture lab desktop thanks to the touch control box (~100 euros/oscillator).

Their reservoir system offers many advantages including; the possibility to easily change the reservoir in a sterile culture hood using sterile filter tips, the possibility to sample culture media, not using any microfluidic tubings thus decreasing the risk of bubbles appearing, long autonomy (several days) with low to medium flow rates.

2.5 Characterization of cell differentiation

2.5.1 Cell culture characterization

Prior cultivating cells in co-culture in microsystems, CiPodocytes, HUVECs, CiGEnCs, and CirPECs were characterized after inducing their differentiation on 2D substrate, to assess any phenotypical changes in 3D co-culture later on.

The cell lines were seeded on human fibronectin coated glass coverslips and allowed to differentiate 1 week at 37°C before fixation with 4% PFA for 15 min at room temperature. Before immunolabelling, cells were permeabilized with a 0.1 % Triton, 1% BSA solution for 1h before blocking (5% BSA for 1h). Cells were then labeled by immunohistochemistry for characterization. Cells were then stained for markers of differentiation and imaged either using epi-fluorescence imaging or confocal imaging.

2.5.1.1 CiPodocytes express Podocin and WT1

WT1 (Wilms' tumor 1 protein) is a transcription factor that is of particular significance in podocytes due to its role in kidney development, maintenance, and disease. Mutations or dysregulation of WT1 expression in podocytes have been linked to various kidney diseases (Morrison et al., 2008).

Podocin is a transmembrane protein that is primarily located in the slit diaphragm, a specialized intercellular junction between adjacent foot processes of podocytes. Podocin is one of the key components involved in maintaining the structural integrity of podocytes and ensuring their proper function (Saleem, Ni, et al., 2002).

Differentiated podocytes both expressed podocin and WT1 (Figure 59). However, podocin localization seemed diffuse in the cell (Figure 58) and did not permit to observe slit diaphragm formation at cell-cell junctions. These differentiation markers are typically found in podocytes (Morrison et al., 2008; Schwarz et al., 2001), indicating a correct differentiation.

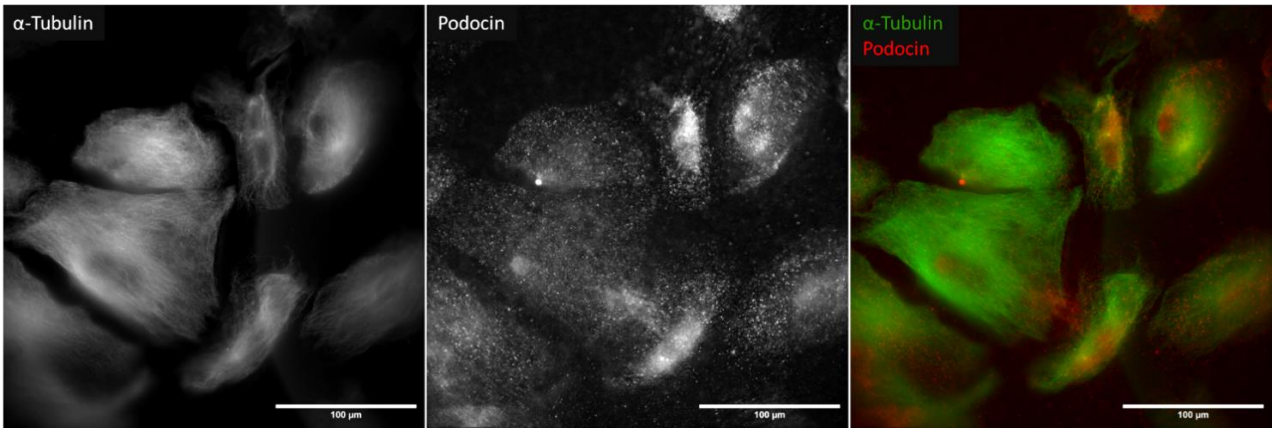

Figure 58: Epifluorescence images of CiPodocytes differentiated for 1 week at 37°C grown on glass coverslip coated with fibronectin, and stained for α-tubulin (CF 568) and podocin (Alexa Fluor 647) 60X magnification.

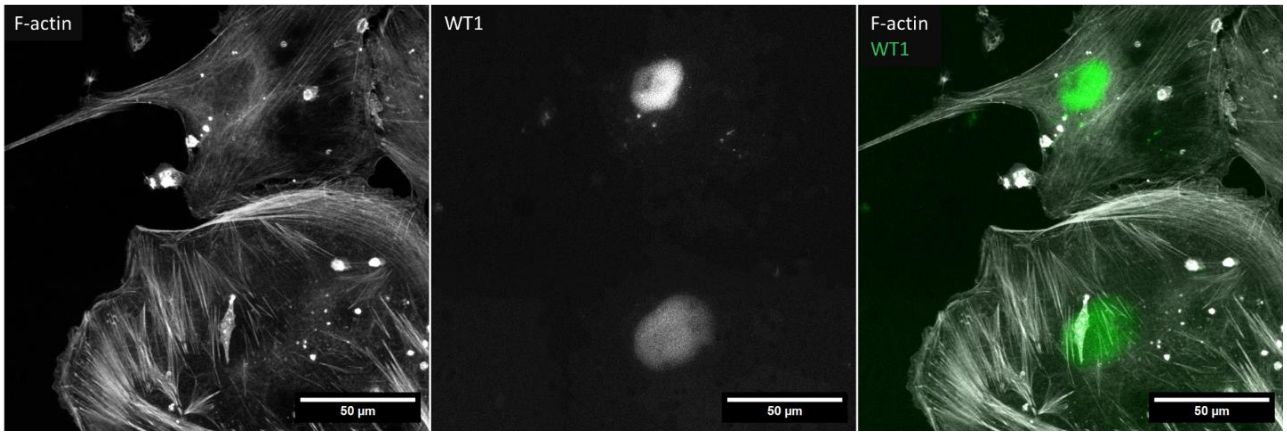

Figure 59: Confocal images of CiPodocytes differentiated for 1 week at 37°C grown on glass coverslip coated with fibronectin, and stained for WT1 (Alexa Fluor 488) and f-actin (Phalloidin 590) 60X magnification.

2.5.1.2 HUVECs and GEnCs express vascular endothelial-cadherin (VE-cadherin)

Vascular Endothelial-cadherin (VE-cadherin) is a critical component of cell-cell adhesion in the endothelium, ensuring the integrity of blood vessel walls and regulating various physiological processes. VE-cadherin is a transmembrane protein that belongs to the cadherin family of adhesion molecules. It is primarily located at the adherent junctions of endothelial cells (R. R. Foster et al., 2008).

Both endothelial cells types expressed VE-cadherin at cellular junctions but also close to the nuclei where the protein is probably maturating (Golgi, endoplasmic reticulum) (Figure 60, Figure 61).

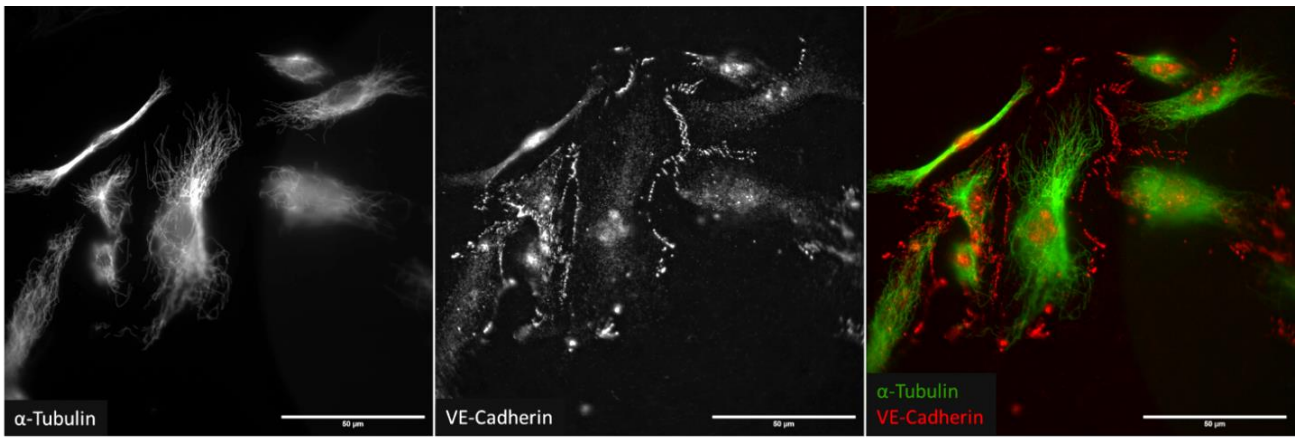

Figure 60: Epifluorescence images of HUVECs grown for 1 week at 37°C grown on glass coverslip coated with fibronectin, and stained for α-tubulin (CF 568) and VE-Cadherin (Alexa Fluor 647) 60X magnification.

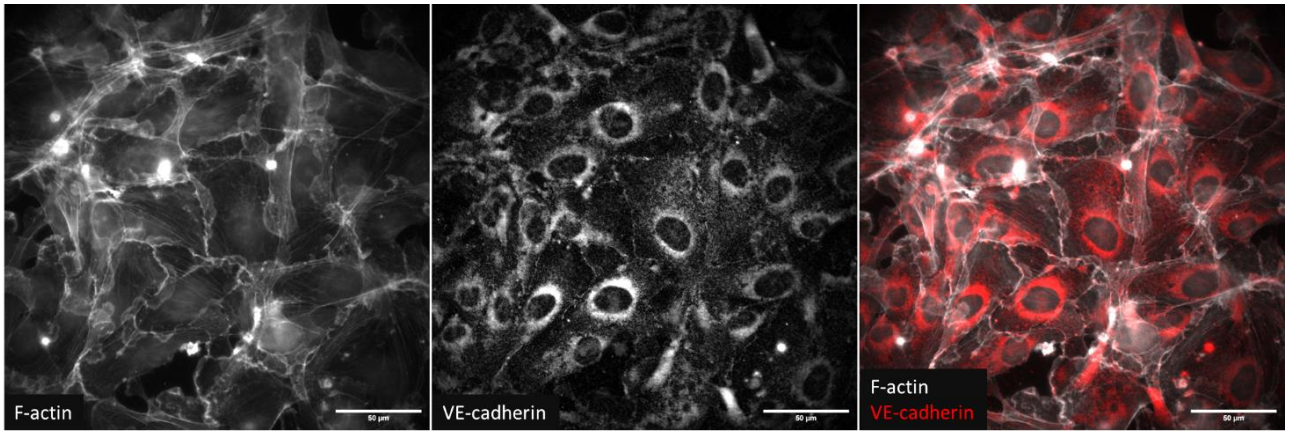

Figure 61: Epifluorescence images of CiGEnCs differentiated for 1 week at 37°C grown on glass coverslip coated with fibronectin, and stained for f-actin (Phalloidin 590) and VE-Cadherin (Alexa Fluor 488) 60X magnification.

2.5.1.3 CirPECs express Claudin-1

Claudin-1 is a protein that belongs to the claudin family, which are integral membrane proteins found in tight junctions of epithelial and endothelial cells. Claudin-1 is a specific marker of PECs in the kidney (Smeets et al., 2014).

CirPECs expressed at least partially Claudin-1 when grown confluently (Figure 62). The staining however showed that tight junctions are only partially resolved.

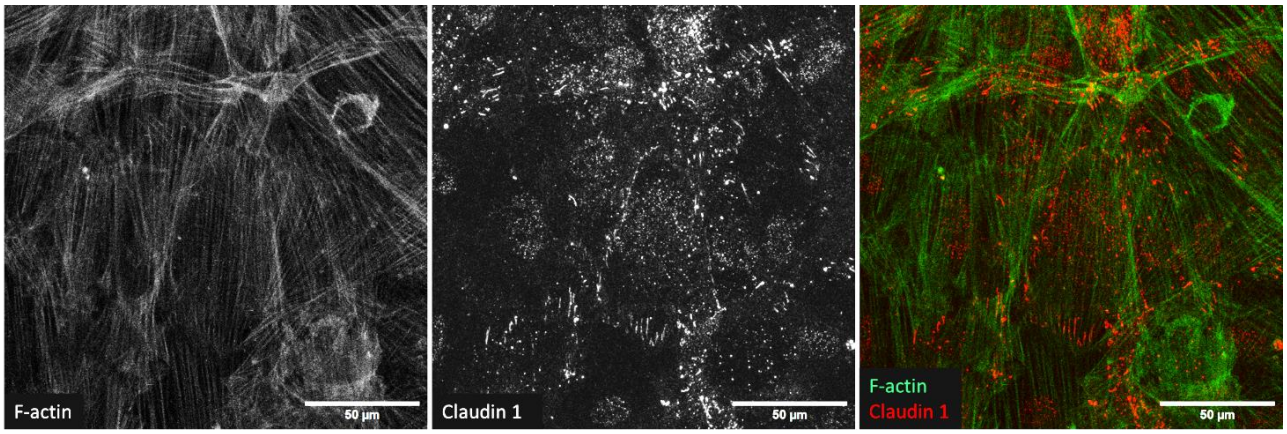

Figure 62: Confocal images of CirPECS differentiated for 1 week at 37°C grown on glass coverslip coated with fibronectin, and stained for F-actin (Phalloidin 647) and Claudine-1 (Alexa Fluor Plus 488) 63X magnification.

All cell types thus exhibited markers of differentiation when grown separately on simple 2D surfaces (glass coverslips). These staining will serve a reference to compare differentiation markers expression in co-culture and in 3D arrangement. All the cells expressed typical markers after induced differentiation indicating that these cells are relevant to mimic the glomerular organization and function. We tough observed that CirPECs behaved differently than CiPodocytes and CiGEnCs in culture and that their proliferation rate seemed high.

2.5.2 CirPECs remain proliferative while differentiated

While growing CirPECs on glass coverslips confluently we realized that PECs continued proliferating while being cultured at 37°C and thus differentiated. This was not observed for

CiPodocytes nor for CiGEnCs. We quantified this proliferation state by using a variation of TransEpithelial/TransEndothelial Electrical resistance TEER assay to attest the proliferating state of the cells, and wound healing experiment to assay for cell migration and division rate of CirPECs.

2.5.2.1 Transepithelial/transendothelial electrical resistance (TEER)

TEER measures cell confluency in cell culture models, particularly in epithelial/endothelial cell monolayers. The method involves the application of a small electric current across the cultured cell layer, and the resulting electrical resistance is then measured (Srinivasan et al., 2015). As the cells become more confluent and form tight junctions, the resistance to the electric current increases. This increase in electrical resistance serves as a quantitative indicator of cell confluency and integrity of the cell layer. TEER is measured using 4 electrodes (2 references electrodes, and two measurement electrodes) placed on both sides of the membrane and cells inserts, as illustrated in Figure 63.

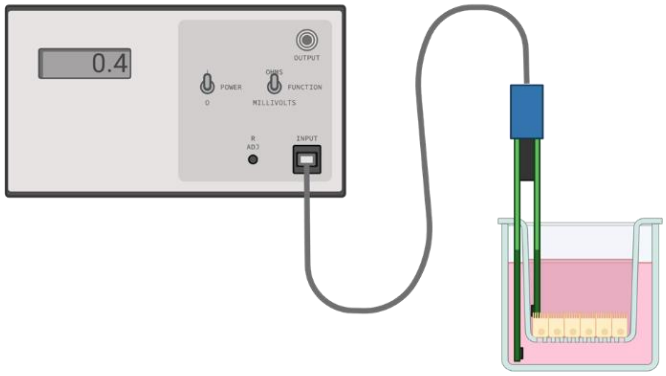

Figure 63: TEER measurements illustration.

We thus plated subconfluently, proliferating CiPodocytes, CiGEnCs, and CirPECs on the apical (upper) side of Transwells inserts (PET, 12 mm diameter, 3 µm pores), let the cells adhere and placed them at 37°C to induce their differentiation. We then monitored the TEER values once a day for 11 days using a chopstick electrode (EVOM) (Figure 64). The EVOM instrument measures the TEER value in ohms (Ω) typically within a few seconds. To calculate the corrected TEER values, we subtract the background resistance of inserts without cells (blank value) and normalize by the surface of the insert (1.12 cm^2). Since TEER measurements are sensitive to various factors, including cell density, temperature, and culture medium. The electrode was equilibrated 15 min in warm media prior performing the readings.

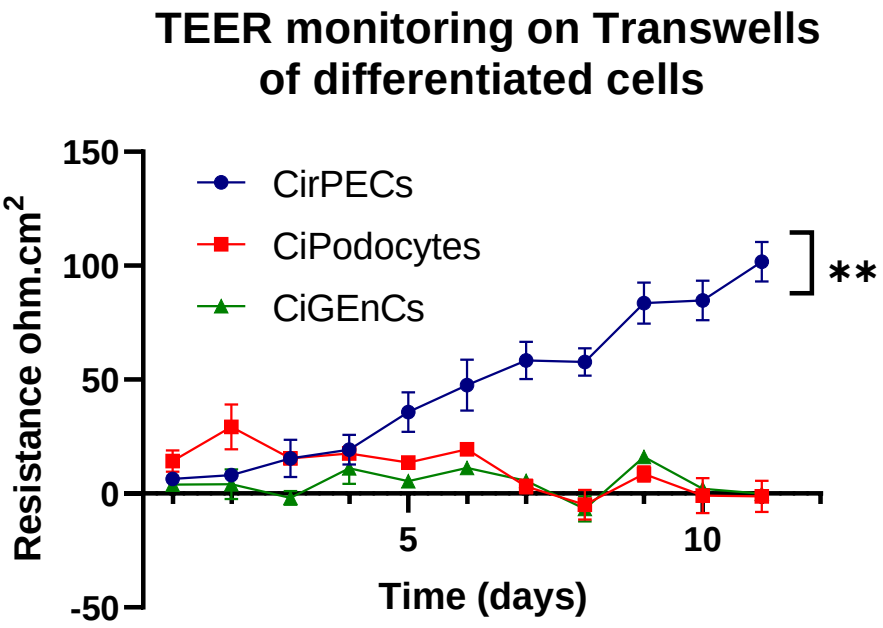

Figure 64: Normalized TEER values of differentiated cells grown on apical side of Transwell inserts (PET, 12 mm, 3 µm pores) (n=3) area under curve was compared for each cell line (error bars are SEM, stars from Friedman test).

Plating the cells subconfluently allows to ensure that if cells remain quiescent, no resistance will be observed. In this case TEER values continued to increase significantly for CirPECs after 1 week of culture at 37°C. This was not observed for CiPodocytes nor for CiGEnCs. This indicates that either oncogene repression with temperature is impaired for CirPECs or that CirPECs continue proliferating on the membrane.

CirPECs migration and proliferation was also studied using a migration assay (Wound-healing) using live imaging.

2.5.2.2 Wound-healing migration assay

Wound healing assay, or scratch assay, is a common experimental technique used in cell biology and tissue culture to study cell migration and wound repair processes. We create a wound or cell-free gap in a confluent monolayer of cells and observe how the cells migrate to close the gap over time (Robles-Flores, 2021). The wound healing assay can be performed by scratching a confluent cell monolayer using a sterile tool, or by using an insert/stencil placed on the culture surface before cell seeding using special chambered inserts (Figure 65) that allows physical cell exclusion or separation of controlled thickness when it is removed to create the wound.

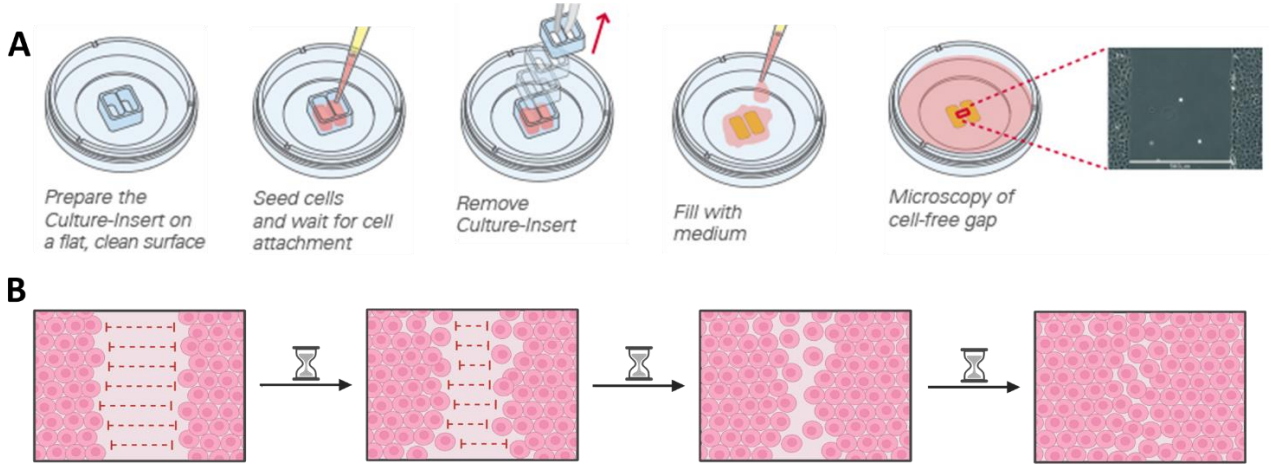

Figure 65: A) Principle of wound healing assay using chambered inserts (illustration from supplier Ibidi), B) illustration of wound closure and analysis over time with cells migrating to close the wound.

CirPECs were cultured proliferating (permissive temperature of 33°C) on chambered culture dishes (IBIDI culture-insert 2 wells) in which cells are separated with a 500 µm stencil until they form a confluent monolayer. The wound is then created by removing the stencil with forceps. After creating the wound, the cell culture was washed with growth medium to remove any cell debris or detached cells. Cell migration/divisions are observed using time-lapse imaging using either phase contrast microscopy or epifluorescence microscopy (for CirPECs stably expressing GFP). Cells were observed on an inversed microscope equipped with a with a live-cell imaging system.

Once the wound was created, cells were followed either at 33°C (permissive temperature) or 37°C (differentiation of cells) with 5% CO_2 and 100% humidity taking one axial series of images (Z-stack) with a 5 µm spacing over 25 µm, every 15 min for several days until the wound closes. Taking a z-stack allows to unsure that cells remains at least partially in focus during the course of the experiment (days, Figure 66).

The analysis of the time-lapse images allows to measure and quantify the rate of wound closure (area of wound closing/time) and division rate of the cells. For this two ImageJ plugins were used. The first plugin (Suarez-Arnedo et al., 2020) enables the measurement of the distance between the advancing edges of migrating cells over time, adjusts the average wound width to account for its inclination, and quantifies other key parameters such as area, wound area fraction, average wound width, and width deviation.

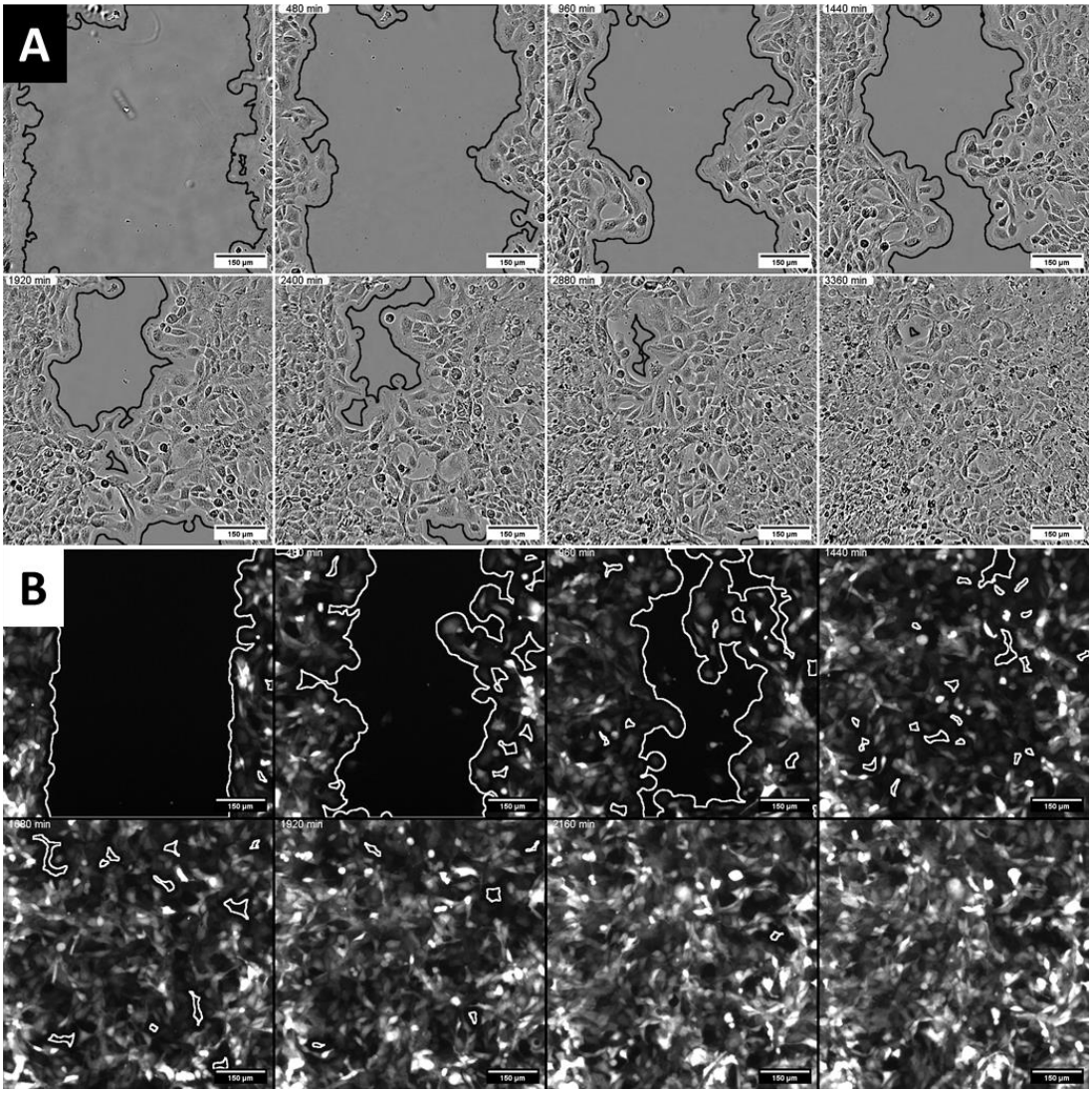

Figure 66: Wound healing migration assay images using A) transmission phase contrast imaging and B) epifluorescence microscopy (10X magnification), dark and white lines indicate wound limits obtained using the wound healing plugin in ImageJ. The plugin was run with the following parameters (variance = 20, pixel saturation = 0,001, threshold = 10).

To analyze the wound healing area closure, first the average of the Z-stack was projected for each time point, and images were then corrected for each time point by the median time projection to remove field illumination inhomogeneities. We obtain for each time point the area fraction of the wound. This was then normalized to the initial time point area to compare the different datasets since the stencil creating the wound has a 10% thickness variation (IBIDI documentation). Wound area closure as a function of time are presented in Figure 68.

We moreover counted cell divisions during the timelapse of the wound closure. To localize and count cell divisions a second ImageJ plugin, TrackMate based on Difference of Gaussians (DoG)detection, was used (Tinevez et al., 2017). This plugin is designed to track and analyze the movement of particles or objects in time-lapse image sequences. It is commonly used to track cell trajectories, microbeads, vesicles, or any other moving objects. A manual oversight of detected object was then performed to get rid of false positive detection of division events. We then obtained localization maps of dividing cells in time, and one example has been plotted in Figure 67.

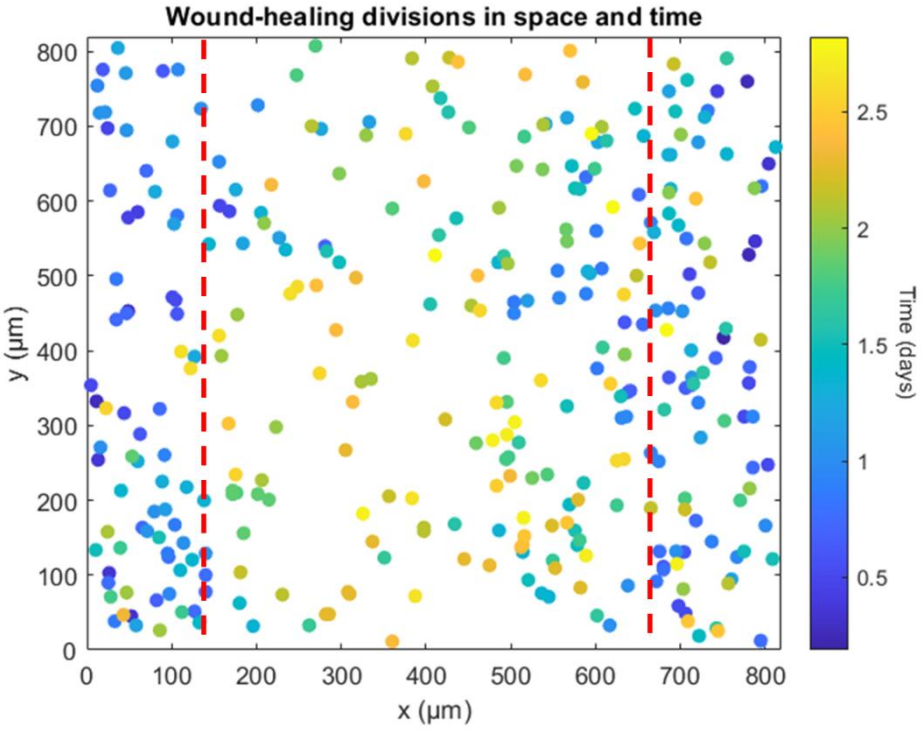

Figure 67: Space/time plot of CirPECS division events in a wound healing experiment (red dashed lines indicate initial wound) when grown under non-permissive conditions at 37°C

From this map we can observe that cellular divisions first occur at the edges of the wound, and then as the wound closes divisions occur everywhere in the field of view. This suggest that the wound closing could be mostly driven by cell division and not by cell migration.

To analyze the division rate of different conditions the cumulative number of cell division was plotted against time (Figure 68: A). We compared wound closure for CirPECs under permissive and non-permissive conditions with different time scales of differentiation (0 and 2 days). Differentiation of cells decreases their proliferation as expected but the division rate remained high even for cells exposed to permissive conditions during 5 days (2 days, + 3 days of experiments). To extract a division rate we then fitted the curves with a Gompertz equation, which is a mathematical model commonly used to describe the growth of biological populations (Tjorve & Tjorve, 2017).

The Gompertz equation is characterized by three main phases; at the beginning the growth rate is relatively slow while the population is adjusting to the new environment, as time progresses, the population starts to grow at an exponential speed, and finally as the population size approaches a carrying capacity or limiting factor, the growth rate decreases. This function is well tailored to fit cell proliferation that should have contact inhibition once confluency is reached.

Assuming a simple model to simulate wound area closing driven only by cell division and not by cell migration. In this model the area closing is defined by the initial wound area to which is subtracted twice a constant cell area per division event with occurrences defined by the Gompertz fits for each conditions. The mean cell area was estimated to 1500 µm^2 by segmenting the cells manually on several images. The model area closure curves are plotted against the actual wound area fraction closure in Figure 68, B.

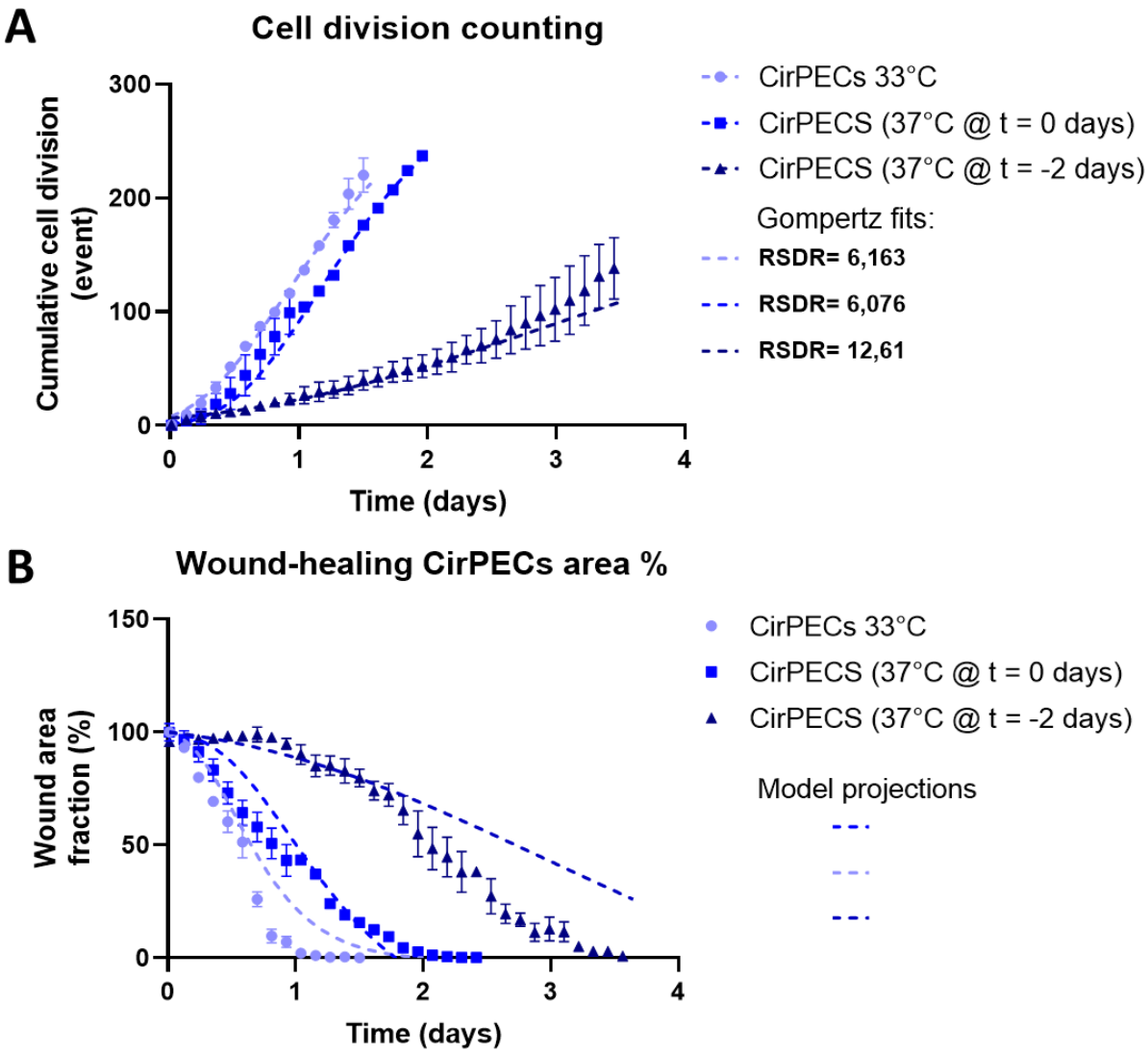

Figure 68: A) Cumulative cell division number fitted with gompertz equation during wound healing experiments, B) Wound healing area closure measured and projected with the gompertz model (error bars are SEM, n=3, RSDR = Robust Standard Deviation of the Residuals).

We first observe from these curves that CirPECs division rates decrease with the differentiation time. This rate can be fitted with a good accuracy with a Gompertz growth model. We can also observe that the wound closing speed decreases with differentiation time. This simultaneous effect might suggest that the decrease in division is responsible for the wound closure speed decrease.

To isolate the division and migration component leading to wound closure, we can use our model with the fitted Gompertz growth to obtain the projection for the wound closure driven only by cell division (Figure 68, B dashed lines). By looking at the difference between integrals of measured and projected wound area closing, we can estimate a migration wound closing component presented in Figure 69. Interestingly we can notice that while the division rate decreases the apparent migration component of the cells remain constant once the cells shift to their permissive state.

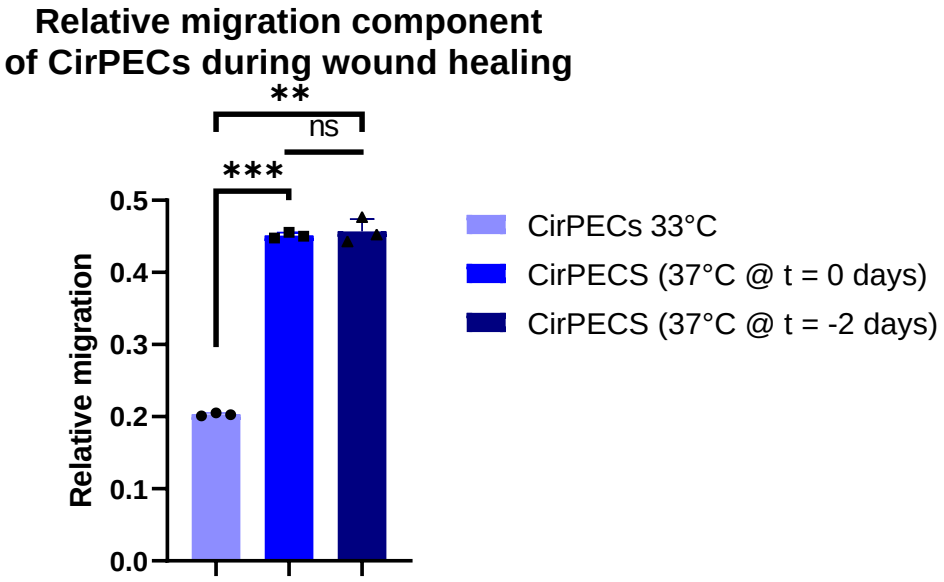

Figure 69: Migration component of wound healing experiments with CirPECS (n= 3).

Overall healing experiments for CirPECs are mainly dominated by cell division while cells are permissive and migration plays a more important part in wound closure as the cells differentiate. TEER and wound healing assays showed that CirPECs are still proliferative when differentiated and showed and increase motility. This could suggest that CirPECs could be particularly proliferating in our glomerulus-on-chip.

2.6 Functional and phenotypic characterization of the "glomerulus-on-chip"

2.6.1 Validation of cell co-culture in microsystems

2.6.1.1 Long term cell culture is possible in microsystems

As the first proof of concept for cell culture and imaging capabilities in our microsystem, we used HeLa cells seeded on top/bottom of PET membranes as well as on the glass coverslip. The perfusion was provided by syringe pumps in line with custom bubble traps (previously described in section: 2.4.2.1) for a week. Systems used at the time had a relatively higher urinary chamber (around 100 µm high).

Systems were then fixed and permeabilized as previously described. Cells were then labeled with primary antibodies and secondary fluorescent antibodies. HeLa cells were labeled for cytoskeleton markers (tubulin, actin) and observed on a confocal microscope (Leica SP8X) to allow good optical sectioning of the 3 cell layers (Figure 70) and 3D reconstruction.

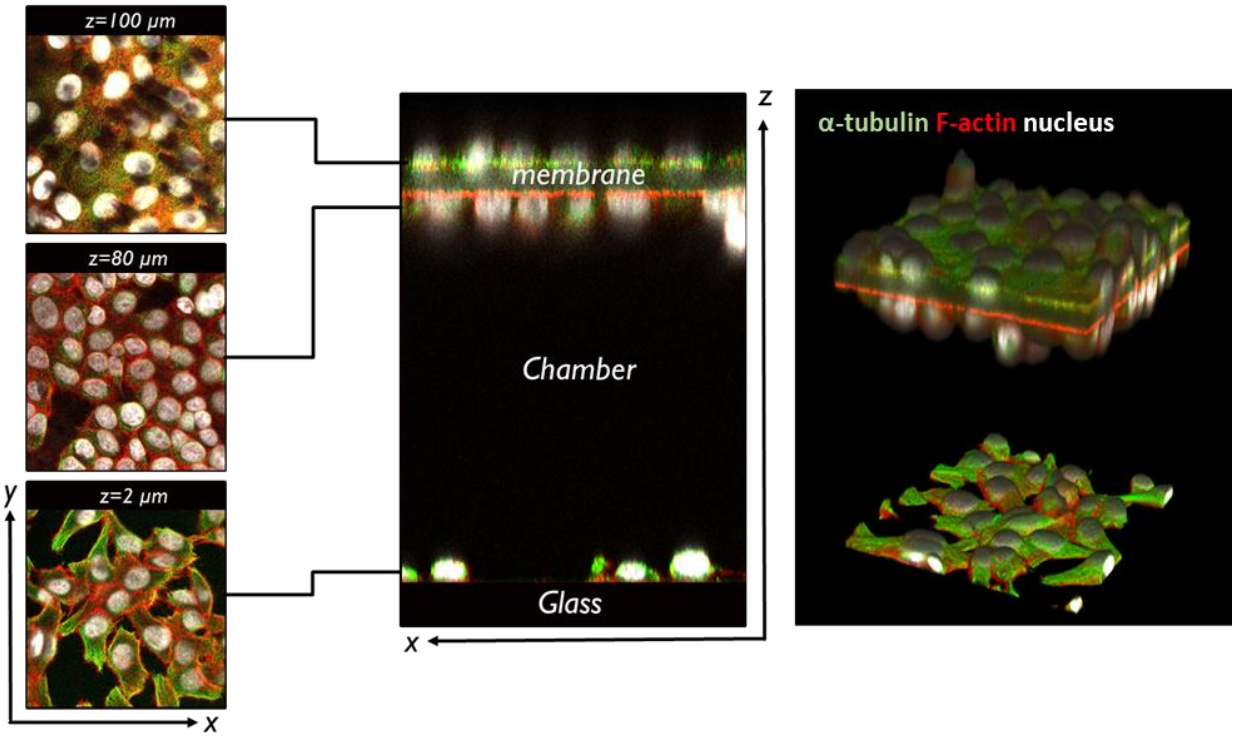

Figure 70: Confocal images of HeLa cells in the 3 layers microsystem with a 100 µm chamber and a PET membrane. Cells are cultured under perfusion for 7 days and stained for cytoskeleton: f-actin (phalloidin rhodamine red), α-tubulin (Alexa Fluor 488) and DAPI (40X magnification).

After 7 days, we could observe monolayers of cells which confluency levels reached 100% on both sides of the membrane and 80% on the surface of the glass coverslip. The confluency level depended mainly on seeding density and perfusion efficacy. The cells showed normal cytoskeleton phenotype (Tubulin/F-actin) as expected for epithelial cells monolayers. Interestingly the density on the lower side of the membrane was high, indicating that the cell seeding by gravity procedure was adapted.

This demonstrated that the prolonged cell culture in microsystems was possible. The fabrication process of the microsystems is thus compatible with cell culture (surface and sterility). The surface of the microsystem, glass coverslip and PET allowed cell attachment spreading and division, as they would in simple 2D culture system. The systems are efficiently sterilized by both plasma and UV treatment.

2.6.1.2 Co-culture of CiPodocytes and HUVECs

Using the same perfusion approach, we investigated if co-culturing cells that normally grow in different media was possible. For this we decided to culture Human Umbilical Vein Endothelial Cells (HUVECs) and CiPodocytes as purposes to recapitulate a glomerular filtration barrier (GFB) on PET membranes.

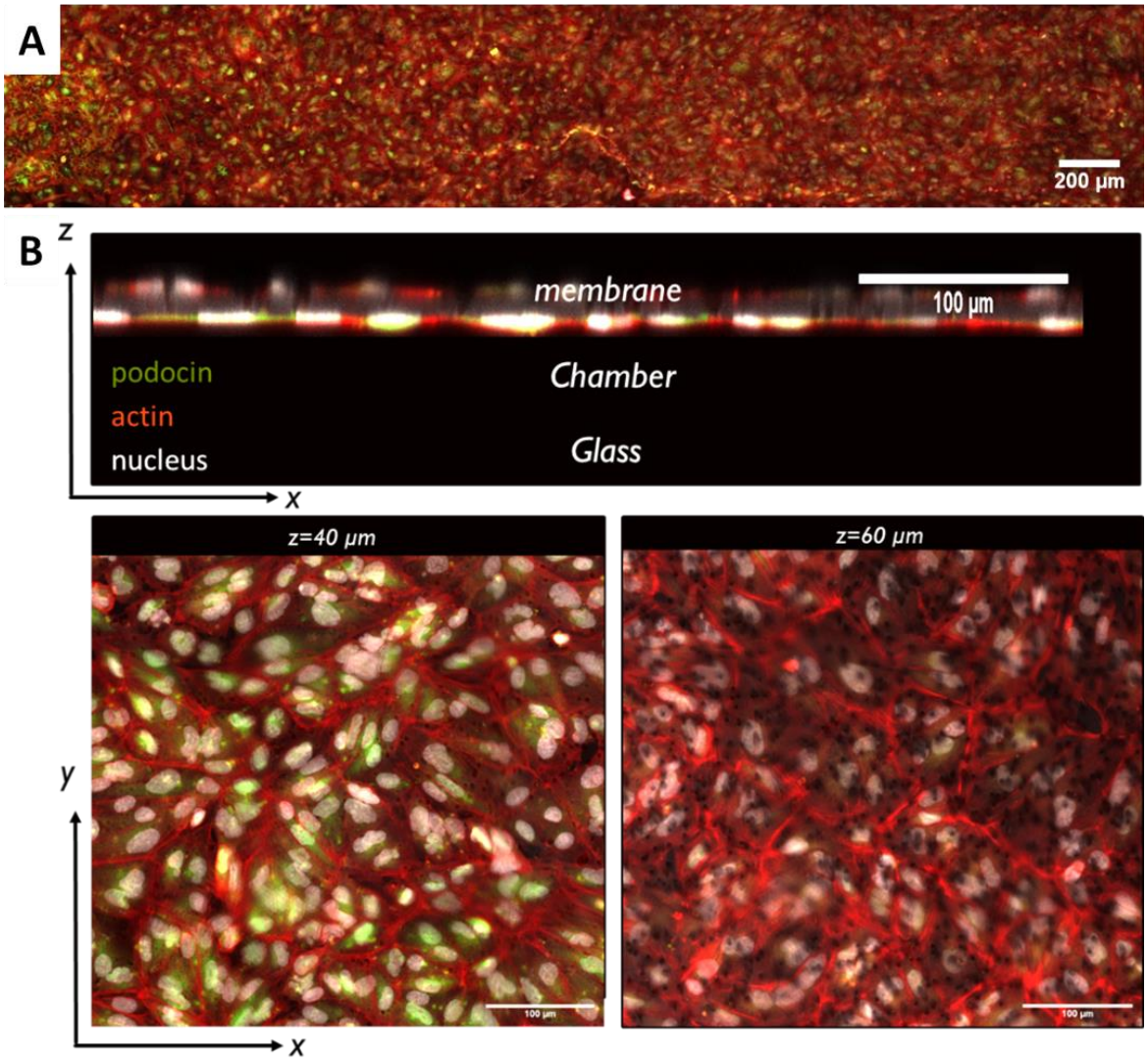

Figure 71: Confocal tilescan images of HUVECs and differentiated podocytes in a microsystem with a 50 µm chamber on both sides of a PET membrane coated with fibronectin. Cells are cultured under perfusion for 7 days and stained for cytoskeleton: F-actin (phalloidin rhodamine red), podocin (Alexa Fluor 488) and DAPI A) Z-average projection 10X magnification tilescan of a whole system B) 40X magnification tilescan.

In microsystems, cells reached 100% confluency (Figure 71) along the whole channel after 1 week of culture, and on both sides of the PET membrane. Cells were labeled for differentiation markers (VE-cadherin for HUVECs and podocin for CiPodocytes). CiPodocytes are almost all expressing podocin (Figure 71) indicating that they differentiated over the culture period of 1 week. Vascular cell staining for adherent junctions was often inconsistent, and the signal was confused within the scattering induced by the PET membrane pores. Imaging on the upper part of the membrane was challenging.

It is thus possible to co-culture HUVECs and CiPodocytes in microsystems for a long term (~1 week) using syringe driven perfusion techniques. However, many microsystems were inhomogeneous in term of cell density. Furthermore the throughput of the perfusion technique was very low (limited by the number of syringe pumps available, complex tubing interconnects, bubble traps filling, perfusion changes,…).

2.6.1.3 Overcoming Imaging and perfusion limitations

As the systems are observed from the glass coverslip towards the membrane on an inverted microscope, the fluorescence signal is well preserved in the lower compartment but up to a 50% signal loss is observed in the upper channel (Figure 72). Many of this signal loss is due to laser absorption, scattering or reflection of the PET membrane. Figure 73 shows an example of the signal that can be obtained for PET membranes alone when using conventional confocal imaging.

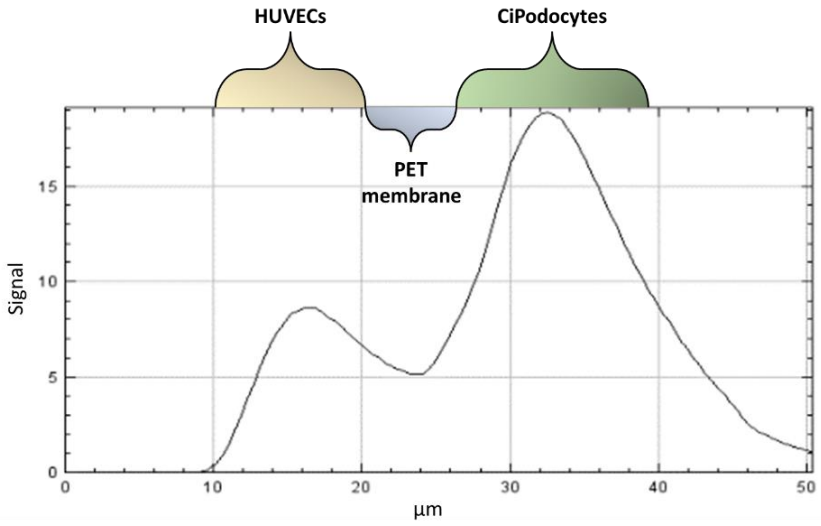

Figure 72: Intensity profile obtained from a Z-axis profile of Figure 40.

To improve imaging on the upper part of the membrane, we used time-gated detection during confocal imaging. This was made possible through the use of the confocal nanosecond pulsed supercontinuum laser, allowing efficient temporal selection of a delay (ns) before collection of the signal after each excitation pulse. Gating the detection of the emission of fluorophores allows to get rid of reflected light, and most of the autofluorescence. This allowed imaging up to the upper part of the membrane (endothelial layer, Figure 74).

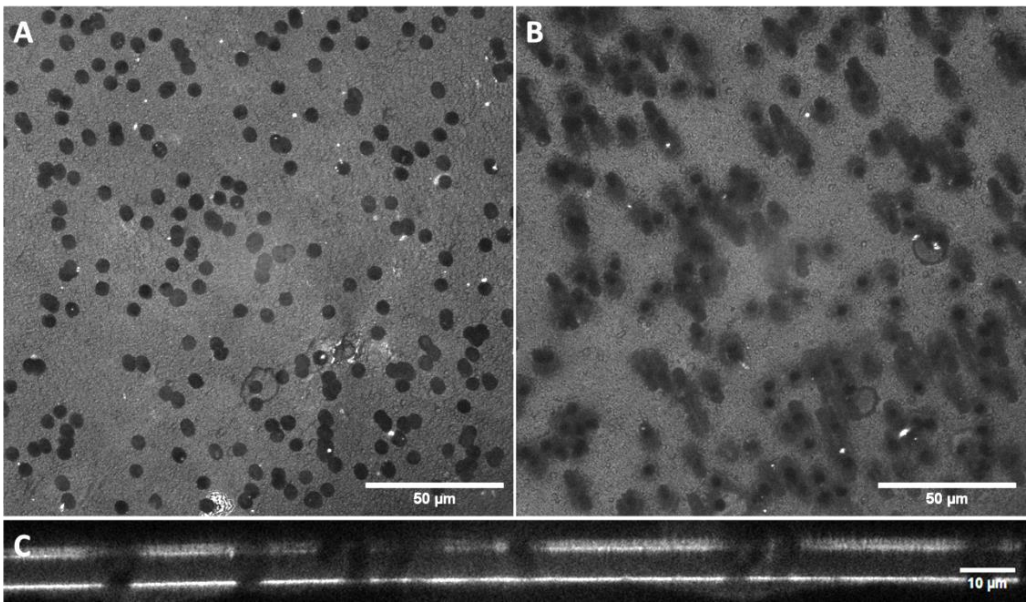

Figure 73: Confocal images of PET membrane light scattering and autofluorescence, observed when illuminated at 647 nm and detection window is 660-770 nm A) lower edge of the membrane, B) upper edge of the membrane, C) axial view of PET membrane (63X).

However a signal loss is still observed after the PET membrane, which is probably due to absorption of the membrane, that limits both excitation and collection. To compensate for this loss we implemented a laser power and gain correction. While acquisition is performed from the bottom to the top of the system for example, the excitation laser power will increase as well as the detection gain.

This excitation/detection correction profile and time gated detection allowed a deep imaging in our microsystems with a subcellular resolution when using high magnification (see in the next section: Figure 74 & Figure 75)

2.6.2 Phenotypic characterization of the glomerulus-on-chip

We then developed a full recapitulation of a glomerulus using human resident endothelial cells from the glomerulus (CiGEnCs), human podocytes (CiPodocytes), and rat parietal epithelial cells (CirPECS) in co-culture in our microsystems. Cells differentiation was fully characterized when grown and differentiated together on-chip. To this end, we performed systematic multicolor imaging of the whole systems (800 µm x 2 mm co-culture area in the whole depth of the systems +/- 100 µm).

2.6.2.1 CiPodocytes, CiGEnCs, and CirPECs co-culture

We first characterized the growth and differentiation of CiPodocytes, CiGEnCs, and CirPECs in co-culture under gravity driven perfusion for 2 weeks.

Cells were seeded sequentially in microsystems previously coated with laminin and collagen IV, as previously described (section: 2.4.1.2). When adding CirPECs we replaced the urinary medium (basal CiPodocyte medium) with CirPECs basal medium. From this point on CiPodocytes will be grown in CirPECs medium. The systems were checked individually for confluence using a phase contrast cell culture microscope. When cells reached confluence, systems were then switched to 37°C, and let to grow and differentiate for two weeks with a full reservoir media change every 4-5 days. Systems were then fixed using 4% PFA, permeabilized and stained for differentiation markers for each cell line. Antibodies used to perform immunostainings are listed in the Appendix: 4.4.2.

By implementing time gated detection and illumination corrections we could bypass imaging limitations and clearly resolve CiGEnCs on the upper part of the membrane (Figure 74). Thought artifacts remained, corresponding to membranes holes that were still visible in the vascular chamber at the level of CiGEnCs monolayers (Figure 74).

We can observe the formation of fully confluent monolayers of cells, expressing expected differentiation markers. CirPECS expressed claudin-1 at cell junctions, CiPodocytes showed expression of podocalyxin and CiGEnCS of VE-cadherin (Figure 74, Figure 75). The staining was consistent over different systems (see Figure 74, Figure 75, Figure 79, Figure 81 & Figure 92). The cell confluency reached 100% in all systems. This indicated that it is possible to grow these cells in co-culture for a long period of time on chip (≥ 2 weeks), and that cells differentiate and form monolayers during this time.

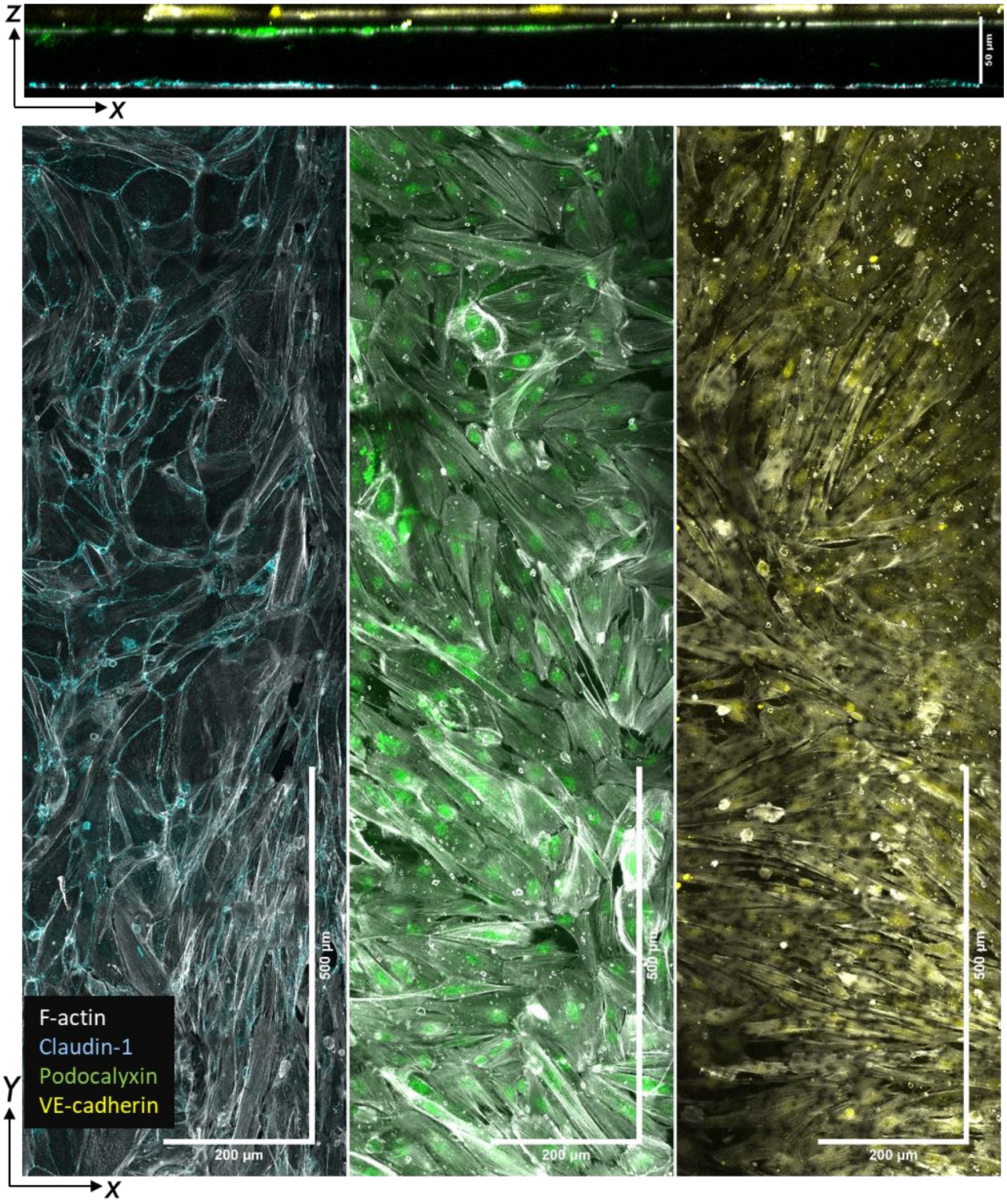

Figure 74: Confocal tilescan images of a microsystem seeded with CirPECs, CiPodocytes, and CiGEnCs cultured and differentiated for 2 weeks with permanent perfusion, stained for claudine-1 (Alexa Fluor 594), podocalyxin (DyLight 550), VE-cadherin (Alexa Fluor Plus 488), and f-actin (phalloidin iFluor 647), 40X magnification.

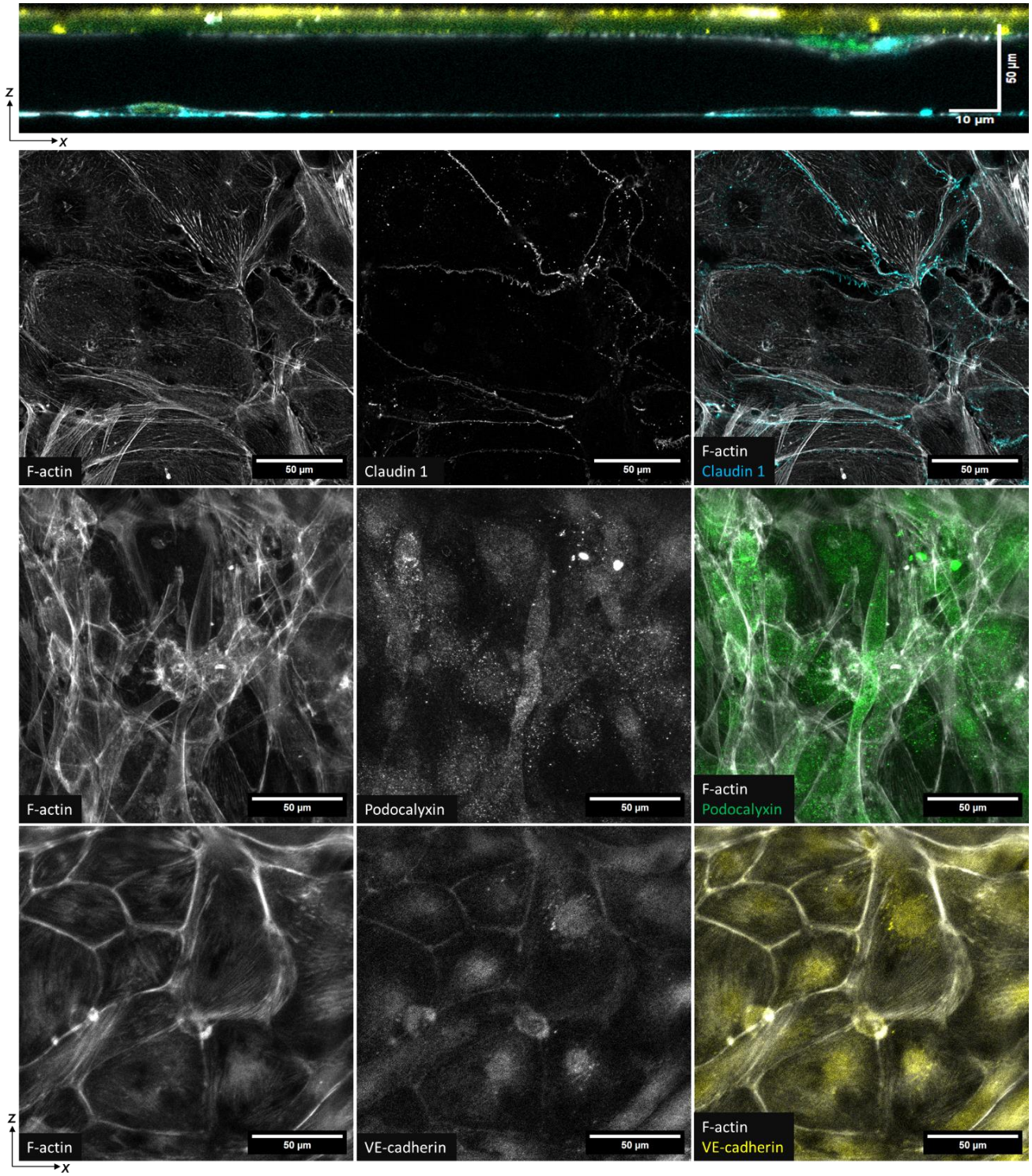

Figure 75: Confocal images of a microsystem seeded with CirPECs, CiPodocytes, and CiGEnCs cultured and differentiated for 2 weeks with permanent perfusion, stained for claudine-1 (Alexa Fluor 594), podocalyxin (DyLight 550), VE-cadherin (Alexa Fluor Plus 488), and f-actin (phalloidin iFluor 647), 40X magnification.

We further quantified the cells differentiation by staining for different markers expressed by each cell types.

2.6.2.1.1 CiGEnCs express VE-Cadherin and VEGFR-2

Like shown previously on glass coverslips, CiGEnCs express VE-cadherin at cellular adherent junctions (Figure 76). However, staining intensity was essentially localized at the cell junctions. VE-

Cadherin staining also shows a preferential orientation of the cells in the microsystem that is fully characterized in the next section: 2.6.2.2.

VEGFR-2 is a key component of the vascular endothelial growth factor (VEGF) signaling pathway and is critical for survival, proliferation and migration of GEnCs, and increase vascular permeability *in vivo* (R. R. Foster et al., 2008). Since Podocytes secrete VEGF-A they may influence GEnCs when grown in co-culture. The culture medium of CiGEnCs contains VEGF, it should thus influence VEGFR expression. Thus, by changing the medium composition one could study VEGF-A, GEnCs/podocytes signaling crosstalk, that play a major role in fenestration and glycocalyx formation, and GEnCs homeostasis in general (Bertuccio et al., 2011; R. R. Foster et al., 2013; Satchell et al., 2006). CiGEnCs express VE-cadherin and VEGFR-2 indicating a good level of differentiation and possibly of a response to podocytes VEGF-A production, or to the VEGF contained in the culture medium.

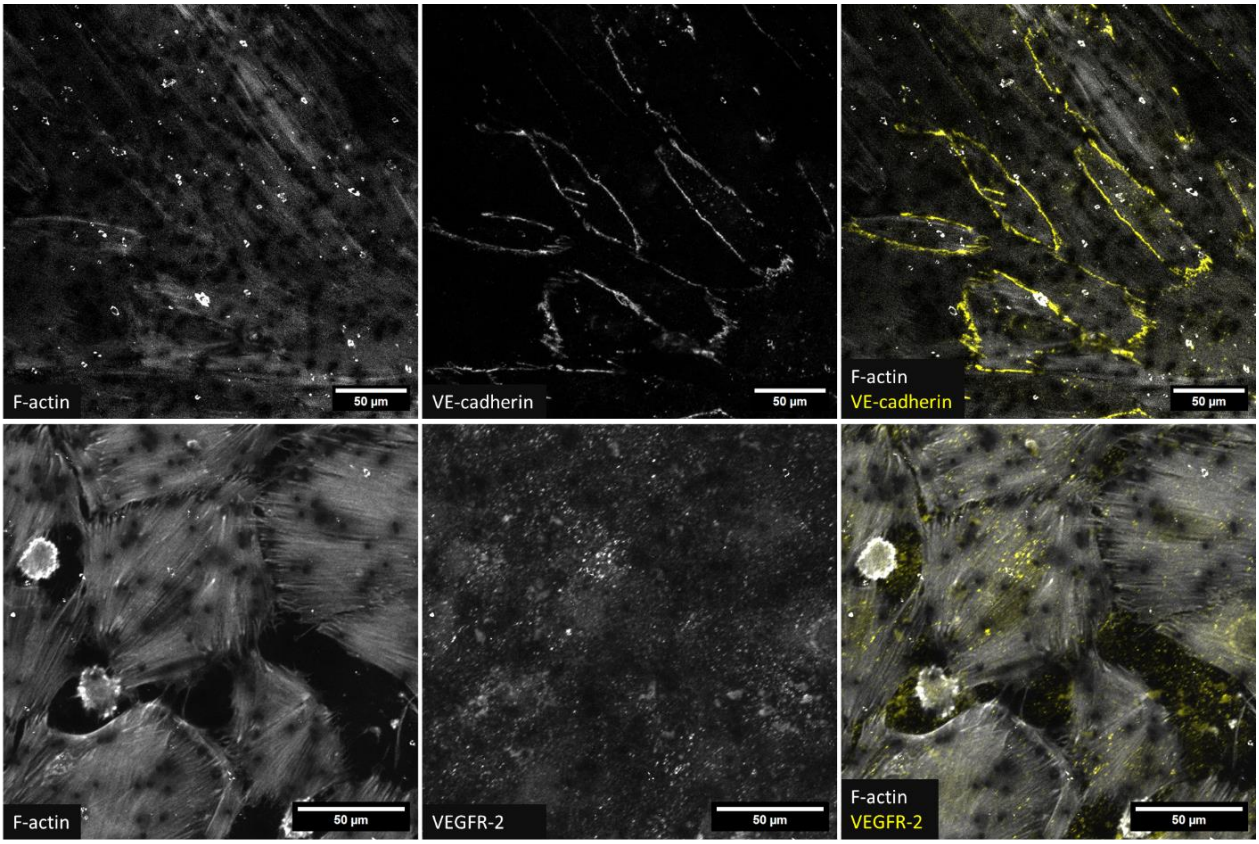

Figure 76: Confocal images of CiGEnCs in a microsystem also seeded with CirPECs, and CiPodocytes cultured and differentiated for 2 weeks with permanent perfusion, stained for VE-cadherin (Alexa Fluor 594) or VEGFR-2 (Alexa Fluor 594), and f-actin (phalloidin iFluor 647), 40X magnification.

2.6.2.1.2 CiPodocytes maintain WT1 and podocin expression

CiPodocytes were stained for WT1 and podocin. Cells retain a strong level of expression after 2 weeks of differentiation. Interestingly, CiPodocytes showed an accumulation of podocin at the membrane holes. This could indicate that CiPodocytes can sense substrate topology changes and accumulate slits diaphragm proteins at this location.

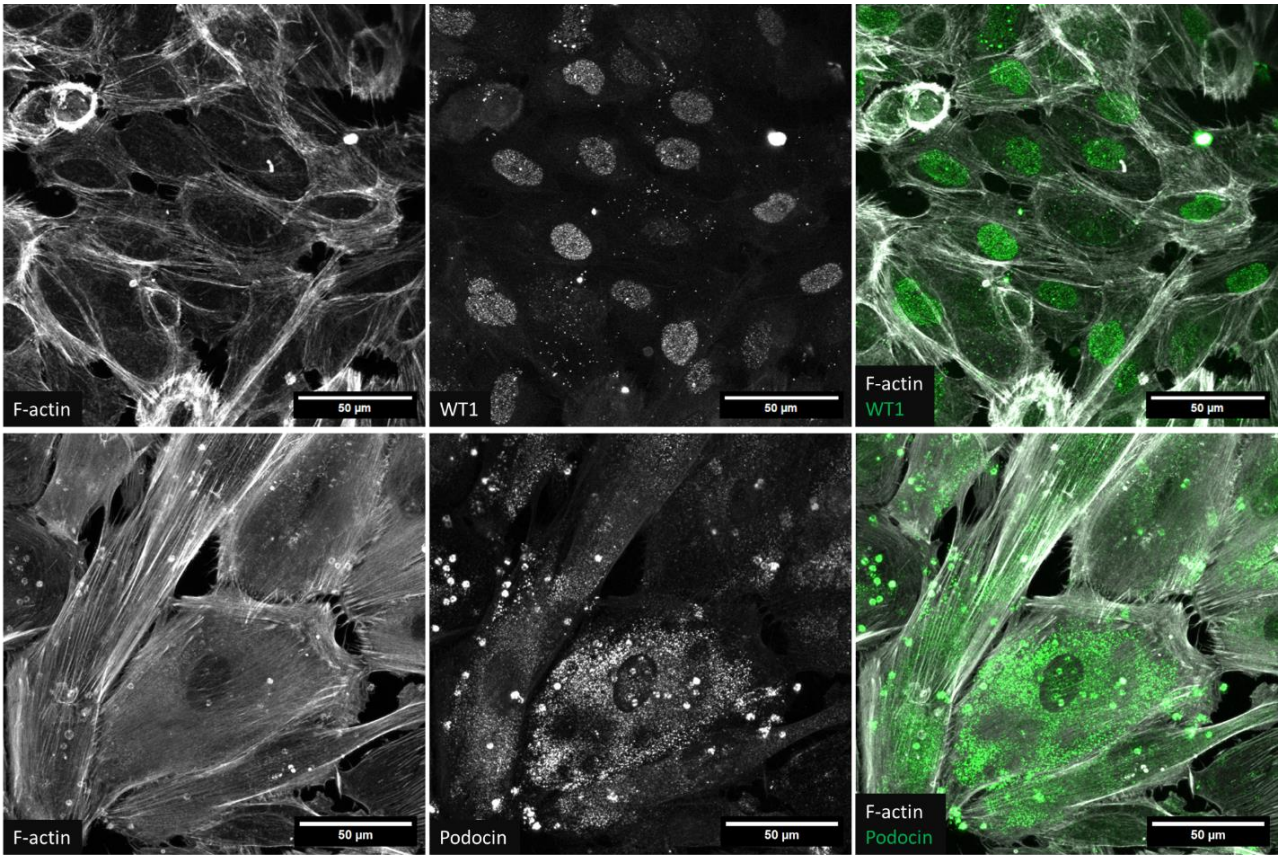

Figure 77: Confocal images of CiPodocytes in a microsystem also seeded with CirPECs, and CiGEnCs cultured and differentiated for 2 weeks with permanent perfusion, stained for WT1 (Alexa Fluor Plus 488) or podocin (Alexa Fluor Plus 488), and f-actin (phalloidin iFluor 647), 40X magnification.

2.6.2.1.3 CirPECs form a tight monolayer.

Claudin-1 expression pattern showed total localization of the protein at cell-cell junctions, completely delimiting cells individually. This continuous delimitations is indicating the formation of tight-junction between cells. This epithelium *in vivo* prevents leakage of primary urine in the peri-glomerular space (Miesen et al., 2022). Thus the formation of this tight epithelium plays a very important role in actual kidneys and in diseases such as RPGN and FSGS, where PEC loose this strong claudin-1 expression in tight-junctions, and initiate the epithelial to mesenchymal transition (Ikenouchi et al., 2003; Ohse, Pippin, et al., 2009).

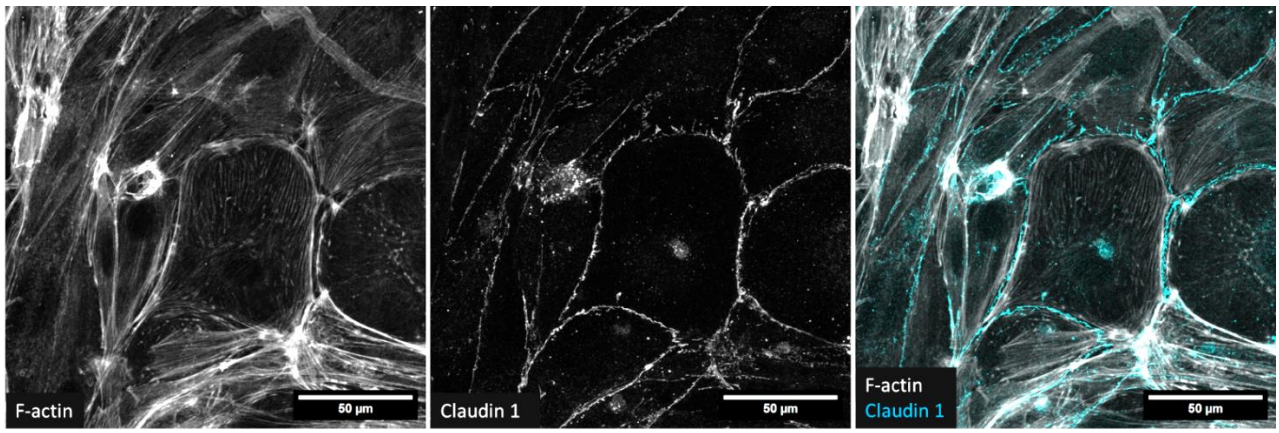

Figure 78: Confocal images of CiPECs in a microsystem also seeded with CirPodocytes, and CiGEnCs cultured and differentiated for 2 weeks with permanent perfusion, stained for claudin-1 (Alexa Fluor Plus 488), and f-actin (phalloidin iFluor 647), 40X magnification.

Overall, we demonstrated that co-culture of the glomerular cell types in microsystems was possible. Cells grown confluently and expressed several markers of differentiation typically expressed *in vivo*. Gravity driven perfusion was more reproducible, and allowed multiple systems to grow simultaneously. This is necessary for efficient and accurate functional characterization, such as filtration assays, were a single defect in the cell confluency could lead to filtration measure anomalies.

2.6.2.2 Cell orientation

Cell monolayers in our glomerulus-on-chip are subjected to flow and shear stress on their apical (upper) side due to the gravity induced perfusion (see section: 2.4.2.2). Cells can respond in various ways depending on factors, such as the type of cells, the magnitude of the flow, the duration of exposure, and the specific conditions of the experiment (Choublier et al., 2022; Dessalles et al., 2021). The behavior of the cell monolayers in the microsystems was studied by analyzing the orientation of the actin cortex of the cells. This is particularly important for GEnCs since evidences showed that GEnCs act as mechanosensors in the glomerulus though their glycocalyx and ESL (Curry & Adamson, 2012; Fu & Tarbell, 2013).

Cell orientation in the systems was thus characterized like described previously (see section: 2.3.3.2). Briefly images of F-actin for each layer of cells were analyzed in ImageJ with the OrientationJ plugin to recover the orientation distributions and create orientation color coded images (Figure 79).

Qualitatively we can first observe that CiGEnCs are typically oriented with an angle between 45° and 60° taking the long axis of the channel as a reference. This could suggest that when exposed to the flow in the microsystems CiGEnCs tend to align to the flow direction (parallel to the long axis of the channel). CiPodocytes and CirPECs preferential orientation is more difficult to interpret qualitatively, but the mean orientation aligns with the channel long axis. Overall we can observe very few cells that are perpendicular to the flow (light blue on Figure 79) in both vascular and urinary chambers.

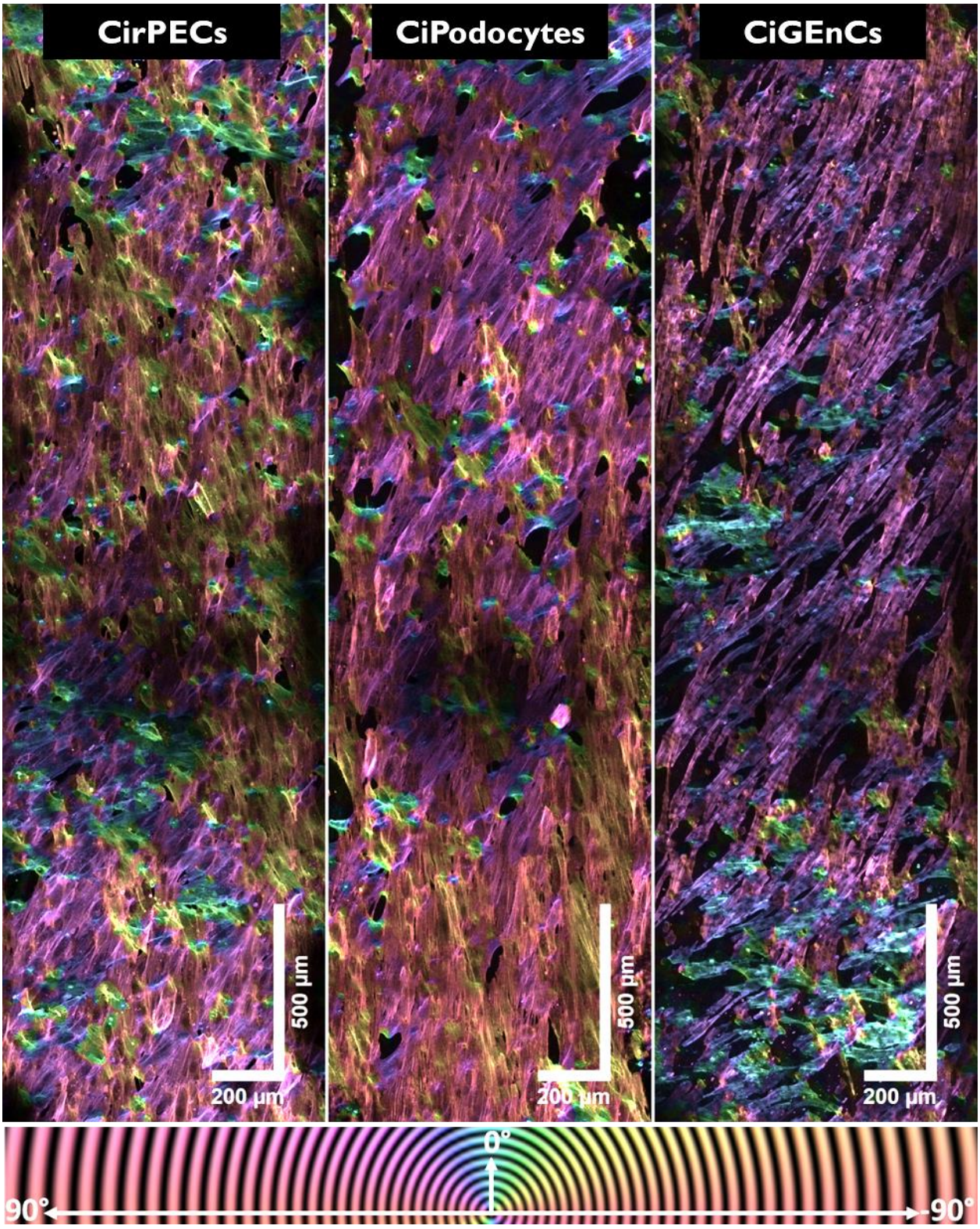

Figure 79 : Confocal tilescan images of a microsystem seeded with CirPECs, CiPodocytes, and CiGEnCs cultured and differentiated for 2 weeks with permanent perfusion, stained for f-actin (phalloidin iFluor 647), cells are color coded with their orientation respecting the bottom colormap using OrientationJ plugin, σ=10 pixels, 20X magnification.

Normalized distributions of orientation were then fitted with Von mises distributions (Figure 80) to extract the orientation of the cells (F-actin stress fibers is a good approximation of cell orientation).

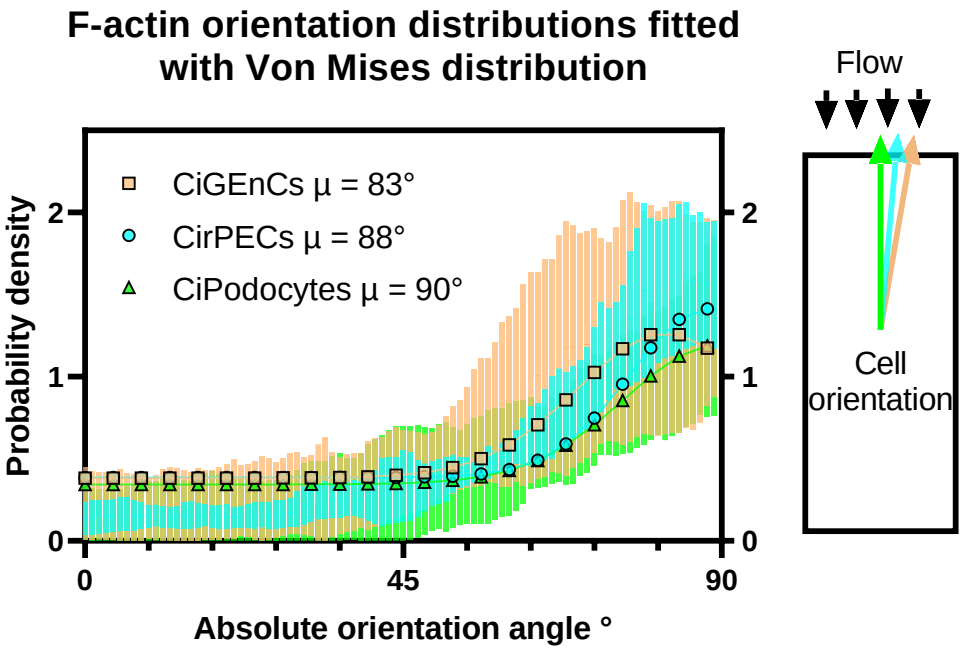

Figure 80: F-actin orientation distributions obtained from microsystems with CirPECs, CiPodocytes, and CiGEnCs cultured and differentiated for 2 weeks with permanent perfusion, bars represent standard deviation of n=6 microsystems, or around 4000 cells per condition (Solid lines and shapes are Von Mises fits, μ indicates mean orientation angle of the cells.

Average cell orientation was comparable for the 3 cell monolayers with an absolute mean orientation angle over 80°. The cell preferred orientation is thus parallel to the flow in both vascular and urinary channel. Angle distributions show an important spread, thus limiting our ability to conclude. Laminar shear stress induced orientation of CiGEnCs parallel to the direction of flow has been previously observed (Bevan et al., 2011).

The angle distribution indicate that the cells (CirPECs, CiPodocytes and CiGEnCs) adopt a preferential vertical orientation in response to the forces generated by the flow in the device (alignment with the flow).

2.6.2.3 ECM deposition

We then checked whether cells in co-culture secreted their own extracellular matrix. Collagen IV and laminin are indeed two important components of the basement membrane, a specialized extracellular matrix (ECM) structure that underlies and supports various tissues and organs, including the glomerular basement membrane (GBM) in the kidneys (Tuffin et al., 2021).

To study ECM deposition by the cells, we co-cultured CirPECs, CiPodocytes and CiGEnCs like previously in microsystems without prior ECM coating to detect only newly deposed extracellular matrix proteins. We performed immunostaining for collagen IV and laminin and also stained the cells for F-actin, podocalyxin and VE-cadherin (Figure 81). First, even without prior initial ECM coating, systems showed similar levels confluency of the different cell monolayers. This indicates that cells have the ability to adhere and grow confluently on plain surfaces (glass coverslips and PET membranes) .

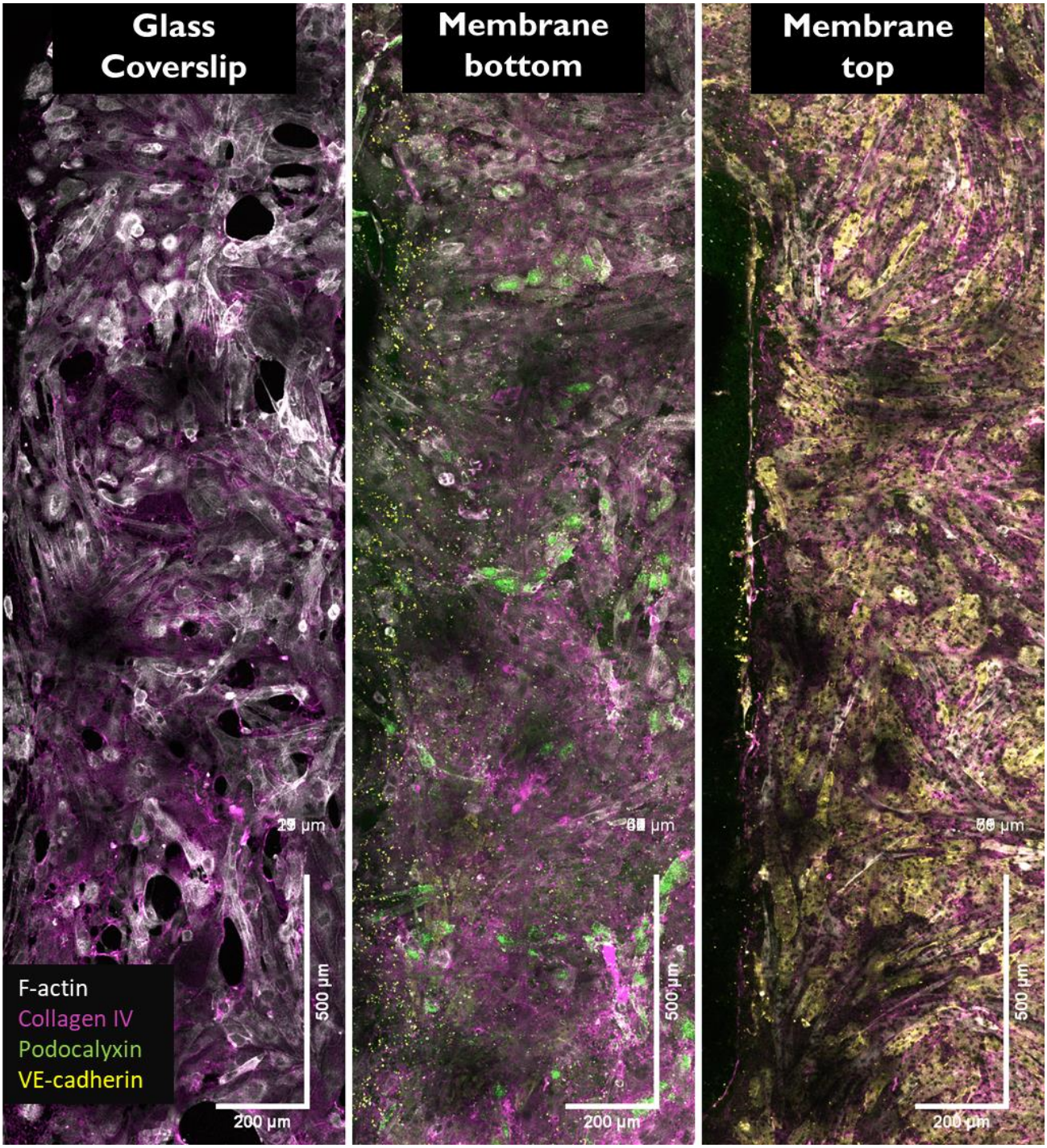

Figure 81: Confocal tilescan images of a microsystem seeded with CirPECs, CiPodocytes, and CiGEnCs cultured and differentiated for 2 weeks with permanent perfusion, stained for collagen IV (Alexa Fluor Plus 488), podocalyxin (DyLight 550), VE-cadherin (Alexa Fluor 594), and f-actin (phalloidin iFluor 647), 20X magnification.

A strong signal for both Laminin and Collagen IV was observed on the 3 layers of the system (Figure 82). This demonstrates that the cells actually secrete their own ECM proteins after 2 weeks of co-culture. Since we perform systematic imaging of the whole systems, we could obtain ECM deposition profiles for each cell type.

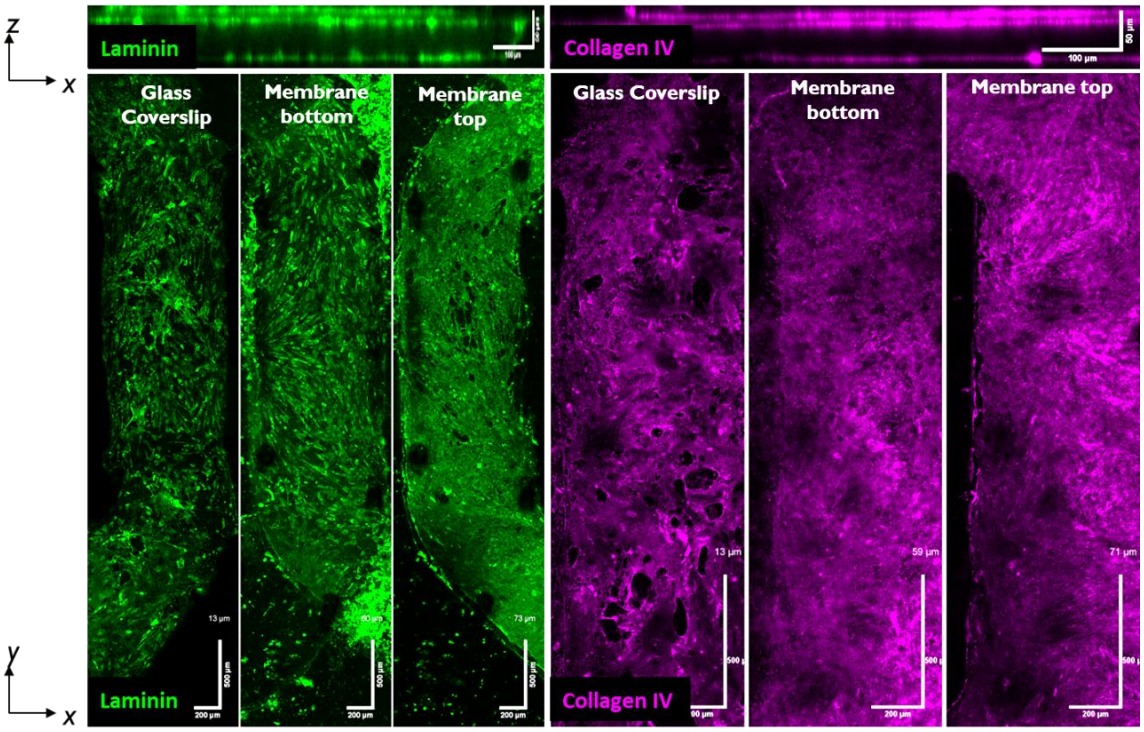

Figure 82: Confocal tilescan images of microsystems seeded with CirPECs, CiPodocytes, and CiGEnCs cultured and differentiated for 2 weeks with permanent perfusion, stained for collagen IV or laminin (Alexa Fluor Plus 488), 20X magnification.

To quantify the level of proteins deposition we then plotted the Z-axis profile of the secreted proteins and normalized it by the profile obtained for F-actin. This unsured that illumination variations and cell density was accounted for before analyzing the profiles.

The profiles obtained correspond to a multi Gaussian component curve where the signal of each layer of proteins contributes as a Gaussian (*Figure 83*). To recover contribution of each layer we thus plotted a multiple Gaussian fitting of the profiles (*Figure 83*)[1].

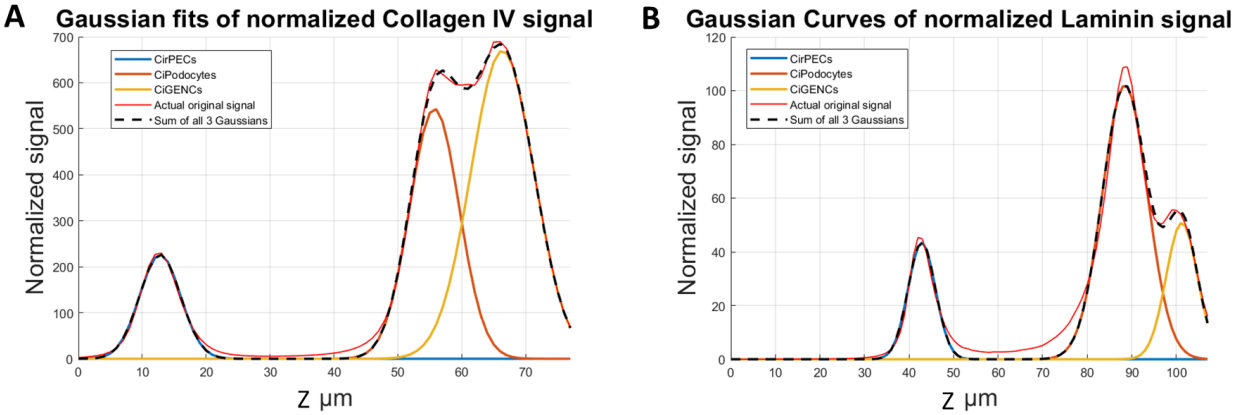

Figure 83: Red lines are normalized Z-axis profiles of A) collagen IV B) laminin signal obtained in microsystems with CirPECs, CiPodocytes, and CiGEnCs cultured and differentiated for 2 weeks with permanent perfusion, signal was fitted (dashed dark line) using MATLAB with a 3 component Gaussian to evaluate protein deposition of each cell type.

[1] Inspired from Image Analyst (2023). Fit Multiple Gaussians https://www.mathworks.com/matlabcentral/fileexchange/74408-fit-multiple-gaussians, MATLAB Central File Exchange. Retrieved August 9, 2023.

Since we obtain the amplitude width and localization of each Gaussian component we can compare them to extract protein deposition from each cell type. First, amplitudes were normalized for each individual profile to get rid of signal variation between acquisitions. We then plotted the contribution of each cell type to collagen IV and laminin deposition (Figure 84).

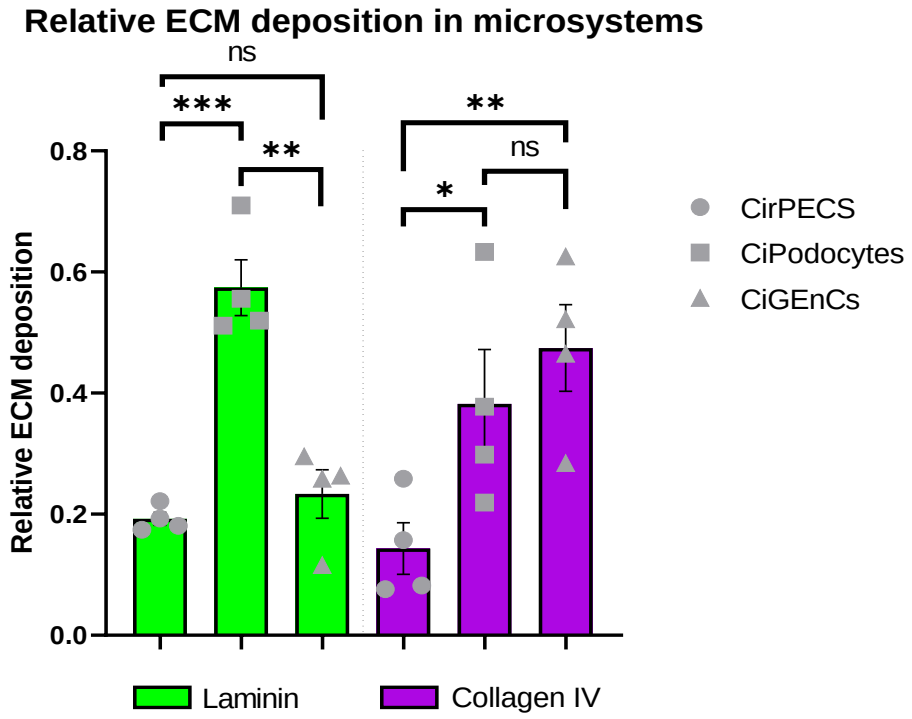

Figure 84: Relative ECM deposition (normalized gaussian amplitude from multi-gaussian fits) assessed for CirPECs, CiPodocytes, and CiGEnCs from microsystems, cultured and differentiated for 2 weeks with permanent perfusion (n= 4 for collagen IV & laminin) (error bars are SEM, stars are Mann-Whitney one tailed t-test).

Interestingly, laminin deposition from CiPodocytes was much higher than from CirPECs an CiGEnCs. Moreover, CiPodocytes and CiGEnCs both secreted high levels of collagen IV compared to CirPECs. It was previously observed by Correlative Light and Electron Microscopy (CLEM) that podocytes line on a thicker network of laminin (Scott & Quaggin, 2015; Suleiman et al., 2013).

Overall we demonstrated that basement membrane proteins are secreted, like *in vivo*, mostly at the membrane by CiGEnCs and CiPodocytes (Abrahamson, 2012). CiPodocytes secreting a denser network of laminin than CiGEnCs. This physiological ECM deposition further indicates that our glomerulus-on-chip is a relevant model to study kidney diseases and potentially study and model diseases such as anti-GBM glomerulonephritis (Godpasture disease).

2.6.3 Functional filtration assay

Blood filtration is the primary function of the glomerulus to form the primitive urine, thus ensuring that our glomerulus-on-chip is capable of selective filtration is crucial to validate that our microsystems are functional. The glomerulus has selective filtration barrier properties due to several factors. First, the presence of endothelial fenestrations *in vivo* is essential for the glomerular filtration by contributing to the high hydraulic conductivity of the glomerular filtration barrier (Satchell et al., 2006). It is also theorized that the glycocalyx plays a role in regulating filtration, with estimates suggesting that it might contribute to as much as half of the total hydraulic resistance of the capillary wall (Fogo & Kon, 2010). The Glomerular Basement Membrane (GBM) also plays a role in the

selective barrier properties of the glomerulus. The dense structures of interconnected BM protein networks act as a barrier to the passage of both cells and large molecules (Leclech et al., 2021). Finally, podocytes whose tight entanglement with the GBM results in the formation of a filtration window between the feet of podocytes whose diameter is of the order of 3.5 nm are the final filter composing the Glomerular Filtration Barrier (GFB, Pavenstädt et al., 2003).

We perform this task by injecting labeled-dextran filtration, of relevant (from 20 to 150 kDa) molecular weights, with molecules typically smaller albumin (68 kDa), of around the same size (70 kDa), and of very important size (150 kDa), in the capillary-like chamber and measuring its concentration, through fluorescence diffusion, in the urinary-like chamber. From a practical point of view, we proposed an operational protocol for the detection of possible proteinuria. Since the PET membrane pores are significantly larger than a typical protein size (3 µm in diameter), we expect that the absence of dextran above 150kDa within the first minutes of perfusion will be proof of an on-chip formation of an efficient filtering barrier by endothelial cells and podocytes.

Measurements were performed by live confocal imaging at 37 °C. Briefly systems with CirPECs, CiPodocytes, and CiGEnCs cultured and differentiated for 2 weeks with permanent perfusion, are first equilibrated in warmed endothelial cell basal medium ECBM (without phenol red), HEPES (30 mM), 0,1% FBS, sodium pyruvate, PS solution (latter referred to imaging buffer) to eliminate the autofluorescent medium. Vascular chambers of the systems are connected to a syringe pump filled with imaging buffer and 0.1 mg/ml of fluorescent dextran of a given molecular weight. Fluorescent reporters are perfused at 3µl/min to induce a physiological flow in the vascular channel and acquisition is launched. To limit photobleaching and phototoxicity, the confocal is used in resonant mode (8000 Hz). The high concentration of the fluorescent reporter allows high imaging speed (up to 14 frames per seconds). Indeed since the pixel dwell time is very short (~2.90 10^{-7} s) the signal has to be strong to be observed.

To access diffusion dynamics from the vascular to the urinary chamber we acquire a Z-stack of the whole system depth (~100 µm) every 30 seconds using a 20X water immersive objective with an optical section of 2.5 µm. A kymograph of a typical experiment is shown Figure 85. From this figure we can observe that the signal increases in the lower urinary channel as time progresses. However the signal in the upper urinary channel remains constant. This indicates that the vascular channel is quickly loaded with the fluorescent reporter (a few tens of seconds usually), and that there is a slow diffusion in the bottom channel. Since the diffusion in control systems (no cells seeded) reached equilibrium typically in less than a minute (Figure 87), diffusion times significantly higher than a minute are due to a filtration effect.

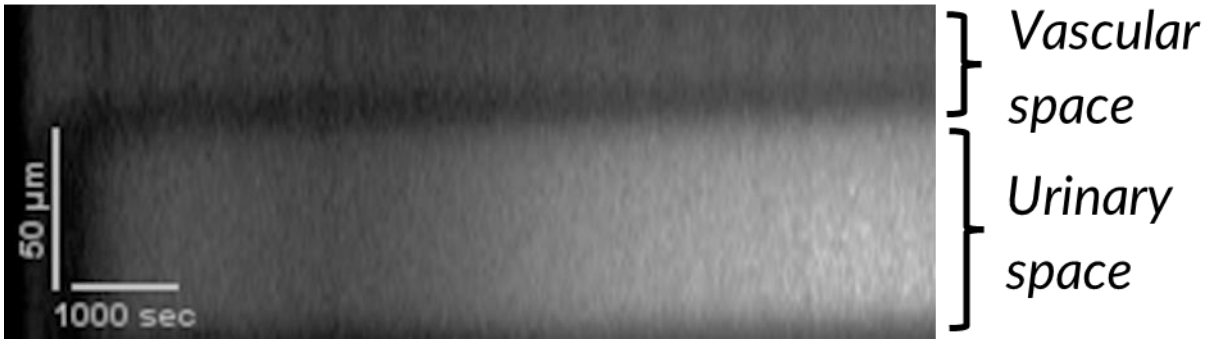

Figure 85: Kymograph obtained from confocal images of perfusion experiment where 150kDa FITC-Dextran (0.1mg/ml in ECBM-HEPES) is perfused (3µL/min) in the vascular chamber of

microsystems with CirPECs, CiPodocytes, and CiGEnCs cultured and differentiated for 2 weeks with permanent perfusion, filtration in the lower urinary compartment is monitored by taking a full Z -stack (2.7s acquisition) every 30s with a confocal with resonant galvanometer (8000 Hz), 20X magnification, optical sections of 2.5 µm.

To analyze the filtration profiles, we analyze the kinetics of this diffusion, by plotting the temporal increase of the signal in the lower urinary chamber. One example is shown Figure 86. The profiles are then fitted with an exponential to determine the characteristic times of filtration.

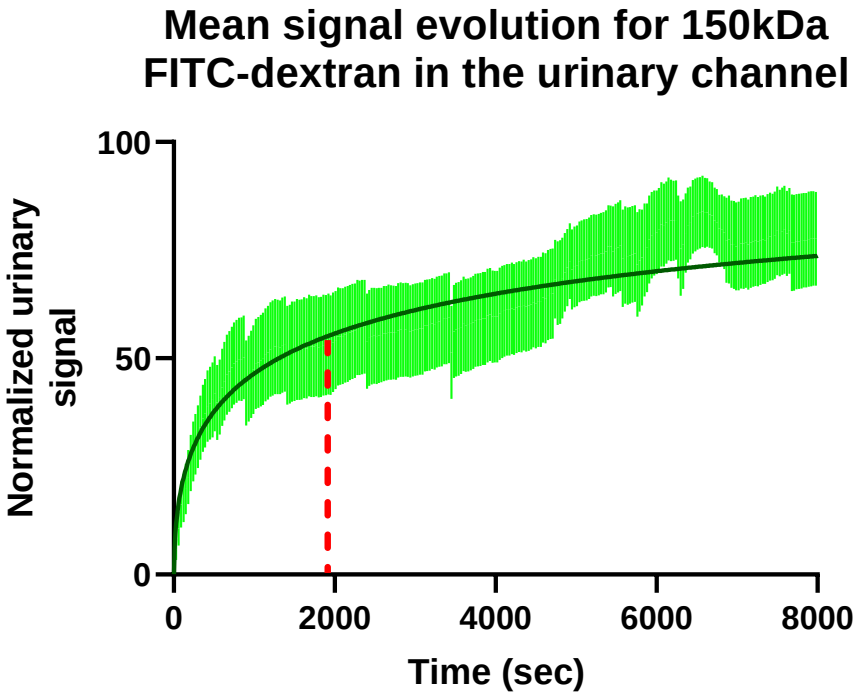

Figure 86: Temporal profile of 7 independent experiments (3 glomeruli-on-chip) of filtration with 150 kDA FITC-dextran accumulation in the urinary (green error bars represent SD), is fitted with an exponential (black line). This gives a characteristic filtration time of 1913 sec or 31.8 min for example.

We thus have a methodology to compare filtration efficiency in different systems, that is able to depict quantitatively filtration (characteristic time) for a wide range of molecular sizes.

2.6.3.1 Filtration with HUVECs and CiPodocytes.

We performed a first set of experiments with CiPodocytes and HUVECs as a first attempt to recapitulate a glomerular filtration barrier and demonstrate co-culture capabilities of the systems. This is important because the results obtained can be compared with the filtration efficiency of a fully developed model using GEnCs, CiPodocytes, and PECs.

We first compared filtration between control systems (no cells seeded) and systems seeded with HUVECs and CiPodocytes, grown and differentiated on PET membranes (3 µm pores) in microsystems, for 2 weeks with a permanent perfusion by gravity. Characteristic times of filtration are obtained for every molecular weights and are plotted Figure 87.

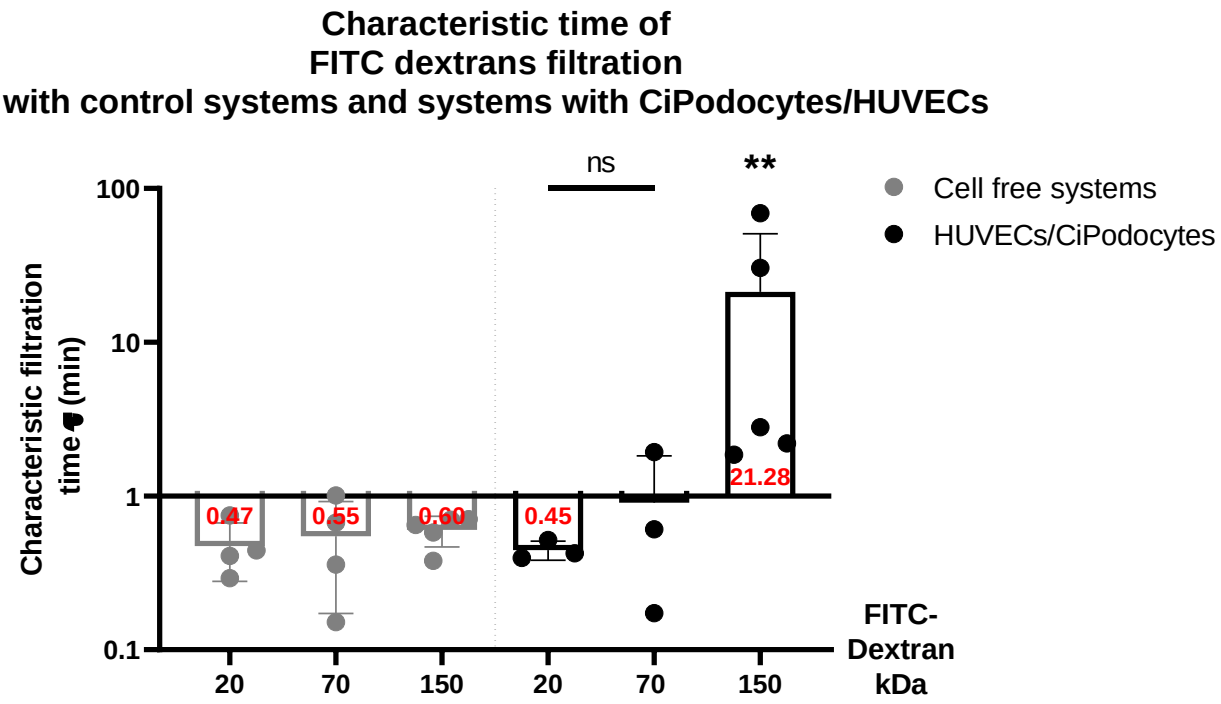

Figure 87: Characteristic time of filtration obtained from fitting diffusion profiles from confocal perfusion experiments where FITC-Dextrans of different molecular weights (0.1mg/ml in ECBM-HEPES) are perfused (3µL/min) in the vascular chamber of microsystems without cells (control) and microsystems seeded with HUVECs and CiPodocytes differentiated for 2 weeks with permanent perfusion (error bars are SEM, stars are Mann-Whitney one tailed t-test).

From this first set of experiments, we can observe that the characteristic time of dextran diffusion is significantly increased for a high molecular weight (150 kDa) reaching a mean characteristic time of ~21 minutes. The results show that smaller molecules freely diffuse across the membrane and cells.

This hybrid system based on CiPodocytes and HUVECs thus shows a filtration for molecules ≥ 150 kDa. This is a good reference to compare filtration of more elaborate and biomimetic systems that use glomerular resident cells, and add the parietal layer of PECs.

2.6.3.2 Synergistic effect of CiGEnCs and Podocyte co-culture on filtration

We thus conducted the same measurements in systems with CirPECs, CiPodocytes, and CiGEnCs, recapitulating fully the glomerular filtration barrier and the bowman membrane. The results are shown in Figure 88.

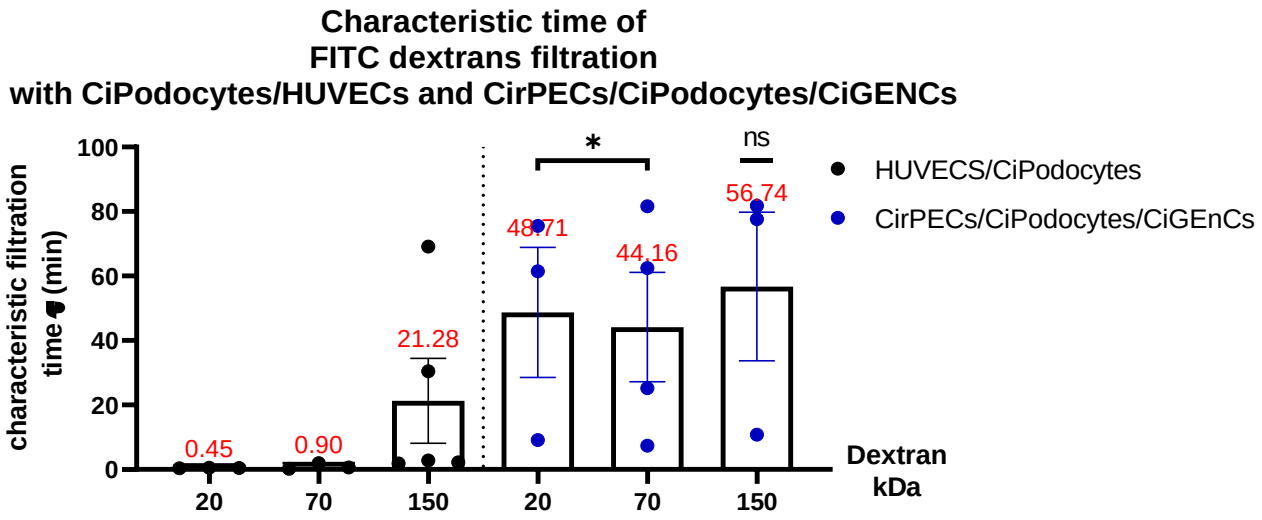

Figure 88: Characteristic time of filtration obtained from fitting diffusion profiles from confocal perfusion experiments where FITC-Dextrans of different molecular weights (0.1mg/ml in ECBM-HEPES) are perfused (3µL/min) in the vascular chamber of microsystems with HUVECs and CiPodocytes, and microsystems with CirPECs, CiPodocytes, and CiGEnCs cultured and differentiated for 2 weeks with permanent perfusion (error bars are SEM, stars are Mann-Whitney one tailed t-test).

We can observe in glomerular like systems that a significant increase in diffusion time across the GFB was observed for small and medium size molecules (20 and 70 kDa) reaching filtration times of more than 40 minutes. Filtration time of larger molecules also increased reaching up to 1 hour though not significative compared to the previous systems. This further indicates that when growing CiGEnCs and CiPodocytes in co-culture, a more efficient filtration barrier is formed than with endothelial cells not resident of the glomerulus.

This filtration effect for both small and large molecules is indeed a characteristic of the glomerular filtration barrier. This multi-cellular system actively filtrates molecules, and this functional behaviors was critical in the demonstration of obtaining a glomerulus-on-chip.

Being able to detect filtration variations for a range of molecular weights further indicates that the systems differentiation and confluency are well preserved during co-culture and that our microsystem recapitulates the glomerular organization and functions. From a practical point of view, this method provides us with an operational protocol for the detection of possible induced proteinuria.

2.6.4 EGF role in glomerular signaling

Since our hypothesis is that EGF may be responsible for PEC activation and RPGN/FSGS progression, we investigated the role of EGF signaling in our glomerulus-on-chip at the functional level. In physiological glomerular condition, no EGF is present in the urinary chamber. CirPECs are routinely cultured in a rich medium containing human recombinant Epidermal Growth Factor (hEGF). Since our hypothesis is that EGF could triggers PECs activation (migration and proliferation), we formulated 2 media to decipher EGF implication in PECs activation and EGF global effect on glomerular signaling.

A basal medium was composed with a reduced amount of fetal bovine serum (which contains EGF) and without the supplemented EGF normally present in the routine culture medium. A second EGF enriched medium containing both hEGF and increased serum concentration was formulated (see Table 2 for detailed composition of the media). EGF is naturally present in FBS so reducing the serum concentration to 1% put the systems in a minimal EGF concentration. EGF was also removed, and serum reduced to 1% for CiGEnCs medium in basal conditions in the upper vascular channel.

The basal medium mimics the physiological glomerular condition, while the EGF enriched medium will simulate the leakage of EGF in the urinary chamber (potential trigger of PECs activation).

Table 2: Components of CirPECs basal and enriched medium

Basal medium	**Enriched medium**
1:1 Endothelial Growth Medium EGM-MV/RPMI	
Bovine Brain Extract (BBE)	
Insulin-Transferrin-Selenium (ITS)	
10 mM HEPES, sodium pyruvate	
Hydrocortisone (HC), GA, PS	
1% FBS	**7,5% FBS**
-	**hEGF**

2.6.4.1 EGF role on CiGEnCs and CiPodocytes phenotype

We first checked if the EGF and serum deprived medium had an impact on CiGEnCs and CiPodocytes differentiation. The objective was to assay for any structural changes on both these cells lines induced by EGF stimulations.

This was done through SEM imaging allowing characterization of fine ultrastructural changes as previously demonstrated. Since we do not have the ability to perform SEM imaging in our glomerulus-on-chip, we co-cultured CiGEnCs and CiPodocytes on PET Transwells inserts (3 µm pores) and let them differentiate for 2 weeks. These systems are clones of the glomerulus-on-chip, but lack flow and thus shear stress. Since these inserts are open on their surface, they can be easily prepared for SEM. Membranes were first fixed and dehydrated before SEM preparation as previously described (see section: 2.3.5).

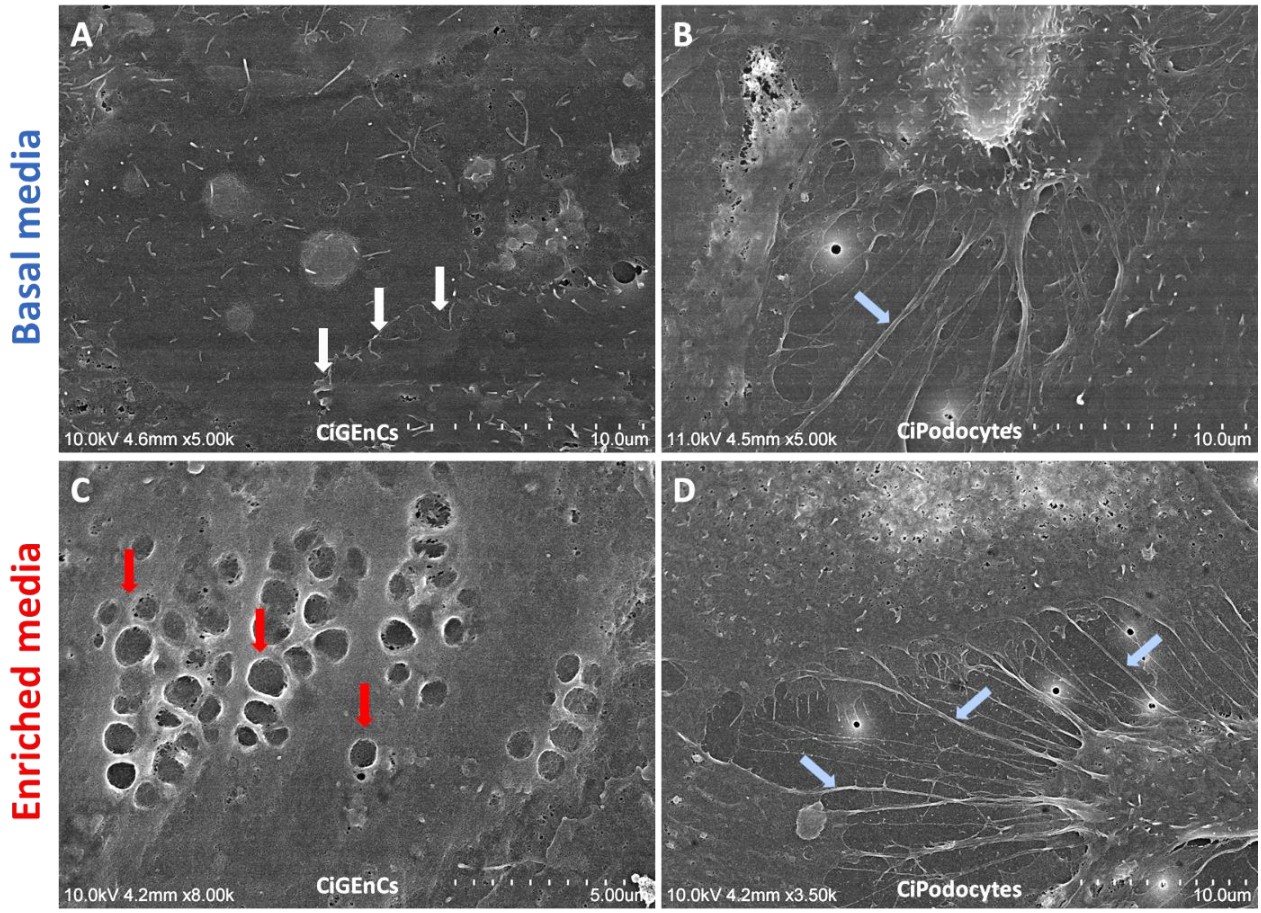

Figure 89: SEM images of B& D) CiPodocytes (basolateral side), and A&C) CiGEnCs (apical side) cultured and differentiated for 2 weeks in co-culture on Transwell inserts (PET, 12 mm, 0.4 µm pores) either in EGF deprived conditions (basal media) or EGF enrichment. White arrows indicate cell-cell junction, blue arrows pedicel like structures, and red arrows indicate fenestrations.

In basal medium, CiGEnCs exhibited a normal endothelial phenotype with flat cells forming adherent junctions (Figure 89: A). When CiGEnCs are co-cultured in enriched media (containing EGF), CiGEnCs started to form fenestrations (Figure 89: B). These observed fenestrations had a grape fruit shape, growing in clusters. Fenestration are typical for GEnCs and found *in vivo* (Satchell & Braet, 2009), indicating increased differentiation since such structure are almost exclusively found *in vivo*. These fenestration covered around 20 to 30% of the endothelium which is consistent with the fenestration of the glomerular microvasculature (Hjalmarsson et al., 2004; Levick & Smaje, 1987; Rostgaard & Qvortrup, 2001; Satchell & Braet, 2009).

GEnCs *in vivo* are exposed to EGF and high serum concentrations from the bloodstream that may be required for their complete differentiation while podocytes, that are found in the urinary space, normally evolve in a serum/EGF free environment. EGF thus may be required for proper CEnCs differentiation and efficient fenestration formation.

CiPodocytes exhibited, like previously observed on PET membranes (see section: 2.3.5.3), many cytoplasmic projections that could resemble pedicel formation. Growing CiPodocytes in basal medium or EGF enriched medium did not induce changes in morphology, with cells continuingly forming many long cellular processes.

This showed that it is possible to grow CiGEnCs and CiPodocytes in EGF deprived medium even though CiGEnCs requires EGF and Serum for a full differentiation towards a fenestrated

endothelium.

2.6.4.2 Effect of EGF on the filtration function

To assay for any chemio-mediated effect of EGF on the glomerular function, we performed dextran filtration experiments again in systems cultured either in EGF deprived conditions (basal media) or EGF enrichment.

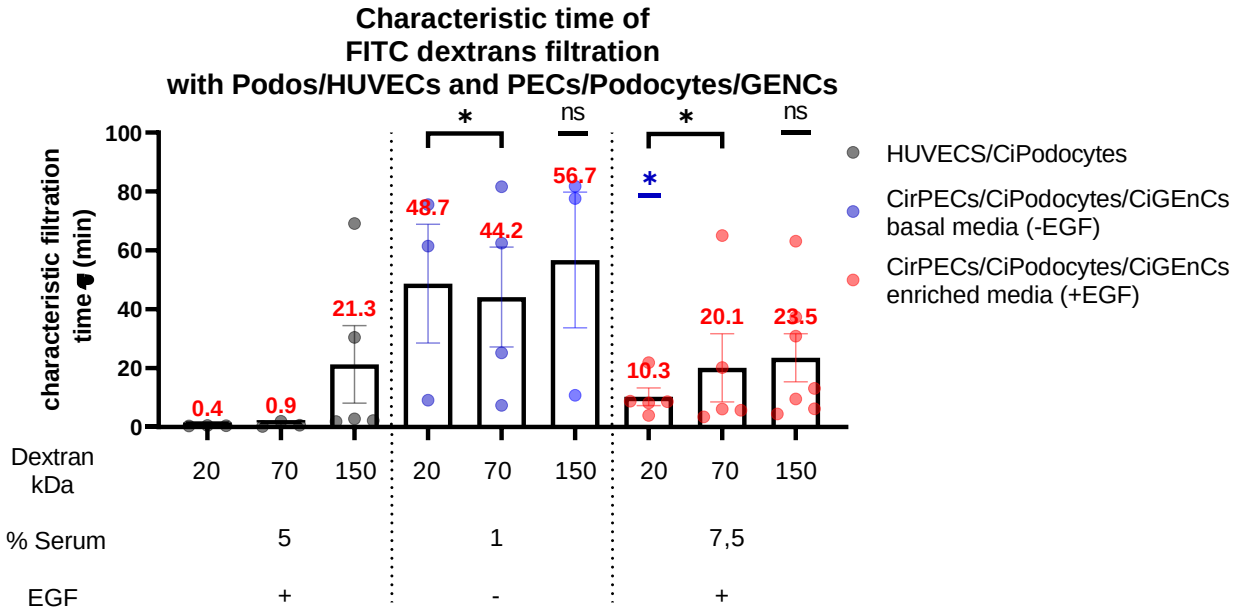

Figure 90: Characteristic time of filtration obtained from fitting diffusion profiles from confocal perfusion experiments where FITC-Dextrans of different molecular weights (0.1mg/ml in ECBM-HEPES) are perfused (3µL/min) in the vascular chamber of microsystems with HUVECs and CiPodocytes, and microsystems with CirPECs, CiPodocytes, and CiGEnCs cultured either in EGF deprived conditions (basal media) or EGF enrichment and differentiated for 2 weeks with permanent perfusion (error bars are SEM, stars are Mann-Whitney one tailed t-test).

Systems grown in enriched medium showed (Figure 90) an overall filtration capabilities reduction compared to basal systems. The filtration characteristic time decreased from 49 to 10 minutes for 20 kDa dextran and went from more than forty minutes to around 20 for larger molecular weight dextrans. The filtration, from EGF deprived to enriched conditions, reduction was significantly lower only for small molecules (20 kDa). However the filtration efficiency of EGF stimulated systems was still significantly higher than systems grown with HUVECs as an endothelial layer. This only partial filtration efficiency reduction, when EGF is supplemented to the system, is interesting because *in vivo* the same filtration reduction is observed in glomerulopathies (Couser, 1988; M. Li et al., 2020). Thus indicating that EGF, when present in the urinary chamber, might be responsible for filtration defects. On a technical point of view this underlines the sensitivity of the measurement technique, being able to quantify changes in filtration efficacy or size selectivity.

To investigate more than the effect on the filtration size threshold of molecules we also performed a second type of filtration assay with a biologically relevant protein, albumin. Albuminuria is a sign of disease progression in many kidney pathologies (Butt et al., 2020), so being able to detect changes in albuminuria is of critical importance for our model.

This perfusion experiment was not performed with the above mentioned confocal technique, but by performing a dosing of FITC-Albumin with a fluorescence spectrophotometer allowing to

determine the absolute concentration of filtered molecules.

Briefly, microsystems with CirPECs, CiPodocytes, and CiGEnCs, cultured either in EGF deprived conditions (basal media) or EGF enrichment, and differentiated for 2 weeks with permanent perfusion were used. We also created intermediary EGF stimulation profiles by first culturing cells for 1 week in basal or enriched medium, and switching media for an EGF enriched only medium or basal medium respectively for the second week of culture and differentiation.

We first replaced the medium containing phenol red with an imaging endothelial medium (ECBM without phenol red, 0,1% FBS, sodium pyruvate, PS solution) and let the cells equilibrate for 1 h in the incubator with permanent perfusion. We then replaced the reservoir of the vascular channer with imaging medium containing a physiological concentration of albumin and FITC-albumin (final concentration of 40 mg/ml total albumin with 5mg/ml of FITC-albumin) and placed the systems back in the incubator for 1.5 hours under gravity induced permanent perfusion (angle 5°, oscillation period 15 min). After 1.5 hours, the medium contained in all reservoirs was pooled for the vascular and the urinary channels, and concentration of FITC-albumin was determined using fluorescence spectrophotometry. This techniques allowed to determine the Glomerular Sieving Coefficient (GSC) for albumin of our systems, with:

$$GSC = \frac{Concentration\ of\ protein\ in\ filtrate}{Concentration\ of\ protein\ in\ plasma}$$

If GSC = 0, the glomerular barrier is completely impermeable to that protein. If GSC = 1, the protein passes through the glomerular barrier as easily as water, with no restriction. For most plasma proteins, the GSC is very low, indicating that they are largely restricted from passing into the filtrate. For example, albumin, the major plasma protein, has a GSC that has been reported at around 0.02 using 2-photon microscopy intravital imaging on rats (Russo et al., 2007), and 0.0006 with the micropuncture technique (Tojo & Endou, 1992).

Since the final vascular concentration of albumin perfused in the vascular chamber system is 40 mg/ml (or 40 µg/µl), and since 1.5 h represents around 6 oscillations or total displaced volume of fluid (10 µL), around 60 µl of "plasma" has been filtrated or ~2400 µg of albumin has been exposed to the filter. In Figure 91, we present both the GSCs obtained, and the total amount of albumin that has escaped the filter.

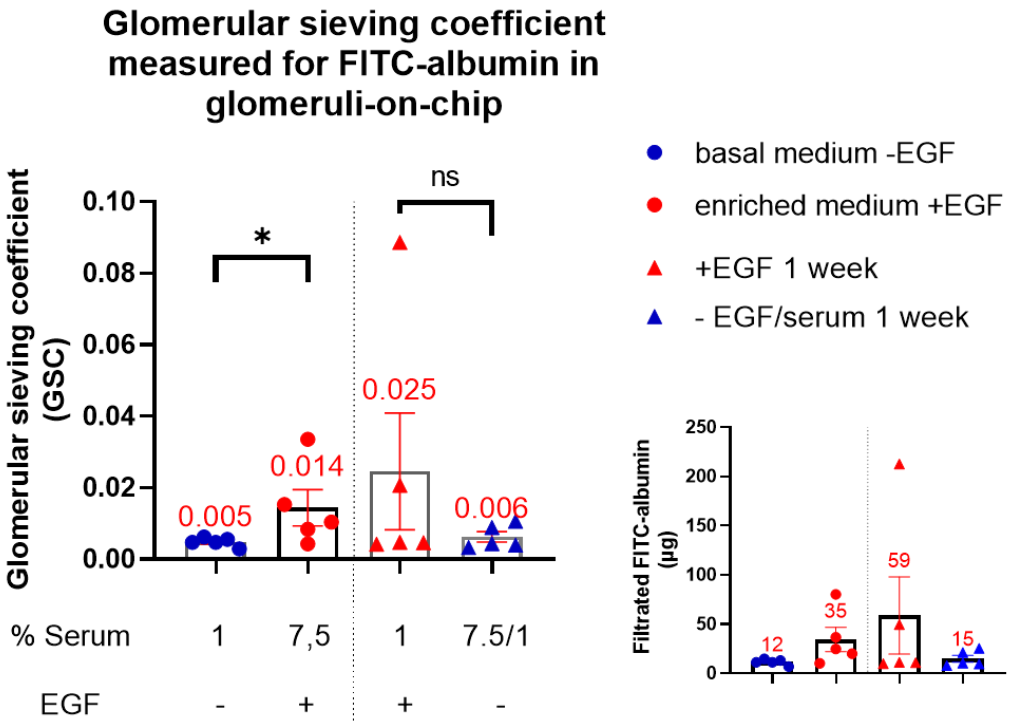

Figure 91: FITC-albumin glomerular sieving coefficient (GSC) and total amount of filtrated albumin (µg) obtained from fluorescence spectrophotometry measurements where FITC-albumin/albumin is supplied at physiologic concentration (40 mg/ml final concentration in ECBM) in the vascular chamber of microsystems with the permanent perfusion (oscillation 15 min, angle 5°) and urinary filtrate is recovered after 1h 30, in systems with CirPECs, CiPodocytes, and CiGEnCs cultured either in EGF deprived conditions (basal media) or EGF enrichment and differentiated for 2 weeks with permanent perfusion (error bars are SEM, stars from Mann-Whitney one tailed t-test).

The results obtained (Figure 91) showed that the amount of albumin filtrated in the urine compartment reached 35 µg for systems grown in EGF enriched conditions while being significantly smaller (12 µg) for systems in physiological medium. Interestingly, when first growing the cells in EGF deprived condition then exposing them to EGF the albumin filtrating in the urine reached the highest levels at almost 60 µg. On the contrary systems first grown in EGF rich medium then starved for EGF showed reduced level of filtrated albumin reaching almost the level of physiological like systems.

In physiological like conditions (EGF deprived) around 12 µg of albumin has been measured in the lower channel, this means that the GSC is 0.005 (fraction of albumin that has escaped the glomerular filter). This value falls within the range of *in vivo* measurements (Moeller & Tenten, 2013; Russo et al., 2007; Tojo & Endou, 1992), obtained by different techniques.

We can thus conclude that our glomerulus-on-chip exhibit both size and molecular filtration selectivity similar of what is expected of an actual glomerulus. This validates that we have recapitulated a fully functional glomerulus-on-chip. EGF exposure may further lead to filtration defects as observed for RPGN and FSGS.

2.6.4.3 Effect of EGF on urinary chamber invasion

To better understand the role of CirPECs in filtration defects in EGF enriched condition, we performed imaging of systems grown in control (basal) and disease-like (+EGF) conditions, and quantified the invasion of PECs in the lower urinary channel.

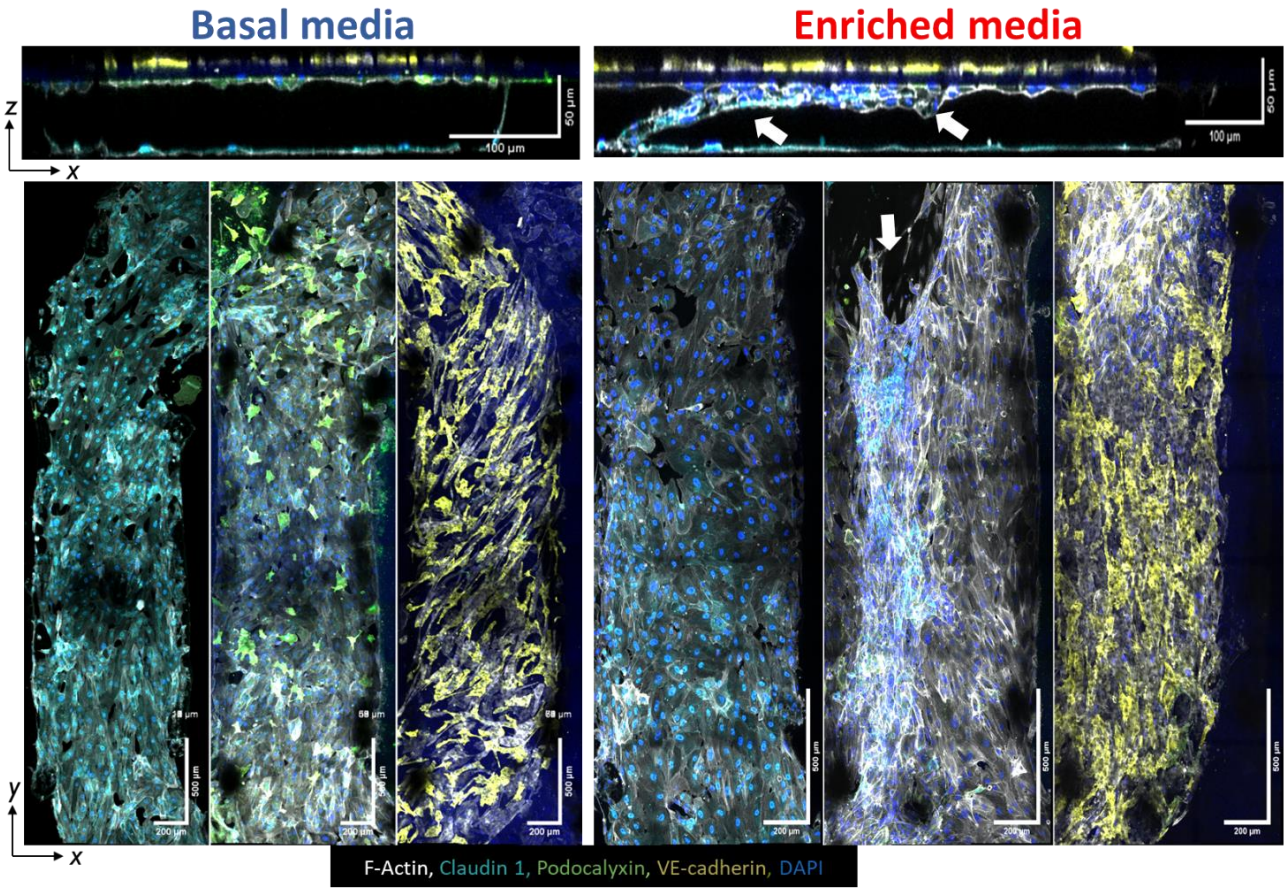

Figure 92: Confocal tilescan images of microsystem seeded with CirPECs, CiPodocytes, and CiGEnCs cultured in either EGF deprived conditions (basal media) or EGF enrichment, and differentiated for 2 weeks with permanent perfusion, stained for claudin-1 (Alexa Fluor Plus 488), podocalyxin (DyLight 550), VE-cadherin (Alexa Fluor 594), and f-actin (phalloidin iFluor 647), 20X magnification, white arrows indicate CirPECs invasion.

In systems grown in basal medium differentiated cells organize in confluent monolayers (Figure 92). However, when systems are grown in EGF enriched conditions we could observe a different phenotype where CirPECs migrate and proliferate and start to invade the urinary space towards the membrane and the CiPodocyte layer (with a occupation of the urinary space reaching 14%), even destabilizing it in some cases (Figure 92 & Figure 93).

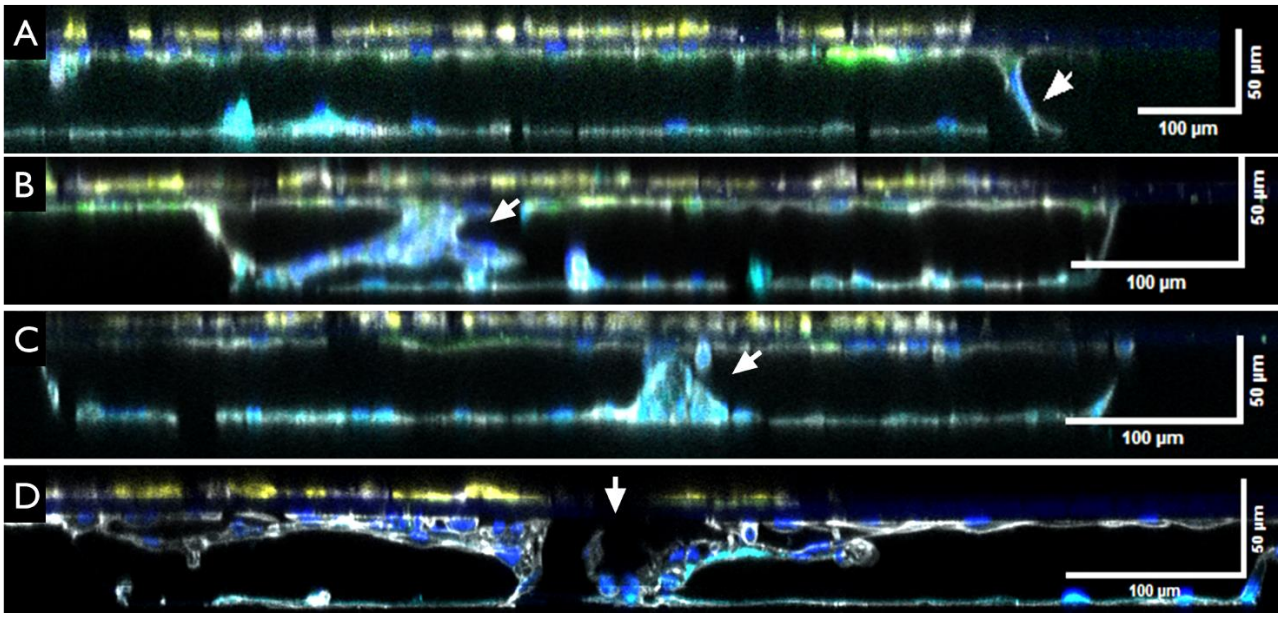

Figure 93: Confocal tilescan images of microsystems seeded with CirPECs, CiPodocytes, and CiGEnCs cultured in EGF enriched conditions and differentiated for 2 weeks with permanent perfusion, stained for claudin-1 (Alexa Fluor Plus 488), podocalyxin (DyLight 550), VE-cadherin (Alexa Fluor 594), and f-actin (phalloidin iFluor 647), 20X magnification (arrows indicate CirPECs invasion A) cell contact from the coverslip to the membrane, B&C) clusters of cells reaching the membrane, D) hole in the CiPodocyte layer from severe CirPECs invasion).

We could observe different levels of PEC invasion, as illustrated by Figure 93, going from simple cell contacts to the CiPodocytes layer (Figure 93: A), to the formation of clusters of CirPECs starting to invade the membrane (Figure 93: B&C). Figure 93: D shows an extreme example of CirPECs invasion where a full rupture podocyte and PECs continuum is observed. This invasion phenotype seems homologous to the PECs invasion process *in vivo*, with PECs invading both the Bowman space and the podocytes layer, while maintaining a continuous epithelium (Kuppe et al., 2019; Miesen et al., 2022; Shankland et al., 2014).

We then quantified quantitively CirPECs proliferation in the urinary chamber. To obtain the actual volume occupied by CirPECs in the lower channel we first determined a common analysis volume for every systems. A 800 by 2000 µm^2 window, covering the whole surface of CirPECs below the membrane and co-culture area was defined as lateral dimensions. The height of the analysis window was varying from a system to another, due to slight variations in the membrane height from the coverslips. To account for this variation we restricted the analysis for each system to the top of the Z-axis profiles for CirPECs to that of the CiPodocytes.

The segmentation was then performed on claudin-1 stacks using the 3D object counter plugin in ImageJ using the automatic threshold detection. This plugin performs a thresholding to obtain binarized stacks were objects are segmented, then it analyses every group of connected components in 3D and returns a list of connected objects volume, area, location... An example of segmentation of a claudin-1 stack in a urinary channel is shown Figure 94. We then obtained the overall volume coming from the CirPECs signal in the lower channel and determined a fraction of total occupation from the actual volume of analysis window.

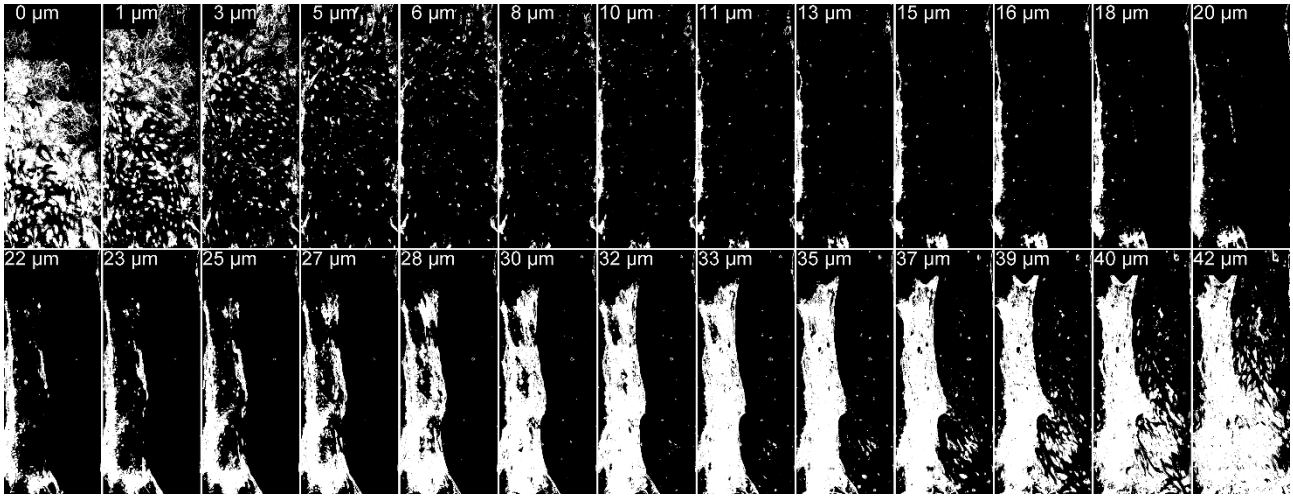

Figure 94: Example of segmentation of CirPECS signal (claudin-1) from the glass coverslip to the membrane to determine volume occupied by the cells.

The resulting occupation ratio of systems grown in either EGF deprived conditions (basal media) or EGF enrichment, and systems where cells were kept proliferating at 33°C are presented Figure 95.

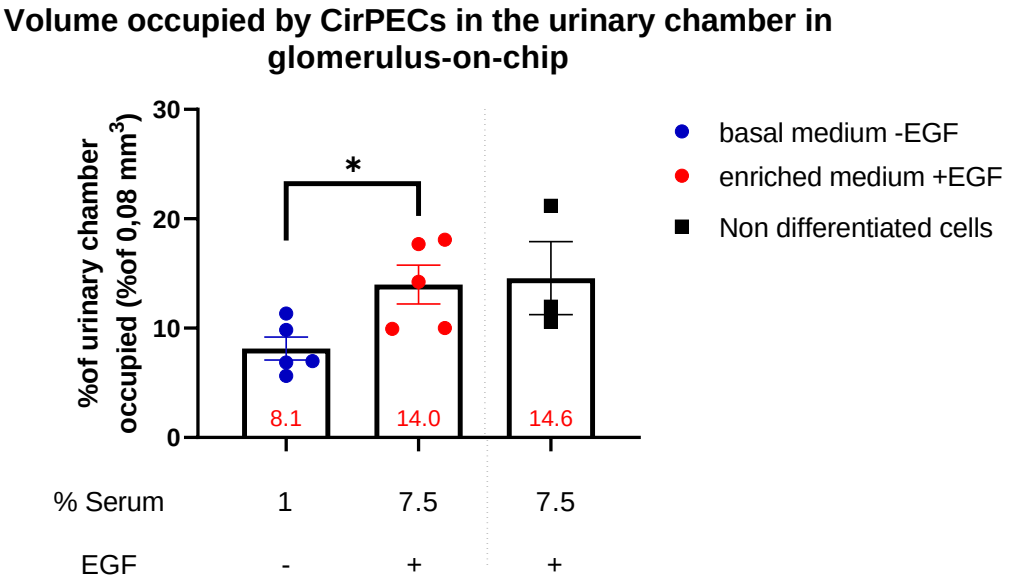

Figure 95: Volume of urinary chamber occupation from CirPECs obtained from segmenting claudin-1 signal in systems seeded with CirPECs, CiPodocytes, and CiGEnCs cultured in either EGF deprived conditions (basal media) or EGF enrichment, intermediary EGF stimulation profiles, and systems kept proliferating at 33°C *(error bars are SEM, stars from Mann-Whitney one tailed t-test)*

We can first notice that the space occupied by CirPECs in the lower channel significantly increased when systems are exposed to EGF, reaching 14% of total Bowman space. This level was similar to that of systems with no cell differentiation (temperature switch) was not induced, thus leaving the cells in their proliferating state.

Overall, CirPECs proliferation, migration, and invasion is increased in EGF enriched conditions compared to physiologically relevant basal medium which contains a minimal amount of EGF. As observed *in vivo*, this proliferation leads to the invasion of the urinary chamber and in some cases to the destabilization on the glomerular filtration barrier (CiPodocytes and CiGEnCs). This

could explain at least partially the deficient filtration of the systems grown in similar conditions. Thus EGF induced Bowman space invasion by PECs could trigger a functional impairment.

2.6.4.4 Effect of EGF on CirPECs proliferation and migration

To better understand the mechanisms underlying CirPECs proliferation, migration and invasion in the urinary chamber, when systems are stimulated with EGF. We investigated EGF effects on CirPECs proliferation and migration in simple 2D assays.

We first performed TEER measurements and wound healing migration assays with CirPECS in either EGF deprived conditions (basal media) or EGF enrichment. Experiments were done as previously described (see section: 2.5.2). For TEER experiments, subconfluent PET Transwell inserts (3 µm pores) with CirPECs seeded on the apical side of the membrane were differentiated and TEER was monitored for 2 weeks (Figure 96).

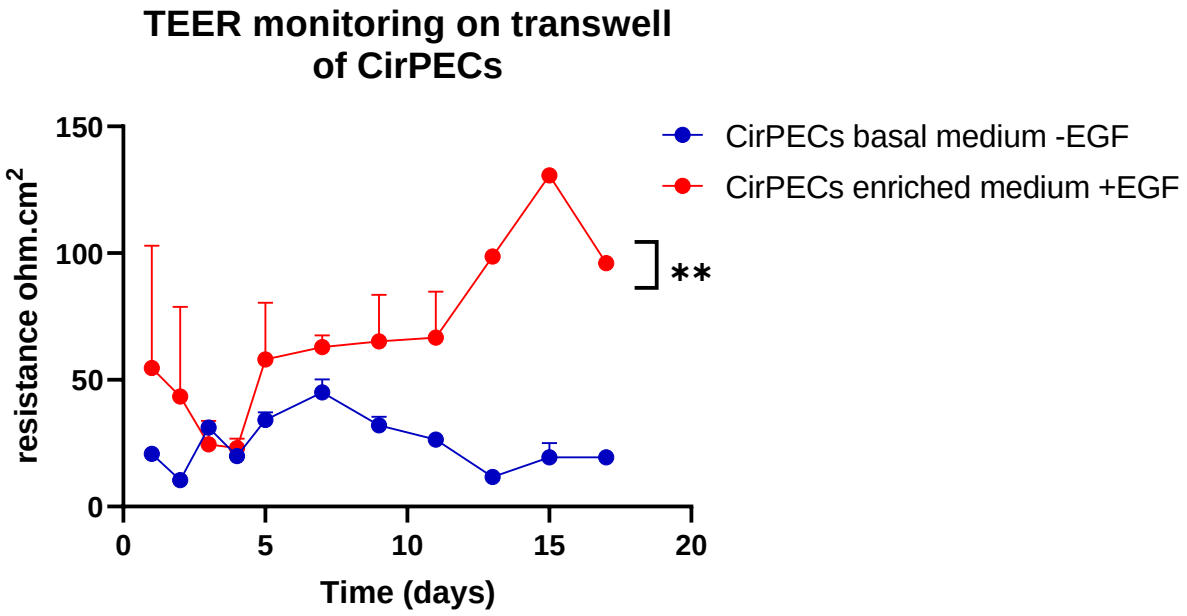

Figure 96: Normalized TEER values of differentiated CirPECs grown either in EGF deprived conditions (basal media) or EGF enrichment, on apical side of Transwell inserts (PET, 12 mm, 3 µm pores) (n=3, error bars are SEM, stars from Friedman test).

TEER experiments showed that CirPECs proliferation in EGF enriched medium was significantly higher than in basal conditions reaching resistance levels around 100 $\Omega.cm^2$. This confirms the ability of PECs to proliferate in EGF enriched conditions.

Wound healing experiments were done under the same conditions with GFP-CirPECs differentiated for 1 day prior to creating the wound. Wound closure was followed by epifluorescence microscopy for 3 days until wound closure. Division rate and wound closure were analyzed as previously described (see section: 2.5.2.2).

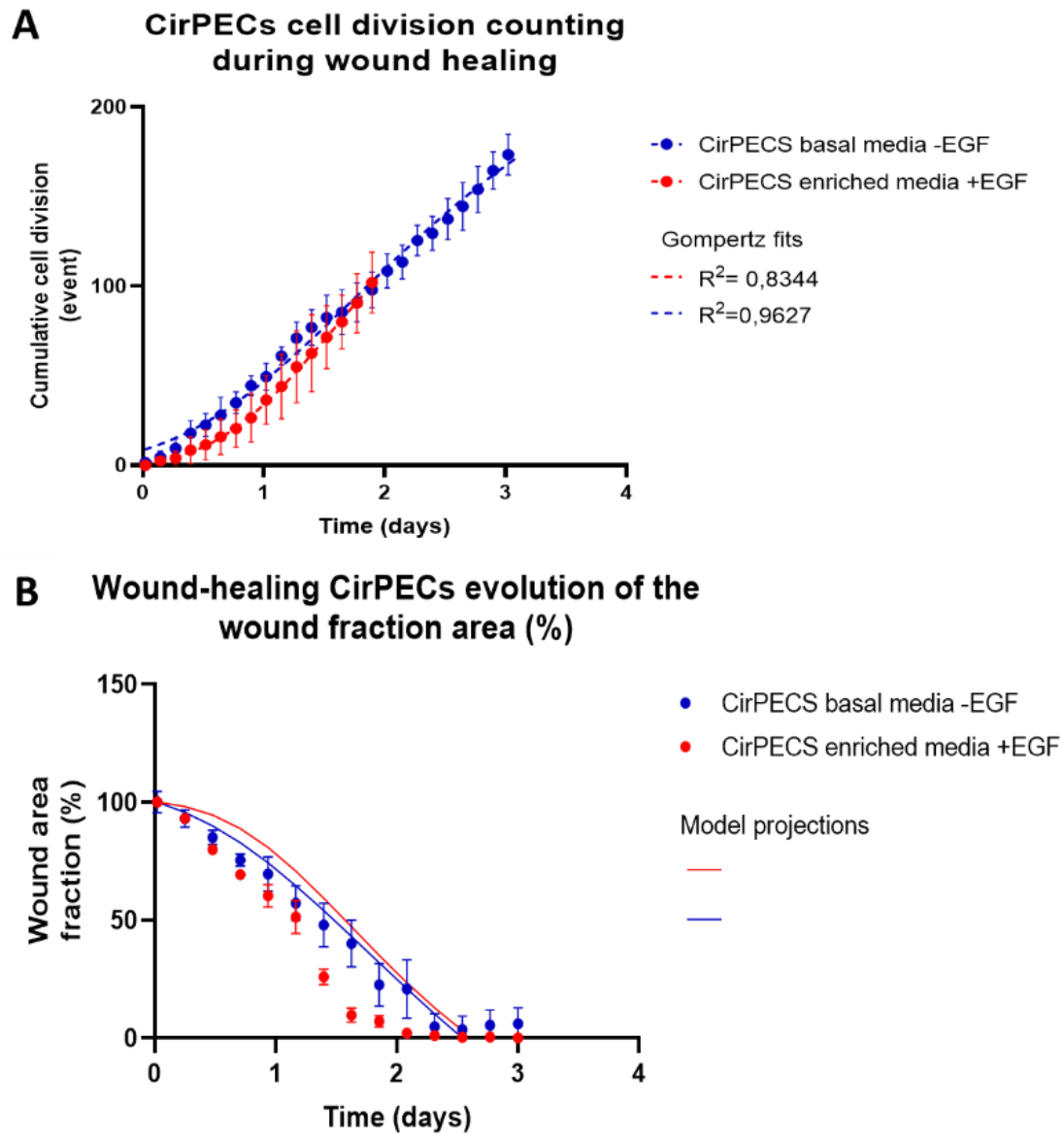

Figure 97: A) Cumulative cell division number fitted with Gompertz equation during wound healing experiments, B) Wound healing area closure measured and projected with the Gompertz model for CirPECs differentiated at t = -1 days and in either EGF deprived conditions (basal media) or EGF enrichment, (error bars are SEM, n=3).

Wound healing experiments showed (*Figure 97*) that division rate seemed not to be impacted by media composition during the course of the experiment (3 days), as observed for TEER experiment where proliferation increased after more than 10 days in culture.

However a reduced wound closure speed was observed for CirPECs in basal conditions. This is confirmed by the fact that the apparent migration component (extracted accordingly as previously described in section: 2.5.2.2) of CirPECs in basal medium is significantly smaller than in EGF enriched conditions (Figure 98).

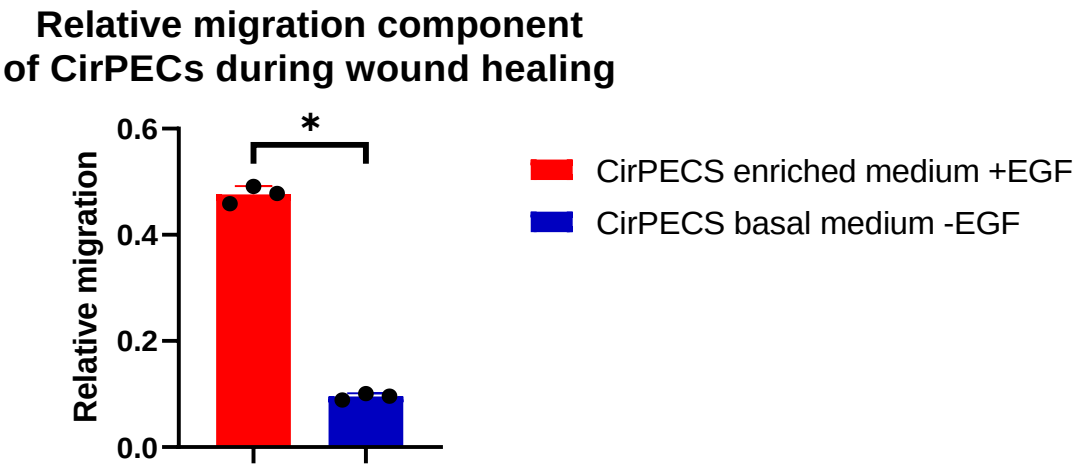

Figure 98: Migration component of wound healing experiments (Star from t-test).

Overall, these results suggest that CirPECs basal proliferation and migration rate can be increased when in presence of EGF. This induced proliferation correlates with our observation *in vitro* in our glomerulus-on-chip where CirPECs proliferate, migrate and invade the bowman space thus mimicking disease progression as in RPGN or FSGS.

2.7 Conclusion

Our goal was to first develop a microsystem allowing combining a systematic organ-on-chip approach with advanced quantitative noninvasive measurement methods, to identify mechanisms leading to pathophysiological responses, at the cell and organ scales.

To that end, we first designed biocompatible microsystems with dimensions tailored to suit both biomimetic dimensions of an actual glomerulus and allow for good imaging capabilities. The devices are built using classical microfabrication techniques allowing good overall control of systems dimensions and fabrication repeatability. The systems are composed of two small compartments mimicking the vascular and urinary space of an actual glomerulus separated by a membrane.

The systems were characterized for both synthetic and bioartificial membranes (PET or collagen based membranes) that provided support for co-culture of conditionally immortalized glomerular endothelial cells (CiGEnCs) and Podocytes (CiPodocytes) that recapitulate the glomerular filtration barrier (GFB). Both membrane types had advantages and inconveniences. The Bowman space in such systems is delimitated by a third parietal epithelial cell layer (CirPECs) directly lining the bottom of the device which appends to be optically accessible, offering an optical window to observe the systems with virtually any microscope. When cells were co-cultured in such devices, a continuous renewal of culture medium and controlled shear stress was provided by a gravity driven perfusion approach that allowed sustained culture (weeks).

After 2 weeks of co-culture and on-chip differentiation the 3 cell types used to recapitulate the glomerular organization all exhibited specific markers found *in vivo.* Cells formed confluent monolayers of cells on the whole surface of the system. Cells also secreted ECM relevant quantities of specific proteins of the basement membrane and showed a response to shear stress by aligning with the flow in the device. The glomerulus-on-chip organization recapitulation is summarized in Figure 99.

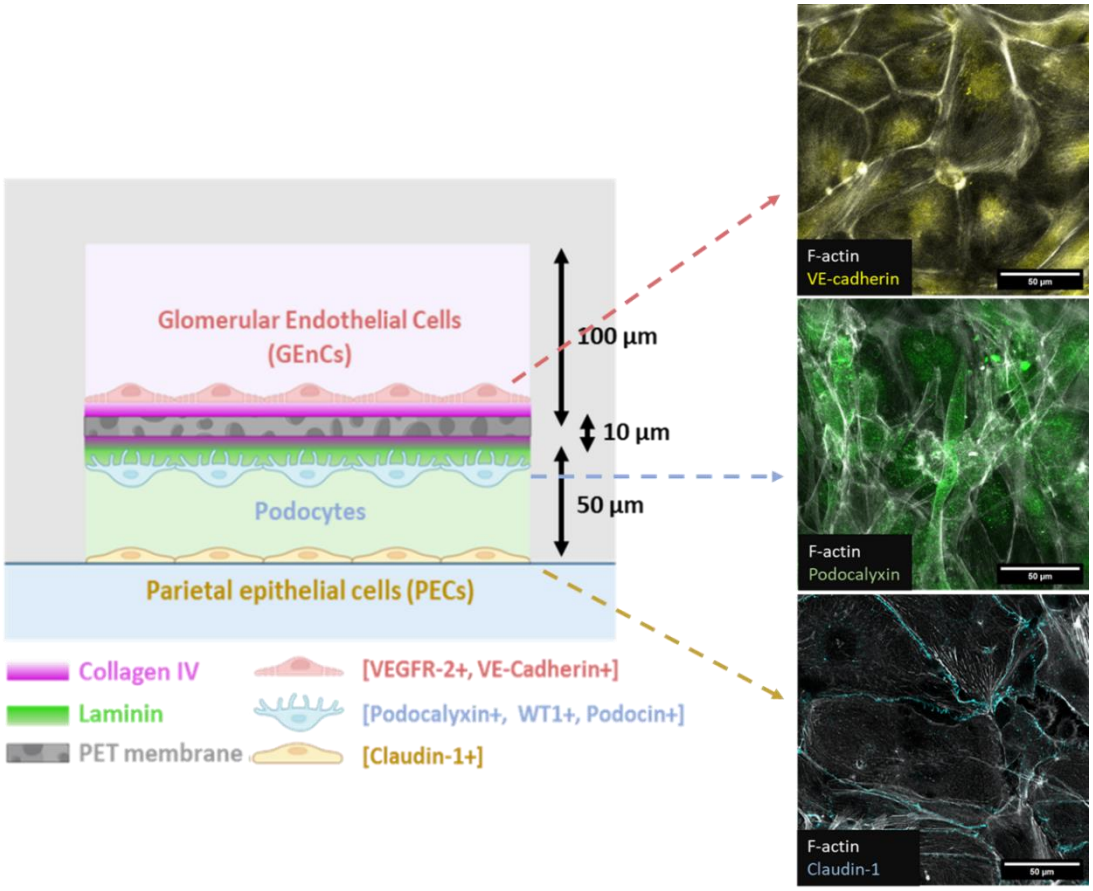

Figure 99: Scheme recapitulating the glomerulus-on-chip organization properties.

A functional assay showed that systems exhibited filtration properties similar to what is expected of an actual glomerulus when compared to an hybrid immature co-culture model (HUVECs and Podocytes) with an enhanced filtration for small molecules (below 70 kDa). Furthermore, albumin filtration (or sieving coefficient) were also measured to values closely matching *in vivo* values. This confirmed that our system behaved functionally like an actual glomerulus.

We then investigated the system response to EGF by stimulating artificially the systems with EGF for several weeks. EGF stimulated systems showed reduced filtration capabilities of both albumin and small molecules. EGF also induced a strong proliferation of CirPECs leading ultimately to the urinary chamber invasion and CiPodocytes layer destabilization. These are also markers of FSGS and RPGN progression observed *in vivo* (Kuppe et al., 2019; Lazareth et al., 2019; Moeller & Smeets, 2014).

Overall, we recapitulated a glomerular organization and function on-a-chip in the course of few weeks using resident cells of the glomerulus, while being able to trigger a disease-like phenotype by EGF stimulation leading to CirPECs activation (migration and proliferation), and urinary chamber invasion.

By studying these phenomena (filtration, migration, proliferation, differentiation) at different levels of complexity, these “meso-scale” biomimetic devices are able to create a more relevant but complex environment to decipher complex signaling pathways and possibly elaborate control strategies, in a future therapeutic perspective.

Chapter 3. Single molecule imaging to study EGFR and CD9 membrane organization and ROS signaling in PECs

Abstract:

Previous research highlighted that knocking-out CD9 proteins in mouse primary PECs (mPECs) resulted in several noticeable differences when compared to wild-type cells (Hoang, 2022; Lazareth et al., 2019). For instance, clusters (membrane nano-domains) of EGFR in CD9-KO mPECs were larger, and fewer EGF molecules are localized in these clusters. It was observed that EGFRs likely are localized in CD9-rich (or tetraspanin-enriched) domains on the cell membrane. Using super-resolution imaging (dSTORM), we further revealed an increased interaction between EGFR and CD9 upon HB-EGF stimulation in mPECs, suggesting that upon activation, EGFRs move towards CD9-rich areas, promoting dimerization in these regions.

Lanthanide-based nanoparticles, particularly those doped with Europium like YVO_4:Eu have been used effectively for quantitative detection of H_2O_2 in different cell types (Casanova et al., 2009). The technique is based on the loading of nanoparticles by pinocytosis and recovery after internalization, which enabled us to quantitatively measure intracellular levels of H_2O_2 in mPECs cells post-HB-EGF stimulations. When analyzing H_2O_2 concentration after HB-EGF exposure, the levels in wild-type mPECs exceeded greatly the levels measured in CD9 deficient mPECs.

In summary, this data not only emphasize the vital role of CD9 in organizing EGFR confinement in nanodomains and its influence on signaling upon HB-EGF stimulation but also independently confirm the potential implications of EGF in PEC activation and kidney inflammatory diseases.

Graphical abstract

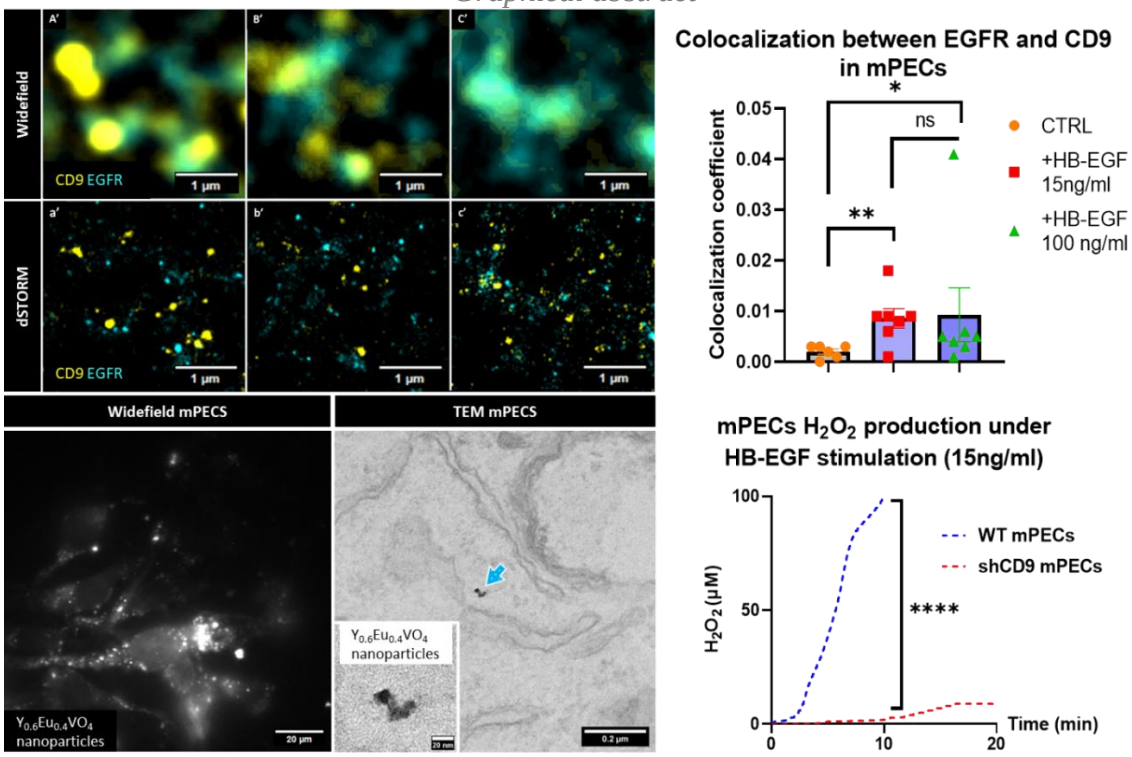

Keywords: *dSTORM, EGFR, CD9, Co-localization, HB-EGF, Eu nanoparticles, ROS, H_2O_2 signaling.*

3.1 Single Molecule Localization Microscopy to study EGFR and CD9 membrane organization in PECs in response to HB-EGF

To better understand EGFR organization in nano-domains (Hoang, 2022), its signaling and how CD9 is involved in both mechanisms, we characterized EGFR and CD9 single molecule nano-organization in PECs membrane domains.

Fluorescence microscopy is widely used in molecular and cell biology for imaging with high biochemical specificity. Despite its advantages, standard fluorescence microscopies such as epifluorescence, confocal microscopy, and light-sheet microscopy (Huisken et al., 2004) are less useful to define the nano-organization due to a resolution limit set by the diffraction of light.

The diffraction barrier in optical microscopy was described by Abbe's lateral resolution for fluorescence microscopy $(x, y) = \frac{\lambda}{2N.A.}$, or by the Rayleigh criterion for image resolution $(x, y) = \frac{0.61\lambda}{N.A.}$, which is the smallest observable distance between two single sources. With the numerical aperture $N.A. = n.sin(\theta)$, excitation wavelength λ, refractive index of the medium n, aperture angle θ.

The spot size produced (Airy disc) by a molecule emitting in the green wavelength and observed with a 100X oil immersive objective of numerical aperture 1.4 is approximately 200 nanometers. This restricts the amount of information that may be captured with standard microscopes.

Several approaches have been used to overcome this diffraction limit, such as Stimulated Emission Depletion (STED) (Hell & Wichmann, 1994), Structured-Illumination Microscopy (SIM) (Gustafsson, 2000), and Single Molecule Localization Microscopy (SMLM) (Betzig et al., 2006; Hess et al., 2006; Rust et al., 2006). Super-resolution microscopy (or nanoscopy) can resolve biological structures at the nanometer scale (in the tens of nanometers lateral resolution), circumventing Abbe's diffraction limit.

SMLM achievable with an epifluorescence microscopy setup, has opened new opportunities in life science research. In biological experiments, SMLM methods routinely achieves 20 nm lateral and 50 nm axial resolution (B. Huang et al., 2008). This gain in resolution enables a better understanding of biological processes such as molecular assembly dynamics, trafficking or protein-protein interaction (Baddeley & Bewersdorf, 2018). SMLM techniques mostly regroup two approaches: PhotoActivated Localization Microscopy (PALM) (Betzig et al., 2006; Hess et al., 2006) and direct Stochastic Optical Reconstruction Microscopy (dSTORM) (Heilemann et al., 2008) experiments.

Structured Illumination Microscopy (SIM) (Gustafsson, 2000) and stimulated emission depletion (STED) microscopy (Hell & Wichmann, 1994) both employ specific illumination patterns to achieve resolutions that surpass the diffraction limit, albeit through distinct physical mechanisms. SIM leverages a periodic pattern that interacts with the sample structure to generate Moiré fringes. In contrast, STED utilizes a hole pattern obtained with saturated stimulated emission to produce a smaller effective point spread function (PSF). The intricacies of these two techniques are briefly discussed in the subsequent sections.

3.1.1 Super resolution microscopy techniques

3.1.1.1 Structured Illumination Microscopy (SIM)

In SIM (Gustafsson, 2000), a predetermined structured light pattern is projected onto the sample being imaged. This structured light pattern interacts with the sample intrinsic structural patterns, resulting in the Moiré effect. In Fourier space, the diffraction limit acts like a low-pass filter, allowing low-frequency signals to pass while blocking high-frequency signals. By taking multiple images with different light pattern orientations, the shift in Fourier space allows to access more frequency information of the original structure. Images are subsequently deconvolved to produce super-resolution images of the sample. This method can achieve a resolution that is approximately twice as fine as that constrained by the diffraction limit.

SIM offers several advantages over other microscopy techniques such as confocal and wide-field microscopy. Notably, it does not necessitate the use of specific fluorophores or specific imaging media. It also has lower phototoxicity, making it suitable for multicolor imaging. Compared to single-molecule localization microscopy methods, SIM is faster, which makes it a viable option for live and 3D imaging. However, its resolution is relatively limited, at around 100 nm, which is coarser compared to other super-resolution techniques that can achieve resolutions between 10 nm and 50 nm.

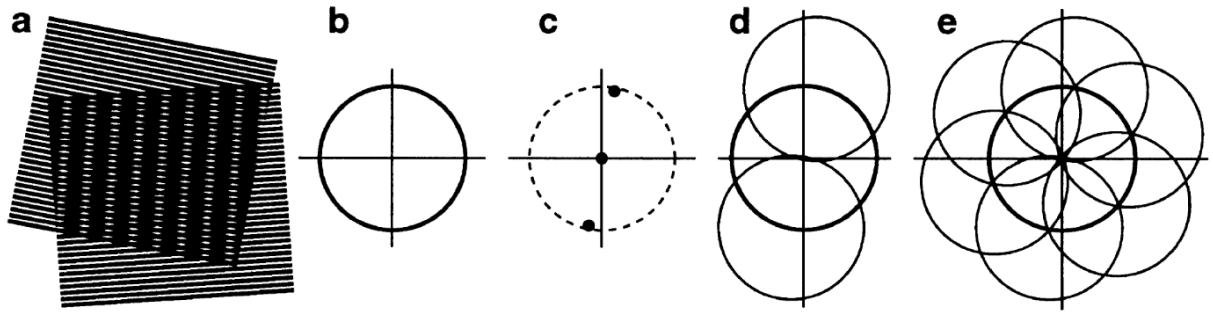

Figure 100: (a) Moiré fringes, visible as darker stripes, form due to the interference between two striped patterns: the excitation pattern and the emission pattern resulting from the sample's structure. Fourier Space: (b) In traditional microscopy, the observable region in Fourier space is circumscribed by a circle, and regions outside this circle remain unobservable. (c) The sinusoidal pattern commonly used to excite the sample is represented by three points in reciprocal space, which indicate the observation range constrained by the diffraction limit. (d) When the sample is illuminated with a striped pattern, Moiré fringes are produced, and the observable area in Fourier space is expanded. (e) Utilizing various orientations and phases of the striped pattern enables the image resolution to be twice as fine as that achievable under standard wide-field conditions, image from (Gustafsson, 2000).

3.1.1.2 Stimulated Emission Depletion (STED) microscopy

In STED microscopy (Hein et al., 2008; Hell & Wichmann, 1994), fluorescent molecules are initially excited by a pulsed laser, elevating them from the ground state to an excited state. A second donut-shaped laser pulse is then employed to deplete the fluorescence of molecules outside the central focal region through stimulated emission. To accomplish this peripheral depletion, the intensity of the second laser pulse must reach saturation levels, effectively suppressing all peripheral fluorescence

while preserving central fluorescence. This process results in an effective point spread function (PSF) that is smaller than the conventional PSF.

The method is fast, making it suitable for live imaging. However, due to the high-intensity lasers used in STED, and the sparse labelling of live probes, that limits the achievable resolution (Hein et al., 2008), the technique poses a greater risk of phototoxicity to cells (Mubaid & Brown, 2017; Tosheva et al., 2020), and may not be appropriate for probing receptor organization.

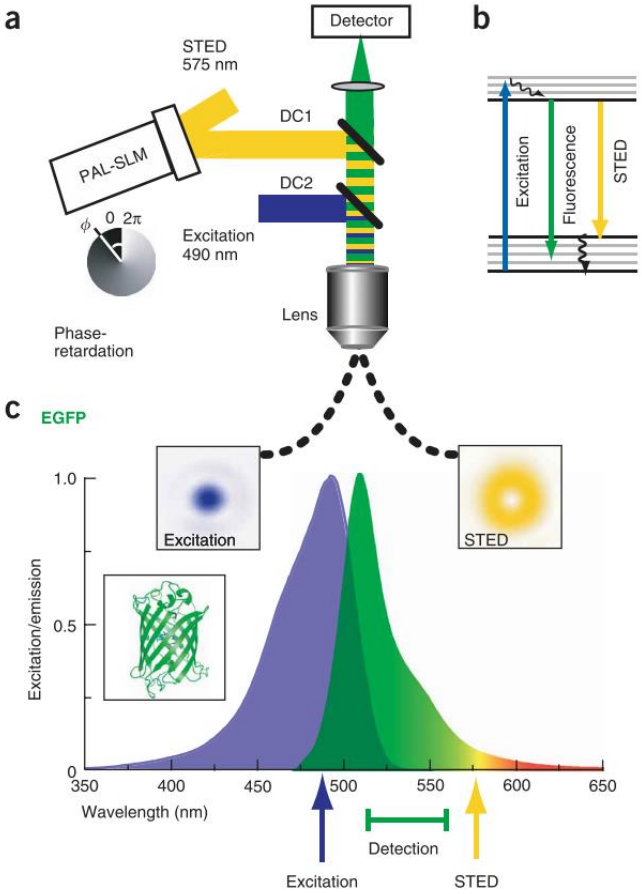

Figure 101: STED Excitation and Emission Principles: (a) In the STED setup diagram, the initial laser (DC2) triggers the fluorescence in the molecules. The STED laser (DC1), which is red-shifted, goes through a phase mask, forming a pattern that lacks intensity at the center, (b) The Jablonski diagram outlines the transitions that fluorophores undergo in STED. Here, molecules are elevated from the ground state (S_0) to an excited state (S_1) when they absorbe a photon. A subsequent STED laser, red-shifted to align with the emitted photons, encourages the stimulated emission process, (c) the point spread function (PSF) resulting from the EGFP excitation is shown (left), and on the right is the shape of the depletion beam that blocks fluorescence, effectively reducing the PSF spread, image from (Willig et al., 2006).

3.1.2 Super-resolution techniques based on single-molecule localization

3.1.2.1 Single Molecule Localization Microscopies (SMLM) principle

SMLM techniques, such as direct Stochastic Optical Reconstruction Microscopy (dSTORM) (Heilemann et al., 2008) or PhotoActivated Localization Microscopy (PALM) (Betzig et al., 2006; Hess et al., 2006), rely on series of imaging cycles in which only a very small fraction of the fluorescent molecules in the field of view are activated, so that each of the active fluorophores is independently resolvable from the others, as their Point Spread Function (PSF) emissions do not

overlap. This allows the localization of these fluorophores to be determined with high accuracy (~10 nm) (Heilemann et al., 2008; B. Huang et al., 2008; Rust et al., 2006). These subsets of molecules, blinking stochastically on thousands of frames, allow at the end of the experiment to position all the emitters with an increased accuracy and then the overall image to be reconstructed.

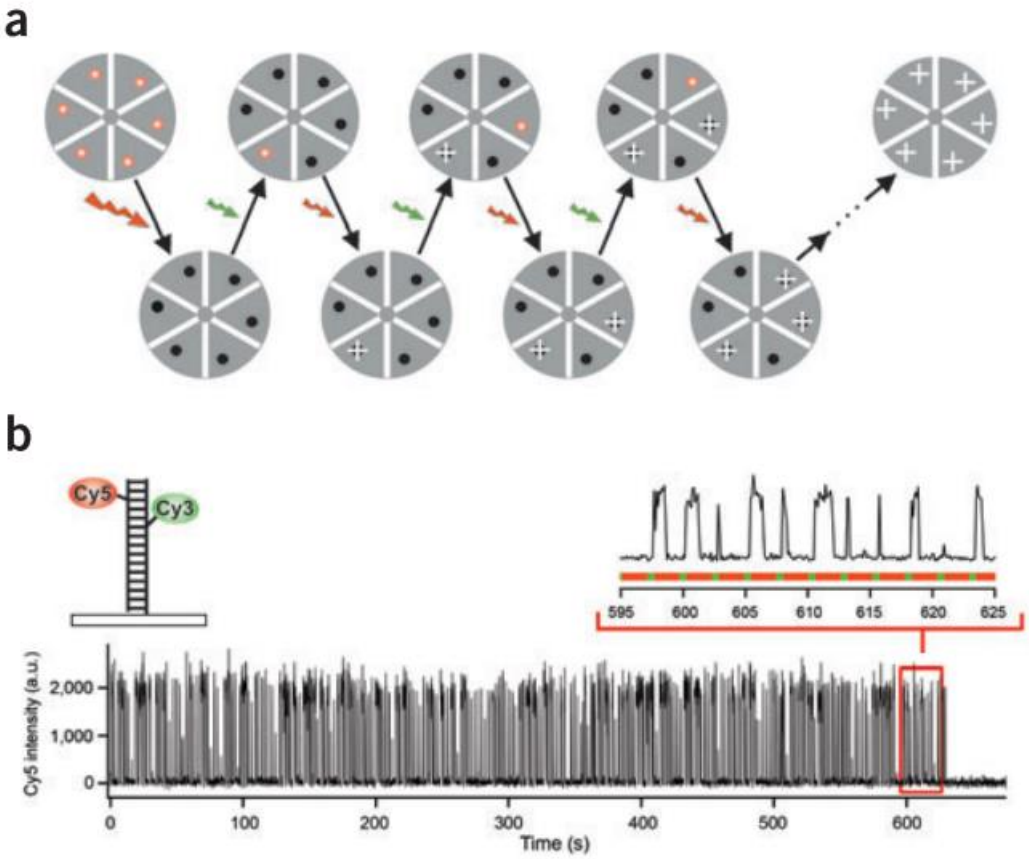

Figure 102: STORM Imaging (a) example of a structure tagged with red fluorophores capable of toggling between a fluorescent and a non-fluorescent state when exposed to red and green lasers, respectively. Initially, a potent red laser pulse turns all fluorophores to their dark, non-fluorescent state. During each imaging cycle, a green laser activates a subset of these fluorophores, making them optically distinguishable. These activated fluorophores are then illuminated with red light, emitting fluorescence until they return to their dark state. Their precise locations (represented by white crosses) can be ascertained with high accuracy. The final image is composed by aggregating the positions of fluorophores from multiple cycles. (b) A single Cy5 molecule attached to DNA can undergo numerous cycles of activation and deactivation before permanent photobleaching occurs. Fluorescence is elicited from Cy5 using a red laser (633 nm, 30 W/cm^2) and this same laser also switches Cy5 to its non-fluorescent state. To reactivate Cy5, a green laser (532 nm, 1 W/cm^2) is used. The laser excitation pattern is indicated by alternating red and green lines, and the emission of fluorescence is tracked by the black line, image from (Rust et al., 2006).

SMLM analysis essentially is the localization of molecules from the raw blinking stack. This is done through fitting single molecule point spread functions (PSF) with a mathematical function (*e.g.* Gaussian like) in order to determine coordinates of the molecule.

Single molecule methods provide lists of molecule positions. Owing to that fundamental difference with diffraction limited conventional imaging techniques, processing and analysis of the

results show a genuine paradigm shift. Proper analysis of the molecule coordinates enables quantitative characterization of the density, size, composition, and spatial distribution of cellular structures at a near-molecular precision.

Interactions are not directly observed, as in FRET, but we can estimate the proximity of two types of molecules to each other. SMLM owing to its high resolution is though well suited to the nano-organization of molecules into assemblies such as clusters (or membrane nano-domains).

3.1.2.2 STORM principle

Stochastic Optical Reconstruction Microscopy (STORM) technique was first demonstrated using paired cyanine dyes (Cy3-Cy5, Bates et al., 2005) attached to nucleic acids or antibodies therefore limiting STORM to fixed samples. These dyes can be switched between a fluorescent and a dark state when placed in a well-defined chemical environment, and the transition can be controlled in a reversible manner by light of different wavelengths. Indeed, when almost all the molecules are in the dark state, a laser is used to switch "on" only a fraction of the fluorophores to give an optically resolvable set of active fluorophores. Such a switch, can be cycled "on" and "off" hundreds of times before permanent photobleaching occurs. These steps are repeated until the density is sufficient to reconstruct the overall image.

Working with common, single organic dyes (such as Alexa Fluor 488, Alexa Fluor 568, Alexa Fluor 647, and Cy5), other research groups developed direct STORM (dSTORM) (Heilemann et al., 2008; Linde et al., 2011). This method aims to reach the dark state with conventional dyes using aqueous buffers containing both reducing agents such as mercapto-ethylamine (MEA), and an oxygen scavenging system (often based on the enzymes glucose oxidase and catalase, Figure 103).

Upon excitation, fluorophores are promoted from the singlet ground state (F_0) to the excited state (F_1). Either de-excitation can occur through fluorescence emission or the fluorophore can undergo intersystem crossing (k_{isc} rate) upon irradiation. In the triplet state (^3F), the molecule can react with molecular oxygen to recover the singlet ground state F_0 and produce singlet oxygen or react with thiolate (k_{red} rate) to form the radical anion of the fluorophore (F•). This particular form of the fluorochrome is essential for super-resolution because it is a stable dark state that can last a few seconds. Depending on the dye, the radical anion can be fully reduced (FH) to form a stable non-fluorescent molecule with "off" times in the order of minutes. To reach this reduction state the dSTORM buffer has to provide a reducing agent and, in the meantime, limit all the oxidation reactions (oxygen scavengers).

Because reduced forms of most Alexa Fluor derivatives show pronounced absorption at ~400 nm, an irradiation at 405 nm is a convenient way to control the slow recovery of the fluorescent form, and restoring the dye in its ground state (F_0).

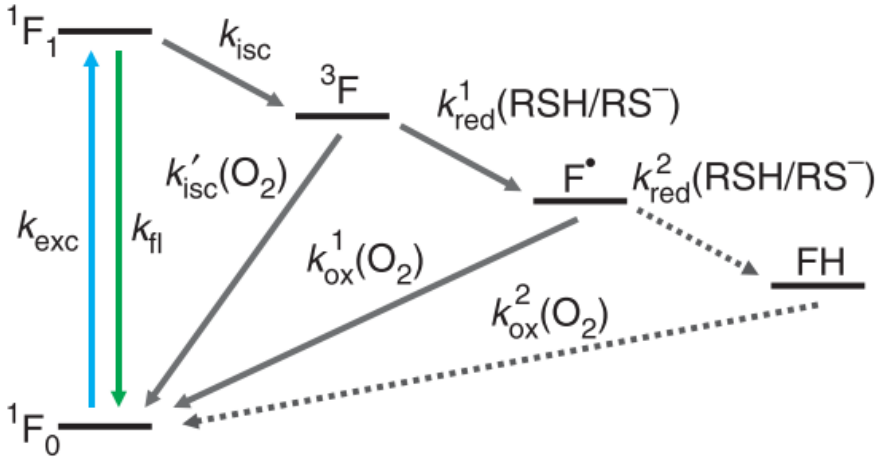

Figure 103: Reversible photoswitching of Alexa Fluor and ATTO dyes in the presence of thiols, image from (Linde et al., 2011).

Recently, my colleagues engineered an improved buffer solution specifically designed for consistent multicolor STORM imaging (Abdelsayed et al., 2022). This enhanced buffer formulation supports high-quality 2-color imaging with Alexa-647 and CF-568. Notably, the buffer remains stable for over a week, can be frozen and stored at -20°C, and is cost-effective to produce. This enables simultaneous multi-protein dSTORM imaging.

3.1.2.3 Localization of the molecules

PALM and dSTORM rely on the photochemical properties of the fluorophore to switch from a low emissive or non-emissive "dark" state from which very small populations of fluorophores are returned to an emissive state and individually detected and localized.

In SMLM we obtain a raw stack of diffraction limited spots, or PSF of single molecules emitting. The spatial resolution of such spots is limited by the diffraction of light. Since all the emitters are temporally separated, their spatial localization (centroid position of molecules) can be determined by fitting a mathematical function with a precision depending on the number of detected photons (Coltharp et al., 2014; Hess et al., 2006). Figure 104 shows a 2D modeled PSF and its Gaussian fitting to determine the molecule centroid coordinates.

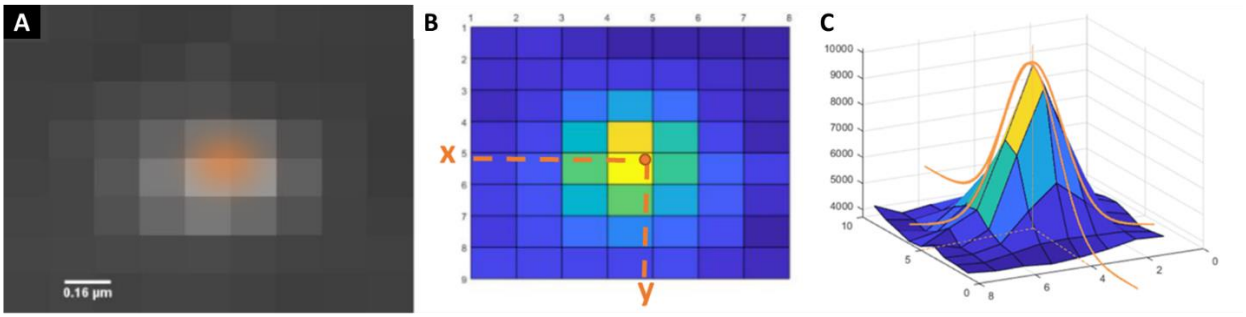

Figure 104: A) Gray level image of a blinking event, B&C) representation of the raw pixel matrix in 2D with localization x,y determination from gaussian fits, the orange spot in A) represents the molecule localization and the spot width reflects the localization precision.

The Gaussian-fitted positional error of the fluorophores is represented by the following equation:

$$\sigma = \sqrt{\frac{s^2}{N} + \frac{\frac{a^2}{12}}{N} + \frac{4\pi s^3 b^2}{aN^2}}$$

In this equation, σ represents the localization precision, s is the standard deviation of the point spread function, N is the total number of photons captured by the camera, a refers to the pixel size of the imaging detector, and b is the standard deviation of the background noise.

SMLM techniques are often combined with Total Internal Reflection Fluorescence (TIRF) microscopy (Z. Fan et al., 2020; Jacquemet et al., 2020), which provides an excellent Signal to Noise Ratio (SNR), with an electron-multiplying charge coupled device (EM-CCD) camera that can detect up to single photons.

For TIRF microscopy, light is directed at a total critical reflection angle to create an evanescent wave that selectively activates nanoparticles within approximately a few hundred nanometers from the substrate surface (Axelrod, 1981; Mattheyses et al., 2010). For TIRF to occur, the sample refractive index must be lower than that of the coverslip (Figure 105). This results in a highly localized excitation, offering an increased Signal-to-Noise Ratio (SNR) and reduced phototoxicity compared to other fluorescence microscopy methods.

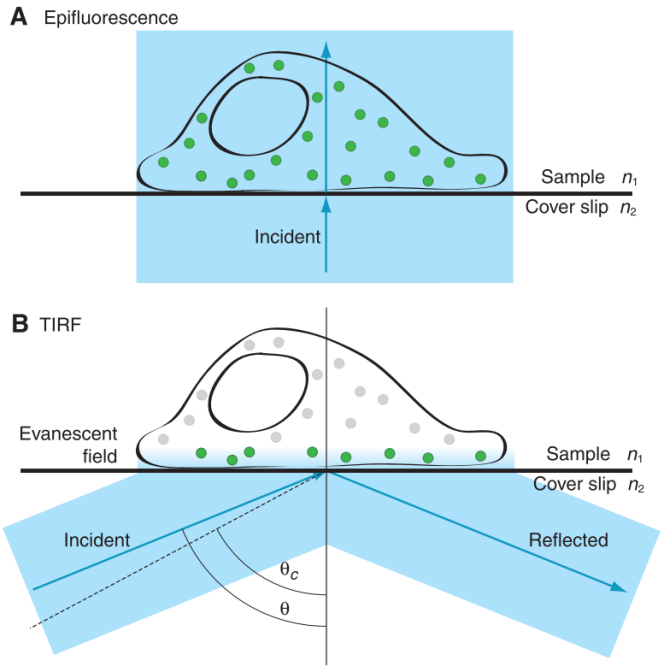

Figure 105: Schematic of epifluorescence and Total Internal Reflection Fluorescence (TIRF) illumination, A) in epifluorescence, the excitation light beam directly penetrates the sample, thereby exciting all fluorophores throughout the sample, B) In TIRF, the excitation light enters at an angle of incidence greater than the critical angle, the light is internally reflected at the coverslip–sample interface, generating an evanescent field within the sample on the other side of the interface. Only the fluorophores within this evanescent field are excited, image from (Mattheyses et al., 2010).

To achieve better-quality reconstructed images, it is important for fluorescent molecules not to remain in the on state for an extended period. The duty cycle, defined as the ratio of the time a fluorescent molecule is in the on state to the time it's in the off state, plays a crucial role here (Rust et al., 2006). A high duty cycle can result in overlapping fluorescent molecules, making them difficult to separate and, consequently, reducing the localization precision. Moreover, high duty cycles

necessitate the use of more computationally demanding and time-consuming methods to identify multiple emitters of the same molecule within the images (Marsh et al., 2018), requiring additional post-processing steps for correction.

3.1.3 Analysis, clustering and colocalization using SMLM

3.1.3.1 Localization correction methods, Drift and Chromatic corrections.

Movements of the stage or sample with respect to the objective lens is an issue in optical nanoscopy (*e.g.* when temperature changes, the microscope stage slowly drifts laterally and axially) because SMLM image acquisition time is long (minutes) and the resolution is high (tens on nm). If the stability of the experimental setup does not limit mechanical drifts to less than about half the resolution uncertainty, drift compensation is essential (Y. Wang et al., 2014). It allows the correction of movement-induced image degradations and distortions. Drift impact has to be limited as much as possible using active stabilization during acquisition and then through several methods of post-acquisition corrections.

Fiduciary markers like gold nanoparticles, quantum dots or fluorescent beads can be introduced in the field of view to estimate the drift of the sample. Those markers are supposed stationary with respect to the target structure over time so that the sample drift (mainly translation) can be easily monitored and corrected. This requires an addition of markers in the sample which means that this correction method is not compatible with all experiments.

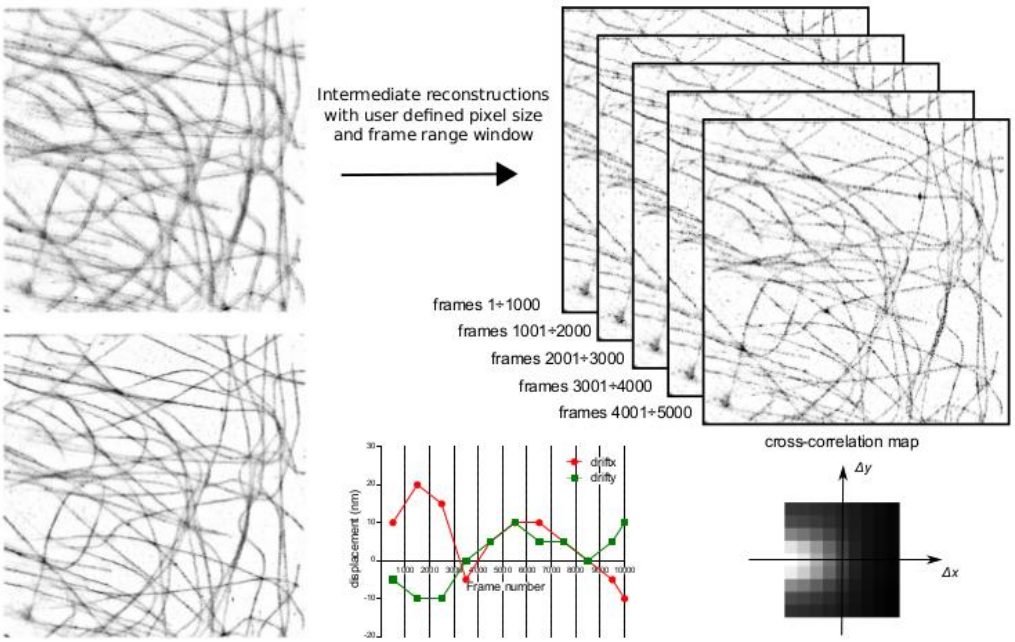

Figure 106: Left, dSTORM images of microtubules before and after cross-correlation drift correction, right, for cross correlation the image is periodically reconstructed (here once every 1000 frames) and resulting dSTORM images are correlated in the Fourier space, the x,y translations are monitored and then all molecules localizations are corrected depending on their tile position in the initial raw blinking stack, image from (Katrukha, 2020).

The cross-correlation analysis method (Y. Wang et al., 2014) is based on intrinsic sample structure, which is assumed to be invariant during the data acquisition time, and does not require the addition of any marker. All localization points, at the same time point, share the same drift compared

to other time points, regardless of where they are in the view field. Furthermore, the super-resolution images obtained at two time points, should describe the identical structures, even if they contain an incomplete subset of all fluorophore localizations. Thus, the localization events-based cross correlation methods use this fact and then calculate the cross-correlation function on partial reconstructed images representing only subsets of all the localizations. Localization points are split along time to generate intermediary images. The split step size should be small enough to reveal structure features and should be large enough so that each intermediate image contains a reasonable number of localization points.

For minimizing focus drift during experiments, dSTORM imaging systems should be equipped with an automatic focus system that keeps constant the distance between the coverslip and the objective. The accuracy of multicolor SMLM is further challenged by color channel cross talk and chromatic alignment errors. Usually, this problem is solved by calibrating with a stack of fluorescent multicolor beads, so that the chromatic localization aberration can be detected and corrected.

3.1.3.2 Clustering analysis

A cluster can be defined as a nanometer-scale organization of molecules whose spatial distribution is not randomly distributed but rather "clustered" within the region of interest. SMLM can provide such spatial hierarchical description: from molecules, to protein complexes, and at the cell level (Pageon et al., 2016).

Cluster characterization requires automatic segmentation for unbiased statistical descriptions of molecular assemblies. Unfortunately, segmentation requires the implementation of complex techniques even when working on classical microscopy images. The methods described here take in consideration the coordinate nature of localization-based super-resolution data.

Different solutions such as K-Ripley function, and DBSCAN have been suggested for directly quantifying clusters from the positions of molecules, and these have been utilized to measure protein organization in SMLM data (Khater et al., 2020).

Ripley's function

Ripley's function (Ripley, 1977) is as a popular tool for analyzing spatial distributions and clustering patterns in data sets. It focuses on two main aspects of a distribution: the density of data points and the expected number of points (N) found within a domain of specific radius (r) around a given point. The function employs a normalized second-moment property, known as the Ripley K function, to characterize these distributions. The Ripley K function offers a standardized measure that can be used to effectively study and compare spatial patterns across different data sets.

$$K(r) = \frac{1}{n}\sum_{i=1}^{n}\frac{N_{pi}(r)}{\lambda}$$

Where λ is the density or the number of points per area (*N/A*), N_{pi} is the number of points around the i^{th} point and the sum is taken over *n* points.

The L-function was proposed by Besag (Besag, 1977) as a normalization for the K function:

$$L(r) = \sqrt{\frac{K(r)}{\pi}}$$

The K-function can be further normalized, yielding the so-called H-function (Kiskowski et al., 2009):

$$H(r) = L(r) - r$$

The H-function, derived from the K-function, provides further insights into the nature of the distribution. A negative value of the H-function suggests that the points are dispersed, while a positive value indicates a clustered distribution. When the H-function value is zero, it indicates a uniform distribution of points (Figure 107).

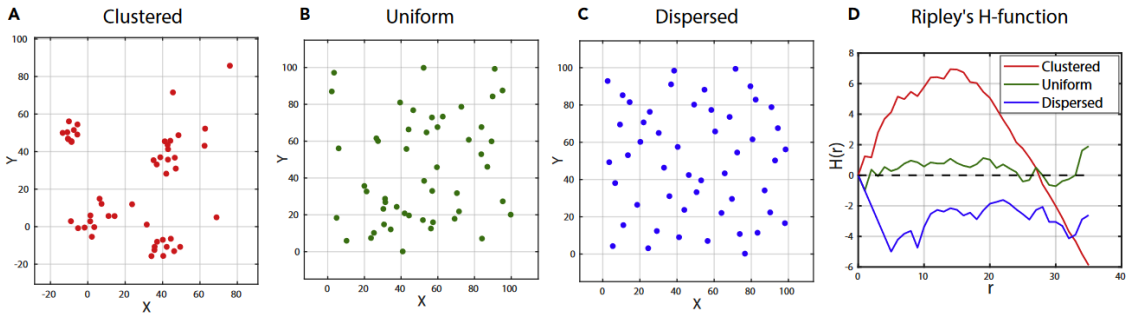

Figure 107: Illustrating how the H(r) function reflects various spatial point patterns: The H(r) function (D) registers positive values for points that are clustered together (A), oscillates around zero for points that are uniformly scattered (random) (B), and records negative values for points that are spread apart (C). In each of the patterns shown in (A) through (C), the generated data includes a set of 50 points from (Khater et al., 2020).

Recent research has extended the utility of the H-function, using its maximal value, denoted as H(r), to ascertain the size of clusters within the distribution. Kiskowski's (Kiskowski et al., 2009) work has further discussed this approach, finding that the maximum value of the H-function (radius of maximal aggregation) approximates the typical radius of the clusters in the distribution. However, even for well-separated domains with radius R in idealized distributions, the radius of maximal aggregation varies between R and 2R.

This additional layer of analysis allows researchers to not only determine the type of distribution (clustered, dispersed, or uniform) but also to quantify the size of clusters when they exist.

Density-based clustering methods

Density-based clustering methods, like DBSCAN developed by (Ester et al., 1996), are efficient for identifying clusters of varying shapes and sizes. DBSCAN works particularly well when there is a stark contrast in density between clusters and background. This algorithm minimizes the need for prior domain knowledge in determining input parameters, which is especially useful when dealing with extensive datasets. It uses only two parameters, a minimum number of points (MinPts) and neighborhood radius (ϵ), to classify each point as belonging to a cluster or not. To maintain cluster qualification, the associated molecules within a cluster should meet the MinPts condition within the

radius ε. This condition should hold as one molecule connects to another within the same cluster, continuing until the boundary molecules are reached, where the MinPts condition is no longer met.

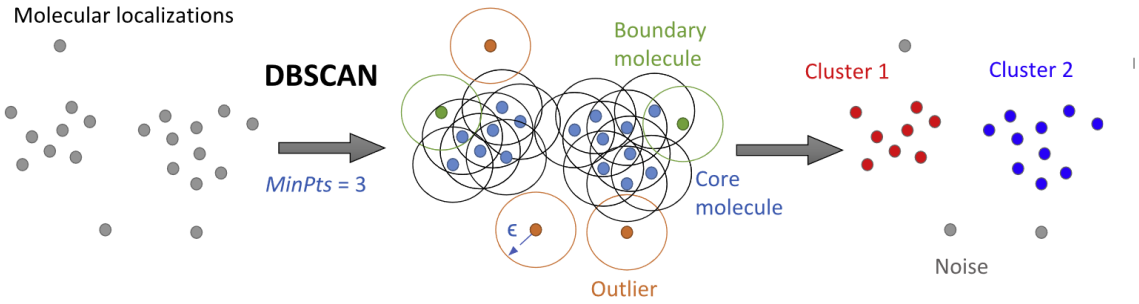

Figure 108: DBSCAN algorithm example when implemented with parameters ε and a minimum number of points (MinPts) set to 3, image from (Khater et al., 2020).

However, the choice of these parameters can be arbitrary and may significantly impact the clustering outcome. Imaging anomalies and the repeated blinking of a single fluorophore can thus lead to the creation of pseudoclusters. The presence of such pseudoclusters in SMLM data can make the selection of appropriate algorithm parameters more challenging (Khater et al., 2020).

Voronoi tessellation

Voronoi tessellation methods are commonly used in various fields like computational geometry, astrophysics, and biology to analyze spatial distributions. In SMLM, Voronoi diagrams help segment molecular localizations into regions, or Voronoi cells, based on the Euclidean distance between molecules, and provide information on the neighborhood surrounding the seeds (molecule localizations). The regions determined by all seeds, called polygons, form the mosaic of tiles that defines the Voronoï diagram (Figure 109).

Recently, Levet et al., have used geometric properties of these Voronoi cells, specifically their area, to cluster molecular localizations. These areas inversely correlate with molecular density, allowing for effective differentiation between clustered and non-clustered regions. Once the Voronoï diagram has been constructed, polygons with a density threshold are selected. The identification of clusters is done by merging all selected neighboring polygons, and defines object outlines by connecting all localizations belonging to the borders of the objects (Figure 109).

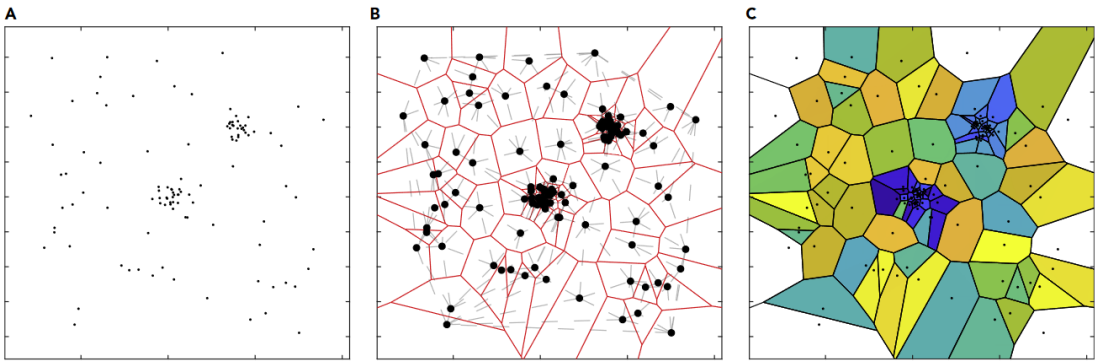

Figure 109: A) The initial molecular localization space, featuring two clusters along with noisy or background localizations, B) Voronoi tessellation divides the space into polygonal areas (Voronoi cells), shown in red. The corresponding Delaunay triangulation, which is the dual of the Voronoi diagram, is indicated by gray dashed lines, C) Various colors indicate different Voronoi cells. The white areas represent Voronoi cells that are open regions, image from (Khater et al., 2020).

However, Voronoi-based methods have limitations: effectiveness may diminish when handling SMLM data affected by artifacts like multiple blinking of a single fluorophore, the tessellation cell areas are influenced by underlying molecular densities and proximities of adjacent clusters, complicating the analysis of SMLM data with varying cluster densities (Khater et al., 2020).

3.1.3.3 Co-localization analysis

The objectives are: (i) to identify whether and where co-localization exists by overlaying two sets of images, (ii) quantify of how much the two sets of images coincide (Bolte & Cordelieres, 2006).

Due to the limitations of diffraction limited imaging technologies, it is crucial to approach co-localization findings with caution. Technologies like SMLM shown that what appears to be co-location at a lower resolution can be differentiated at higher resolutions (Cordelières & Bolte, 2008).

SMLM does not allow for the direct observation of interactions, as FRET, but can describe if two proteins share the same nano-organization.

Co-localization was quantified using intensity or object-based methods. However, in the case of coordinate-based objects like those in SMLM, it is more appropriate to use point distribution analytical tools. The co-localization coefficients defined for image based colocalization, however, remain applicable to SMLM data. It is important to note that the degree of co-localization can be affected by changes in molecular density across different experiments (Pageon et al., 2016).

Pearson's coefficient

The most common approach for estimating co-localization is through the use of a cytofluorogram. In this graphical representation, the intensities from Channel R and Channel G (designated as R_i and G_i with i the pixel index, and R_{avg} and G_{avg} being the average intensities for each channel) act as coordinates for individual points on the graph. If there is a unique stoichiometric relationship between the two proteins being studied, the distribution of points will form a line. The slope of this median line is influenced by both the stoichiometry and the unique properties of the chromophores used for detection. Although it cannot precisely determine the association ratio, it can be useful for comparative analyses between samples processed simultaneously and in the same manner (Cordelières & Bolte, 2008). The dispersion of the points around this median line can be quantified using the Pearson's correlation coefficient (r_P) which describes the level of co-occurence (Mukaka, 2012).

$$r_P = \frac{\sum_i\left(\left(R_i - R_{avg}\right)\left(G_i - G_{avg}\right)\right)}{\sqrt{\sum_i\left(R_i - R_{avg}\right)^2 \times \sum_i\left(G_i - G_{avg}\right)^2}}$$

The r_p value, which ranges between -1 and 1, quantifies the linear relationship between the red (R) and green (G) channels in an image, where R_{avg} and G_{avg} are the respective channel averages. The inclusion of these averages renders the coefficient insensitive to the image background. The r_p value remains valid even if the detectors for each channel have different intensity outputs. r_p indicates the degree of linear correlation between the two channels, the closer r_p is to +/- 1.0, the stronger the linear correlation between voxel intensities in the two channels.

Pearson's coefficient is not an accurate measure of co-localization *per se*, but rather serves as an approximation of the degree of association between two proteins. The coefficient ranges from -1

to 1, with -1 indicating an inverse correlation (usually implying exclusion), 0 signifying no correlation, and 1 indicating complete correlation. In biological contexts, a Pearson's coefficient of 1 is typically only observed when the same image is being compared with itself (Cordelières & Bolte, 2008).

The Spearman coefficient is an extension of the Pearson coefficient, but it uses intensity ranks rather than actual intensity values. The position of a specific intensity value (*Ri* or *Gi*) in a sorted list of all channel intensities determines its intensity rank (R_r or G_r).

This distinction endows Spearman's coefficient with the added capability of capturing all types of monotonic relationships between two channel, whereas Pearson's coefficient is limited to measuring only linear dependencies (Mukaka, 2012).

Manders coefficient

In cases where negative values in Pearson's coefficient are difficult to interpret, the subtraction of the averages can be omitted to create an overlap coefficient. This adjustment simplifies the interpretation of the measure by focusing on the degree of overlap between the two datasets:

$$r_0 = \frac{\sum(R_i G_i)}{\sqrt{\sum {R_i}^2 \sum {G_i}^2}}$$

The value of r_o ranges from 0 to 1 and serves as a measure of the correlation between two channels in an image. Unlike Pearson's coefficient, which is independent of both the relative channel strengths and the background intensity, r_o is sensitive to the background intensity level.

Due to the symmetric contribution of both channels to r_o, this coefficient cannot differentiate between situations where non-colocalized components are present in one of the two channels. For instance, all red pixels might overlap with green ones, while many green pixels do not have corresponding red signals. To address this limitation, r_o can be separated into specific coefficients:

$$k_1 = \frac{\sum(R_i G_i)}{\sum {R_i}^2}$$

and

$$k_2 = \frac{\sum(R_i G_i)}{\sum {G_i}^2}$$

These coefficients enable us to differentiate between the scenari described earlier, *e.g*. adding non-colocalized signals to the G channel will impact k_2 but not k_1. However, these coefficients come with their own limitations: k_1 scales in proportion to the signal strength in the G channel, and similarly, k_2 scales with the signal strength in the R channel.

These coefficient are implemented for image analysis in multiple plugins in ImageJ (Cordelières & Bolte, 2008), as well as for SMLM localization in Coloc-tesseler (Levet, Julien, Galland, Butler, Beghin, Chazeau, Hoess, et al., 2019).

These descriptors quantify co-localization of membrane nano-domains allowing description of their degree of co-organization in the cell membrane, which is important to understand molecular mechanisms of EGFR activation and signaling.

3.1.4 Tetraspanin enriched membrane domains

The cell membrane is a vital boundary, enclosing the cell internal components and acting as a selective barrier. It permits only specific molecules to enter or exit, thus maintaining the cellular internal environment.

Comprising lipids, proteins, and carbohydrates, the cell membrane has a complex makeup. Lipids form roughly 50% of the membrane's mass, with proteins contributing about 42%, and carbohydrates making up the remainder (Steck, 1974). The lipids are amphiphilic, possessing both hydrophilic and hydrophobic moieties, which lead them to naturally form a bilayer. Phospholipids are the most prevalent type of lipids and play a key role in membrane fluidity. Their structure includes a hydrophilic "head" and two hydrophobic "tails," one of which is often unsaturated, that prevent tight packing and thus affect the membrane overall fluidity (Meer et al., 2008).

Besides phospholipids, the membrane also contains other lipid types like sphingolipids and cholesterol, each contributing unique attributes (Meer et al., 2008). Sphingolipids, with their saturated chains, form tightly-packed regions known as lipid rafts (Simons & Ikonen, 1997). Cholesterol, on the other hand, adds rigidity and varies in proportion across different types of cells (Brown & London, 2000).

Proteins, both integral and peripheral, facilitate a range of membrane functions. Integral proteins embed in the lipid bilayer, while peripheral ones reside at the interface and are more mobile. Carbohydrates, though less described, are vital for cell-cell interactions and pathogen binding, often forming complexes with lipids or proteins.

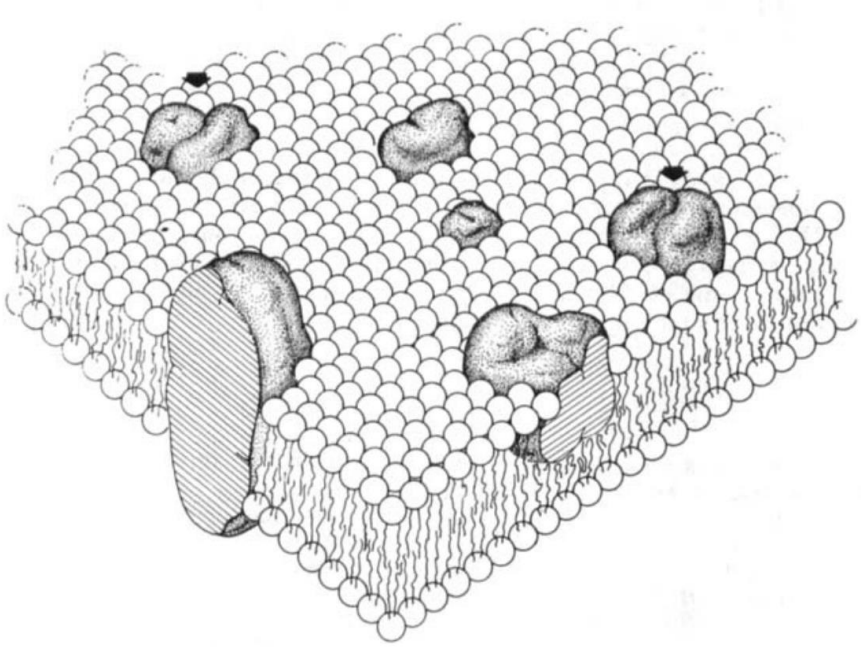

Figure 110: The diagram shows how the membrane's complex 3D structure is organized. Phospholipids create the membrane's foundational layer, while globular proteins are both partially sunk into and sticking out of this layer. While the placement of these proteins appears random over larger distances, there may be small clusters of proteins or lipoproteins (indicated by arrows) that form due to short-range interactions between proteins. image from (Singer & Nicolson, 1972).

3.1.4.1 The different membrane domains

The Fluid Mosaic Model, formulated by Singer and Nicholson in 1972 (Singer & Nicolson, 1972), describes the membrane as a dynamic structure with lipids and proteins (Figure 110). The Fluid Mosaic Model provided the initial framework for understanding the cell membrane, and has evolved to accommodate more nuanced insights into the lipid and protein organization.

A key advancement was the discovery of “lipid rafts”, specialized membrane domains rich in certain lipids and proteins (Simons & Ikonen, 1997). While these rafts were initially identified using detergents like Triton X-100, the methodology and the universal presence of cholesterol in these rafts have been subjects of debate (Almeida et al., 2003). Advanced techniques such as nanoSIM and FRET have been employed to investigate these domains, revealing their composition to be more variable and complex than initially thought (Lu & Fairn, 2018).

In addition, A. Kusumi and colleagues introduced the Picket-Fence Model (Figure 111) (Kusumi et al., 1993; Kusumi & Sako, 1996). Contrary to the Fluid Mosaic Model, which suggests free diffusion of membrane components, the Picket-Fence Model proposes that proteins can be temporarily confined within specific domains by an underlying actin "fence." This model finds support from single-molecule tracking experiments (Freeman et al., 2018; Kusumi et al., 1993), revealing that membrane components, including phospholipids, show restricted diffusion patterns. Super resolution live imaging of actin coupled with Single particle Tracking (SPT) (Sadegh et al., 2017) further corroborated these findings by revealing the ultrastructure of the actin cytoskeleton beneath the membrane, providing a structural basis for this temporary confinement.

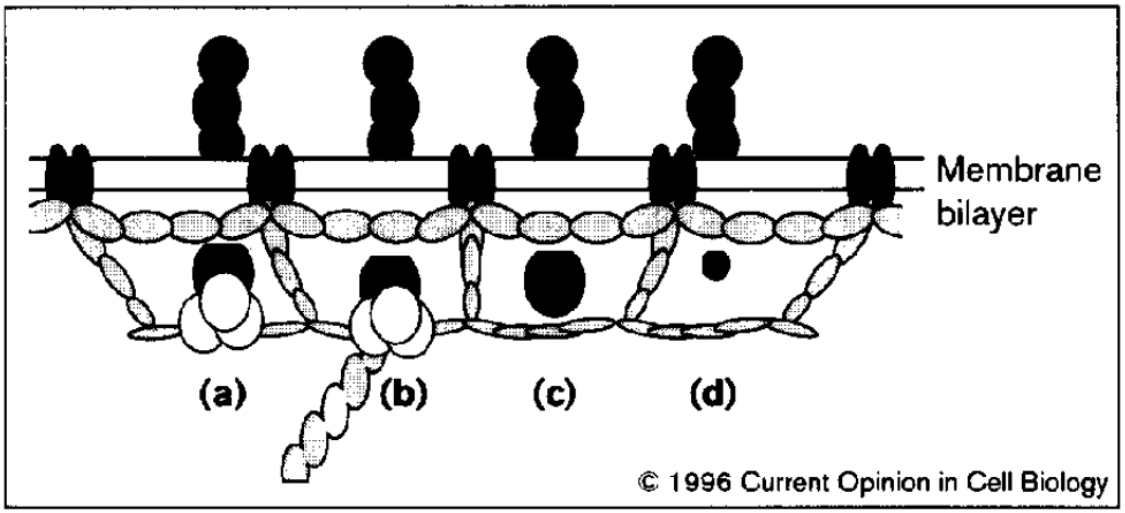

Figure 111: Fence and Picket Model: a) actin filaments limit the mobility of the receptors (fence), b) some proteins are bound to actin filaments (pickets), image from (Kusumi & Sako, 1996).

The concept of membrane proteins being tethered to the cytoskeleton has emerged as an additional mechanism influencing membrane dynamics (Goswami et al., 2008; Winder et al., 2005). Such tethering is dynamic, altering in response to cellular events like activation. The restructuring of rafts and actin filaments upon activation could have downstream implications for cellular signaling and responses. This tethering adds complexity to the membrane dynamics and could be critical for spatial organization of membrane proteins, influencing localized cellular functions such as signal transduction and cellular adhesion (Viola & Gupta, 2007). These ongoing discoveries underline the cell membrane as a dynamic, complex system, not merely a passive barrier. The organization within

these membrane domains is assumed to play a role in the regulation of cell activity (Sezgin et al., 2017).

3.1.4.2 Tetraspanin enriched membrane domains, CD9 and EGFR

Tetraspanins are transmembrane proteins involved in various cellular processes such as cell adhesion and endocytosis (Hemler, 2005). They interact not only with each other but also with other membrane proteins and lipids to form specialized areas known as Tetraspanin-Enriched Microdomains (TEMs) (Yanez-Mo et al., 2009). TEMs either remain stable or are only partially affected when cholesterol is depleted: in contrast, lipid rafts become unstable following cholesterol depletion (Charrin et al., 2003; Claas et al., 2001). At low temperatures, 1% Triton X primarily dissolves TEMs, whereas lipid rafts remain insoluble. TEMs are also soluble in other non-ionic detergents like Brij and CHAPS (Claas et al., 2001). While palmitoylation does not significantly affect the solubility or density of TEM proteins, it does increase the solubility of proteins in lipid rafts (Berditchevski et al., 2002; Charrin et al., 2002; X. Yang et al., 2002).

In TEMs, integrins are commonly found as partners of tetraspanins. Other proteins, like the junction protein claudin-1, are also associated with tetraspanins (Kovalenko et al., 2007). On the other hand, GPI-linked proteins, caveolin, and Src-family kinases are typically located in lipid rafts but not in TEMs (Brown & London, 1998; L. J. Foster et al., 2003). The TEMs could be signaling platforms by regulating the organization of receptors such as EGFR.

Advanced imaging techniques like STED have provided deeper insights into the size and density of these domains (Zuidscherwoude et al., 2015). Different tetraspanins like CD53, CD37, CD81, and CD82 occupy distinct domains. CD53 is found in the smallest, and CD37 in the largest domains. Most domains range in size from 100 nm to 150 nm.

During her thesis, Thi Thuy Hoang (Hoang, 2022) used dSTORM and Single-Particle Tracking (SPT) to scrutinize how the depletion of CD9 proteins affects the distribution, clustering, and behavior of EGF receptors (EGFR) in mouse primary Parietal Epithelial Cells (mPECs). When CD9 proteins are removed (in shCD9 mPECs), several features emerge (Figure 112):

1. EGFRs mainly exist in small domains or clusters in both cell types, but in shCD9 mPECs, the number of receptors is only about half that in normal mPECs
2. The clusters of EGFR have a larger area and diameter in shCD9 mPECs than in normal mPECs.
3. The count and density of EGF molecules in these clusters are lower in shCD9 mPECs.

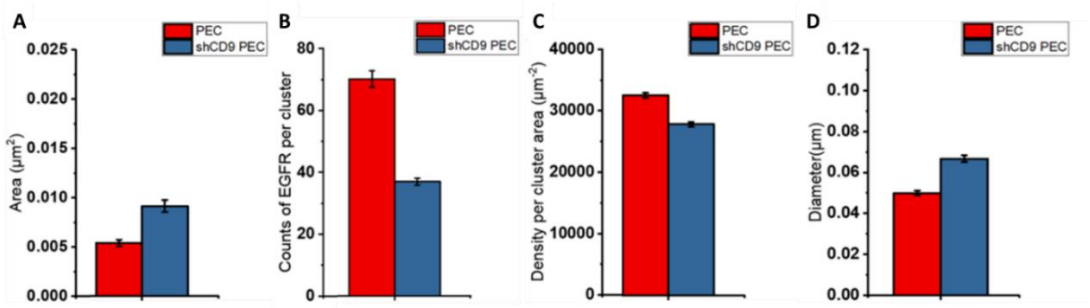

Figure 112: EGFR cluster analysis in mPECs and shCD9 mPECs of the dSTORM data, parameters are: A) cluster area, B) EGFR counts per cluster, C) EGFR density inside the cluster, and D) cluster diameter, from (Hoang, 2022).

CD9 thus regulates EGFR organization in membrane domains.

The study also compares the behavior of EGFR with other receptors like transferrin receptors, which are known to be localized outside rafts, and finds that there is more overlap between CD9 and EGFR clusters than with transferrin and EGFR, further supporting the idea that EGFRs are present in CD9 domains (Figure 113).

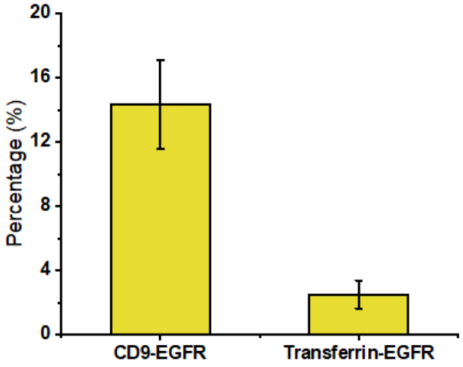

Figure 113: Percentages of overlap between CD9 clusters and EGFR clusters and between transferrin receptor and EGFR clusters. Two clusters are considered overlapping if the distance between their centers is smaller than 100 nm, from (Hoang, 2022).

Additionally, SPT tracking data align with these findings, showing larger confinement domains for EGFRs in shCD9 PEC cells, without significantly affecting the diffusion properties and the energy landscape in which these receptors evolve (Figure 114).

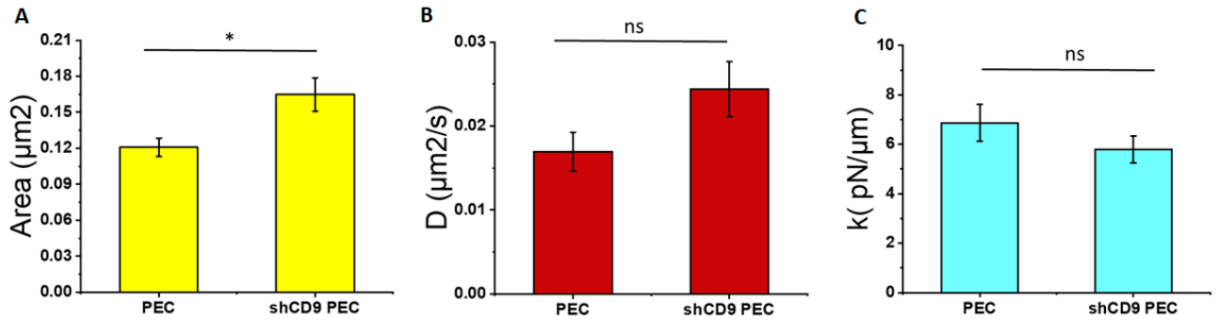

*Figure 114: EGF receptor confinement in mPECs and shCD9 mPECs, A) Confinement domain area, B) diffusion coefficient, C) spring constant of the harmonic potential felt by the receptors, from (Hoang, 2022) (T-test *: $P < 0.05$).*

Overall, the data suggest that EGFR is likely present in CD9-rich areas, or tetraspanin-enriched microdomains, on the cell membrane. When CD9 is depleted, EGFR stability in the membrane may be impaired. This leads to quicker internalization and degradation of the receptors, resulting in fewer receptors in the membrane of shCD9 mPECs. The size of these domains also appears to increase, possibly due to less compact tetraspanin domains. CD9 might thus play a role in EGFR signaling by regulating its organization.

We thus decided to study the organization of both EGFR and CD9 in response to HB-EGF stimulations to better understand the EGF role of these TEM nanodomains upon activation in order to achieve a better comprehension of signal transduction regulation.

3.1.5 Characterization of EGFR and CD9 organization in mPECs by dSTORM after HB-EGF stimulations

3.1.5.1 dSTORM imaging and detection efficacy

Mouse primary Parietal Epithelial Cells (mPECs) were cultured as previously described on fibronectin coated glass coverslips, and let to grow until 70% confluence is reached. Cells were then serum-deprived in unsupplemented ECBM (1% FBS, no growth factors) medium overnight. Cells were then incubated with either 15 or 100 ng/ml HB-EGF in ECBM for 20 minutes prior to fixation.

The fixation and permeabilization protocols are provided in Appendix: 4.4. After cell fixation and permeabilization, mPECs were labeled for EGFR (rat primary antibody, secondary antibody labeled with CF568) & CD9 (primary antibody labeled with Dylight 650 generously provided by Eric Rubinstein). Cells were imaged on a inversed microscope with laser epi-illumination (imaging setup and lasers used described in Appendix: 4.4.1).

For dSTORM imaging, the glass coverslips with cells are mounted in imaging chambers and filled with dSTORM buffer (Appendix: 4.4) and covered with a coverslip to create an air tight structure. A fraction of the fluorophores was first turned off using high laser intensities at the excitation wavelength before imaging at lower intensity. Time series of 15000 frames were then acquired for each fluorophore sequentially (first 568 nm for EGFR, then 650 nm for CD9) using a 2x2 binning on the camera providing an image pixel size of 130 nm.

For the analysis of the raw blinking stacks, detection and quantification were performed using Detection of Molecules (DoM) plugin v.1.2.5 for ImageJ (Katrukha, 2020). The entire image is processed for spots detection, but spots near the image borders (less than 3 *SD* of the PSF) are excluded. A specialized module adjusts for stage drift (see section: 3.1.3.1) by employing normalized cross-correlation on partially reconstructed images.

We first measured the total number of EGFR and CD9 localizations obtained per cell area (Figure 115). From this graph we can observe that the number of EGFR and CD9 localizations per cell area decreases with the stimulation by HB-EGF. This decrease was significative for a saturating stimulation with 100ng/ml for both proteins. The number of EGFR molecules per μm^2 dropped from 73 to 28 and CD9 from 34 to 9 on average. This indicates that the result obtained by semi-quantitative Western-Blot analysis of the total cell EGFR population presented in section: 1.3.2, *i. e.* a decrease of EGFR receptors upon stimulation is actually also true for the EGFR population in the membrane, and indicates that upon stimulation, EGFR are internalized and recycled (Madshus & Stang, 2009). The fact that the CD9 localization number also decreases upon HB-EGF stimulation has however not yet been observed. A possible explanation could be that EGFR receptors are internalized together with their surrounding TEM CD9-containing nanodomain.

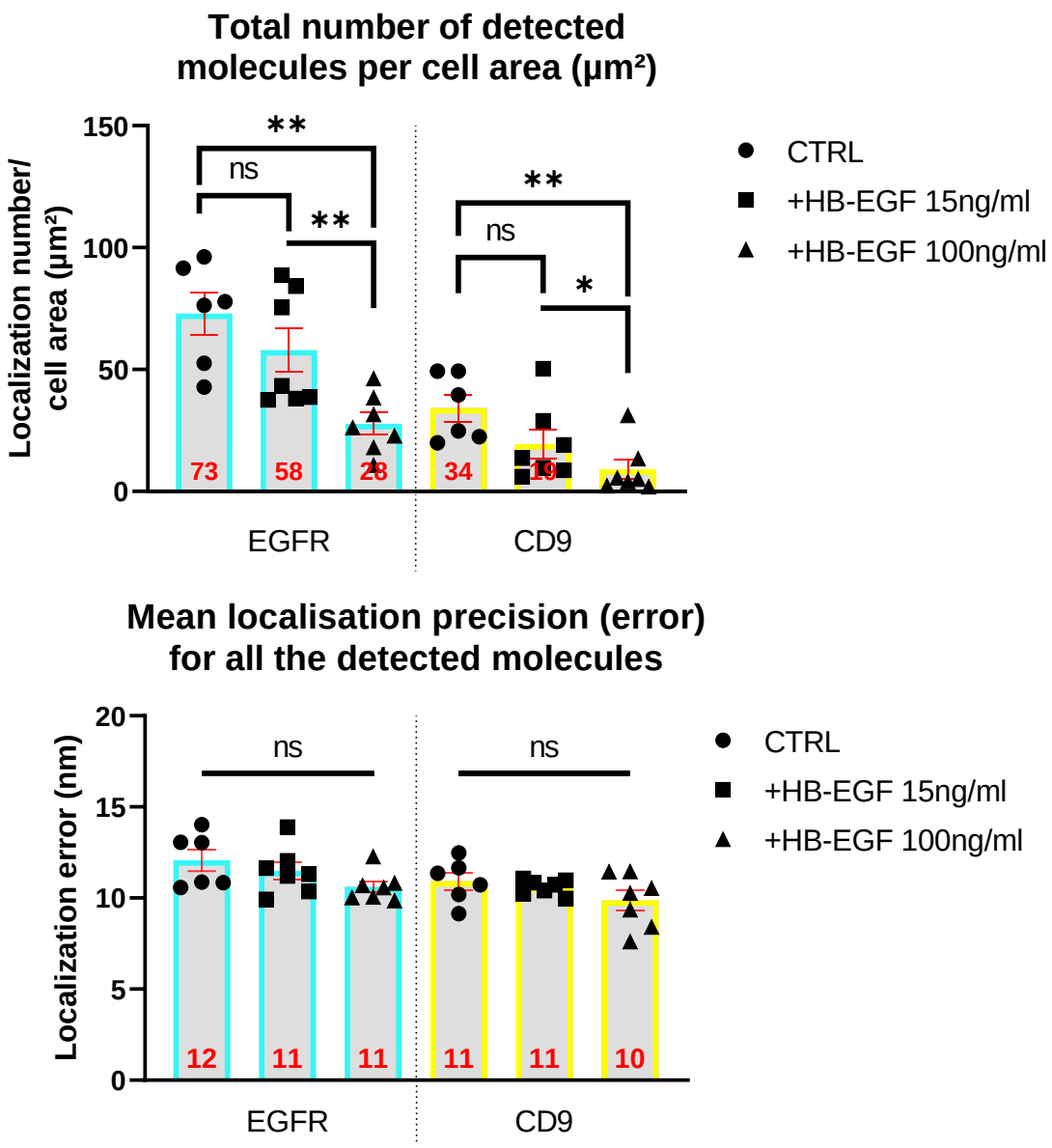

Figure 115: Top, total EGFR and CD9 localization count per images, and bottom, average localization error from molecule fits for mPECs grown on glass coverslips and labeled for EGFR (Cyan, labeled with CF568) & CD9 (Yellow, labeled with Dylight 650) with control cells, cells stimulated with 15 ng/ml or with 100 ng/ml HB-EGF (n=6, error bars are SEM, stars from t-test).

The localization precision of molecules is not affected by this density decrease, indicating that the decreased localization number is indeed due to fewer molecules being present and not a global decrease in imaging quality. We then analyzed quantitatively the effect of HB-EGF of EGFR and CD9 cluster size density and possible co-localization.

3.1.5.2 EGFR and role of HB-EGF on clustering and density in mPECs

We present here both diffraction limited images of EGFR obtained from plotting the standard deviation of the raw molecule blinking stack versus the images reconstructed from localization obtained by the dSTORM analysis. The reconstructions to obtain super resolution images are 32-bit image where each molecule is represented as a 2D Gaussian with integrated intensity of 1 and where the widths of the Gaussian spots are the standard deviation X,Y of localization precision.

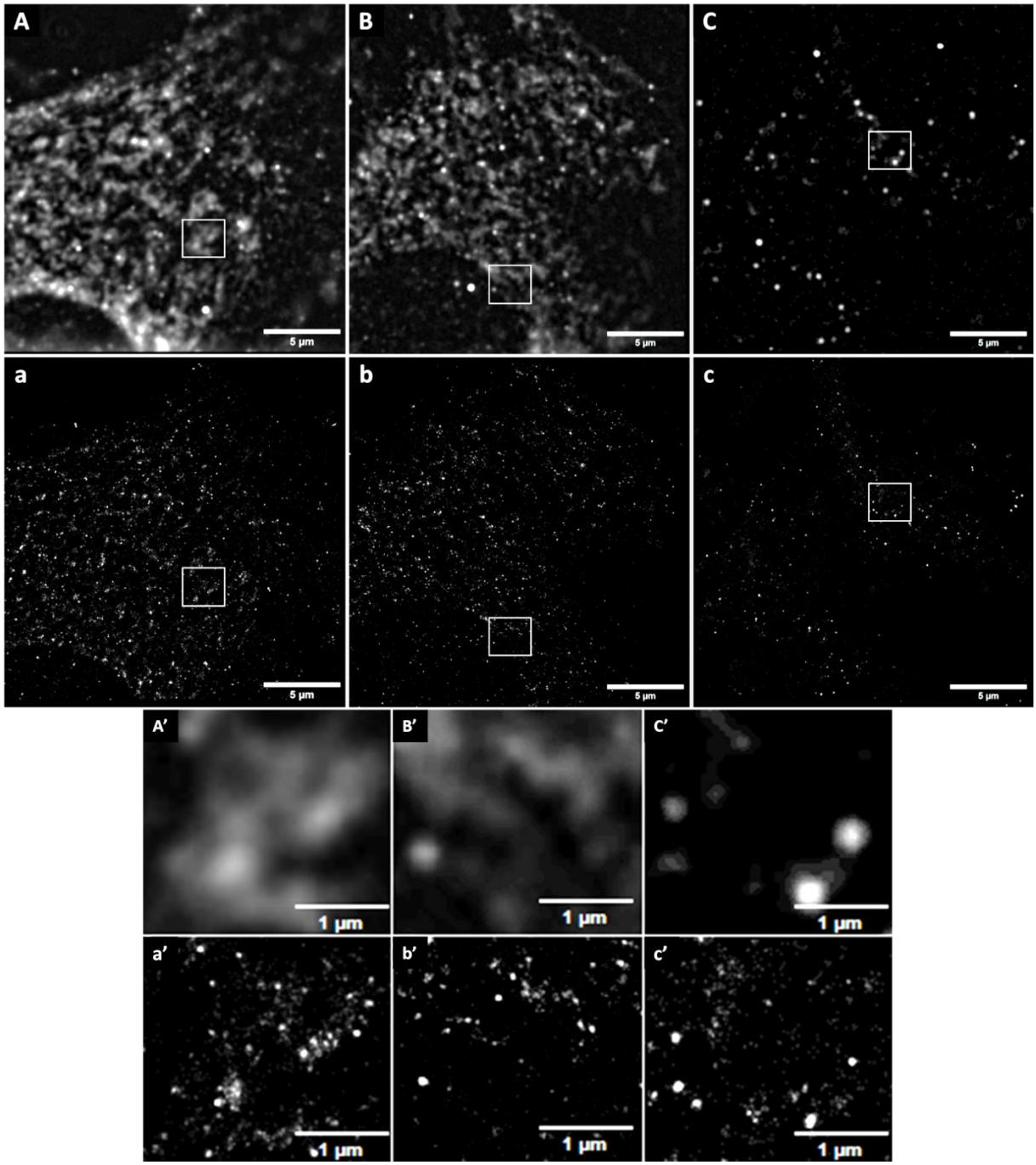

Figure 116: A, B, & C) Diffraction limited images of mPECs labeled ***for EGFR*** *(labeled with CF568) a, b,& c) dSTORM super resolution reconstructed images, squares indicate region of interest enlarged in A', a', B', b', C', & c') A&a) are control cells, B&b) are cells stimulated with 15 ng/ml HB-EGF, C&c) are cells stimulated with 100 ng/ml HB-EGF (pixel = 20 nm, magnification 100X).*

From these images (Figure 116), we can observe first observe qualitatively that EGFR organizes in small clusters (or nanodomains), typically much smaller than the diffraction limit 200 nm, and that the cluster number seems to decrease with HB-EGF stimulation of mPECs. We quantified this effect by analyzing the cluster size, the molecule density inside clusters, and overall cluster cell density from the localization files.

This quantitative analysis of clusters is performed using both the H-Function obtained from

the K-Ripley clustering (Ripley, 1977) analysis methods and a density based approach called DBSCAN (Ester et al., 1996) implemented in the SR-tesseler software (Levet et al., 2015). Both approaches are complementary and give different information. The H-Function determines if a clustering tendency is observed, and will help to determine the radius of aggregation of the whole spatial distribution of points (Kiskowski et al., 2009), hence allowing to obtain an approximation of the cluster diameter. And the DBSCAN will give the number of clusters, their size, and density of molecules distributions.

To obtain the H-Function, the K-Ripley index was calculated, with an increasing step radius of 10 nm, over a 200 nm range, for each obtained dSTORM localization file. The curves obtained for each cell are then normalized and averaged to obtain Figure 117, (top). The maximum value of the H-function approximates the radius of the clusters in the distribution, (Figure 117, bottom).

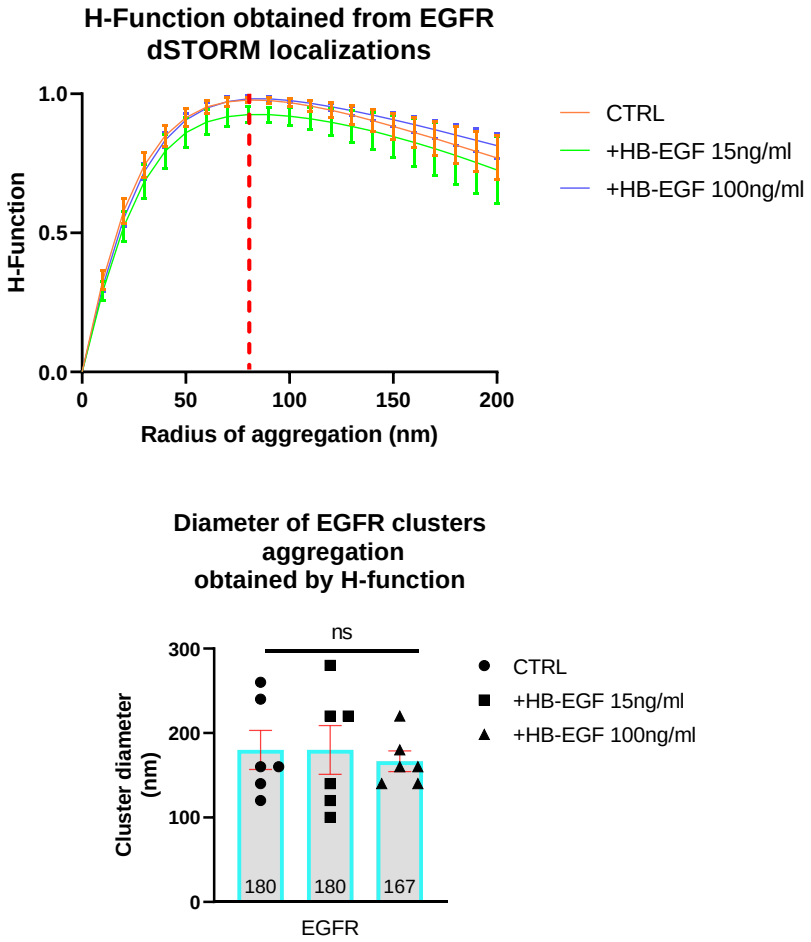

Figure 117: Top) H-Function averaged per experimental condition, Bottom) The aggregation radius leading to the maximum H-function value yields a close approximation of the actual radius of the cluster in the distributions (error bars are SEM).

A radius of maximal aggregation was found for the EGFR spatial distribution indicating first that a clustering tendency of the molecules was detected. The maximum of the H-function yields a cluster diameter in the distribution of around 175 nm (below the diffraction limit for this fluorophore 200 nm). The absence of significant variations in cluster size can be noticed, though a slight decrease in EGFR cluster diameter is observed when stimulating with 100 ng/ml HB-EGF.

To more precisely quantify the cluster properties, we employed a DBSCAN (Density-Based Spatial Clustering of Applications with Noise) algorithm on the data. To run the algorithm we chose a minimal number of localizations per cluster of 30, with a radius search ε of 50 nm. This ensures that identified clusters, within a 100 nm diameter search area, have at least one order of magnitude higher localization density than the average localization density per cell area (~30 molecules per μm^2).

Figure 118 shows examples of identified clusters in the previous dSTORM images. From these images we can observe that their size is indeed below the diffraction limit, and that their number seems to decrease with HB-EGF stimulations.

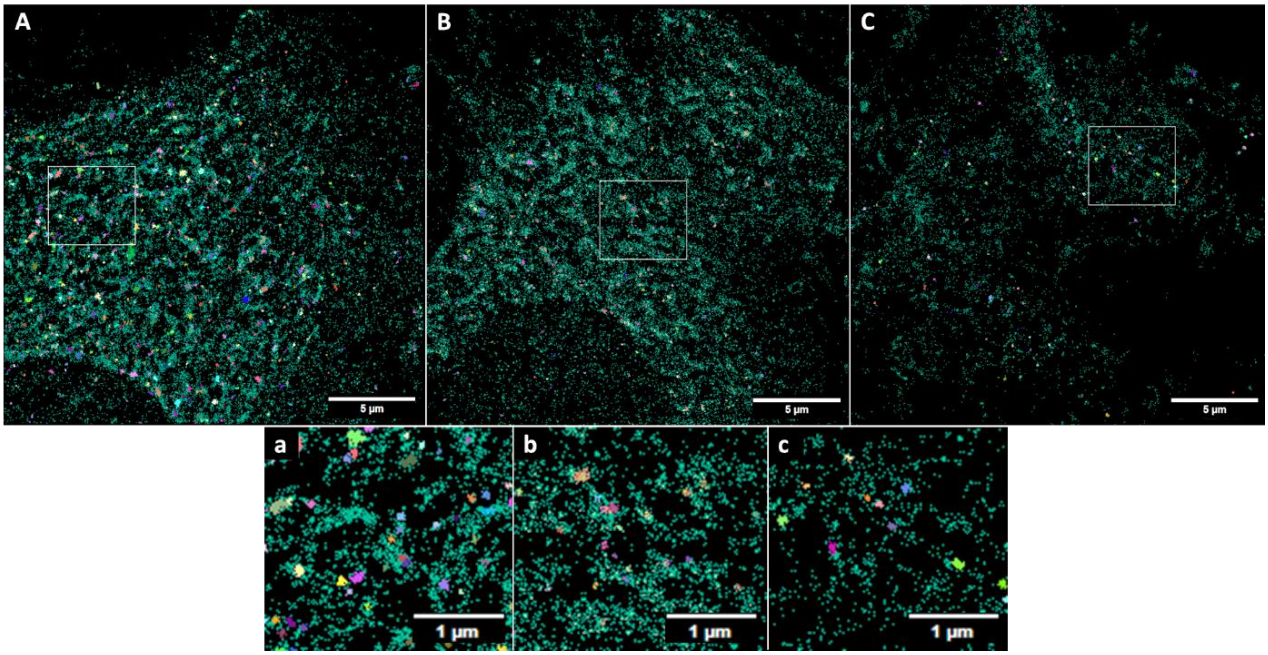

*Figure 118: A, B, & C) dSTORM super resolution reconstructed images of mPECs labeled for **EGFR** (labeled with CF568) processed with DBSCAN (each localization is shown as a green spot while each detected cluster is shown as a spot with a different color), squares indicate region of interest enlarged in a, b,& c, A&a) are control cells, B&b) are cells stimulated with 15 ng/ml HB-EGF, C&c) are cells stimulated with 100 ng/ml HB-EGF (pixel = 20 nm, magnification 100X).*

We then quantified the cluster number, size distribution, and molecule (or localization) density (Figure 119). We observe that the mean membrane density of EGFR clusters decreases significantly for a stimulation with 100 ng/ml of HB-EGF, confirming the visual observation of less clusters being present after stimulation.

The cluster mean diameter, and localization count per cluster decreased with both 15 and 100 ng/ml HB-EGF stimulations. While the cluster mean diameter decreased significantly for a 15 ng/ml stimulation, the cluster mean area however only decreases significantly for a 100 ng/ml HB-EGF stimulation.

While the count number per cluster decreases, the EGFR cluster density increases. This implies that EGFR are more tightly packed inside clusters after a 100 ng/ml HB-EGF stimulation.

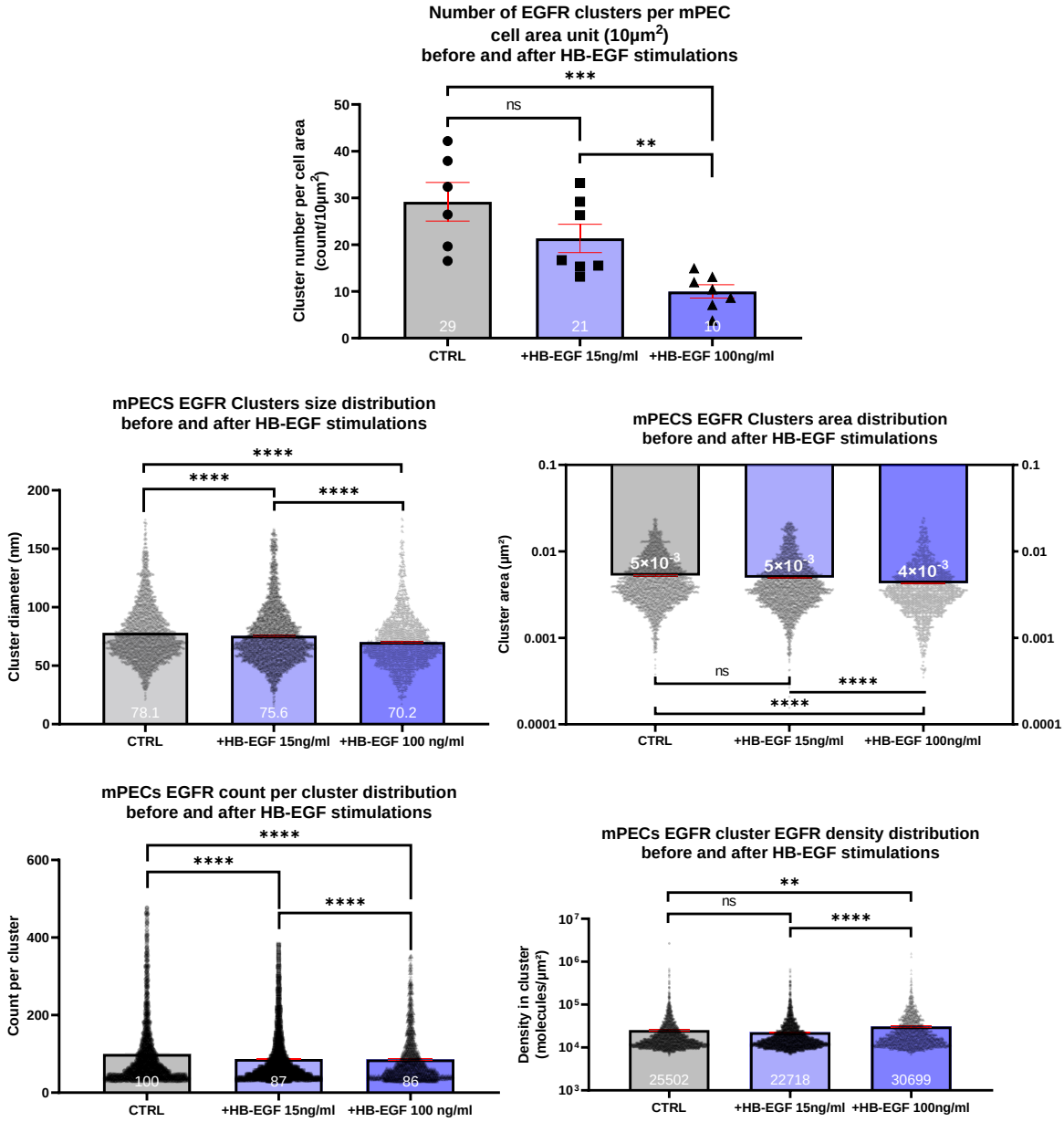

*Figure 119: Top, **EGFR** cluster number per cell area (per 10 µm²) evolution in mPECs after cells are stimulated with 15 or 100 ng/ml HB-EGF, middle left, evolution of cluster diameter, middle right, evolution of cluster area, bottom left, evolution of EGFR count per cluster, bottom right, evolution of EGFR density inside clusters, (error bars are SEM, stars from significative t-test).*

The overall EGFR clusters response to HB-EGF leads to a decrease in cluster number, diameter, and area with EGFR molecules packing more tightly in clusters for a stimulation with 100 ng/ml. Upon activation, EGFR receptors dimerize and are recycled through internalization (Madshus & Stang, 2009), which may explain the global EGFR count diminution.

Moreover, the increase in EGFR cluster density and the nanodomains size variation may suggest two hypothesis: either HB-EGF stimulation induces a EGFR nanodomains modulation (*e.g.* receptor packing), or the remaining receptors are relocating to a different type of membrane

nanodomains upon stimulation.

3.1.5.3 CD9 and HB-EGF role on clustering and density in mPECs

The same analysis was performed for CD9 dSTORM images. Figure 120 shows that the CD9 cluster size is also below the diffraction limit, and clusters (or nanodomains) are evenly distributed at the cell surface. The stimulation with HB-EGF also seems to have an effect on the cluster number per cell.

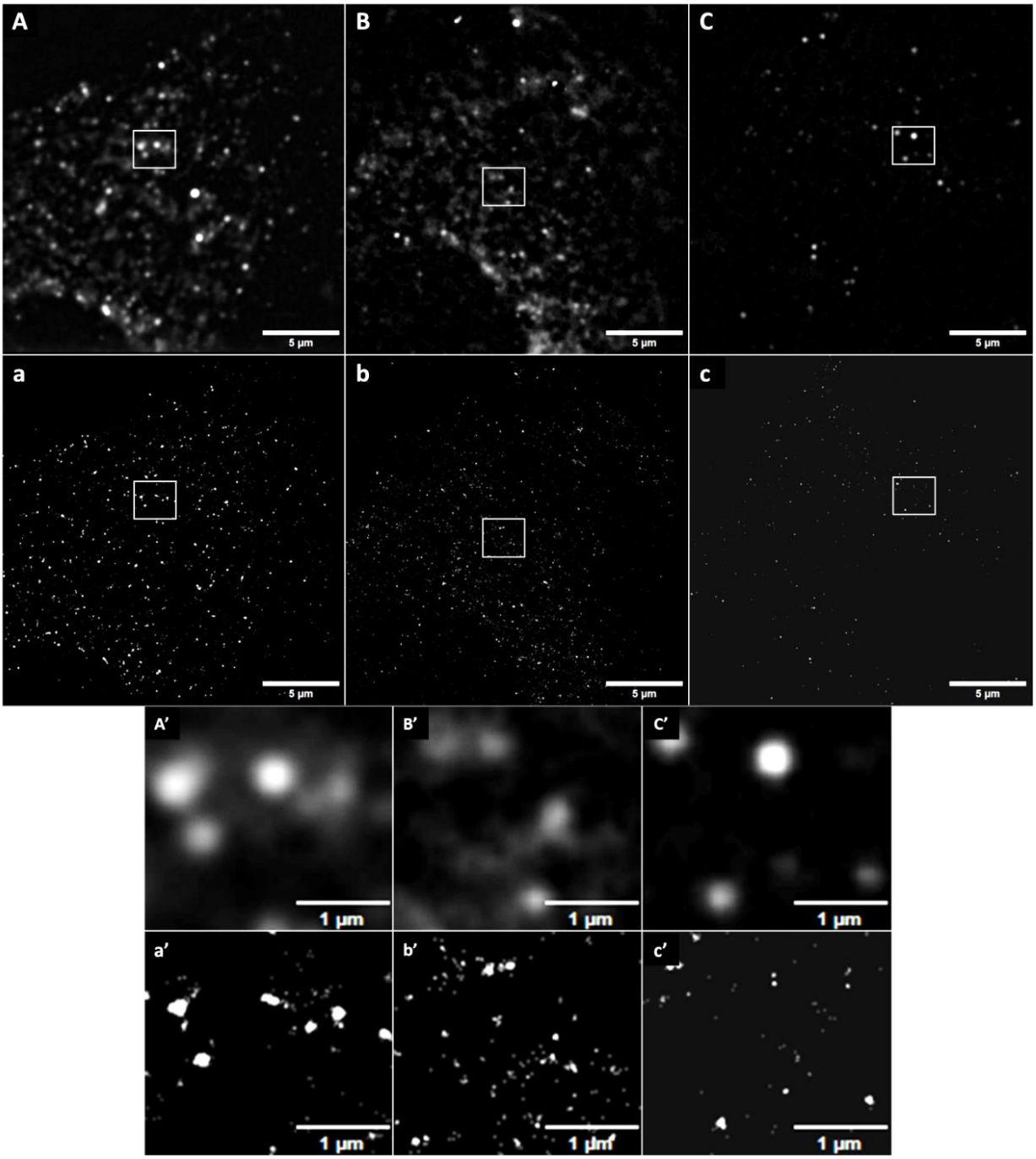

*Figure 120: A, B, & C) Diffraction limited images of mPECs labeled for **CD9** (labeled with Dylight 650) a, b,& c) dSTORM super resolution reconstructed images, squares indicate region of interest enlarged in A', a', B', b', C', & c') A&a) are control cells, B&b) are cells stimulated with 15 ng/ml HB-EGF, C&c) are cells stimulated with 100 ng/ml HB-EGF (pixel = 20 nm, magnification 100X).*

The H-function quantification (Figure 121) yields a radius of aggregation for the CD9 spatial distribution, with a cluster diameter of around 190 nm (which is indeed below the diffraction limit for this fluorophore 230 nm). This diameter is comparable to EGFR domains diameter.

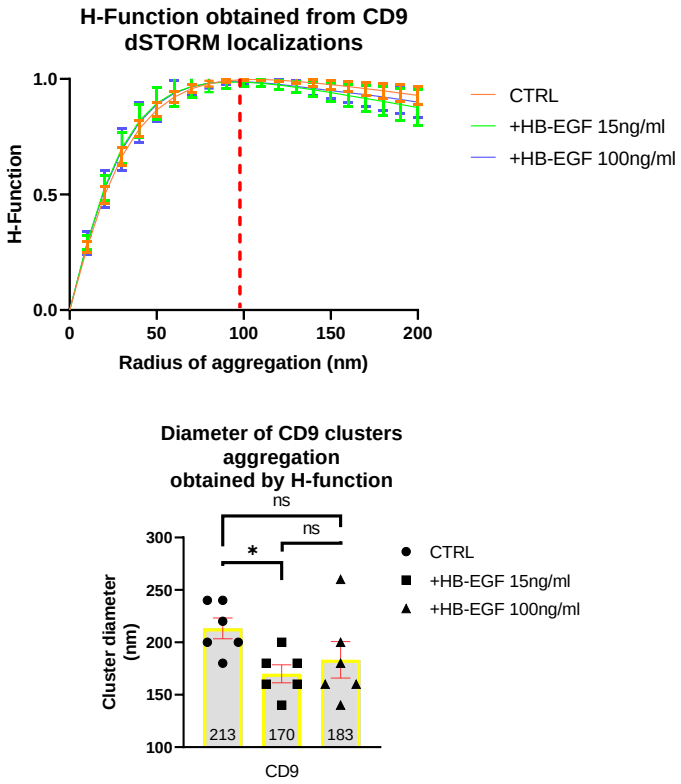

Figure 121: Top) H-Function averaged per experimental condition, Bottom) The aggregation radius leading to the maximum H-function value yields a close approximation of the actual radius of the cluster in the distributions, (error bars are SEM, star from t-test).

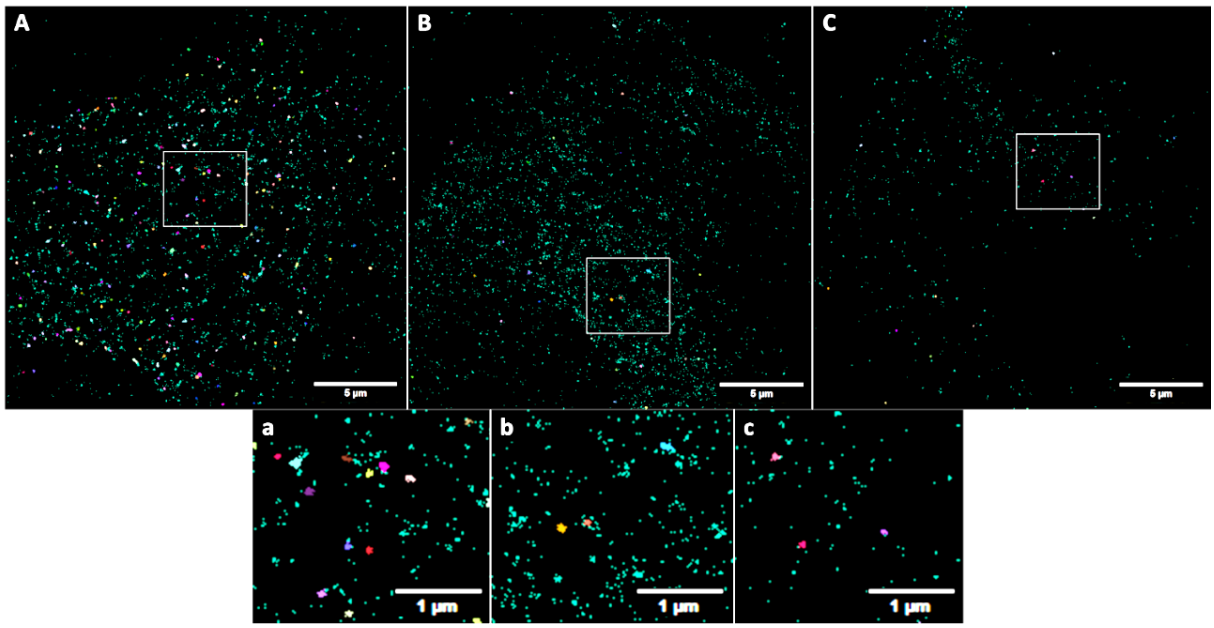

*Figure 122: A, B, & C) dSTORM super resolution reconstructed images of mPECs labeled for **CD9** (labeled with Dylight 650) processed with DBSCAN (each localization is shown as a green spot while each detected cluster is shown as a spot with a different color), squares indicate region of interest enlarged in a, b,& c, A&a) are control cells, B&b) are cells stimulated with 15 ng/ml HB-EGF, C&c) are cells stimulated with 100 ng/ml HB-EGF (pixel = 20 nm, magnification 100X).*

The DBSCAN algorithm was successful in identifying CD9 clusters as well (*Figure 122*). From this figure we observe qualitatively a decrease in CD9 cluster density when stimulating with HB-EGF.

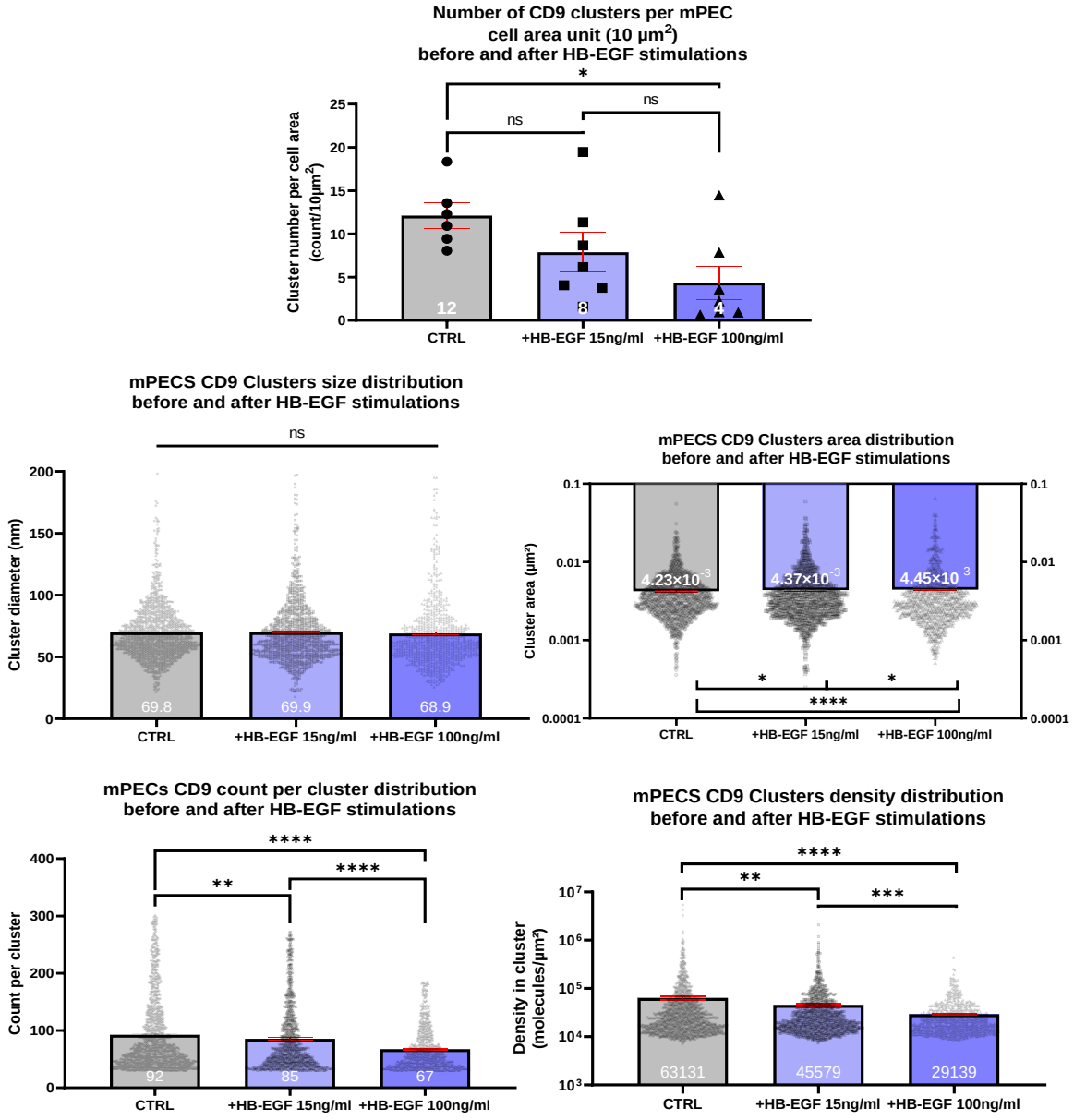

*Figure 123: Top, **CD9** cluster number per cell area (per 10 µm²) evolution in mPECs after cells are stimulated with 15 or 100 ng/ml HB-EGF, middle left, evolution of cluster diameter, middle right, evolution of cluster area, bottom left, evolution of CD9 count per cluster, bottom right, evolution of CD9 density inside clusters (error bars are SEM, stars from t-test).*

Quantifying further the cluster number, size distribution, and molecule (or localization) density by DBSCAN gave the graphs in Figure 123. From these charts, it is evident that cluster density drops significantly when the cells are stimulated with 100 ng/ml of HB-EGF. The number of molecules within each cluster and the density of CD9 inside clusters also decreases in response to both 15 and 100 ng/ml HB-EGF stimulations.

The CD9 cluster diameter does not change significatively despite HB-EGF stimulations indicating that TEMs remain stable under stimulation. However the decrease in both cluster density and number indicates a possible internalization of total nanodomains unpon HB-EGF stimulation.

We characterized EGFR and CD9 clusters based on dSTORM localization files after HB-EGF stimulations. We observed that both EGFR and CD9 cluster numbers are reduced when stimulated with 100 ng/ml of HB-EGF, and their number within each cluster also declines with HB-EGF stimulations at both 15 and 100 ng/ml concentrations.

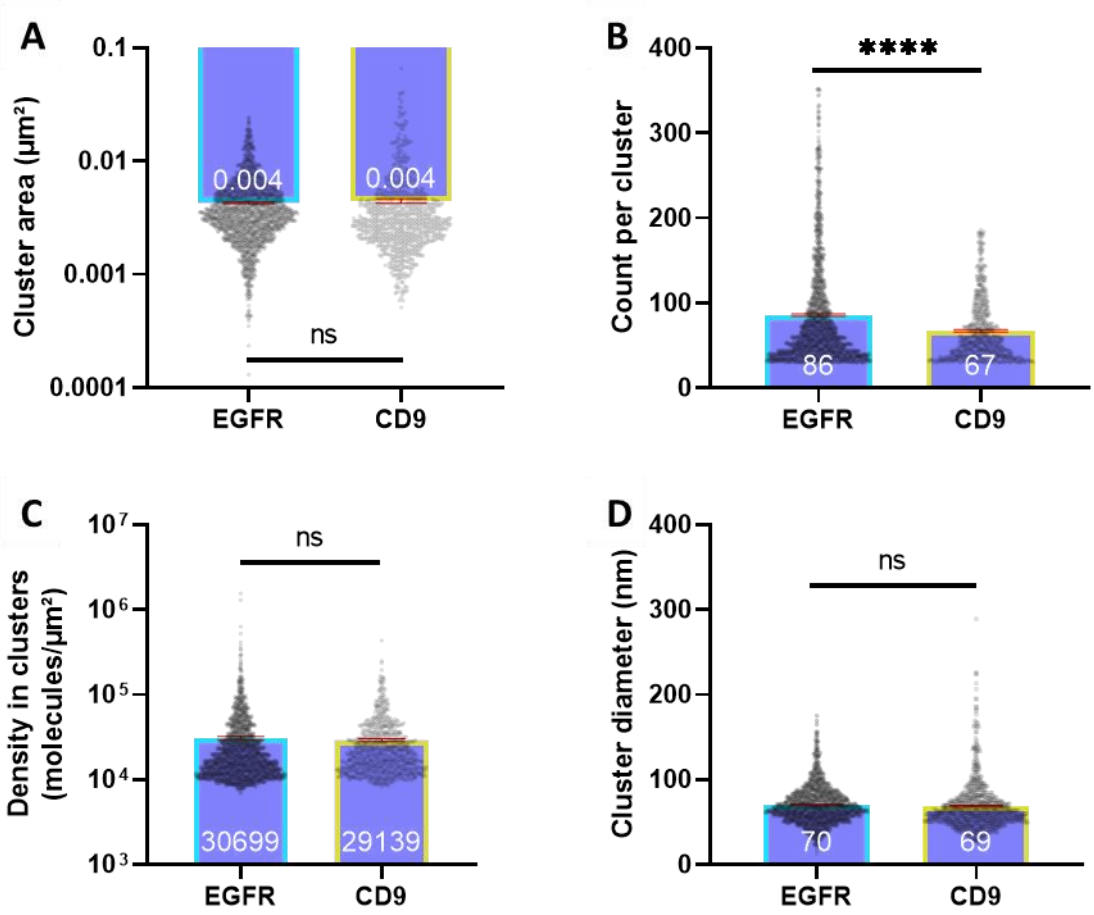

Figure 124: Distribution of EGFR and CD9 A) cluster area, B) count per cluster, C) Density inside clusters, D) cluster diameter in mPECs after ***100 ng/ml HB-EGF*** *stimulations for 20 min (n=7, 1701 EGFR and 782 CD9 clusters analyzed,* error bars are SEM, *stars from t-test).*

After a 100 ng/ml HB-EGF stimulation, EGFR and CD9 cluster nanodomain size and molecule density are compared in Figure 124. The cluster area, diameter and molecular density were similar. This suggests that EGFR and CD9 nanodomains could be shared. To verify this assumption we quantified the effect of HB-EGF on CD9 and EGFR co-localization.

3.1.5.4 HB-EGF role on CD9 and EGFR localization in mPECs

We performed 2-color dSTORM simultaneous acquisition of both EGFR and CD9, in order to probe their localization with respect to each other. From the 2-color diffraction limited images (Figure 125), we can clearly observe an overlap in EGFR and CD9 signal. This overlap seems also to increase with the HB-EGF stimulation, but is not sufficient to conclude on a possible interactions due to the limited resolution.

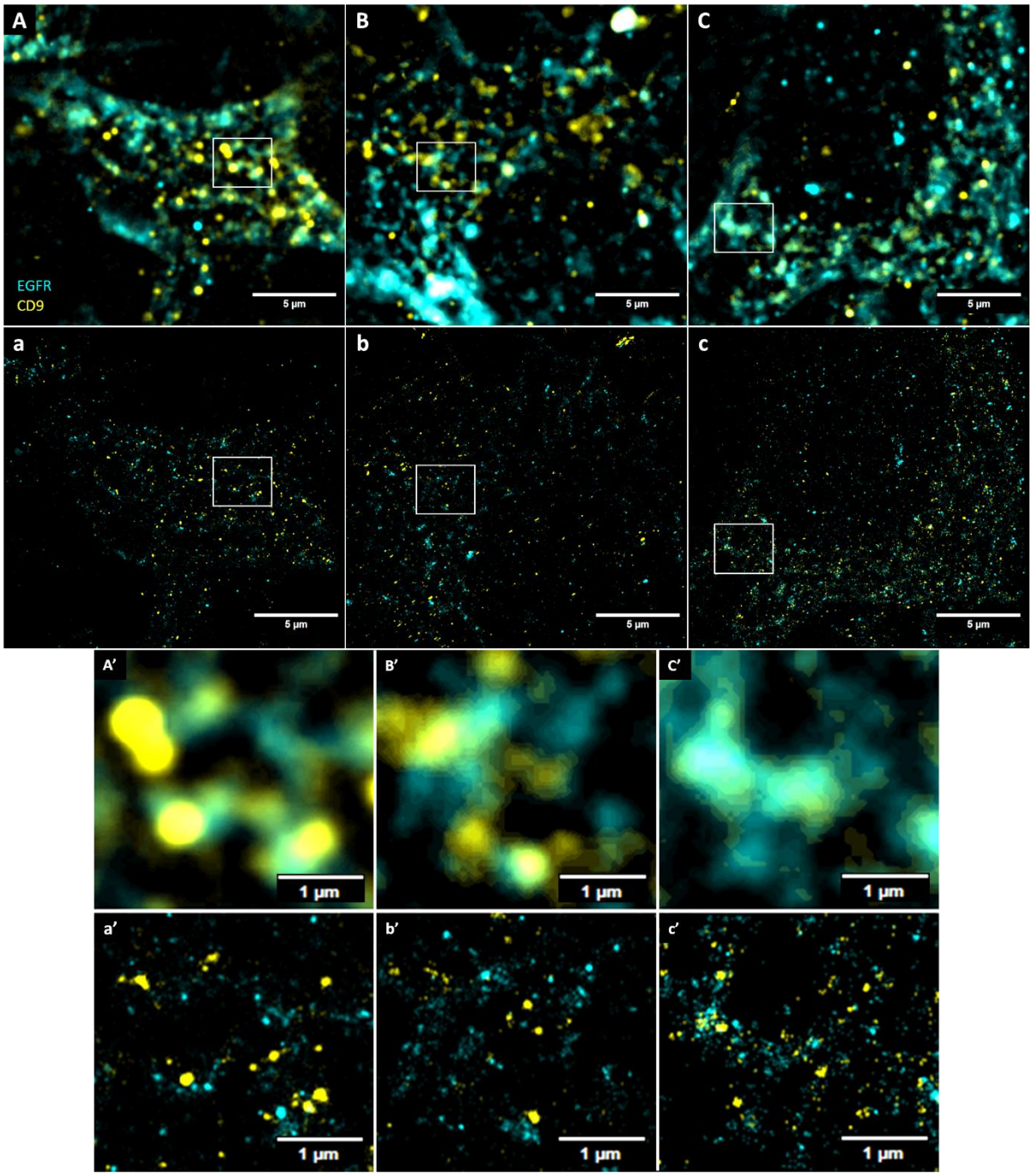

*Figure 125: A, B, & C) 2 color diffraction limited images of mPECs labeled for **EGFR** (Cyan, labeled with CF568) & **CD9** (Yellow, labeled with Dylight 650) a, b,& c) dSTORM super resolution reconstructed images, squares indicate region of interest enlarged in A', a', B', b', C', & c') A&a) are control cells, B&b) are cells stimulated with 15 ng/ml HB-EGF, C&c) are cells stimulated with 100 ng/ml HB-EGF (pixel = 20 nm, magnification 100X).*

The dSTORM images show that previously overlapping signals, from the diffraction limited images, now appear mostly spatially separated (Figure 125), except for a 100 ng/ml HB-EGF stimulation where some overlap between EGFR and CD9 can be qualitatively observed (Figure 125, c').

To study the effect of HB-EGF on CD9 and EGFR localization, we first performed a simple pixel based co-localization analysis from reconstructed dSTORM images. The Pearson correlation

coefficient was computed using the JACoP:V2 plugin in ImageJ (Cordelières & Bolte, 2008) for all images and the results are presented in Figure 126.

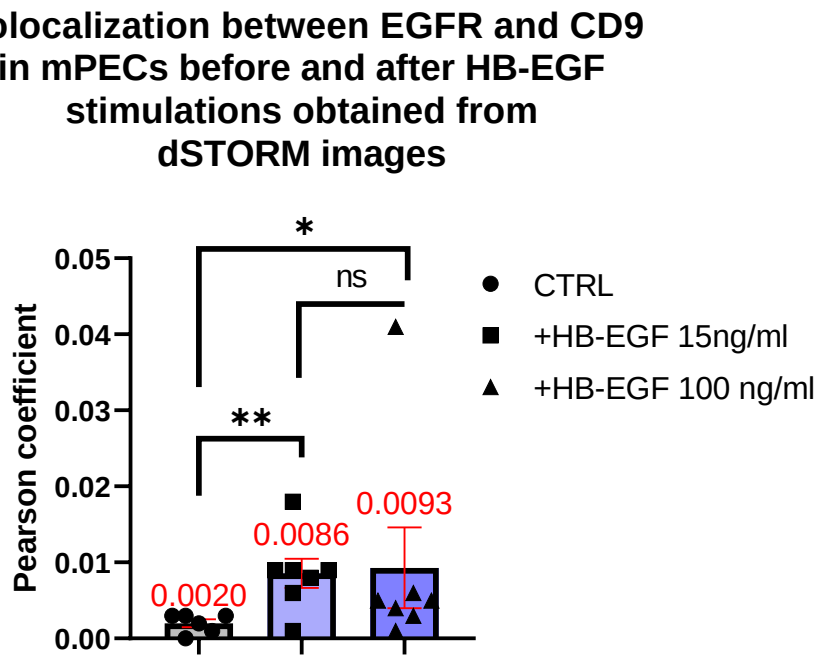

*Figure 126: Evolution of the Pearson colocalization coefficient between **EGFR** and **CD9** from reconstructed 2-color dSTORM images obtained unsig JACoP, in mPECs after cells are stimulated with 15 or 100 ng/ml HB-EGF (error bars are SEM, stars from t-test).*

We observe a significant increase in co-localization for both 15 and 100 ng/ml HB-EGF stimulations. The Pearson coefficient is initially low (0.0020) and increases slightly (up to 0.0093) when the cells are stimulated. While we detected a significant increase in co-localization, the coefficient values remained small (below 0.001 on average) suggesting that few pixels are actually overlapping.

We then analyzed the localizations of EGFR and CD9 which should lead to an artifact free measure of co-localization. This was quantitatively assessed by analyzing the spatial distribution by tessellation followed by a co-localization test implemented in the Coloc-tesseler software (Levet, Julien, Galland, Butler, Beghin, Chazeau, Hoess, et al., 2019). Coloc-Tesseler uses the normalized pair-density metric, derived from the intersecting Voronoi diagrams of two molecular types, to robustly measure their spatial co-organization without relying on density or adjustable parameters. This enables the straightforward calculation of widely-used image-based colocalization metrics like Manders and Spearman's coefficients, directly from the molecular coordinates. This approach has the added benefit of being both parameter-free and resistant to fluctuations in molecular density. An example of Voronoi tessellation for CD9 and EGFR is shown in Figure 127.

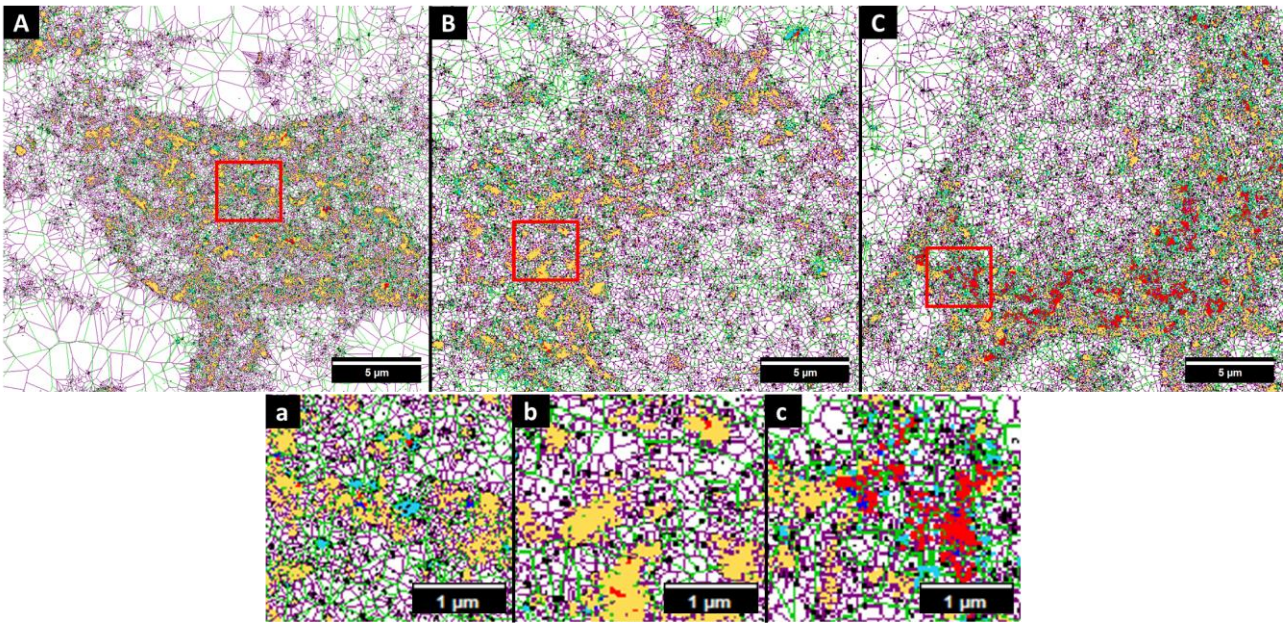

*Figure 127: A, B, & C) 2 color dSTORM super resolution reconstructed images of mPECs labeled for **EGFR** (Magenta, labeled with CF568) & **CD9** (Green, labeled with Dylight 650) processed with Voronoï tessellation (overlapping clusters are red, isolated clusters are blue, close clusters are yellow), red squares indicate region of interest enlarged in a, b,& c, A&a) are control cells, B&b) are cells stimulated with 15 ng/ml HB-EGF, C&c) are cells stimulated with 100 ng/ml HB-EGF (pixel = 20 nm, magnification 100X).*

From the tessellation co-localization analysis we obtain the Spearman's rank correlation coefficient and Manders coefficient.

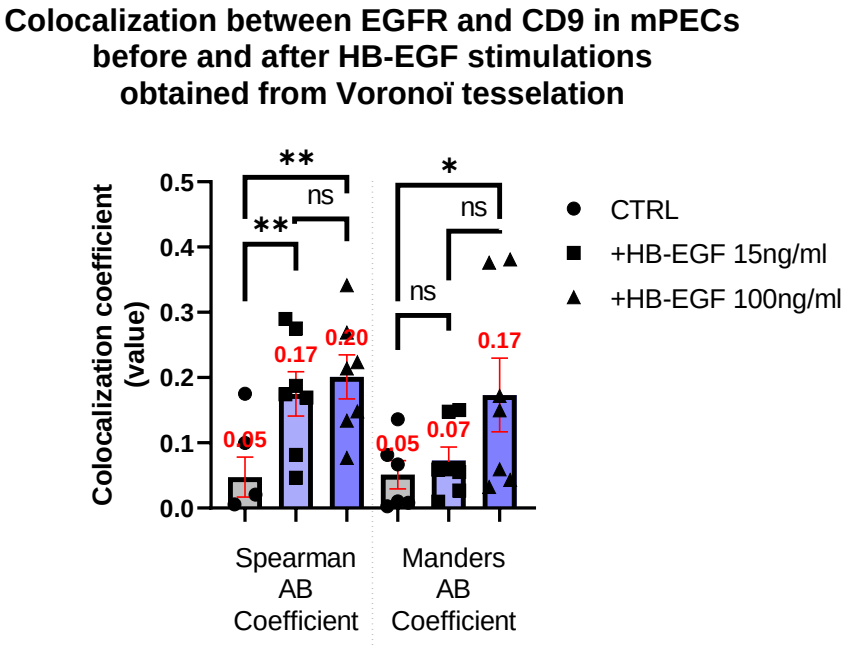

Figure 128: Evolution of the colocalization coefficient (Spearman and Manders coefficient) from Voronoï tesselation of both EGFR and CD9 clusters obtained using coloc-tesseler (Levet et al., 2019) in mPECs after cells are stimulated with 15 or 100 ng/ml HB-EGF (error bars are SEM, stars from t-test).

We can observe that the Spearman coefficient increases significantly for both 15 and 100 ng/ml HB-EGF stimulations, going from 0.05 to ~0.2 after stimulation. The Manders coefficient increases significantly for 100 ng/ml HB-EGF stimulations, going from 0.05 to 0.17 (Figure 128).

Upon stimulation with HB-EGF, there is an increased co-localization between EGFR and CD9 in mPECs. Furthermore, after stimulation the size and molecular density of both domains are identical. This suggest that EGFR translocate within the CD9 rich nanodomains upon HB-EGF stimulation. When EGFR are stimulated, they are activated and are recycled through endocytosis (Madshus & Stang, 2009), thus explaining EGFR total count decrease. We can hypothesize that since CD9 and EGFR share membrane domains, CD9 is at least partially internalized during this process, leading to the total CD9 count decrease after stimulation. The fact that EGFR domains are larger in CD9-KO mPECs (Hoang, 2022), and our findings showing that EGFR translocate to CD9 nanodomains suggest that CD9 plays an important role in EGFR activation and signaling. The link between the regulation of EGFR domains by CD9, and EGFR signaling is investigated in the next section.

3.2 ROS production induced by HB-EGF and PDGF-BB stimulations in mPECs

In order to probe EGFR downstream signaling and the possible functional role of CD9, we measured Reactive Oxygen Species (ROS) levels in mPECs and CD9-KO mPECs. ROS is a secondary messenger of EGFR (Bae et al., 1997; DeYulia et al., 2005; Jaenen et al., 2021; Rhee, 2006), and of PDGFR (Abdesselem et al., 2017; Bouzigues et al., 2014; K. C.-W. Chen et al., 2007) either through ligand interaction or receptor transactivation. We thus hypothesize that ROS signaling plays a central role in crescent glomerulonephritis and in PEC activation, and that ROS concentration monitoring is a good indicator of cell response.

Measuring ROS signaling levels in cells quantitatively is however complex. Many fluorescent probes (Lippert et al., 2011; X. Wang et al., 2013a) or fluorescent proteins (Belousov et al., 2006; Enyedi et al., 2013; Erard et al., 2018; Meyer & Dick, 2010) have been engineered but do not allow to monitor quantitatively the ROS signaling levels in cells at good spatio-temporal resolution.

To that end, we used Europium doped nanoparticles luminescence imaging to follow quantitatively the H_2O_2 levels produced by NADPH oxidase (NOX) transactivation after HB-EGF and PDGF-BB stimulations in mPECs.

3.2.1 Reactive Oxygen Species

Oxidative stress and more generally the oxidative response is essential in physiological processes (Erard et al., 2018). This has justified an interest for redox processes and the development of methods of observation.

The molecules primarily responsible for oxidation are identified as Reactive Oxygen Species (ROS), Reactive Nitrogen Species (RNS), and Reactive Sulfur Species (RSS) (Uusitalo & Hempel, 2012). ROS are assumed to play a major in signaling (Rhee, 2006).

3.2.1.1 ROS types

ROS are transient molecules, including types like superoxide ($O_2^{\cdot-}$), hydrogen peroxide (H_2O_2), hydroxyl radical ($HO^{\cdot}$), as well as peroxynitrite ($ONOO^-$) and hypochlorous acid (HOCl). They can be generated in multiple ways, such as by-products of cellular metabolism or by enzymes like NADPH oxidases (NOXs) (Figure 129) (Rhee, 2006). NADPH oxidases in humans are categorized into seven types, with the first known being phagocytic NADPH oxidase, which has two transmembrane subunits, NOX2 ($gp91^{phox}$) and $p22^{phox}$, and four cytosolic partners ($p67^{phox}$, $p47^{phox}$, $p40^{phox}$, and Rac) which are recruited to the membrane when the NOX is activated (Bedard & Krause, 2007).

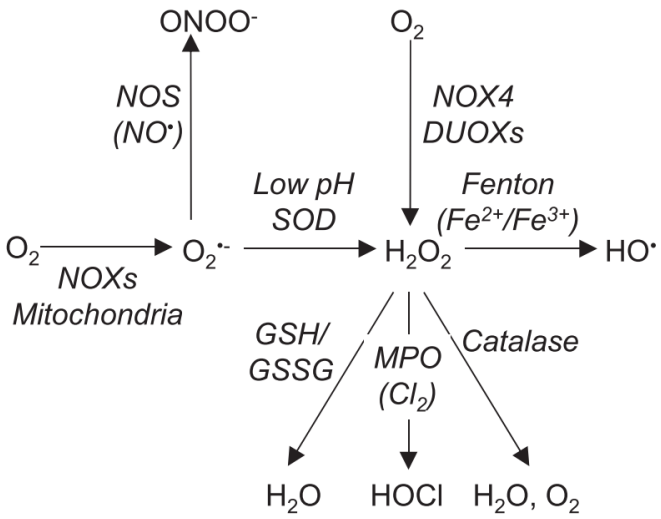

Figure 129: Key pathways for the production and reactions of reactive oxygen species (ROS). GSH (Glutathione) is a tripeptide made up of cysteine, glycine, and glutamate, and a primary antioxidant in cells, neutralizing free radicals. When oxidized, two GSH molecules form GSSG. NOX refers to NADPH oxidase. Catalase is a heme-containing oxidoreductase that catalyzes the dismutation of hydrogen peroxide into water and oxygen. Superoxide dismutases (SOD) are metalloproteins that are also oxidoreductases catalyzing the dismutation of superoxide anion ($O_2^{\cdot-}$), into oxygen O_2 and hydrogen peroxide H_2O_2. The Fenton reaction generates $HO^{\cdot}$ from H_2O_2 in the presence of Fe^{2+} cations, image from (Erard et al., 2018).

The superoxide anion ($O_2^{\cdot-}$), is a mild oxidant with limited ability to permeate membranes. It rapidly converts to hydrogen peroxide (H_2O_2) or peroxinitrite ($ONOO^-$) when nitrogen monoxide ($NO^{\cdot}$) is present. H_2O_2, which can move across membranes (Bienert et al., 2006) and travel away from its production site, participates in various oxidative reactions involving thiols, peroxidases like myeloperoxidase (MPO), and iron ions (Erard et al., 2018). Both $ONOO^-$ and $HO^{\cdot}$ are highly reactive, short-lived species capable of oxidizing a wide array of molecules. Meanwhile, the nonradical HOCl, a potent oxidant, can interact with thiols, amines, and unsaturated bonds in general (Erard et al., 2018).

Other sources of ROS includes peroxisomes and several enzymes like nitric oxide synthases, xanthine oxidase, cyclooxygenases, cytochrome p450 enzymes, the redox enzyme p66Shc, and lipoxygenases. Additionally, oxidants are formed in the endoplasmic reticulum (ER) during oxidative protein folding (Erard et al., 2018). ROS homeostasis is essential for cell response, signaling,…

To regulate ROS, cells use various detoxifying methods, involving both non-enzymatic components like flavonoids and glutathione, and enzymatic antioxidants such as superoxide dismutase and catalase. The genes for these enzymes are controlled by nuclear factor erythroid 2-related factor (NRF2), which is itself regulated by the ROS level in cells (X. Wang et al., 2013b). Catalases, glutathione peroxidases, and peroxiredoxins catalyze the decomposition of H_2O_2. Glutathione peroxidases turn free H_2O_2 into water using reduced glutathione (GSH) as the reducing agent. The process forms glutathione disulfide (GSSG), which is then converted back to GSH by glutathione reductases with the help of NADPH. Glutathione, being the primary nonprotein thiol in most cells, plays a crucial role in maintaining the intracellular redox balance (X. Wang et al., 2013b).

3.2.1.2 H_2O_2 role in signaling

While ROS are often associated with cellular damage, they also play crucial roles in signaling pathways. Low concentrations of hydrogen peroxide (H_2O_2) mediate numerous signaling processes in the cell (Rhee, 2006).

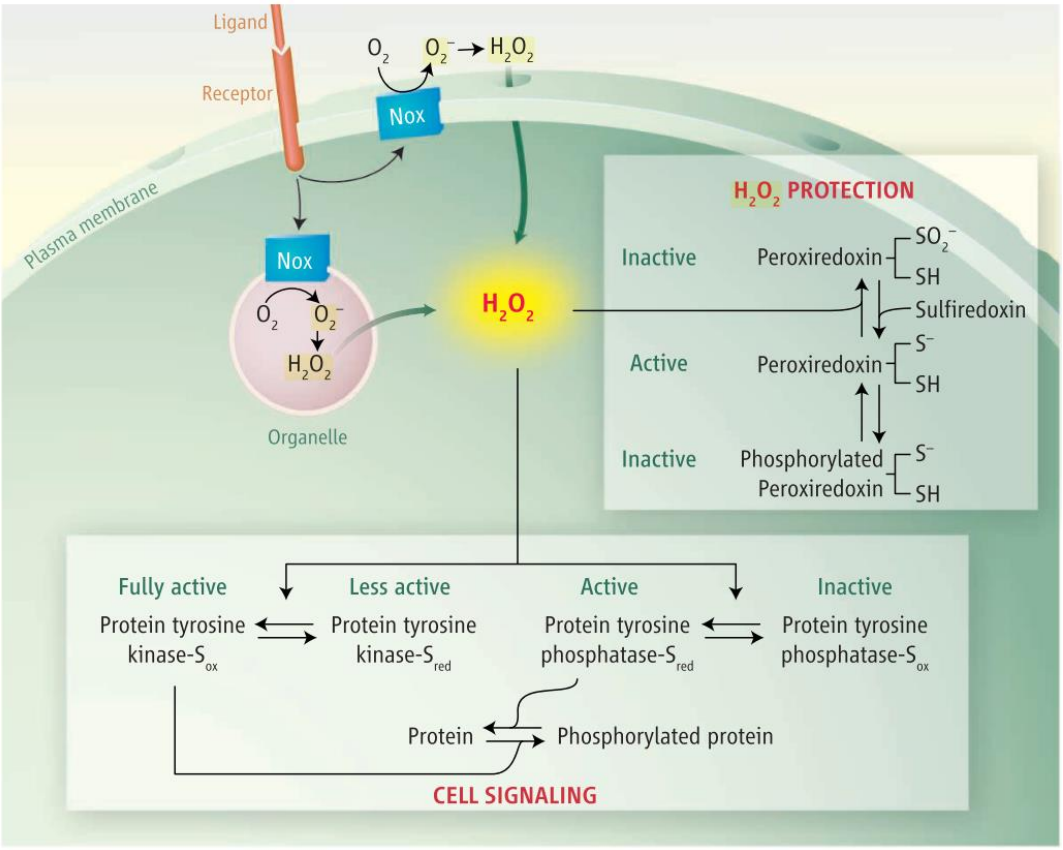

Figure 130: Activation of specific cell surface receptors stimulates NOXs, located in the plasma membrane or organellar membranes like endosomes, leading to H_2O_2 production. For H_2O_2 to serve as an intracellular signaling agent, it needs to be transported into the cytosol. Once in the cytosol, H_2O_2 promotes protein tyrosine phosphorylation by deactivating protein tyrosine phosphatases and activating protein tyrosine kinases. The transient protection of the H_2O_2 signal against abundant cytosolic peroxiredoxin seems to arise from the temporary inactivation of these enzymes, either through hyperoxidation or phosphorylation, image from (Rhee, 2006).

In vivo, ROS can inhibit some key phosphatases like the ones belonging to the protein tyrosine phosphatase family (PTP). For example, PTP1B, which inactivates both EGFR and PDGFR, is inactivated by H_2O_2 (J. Zhang et al., 2016).

Additionally, ROS can influence cell signaling either by directly oxidizing molecules such as Src, or by affecting the interactions between signaling and antioxidant proteins. An imbalance in ROS levels can disrupt normal cell functions; elevated ROS levels can oxidize lipids, proteins, and DNA, leading to cellular damage. To keep ROS levels within a safe range, cells utilize detoxification methods involving nonenzymatic elements (like flavonoids or glutathione) and antioxidant enzymes including superoxide dismutase, catalase, peroxiredoxin, and thioredoxin (Rhee, 2006; J. Zhang et al., 2016).

ROS can influence the function of proteins by modifying their thiol groups. This can change protein conformation, and thereby its activity, leading to alterations in downstream signaling (Rhee, 2006).

To truly grasp redox dynamics, and cell ROS dependent response, it is thus crucial to understand their spatial regulation, distribution, and compartmentalization within cells.

3.2.2 Probes for H_2O_2 detection

The specificity and sensitivity of ROS detection is essential. The existence of quantitative, dynamic, and local ROS sensors is thus crucial for this objective. Several methods and probes have been developed to detect and quantify ROS, and are presented in this section.

The ideal probe should be highly sensitive to relevant fluctuations in redox species levels and specific to a distinct molecule, such as H_2O_2. It should display a broad dynamic range and kinetics that match the redox signal's timeline, and exhibit reversibility. The probe should also offer subcellular precision in mapping redox signaling. Quantitative or semi-quantitative (ratiometric) capabilities are preferable. It should remain unaffected by environmental factors like pH changes and be expressible or addressable in living organisms, while ensuring it does not disrupt the biological system under observation.

The dynamics of ROS production moreover spans over several scales. For instance, a phagocyte NADPH oxidase activates rapidly and functions briefly (Tlili et al., 2011), while conditions like inflammatory disease can persist for years with ongoing redox imbalances (Federico et al., 2007).

3.2.2.1 Organic probes for H_2O_2 detection

Soluble synthetic probes tailored for H_2O_2 detection are commonly used fluorescent markers for in cells. For instance, dihydrodichlorofluorescein ($DCFH_2$), dihydrorhodamine (DHR), Amplex red assay, and Boronate based probes are used (Erard et al., 2018; Lippert et al., 2011; Walrand et al., 2003). All of these are irreversible dyes that activate upon oxidation.

Dihydrodichlorofluorescein diacetate $DCFH_2$-DA, $DCFH_2$-SE, the amine-reactive succinimidyl-ester of $DCFH_2$ (Tlili et al., 2011), $DCFH_2$, and DCF share structural similarities with other fluorescent markers like fluorescein and dihydrorhodamine (DHR) (X. Chen et al., 2010). Initially, both $DCFH_2$-DA/-SE and $DCFH_2$ are non-fluorescent, but when excited, DCF (which is yellow) intensely fluoresces, with an excitation wavelength of roughly 485–500 nm and an emission wavelength of about 515–530 nm (Tlili et al., 2011). Inside cells, the non-fluorescent and fat-soluble $DCFH_2$-DA enters and traverses the cellular barrier. When acted upon by internal cell esterases, $DCFH_2$-DA is deacetylated to form $DCFH_2$. This transformed version remains non-fluorescent but can no longer cross the cell membrane. $DCFH_2$ then interacts with internal ROS to produce the glowing DCF molecule (X. Chen et al., 2010).

DHR can penetrate the cell membrane, and upon oxidation by ROS, it transforms into rhodamine 123 (RHO) which emits a strong red fluorescent signal. Since RHO binds to cell membranes, this fluorescence is contained within the cell (Ribou, 2016).

$DCFH_2$, and DHR are currently recognized as fluorescent markers to identify respiratory burst activities. Walrand et al. (Walrand et al., 2003) found that when PolyMorphonuclear Neutrophils

(PMNs) are activated, $DCFH_2$ (5µM) & DHR (1µM), displayed a similar rise in fluorescence intensity.

The Amplex Red assay operates on the enzymatic transformation of the non-fluorescent, colorless substance AmR through a radical intermediary. In the presence of horseradish peroxidase, AmR interacts with H_2O_2, producing the stable, colored, and fluorescent compound, resorufin. AmR doesn't enter cells, so it measures H_2O_2 outside of them (Erard et al., 2018).

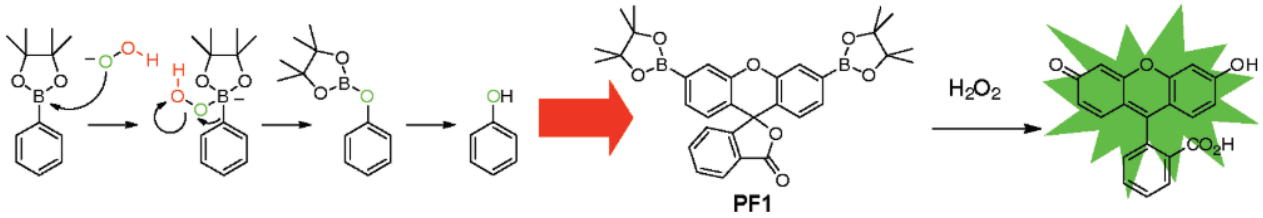

Figure 131: Example of first-generation H_2O_2 probe, Boronate-masked fluorescein peroxyfluor 1 (PF1), utilizes boronates to push the molecule into a non-absorbing, non-emitting closed lactone form in the visible spectrum. Upon reacting with H_2O_2, the boronates change to phenols, causing the lactone to open. This transformation leads to an over 1000-fold enhancement in fluorescence as the molecule shifts to the brightly fluorescent green fluorescein product, image from (Lippert et al., 2011).

Bio-orthogonal reactions (Figure 131), along with various reaction-based molecular probes, are commonly employed for the alteration and identification of biological molecules and mechanisms. Numerous "turn-on" probes were crafted based on H_2O_2 capacity to convert aryl boronates to phenols. A vast assortment of fluorogenic and luminescent molecules were developed to detect H_2O_2 *via* boronate oxidation. Notably, these reactions show a preference for H_2O_2 over other ROS (Lippert et al., 2011).

However these organic probes are neither dynamic nor quantitative *in situ*, and several other approaches aim at bypassing these issues.

3.2.2.2 Fluorescent proteins

Fluorescent protein sensors have been developed to study ROS in living cells and organisms (Erard et al., 2018; Meyer & Dick, 2010; Pouvreau, 2014). Among these, H_2O_2-sensitive green fluorescent proteins (roGFP family) (Gutscher et al., 2009), HyPer family (Belousov et al., 2006), and the FRET based sensors OxyFRET and PerFRET (Enyedi et al., 2013) have been employed in various cells and *in vivo*.

The detection of H_2O_2 in yeast is based on the collaborative effects of two redox proteins: the oxidant receptor 1 (Orp1) and yeast activator protein 1 (Yap1). Together, they create a redox relay system in which the transcription factor Yap1 undergoes oxidation by the peroxidase Orp1 when H_2O_2 is present (Enyedi et al., 2013). Using this Orp1-Yap1 redox relay system (found in *S. Cerevisae)*, two teams have crafted two distinct H_2O_2 sensors that incorporate H_2O_2-sensitive component in fluorescent protein variants (Enyedi et al., 2013; Gutscher et al., 2009).

Genetically encoded sensors like roGFP2-Orp1 (redox-sensitive green fluorescent protein) (Gutscher et al., 2009) undergo reversible conformational changes upon oxidation, leading to shifts in their fluorescence spectra (Pouvreau, 2014). Orp1 is a peroxiredoxin and facilitates the oxidation of roGFP2 based on their proximity, both in a test environment or within living cells.

Later, two unique FRET-based redox sensors, OxyFRET and PerFRET, which embed H_2O_2-sensitive elements Orp1 & Yap1 between the fluorescent protein versions of Cerulean and Venus, have moreover been developed (Enyedi et al., 2013). OxyFRET and PerFRET display opposite FRET signal variation upon oxidation. By combining both sensors, one can achieve ratiometric quantitative assessments of H_2O_2 concentrations ranging from 1 to 100 µM, after which the probe reaches its saturation point (Enyedi et al., 2013).

HyPer is a fluorescent protein where the circularly permuted YFP (cpYFP) is integrated into the OxyR-RD, which is the H_2O_2-detecting regulatory domain of the OxyR transcription factor from *Escherichia coli* (Belousov et al., 2006). Structural changes in the sensing domain may result in shifts in the fluorescent protein, leading to a fluorescence change. HyPer is highly responsive to H_2O_2, detecting even low nanomolar concentrations and saturates at 100 µM for HyPer 3 the evolution of the initial sensor (Bilan et al., 2013). It possesses faster kinetics than roGFP2-Orp1, consistent with its direct reaction mechanism as opposed to the Orp1-mediated process in roGFP2-Orp1. Furthermore, HyPer has been demonstrated to be completely reversible in eukaryotic organisms (Pouvreau, 2014).

Genetically encoded sensors can be precisely directed to certain subcellular regions, allowing for detailed spatial analysis of cellular ROS production (Meyer & Dick, 2010). By utilizing various targeting sequences, these probes can be addressed to specific cellular compartments. Additionally, a number of these probes are ratiometric (Belousov et al., 2006; Enyedi et al., 2013; Gutscher et al., 2009), enabling measurements independent of the sensor concentration within the cells and allow quantitative detection when calibrated appropriately.

Organic, or genetically encoded sensors, such as the commonly used DCF or Hyper proteins, are though not quantitative. Furthermore, DCF or Hyper photobleaching prevents long-term or single-molecule observation, thus limiting the achievable temporal and spatial resolution.

Over the past three decades, various electrochemical methods like voltammetry, chronoamperometry, potentiometry, coulometry, and electrochemical impedance spectroscopy have been employed to efficiently measure H_2O_2 in both *in vitro* and *in vivo* environments. However, despite the considerable progress in creating electrochemical sensors for accurate H_2O_2 quantification in *in vitro* settings, achieving, highly sensitive, selective, reproducible, and rapid-response sensors remains a challenge. The task of implementing these refined electrochemical techniques in living systems is even more complex, often hindered by the toxic substances used in electrode design and operation (Gulaboski et al., 2019).

H_2O_2 sensors offering both high dynamics, reversibility, photostability, and quantitative measurement are required for probing cell signaling on relevant time scales (at least several minutes). The previously mentioned sensors fail to combine all these properties. We thus used Eu-doped nanoparticles that allow to track H_2O_2 production induced by EGF and PDGF in PECs.

3.2.3 YVO_4:Eu Nanoparticles

Lanthanide-based nanoparticles, such as Eu-doped nanoparticles (YVO_4:Eu, $GdVO_4$:Eu,…) have been used as probes (Abdesselem et al., 2015, 2017; Bouzigues et al., 2014; Casanova et al., 2009) for quantitative H_2O_2 detection in the cytoplasm in different cell types (HeLa, VSMCs) in response to Platelet Derived Growth Factor (PDGF) or Edothelin-1 (ET-1) for example.

Since intracellular H_2O_2 concentrations is pivotal for understanding cellular response, we used nanoparticles imaging to study how ROS production varies in time and space within PEC under PDGF and EGF stimulations.

3.2.3.1 Nanoparticle properties

The luminescence of YVO_4:Eu nanoparticles is due to Eu^{3+} ions, and is modulated oxidant levels, offering a unique way to measure intracellular H_2O_2 concentrations in both space and time (Beaurepaire et al., 2004; Casanova et al., 2006). The latter property is also responsible for the narrow emission (10 nm at 617 nm) and important Stokes shift in luminescence (excitation at 396 or 466 nm) allowing multiplexing with other fluorophores.

This method stands out from organic sensors like dichlorofluorescein (X. Chen et al., 2010) or boronate-based probes (Lippert et al., 2011), which lack reversibility and time precision. It also differs from genetically encoded sensors that have a restricted range and might need ratiometric techniques for accurate results (Belousov et al., 2006; Enyedi et al., 2013; Meyer & Dick, 2010).

YVO_4:Eu nanoparticles can be chemically or photo-reduced and oxidants such as H_2O_2 or HOCl induce a luminescence recovery dependent on the oxidant concentration (Figure 141, A). Even though these nanoparticles are not exclusive H_2O_2 detectors, in previous studies, only H_2O_2 was identified in cells (Casanova et al., 2009).

It was furthermore demonstrated in my team, that they are efficient nanosensors with high temporal resolution (tens of ms), and allow accurate ROS sensing in a large concentration range (1-100 µM), and can reveal the absolute ROS concentration in response to specific stimulation in living cells after proper calibration (Abdesselem et al., 2015, 2017; Bouzigues et al., 2014; Casanova et al., 2009).

Besides their ability to detect oxidant levels, these nanoparticles have several imaging advantages over traditional fluorescent probes. They are individually detectable under optical microscopy through the fluorescence they emit, and show no emission intermittency (Casanova et al., 2006). These particles can furthermore be functionalized with proteins, which make them addressable to different cell compartments, and allowing Single Particle Tracking (SPT) (Richly, 2015; Türkcan et al., 2013).

3.2.3.2 Synthesis

Europium-doped nanoparticles were provided by T. Gacoin team and synthesized at room temperature by salt co-precipitation in aqueous buffer. Briefly, 25 ml of a sodium orthovanadate aqueous solution (Na_3VO_4, 0.1 M, pH 12.5~13) was freshly prepared. The same volume of an aqueous solution of yttrium and europium nitrates (0.06 M of Y^{3+} and 0.04 M of Eu^{3+}) was then added dropwise using a peristaltic pump and the solution was kept under vigorous stirring until the pH stabilized. The solution was purified by centrifugation followed by redispersion *via* sonication in MilliQ water. Particles were then silica coated. 2.5 ml of sodium silicate (10% in water) were added dropwise to 50 ml of nanoparticles at 60 mM of vanadate. The silica layer thus created is amorphous and permeable to small molecules.

Thus these nanoparticles are readily available after synthesis at high concentration in aqueous solution. This allows straightforward preparation to use with biological molecules of *in vitro/vivo* experiments.

The europium doped and silicated NPs (NanoParticles) were studied after synthesis. The size distributions, zeta potential and quantum yield were obtained by dynamic light scattering (DLS), transmission electron microscopy (TEM) and UV-vis spectroscopy.

3.2.3.3 Characterization

3.2.3.3.1 Quantum yield

The quantum yield of silica-coated nanoparticles was determined by the "Relative Determination Method" (Würth et al., 2013). Absorption and fluorescence spectra were measured for Rhodamine 6G (5 µM) and $Y_{0.6}Eu_{0.4}VO_4$:SiO_2 (10 mM of vanadate) in absolute ethanol and pure water respectively. The quantum yield Φ was then calculated following the formula of Demas and Crosby:

$$\Phi = \Phi_r * \left(\frac{n_s}{n_r}\right)^2 * \frac{1-10^{-A_r}}{1-10^{-A_s}} * \frac{I_s}{I_r} * \frac{f_r}{f_s}$$

In this formula, the subscripts s and r represent the sample and the reference, respectively. Φ_r is the fluorescence quantum yield of the reference, with a value of 0.95 here. The term n refers to the refractive indices of the solvents ($n_s = 1.33$ for water and $n_r = 1.36$ for absolute ethanol). A stands for the absorbance at the excitation wavelength used for fluorescence measurements, which is 280 nm in this case. I indicates the total spectral fluorescence, and f represents the instrumental function. The same measurement conditions (such as excitation wavelength, spectral slots, integration times, and spectral range) are maintained for both the sample and the reference ($f_s = f_r$).

Absorbance and emission spectra of both rhodamine 6G and $Y_{0.6}Eu_{0.4}VO_4$ nanoparticles are presented in Figure 132.

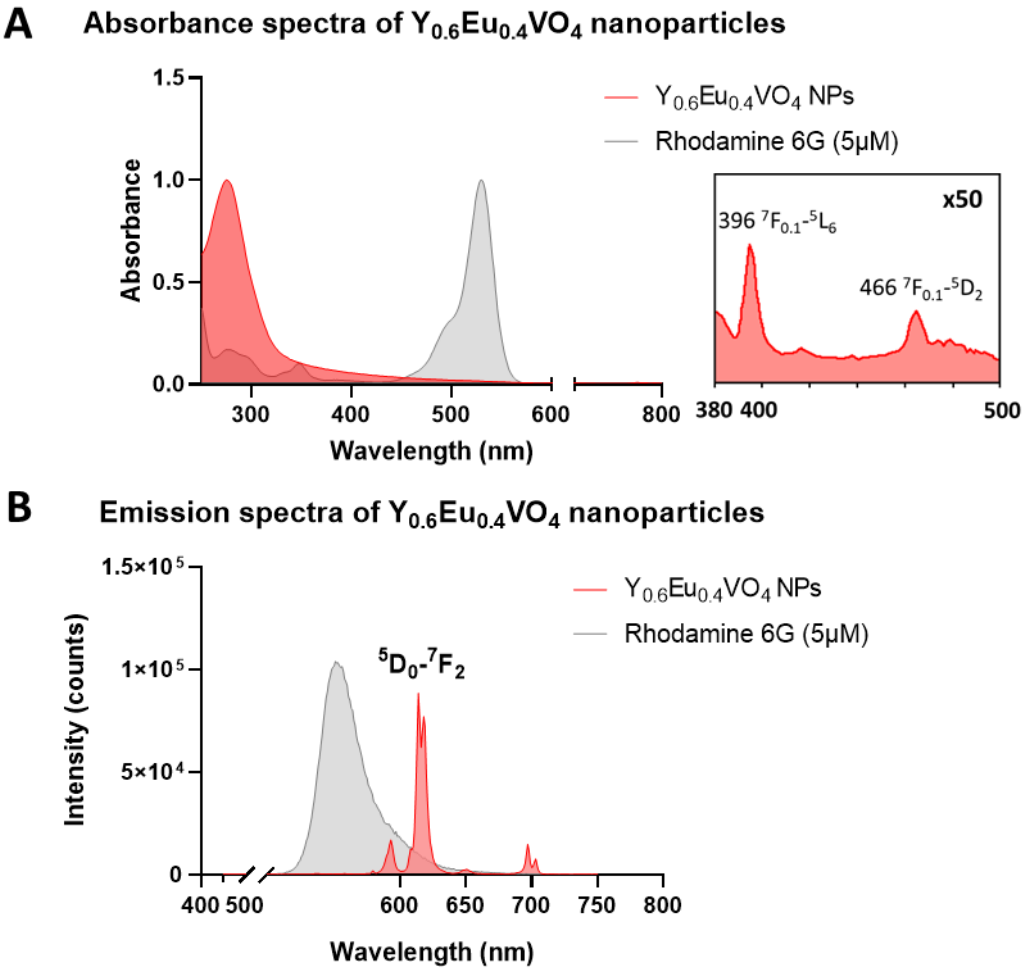

Figure 132: A) left, full absorption spectra of rhodamine 6G (grey) and silica coated $Y_{0.6}Eu_{0.4}VO_4$ nanoparticles, right, nanoparticles absorption spectra of concentrated nanoparticles solution (50x) B) emission spectra when excited at 280 nm.

Silica-coated $Y_{0.6}Eu_{0.4}VO_4$ nanoparticles present a strong absorbance in the UV spectra. The absorption pic is at 280 nm and corresponds to the orthovanadate matrix absorption. Other absorption pics are present, centered on 396 and 466 nm, in the visible region of the spectra and correspond to the direct Eu^{3+} excitation, with absorption pics corresponding to the $^7F_{0.1}$-$^5L_6$ and $^7F_{0.1}$-$^5D_2$ transitions of Eu^{3+} ions respectively (Brecher et al., 1967; Huignard et al., 2003).

The emission spectra is obtained by exciting nanoparticles at 280 nm. Two emission pics in the red region of the spectra are particularly intense at 615 and 619 nm. They correspond to the radiative deexcitation of Eu^{3+} ions following the $^5D_0$-$^7F_2$ transition. These wavelength will be used to detect nanoparticles for luminescence imaging (Beaurepaire et al., 2004; Huignard et al., 2003).

Using this method, the quantum yield of the silica coated $Y_{0.6}Eu_{0.4}VO_4$ nanoparticles was determined to be 5,7 %.

3.2.3.3.2 Hydrodynamic radius and zeta potential

We measured nanoparticles size through Dynamic Light Scattering (DLS), also known as photon correlation spectroscopy, is a widely used technique for characterizing the size distribution of

nanoparticles suspended in a fluid. It is particularly useful for measuring hydrodynamic radius in the range of 1 nm to a few micrometers (Bhattacharjee, 2016).

ζ potential is a measure of the magnitude of the electrostatic surface potential or charge repulsion/attraction between particles, and it is one of the fundamental parameters known to affect nanoparticle stability (Bhattacharjee, 2016). It provides insight into the charge stability of the particles in a particular medium,

To determine the PDI (PolyDispersity Index), Z average size and ζ potential, bare or silica-coated nanoparticles (100µl) from a stock solution of 60 mM or 49 mM of vanadate respectively, were diluted 100 times in ΔH_2O, centrifugated (1000g, 15 min) to remove nanoparticles aggregates (pelleted). The solution was then sonicated again prior DLS or ELS (Electrophoretic Light Scattering) measurements. Both measurements were conducted on a Zetasizer (Malvern) that combine both measurement methods .

Table 3: Bulk solution characterization of bare and silica-coated $Y_{0.6}Eu_{0.4}VO_4$ nanoparticles

	$Y_{0.6}Eu_{0.4}VO_4$	**$Y_{0.6}Eu_{0.4}VO_4$:SiO_2**
Size measured by DLS (nm)	198 ± 3	90 ± 4
PolyDispersity Index (PDI)	0.188	0.233
Z-average (nm)	188 ± 2	110 ± 2
ζ potential (mV)	+27 ± 5	-34 ± 8

The ζ potential of nanoparticles coated with silica is -34 mV, since the typical zeta potential to reach stability in water is -20 mV the particles will have colloidal stability in water. This observation can also shed light on the DLS size determinations. If nanoparticles tend to clump together because of inadequate colloidal stability, the measured Z-average will appear larger than it truly is. This is why the Z-average value is lower for nanoparticles coated with silica.

3.2.3.3.3 Size distribution by TEM

Accurate size measurement of nanoparticles is essential. If the nanoparticles are overly small, then distinguishing individual emitters using optical microscopy is not possible. On the other hand, if the nanoparticles are too large, they can interfere with cellular structures upon internalization. Transmission Electron Microscopy (TEM) is considered the benchmark method for determining nanoparticle size.

For TEM, 2 µL of silica-coated $Y_{0.6}Eu_{0.4}VO_4$ nanoparticle suspension was dropped on a carbon-coated formvar 400 mesh copper grid for 3 min. Then the excess solution was absorbed on a filter paper and the grid was air-dried. NPs were observed on a JEOL JEM-2010F transmission electron microscope operating at 200 kV accelerating voltage with a Field Emission Gun (FEG), using a US4000 CCD camera (Gatan), processed with Digital Micrograph (Gatan), and analyzed quantitatively with the ImageJ software.

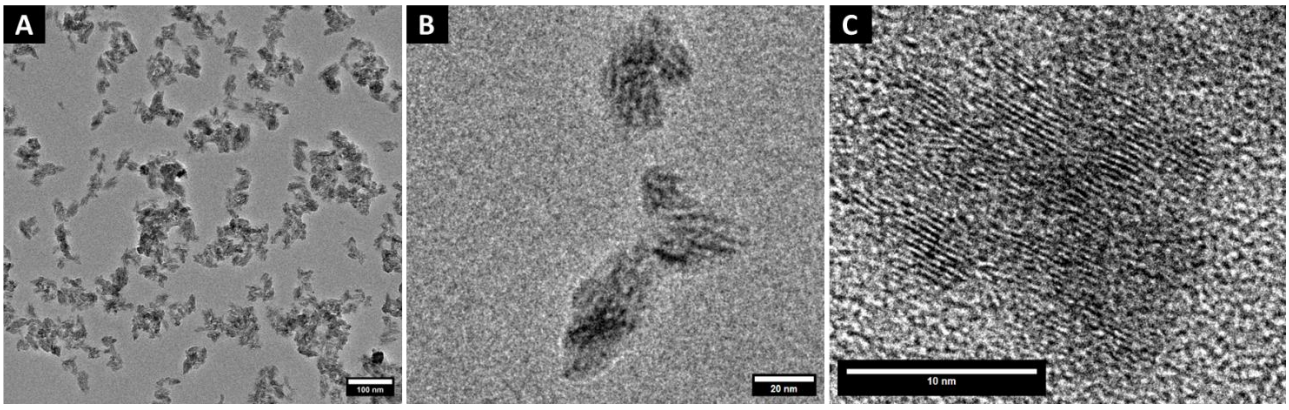

Figure 133: TEM images of silica-coated $Y_{0.6}Eu_{0.4}VO_4$ nanoparticles at different magnifications.

TEM images allows to measure the absolute size of nanoparticles since they can be observed with a sufficient contrast (Figure 133). Images of the silica-coated $Y_{0.6}VO_4Eu_{0.4}$ nanoparticles show that the nanoparticles are oblong and that the size distribution is broad, and that they tend to aggregate on the TEM grid. From the TEM images, small and long axis were manually measured for 200 NPs (Figure 134). By fitting the distributions with a log-normal curve we can extract the geometric mean length and width of nanoparticles. The geometric mean length was 32 ± 1.4 nm and the width was measured at 15 ± 1.3 nm. These sizes differ from the ones observed by DLS due to the fact that nanoparticles tend to aggregate in solution hence the hydrodynamic radius observed may be polluted by aggregates.

High magnification images of nanoparticles (Figure 133: C) shows interferences pseudo-lattice fringes (so-called Moiré patterns) that are commonly observed for nanocrystalline structures (Casanova, 2008), indicating that nanoparticles are at least partially crystalline.

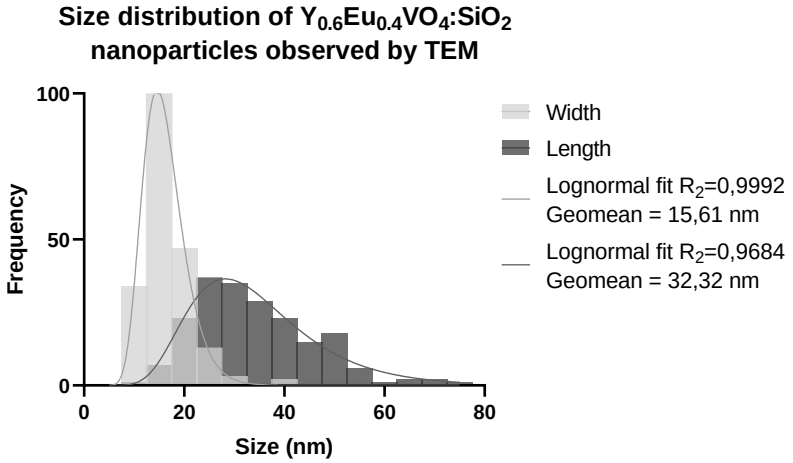

Figure 134: Size distribution of silica-coated $Y_{0.6}Eu_{0.4}VO_4$ nanoparticles obtained from TEM images (200 individual nanoparticles were analyzed).

3.2.3.4 Fluorescence imaging size determination of $Y_{0.6}Eu_{0.4}VO_4$ nanoparticles

The dimensions of nanoparticles are commonly assessed using techniques such as Transmission Electron Microscopy (TEM), or Dynamic Light Scattering (DLS). However, interpreting DLS data can be challenging when dealing with solutions that have a varied range of particle sizes, and TEM induced the formation of nanoparticle aggregates.

An alternative is to measure their size *in situ*, through the fluorescence intensity of the nanoparticles. Indeed, the number of emitters (Eu ions) is proportional to the volume of the nanoparticle. It is therefore possible to determine the relative size of the nanoparticle by measuring its signal (Casanova et al., 2006).

We carry out the fluorescence imaging on an inverted microscope (IX71 Olympus) under wide-field illumination by a custom-modified diode laser at 396 nm (Stradus 405, Vortran, 100mW) or a 466 nm (Modulight, 1W) diode laser. Nanoparticle luminescence was collected by an apochromat 60X, 1.42 numerical aperture oil-immersion objective (Olympus) equipped with a D617/8 nm bandpass filter (FWHM 8 nm, Chroma). The image acquisition is performed on an EM-CCD camera (Hamamatsu). The detailed microscope setup is presented in Appendix 4.4.1.

Nanoparticles from a stock solution (200 µl, 49 mM of vanadate) were diluted in distilled H_2O (ΔH_2O) to obtain a final solution of 1mL. The solution was sonicated and centrifuged (1000g, 5 min) to remove nanoparticles aggregates. The solution was then sonicated again prior use.

Diluted solutions of nanoparticles are deposed on glass coverslips, previously cleaned in a plasma cleaner, for 1h at room temperature (High power, 45 s; PDC-002-HPCE, Harrick Plasma), and rinsed three times with ΔH_2O. Nanoparticles are nonspecifically adsorbed on the glass surface as shown Figure 135.

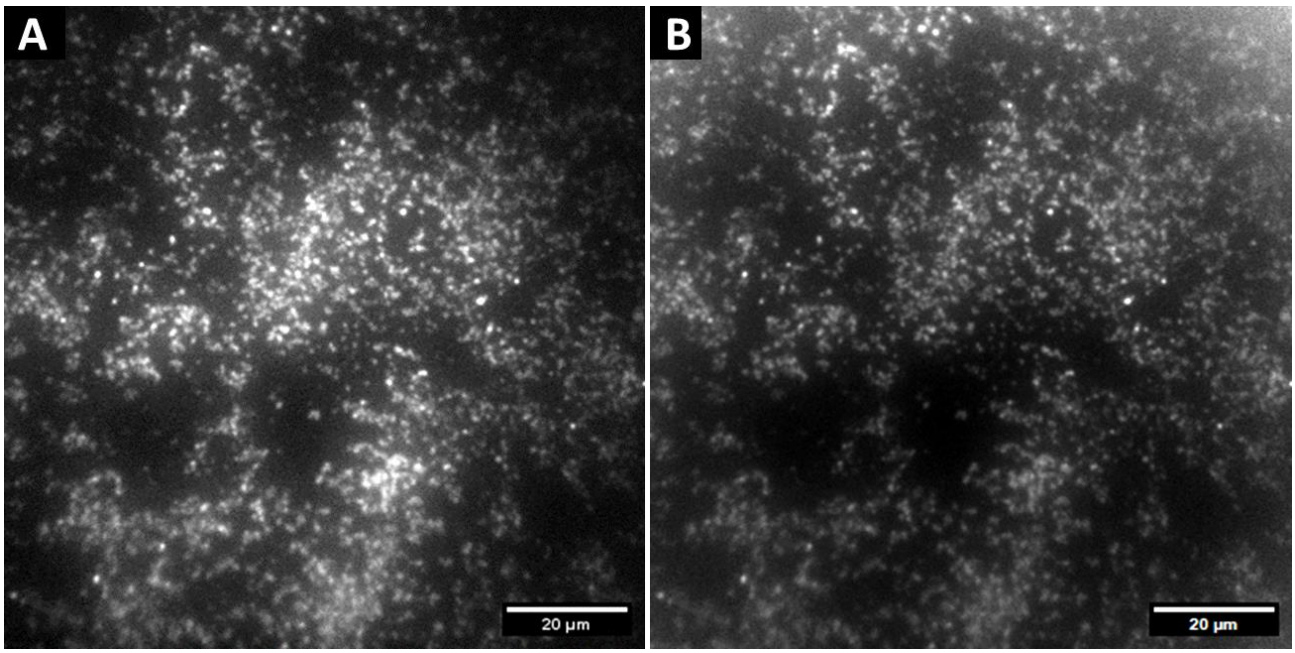

Figure 135: A) Image of silica-coated $Y_{0.6}Eu_{0.4}VO_4$ nanoparticles deposited on a glass coverslip after plasma activation (45s) by adsorption for 1h, nanoparticles are excited at 396 nm (28.5 W.cm^{-2}) and luminescence collected through a 617 ± 8 nm emission filter with a EM-CDD camera, B) image corrected for intensity illumination from the gaussian laser beam profile (magnification 60X).

While deposited by adsorption on the glass surface, the nanoparticle density was high yet allowing many individual nanoparticles to be resolved (Figure 135). Although some nanoparticles aggregated to form small clusters thus limiting the ability to resolve single particle emitters. From the images we can observe a Gaussian like illumination profile from the excitation laser creating inhomogeneities in nanoparticles signals.

This profile has been characterized in order to correct images and allow a quantitative analysis of nanoparticles on almost the whole field of view.

3.2.3.4.1 Illumination profile correction

By imaging plain glass coverslips covered with PBS, we recover images of the medium/coverslip autofluorescence that reveals the shape of the laser beam profile (Figure 136: A). We performed acquisition of time series images to assay for illumination intensity time variations (Figure 136: A&B). The intensity profiles were obtained by plotting the radial profile of intensities from the center of the images for every time points (Figure 136: B colored curves) using the ImageJ radial profile extended plugin[2].

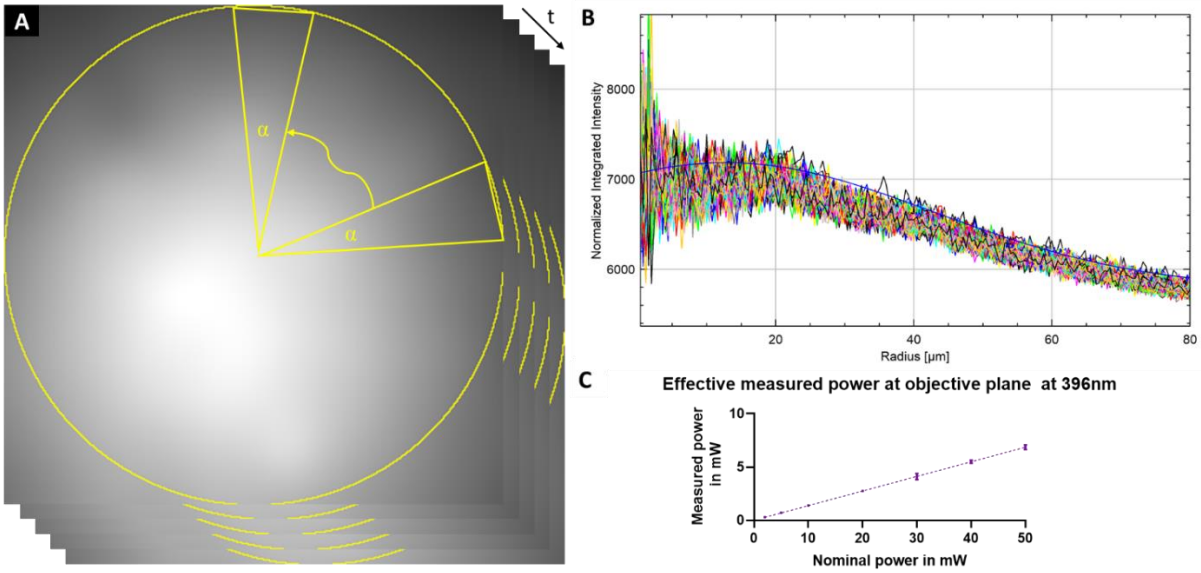

Figure 136: A) Stack of images showing intensity profiles from 396 nm excitation on a glass coverslip. B) Radial intensity profiles for varying α and t averaged and fitted with a Gaussian (blue line). C) Relation between nominal power of the laser and measured power at the objective focus plane.

By fitting the multiple Gaussian intensity profile of the laser ($I_{(r,z)}$) from these images we can determine the beam parameters (waist). I_0 is the intensity at the center of the beam at its waist, and if P_0 is the total power of the beam measured at the focal plane:

$$I_{(r,z)} = I_0 \left(\frac{w_0}{w_{(z)}}\right)^2 exp\left(\frac{-2r^2}{{w_{(z)}}^2}\right), \text{ with: } I_0 = \frac{2P_0}{\pi {w_0}^2}$$

From the Gaussian profile fits we have a beam waist $D_{(z)} = 2w_{(0)}$ of 175 ± 5.8 µm.

This allows to compute the absolute intensity of the laser excitation for each pixel for a given excitation power. An example of excitation profile is shown in Figure 137.

[2] Philippe Carl, (philippe.carl at unistra.fr), available at: https://imagej.nih.gov/ij/plugins/radial-profile-ext.html

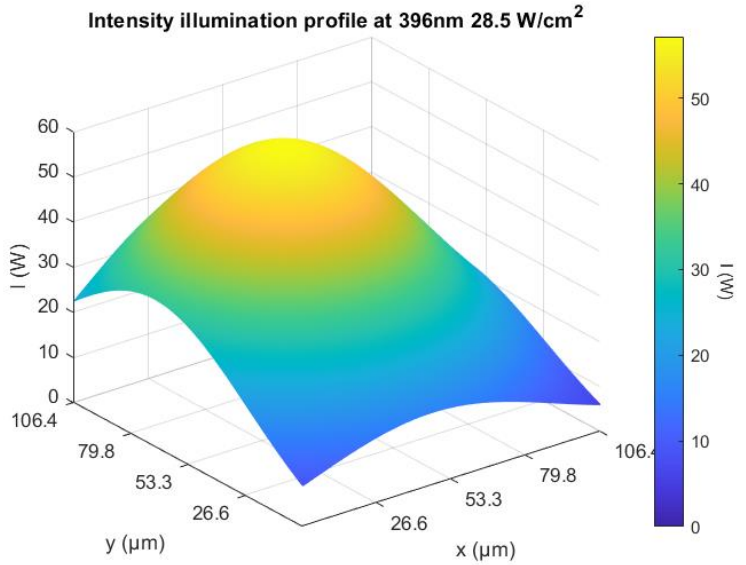

Figure 137: Absolute laser intensity (396 nm) profile for a 50 mW nominal power (6.86 mW at the objective plane) giving a total illumination of 28.5 W/cm² calculated from the beam waist.

This intensity profile can then be used to correct the images by normalizing the luminescence images by the excitation profile (Figure 135: B), allowing to determine precisely the number of photons emitted per nanoparticle.

3.2.3.4.2 Calculation of the nanoparticle size from the number of emitted photons

The crystal structure of Yttrium orthovanadate (YVO_4) is quadratic and of the zircon-type with space group $I4_1/amd(D_{4h}^{19})$. The lattice parameters for the undoped crystal are given as $a_0 = b_0 = 7.123$ Å and $c_0 = 6{,}291$ Å (Finch & Hanchar, 2003). Yttrium is homogeneously replaced by Europium in the vanadate lattice during the synthesis (Buissette et al., 2006).

A spherical nanoparticle of radius R has $N_{mesh} = \frac{4}{3}\pi \frac{R^3}{a_0 b_0 c_0}$ crystal mesh of size $V = a_0 b_0 c_0 = 0.323nm^3$ for a 40% Eu doping. After Yttrium substitution by Europium each mesh has $N_{Eu^{3+}} = 4N_{mesh}.0.4$ emitting europium ions.

The number of detected photons per second N_{det} is thus given by:

$$N_{det} = -\Phi\eta \frac{\sigma I}{h\nu} 4x \frac{(4/3)\pi(R)^3}{V}$$

Where;

- Φ is the luminescence quantum yield (5.7%),
- η is the detection efficiency of the optical setup; η is the product of the fraction of emission volume collected through the objective, $\frac{\pi N.A.^2}{4\pi}, N.A. = 1.42$, and of the objective, lens and interference filter transmission at emission wavelength (0.9, 0.98, 0.99 respectively at 617 nm), and reflectivity of mirrors (silver and dichroic 0.98 and 0.99 respectively),
- σ the absorption cross section of the 395 nm Eu^{3+} absorption line,
- *I* the excitation intensity, $h\nu$ the excitation photon energy,
- *x* the fraction of Y^{3+} ions replaced by Eu^{3+} ions (40%),

- *R* the nanoparticle radius,
- *V* the unit cell volume of the $Y_{0.6}Eu_{0.4}VO_4$ crystal.

The first fraction in the equation corresponds to the number of absorbed photons per Eu^{3+} ion, while the second is equal to the number of unit cells in a NP of diameter D.

The number of emitted photons per nanoparticles was determined by fitting the signal of each nanoparticle with a 2D-Gaussian allowing integration of the total signal collected for each nanoparticle (surface under the Gaussian) and the detection of the background level (offset of the gaussian). This was done with a custom analysis MATLAB code.

We then determined the equivalent spherical diameter of nanoparticles from their emitted photon number using the previous equation. Results are presented in *Figure 138*. We obtain a nanoparticle equivalent diameter of 19 ± 1.3 nm from TEM and of respectively 15 ± 1.5 and 18 ± 1.4 nm for nanoparticles measured through their luminescence intensity before and after illumination corrections.

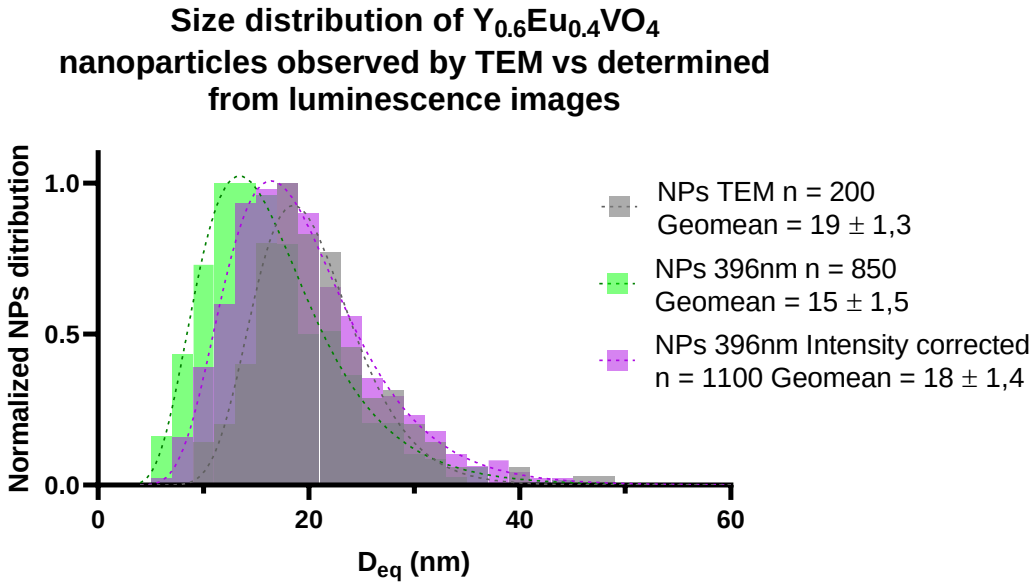

Figure 138: Spherical equivalent diameter (D_{eq}) determined by analyzing luminescence signal of nanoparticles before (green) and after (purple) intensity correction of the field of view compared to the volume measured by TEM converted to a spherical equivalent diameter (gray).

We can observe a good agreement between the measurements done by optical microscopy and TEM. This indicates first that we observe single nanoparticles deposed on the glass coverslip, and that we could determine the size of nanoparticles (~20 nm) from luminescence images alone, without needing to resort to electron microscopy.

3.2.3.5 Quantitative ROS sensors

The fluorescence of most fluorescent organic molecules photobleaches with illumination (Hoebe et al., 2007; Ludvikova et al., 2023). This non-reversible photodegradation explains why they must be kept out of the light. In contrast, most fluorescent nanoparticles and quantum dots exhibit low or no photobleaching (Courty et al., 2006).

In the case of $Y_{0.6}Eu_{0.4}VO_4$ nanoparticles, luminescence can decreases with laser illumination tough this decrease is never total (for both 396 and 466 nm), and no spontaneous recovery is observed (Abdesselem et al., 2015, 2017; Casanova et al., 2009). Europium and more generally the lanthanides $[Xe]6s^24f^n$ exist in their twice-oxidized form $[Xe]6s^24f^n$. The Eu^{3+} ion $[Xe]4f^6$ is among the lanthanides the strongest oxidizing agent and is therefore easily reduced ($E^0_{Eu^{3+}/Eu^{2+}} = -0.35$ mV) (Casanova, 2008). Broad excitation and emission lines typical of the Eu^{2+} ion appear after luminescence reduction (Casanova et al., 2009). The phenomenon is therefore related to a reduction of the Eu^{3+} ions to Eu^{2+}.

Since laser illumination leads to a reduction of the Eu^{3+} ions in the nanoparticles, it may be possible to oxidize them to reform the ions Eu^{3+}. After photoreduction, the intensity of their photoluminescence (PL) increases upon the addition of hydrogen peroxide (Casanova et al., 2009). This increase starts as soon as the hydrogen peroxide is added. The increase is such that for high concentrations, the PL returns to its initial level (Casanova et al., 2009). Even after a few cycles of photobleaching and recovery, the behavior is reproducible with the same dynamics. The recovery occurs much more slowly in the absence of illumination, and illumination with a resonant wavelength also accelerates the recovery (Casanova et al., 2009). The observed signal is therefore the result of a complex equilibrium between photoreduction and reoxidation. The kinetics and amplitude of the recovery depends on the H_2O_2 concentration, allowing for a precise determination of the ROS concentration nearby the particles.

3.2.3.5.1 Sensor response

We measured the photoreduction of nanoparticles deposed on glass coverslips in physiological buffers (Figure 139).

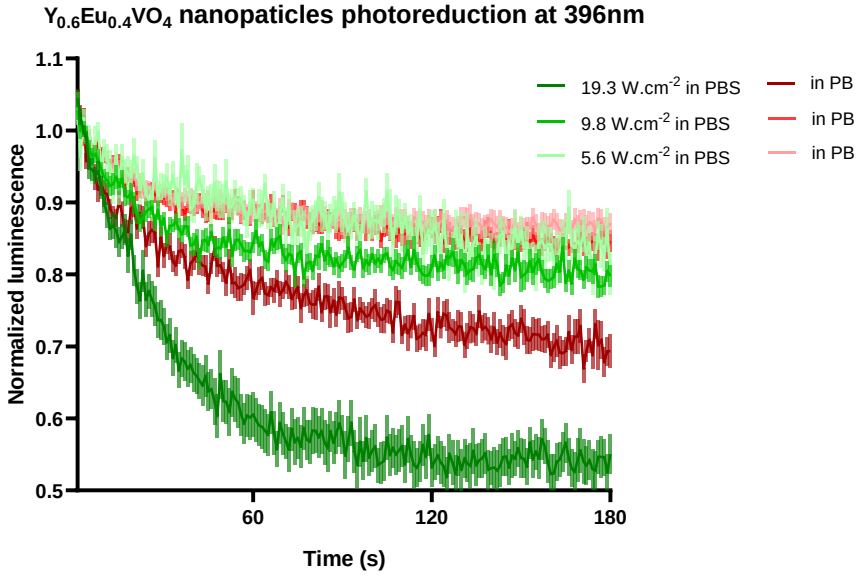

Figure 139: Silica-coated $Y_{0.6}Eu_{0.4}VO_4$ nanoparticles photoreduction curves (averaged over 20 individual nanoparticles per curve), in buffered media (PBS or PB), pH 7,4, exposed to 396 nm laser illumination for 3 minutes at varying laser intensities, error bars indicate SEM.

We observed a correlation between laser power and the extent of photoreduction observed. Higher laser power results in greater photoreduction of the nanoparticles. The rate of photoreduction

varies depending on the salinity of the buffer, and is more pronounced in Phosphate-Buffered Saline (PBS) than in PB. The solvent has thus an effect on the reduction dynamics of the probe. This implies that for sensor calibration, photoreduction and nanoparticle signal tracking should be conducted in a buffer that most closely mimics cellular homeostasis (pH and salinity).

To perform a quantitative calibration of the nanoparticles response to H_2O_2, we first determined concentration of oxidant that fully regenerated the sensor. Once the nanoparticles are photoreduced, when adding a high concentration of hydrogen peroxide (500 µM) the sensor can be fully reoxidized (Figure 140).

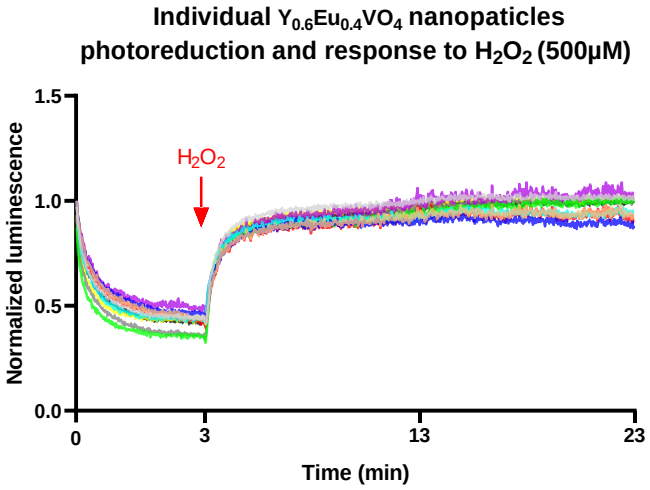

Figure 140: Example of individual $Y_{0.6}Eu_{0.4}VO_4$ nanoparticle photoreduction (3 minutes at 396 nm, 19 W.cm^{-2}) followed by the tracking of the luminescence recovery when adding 500 µM of hydrogen peroxide H_2O_2 (20 minutes at 396 nm, 3 W.cm^{-2}).

To characterize the sensor over a full range of oxidant concentrations, the response of nanoparticles to hydrogen peroxide is assessed by following the luminescence response after the addition of hydrogen peroxide concentrations ranging from 1 to 100 µM in the solution for 20 minutes at laser intensities of 3 W.cm^{-2} for 396 nm after photoreduction. We performed the calibration on immobilized nanoparticles plated on glass coverslips. Each luminescence recovery line is the average of at least 25 individual intensity tracking over 3 individual experiments.

Upon introducing different concentrations C of H_2O_2 to the photo-reduced nanoparticles, the luminescence recovery vary with C. Without H_2O_2, there is no notable deviation from the zero baseline, suggesting that spontaneous re-oxidation does not occur. It is possible to detect H_2O_2 concentrations as low as 1 µM, after averaging across several nanoparticles (Figure 141, A). The final luminescence value reached after recovery depends on the H_2O_2 concentration in the 1–100 µM range. The recovery curves following a step-like addition of H_2O_2 can be fitted by exponentials with two concentration-dependent parameters, the characteristic time $\tau(C)$ and the final value $A(C)$ following this equation :

$$\Delta S/S_0 = A(C) \cdot \left(1 - e^{-\frac{t}{\tau(C)}}\right)$$

Based on this property, and given that the monotonous relations $\tau(C)$ and $A(C)$ provide a unique solution for C(t) (Figure 141: B, C, D), this equation can be used to extract $C(t)$, the

instantaneous H_2O_2 concentration. The temporal resolution is determined by accuracy of the measurement of $(\Delta S/S_0)(t)$ and its first derivative and is typically 10–30 s. We can use this relation to build a parametrized sheet (Figure 141, D) giving this relation:

$$[H_2O_2] = u\left(\Delta S/S_0, \frac{d(\Delta S/S_0)}{dt}\right)$$

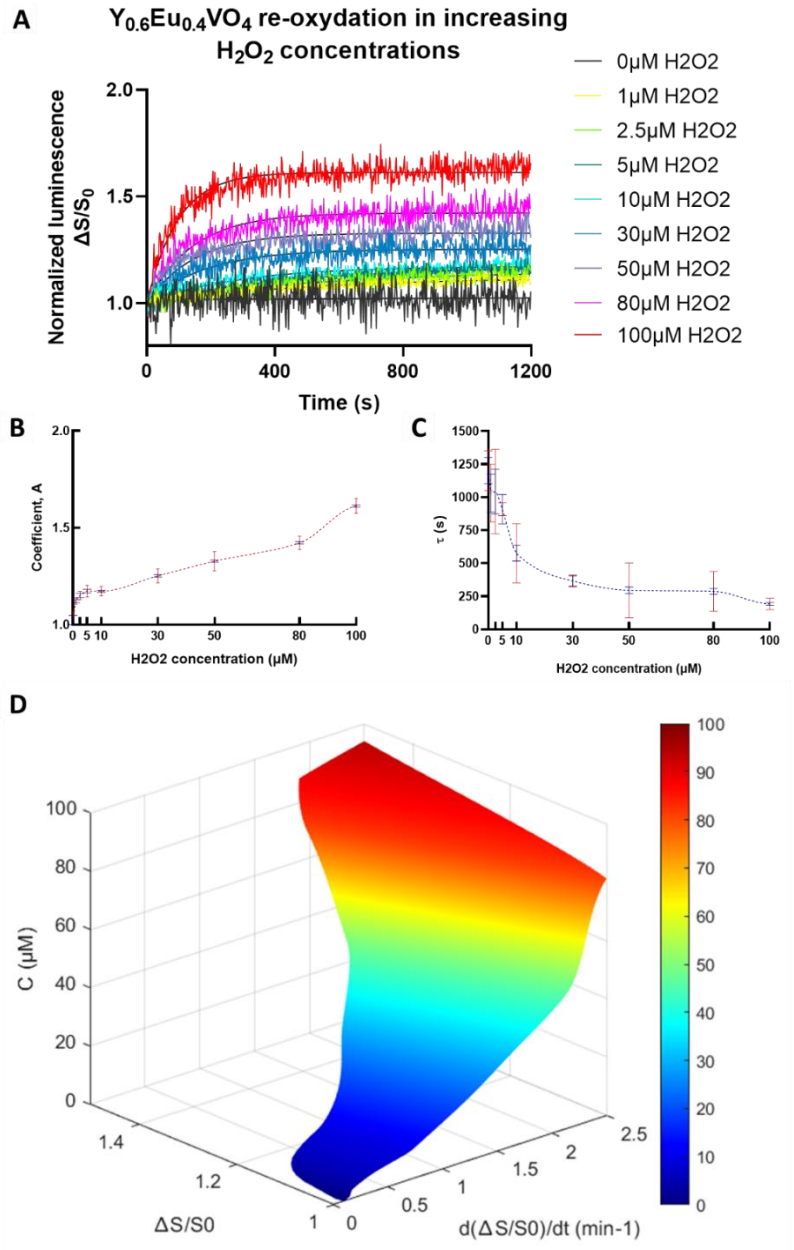

Figure 141: Calibration of ROS quantitative measurement, A) Normalized luminescence recovery averaged over 25 $Y_{0.6}Eu_{0.4}VO_4$ nanoparticles for each given H_2O_2 concentrations fitted with $\Delta S/S_0 = A(C) \cdot (1 - e^{-t/\tau(C)})$, B&C) coefficient A and characteristic time τ obtained from fitting nanoparticles response to H_2O_2 (blue error bars of the fits, red error bars are standard deviation for the collection of individual nanoparticles that gave the averages, the red dashed and blue lines are piecewise cubic Hermite interpolations), D) Parameterized sheet linking luminescence recovery to the instantaneous H_2O_2 concentration in the vicinity of the nanoparticles (calculated numerically from A(C) and τ(C) showing the H_2O_2 concentration C corresponding to sets of $\Delta S/S_0$ values and its derivative, valid for the excitation intensity used to obtain A(C) and τ(C) 396 nm, 3 W.cm^{-2}).

Illumination of the nanoparticles was realized at low power in the same conditions as for the *in cellulo* particle tracking enabling a sensitivity range of detection to 1 µM. These nanoparticles are thus interesting sensors to measure H_2O_2 signaling levels quantitatively in signaling processes. In the following section we discuss how they can be used to detect intracellular levels of hydrogen Peroxide in PECs in response to different stimulations.

3.2.4 Nanoparticles internalization in mPECs

We plan to measure intracellular signaling levels of H_2O_2 in PECs in response to HB-EGF and PDGF-BB. To that end we internalized $Y_{0.6}Eu_{0.4}VO_4$ nanoparticles in the cells cytoplasm. Indeed, the presence of a lipid bilayer around nanoparticles would limit H_2O_2 diffusion (Bienert et al., 2006) and thus prevent the actual measure of the cellular internal concentration.

This has previously been performed by colleagues using osmotic lysis of pinocytic vesicles (Casanova et al., 2009). Pinocytosis delivery of nanoparticles is more robust in delivering a consistent amount of nanoparticles to adherent cells, at the cost of introducing cytotoxicity to the cells *via* an osmotic shock to deliver nanoparticles. The main advantage for us is that nanoparticles, once internalized, may remain in the cells cytoplasm for several days without being secreted by the cells.

In this section we will describe the protocol of internalization, how we monitored the induced cytotoxicity, and how we ensured that nanoparticles were realized in the cell cytoplasm.

3.2.4.1 Osmotic shock mediated pinocytosis

Osmotic shock-mediated pinocytosis is used to introduce macromolecules or other substances into cells (Okada & Rechsteiner, 1982). Pinocytosis itself is a form of endocytosis, where a cell engulfs extracellular fluid and its dissolved solutes into vesicles. Osmotic shock can be used to increase the uptake of these materials, particularly when traditional methods of material delivery into cells may not be effective.

Cells are first exposed to a hypertonic solution containing the nanoparticles. This destabilizes the plasma membrane, creating more surface area. The cellular membrane, perturbed by the osmotic imbalance, may be more prone to the engulfment of extracellular material at this stage. After 10 minutes in the hypertonic solution, the cells are exposed to a hypotonic solution for 2 minutes, leading to vesicles rupture and cargo delivery in the cell cytoplasm. Finally, the cells are returned to an isotonic solution to restore normal osmotic balance and physiological conditions. The process is illustrated in Figure 142: A. This technique can be used for a variety of cell types and materials, including proteins, DNA, and other macromolecules. However, the drastic changes in osmotic conditions can stress cells, sometimes leading to cell death or other types of cellular damage. The technique requires fine-tuning and optimization for different cell types or materials.

Primary mouse Parietal Epithelial Cells (mPECs) (Kabgani et al., 2012) (kind gift from M. Moeller, University Hospital of the Aachen University of Technology) were isolated using transgenic mouse lines and Fluorescence-Activated Cell Sorting (FACS). mPECs were cultured at 5% CO_2, and 37°C in supplemented ECBM with PS and 20% FBS until 70% of confluence before passaging. A stable mPEC-shCD9 knockout cell line was obtained (kind gift from O. Lenoir, PARCC) by lentiviral transduction of a shRNA targeting CD9 (Lazareth et al., 2019). Cells were placed in an incubator at 37°C under a 5% CO_2 atmosphere until they reached 70% confluence. Cells were then plated on

fibronectin-coated glass coverslips (0,01mg/ml coating overnight at 4°C) 24h before nanoparticle internalization.

For cellular internalization, silica-coated nanoparticles from a stock solution of 49 mM Vanadate preparation were diluted 5 times in ultrapure water before homogenization by sonication (6 times 5 s at 70% power, Sonics vc18) at 4°C. Aggregating particles were sedimented by centrifugation at 1000g 5 min, supernatant was then recovered and homogenized again by sonication following the same steps. Nanoparticles were prepared following these steps before each reinternalization and not kept longer than 10 minutes at 4°C before use.

We internalized silica-coated $Y_{0.6}$ $Eu_{0.4}VO_4$ nanoparticles in cells by pinocytosis using a three-step process:

- incubation of the cells with 500 µL of hypertonic medium (10% PEG 1000, 0.5 M Sucrose, Sigma) solution in ECBM-HEPES media supplemented with 50 µL of lanthanide-based colloid (where rare-earth concentration was approximately 0.1 mM) for 10 min leading to the formation of intracellular vesicles containing the nanoparticles,

- incubation of the cells with hypotonic medium (60:40 ECBM medium:water) for 2 min to burst the intracellular vesicles and release free nanoparticles in the cytosol,

- cell recovery at 37°C under a 5% CO_2 atmosphere for 30 min in complete ECBM supplemented media.

A MTT (3-(4,5-dimethylthiazol-2-yl)-2,5-diphenyltetrazolium bromide) assay was then performed to monitor cell viability after loading of nanoparticles by pinocytosis.

3.2.4.2 Viability assay

The MTT assay is a widely-used colorimetric assay for assessing cell metabolic activity, and by extension, cell viability and proliferation (Ghasemi et al., 2021). This assay is often used to evaluate the effectiveness of drugs, toxins, or other agents on cell survival or growth. In living cells, MTT is reduced to formazan, a purple, insoluble compound, by cellular enzymes such as NAD(P)H-dependent oxidoreductase enzymes. These enzymes are found in the mitochondria of metabolically active cells. The amount of formazan produced is directly proportional to the number of viable cells (Ghasemi et al., 2021) and ca be assayed by a spectrophotometer.

WT and shCD9 mPECs were seeded in a 96-well plate coated with Fibronectin (0.01 mg/ml) and allowed to adhere and grow. Once the cells have adhered, they were subjected to pinocytosis with or without nanoparticles and left to recover overnight as previously described. After this period, MTT solution is added to each well. mPECs medium was first changed for HBSS, and 10 % of MTT stock solution was added on the cells and incubated at 37°C for 3h and protected from light. An equal volume of lysis buffer is then added to the cells and the plate is incubated overnight with agitation at 37°C (formazan crystals are dissolved in lysis buffer under a fume-hood since SDS and DMF vapors are highly toxic). The plate is then read on a spectrophotometer to measure the absorbance of the formazan solution, the absorbance is measured at a wavelength of around 570 nm and normalized by the values at 650 nm. The higher the absorbance, the greater the number of viable, metabolically active cells.

We can a observe (Figure 142: B) a significative reduction in absorbance compared to control cells indicating a reduced cell viability or metabolic activity after pinocytosis for both wild type and

CD9-KO mPECs. The absorbance decrease of around 25% for wild-type mPECs and 15% for CD9-KO mPECs. Pinocytosis with nanoparticles loaded increased cell mortality slightly but significantly compare to loading control for both cell types reaching up to 30% of cell mortality 24 hours after loading.

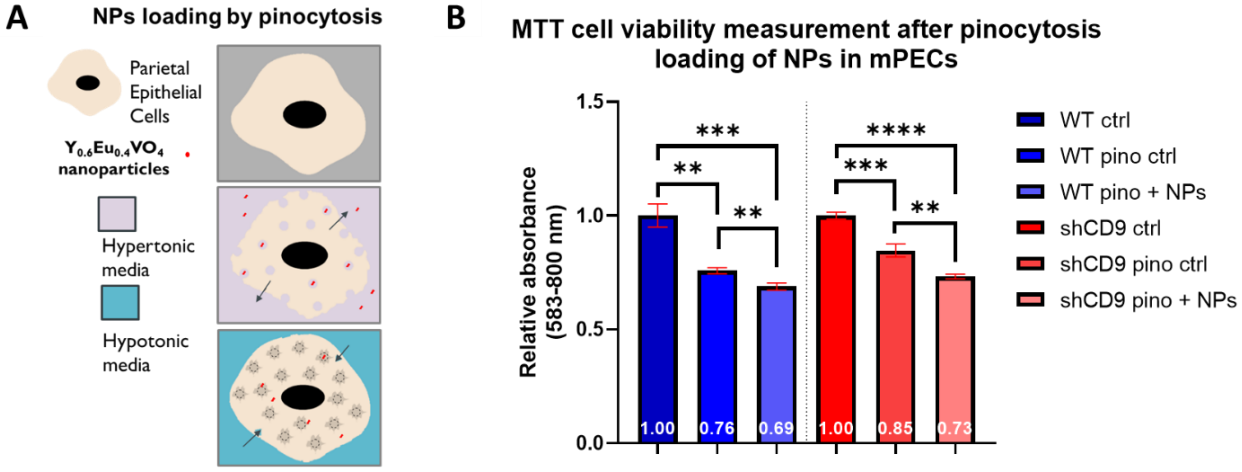

Figure 142: A) principle of osmotic shock mediated pinocytosis, B) MTT viability assay for WT & shCD9 mPECs after osmotic shock mediated pinocytosis with (pino + NPs) or without (pino ctrl) nanoparticles (n=12 for controls conditions and n=24 for NPs loading, error bars are SEM, stars from Kolmogorov-Smirnov t-test).

Loading of nanoparticles *via* pinocytosis is thus possible allowing cytoplasmic measurement of H_2O_2 levels, with a moderate cytotoxicity.

3.2.4.3 Nanoparticle localization after pinocytosis

PECs were fixed after pinocytosis to determine if nanoparticles were released in the cytoplasm of the cells or did show any specific addressing to a subcellular compartment. To determine this, we used TEM on ultrathin cell sections prepared from adherent mPECs (this was done at Imagerie-Gif imaging platform, I2BC).

After pinocytic treatment adherent cells were fixed with 2.5% Glutaraldehyde, 2% Paraformaldehyde solution in 0,2 M Phosphate Buffer PB for 1h at room temperature. Cells were then rinsed twice for 15 min for in PB. Cells were post-fixed in 1% Osmium and 1.5% potassium ferrocyanide in distilled water for 1h. Cells were rinsed 5 times for 5 min in distilled water. Cells were then sequentially dehydrated in 10 min in 50%, 70%, 90%, and twice in absolute ethanol baths. Cells were then embedded in 1:1 ethanol:Epon resin (R1165, Oxford Instruments) using a capsule directly on the glass coverslip. The resin was left to polymerize for 16h at 60°C. The obtained resin block was trimmed, and semi-thin sections were realized followed by toluidine blue staining to assess cell presence. Then ultrathin sections of 70 nm were performed and collected on formvar/carbon-coated 400 mesh copper grids. Then a 1% uranyl acetate solution was applied for 15 min on sections and rinsed 3 times with distilled water before lead citrate staining. Cells were observed on a JEOL JEM-1400 microscope operating at 80 kV. Images were acquired with a high-speed camera (SC1000 Orius, Gatan), processed with Digital Micrograph (Gatan), and analyzed quantitatively with the ImageJ software.

Cells treated by pinocytosis show a population of highly contrasted vesicles, easily observable and different from normal secretory vesicles (Figure 143). These vesicles are large (around 0.5 µm) and probably result from the pinocytosis process, and could be fused vesicles unruptured from the hypotonic shock. As the hypertonic medium is loaded with polyethylene glycol (PEG 1000) it could explain their high contrast under TEM. Another explanation would be that these vesicles are granules containing proteins normally present in PECs which number may increase due to the pinocytosis process (Ohse, Pippin, et al., 2009; Shankland et al., 2014).

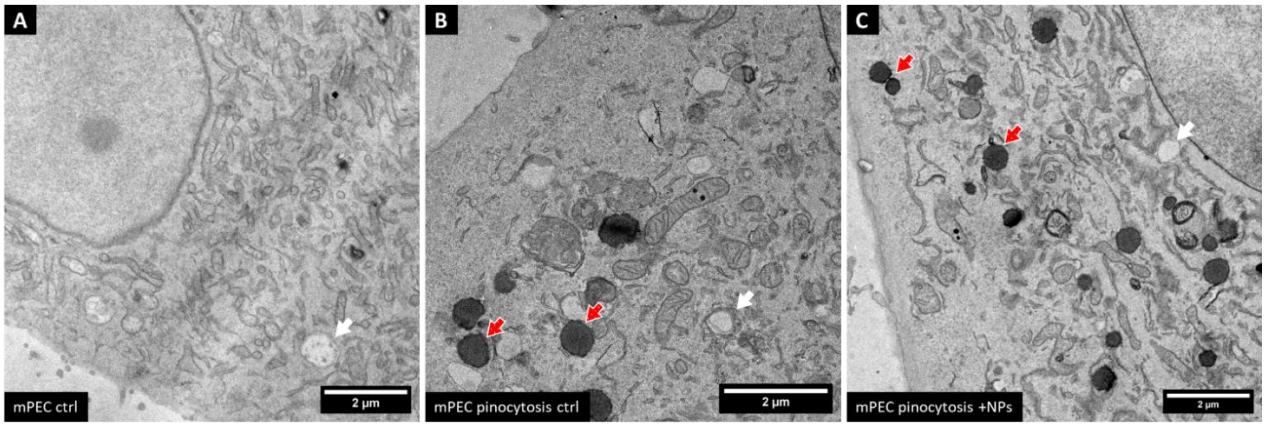

Figure 143: TEM images of mPECs in A) control conditions, B) pinocytosis induced loading control, C) loading of nanoparticles, white arrows indicate normal secretory vesicles, red arrows indicate new population of vesicles induced by pinocytosis.

At higher magnification (~7000X), we could identify highly contrasted nanostructures in the cell cytoplasm of mPECs loaded with nanoparticles (Figure 144, Figure 145), that were absent in control or nanoparticle free pinocytosed cells, as nanoparticles.

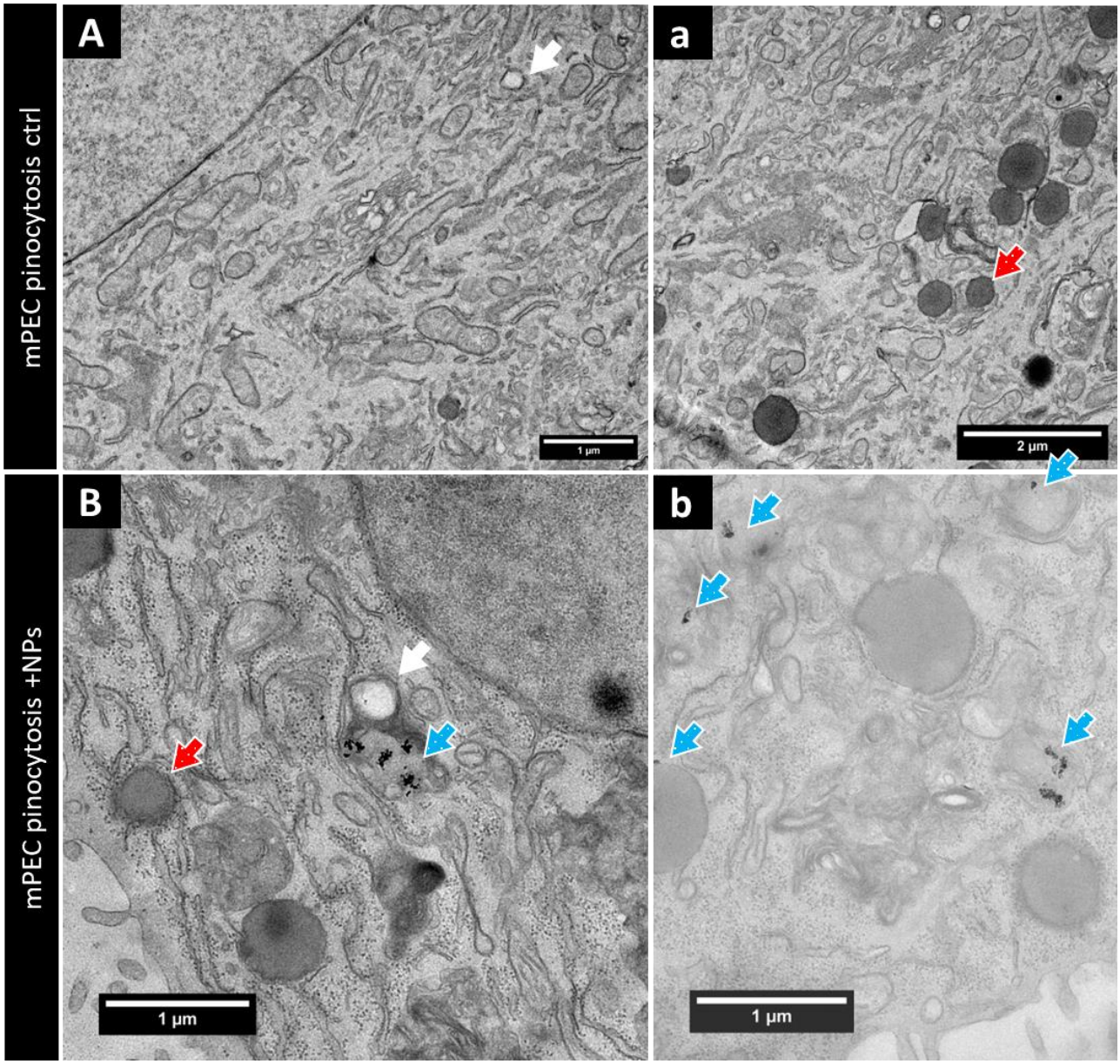

Figure 144: TEM images of mPECs in A&a) pinocytosis induced loading control, B&b) loading of $Y_{0.6}Eu_{0.4}VO_4$ nanoparticles, white arrows indicate normal secretory vesicles, red arrows indicate new population of vesicles induced by pinocytosis, blue arrows indicate silica-coated $Y_{0.6}Eu_{0.4}VO_4$ nanoparticles.

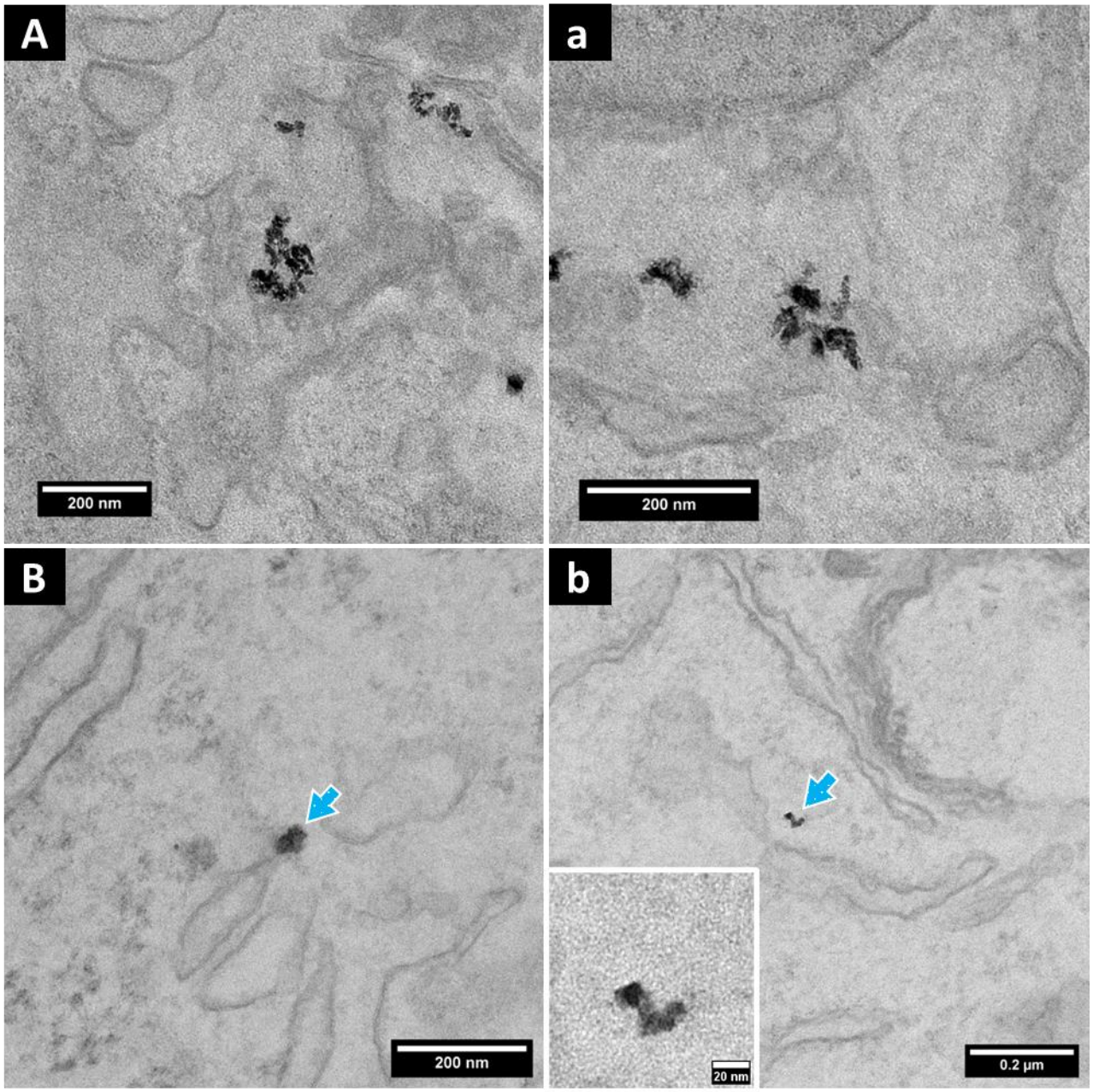

Figure 145: TEM images of mPECs with pinocytosis induced loading of $Y_{0.6}Eu_{0.4}VO_4$ nanoparticles (blue arrows), A&A) show aggregated particles and B&b) isolated nanoparticles.

Nanoparticles are visible in the cytoplasm of mPECS (*Figure 145*). Although some nanoparticles are aggregated in the cytoplasm of the cells, many nanoparticles are isolated in the cytoplasm not surrounded by membrane compartments.

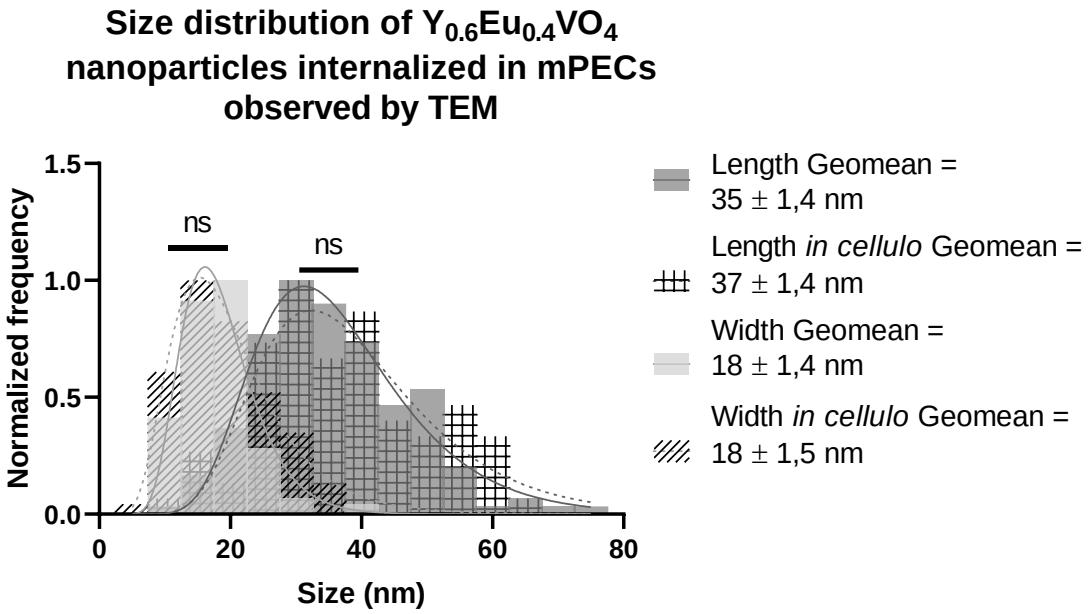

Figure 146: Size distribution of nanoparticles measured in mPECs (n= 83) after pinocytosis compared to size distribution of nanoparticles on EM grids (n=125).

The size distribution of nanoparticles internalized in mPECs obtained from TEM images was compared to the distribution obtained from nanoparticles deposed on EM grids (*Figure 146*). We can observe that the size distributions are similar. This ruled out the possibility of such structures being impurity included during contrast or preparation for electron microscopy.

We can thus use pinocytosis to deliver nanoparticles into the cell cytosol. By combining osmotic lysis of pinocytic vesicles with long recovery time of cells after nanoparticles internalization we were able to get minimal cytotoxicity and maximal throughput for our experiments. This method is thus suitable to address nanoparticles in the cytoplasm of primary mouse PECs.

3.2.5 HB-EGF and PDGF-BB stimulations in WT and shCD9 mPECs

3.2.5.1 Observation of nanoparticles in living mPECs

To track the ROS response to HB-EGF or PDGF-BB we first determined the excitation wavelength at which the experiments would be performed. Since Europium ions can be directly excited at either 396 nm or 466 nm both wavelengths could be used. Most of the experiments realized so far using lanthanides nanoparticles were performed using a 466 nm excitation (Abdesselem et al., 2015, 2017; Casanova et al., 2009). This choice seems reasonable to limit phototoxicity during nanoparticles luminescence tracking. However, the absorption at 466 nm is smaller than at 396 nm (Figure 132, A), thus imaging at 396 nm allows to detect nanoparticles using reduced illumination power, and potentially use GFP expressing cells.

We thus compared photoreduction dynamics at both wavelength and compared quantitatively the amplitude of the photoreduction and Signal to Noise Ratio (SNR) that could be obtained for both excitations. We carried out the *in cellulo* nanoparticles imaging on the previously described microscope (Appendix: 4.4.1) using either the 396 nm or 466 nm laser diodes. We used HBSS-HEPES (30 mM) pH 7.4 as imaging medium in cell imaging experiments. Typical images of

nanoparticles internalized in mPECs cytoplasm, before and after photoreduction, are shown in Figure 147.

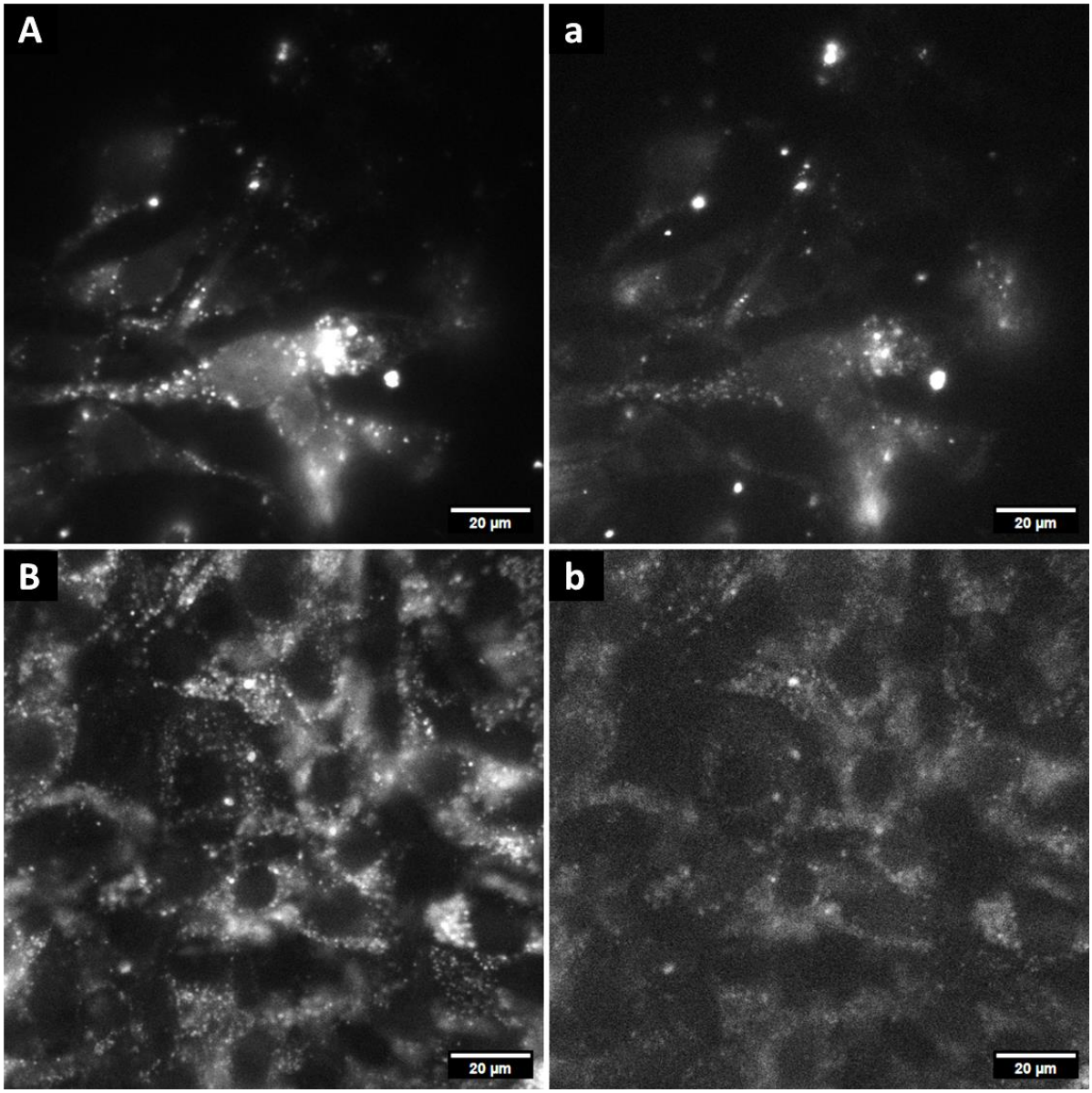

Figure 147: Luminescence images of $Y_{0.6}Eu_{0.4}VO_4$ nanoparticles internalized in mPECs, A&a) exited at 396 nm before (A) and after 3min photoreduction (a, at 19 W.cm^{-2}) and B&b) before (B) and after 3min photoreduction at 466 nm (b, at 254 W.cm^{-2}).

The images show that a cellular autofluorescence background is present for both excitations, however its localization pattern is slightly different. When exciting the cell at 396 nm the cell background is homogeneously autofluorescent, while using the 466 nm laser leads to revealing more point like structures (probably vesicles containing fluorescent culture medium) that could be confused with nanoparticles.

After background photobleaching (3min), we see that nanoparticles excited with the 396 nm laser could be more easily identified than in the images performed at 466 nm. A quantitative tracking of both nanoparticles and cell background bleaching dynamics was performed (Figure 148).

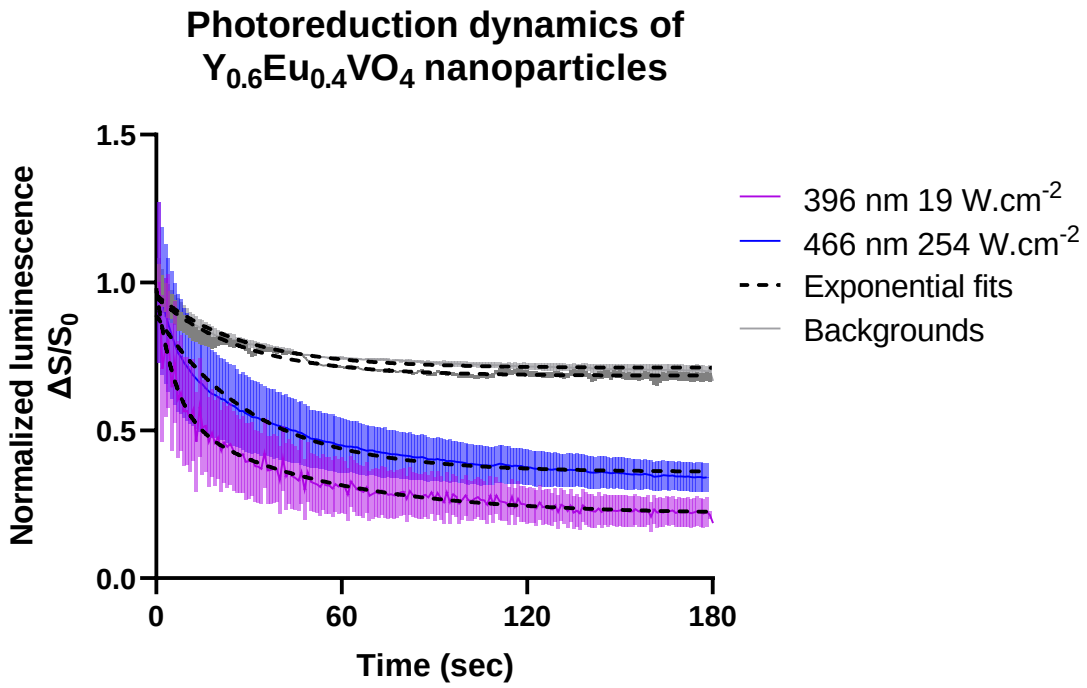

Figure 148: Nanoparticles and background luminescence tracking when performing photoreduction using either the 396 or 466 laser diodes, photoreduction dynamics can be fitted with a bi-exponential function (dashed curves).

We first observed that the background bleaching dynamic is the same for both excitations with a signal reduction (~20%) reaching quickly equilibrium (~1min). The photoreduction induced by near UV illumination (396 nm) is larger than at 466 nm even when using one order of magnitude less light intensity on the cells, which enlarge the range of the sensor sensitivity.

The nanoparticles, with a diameter of approximately 30 nm, fall below the optical diffraction limit and are thus represented as a Point Spread Function (PSF) in the image.

We tracked the nanoparticles, through a MATLAB algorithm used to fit a 2D Gaussian curve to the nanoparticle. The peak of the Gaussian curve indicates the nanoparticle's position with an accuracy depending on the number of emitted photons (see section: 3.1.2.3). The signal-to-noise ratio (SNR) significantly influences the level of precision attainable in localizing a label during Single Particle Tracking (SPT, (Richly, 2015). Extending the image acquisition time (~1 second) will increase the photon count, thereby reducing the positional error. However, this will compromise time resolution. Additionally, any motion of the probe while capturing images can cause distortions in the PSF. The SNR can be calculated as:

$$SNR = \frac{N}{\sqrt{N}}$$

The photon number is determined by the Gaussian fits on the nanoparticle signal. The total count for a nanoparticles corresponds to the amplitude under the Gaussian fit. Knowing the EM-CCD camera gain, photoelectron per count, and quantum yield we can calculate the number of emitted photons. An example of photon count for different nanoparticles from a live experiment, and the leading changes in SNR is illustrated in Figure 149.

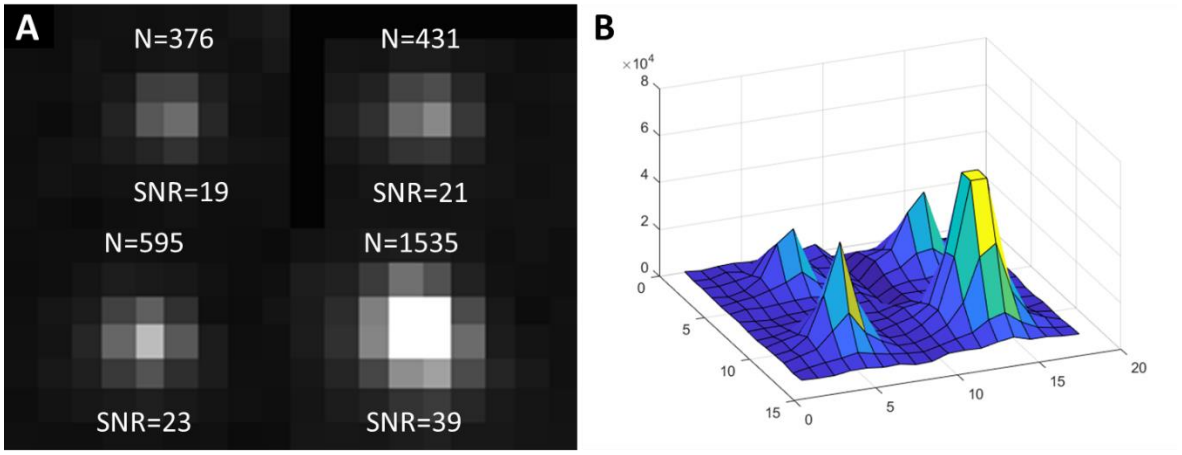

Figure 149: A) Effect of photon number on Signal to Noise Ratio (SNR). The localisation of the probe becomes more precise as the number of photons, N, increases from 376 to 1535, B) raw signal of the nanoparticles in count per pixel.

We quantified the SNR of individual nanoparticles for both 396 and 466 nm excitations, before and after photoreduction (Figure 150).

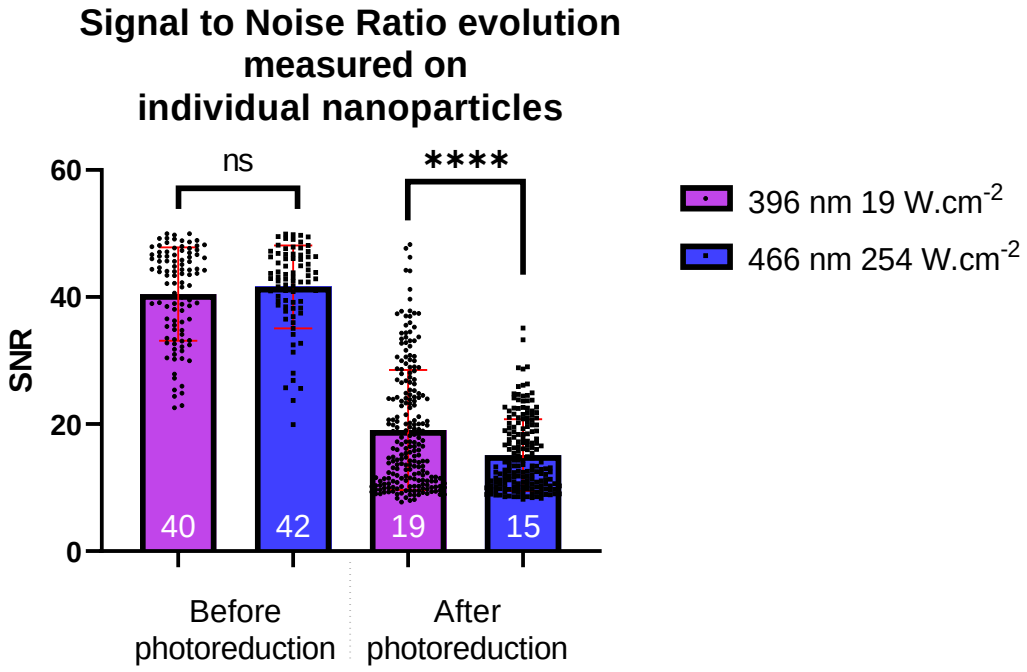

Figure 150: Individual nanoparticles SNR extracted from photoreduction experiments using either 396 or 466 nm excitations (n=5 images each ~20 NPs per image, error bars are SEM, stars indicate significant Kolmogorov-Smirnov t-test).

The SNR distributions are similar before photoreduction of the nanoparticles for 396 and 466 nm excitations, with a high SNR around 40. After photoreduction of the nanoparticles, the SNR drops for particles excited with both wavelengths, however, nanoparticles excited with the 396 nm laser diode have a significantly higher SNR than those excited at 466 nm. Performing imaging at 396 nm thus enables easier tracking of the nanoparticles photoluminescence for long term experiments (≥ 10 minutes).

To assay the potential cytotoxicity of the 396 nm laser line we systematically performed a trypan blue viability assay, after the photoreduction, and tracking of the nanoparticles for a total

continuous illumination of 26 minutes. Dead cells will be permeable to the dye that will stain their nuclei (Figure 151, b), and were removed from the analysis.

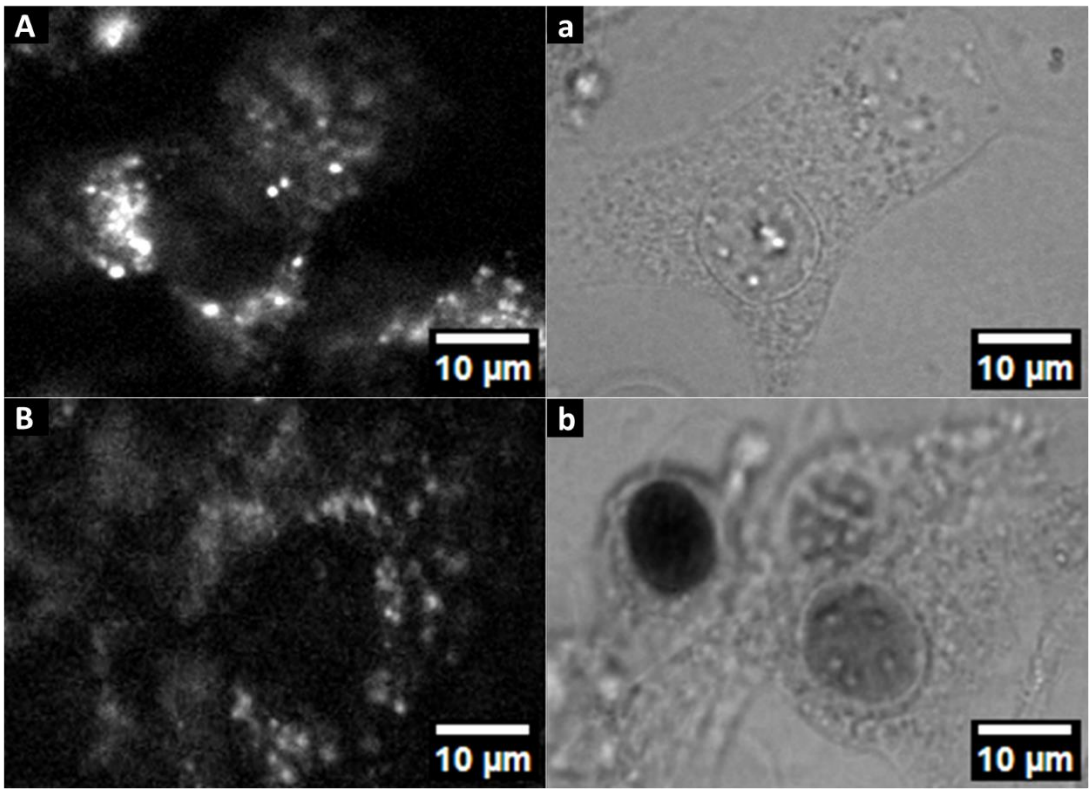

Figure 151: A&B) Luminescence images of $Y_{0.6}Eu_{0.4}VO_4$ nanoparticles internalized in mPECs, exited at 396 nm for 3 minutes of photoreduction at 19 W.cm^{-2} and tracking for 23 minutes at 3W.cm^{-2} a&b) are transmission images of the same cells after trypan blue staining.

We thus showed that imaging of nanoparticles at 396 nm offered interesting features; an increased dynamic of the sensor and a better SNR allowing easier tracking for long experiments (several tens of minutes), while being compatible with live cell imaging.

3.2.5.2 HB-EGF and PDGF-BB stimulations

In PECs cells, HB-EGF and PDGF-BB regulate proliferation and migration by producing H_2O_2 (Lazareth et al., 2019). CD9 is a tetraspanin organizing EGF-receptor membrane confinement in nanodomains, and CD9 knock-out (KO) mice were shown to have a slower RPGN progression (Lazareth et al., 2019).

mPECs were plated on fibronectin coated coverslips and let to grow until 70% confluence. We internalized silica-coated $Y_{0.6}Eu_{0.4}VO_4$ nanoparticles into mPECs using pinocytosis as previously described. To detect the H_2O_2 produced in signaling processes in wild-type and CD9-KO mPECs, cells were first serum-deprived in unsupplemented ECBM (1% FBS, no growth factors) medium overnight. Cells were then observed for nanoparticle luminescence upon EGF or PDGF stimulations.

We used HBSS-HEPES (30 mM), pH 7.4, as imaging medium in cell imaging experiments. *In situ* photoreduction of nanoparticles was achieved by illuminating the cells at high power at 396 nm for 3 min (19 W.cm^{-2}). The luminescence of the nanoparticles was then tracked at low laser power (3 W.cm^{-2}) for 3 minutes before stimulation to assess the absence of residual photoreduction.

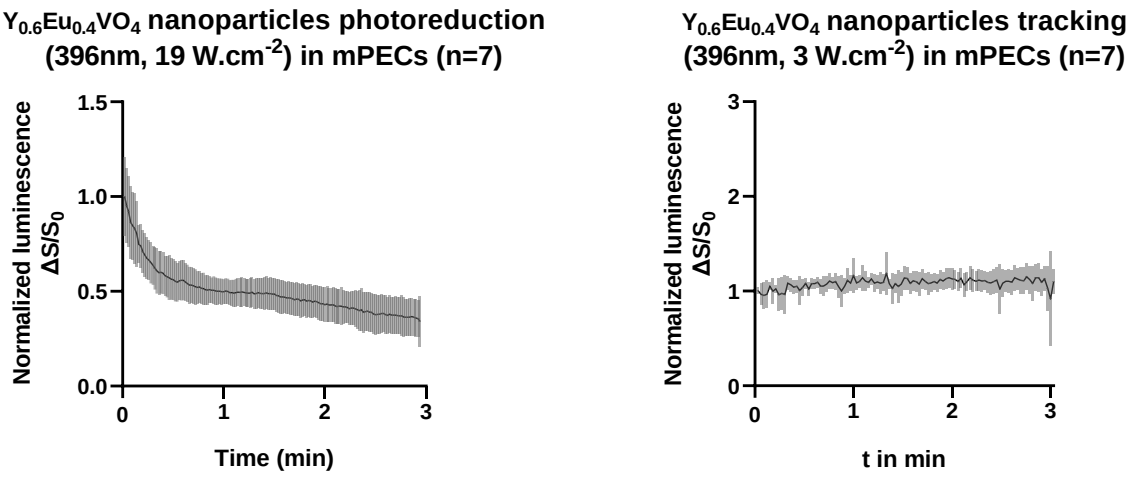

Figure 152: Left, mean photoreduction rate of $Y_{0.6}$ $Eu_{0.4}VO_4$ nanoparticles internalized in mPECs (n=7 cells, at least 5 NPs analyzed per cell, 396 nm, 19 W.cm^{-2}), right, luminescence tracking before stimulation of mPECs (n=7 cells, at least 5 NPs analyzed per cell, 396 nm, 3 W.cm^{-2}).

In situ photoreduction of nanoparticles shows ~60% nanoparticles intensity reduction. The luminescence intensity before stimulation with growth factors remains constant under low illumination. This indicates that no spontaneous reoxidation (or potential stress induced production) of the nanoparticles is observed in mPECs after photoreduction.

Cells were then incubated with either 15 ng/ml HB-EGF or 15 and 100 ng/ml PDGF-BB (Sigma) at t=0, and nanoparticle luminescence was followed at 396 nm for 20 minutes at low laser power (3 W.cm^{-2}). Cells were then subjected to a trypan blue test to check viability after imaging. The average luminescence recovery induced by HB-EGF or PDGF-BB stimulations of mPECs is shown in Figure 153, & Figure 154.

The nanoparticle signal analysis was done by fitting the signal of each nanoparticle with a 2D-Gaussian and the surface under the Gaussian was calculated to determine the total signal collected for each particle. In most cell experiments, the particles movement inside the cell is neglectable compared to the cells motion. This is most probably because nanoparticles of this size are restricted in their movement within the dense milieu of the cytosol and the cytoskeleton network. Our analysis was limited to particles that stayed in focus throughout the experiment. By monitoring the emission width of the particles, we identified any potential defocusing that might cause false signal variations, and these defocused particles were excluded from our analysis. A minimum a 10 nanoparticles/cell were analyzed to give a cell average response, and an average of all cells response is presented in Figure 153.

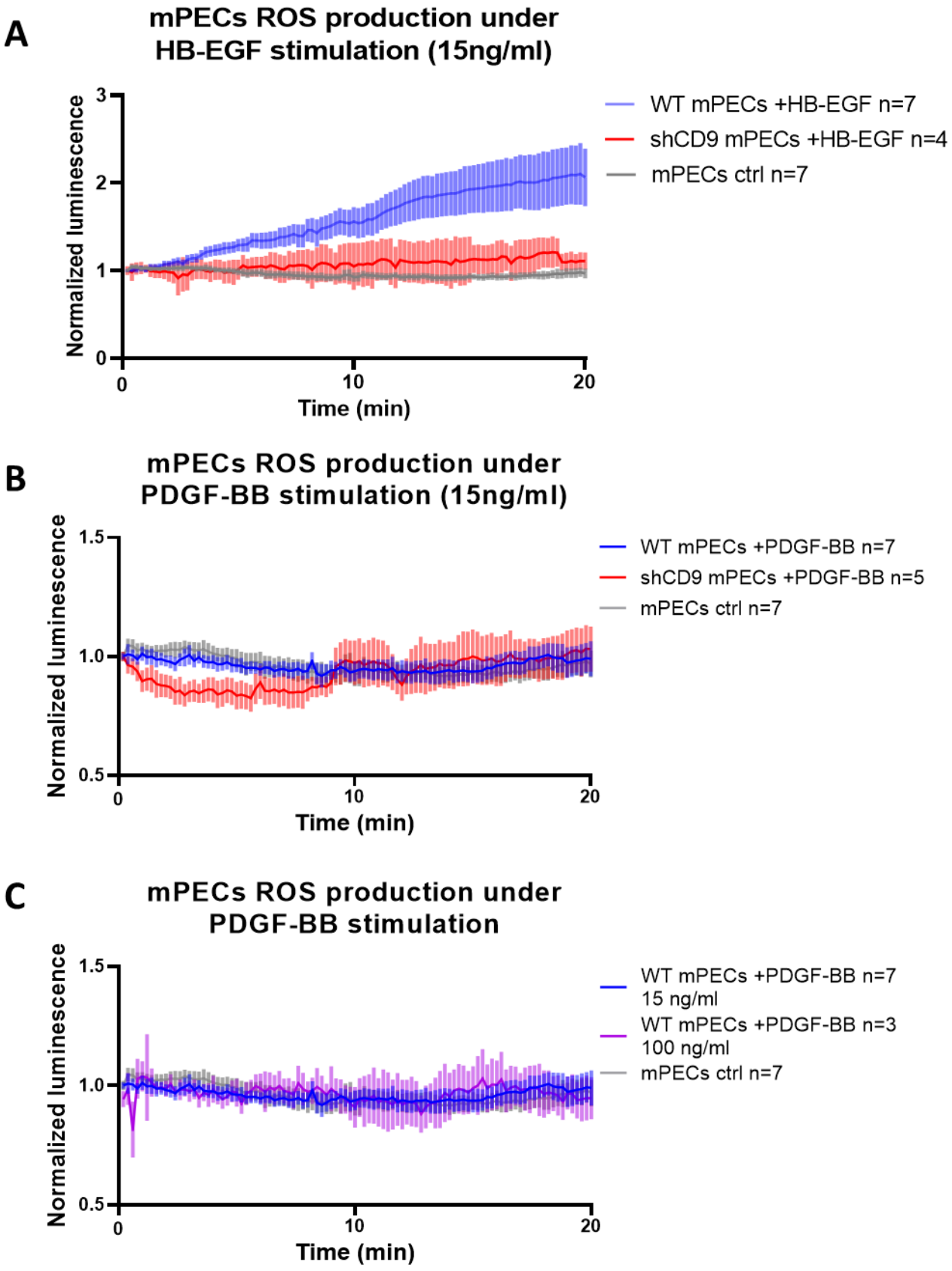

Figure 153: Luminescence tracking of $Y_{0.6}Eu_{0.4}VO_4$ nanoparticles internalized in WT and shCD9 mPECs (averaged by cell at least 5 NPs analyzed per cell, 396 nm, 3 W.cm^{-2}) in control conditions, stimulation with HB-EGF 15ng/ml, PDGF-BB 15 and 100 ng/ml (error bars are SEM).

For unstimulated cells no significant deviation from the baseline was observed indicating that no spontaneous reoxidation of nanoparticles occurred during the course of the experiment. HB-EGF stimulation on CD9-KO in PECs induced a lower oxidative response than wild-type cells (Figure 153). PDGF stimulations of mPECs did not show any increase in H_2O_2 production levels for the same used EGF concentration, even when increasing PDGF concentration to 100ng/ml (Figure 153).

We compared quantitatively these responses by determining the final level of luminescence of the different cells average. This indicates the difference in the relative H_2O_2 production and if cells responded or not (Figure 154).

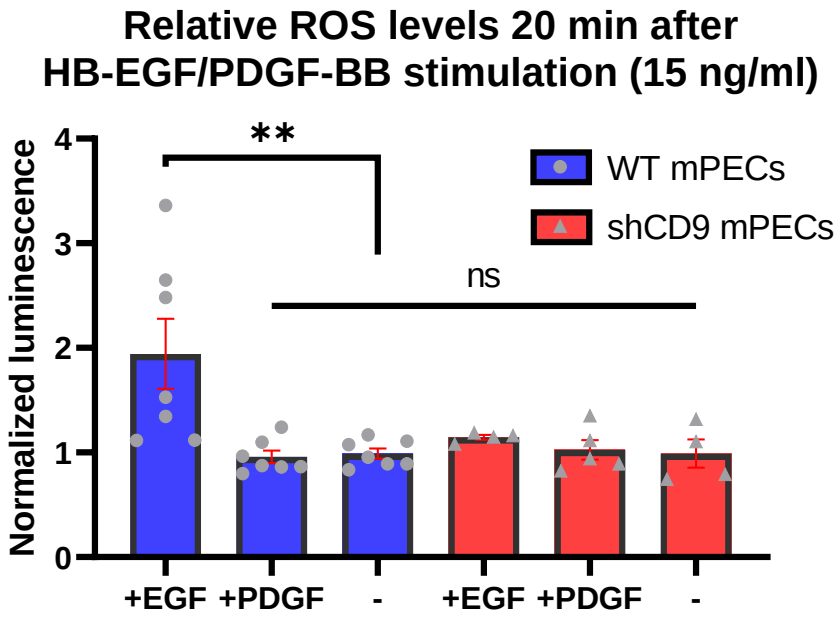

Figure 154: Final mean luminescence level of $Y_{0.6}$ $Eu_{0.4}VO_4$ nanoparticles in WT and CD9 mPECs (averaged by cell at least 5 NPs analyzed per cell, 396 nm, 3 W.cm^{-2}) in control conditions, stimulation with HB-EGF 15ng/ml, PDGF-BB 15 and 100 ng/ml (stars from t-test, error bars are SEM).

We can observe that a significant increase of luminescence is observed for wild type mPECs in response to HB-EGF. A slight increase is also observed for shCD9 mPECs tough not significative.

Then, from the quantitative calibration of the sensor, we perform the extraction of the H_2O_2 concentration produced by mPECs when stimulated with 15 ng/mL of HB-EGF (Figure 155).

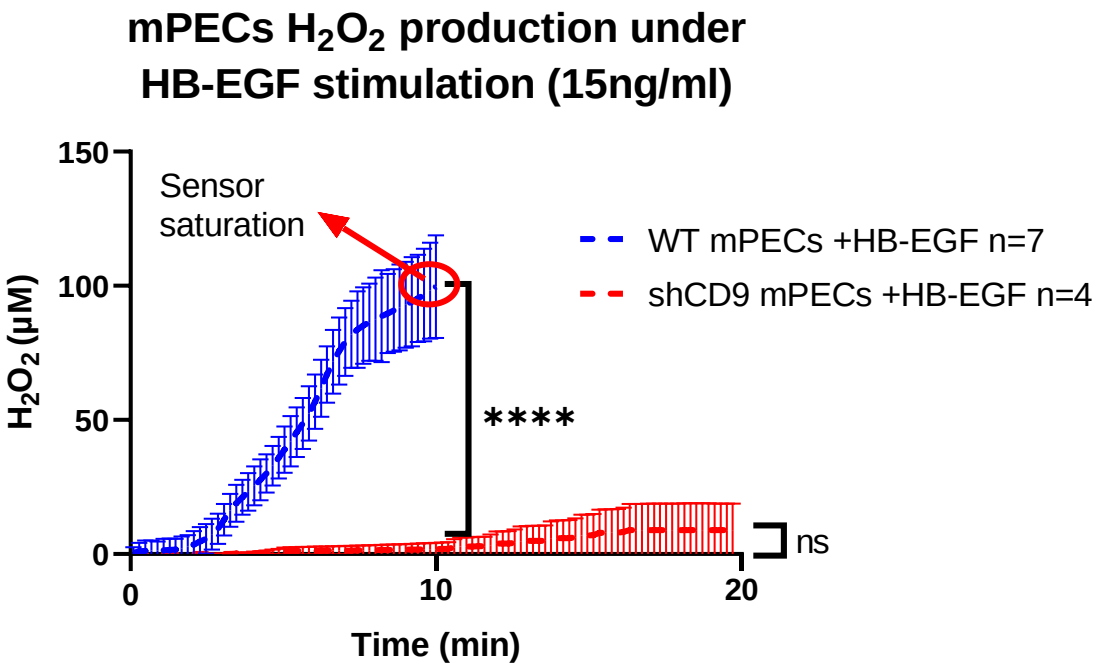

Figure 155: WT and shCD9 mPECs H_2O_2 concentration produced in response to HB-EGF (error bars are SEM, stars from t-test at t=10 min, values are averaged on 30 second interval).

The level of local intracellular concentration of H_2O_2 produced in response to HB-EGF for wild-type mPECs is very high, and quickly exceed the sensor calibration range (100 µM). Thus, we can only compare the production in WT vs shCD9 mPECs for the first 10 min after HB-EGF stimulations. We can observe a very significative decrease of H_2O_2 production in CD9 KO mPECs.

This production in shCD9 mPECs reaches after 20 minutes a level of ~9 µM of H_2O_2 produced thought not significant from the baseline. This concentration is comparable to other signaling concentration measured in cancer cells for example (Casanova et al., 2009). The fact that the production levels in WT mPECs is one order of magnitude higher at least, could further support our hypothesis and previous results, that upon EGF stimulations, PECs are activated (before starting to migrate and proliferate) at least partly through EGF signaling. CD9 thus not only regulates EGFR organization but also its signaling in PECs.

Overall this approach allows to decipher fine changes in signaling at good spatio-temporal resolution providing a unique quantitative information on ROS instantaneous production.

3.3 Towards embedding ROS sensors in Organ-on-chip

In this section, we will explore the potential of incorporating YVO_4Eu nanoparticles as sensors for Reactive Oxygen Species (ROS) within the organ-on-chip platform we previously engineered (Chapter 2). Our objective is to enhance the monitoring of ROS generation in Parietal Epithelial Cells (PECs) under more physiologically relevant conditions, such as in reaction to HB- EGF stimulations. This could offer more precise insights into the initial mechanisms governing PEC activation, migration, and proliferation, thereby enriching our understanding of histopathological transitions.

Given that the uptake of nanoparticles through pinocytosis seems impractical in a microfluidic environment, our principal focus has been to create "smart surfaces" that enable imaging techniques specific to ROS detection. Hydrogen peroxide (H_2O_2), which is primarily generated by membrane-bound NADPH oxidase (Erard et al., 2018; Rhee, 2006), contributes significantly to membrane-specific ROS production. Additionally, H_2O_2 has the ability to diffuse quickly and freely both intracellularly and across membranes trough aquaporins (Bienert et al., 2006; Jaenen et al., 2021; Rhee, 2006). Consequently, engineering surfaces that allow for close-proximity imaging of nanoparticles to Parietal Epithelial Cells (PECs) presents a compelling alternative approach to internalized nanoparticles. Such surfaces should facilitate imaging of all nanoparticles on a unique plane, thereby increasing the total number of nanoparticles that can be concurrently imaged. The utility of these surfaces is further accentuated when coupled with Total Internal Reflection Fluorescence (TIRF) imaging techniques that increase SNR and reduces cell phototoxicity for long term imaging (Mattheyses et al., 2010).

We tested two methodologies for creating an active surface conducive to single nanoparticle imaging for ROS detection through TIRF imaging: the direct adsorption of nanoparticles on glass coverslips and the deposition of a thin gel layer embedded with nanoparticles. This project (section 3.3) was executed by Joanna DUFFRENE during her second-year master's internship, under my guidance.

3.3.1 Principle

We first investigated the nanoparticle deposition technique previously described (adsorption on plasma activated glass coverslips). Our goal was to identify the parameters that would optimize nanoparticle density, while preserving the capability for individual nanoparticle imaging, and being compatible with PEC culture.

Subsequently, we developed a method to produce thin (typically a µm thick) polyacrylamide gels embedding nanoparticles. This method offers a number of advantages, including enhanced biomimicry as stiffness is closer to the *in vivo* one, along with the possibility of studying cellular stress and cell contraction by measuring the Young Modulus, as done with Traction Force Microscopy (TFM), even if it makes implementation in organ-on-chip more challenging (Plotnikov et al., 2014).

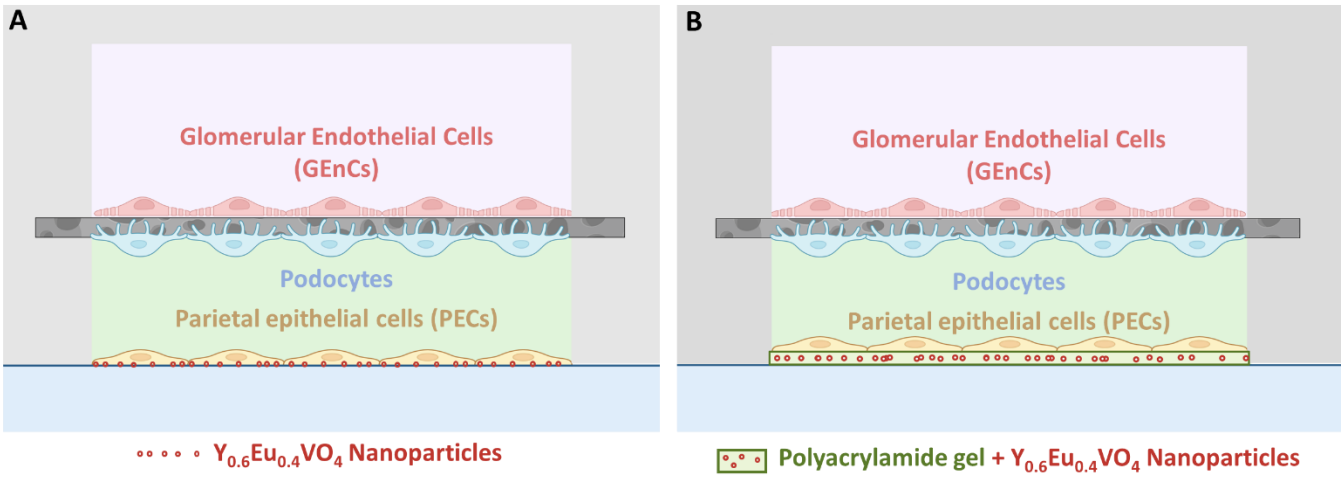

Figure 156: Schematic of active surfaces for ROS detection in our glomerulus-on-a-chip, (A) deposition of silica-coated $Y_{0.6}$ $Eu_{0.4}VO_4$ nanoparticles (small red dots) directly on the glass coverslip, below the parietal epithelial cells (PEC). (B) Deposition of a thin layer of polyacrylamide gel containing nanoparticles on the glass coverslip, on which PECs are grown.

These surfaces may offer various advantages compared to the previous internalization methods. For instance, these surfaces allow for imaging nanoparticles on a single focal plane, increasing the quantity of nanoparticles that can be imaged at the same time, and the mapping density. Furthermore, utilizing TIRF imaging technique is particularly effective for observing biological processes occurring near the cell membrane.

We first describe how integrating this optimized surface into the microfluidic chip could be done. Then, how do cells grow and behaves on such surfaces. The final phase of our study involved evaluating the sensitivity of these surfaces to varying concentrations of hydrogen peroxide, thereby assessing their effectiveness in ROS detection.

3.3.1.1 Methodology to prepare "smart surfaces" for ROS detection

Both methods use the same nanoparticles size sorting protocol to obtain monodisperse nanoparticles working solutions. 200 µl of nanoparticles stock solution (49 mM of vanadate) were diluted in ΔH_2O to obtain a final solution of 1mL. The working solution was sonicated and centrifuged (1000 g, 5 min) right before use to remove pelleted aggregates, and then sonicated again prior use.

To prepare nanoparticles adsorbed on glass surfaces, 25 mm glass coverslips (1.5 H#) were activated/sterilized by treatment with oxygen plasma (High power, 45 s; PDC-002-HPCE, Harrick Plasma) and placed in a 6-well plate. 800 μl of the working NP solution were diluted in 11.2 ml ΔH2O and sonicated. Then, 2 ml was added to each well under sterile conditions within 10 minutes of plasma treatment. After 1h deposition, coverslips were washed with ΔH_2O and PBS. For cell culture, 2ml of 10 μg/ml of human fibronectin (Corning) per well was added and incubated 1h at 37°C.

Thin gels, 30 kPa polyacrylamide (PAM) gels, were prepared by modifying a previously published protocol by Plotnikov and al (Plotnikov et al., 2014). A stock solution of acrylamide/bisacrylamide was made and stored at 4°C, while the working solution containing both the nanoparticles and initiator of polymerization (ammonium persulfate APS and Tetramethylethylenediamine TEMED) was prepared fresh before each experiment. Immediately after the addition of initiator, the working solution was vortexed and 20 µl was deposited between parafilm and plasma-activated glass coverslips under sterile conditions. After gel polymerization, the

coverslips were transferred to 6-well plates and washed 3 times with PBS. A coating (2ml of 10 μg/mL of human fibronectin) per well was added and incubated 1h at 37°C.

Both of these protocols obtained high density of nanoparticles (~0.2 NPs/µm^2, Figure 157). This is crucial to map extracellular ROS production near the PEC membrane, capturing the cellular response. Interestingly, whether embedded in thin polyacrylamide gels or adsorbed directly onto glass, the nanoparticles appear to reside within the depth of the field of view (~2 µm). This suggests that the gel layer applied to the glass surface is thin (≤ 2 µm).

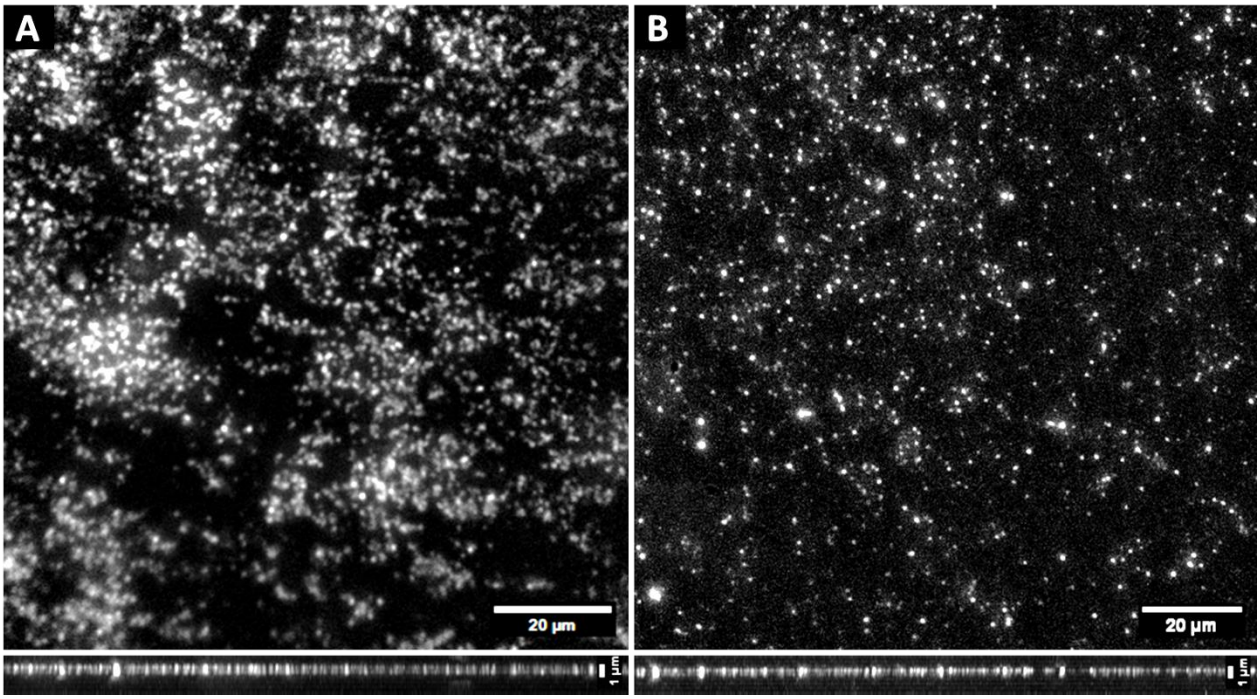

Figure 157: TIRF images of A) silica-coated $Y_{0.6}Eu_{0.4}VO_4$ nanoparticles deposed on a glass coverslip after plasma activation (45s) by adsorption for 1h, B) $Y_{0.6}Eu_{0.4}VO_4$ nanoparticles embedded in a 30 kPa polyacrylamide thin gel, (nanoparticles are excited at 396 nm, 15 W.cm^{-2}).

When examining nanoparticle dispersion, the adsorbed nanoparticles showed aggregation (Figure 157, A). This phenomenon was not observed for nanoparticles within polyacrylamide gels, with a more uniform distribution (Figure 157, B).

3.3.1.2 Cell culture compatibility.

Conditionally immortalized human parietal epithelial cells (CihPECs) (MTA C. Meyer-Schwesinger, University Medical Center Hamburg-Eppendorf) cell line was generated through the introduction of the temperature-sensitive SV40-T gene *via* transduction in isolated primary human PECs. These cells proliferate at a "permissive" temperature of 33°C, and they undergo growth arrest and exhibit markers of differentiated PECs found *in vivo* at 37°C. CihPECs were cultured in 1:1 Endothelial Growth Medium EGM-MV/RPMI with supplement (Bovine Brain Extract (BBE), hEGF, Insulin-Transferrin-Selenium (ITS), 10 mM HEPES, sodium pyruvate, HC, GA, PS) and 7,5% FBS at 5% CO2, and kept at 33°C for passaging.

CihPECs were added to both substrates and grown at 33°C, in 5% CO_2 until confluence. After cells reached confluence, cells were differentiated for a week at 37°C, as they would in glomeruli-on-chips.

Nanoparticle imaging was then performed in a 30 mM HBSS/HEPES buffer solution on the previously described microscope (Appendix: 4.4.1), with TIRF illumination at 396 nm.

Directly adsorbed NPs were difficult to observe by TIRF with CihPECs grown for several days on the surface. By performing a z-stack of the samples with an epi-fluorescence illumination coupled with deconvolution (Figure 158, C), we observed NPs at different levels across the cells, even though these particles were initially deposited on the glass flat surface. NPs were thus internalized during the several days in presence of cells. consistently with the literature, reporting that certain cell types have been shown to endocyte inorganic NPs adsorbed on surfaces (J. A. Yang et al., 2013). CihPECs internalize NPs as early as 3 days in culture, thus direct deposition is not suitable for our microsystems, where cells are kept in culture for around ten days.

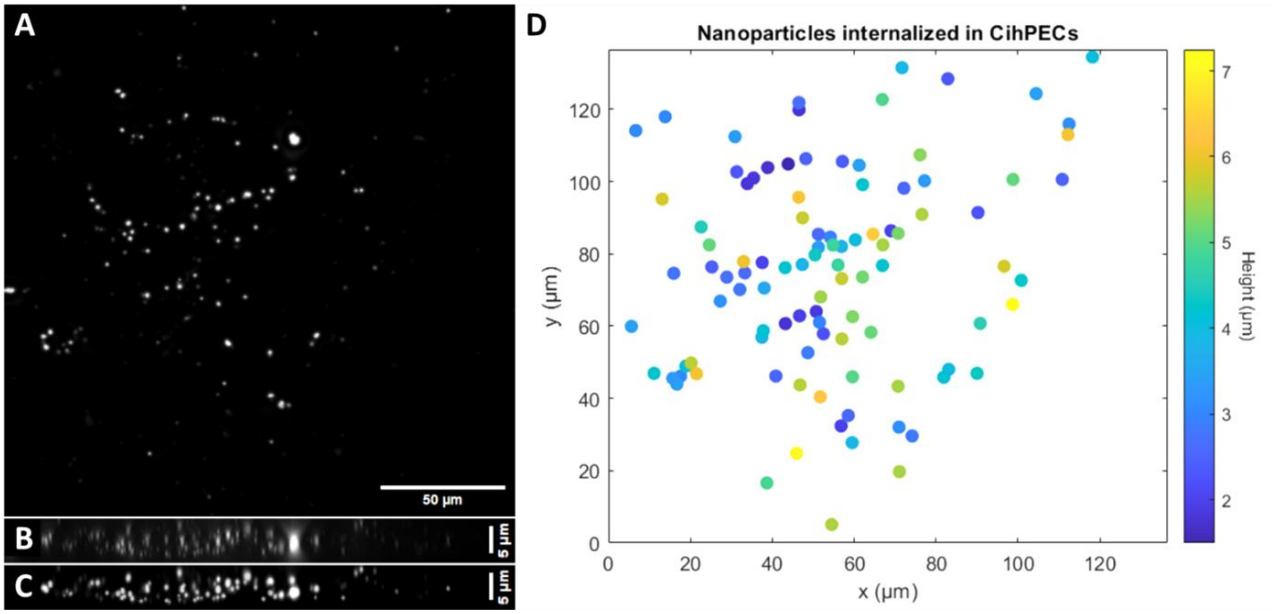

Figure 158: A) Z-stack of $Y_{0.6}Eu_{0.4}VO_4$ nanoparticles within CihPECs grown on nanoparticles and fibronectin coated glass coverslips, B) XZ view, C) deconvolved XZ view, and D) color coding of nanoparticles height in the Z -stack (60X magnification, epi-fluorescence, microscopy at 396 nm, 15 $W.cm^{-2}$).

In contrast, TIRF microscopic observation of nanoparticles dispersed in thin gels was not impacted by cell culture on the substrate for several days. PAM gel thus prevents NPs from being internalized by CihPECs, keeping all nanoparticles in the same plane (Figure 159). CihPECs normally grow to confluence on these gels and to have sizes and morphologies similar to those obtained on glass, for 10 days in culture. CihPECS expressed differentiation markers (Claudin-1) indicating a correct differentiation with the formation of tight junction from the monolayer of cells.

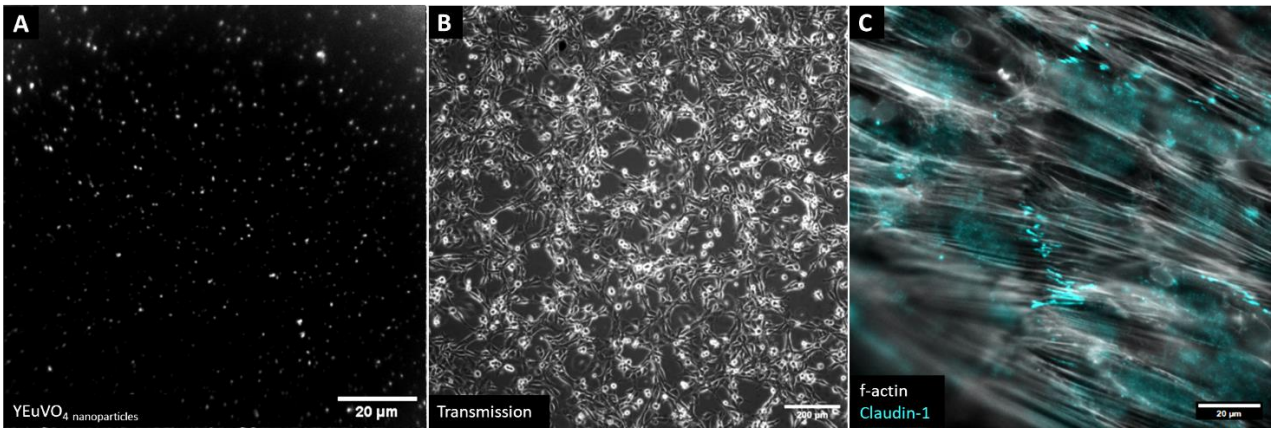

Figure 159: A) TIRF image of $Y_{0.6}Eu_{0.4}VO_4$ nanoparticles embedded in a 30 kPa polyacrylamide thin gel, (60X, nanoparticles are excited at 396 nm, 15 W.cm^{-2}), B) Phase contrast transmission image of CihPECS grown on such gels for 10 days (10X), C) Immunofluorescence of CihPECs grown confluently (~3 days) and differentiated for 7 days, stained for f-actin (phalloidin rhodamine) and claudin-1 (Alexa Fluor Plus 488) of CihPECs on such gels (60X, epifluorescence).

We thoroughly characterized the system through the analysis of the effect of the PAM gel substrate on CihPECs differentiation, or nuclear size evolution.

3.3.2 Effect of the sensor substrate on CihPECs differentiation

3.3.2.1 CihPECs grown on glass vs. on PAM gels

Tight junction formation and differentiation marker expression (Claudin-1) was quantified using immunostaining and confocal imaging in different conditions (basal EGF deprived medium and EGF enriched medium). Figure 160 shows typical confocal images obtained from the same different experimental conditions.

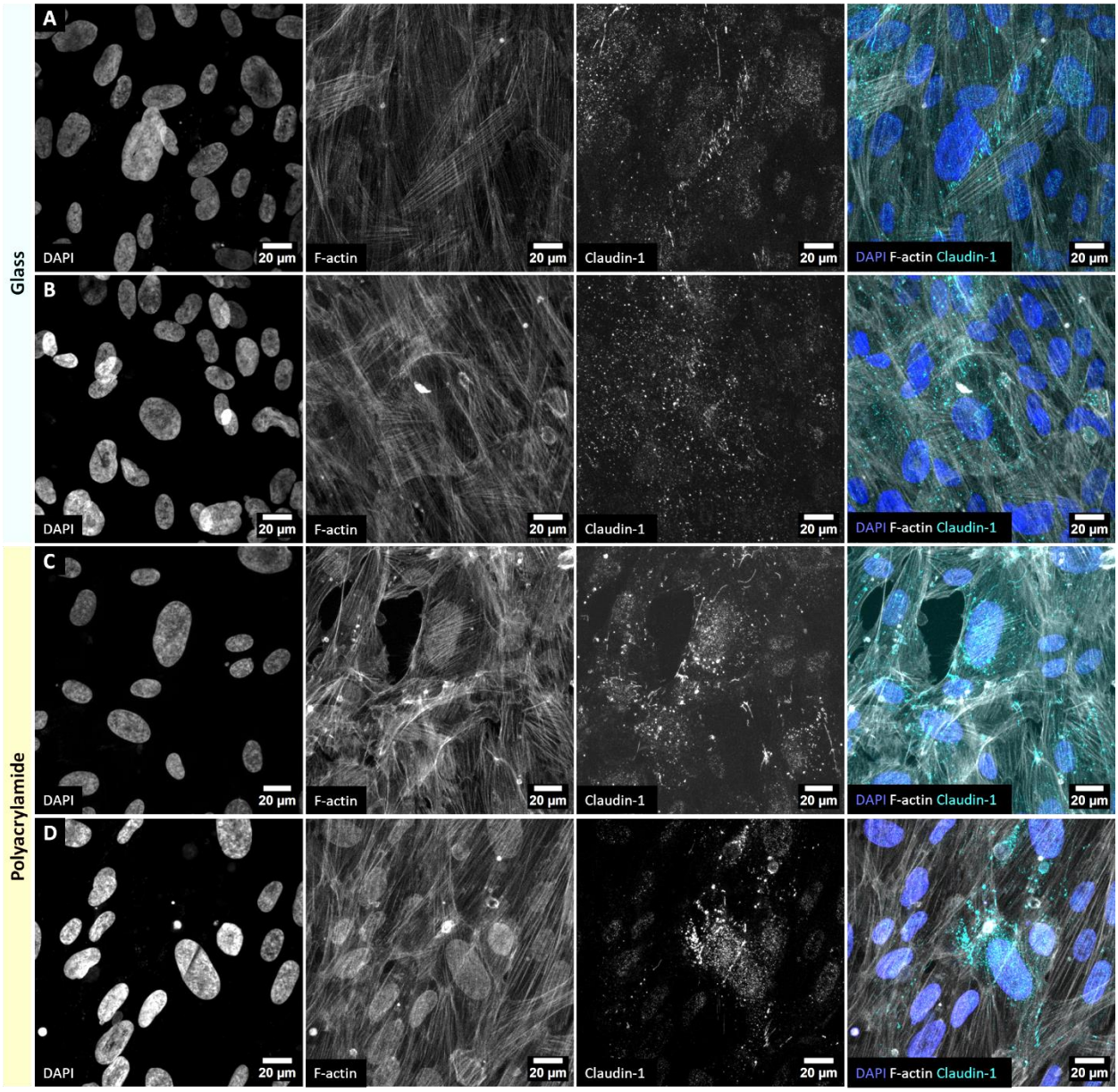

Figure 160: Confocal images (z-stack projections) of CihPECs grown confluently (~3 days) and differentiated for 7 days on fibronectin coated glass coverslips A&B) or PAM thin gels coated coverslips C&D) stained for nucleus (DAPI), f-actin (Phalloidine rhodamine red), and Claudin-1 (Alexa Fluo Plus 488), cultured either in EGF deprived conditions A&C) (basal media) or EGF enrichment B&D) (63X).

We can first observe that CihPECs reached good levels of confluence (~100%) on both glass and PAM gels. No visible difference in morphology was observed. However a difference in claudin-1 expression was observed and further quantified in the next section.

3.3.2.2 Quantification

The nuclear and claudin-1 channels were extracted and segmented using a simple threshold method (ImageJ). Binarized images were then analyzed with different parameters. We measured nucleus sizes with the constrain of a minimal object area of 10 µm^2 to get rid of isolated pixels. We compared the object Feret's diameter, area, and perimeter. Feret's diameter corresponds to the maximum caliper, or the longest distance between any two points along the selection boundary.

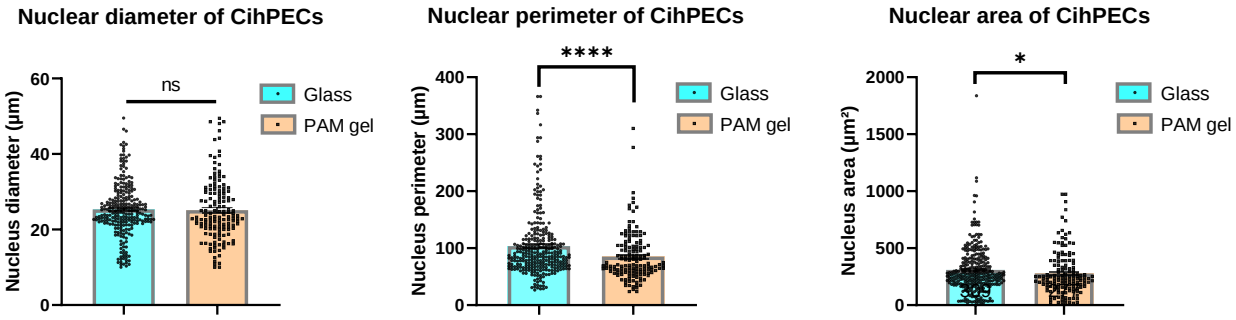

Figure 161: Distributions of cell nuclear diameter, perimeter and area obtained from confocal images simple nuclear signal thresholding for both CihPECs grown either on glass coverslips or on PAM gels (error bars are SEM, stars from Kolmogorov-Smirnov t-test, n=8).

An average area of 276 ± 15 and 309 ± 3 μm^2, an average perimeter of 85 ± 3 and 103 ± 3 μm, and an average diameter of 25 ± 0.7 and 25 ± 0.4 μm were found for CihPECs on PAM gels and on glass respectively. No significant diameter difference was observed, but a significant area and perimeter difference between cells grown on PAM gels vs glass. The diminution of the substrate stiffness could lead to this nucleus size diminution.

We quantified Claudin-1 signal at cell-cell junction, from binarized images (Figure 162). Object with a circularity above 0.3 (ratio = $\frac{Ferret\ min}{Ferret\ max}$) and smaller than 5 µm² were also removed. We identified patches of claudin-1 at cellular junctions.

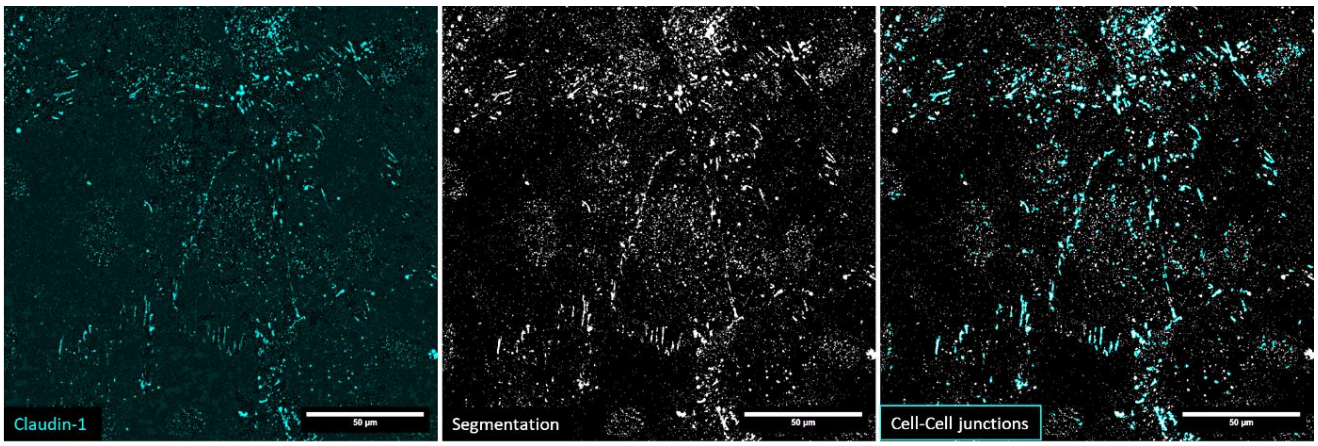

Figure 162: Left, confocal image of CihPECs grown confluently (~3 days) and differentiated for 7 days on fibronectin coated glass coverslips stained for Claudin-1 (Alexa Fluo Plus 488), cultured in EGF deprived conditions, middle, thresholding based segmentation of Claudin-1(binary image), right, adherent junction selection (cyan) based of circularity and size parameters (63X).

Quantifying the total claudin-1 area at cell junction area per image, in which cells are fully confluent on different substrates, and in EGF enriched or basal medium, yields the following results (Figure 163).

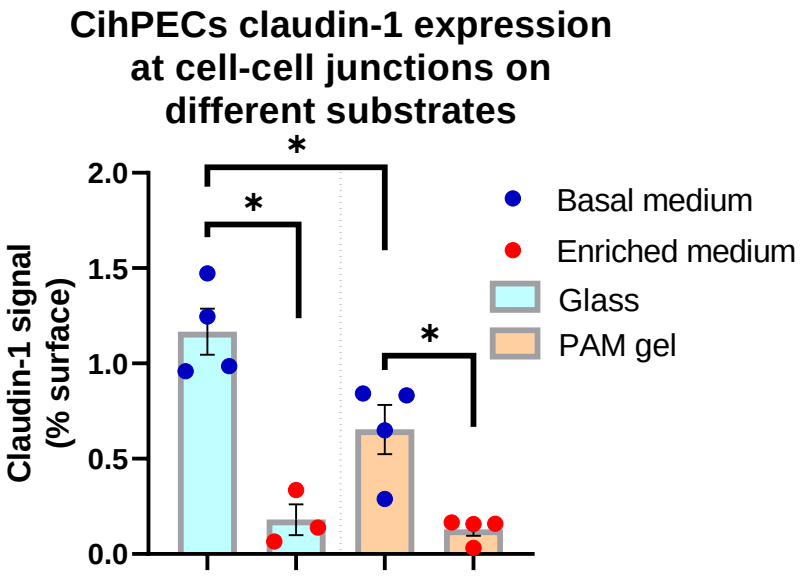

Figure 163: Surface quantification of Claudin-1 signal at cell-cell junction (in % of total image area) for CihPECs grown confluently (~3 days) and differentiated for 7 days on fibronectin coated glass coverslips or PAM thin gels coated coverslips cultured either in EGF deprived conditions (basal media) or EGF enrichment (error bars are SEM, stars indicate t-test significance).

A noteworthy decrease in claudin-1 expression at cell junctions was observed when cultivating CihPECs on Polyacrylamide (PAM) gels, and when the cells were grown in a medium supplemented with EGF. We have previously observed in CirPECs (derived from rats) that an excess of EGF in the culture medium enhances both cell proliferation and migration. Therefore, the observed reduction in claudin-1 at intercellular junctions could be related to the cells proliferative state, which may interfere with their ability to form a tightly connected epithelial layer as they undergo epithelial to mesenchymal transition (EMT, see section: 1.2.2). On PAM gels PECs had a slightly different behavior.

3.3.3 Sensor integration in the microsystem

We incorporated the sensor surface polyacrylamide gel, embedded with nanoparticles (NPs), into the urinary microchannel of our microfluidic device (Figure 156, B).

A crucial factor in this implementation is the surface thickness. Given that the urinary microchannel has a height of 50 µm, the aim was to create a gel with a thickness of less than 10 µm to prevent obstruction of fluid flow within the channel. To achieve this target thickness while maintaining uniformity throughout the channel, we opted for a spin-coating technique directly applied within the microchannel itself before systems final assembly. By fine-tuning various parameters of the spin-coater—such as the rotations per minute (rpm), acceleration, and duration—we were able to adjust the gel thickness to less than 1 µm thick (Figure 164).

The embedded gel in the microchips was characterized by confocal imaging with a fluorescent gel (Rhodamine 6G, Sigma) and by line scanning confocal optical coherence tomography (LC-OCT).

In PAM gels the nanoparticle volume was substituted with an equal volume of a 1mg/ml rhodamine solution (Figure 164). After activating the glass coverslips with plasma, 2 µl of PAM gel were placed at the center of the microchannels and then spin-coated for one minute at 800 rpm with an acceleration of 50 rpm. The PAM gel was added after allowing a few minutes for polymerization,

allowing viscosity to increase due to polymerization, preventing its ejection when spin-coating starts. A thin gel layer was successfully formed (>1 µm Figure 164).

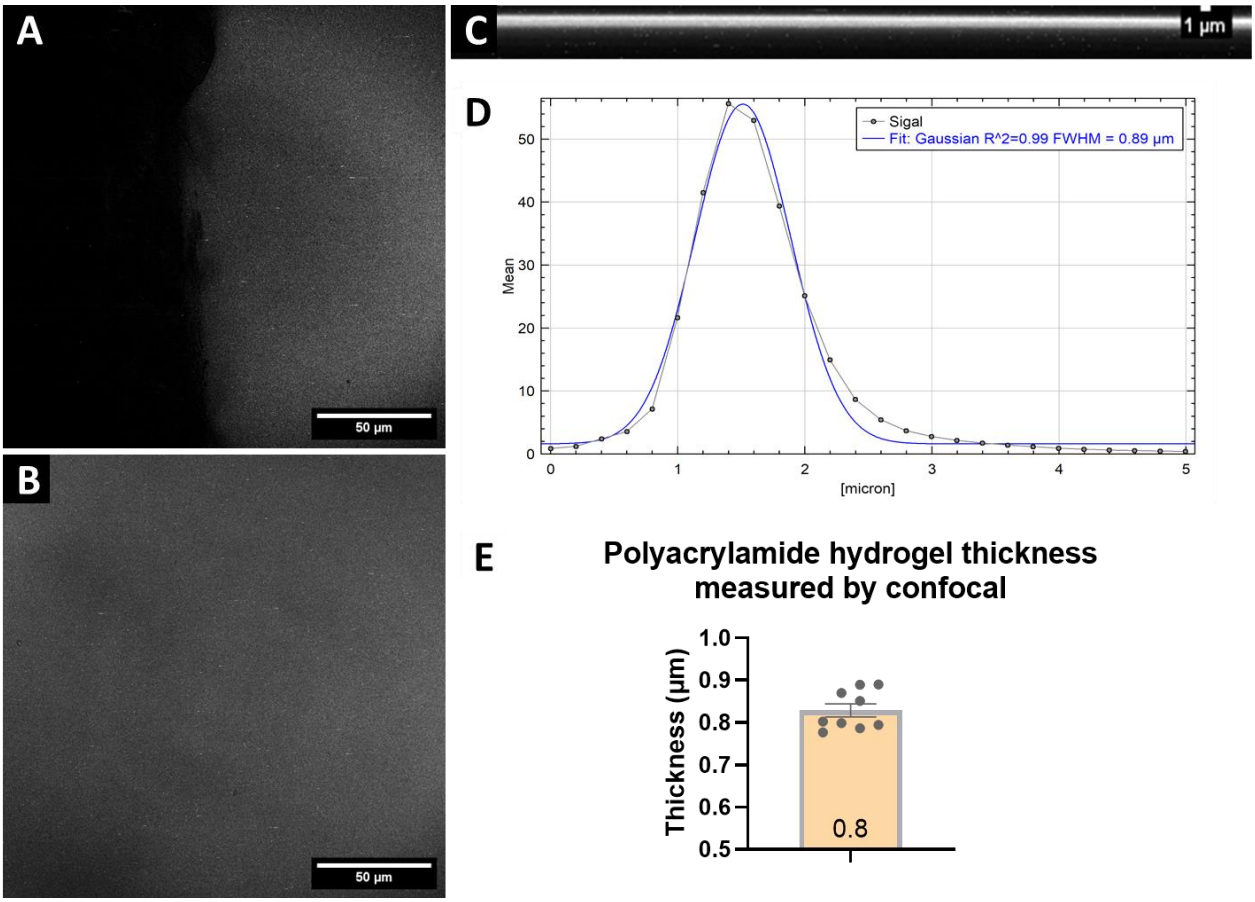

Figure 164: A,B, & C) Confocal images of Rhodamine 6G loaded PAM gels spin coated at the glass coverslip layer of the microsystems, A) channel border view, B) center channel view, C) XZ view (magnification 63X), D) Gaussian fit of the z-axis profile intensity distribution, E) thickness distribution of PAM gels (error bars are SEM).

The microsystems were then imaged with a confocal microscope to analyze the thickness of the gel layer. This enabled us to obtain a Z-axis projection of the rhodamine intensity. A Gaussian fit of the intensity distribution gives an average thickness of $0.82 \pm 0.02\ \mu m$ (n=9).

To support the results obtained with the confocal microscope, we also imaged the microsystems using line scanning confocal optical coherence tomography (LC-OCT, Figure 165). We notice the absence of a visible interface between the glass and the urinary canal. The lack of such a demarcation indicates that our gel thickness is close or less than the OCT axial resolution (~1µm).

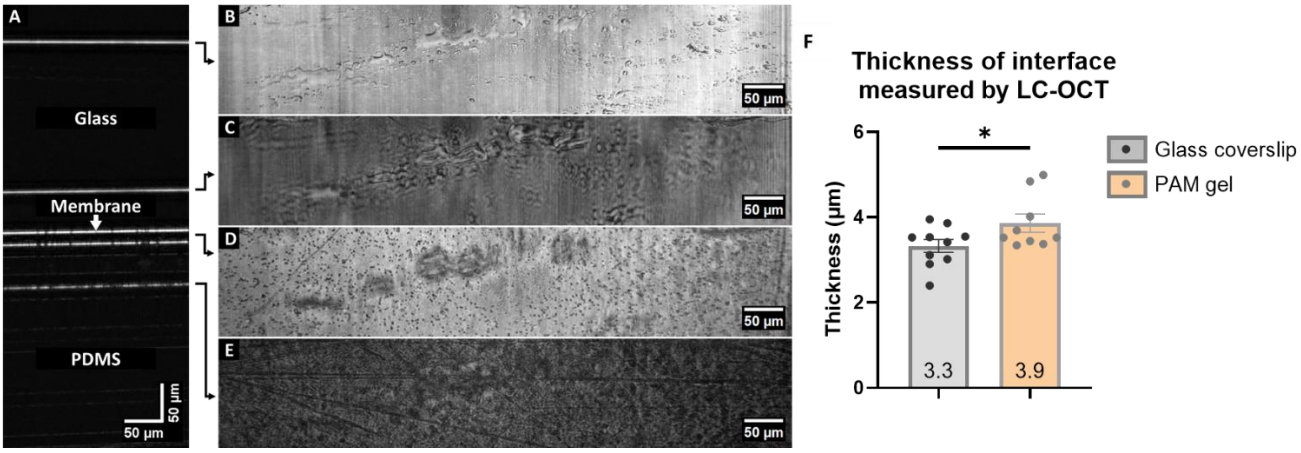

Figure 165: A,B,C,D, & E) LC-OCT images of a microsystem with a PAM thin gel with all the interfaces lateral views visible (1 for each interface), F) thickness measured from the bottom of the glass coverslip interface with and without PAM gels (stars form t-test, error bars are SEM).

We nevertheless quantified the interface thickness obtained from LC-OCT and found a significant increase in thickness for systems embedding a PAM thin gel at the bottom of the urinary channel (0.6 µm increase with PAM gels).

Overall, this indicates that embedding a submicrometric PAM gel in organ-on-chip microsystem was possible, and with a good repeatability.

3.3.4 ROS detection using NPs embedded in PAM gels

Unlike the direct deposition alternative or cellular internalization, with the PAM gel method, NPs are not in direct contact with cell membranes and the extracellular medium. Nevertheless, PAM gel is porous and may allow the diffusion of small molecules such as H_2O_2. We thus checked that H_2O_2 is indeed able to diffuse through the gel to re-oxidize the NPs.

Recently, colleagues from PMC (Laboratoire de la matière condensée, Ecole Polytechnique; Thierry Gacoin, Raphael Vieira Perrella, and LOB; Robin Khuner) have developed a new synthesis protocol for $YEuVO_4$ nanoparticles.

A first step is carried out by reacting rare earth nitrates (Eu/Y: 0.05/0.95) with urea in a water/ethylene glycol mixture (60%) at 95°C. Under these conditions, the urea is gradually hydrolyzed to form carbonate ions. The slow addition of these ions, which will interact with europium or yttrium ions, will lead to the nucleation and controlled growth of dispersed nanoparticles. After purification, the nanoparticles are brought into contact with ammonium metavanadate, also in an ethylene glycol mixture (60%) at 100°C, where the carbonate ions are gradually replaced by metavanadate, giving YVO_4:Eu nanoparticles (there is no longer any carbonate, the reaction is complete).

Nanoparticles new synthesis route had a major impact on their properties. These new NPs are round and more porous, as well as being larger and more monodisperse (around 100 nm) than the previous synthesis (around 30 nm). A TEM images of these nanoparticles is shown in Figure 166.

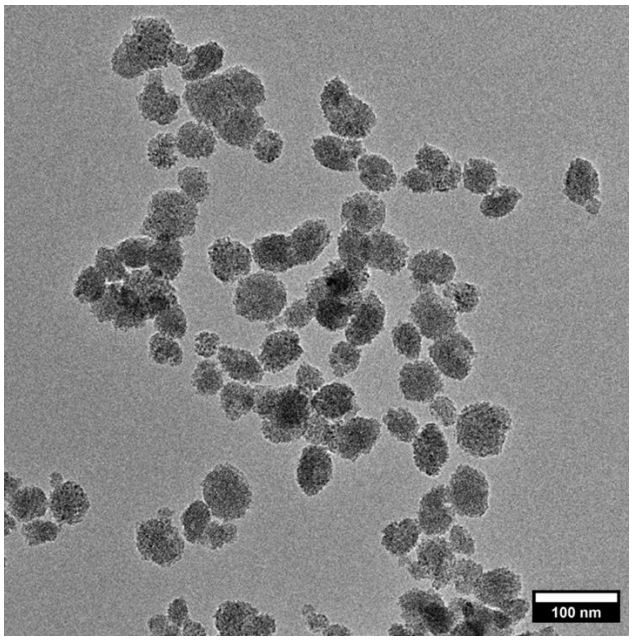

Figure 166: TEM image of $Y_{0.95}$ $Eu_{0.05}VO_4$ nanoparticles.

This monodisperse size distribution is important to obtain a reliable ROS mapping. We thus decided to perform H_2O_2 detection in PAM gels using these nanoparticles and in presence of a confluent cell layer on this PAM gel.

The preparation of the PAM gels containing the NPs was described previously, and the H_2O_2 response tests followed the same protocol as in section: 3.2.3.5. Cells were grown for ~3 days to confluence and differentiated for a week on thin gels before H_2O_2 stimulations. For re-oxidation detection experiments, nanoparticles were photoreduced for 3 minutes at ~19 W.cm^{-2}, oxidant detection was performed by addition of 0-10-100-500μM H_2O_2, and nanoparticles photoluminescence intensity was tracked quantitatively using the same Gaussian integration technique. The absence of cellular photodamages was controlled using trypan blue viability assay.

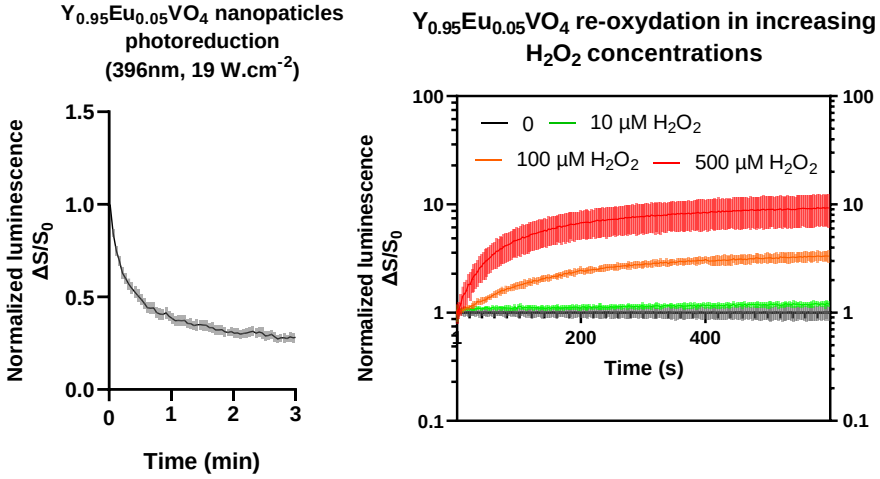

Figure 167: Left, photoreduction of $Y_{0.95}$ $Eu_{0.05}VO_4$ nanoparticles using TIRF illumination (396 nm at ~19 W.cm^{-2}), right, luminescence tracking after H_2O_2 addition to the CihPECs/polyacrylamide gel layer (error bars are SEM).

The observations made from monitoring responses to H_2O_2 addition clearly indicate a

concentration-dependent recovery of luminescence (*Figure 167*). Cells and in particular the cell junctions, do not appear to prevent H_2O_2 diffusion into the PAM gel.

While the range of photoreduction remained roughly the same as in previous experiments—accounting for about 60% of the signal reduction but with TIRF illumination—the luminescence recovery saw a substantial increase, by an order of magnitude, compared to the earlier nanoparticle synthesis protocol. This suggests that these newly synthesized nanoparticles are more suitable for quantitative H_2O_2 detection, given their expanded dynamic range for photoreduction and oxidation.

The PAM gel thus appears to be permeable to H_2O_2, confirming that an active surface made of PAM gel embedded with nanoparticles is both sensitive and viable for measuring membrane-associated H_2O_2 production by CihPECs in our microfluidic systems, within a concentration range of at least 10 μM to 500 μM.

Overall, this methodology had the benefit of achieving a uniform distribution of nanoparticles in thin polyacrylamide gels, with thicknesses below 1 μm. This makes it particularly advantageous for imaging individual nanoparticles. The technique accommodates the use of TIRF imaging, which is less phototoxic and thus better suited for long-term live cell imaging, as well as offering easy integration into organ-on-chip (OoC) platforms as a ROS detection surface, on which CihPECs were capable of both long-term growth and differentiation.

3.4 Conclusion

We know from previous work (Thi Thuy Hoang thesis, LOB 2022) that when CD9 proteins are removed in mPECs cells, several differences from the wild-type cells emerge. The clusters of EGFR have a larger area and diameter in CD9-KO mPECs than in normal PEC cells. This is further supported by SPT tracking data showing larger confinement domains for EGFRs in shCD9 PEC cells, without significantly affecting the force or diffusion properties of these receptors.

The count and density of EGF molecules in these clusters are lower in shCD9 mPECs. EGFRs mainly exist in smaller domains or clusters in both cell types, but in shCD9 mPECs, the number of receptors is only about half that in normal mPECs. Furthermore, there is more overlap between CD9 and EGFR clusters than with transferrin and EGFR, further supporting the idea that EGFRs prefer CD9-enriched domains. Hence we knew that EGFRs likely inhabit CD9-rich areas, or tetraspanin-enriched domains, on the cell membrane. When CD9 is depleted, these receptors internalized, resulting in fewer receptors in shCD9 mPECs. The size of these domains also appears to increase, possibly due to less compact tetraspanin domains.

Our first work aimed at understanding how EGFR and CD9 interact upon HB-EGF stimulations, with a focus on their organization within the nanodomains they form. We revealed though dSTORM imaging, that with HB-EGF stimulation, both EGFR and CD9 localizations per cell area decreased. However, the precision of their localization remained consistent, indicating an actual reduction in molecules and not a compromise in imaging quality. This finding is in agreement with previous work done on the same cells by Western-Blot semi-quantitative analysis showing a reduction in EGFR total number after HB-EGF stimulations.

EGFR and CD9 were observed to form small clusters (or membrane nanodomains), the numbers of which decrease with HB-EGF stimulation. The size of EGFR clusters decreased with HB-EGF stimulation, while the CD9 clusters size did not change. HB-EGF stimulation resulted in denser

packing of EGFR molecules within clusters. This suggested that EGFR nanodomains change upon stimulation, or that EGFR relocate to another type of membrane domains.

An interesting observation was that the size and molecule density of both receptor cluster domains seemed to converge post-stimulation, hinting at a potential interaction between EGFR and CD9. Furthermore, advanced dSTORM molecules localization analysis indicated increased co-localization between EGFR and CD9 upon HB-EGF stimulation which further supports our hypothesis that active EGFR translocate in CD9 enriched domains, and that CD9 deletion could have implication in downstream EGF signaling in PECs.

We used Eu-doped nanoparticles to gauge intracellular hydrogen peroxide levels in wild-type and CD9 deficient mPECs following distinct HB-EGF and PDGF-BB stimulations. When assessing the intracellular H_2O_2 concentration in response to HB-EGF in wild-type mPECs, the levels rapidly surpassed the sensor calibration threshold of 100 µM. This was not expected as previous H_2O_2 signaling measurements in cancer cells for example reached levels as high as a few tens of µM produced (Bouzigues et al., 2014). However, a comparative analysis between WT and shCD9 mPECs during the initial 10 minutes post HB-EGF stimulation revealed a marked reduction in H_2O_2 production in CD9-KO mPECs.

Overall, these results support the hypothesis and previous findings suggesting that in PECs CD9 at least partially organizes EGFR confinement in nanodomains and regulates its signaling. Since CD9 depletion has been shown to have a protective phenotype for RPGN and FSGS progression (Lazareth et al., 2019), and that EGF is absent in the Bowman space, this provides molecular basis on the regulation of EGF dependent pathological transition.

General conclusion

Glomerulonephritis and glomerulosclerosis correspond to acute or chronic damage to the glomerulus. During these pathologies which are of various causes, there is an activation of the resident glomerular cells (podocytes, parietal epithelial cells) which undergo phenotypic modifications (proliferation, migration) leading to glomerular destruction and ultimately to renal insufficiency. Potential factors that lead to this uncontrolled activation of glomerular cells include CD9, HB-EGF and PDGF, but remain imperfectly understood.

Such mechanisms are complex to decipher using a standard procedure such as simple cell culture-based experiments, animal models or from clinical cues only. We believe that this issue can be addressed by modeling the complex environment of the glomerulus using a systematic organ-on-chip approach with advanced quantitative measurement, to identify mechanisms leading to pathophysiological responses, at the cell and organ scales.

We thus have developed an organ-on-chip microfluidic system mimicking the glomerular organization and cell types, with advanced imaging capabilities. Using these systems, we first showed that it is possible to control the co-culture of the 3 cell type/layer systems mimicking the glomerular organization by using conditionally immortalized glomerular endothelial, podocytes and parietal epithelial cell lines. Using gravity-driven perfusion, we were able to easily maintain these cells in culture in our microfluidic chip for more than 2 weeks allowing proper cell expression of differentiation markers typically found *in vivo*. Cells also secreted their own extracellular matrix with expression profiles consistent with those expected of a glomerular basement membrane. We also showed that the glomerulus-on-chip retained filtration properties which included both a molecular size and protein (albumin) selectivity.

We have further investigated the effects of EGF on such cells. We showed that supplementing the medium with EGF induced an increased PECs proliferation both in two dimensions and in our organ-on-chip system. This observation correlated with a reduced albumin and small molecular weight dextran filtration capabilities of the glomerulus-on-chip. PECs also showed reduced tight junction formation in simple cultures when exposed to EGF, possibly indicating an EMT transition. The proliferation of PECs eventually lead to the invasion of the urinary chamber on-chip and even destabilization on the biomimetic glomerular filtration barrier. This recapitulates well the characteristics of PECs during RPGN and FSGS progression observed *in vivo*. We thus have the access to a fully biomimetic system in which we can trigger the diseases, and thus study the mechanism leading to RPGN and FSGS progression.

Concomitantly, we investigated the molecular mechanisms that could lead to PECs activation by the EGF pathway. Using a single molecule super-resolution imaging technique (dSTORM), we showed that CD9 rich areas are preferential sites for EGFR translocation during the receptor activation by HB-EGF in PECs. We also used ROS-sensitives nanoparticle probes to detect quantitatively the levels of H_2O_2 signaling induced by HB-EGF both in wild type and CD9 deficient PECs. We showed that HB-EGF signaling was impaired in CD9-deficient PECs. CD9 therefore regulates EGFR organization and its signaling.

These findings are summarized in Figure 168.

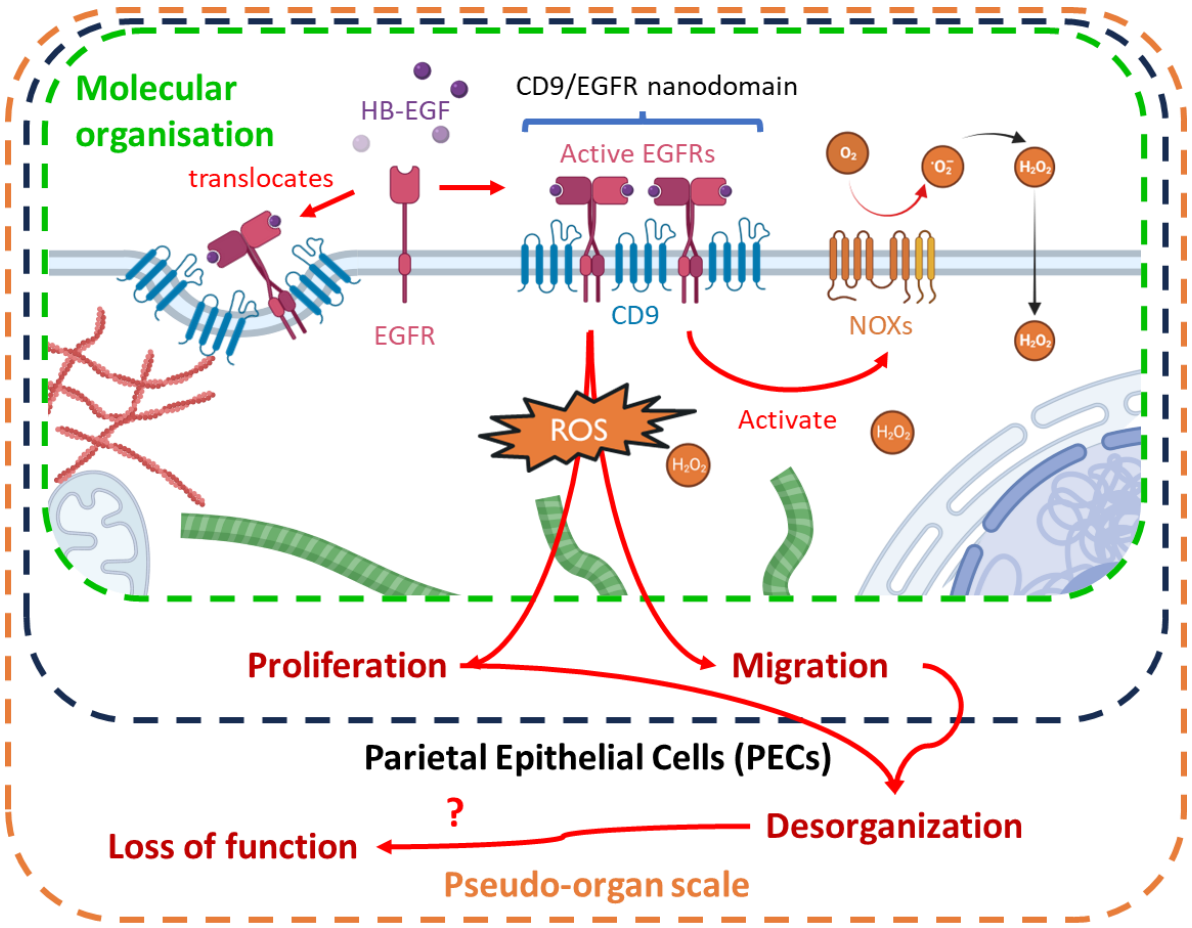

Figure 168: Molecular and cellular mechanisms implicating CD9 and EGF signaling in PECs and role at the pseudo-organ scale, possibly explaining RPGN and FSGS progression.

Finally, we developed innovative surfaces for ROS detection in our glomerulus-on-chip platform. We can now associate powerful *in situ* measurement tools with microsystems, which has never been achieved before. Based on this system, we could investigate ROS signaling in parietal epithelial cells directly in a glomerulus-on-chip and compare production levels with those of simple PEC monoculture. Hopefully, this will enable us to decipher cues leading to pathological transition in RPGN and FSGS.

Our microfluidic biomimetic framework aims to bridge the gap between *in vitro* and *in vivo* studies by bringing a relevant complexity (*e.g.* 3D microenvironment and controlled co-cultures) while answering a biological question at the "mesoscale" of a tissue construct confined in an environment allowing the quantitative study of molecular, cellular, and up to the tissue responses.

RPGN and FSGS are terminal diseases and have no effective treatments to date, with the exception of transplantation. This work could have important medical and ethical consequences. In short term, it could first constitute a valuable tool to support biomedical studies. It could indeed provide information that is only accessible through *in vivo* studies, whose sacrifices could thus be limited. Our technology thus addresses the growing pressure for economic and ethical reasons to limit the use of animal models. In medium term, our technology could provide quantitative data, and be adapted to a large range of stimuli, *e.g.* for drug screening, and could establish itself as a new reference approach in the processes of understanding the molecular basis of complex pathologies.

A molecular Toolkit for mechanisms of PEC activation

dSTORM to probe organization

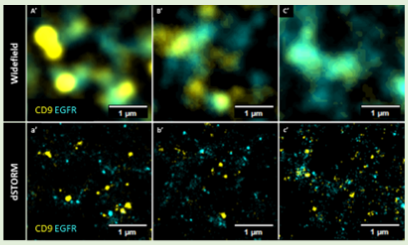

Single nanoparticles for ROS detection

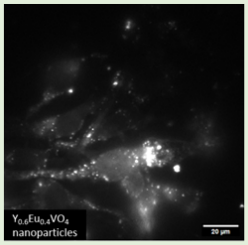

+HB-EGF on PECs

Organization	Function
CD9 organizes EGFR in membrane nanodomains	CD9 regulates EGFR signaling

RPGN and FSGS progression

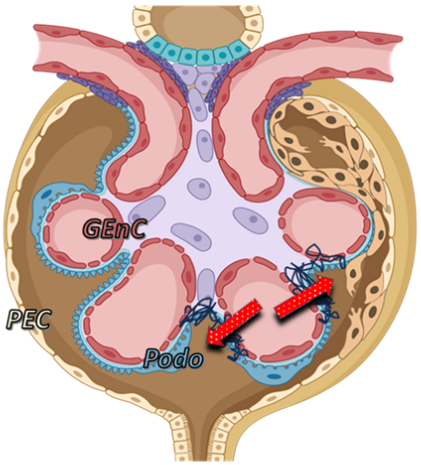

1. *Glomerular filtration barrier destabilization*
2. *Possible leakage of cues responsible for PEC activation: EGF, HB-EGF…*
3. *PEC proliferation, migration leading to invasion and crescent formation*

A multi-scale approach to decipher complex pathologies ?

A glomerulus-on-chip to model renal disease progression

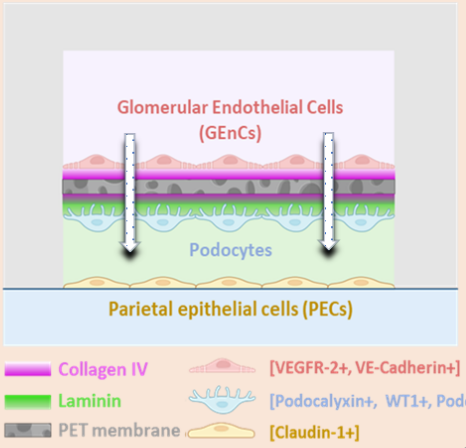

Physiological filtration function :

- **molecules from 20 to 150 kDa**
- **Albumin glomerular sieving coefficient 0.005 (~*in vivo*)**

+ EGF

Organization	Function
GEnCs : + Fenestration formation PECs: ↘ Claudin-1 tight junctions ↗ Proliferation, Migration & Invasion	↘ Small molecule filtration ↘ Albumin filtration

Appendix

4.1 Protocols for cell cultures

HeLa cells are cultured in Dulbecco/Vogt Modified Eagle's Minimal essential medium (DMEM GlutaMAX, Gibco) medium supplemented with 10% Fetal Bovine Serum (FBS, Gibco), and 100 units/ml Penicillin/Streptomycin (PS, Invitrogen) at 5% CO_2, and 37°C.

HUVECs are cultured in Endothelial Cell Basal Medium (ECBM, Promocell) medium with supplement; Endothelial Cell Growth Factor (ECGS), human recombinant Epidermal Growth Factor (hEGF), HydroCortisone (HC), Heparin and human recombinant Fibroblast Growth Factor (hFGF), 5% FBS, and 100 units/ml PS at 5% CO_2, and 37°C.

CiPodocytes are cultured in Roswell Park Memorial Institute medium (RPMI 1640 GlutaMAX, Gibco) medium supplemented with 10% FBS, and 100 units/ml PS at 5% CO_2, and 33°C.

Primary mouse Parietal Epithelial Cells (mPECs) were cultured at 5% CO_2, and 37°C in supplemented ECBM with PS and 20% FBS until 70% of confluence before passaging.

CiGEnCs are cultured in Endothelial Growth Medium 2 (EGM2-MV, Lonza) with supplement; hFGF, Vascular Endothelial Growth Factor (VEGF), hEGF, HC, Ascorbic Acid (AA), heparin, Gentamicin sulfate/Amphotericin B (GA), and a recombinant analog of Insulin-like Growth Factor (R3-IGF), and 5% FBS at 5% CO_2, and kept at 33°C.

CirPECs and CihPECs are cultured in 1:1 Endothelial Growth Medium EGM-MV/RPMI with supplement; Bovine Brain Extract (BBE), hEGF, Insulin-Transferrin-Selenium (ITS), 10 mM HEPES, sodium pyruvate, HC, GA, PS, and 7,5% FBS at 5% CO_2, and kept at 33°C.

All the cell lines maintenance cultures were passaged once a week by gentle trypsinization by using trysin/EDTA 0.05% (Thermo Fisher Scientific). After cells are dissociated and resuspended in culture medium, and before cells are seeded in the different channels of the microsystems, centrifugation allows for a high cell concentration (~10^7 cells/ml).

4.2 Collagen I membranes observed by SEM

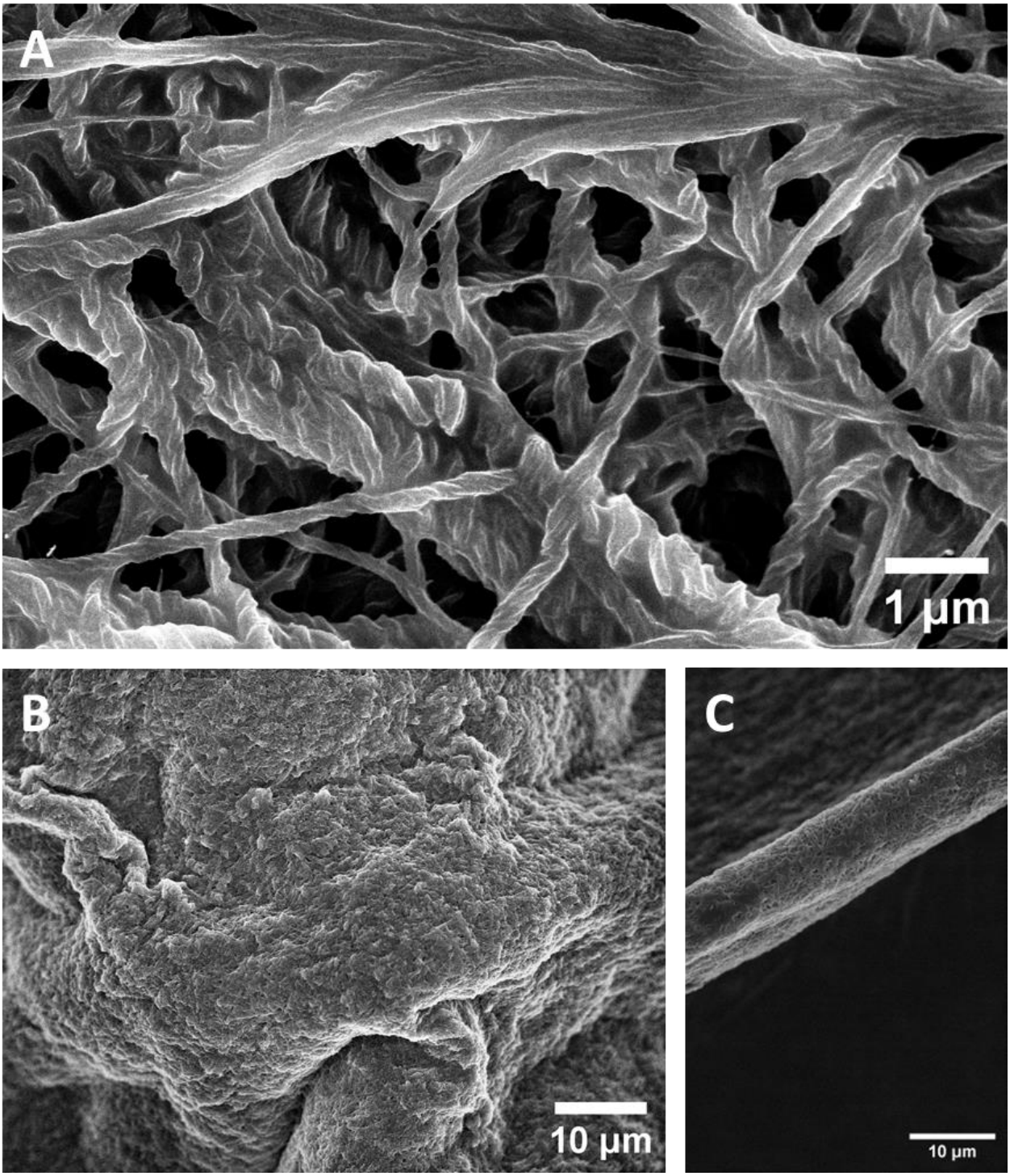

Figure 169: SEM images of Collagen I membranes at high (A) or low (B&C) magnification, A) Collagen fibril bundling fibers up to a few µm diameter, B) membrane ruffles, and C) edge view of a membrane.

4.3 Differentiated CiPodocytes grown on Collagen I membranes

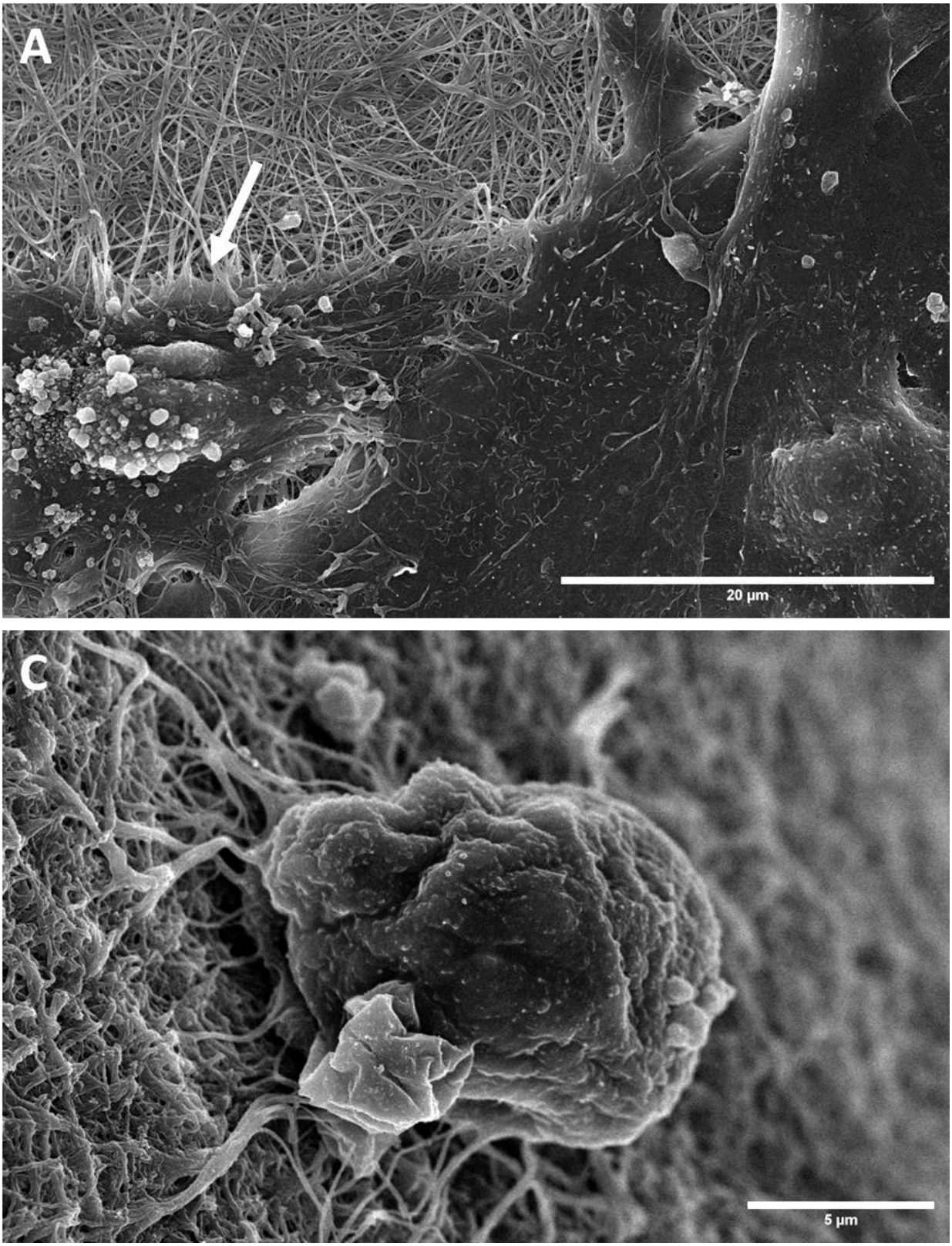

Figure 170: A) Differentiated CiPodocyte exhibiting pre-apoptotic like phenotype B) necrotic CiPodocyte

4.4 Optical setups and list of antibodies and chemicals used for imaging

4.4.1 Optical microscopy set-ups

4.4.1.1 Single nanoparticles imaging/TIRF setup and live imaging setup

An Olympus (IX-71) is equipped with a 60X N.A.=1.42 and a 100X, N.A.=1.49, oil immersion objective and a ImageEM X2 EM-CCD camera (Hamamatsu). The microscope is equipped with a with a live-cell imaging system (whole microscope is enclosed in a temperature controlled chamber and only the stage top is CO_2 and humidity buffered). A X,Y,Z translation stage with a piezo installed on the Z axis allows for precise axial control. Arc lamp provides the epi-illumination light source with custom spectral separating cubes (DAPI, FITC/GFP, TRITC/RFP). Laser diodes for 396 nm (Vortran, 100 mW) or 465 nm (Modulight, ML6500-465, 1W) are installed with a custom epi to TIRF motorized translation stage.

Luminescent nanoparticles imaging of the $Y_{0.6}Eu_{0.4}VO_4$ nanoparticles emission was collected through a 617/8 filter (FWHM 8 nm, Chroma). We recorded series of images at a frame rate of 1 Hz during photoreduction and 0.5Hz during nanoparticles tracking, with an excitation intensity of 19 W/cm^2 and of 3 W/cm^2 respectively. Nanoparticle luminescence was collected by an apochromat 60X, 1.42 numerical aperture oil-immersion objective (Olympus).

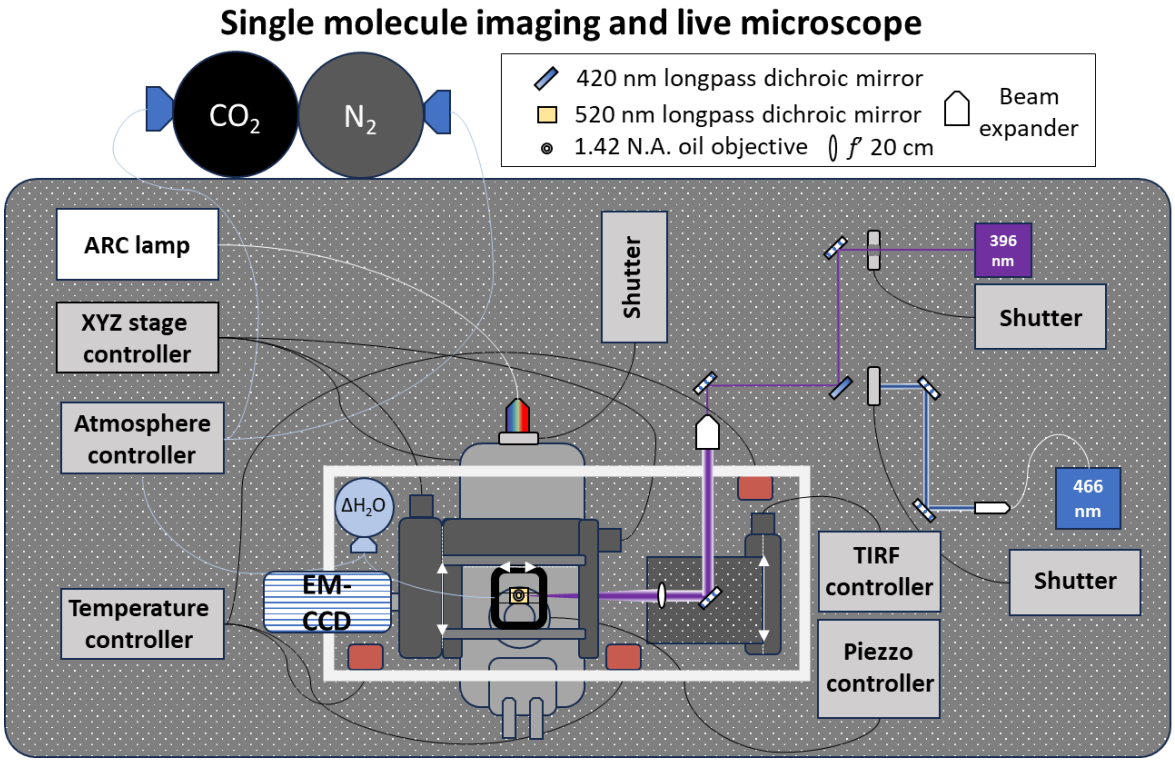

Figure 171: Imaging setup to perform nanoparticle imaging at 396 and 466 nm and live imaging.

4.4.1.2 dSTORM setup

An Olympus (IX-81) is equipped with 60X and 100X, N.A.=1.4 oil immersion objectives, and an Orca Fusion sCMOS camera (Hamamatsu) is used with 2 × 2 binning. The lasers used for Dylight 650 excitation, and CF 568 were mounted in a 4-color laser box (Vortran). We used 150 mW excitation at 640 nm for Dylight 650, and 40 mW excitation at 532 nm for CF 568. We used filter ET

(605/70 nm) and dichroic 560 (FDi01-25x36 Semrock) for CF568 and filter ET620/60x (Chroma) for excitation and T660lpxr (Chroma) and ET700/75m (Chroma) for the emission filters for Dylight 650.

4.4.1.3 dSTORM immunostaining

First, the cells were fixed for 15 minutes at 37°C using a solution comprising 1% paraformaldehyde and 0.2% glutaraldehyde (Sigma). An additional quenching step is performed after fixation in PBS, 0.1% $NaBH_4$ for 8 minutes and finally 3 washes in PBS. Cells are then permeabilized in PBS, 0,25% Triton, 1% BSA for 15 minutes. The samples were then blocked for 1h in PBS, 0.02% Triton, 5% BSA, before performing the immunostaining. We incubated the primary antibodies for 1h in PBS, 0.02% Triton, 1% BSA at 37°C, followed by 3 washes with PBS, and incubation with secondary antibodies for 1h in PBS, 0.025% Triton, 1% BSA at 37°C.

The buffer solution of 2-color STORM imaging was prepared in PBS (1X) pH 8.0 with 30 mM sodium sulfite, 30 mM dithiothreitol (DTT), and 30 mM DABCO and was prepared fresh before each experiment.

4.4.2 Antibodies and chemicals used for imaging

All primary antibodies were used in 1:100 dilutions in PBS, 0.02% Triton, 1% BSA.

Table 4: List of primary antibodies used for immunostaining

Antibodies	Reactivity	Host	reference	Clonality
VE-Cadherin/CD144	Human	Rabbit IgG	ab33168	Polyclonal
VE-Cadherin/CD144	Human	Goat IgG	AF938	Polyclonal
PECAM-1/ CD31	Human	Sheep IgG	AF806	Polyclonal
VEGFR2/KDR/Flk-1	Human	Goat IgG	AF357	Polyclonal
Podocalyxin	Human	Mouse IgG	MAB1658	Monoclonal
Podocin/NPHS2	Human, mouse, rat	Rabbit IgG	ab50339	Polyclonal
Podocin/NPHS2	Human	Rabbit IgG	ZRB1262	Monoclonal
WT1	Human, mouse	Rabbit IgG	ab89901	Monoclonal
P57/Kip2	Human	Rabbit IgG	SC8298	Polyclonal
Claudin-1	Human	Rabbit IgG	ab15098	Polyclonal
α-Tubulin	Human,+…	Mouse IgG	T5168	Monoclonal
EGFR	Human	Rat IgG	ab231	Monoclonal
CD9-Dylight 650	Human	Mouse	Eric Rubinstein, (Lozahic et al., 2000)	Monoclonal
Laminin	Human, mouse	Rabbit IgG	ab11575	Polyclonal
Collagen IV	Human,+…	Rabbit IgG	ab6586	Polyclonal

All secondary antibodies were used a 1:200 dilutions in PBS, 0.02% Triton X100, 1% BSA. Phalloidin was used at a 1:200 dilution and DAPI at 1:500.

Table 5: List of secondary antibodies used for immunostaining

Antibodies	Reactivity	Host	reference	Clonality
Alexa Fluor™ 594	Goat	Donkey IgG	A11058	Polyclonal
DyLight™ 550	Mouse	Donkey IgG	SA5-10167	Polyclonal
Atto-488	Mouse	Goat IgG	62197	Polyclonal
Alexa Fluor™ 488	Mouse	Goat IgG	A11001	Polyclonal
Alexa Fluor™ Plus 488	Rabbit	Donkey IgG	A32790	Polyclonal
Alexa Fluor™ Plus 405	Mouse	Donkey IgG	A48257	Polyclonal
CF™ 568	Rat	Goat IgG	sab4600086-250	Polyclonal
Phalloidin rhodamine red			R415	
Phalloidin 590			93642	
Phalloidin iFluor® 647			ab176759	
DAPI			62248	

Table 6: Fluorescent markers for filtration assays

Fluorescent marker	reference
FITC-dextran Mw 20 000 kDa	FD20S
FITC-dextran Mw 70 000 kDa	46945
FITC-dextran Mw 150 000 kDa	46946
FITC-albumin	A9771

List of figures

References

Abdelsayed, V., Boukhatem, H., & Olivier, N. (2022). An Optimized Buffer for Repeatable Multicolor STORM. *ACS Photonics*. https://doi.org/10.1021/acsphotonics.2c01249

Abdesselem, M., Gacoin, T., Boilot, J.-P., Tharaux, P.-L., Alexandrou, A., & Bouzigues, C. (2015). ROS Detection and Quantification with Lanthanide-Based Nanosensors. *Biophysical Journal*, *108*(2), 483a. https://doi.org/10.1016/j.bpj.2014.11.2640

Abdesselem, M., Ramodiharilafy, R., Devys, L., Gacoin, T., Alexandrou, A., & Bouzigues, C. I. (2017). Fast quantitative ROS detection based on dual-color single rare-earth nanoparticle imaging reveals signaling pathway kinetics in living cells. *Nanoscale*, *9*(2), 656–665. https://doi.org/10.1039/c6nr07413h

Abrahamson, D. R. (2012). Role of the Podocyte (and Glomerular Endothelium) in Building the GBM. *Seminars in Nephrology*, *32*(4), 342–349. https://doi.org/10.1016/j.semnephrol.2012.06.005

Abrahamson, D. R., Hudson, B. G., Stroganova, L., Borza, D., & John, P. L. S. (2009). Cellular Origins of Type IV Collagen Networks in Developing Glomeruli. *J Am Soc Nephrol*, *20*, 1471–1479. https://doi.org/10.1681/ASN.2008101086

Achenbach, J., Mengel, M., Tossidou, I., Peters, I., Park, J., Haubitz, M., Ehrich, J. H., Haller, H., & Schiffer, M. (2008). Parietal epithelia cells in the urine as a marker of disease activity in glomerular diseases. *Nephrol Dial Transplant*, *23*(May), 3138–3145. https://doi.org/10.1093/ndt/gfn235

Akilesh, S., Kopp, J. B., Miner, J. H., Huber, T. B., Wu, H., Wang, G., Roopenian, D. C., Unanue, E. R., & Shaw, A. S. (2008). Podocytes use FcRn to clear IgG from the glomerular basement membrane. *PNAS*, *105*(3), 967–972. https://doi.org/10.1073/pnas.0711515105

Albert-Smet, I., Marcos-Vidal, A., Vaquero, J. J., Desco, M., Muñoz-Barrutia, A., & Ripoll, J. (2019). Applications of light-sheet microscopy in microdevices. *Frontiers in Neuroanatomy*, *13*(January), 1–15. https://doi.org/10.3389/fnana.2019.00001

Almeida, R. F. M. De, Fedorov, A., & Prieto, M. (2003). Sphingomyelin / Phosphatidylcholine / Cholesterol Phase Diagram : Boundaries and Composition of Lipid Rafts. *Biophysical Journal*, *85*, 2406–2416. https://doi.org/10.1016/S0006-3495(03)74664-5

Alvaro, M., J, F., & Shuvo, R. (2005). Characterization of Polydimethylsiloxane (PDMS) Properties for Biomedical Micro/Nanosystems. *Biomedical Microdevices*, *7*(4), 281–293.

Andrae, J., Gallini, R., & Betsholtz, C. (2008). Role of platelet-derived growth factors in physiology and medicine. *Genes and Development*, *22*, 1276–1312. https://doi.org/10.1101/gad.1653708.revealing

Andrassy, K., Küster, S., Waldherr, R., & Ritz, E. (2008). Rapidly Progressive Glomerulonephritis: Analysis of Prevalence and Clinical Course. *Nephron*, *59*(2), 206–212. https://doi.org/10.1159/000186552

Appel, D., Kershaw, D. B., Smeets, B., Yuan, G., Fuss, A., Frye, B., Elger, M., Kriz, W., Floege, J., & Moeller, M. J. (2009). Recruitment of podocytes from glomerular parietal epithelial cells. *Journal of the American Society of Nephrology*, *20*(2), 333–343. https://doi.org/10.1681/ASN.2008070795

Arakawa, M., & Tokunaga, J. (1977). A Scanning Electron Microscope Study of the Human Bowman's Epithelium. *Contr. Nephrol.*, *6*, 73–78.

Arik, Y. B. et al. (2021). Collagen I Based Enzymatically Degradable Membranes for Organ-on-a-

Chip Barrier Models. *ACS Biomaterial Science and Engineering*, *7*. https://doi.org/10.1021/acsbiomaterials.0c00297

Artelt, N., Siegerist, F., Ritter, A. M., Grisk, O., Schlüter, R., Endlich, K., & Endlich, N. (2018). Comparative analysis of podocyte foot process morphology in three species by 3D super-resolution microscopy. *Frontiers in Medicine*, *5*(October), 1–8. https://doi.org/10.3389/fmed.2018.00292

Asakura, M., Kitakaze, M., Takashima, S., Liao, Y., Ishikura, F., Yoshinaka, T., Ohmoto, H., Node, K., Yoshino, K., Ishiguro, H., Asanuma, H., Sanada, S., Matsumura, Y., Hiroshi, T., Beppu, S., Tada, M., Hori, M., & Higashiyama, S. (2002). Cardiac hypertrophy is inhibited by antagonism of ADAM12 processing of HB-EGF: Metalloproteinase inhibitors as a new therapy. *Nature Medicine*, *8*(1), 35–40.

Assoian, R. K. (1997). Anchorage-dependent Cell Cycle Progression. *The Journal of Cell Biology*, *136*(1), 1–4.

Avila, A. M., Bebenek, I., Bonzo, J. A., Bourcier, T., Davis Bruno, K. L., Carlson, D. B., Dubinion, J., Elayan, I., Harrouk, W., Lee, S. L., Mendrick, D. L., Merrill, J. C., Peretz, J., Place, E., Saulnier, M., Wange, R. L., Yao, J., Zhao, D., & Brown, P. C. (2020). An FDA/CDER perspective on nonclinical testing strategies: Classical toxicology approaches and new approach methodologies (NAMs). *Regulatory Toxicology and Pharmacology*, *114*(April), 104662. https://doi.org/10.1016/j.yrtph.2020.104662

Axelrod, D. (1981). Cell-substrate contacts illuminated by total internal reflection fluorescence. *Journal of Cell Biology*, *89*(1), 141–145. https://doi.org/10.1083/jcb.89.1.141

Aydogmus, H., Hu, M., Ivancevic, L., Frimat, J. P., van den Maagdenberg, A. M. J. M., Sarro, P. M., & Mastrangeli, M. (2023). An organ-on-chip device with integrated charge sensors and recording microelectrodes. *Scientific Reports*, *13*(1), 8062. https://doi.org/10.1038/s41598-023-34786-5

Baddeley, D., & Bewersdorf, J. (2018). Biological Insight from Super-Resolution Microscopy: What We Can Learn from Localization-Based Images. *Annual Review of Biochemistry*, *87*(1). https://doi.org/10.1146/annurev-biochem-060815-014801

Bae, Y. S., Kang, S. W., Seo, M. S., Baines, I. C., Tckle, E., Chock, P. B., & Rhee, S. G. (1997). Epidermal growth factor (EGF)-induced generation of hydrogen peroxide. *Journal of Biological Chemistry*, *272*(1), 217–221. https://doi.org/10.1074/jbc.272.1.217

Baker, B. M., & Chen, C. S. (2012). Deconstructing the third dimension-how 3D culture microenvironments alter cellular cues. *Journal of Cell Science*, *125*(13), 3015–3024. https://doi.org/10.1242/jcs.079509

Ballermann, B. J., Dardik, A., Eng, E., & Liu, A. (1998). Shear stress and the endothelium. *Kidney International, Supplement*, *54*(67), 100–108. https://doi.org/10.1046/j.1523-1755.1998.06720.x

Bari, R., Guo, Q., Xia, B., Zhang, Y. H., Giesert, E. E., Levy, S., Zheng, J. J., & Zhang, X. A. (2011). Biochemical and Biophysical Research Communications Tetraspanins regulate the protrusive activities of cell membrane. *Biochemical and Biophysical Research Communications*, *415*(4), 619–626. https://doi.org/10.1016/j.bbrc.2011.10.121

Barisoni, L., Schnaper, H. W., & Kopp, J. B. (2007). A proposed taxonomy for the podocytopathies: A reassessment of the primary nephrotic diseases. *Clinical Journal of the American Society of Nephrology*, *2*(3), 529–542. https://doi.org/10.2215/CJN.04121206

Bates, M., Blosser, T. R., & Zhuang, X. (2005). Short-range spectroscopic ruler based on a single-molecule optical switch. *Physical Review Letters*, *94*(10), 1–4.

https://doi.org/10.1103/PhysRevLett.94.108101

Beaurepaire, E., Buissette, V., Sauviat, M. P., Giaume, D., Lahlil, K., Mercuri, A., Casanova, D., Huignard, A., Martin, J. L., Gacoin, T., Boilot, J. P., & Alexandrou, A. (2004). Functionalized fluorescent oxide nanoparticles: Artificial toxins for sodium channel targeting and imaging at the single-molecule level. *Nano Letters*, *4*(11), 2079–2083. https://doi.org/10.1021/nl049105g

Bedard, K., & Krause, K. H. (2007). The NOX family of ROS-generating NADPH oxidases: Physiology and pathophysiology. *Physiological Reviews*, *87*(1), 245–313. https://doi.org/10.1152/physrev.00044.2005

Belousov, V. V., Fradkov, A. F., Lukyanov, K. A., Staroverov, D. B., Shakhbazov, K. S., Terskikh, A. V., & Lukyanov, S. (2006). Genetically encoded fluorescent indicator for intracellular hydrogen peroxide. *Nature Methods*, *3*(4), 281–286. https://doi.org/10.1038/nmeth866

Berditchevski, F., Odintsova, E., Sawada, S., & Gilbert, E. (2002). Expression of the Palmitoylation-deficient CD151 Weakens the Association of α3β1 Integrin with the Tetraspanin-enriched Microdomains and Affects Integrin-dependent Signaling*. *Journal of Biological Chemistry*, *277*(40), 36991–37000. https://doi.org/10.1074/jbc.M205265200

Bersini, S., Yazdi, I. K., Talò, G., Shin, S. R., Moretti, M., & Khademhosseini, A. (2016). Cell-microenvironment interactions and architectures in microvascular systems. *Biotechnology Advances*, *34*(6), 1113–1130. https://doi.org/10.1016/j.biotechadv.2016.07.002

Bertram, J. F., Douglas-Denton, R. N., Diouf, B., Hughson, M. D., & Hoy, W. E. (2011). Human nephron number: Implications for health and disease. *Pediatric Nephrology*, *26*(9), 1529–1533. https://doi.org/10.1007/s00467-011-1843-8

Bertram, J. F., Soosaipillai, M. C., Ricardo, S. D., & Ryan, G. B. (1992). Total numbers of glomeruli and individual glomerular cell types in the normal rat kidney. *Cell Tissue Res*, *270*, 37–45.

Bertuccio, C., Veron, D., Aggarwal, P. K., Holzman, L., & Tufro, A. (2011). Vascular endothelial growth factor receptor 2 direct interaction with nephrin links VEGF-A signals to actin in kidney podocytes. *Journal of Biological Chemistry*, *286*(46), 39933–39944. https://doi.org/10.1074/jbc.M111.241620

Besag, J. . (1977). Comments on Ripley's paper. *J R Stat Soc*, *39*, 193–195.

Besner, G., Higashiyama, S., & Klagsbrun, M. (1990). Isolation and characterization of a macrophage-derived heparin-binding growth factor. *Cell Regulation*, *1*(October), 811–819.

Betzig, E., Patterson, G. H., Sougrat, R., Lindwasser, O. W., Olenych, S., Bonifacino, J. S., Davidson, M. W., Lippincott-Schwartz, J., & Hess, H. F. (2006). Imaging intracellular fluorescent proteins at nanometer resolution. *Science*, *313*(5793), 1642–1645. https://doi.org/10.1126/science.1127344

Bevan, H. S., Slater, S. C., Clarke, H., Cahill, P. A., Mathieson, P. W., Welsh, G. I., & Satchell, S. C. (2011). Acute laminar shear stress reversibly increases human glomerular endothelial cell permeability via activation of endothelial nitric oxide synthase. *American Journal of Physiology - Renal Physiology*, *301*(4), 733–743. https://doi.org/10.1152/ajprenal.00458.2010

Bhattacharjee, S. (2016). DLS and zeta potential - What they are and what they are not? *Journal of Controlled Release*, *235*, 337–351. https://doi.org/10.1016/j.jconrel.2016.06.017

Bienert, G. P., Schjoerring, J. K., & Jahn, T. P. (2006). Membrane transport of hydrogen peroxide. *Biochimica et Biophysica Acta - Biomembranes*, *1758*(8), 994–1003. https://doi.org/10.1016/j.bbamem.2006.02.015

Bilan, D. S., Pase, L., Joosen, L., Gorokhovatsky, A. Y., Ermakova, Y. G., Gadella, T. W. J., Grabher, C., Schultz, C., Lukyanov, S., & Belousov, V. V. (2013). HyPer-3: A genetically encoded H2O2

probe with improved performance for ratiometric and fluorescence lifetime imaging. *ACS Chemical Biology*, *8*(3), 535–542. https://doi.org/10.1021/cb300625g

Blackstone, B. N., Gallentine, S. C., & Powell, H. M. (2021). Review collagen-based electrospun materials for tissue engineering: A systematic review. *Bioengineering*, *8*(3), 1–16. https://doi.org/10.3390/bioengineering8030039

Blaine, J., & Dylewski, J. (2020). Regulation of the Actin Cytoskeleton in Podocytes. *Cells*, *9*(7), 1–27. https://doi.org/10.3390/cells9071700

Blouch, K., Deen, W. M., Fauvel, J.-P., Bialek, J., Derby, G., & Myers, B. D. (1997). Molecular in healthy configuration and glomerular and nephrotic humans size selectivity. *Am. J. Physiol*, *273*, 430–437.

Blumenthal, A., Giebel, J., Warsow, G., Li, L., Ummanni, R., Schordan, S., Schordan, E., Klemm, P., Gretz, N., Endlich, K., Endlich, N., Schordan, E., Klemm, P., Gretz, N., Endlich, K., & Mechanical, E. N. (2015). Mechanical stress enhances CD9 expression in cultured podocytes. *Am J Physiol Renal Physiol*, *308*, 602–613. https://doi.org/10.1152/ajprenal.00190.2014

Bohle, A., Aeikens, B., Eenboom, A., Fronholt, L., Plate, W. R., Xiao, C., Greschniok, A., & Wehrmann, M. (1998). Human glomerular structure under normal conditions and in isolated glomerular disease. *Kidney International, Supplement*, *54*(67), 186–188. https://doi.org/10.1046/j.1523-1755.1998.06742.x

Bollée, G., Flamant, M., Schordan, S., Fligny, C., Rumpel, E., Milon, M., Schordan, E., Sabaa, N., Vandermeersch, S., Galaup, A., Rodenas, A., Casal, I., Sunnarborg, S. W., Salant, D. J., Kopp, J. B., Threadgill, D. W., Quaggin, S. E., Dussaule, J.-C., Germain, S., … Tharaux, P.-L. (2011). The Epidermal Growth Factor Receptor Promotes Glomerular Injury and Renal Failure in Rapidly Progressive Crescentic Glomerulonephritis. *Nat Med*, *17*(10), 1242–1250. https://doi.org/10.1038/nm.2491

Bolte, S., & Cordelieres, F. P. (2006). A guided tour into subcellular colocalisation analysis in light microscopy. *Journal of Microscopy*, *224*(3), 13–232. https://doi.org/10.1111/j.1365-2818.2006.01706.x

Booth, A. D., Almond, M. K., Burns, A., Ellis, P., Gaskin, G., Neild, G. H., Plaisance, M., Pusey, C. D., & Jayne, D. R. W. (2003). Outcome of ANCA-associated renal vasculitis: a 5-year retrospective study. *American Journal of Kidney Diseases*, *41*(4), 776–784. https://doi.org/10.1016/s0272-6386(03)00025-8

Boucheix, C., Soria, C., Mirshahi, M., Soriat, J., Perrot, J., Fournier, N., Billard, M., & Rosenfeld, C. (1983). Characteristics of platelet aggregation induced by the monoclonal antibody ALBe (acute lymphoblastic leukemia antigen p24). *FEBS Letters*, *161*(2).

Boute, N., Gribouval, O., Roselli, S., Benessy, F., Lee, H., Fuchshuber, A., Dahan, K., Gubler, M., Niaudet, P., & Antignac, C. (2000). NPHS2, encoding the glomerular protein podocin , is mutated in autosomal recessive steroid-resistant nephrotic syndrome. *Nature Genetics*, *24*(april), 349–354. https://doi.org/10.1038/74166

Bouzigues, C. I., Nguyên, T. L., Ramodiharilafy, R., Claeson, A., Tharaux, P. L., & Alexandrou, A. (2014). Regulation of the ROS response dynamics and organization to PDGF motile stimuli revealed by single nanoparticle imaging. *Chemistry and Biology*, *21*(5), 647–656. https://doi.org/10.1016/j.chembiol.2014.02.020

Brecher, C., Samelson, H., Lempicki, A., Riley, R., & Peters, T. (1967). Polarized Spectra and Crystal-Field Parameters of Eu+3 in YVO4. *Physical Review*, *155*(2), 178–187.

Bright, R., & London, C. (1827). Reports of medical cases selected with a view of illustrating the

symptoms and cure of diseases by a reference to morbid anatomy. *Oxford University Press, Vol 2*.

Brown, D. A., & London, E. (1998). Functions of lipid rafts in biological membranes. *Annu. Rev. Cell Dev. Biol*, *14*, :111–36.

Brown, D. A., & London, E. (2000). Structure and Function of Sphingolipid- and Cholesterol-rich Membrane Rafts*. *Journal of Biological Chemistry*, *275*(23), 17221–17224. https://doi.org/10.1074/jbc.R000005200

Buissette, V., Giaume, D., Gacoin, T., & Boilot, J. P. (2006). Aqueous routes to lanthanide-doped oxide nanophosphors. *Journal of Materials Chemistry*, *16*(6), 529–539. https://doi.org/10.1039/b508656f

Butt, L., Unnersjö-Jess, D., Höhne, M., Edwards, A., Binz-Lotter, J., Reilly, D., Hahnfeldt, R., Ziegler, V., Fremter, K., Rinschen, M. M., Helmstädter, M., Ebert, L. K., Castrop, H., Hackl, M. J., Walz, G., Brinkkoetter, P. T., Liebau, M. C., Tory, K., Hoyer, P. F., … Benzing, T. (2020). A molecular mechanism explaining albuminuria in kidney disease. *Nature Metabolism*, *2*(5), 461–474. https://doi.org/10.1038/s42255-020-0204-y

Byron, A., Randles, M. J., Humphries, J. D., Mironov, A., Hamidi, H., Harris, S., Mathieson, P. W., Saleem, M. A., Satchell, S. C., Zent, R., Humphries, M. J., & Lennon, R. (2014). Glomerular cell cross-talk influences composition and assembly of extracellular matrix. *Journal of the American Society of Nephrology*, *25*(5), 953–966. https://doi.org/10.1681/ASN.2013070795

Calderón-Colón, X., Xia, Z., Breidenich, J. L., Mulreany, D. G., Guo, Q., Uy, O. M., Tiffany, J. E., Freund, D. E., McCally, R. L., Schein, O. D., Elisseeff, J. H., & Trexler, M. M. (2012). Structure and properties of collagen vitrigel membranes for ocular repair and regeneration applications. *Biomaterials*, *33*(33), 8286–8295. https://doi.org/10.1016/j.biomaterials.2012.07.062

Casalena, G. A., Yu, L., Gil, R., Rodriguez, S., Sosa, S., Janssen, W., Azeloglu, E. U., Leventhal, J. S., & Daehn, I. S. (2020). The diabetic microenvironment causes mitochondrial oxidative stress in glomerular endothelial cells and pathological crosstalk with podocytes. *Cell Communication and Signaling*, *18*(1), 1–15. https://doi.org/10.1186/s12964-020-00605-x

Casanova, D. (2008). *Interaction toxine-cellule étudiée par imagerie individuelle de nanoparticules d'oxyde fluorescentes.* [Ecole Polytechnique]. https://doi.org/pastel-00003731

Casanova, D., Bouzigues, C., Nguyen, T. L., Ramodiharilafy, R. O., Bouzhir-Sima, L., Gacoin, T., Boilot, J. P., Tharaux, P. L., & Alexandrou, A. (2009). Single europium-doped nanoparticles measure temporal pattern of reactive oxygen species production inside cells. *Nature Nanotechnology*, *4*(9), 581–585. https://doi.org/10.1038/nnano.2009.200

Casanova, D., Giaume, D., Beaurepaire, E., Gacoin, T., Boilot, J. P., & Alexandrou, A. (2006). Optical in situ size determination of single lanthanide-ion doped oxide nanoparticles. *Applied Physics Letters*, *89*(25), 1–4. https://doi.org/10.1063/1.2405871

Chang, A. M., Ohse, T., Krofft, R. D., Wu, J. S., Eddy, A. A., Pippin, J. W., & Shankland, S. J. (2012). Albumin-induced apoptosis of glomerular parietal epithelial cells is modulated by extracellular signal-regulated kinase 1/2. *Nephrol Dial Transplant*, *27*, 1330–1343. https://doi.org/10.1093/ndt/gfr483

Charrin, S., Manie, S., Oualid, M., Billard, M., Boucheix, C., & Rubinstein, E. (2002). Differential stability of tetraspanin/tetraspanin interactions: role of palmitoylation. *FEBS Letters*, *516*, 139–144.

Charrin, S., Manie, S., Thiele, C., Billard, M., Gerlier, D., Boucheix, C., & Rubinstein, E. (2003). A physical and functional link between cholesterol and tetraspanins. *Eur. J. Immunol*, *33*, 2479–2489. https://doi.org/10.1002/eji.200323884

Chasles, F., Dubertret, B., & Boccara, A. C. (2007). Optimization and characterization of a structured illumination microscope. *Optics Express*, *15*(24), 16130. https://doi.org/10.1364/oe.15.016130

Chen, K. C.-W., You, Z., Zhang, W., & Lou, M. F. (2007). Control of PDGF-induced reactive oxygen species (ROS) generation and signal transduction in human lens epithelial cells. *Molecular Vision*, *13*(March), 374–387.

Chen, X., Zhong, Z., Xu, Z., Chen, L., & Wang, Y. (2010). 2′,7′-Dichlorodihydrofluorescein as a fluorescent probe for reactive oxygen species measurement: Forty years of application and controversy. *Free Radical Research*, *44*(6), 587–604. https://doi.org/10.3109/10715761003709802

Chiarelli, F., Basciani, F., Tumini, S., Mezzetti, A., Cipollone, F., Cuccurullo, F., & Verrotti, A. (2000). Vascular endothelial growth factor (VEGF) in children , adolescents and young adults with Type 1 diabetes mellitus : relation to glycaemic control and microvascular complications. *Diabetic Medicine*, *17*, 650–656.

Choublier, N., Taghi, M., Menet, M. C., Le Gall, M., Bruce, J., Chafey, P., Guillonneau, F., Moreau, A., Denizot, C., Parmentier, Y., Nakib, S., Borderie, D., Bouzinba-Segard, H., Couraud, P. O., Bourdoulous, S., & Declèves, X. (2022). Exposure of human cerebral microvascular endothelial cells hCMEC/D3 to laminar shear stress induces vascular protective responses. *Fluids and Barriers of the CNS*, *19*(1). https://doi.org/10.1186/s12987-022-00344-w

Ciani, L., Patel, A., Allen, N. D., & Ffrench-Constant, C. (2003). Mice Lacking the Giant Protocadherin mFAT1 Exhibit Renal Slit Junction Abnormalities and a Partially Penetrant Cyclopia and Anophthalmia Phenotype. *Molecular and Cellular Biology*, *23*(10), 3575–3582. https://doi.org/10.1128/MCB.23.10.3575

Civerchia-Perez, L., Faris, B., LaPointe, G., Beldekas, J., Leibowitz, H., & Franzblau, C. (1980). Use of collagen-hydroxyethylmethacrylate hydrogels for cell growth. *Proc. Nat. Acad. Sci. USA*, *77*(4), 2064–2068. https://doi.org/10.1073/pnas.77.4.2064

Claas, C., Stipp, C. S., & Hemler, M. E. (2001). Evaluation of Prototype Transmembrane 4 Superfamily Protein Complexes and Their Relation to Lipid Rafts*. *Journal of Biological Chemistry*, *276*(11), 7974–7984. https://doi.org/10.1074/jbc.M008650200

Clark, E. A., & Brugget, J. S. (1995). Integrins and Signal Transduction Pathways : The Road Taken. *Science*, *268*(April), 233–239.

Collins, R. D. (2010). Dr Goodpasture: “I was not aware of such a connection between lung and kidney disease.” *Annals of Diagnostic Pathology*, *14*(3), 194–198. https://doi.org/10.1016/j.anndiagpath.2010.02.003

Coltharp, C., Yang, X., & Xiao, J. (2014). Quantitative analysis of single-molecule superresolution images. *Current Opinion in Structural Biology*, *28*(1), 112–121. https://doi.org/10.1016/j.sbi.2014.08.008

Cordelières, F. P., & Bolte, S. (2008). JACoP v2.0 : improving the user experience with co-localization studies. *ImageJ User & Developer Conference*, 174–181.

Courty, S., Bouzigues, C., Luccardini, C., Ehrensperger, M. V., Bonneau, S., & Dahan, M. (2006). Tracking Individual Proteins in Living Cells Using Single Quantum Dot Imaging. *Methods in Enzymology*, *414*(06), 211–228. https://doi.org/10.1016/S0076-6879(06)14012-4

Couser, W. G. (1988). Rapidly Progressive Glomerulonephritis: Classification, Pathogenetic Mechanisms, and Therapy. *American Journal of Kidney Diseases*, *11*(6), 449–464. https://doi.org/10.1016/S0272-6386(88)80079-9

Cui, Z., & Zhao, M. (2011). Advances in human antiglomerular basement membrane disease. *Nature*

Reviews Nephrology, *7*(12), 697–705. https://doi.org/10.1038/nrneph.2011.89

Curry, F. E., & Adamson, R. H. (2012). Endothelial glycocalyx: Permeability barrier and mechanosensor. *Annals of Biomedical Engineering*, *40*(4), 828–839. https://doi.org/10.1007/s10439-011-0429-8

D. Huang, E. A. Swanson, J. G. F. (1991). Optical Coherence Tomography. *Science*, *254*(5035), 1178–1181. https://doi.org/10.1201/b15085-15

D'Agati, V. (1994). The many masks of focal segmental glomerulosclerosis. *Kidney International*, *46*(4), 1223–1241. https://doi.org/10.1038/ki.1994.388

D'Agati, V. D., Fogo, A. B., Bruijn, J. A., & Jennette, J. C. (2004). Pathologic Classification of Focal Segmental Glomerulosclerosis: A Working Proposal. *American Journal of Kidney Diseases*, *43*(2), 368–382. https://doi.org/10.1053/j.ajkd.2003.10.024

D'Agati, V. D., Kaskel, F. J., & Falk, R. J. (2011). Focal Segmental Glomerulosclerosis. *National Kidney Foundation's Primer on Kidney Diseases*, *365*, 2398–2411. https://doi.org/10.1016/B978-0-323-47794-9.00018-4

Dahmane, S., Doucet, C., Gall, A. Le, Chamontin, C., Dosset, P., Murcy, F., Fernandez, L., Pastene, D. S., Rubinstein, E., Mougel, M., Nollmann, M., & Milhiet, P.-E. (2019). Nanoscale Organization of Tetraspanins during HIV-1 budding by correlative dSTORM/AFM. *Nanoscale*. https://doi.org/10.1039/C8NR07269H

Davis-Fleischer, K. M., & Besner, G. E. (1998). Structure and function of Heparin-Binding EGF-like Growth Factor (HB-EGF). *Frontiers in Bioscience*, *3*, 288–299.

Deen, W. M., Lazzara, M. J., & Myers, B. D. (2001). Structural determinants of glomerular permeability. *Am J Physiol Renal Physiol*, *281*, 579–596.

Dems, D., Rodrigues Da Silva, J., Hélary, C., Wien, F., Marchand, M., Debons, N., Muller, L., Chen, Y., Schanne-Klein, M. C., Laberty-Robert, C., Krins, N., & Aimé, C. (2020). Native Collagen: Electrospinning of Pure, Cross-Linker-Free, Self-Supported Membrane. *ACS Applied Bio Materials*, *3*(5), 2948–2957. https://doi.org/10.1021/acsabm.0c00006

Dessalles, C. A., Leclech, C., Castagnino, A., & Barakat, A. I. (2021). Integration of substrate- and flow-derived stresses in endothelial cell mechanobiology. *Communications Biology*, *4*(1). https://doi.org/10.1038/s42003-021-02285-w

DeYulia, G. J., Cárcamo, J. M., Bórquez-Ojeda, O., Shelton, C. C., & Golde, D. W. (2005). Hydrogen peroxide generated extracellularly by receptor-ligand interaction facilitates cell signaling. *Proceedings of the National Academy of Sciences of the United States of America*, *102*(14), 5044–5049. https://doi.org/10.1073/pnas.0501154102

Díaz, L., Zambrano, E., Flores, M. E., Contreras, M., Crispín, J. C., Alemán, G., Bravo, C., Armenta, A., Valdés, V. J., Tovar, A., Gamba, G., Barrios-Payán, J., & Bobadilla, N. A. (2020). Ethical Considerations in Animal Research: The Principle of 3R's. *Rev Invest Clin*, *73*(4), 199–209. https://doi.org/10.24875/RIC.20000380

Dijkman, H., Smeets, B., Laak, J. VAN DER, Steenbergen, E., & Wetzels, J. (2005). The parietal epithelial cell is crucially involved in human idiopathic focal segmental glomerulosclerosis. *Kidney International*, *68*, 1562–1572. https://doi.org/10.1111/j.1523-1755.2005.00568.x

Duffy, D. C., McDonald, J. C., Schueller, O. J. A., & Whitesides, G. M. (1998). Rapid prototyping of microfluidic systems in poly(dimethylsiloxane). *Analytical Chemistry*, *70*(23), 4974–4984. https://doi.org/10.1021/ac980656z

Edington, C. D., Chen, W. L. K., Geishecker, E., Kassis, T., Soenksen, L. R., Bhushan, B. M., Freake, D., Kirschner, J., Maass, C., Tsamandouras, N., Valdez, J., Cook, C. D., Parent, T., Snyder, S.,

Yu, J., Suter, E., Shockley, M., Velazquez, J., Velazquez, J. J., … Griffith, L. G. (2018). Interconnected Microphysiological Systems for Quantitative Biology and Pharmacology Studies. *Scientific Reports*, *8*(1), 1–18. https://doi.org/10.1038/s41598-018-22749-0

Endlich, N., Kress, K. R., Reiser, J., Uttenweiler, D., Kriz, W., Mundel, P., & Endlich, K. (2001). Podocytes respond to mechanical stress in vitro. *Journal of the American Society of Nephrology*, *12*(3), 413–422. https://doi.org/10.1681/asn.v123413

Endlich, N., Schordan, E., Cohen, C. D., Kretzler, M., Lewko, B., Welsch, T., Kriz, W., Otey, C. A., & Endlich, K. (2009). Palladin is a dynamic actin-associated protein in podocytes. *Kidney International*, *75*(2), 214–226. https://doi.org/10.1038/ki.2008.486

Enyedi, B., Zana, M., Donkó, Á., & Geiszt, M. (2013). Spatial and temporal analysis of NADPH oxidase-generated hydrogen peroxide signals by novel fluorescent reporter proteins. *Antioxidants and Redox Signaling*, *19*(6), 523–534. https://doi.org/10.1089/ars.2012.4594

Erard, M., Dupré-Crochet, S., & Nüße, O. (2018). Biosensors for spatiotemporal detection of reactive oxygen species in cells and tissues. *American Journal of Physiology - Regulatory Integrative and Comparative Physiology*, *314*(5), R667–R683. https://doi.org/10.1152/ajpregu.00140.2017

Eremina, V., Cui, S., Gerber, H., Ferrara, N., Haigh, J., Nagy, A., Ema, M., Rossant, J., Jothy, S., Miner, J. H., & Quaggin, S. E. (2006). Vascular Endothelial Growth Factor A Signaling in the Podocyte-Endothelial Compartment Is Required for Mesangial Cell Migration and Survival. *JASN*, *17*(14), 724–735. https://doi.org/10.1681/ASN.2005080810

Eremina, V., Jefferson, J. A., Kowalewska, J., Hochster, H., Haas, M., Weisstuch, J., Richardson, C., Kopp, J. B., Kabir, M. G., Backx, P. H., Gerber, H.-P., Ferrara, N., Barisoni, L., Alpers, C. E., & Quaggin, S. E. (2008). VEGF Inhibition and Renal Thrombotic Microangiopathy. *New England Journal of Medicine*, *358*, 1129–1136.

Eremina, V., Miner, J. H., Quaggin, S. E., Eremina, V., Sood, M., Haigh, J., Nagy, A., Lajoie, G., Ferrara, N., Gerber, H., Kikkawa, Y., Miner, J. H., & Quaggin, S. E. (2003). Glomerular-specific alterations of VEGF-A expression lead to distinct congenital and acquired renal diseases. *J Clin Invest*, *111*(5), 707–716. https://doi.org/10.1172/JCI200317423.Introduction

Ester, M., Kriegel, H.-P., Sander, J., & Xu, X. (1996). A Density-Based Algorithm for Discovering Clusters in Large Spatial Databases with Noise. *AAAI*.

Evens, R. P. (2016). Pharma Success in Product Development—Does Biotechnology Change the Paradigm in Product Development and Attrition. *AAPS Journal*, *18*(1), 281–285. https://doi.org/10.1208/s12248-015-9833-6

Evrova, O., & Buschmann, J. (2017). In vitro and in vivo effects of PDGF-BB delivery strategies on tendon healing : A review. *European Cells and Materials*, *34*(July), 15–39. https://doi.org/10.22203/eCM.v034a02

Eymael, J., Sharma, S., Loeven, M. A., Wetzels, J. F., Mooren, F., Florquin, S., Deegens, J. K., Willemsen, B. K., Sharma, V., van Kuppevelt, T. H., Bakker, M. A., Ostendorf, T., Moeller, M. J., Dijkman, H. B., Smeets, B., & van der Vlag, J. (2018). CD44 is required for the pathogenesis of experimental crescentic glomerulonephritis and collapsing focal segmental glomerulosclerosis. *Kidney International*, *93*(3), 626–642. https://doi.org/10.1016/j.kint.2017.09.020

Fahr, T. (1925). Handbuch der speziellen pathologischen Anatomie und Histologie. In *Springer. Vol. VI/1. Berlin*.

Fan, Y. (2018). Low-cost Microfluidics : Materials and Methods. *Micro Nano Letters*, 2–7.

Fan, Z., Mikulski, Z., McArdle, S., Sundd, P., & Ley, K. (2020). Super-STORM: Molecular Modeling

to Achieve Single-molecule Localization with STORM Microscopy. *STAR Protocols*, *1*(1), 100012. https://doi.org/10.1016/j.xpro.2019.100012

Farjana, S., Ghaderi, M., Rahiminejad, S., Haasl, S., & Enoksson, P. (2021). Dry film photoresist-based microfabrication: A new method to fabricate millimeter-wave waveguide components. *Micromachines*, *12*(3), 1–13. https://doi.org/10.3390/mi12030260

Farquhar, M. G. (2006). The glomerular basement membrane: Not gone, just forgotten. *Journal of Clinical Investigation*, *116*(8), 2090–2093. https://doi.org/10.1172/JCI29488

Farquhar, M. G., Wissig, S. L., & Palade, G. E. (1960). Glomerular permeability: I. Ferritin transfer across the glomerular capillary wall in nephrotic rats. *J Exp Med*, *113*, 47–66.

Farquhar, & Palade. (1961). Glomerular permeability: II. Ferritin transfer across the glomerular capillary wall in nephrotic rats. *J Exp Med*, *114*, 699.

Federico, A., Morgillo, F., Tuccillo, C., Ciardiello, F., & Loguercio, C. (2007). Chronic inflammation and oxidative stress in human carcinogenesis. *International Journal of Cancer*, *121*(11), 2381–2386. https://doi.org/10.1002/ijc.23192

Ferrell, N., Sandoval, R. M., Bian, A., Campos-Bilderback, S. B., Molitoris, B. A., & Fissell, W. H. (2015). Shear stress is normalized in glomerular capillaries following 5⁄6 nephrectomy. *American Journal of Physiology - Renal Physiology*, *308*(6), F588–F593. https://doi.org/10.1152/ajprenal.00290.2014

Finch, R. J., & Hanchar, J. M. (2003). Structure and chemistry of zircon and zircon-group minerals. *Reviews in Mineralogy and Geochemistry*, *53*(1), 1–25. https://doi.org/https://doi.org/10.2113/0530001

Flachsbart, B. R., Wong, K., Iannacone, J. M., Abante, E. N., Vlach, R. L., Rauchfuss, P. A., Bohn, P. W., Sweedler, J. V., & Shannon, M. A. (2006). Design and fabrication of a multilayered polymer microfluidic chip with nanofluidic interconnects via adhesive contact printing. *Lab on a Chip*, *6*(5), 667–674. https://doi.org/10.1039/b514300d

Floege, J., Eitner, F., & Alpers, C. E. (2008). A New Look at Platelet-Derived Growth Factor in Renal Disease. *J Am Soc Nephrol*, *19*, 12–23. https://doi.org/10.1681/ASN.2007050532

Floege, J., Roeyen, C. van, Boor, P., & Ostendorf, T. (2007). The Role of PDGF-D in Mesangioproliferative Glomerulonephritis. *Contrib Nephrol.*, *157*, 153–158.

Fogazzi, G. B. (1997). The description of the renal glomeruli by Marcello Malpighi. *Nephrology Dialysis Transplantation*, *12*(10), 2191–2192. https://doi.org/10.1093/ndt/12.10.2191

Fogo, A. B., & Kon, V. (2010). The glomerulus - a view from the inside - the endothelial cell. *International Journal of Biochemistry and Cell Biology*, *42*(9), 1388–1397. https://doi.org/10.1016/j.biocel.2010.05.015

Foster, L. J., Hoog, C. L. De, & Mann, M. (2003). Unbiased quantitative proteomics of lipid rafts reveals high specificity for signaling factors. *Proc. Nat. Acad. Sci. USA*, *100*(10), 5813–5818.

Foster, R. R., Armstrong, L., Baker, S., Wong, D. W. L., Wylie, E. C., Ramnath, R., Jenkins, R., Singh, A., Steadman, R., Welsh, G. I., Mathieson, P. W., & Satchell, S. C. (2013). Glycosaminoglycan regulation by VEGFA and VEGFC of the glomerular microvascular endothelial cell glycocalyx in vitro. *American Journal of Pathology*, *183*(2), 604–616. https://doi.org/10.1016/j.ajpath.2013.04.019

Foster, R. R., Slater, S. C., Seckley, J., Kerjaschki, D., Bates, D. O., Mathieson, P. W., & Satchell, S. C. (2008). Vascular endothelial growth factor-C, a potential paracrine regulator of glomerular permeability, increases glomerular endothelial cell monolayer integrity and intracellular calcium. *American Journal of Pathology*, *173*(4), 938–948.

https://doi.org/10.2353/ajpath.2008.070416

Freeman, S. A., Vega, A., Riedl, M., Collins, R. F., Ostrowski, P. P., Woods, E. C., Bertozzi, C. R., Tammi, M. I., Lidke, D. S., Johnson, P., Mayor, S., Jaqaman, K., & Grinstein, S. (2018). Transmembrane Pickets Connect Cyto- and Pericellular Skeletons Forming Barriers to Receptor Article Transmembrane Pickets Connect Cyto- and Pericellular Skeletons Forming Barriers to Receptor Engagement. *Cell*, *172*, 305–317. https://doi.org/10.1016/j.cell.2017.12.023

Fridén, V., Oveland, E., Tenstad, O., Ebefors, K., Nyström, J., Nilsson, U. A., & Haraldsson, B. (2011). The glomerular endothelial cell coat is essential for glomerular filtration. *Kidney International*, *79*(12), 1322–1330. https://doi.org/10.1038/ki.2011.58

Friedrich, C., Endlich, N., Kriz, W., & Endlich, K. (2006). Podocytes are sensitive to fluid shear stress in vitro. *American Journal of Physiology - Renal Physiology*, *291*(4), 856–865. https://doi.org/10.1152/ajprenal.00196.2005

Frisch, S. M., & Ruoslahtit, E. (1997). Integrins and anoikis. *Current Opinion in Cell Biology*, *9*, 701–706.

Fu, B. M., & Tarbell, J. M. (2013). Mechano-sensing and transduction by endothelial surface glycocalyx: Composition, structure, and function. *Wiley Interdisciplinary Reviews: Systems Biology and Medicine*, *5*(3), 381–390. https://doi.org/10.1002/wsbm.1211

Fujigaki, Y., Sun, D. F., Fujimoto, T., Yonemura, K., Morioka, T., Yaoita, E., & Hishida, A. (2001). Cytokines and cell cycle regulation in the fibrous progression of crescent formation in antiglomerular basement membrane nephritis of WKY rats. *Virchows Arch*, *439*, 35–45. https://doi.org/10.1007/s004280100433

Fukasawa, H., Bornheimer, S., Kudlicka, K., & Farquhar, M. G. (2009). Slit diaphragms contain tight junction proteins. *Journal of the American Society of Nephrology*, *20*(7), 1491–1503. https://doi.org/10.1681/ASN.2008101117

Gagliardini, E., Conti, S., Benigni, A., Remuzzi, G., & Remuzzi, A. (2010). Imaging of the porous ultrastructure of the glomerular epithelial filtration slit. *Journal of the American Society of Nephrology*, *21*(12), 2081–2089. https://doi.org/10.1681/ASN.2010020199

Garg, P., Verma, R., Cook, L., Soofi, A., Venkatareddy, M., George, B., Mizuno, K., Gurniak, C., Witke, W., & Holzman, L. B. (2010). Actin-depolymerizing Factor Cofilin-1 Is Necessary in Maintaining Mature Podocyte Architecture. *Journal Biological Chemistry*, *285*(29), 22676–22688. https://doi.org/10.1074/jbc.M110.122929

Gates, B. D., Xu, Q., Stewart, M., Ryan, D., Willson, C. G., & Whitesides, G. M. (2005). New approaches to nanofabrication: Molding, printing, and other techniques. *Chemical Reviews*, *105*(4), 1171–1196. https://doi.org/10.1021/cr030076o

Gerke, P., Huber, T. B., Sellin, L., Benzing, T., & Walz, G. (2003). Homodimerization and Heterodimerization of the Glomerular Podocyte Proteins Nephrin and NEPH1. *J Am Soc Nephrol*, *14*(3), 918–926. https://doi.org/10.1097/01.ASN.0000057853.05686.89

Ghasemi, M., Turnbull, T., Sebastian, S., & Kempson, I. (2021). The mtt assay: Utility, limitations, pitfalls, and interpretation in bulk and single-cell analysis. *International Journal of Molecular Sciences*, *22*(23). https://doi.org/10.3390/ijms222312827

Goldberg, S., Adair-kirk, T. L., Senior, R. M., & Miner, J. H. (2010). Maintenance of Glomerular Filtration Barrier Integrity Requires Laminin α5. *J Am Soc Nephrol*, *21*, 579–586. https://doi.org/10.1681/ASN.2009091004

Goodpasture, E. W. (2009). Landmark publication from The American Journal of the Medical Sciences: The significance of certain pulmonary lesions in relation to the etiology of influenza.

The American Journal of the Medical Sciences, *338*(2), 148–151. https://doi.org/10.1097/MAJ.0b013e31818fff94

Goswami, D., Gowrishankar, K., Bilgrami, S., Ghosh, S., Raghupathy, R., Chadda, R., Vishwakarma, R., Rao, M., & Mayor, S. (2008). Nanoclusters of GPI-Anchored Proteins Are Formed by Cortical Actin-Driven Activity. *Cell*, *135*(6), 1085–1097. https://doi.org/10.1016/j.cell.2008.11.032

Guhr, S. S. O., Sachs, M., Wegner, A., Becker, J. U., Meyer, T. N., Kietzmann, L., Schlossarek, S., Carrier, L., Braig, M., Jat, P. S., Stahl, R. A. K., & Meyer-Schwesinger, C. (2013). The expression of podocyte-specific proteins in parietal epithelial cells is regulated by protein degradation. *Kidney International*, *84*(3), 532–544. https://doi.org/10.1038/ki.2013.115

Gulaboski, R., Mirčeski, V., Kappl, R., Hoth, M., & Bozem, M. (2019). Review—Quantification of Hydrogen Peroxide by Electrochemical Methods and Electron Spin Resonance Spectroscopy. *Journal of The Electrochemical Society*, *166*(8), G82–G101. https://doi.org/10.1149/2.1061908jes

Gustafsson, M. G. L. (2000). Surpassing the lateral resolution limit by a factor of two using structured illumination microscopy. *Journal of Microscopy*, *198*(2), 82–87. https://doi.org/10.1046/j.1365-2818.2000.00710.x

Gutscher, M., Sobotta, M. C., Wabnitz, G. H., Ballikaya, S., Meyer, A. J., Samstag, Y., & Dick, T. P. (2009). Proximity-based Protein Thiol Oxidation by H2O2-scavenging Peroxidases. *Journal of Biological Chemistry*, *284*(46), 31532–31540. https://doi.org/10.1074/jbc.M109.059246

Hakroush, S., Moeller, M. J., Theilig, F., Kaissling, B., Sijmonsma, T. P., Jugold, M., Akeson, A. L., Traykova-Brauch, M., Hosser, H., Hähnel, B., Gröne, H. J., Koesters, R., & Kriz, W. (2009). Effects of increased renal tubular Vascular Endothelial Growth Factor (VEGF) on fibrosis, cyst formation, and glomerular disease. *American Journal of Pathology*, *175*(5), 1883–1895. https://doi.org/10.2353/ajpath.2009.080792

Hale, L. J., Howden, S. E., Phipson, B., Lonsdale, A., Er, P. X., Ghobrial, I., Hosawi, S., Wilson, S., Lawlor, K. T., Khan, S., Oshlack, A., Quinlan, C., Lennon, R., & Little, M. H. (2018). 3D organoid-derived human glomeruli for personalised podocyte disease modelling and drug screening. *Nature Communications*, *9*(1), 5167. https://doi.org/10.1038/s41467-018-07594-z

Hamano, Y., Okude, T., Shirai, R., Sato, I., Kimura, R., Ogawa, M., Ueda, Y., Yokosuka, O., Kalluri, R., & Ueda, S. (2010). Lack of Collagen XVIII / Endostatin Exacerbates Immune-Mediated Glomerulonephritis. *J Am Soc Nephrol 21*, *21*, 1445–1455. https://doi.org/10.1681/ASN.2009050492

Hammarback, J. A., Palm, S. L., Furcht, L. T., & Letourneau, P. C. (1985). Guidance of neurite outgrowth by pathways of substratum-adsorbed laminin. *Journal of Neuroscience Research*, *13*(1–2), 213–220. https://doi.org/10.1002/jnr.490130115

Haraldsson, B., Nystrom, J., & Deen, W. M. (2008). Properties of the Glomerular Barrier and Mechanisms of Proteinuria. *Physiol Rev*, *88*, 451–487. https://doi.org/10.1152/physrev.00055.2006.

Harris, R. (2011). EGFR signaling in podocytes at the root of glomerular disease. *Nature Medicine*, *17*(10), 1188–1189. https://doi.org/10.1038/nm.2455

Harskamp, L. R., Gansevoort, R. T., Goor, H. Van, & Meijer, E. (2016). The epidermal growth factor receptor pathway in chronic kidney diseases. *Nature Reviews Nephrology*. https://doi.org/10.1038/nrneph.2016.91

Hart, D. C. ‘t, Yildiz, D., Palacio-Castañeda, V., & Nijenhuis, T. (2023). Co-Culture of Glomerular Endothelial Cells and Podocytes in a Custom-Designed Glomerulus-on-a-Chip Model Improves

the Filtration Barrier Integrity and Affects the Glomerular Cell Phenotype. *Biosensors*, *13*(339). https://doi.org/10.3390/bios13030339

Harvey, S. J., Jarad, G., Cunningham, J., Rops, A. L., Vlag, J. Van Der, Berden, J. H., Moeller, M. J., Holzman, L. B., Burgess, R. W., & Miner, J. H. (2007). Disruption of Glomerular Basement Membrane Charge through Podocyte-Specific Mutation of Agrin Does Not Alter Glomerular Permselectivity. *The American Journal of Pathology*, *171*(1), 139–152. https://doi.org/10.2353/ajpath.2007.061116

Hausmann, R., Grepl, M., Knecht, V., & Moeller, M. J. (2012). The glomerular filtration barrier function : new concepts. *Curr Opin Nephrol Hypertens*, *21*, 441–449. https://doi.org/10.1097/MNH.0b013e328354a28e

Hausmann, R., Kuppe, C., Egger, H., Schweda, F., Knecht, V., Elger, M., Menzel, S., Somers, D., Braun, G., Fuss, A., Uhlig, S., Kriz, W., Tanner, G., Floege, J., & Moeller, M. J. (2010). Electrical forces determine glomerular permeability. *Journal of the American Society of Nephrology*, *21*(12), 2053–2058. https://doi.org/10.1681/ASN.2010030303

He, Y., Wu, Y., Fu, J. Z., Gao, Q., & Qiu, J. J. (2016). Developments of 3D Printing Microfluidics and Applications in Chemistry and Biology: a Review. *Electroanalysis*, *28*(8), 1658–1678. https://doi.org/10.1002/elan.201600043

Heikkila, E., Ristola, M., Havana, M., Jones, N., Holthofer, H., & Lehtonen, S. (2011). Trans-interaction of nephrin and Neph1/Neph3 induces cell adhesion that associates with decreased tyrosine phosphorylation of nephrin. *Biochem. J. (2011)*, *435*, 619–628. https://doi.org/10.1042/BJ20101599

Heilemann, M., Van De Linde, S., Schüttpelz, M., Kasper, R., Seefeldt, B., Mukherjee, A., Tinnefeld, P., & Sauer, M. (2008). Subdiffraction-resolution fluorescence imaging with conventional fluorescent probes. *Angewandte Chemie - International Edition*, *47*(33), 6172–6176. https://doi.org/10.1002/anie.200802376

Hein, B., Willig, K. I., & Hell, S. W. (2008). Stimulated emission depletion (STED) nanoscopy of a fluorescent protein-labeled organelle inside a living cell. *Proc. Nat. Acad. Sci. USA*, *105*(38), 14271–14276. https://doi.org/10.1073/pnas.0807705105

Heldin, C., & Westermark, B. (1999). Mechanism of Action and In Vivo Role of Platelet-Derived Growth Factor. *Physiological Reviews*, *79*(4), 1283–1316.

Hell, S. W., & Wichmann, J. (1994). STED: stimulated-emission-depletion fluorescence microscopy. *Optics Letters*. https://doi.org/10.1364/OL.19.000780

Hemant, S. (2010). Physiologic upper limits of pore size of different blood capillary types and another perspective on the dual pore theory of microvascular permeability. *Journal of Angiogenesis Research*, *2*(14), 1–19.

Hemler, M. E. (2003). Tetraspanin proteins mediate cellular penetration, invasion, and fusion events and define a novel type of membrane nanodomain. *Annu. Rev. Cell Dev. Biol*, *19*, 397–422. https://doi.org/10.1146/annurev.cellbio.19.111301.153609

Hemler, M. E. (2005). Tetraspanin functions and associated microdomains. *Nature Reviews Molecular Cell Biology*, *6*, 801–811. https://doi.org/10.1038/nrm1736

Hendrix, M. J. C., Seftor, E. A., Seftor, R. E. B., & Fidler, I. J. (1987). A simple quantitative assay for studying the invasive potential of high and low human metastatic variants. *Cancer Letters*, *38*(1–2), 137–147. https://doi.org/10.1016/0304-3835(87)90209-6

Hess, S. T., Girirajan, T. P. K., & Mason, M. D. (2006). Ultra-high resolution imaging by fluorescence photoactivation localization microscopy. *Biophysical Journal*, *91*(11), 4258–4272.

https://doi.org/10.1529/biophysj.106.091116

Higashiyama, S., Abraheam, J. A., Miller, J., Fiddes, J. C., & Klagsbrun, M. (1990). A Heparin-Binding Growth Factor Secreted by Macrophage-Like Cells That Is Related to EGF. *Science*, *251*, 936–939.

Higashiyama, S., Iwamoto, R., Goishi, K., Raab, G., Taniguchi, N., Klagsbrun, M., & Mekada, E. (1995). The Membrane Protein CD9/DRAP 27 Potentiates the Juxtacrine Growth Factor Activity of the Membrane-anchored Heparin-binding EGF-like Growth Factor. *The Journal of Cell Biology*, *128*(5), 929–938.

Hilhorst, M., Van Paassen, P., & Tervaert, J. W. C. (2015). Proteinase 3-ANCA vasculitis versus myeloperoxidase- ANCA vasculitis. *Journal of the American Society of Nephrology*, *26*(10), 2314–2327. https://doi.org/10.1681/ASN.2014090903

Hirose, T., Satoh, D., Kurihara, H., Kusaka, C., Hirose, H., Matsusaka, T., Ichikawa, I., Noda, T., & Ohno, S. (2009). An Essential Role of the Universal Polarity Protein, aPKCλ, on the Maintenance of Podocyte Slit Diaphragms. *PLoS ONE*, *4*(1), 1–9. https://doi.org/10.1371/journal.pone.0004194

Hjalmarsson, C., Johansson, B. R., & Haraldsson, B. (2004). Electron microscopic evaluation of the endothelial surface layer of glomerular capillaries. *Microvascular Research*, *67*(1), 9–17. https://doi.org/10.1016/j.mvr.2003.10.001

Hoang, T. T. (2022). *Single-molecule-based imaging study of EGFR receptor nano-organization regulation: to pathophysiological mechanisms in kidney diseases* [Université Paris-Saclay]. https://doi.org/NNT: 2022UPAST012

Hoch, R. V, & Soriano, P. (2003). Roles of PDGF in animal development. *Development*, *130*, 4769–4784. https://doi.org/10.1242/dev.00721

Hoebe, R. A., Van Oven, C. H., Gadella, T. W. J., Dhonukshe, P. B., Van Noorden, C. J. F., & Manders, E. M. M. (2007). Controlled light-exposure microscopy reduces photobleaching and phototoxicity in fluorescence live-cell imaging. *Nature Biotechnology*, *25*(2), 249–253. https://doi.org/10.1038/nbt1278

Holzman, L. B., St. John, P. L., Kovari, I. A., Verma, R., Holthofer, H., & Abrahamson, D. R. (1999). Nephrin localizes to the slit pore of the glomerular epithelial cell Rapid Communication. *Kidney Internationa*, *56*, 1481–1491. https://doi.org/10.1046/j.1523-1755.1999.00719.x

Homan, K. A., Gupta, N., Kroll, K. T., Kolesky, D. B., Skylar-Scott, M., Miyoshi, T., Mau, D., Valerius, M. T., Ferrante, T., Bonventre, J. V., Lewis, J. A., & Morizane, R. (2019). Flow-enhanced vascularization and maturation of kidney organoids in vitro. *Nature Methods*, *16*(3), 255–262. https://doi.org/10.1038/s41592-019-0325-y

Hovind, P., Tarnow, L., Oestergaard, P. B., & Parving, H.-H. (2000). Elevated vascular endothelial growth factor in type 1 diabetic patients with diabetic nephropathy. *Kidney International*, *57*(75), 56–61. https://doi.org/10.1046/j.1523-1755.2000.07504.x

Hu, Q., Klippel, A., Muslin, A. J., Fantl, W. J., & Williamst, L. T. (1995). Ras-Dependent Induction of Cellular Responses by Constitutively Active Phosphatidylinositol-3 Kinase. *Science*, *268*(April), 100–102.

Huang, B., Wang, W., Bates, M., & Zhuang, X. (2008). Three-dimensional super-resolution imaging by stochastic optical reconstruction microscopy. *Science*, *319*(5864), 810–813. https://doi.org/10.1126/science.1153529

Huang, C., Taki, T., Adachi, M., Yagita, M., Sawada, S., Takabayashi, A., Inufusa, H., Yoshie, O., & Masayuki, M. (1997). MRP-1/CD9 and KAI1/CD82 expression in normal and various cancer tissues. *International Journal of Oncology*, *11*, 1045–1051.

Huber, T. B., Simons, M., Hartleben, B., Sernetz, L., Schmidts, M., Gundlach, E., Saleem, M. A., Walz, G., & Benzing, T. (2003). Molecular basis of the functional podocin – nephrin complex : mutations in the NPHS2 gene disrupt nephrin targeting to lipid raft microdomains. *Human Molecular Genetics*, *12*(24), 3397–3405. https://doi.org/10.1093/hmg/ddg360

Hudkins, K. L., Gilbertson, D. G., Carling, M., Taneda, S., Hughes, S. D., Holdren, M. S., Palmer, T. E., Topouzis, S., Haran, A. C., Feldhaus, A. L., & Alpers, C. E. (2004). Exogenous PDGF-D Is a Potent Mesangial Cell Mitogen and Causes a Severe Mesangial Proliferative Glomerulopathy. *J Am Soc Nephrol*, *15*, 286–298. https://doi.org/10.1097/01.ASN.0000108522.79652.63

Huh, D., Matthews, B. D., Mammoto, A., Montoya-Zavala, M., Hsin, H. Y., & Ingber, D. E. (2010). Reconstituting Organ-Level Lung Functions on a Chip. *Science*, *328*, 1662–1668. https://doi.org/10.1126/science.1188302

Huignard, A., Franville, A., & Gacoin, T. (2003). Emission Processes in YVO4:Eu Nanoparticles. *J. Phys. Chem.*, *107*, 6754–6759.

Huisken, J., Swoger, J., Del Bene, F., Wittbrodt, J., & Stelzer, E. H. K. (2004). Optical sectioning deep inside live embryos by selective plane illumination microscopy. *Science*. https://doi.org/10.1126/science.1100035

Hynes, R. O. (2002). Integrins : Bidirectional, Allosteric Signaling Machines. *Cell*, *110*, 673–687.

Iampietro, C., Bellucci, L., Arcolino, F. O., Arigoni, M., Alessandri, L., Gomez, Y., Papadimitriou, E., Calogero, R. A., Cocchi, E., Van Den Heuvel, L., Levtchenko, E., & Bussolati, B. (2020). Molecular and functional characterization of urine-derived podocytes from patients with Alport syndrome. *Journal of Pathology*, *252*(1), 88–100. https://doi.org/10.1002/path.5496

Ichimura, K., Kurihara, H., & Sakai, T. (2003). Actin Filament Organization of Foot Processes in Rat Podocytes. *The Journal of Histochemistry & Cytochemistry*, *51*(12), 1589–1600. https://doi.org/10.1177/002215540305101203

Ichimura, K., Miyaki, T., Kawasaki, Y., Kinoshita, M., Kakuta, S., & Sakai, T. (2019). Morphological processes of foot process effacement in puromycin aminonucleoside nephrosis revealed by FIB/SEM tomography. *Journal of the American Society of Nephrology*, *30*(1), 96–108. https://doi.org/10.1681/ASN.2018020139

Ikenouchi, J., Matsuda, M., Furuse, M., & Tsukita, S. (2003). Regulation of tight junctions during the epithelium- mesenchyme transition : direct repression of the gene expression of claudins /occludin by Snail. *Journal of Cell Science 116*, *116*(10). https://doi.org/10.1242/jcs.00389

Ingber, D. E. (2022). Human organs-on-chips for disease modelling, drug development and personalized medicine. In *Nature Reviews Genetics* (Vol. 23, Issue 8, pp. 467–491). https://doi.org/10.1038/s41576-022-00466-9

Inoue, T., Yaoita, E., Kurihara, H., Shimizu, F., Sakai, T., Kobayashi, T., Ohshiro, K., Kawashi, H., Okada, H., Suzuki, H., Kihara, I., & Yamamoto, T. (2001). FAT is a component of glomerular slit diaphragms. *Kidney International*, *59*, 1003–1012. https://doi.org/10.1046/j.1523-1755.2001.0590031003.x

Ito, Y., Aten, J., Bende, R. J., Oemar, B. S., Rabelink, T. J., Weening, J. J., & Goldschmeding, R. (1998). Expression of connective tissue growth factor in human renal fibrosis. *Kidney International*, *53*, 853–861. https://doi.org/10.1111/j.1523-1755.1998.00820.x

Itoh, M., Nakadate, K., Horibata, Y., Matsusaka, T., Xu, J., Hunziker, W., & Sugimoto, H. (2014). The Structural and Functional Organization of the Podocyte Filtration Slits Is Regulated by Tjp1/ZO-1. *PLoS ONE*, *9*(9), 1–11. https://doi.org/10.1371/journal.pone.0106621

Iwamoto, R., Higashiyama, S., Mitamura, T., Taniguchi, N., Klagsbrun, M., & Mekada, E. (1994).

Heparin-binding EGF-like growth factor, which acts as the diphtheria toxin receptor, forms a complex with membrane protein DRAP27/CD9 , which up-regulates functional receptors and diphtheria toxin sensitivity. *The EMBO Journal*, *13*(10), 2322–2330. https://doi.org/10.1002/j.1460-2075.1994.tb06516.x

Iwamoto, R., Senohs, H., Okadas, Y., Uchidas, T., & Mekada, E. (1991). An Antibody That Inhibits the Binding of Diphtheria Toxin to Cells Revealed the Association of a 27-kDa Membrane Protein with the Diphtheria Toxin Receptor*. *The Journal of Biological Chemistry*, *266*(30). https://doi.org/10.1016/S0021-9258(18)54947-4

Iyoda, M., Shibata, T., Kawaguchi, M., Yamaoka, T., & Akizawa, T. (2009). Preventive and therapeutic effects of imatinib in Wistar-Kyoto rats with anti-glomerular basement membrane glomerulonephritis. *Kidney International*, *75*(10), 1060–1070. https://doi.org/10.1038/ki.2009.43

Iyoda, M., Shibata, T., Wada, Y., Kuno, Y., Shindo-Hirai, Y., Matsumoto, K., & Akizawa, T. (2013). Long- and short-term treatment with imatinib attenuates the development of chronic kidney disease in experimental anti-glomerular basement membrane nephritis. *Nephrol Dial Transplant*, *28*, 576–584. https://doi.org/10.1093/ndt/gfs414

Izumi, Y., Hirata, M., Hasuwa, H., Iwamoto, R., Umata, T., Miyado, K., Tamai, Y., Kurisaki, T., Sehara-fujisawa, A., Ohno, S., & Mekada, E. (1998). A metalloprotease – disintegrin, MDC9/meltrin- γ/ADAM9 and PKCδ are involved in TPA-induced ectodomain shedding of membrane-anchored heparin-binding EGF-like growth factor. *The EMBO Journal*, *17*(24), 7260–7272. https://doi.org/10.1093/emboj/17.24.7260

Jacquemet, G., Carisey, A. F., Hamidi, H., Henriques, R., & Leterrier, C. (2020). The cell biologist's guide to super-resolution microscopy. *Journal of Cell Science*, *133*(11). https://doi.org/10.1242/jcs.240713

Jaenen, V., Fraguas, S., Bijnens, K., Heleven, M., Artois, T., Romero, R., Smeets, K., & Cebrià, F. (2021). Reactive oxygen species rescue regeneration after silencing the MAPK–ERK signaling pathway in Schmidtea mediterranea. *Scientific Reports*, *11*(1). https://doi.org/10.1038/s41598-020-79588-1

Jeansson, M., Björck, K., Tenstad, O., & Haraldsson, B. (2009). Adriamycin alters glomerular endothelium to induce proteinuria. *Journal of the American Society of Nephrology*, *20*(1), 114–122. https://doi.org/10.1681/ASN.2007111205

Jeansson, M., & Haraldsson, B. (2003). Glomerular size and charge selectivity in the mouse after exposure to glucosaminoglycan-degrading enzymes. *Journal of the American Society of Nephrology*, *14*(7), 1756–1765. https://doi.org/10.1097/01.ASN.0000072742.02714.6E

Jeansson, M., & Haraldsson, B. (2006). Morphological and functional evidence for an important role of the endothelial cell glycocalyx in the glomerular barrier. *American Journal of Physiology - Renal Physiology*, *290*(1), 111–116. https://doi.org/10.1152/ajprenal.00173.2005

Jeibmann, A., Halama, K., Theresa, H., Kim, S. N., Kla, C., & Paulus, W. (2015). Involvement of CD9 and PDGFR in migration is evolutionarily conserved from Drosophila glia to human glioma. *J Neurooncol*. https://doi.org/10.1007/s11060-015-1864-4

Jennette, J. C. (2013). Overview of the 2012 revised International Chapel Hill Consensus Conference nomenclature of vasculitides. *Clinical and Experimental Nephrology*, *17*(5), 603–606. https://doi.org/10.1007/s10157-013-0869-6

Jennette, J. C., & Falk, R. J. (1997). ANCA Small-Vessel Vasculitis. *Journal of the American Society of Nephrology*.

Jennette, J. C., Harrington, J. T., Kausz, A., Narayan, G., Ucci, A. A., Levey, A. S., Uhlig, K., Gill,

J., & Balakrishnan, V. (2003). Rapidly progressive crescentic glomerulonephritis. *Kidney International*, *63*(3), 1164–1177. https://doi.org/10.1046/j.1523-1755.2003.00843.x

Jennette, J. C., & Hipp, C. G. (1986). The Epithelial Antigen Phenotype of Glomerular Crescent Cells. *American Journal of Clinical Pathology*, *86*(3), 274–280.

Jiménez-Díaz, E., Cano-Jorge, M., Zamarrón-Hernández, D., Cabriales, L., Páez-Larios, F., Cruz-Ramírez, A., Vázquez-Victorio, G., Fiordelisio, T., & Hautefeuille, M. (2019). Micro-macro: Selective integration of microfeatures inside low-cost macromolds for PDMS microfluidics fabrication. *Micromachines*, *10*(9), 1–16. https://doi.org/10.3390/mi10090576

Johnsson, A., Heldin, C. H., Westermark, B., & Wasteson, A. (1982). Platelet-Derived Growth Factor: identification of constituent polypeptide chains. *Biochemical and Biophysical Research Communications*, *104*(1), 66–74.

Jones, N., Blasutig, I. M., Eremina, V., Ruston, J. M., Bladt, F., Li, H., Huang, H., Larose, L., Li, S. S., Takano, T., Quaggin, S. E., & Pawson, T. (2006). Nck adaptor proteins link nephrin to the actin cytoskeleton of kidney podocytes. *Nature*, *440*(April), 1–6. https://doi.org/10.1038/nature04662

Kabgani, N., Grigoleit, T., Schulte, K., Sechi, A., Sauer-Lehnen, S., Tag, C., Boor, P., Kuppe, C., Warsow, G., Schordan, S., Mostertz, J., Chilukoti, R. K., Homuth, G., Endlich, N., Tacke, F., Weiskirchen, R., Fuellen, G., Endlich, K., Floege, J., … Moeller, M. J. (2012). Primary cultures of glomerular parietal epithelial cells or podocytes with proven origin. *PLoS ONE*, *7*(4). https://doi.org/10.1371/journal.pone.0034907

Kane, R. S., Takayama, S., Ostuni, E., Ingber, D. E., & Whitesides, G. M. (1999). Patterning proteins and cells using soft lithography. *Biomaterials*, *20*(23–24), 2363–2376. https://doi.org/10.1016/S0142-9612(99)00165-9

Kanemoto, K., Usui, J., Tomari, S., Yokoi, H., Mukoyama, M., Aten, J., Weening, J. J., & Nagata, M. (2003). Connective Tissue Growth Factor Participates in Scar Formation of Crescentic Glomerulonephritis. *Laboratory Investigation*, *83*(11), 1615–1625. https://doi.org/10.1097/01.LAB.0000096711.58115.46

Kann, S. H., Shaughnessey, E. M., Coppeta, J. R., Azizgolshani, H., Isenberg, B. C., Vedula, E. M., Zhang, X., & Charest, J. L. (2022). Measurement of oxygen consumption rates of human renal proximal tubule cells in an array of organ-on-chip devices to monitor drug-induced metabolic shifts. *Microsystems and Nanoengineering*, *8*(1). https://doi.org/10.1038/s41378-022-00442-7

Katrukha, E. A. (2020). Detection of Molecules (DoM) plugin for ImageJ, v1.2.1. *Zenodo*. https://doi.org/10.5281/zenodo.4281069

Kaverina, N. V., Eng, D. G., Miner, J. H., Pippin, J. W., & Shankland, S. J. (2020). Parietal epithelial cell differentiation to a podocyte fate in the aged mouse kidney. *Aging*, *12*(17), 1–24. https://doi.org/10.18632/AGING.103788

Kestila, M., Lenkkeri, U., Lamerdin, J., Mccready, P., Putaala, H., Ruotsalainen, V., Morita, T., Nissinen, M., Herva, R., Kashtan, C. E., Peltonen, L., Holmberg, C., Olsen, A., & Tryggvason, K. (1998). Positionally Cloned Gene for a Novel Glomerular Protein — Nephrin — Is Mutated in Congenital Nephrotic Syndrome. *Molecular Cell*, *1*, 575–582. https://doi.org/10.1016/S1097-2765(00)80057-X

Khater, I. M., Nabi, I. R., & Hamarneh, G. (2020). A Review of Super-Resolution Single- Molecule Localization Microscopy Cluster Analysis and Quantification Methods. *Patterns*, *1*(3), 100038. https://doi.org/10.1016/j.patter.2020.100038

Khoshnoodi, J., Sigmundsson, K., Ofverstedt, L.-G., Skoglund, U., Obrink, B., Wartiovaara, J., &

Tryggvason, K. (2003). Nephrin Promotes Cell-Cell Adhesion through Homophilic Interactions. *American Journal of Pathology*, *163*(6), 2337–2346. https://doi.org/10.1016/S0002-9440(10)63590-0

Kihara, I., Tsuchida, S., Yaoita, E., Yamamoto, T., Hara, M., Yanagihara, T., & Takada, T. (1997). Podocyte detachment and epithelial cell reaction in focal segmental glomerulosclerosis with cellular variants. *Kidney International. Supplement*, *63*, S171-6.

Kim, K. M., An, H. J., Kim, S. H., Kim, J. H., Sim, C., Lee, J., Park, S. H., Lee, H. Il, Jang, I., & Lee, S. (2022). Therapeutic Effect of Pericytes for Diabetic Wound Healing. *Frontiers in Cardiovascular Medicine*, *9*(May). https://doi.org/10.3389/fcvm.2022.868600

Kiskowski, M. A., Hancock, J. F., & Kenworthy, A. K. (2009). On the use of Ripley's K-function and its derivatives to analyze domain size. *Biophysical Journal*, *97*(4), 1095–1103. https://doi.org/10.1016/j.bpj.2009.05.039

Kitadokoro, K., Bordo, D., Galli, G., Petracca, R., Falugi, F., Abrignani, S., Grandi, G., & Bolognesi, M. (2001). CD81 extracellular domain 3D structure : insight into the tetraspanin superfamily structural motifs. *The EMBO Journal*, *20*(1), 12–18. https://doi.org/10.1093/emboj/20.1.12

Klinghoffer, R. A., Mueting-nelsen, P. F., Faerman, A., Shani, M., & Soriano, P. (2001). The Two PDGF Receptors Maintain Conserved Signaling In Vivo despite Divergent Embryological Functions. *Molecular Cell*, *7*, 343–354.

Kohler, N., & Lipton, A. (1974). Platelets as a source of fibroblast growth-promoting activity. *Experimental Cell Research*, *87*, 297–301.

Kok, H. M., Falke, L. L., Goldschmeding, R., & Nguyen, T. Q. (2014). Targeting CTGF, EGF and PDGF pathways to prevent progression of kidney disease. *Nature Reviews Nephrology*, 1–12. https://doi.org/10.1038/nrneph.2014.184

Korolj, A., Laschinger, C., James, C., Hu, E., Velikonja, C., Smith, N., Gu, I., Ahadian, S., Willette, R., Radisic, M., & Zhang, B. (2018). Curvature facilitates podocyte culture in a biomimetic platform. *Lab on a Chip*, *18*(20), 3112–3128. https://doi.org/10.1039/c8lc00495a

Kotha, J., Longhurst, C., Appling, W., & Jennings, L. K. (2008). Tetraspanin CD9 regulates β1 integrin activation and enhances cell motility to fibronectin via a PI-3 kinase-dependent pathway. *Experimental Cell Research*, *314*, 1811 – 1 822. https://doi.org/10.1016/j.yexcr.2008.01.024

Kovalenko, O. V, Yang, X. H., & Hemler, M. E. (2007). A Novel Cysteine Cross-linking Method Reveals a Direct Association between Claudin-1 and Tetraspanin CD9. *Molecular and Cellular Proteomics*, *6*(11), 1855–1867. https://doi.org/10.1074/mcp.M700183-MCP200

Kriz, W. (2020). The Inability of Podocytes to Proliferate: Cause, Consequences, and Origin. *Anatomical Record*, *303*(10), 2588–2596. https://doi.org/10.1002/ar.24291

Kriz, W., Hahnel, B., Rosener, S., & Elger, M. (1995). Long-term treatment of rats with FGF-2 results in focal segmental glomeruloscierosis. *Kidney International*, *48*, 1435–1450. https://doi.org/10.1038/ki.1995.433

Kriz, W., Hartmann, I., Hosser, H., Ahnel, B. H., Anzlin, B. K. R., Provoost, A. P., & Gretz, N. (2001). Tracer Studies in the Rat Demonstrate Misdirected Filtration and Peritubular Filtrate Spreading in Nephrons with Segmental Glomerulosclerosis. *J Am Soc Nephrol*, *12*, 496–506.

Kriz, W., & Lemley, K. V. (2015). A Potential Role for Mechanical Forces in the Detachment of Podocytes and the Progression of CKD. *J Am Soc Nephrol*, *26*, 258–269. https://doi.org/10.1681/ASN.2014030278

Kriz, W., Shirato, I., Nagata, M., LeHir, M., & Lemley, K. V. (2013). The podocyte's response to

stress: the enigma of foot process effacement. *Am J Physiol Renal Physiol*, *304*, 333–347. https://doi.org/10.1152/ajprenal.00478.2012.-Progressive

Kubosawa, H., & Kondo, Y. (1985). Ultrastructural organization of the glomerular basement membrane as revealed by a deep-etch replica method. *Cell and Tissue Research*, *242*, 33–39. https://doi.org/http://dx.doi.org/10.1007/BF00225560

Kundra, V., Escobedo, J. A., Kazlauskas, A., Kim, H. K., Rhee, S. G., Williams, L. T., & Zetter. (1994). Regulation of chemotaxis by the platelet-derived growth factor receptor B. *Nature*, *367*, 474–476.

Kuppe, C., Gröne, H. J., Ostendorf, T., Van Kuppevelt, T. H., Boor, P., Floege, J., Smeets, B., & Moeller, M. J. (2015). Common histological patterns in glomerular epithelial cells in secondary focal segmental glomerulosclerosis. *Kidney International*, *88*(5), 990–998. https://doi.org/10.1038/ki.2015.116

Kuppe, C., Leuchtle, K., Wagner, A., Kabgani, N., Saritas, T., Puelles, V. G., Smeets, B., Hakroush, S., van der Vlag, J., Boor, P., Schiffer, M., Gröne, H. J., Fogo, A., Floege, J., & Moeller, M. J. (2019). Novel parietal epithelial cell subpopulations contribute to focal segmental glomerulosclerosis and glomerular tip lesions. *Kidney International*, *96*(1), 80–93. https://doi.org/10.1016/j.kint.2019.01.037

Kuppe, C., Roeyen, C. Van, Leuchtle, K., Kabgani, N., Vogt, M., Zandvoort, M. Van, Smeets, B., Floege, J., Gröne, H., & Moeller, M. J. (2017). Investigations of Glucocorticoid Action in GN. *J Am Soc Nephrol*, *28*, 1408–1420.

Kusumi, A., & Sako, Y. (1996). Cell surface organization by the membrane skeleton. *Current Opinion in Cell Biology*, *8*, 566–574.

Kusumi, A., Sako, Y., & Yamamoto, M. (1993). Confined Lateral Diffusion of Membrane Receptors as Studied by Single Particle Tracking (Nanovid Microscopy). Effects of Calcium-induced Differentiation in Cultured Epithelial Cells. *Biophysical Journal*, *65*(November 1993), 2021–2040.

Lagaudriere-Gesbert, C., Naour, L., Lebel-binay, S., Billard, M., Lemichez, E., Boquet, P., Boucheix, C., Conjeaud, H., & Rubinstein, E. (1997). Functional Analysis of Four Tetraspans, CD9, CD53, CD81, and CD82, Suggests a Common Role in Costimulation, Cell Adhesion , and Migration : Only CD9 Upregulates HB-EGF Activity. *Cellular Immunology*, *112*(182), 105–112.

Lan, H. Y., Mitsuhashi, H., Ng, Y., Nikolic-paterson, D. J., Yang, N., Mu, W., & Atkins, R. C. (1997). Macrophage Apoptosis in Rat Crescentic Glomerulonephritis. *American Journal of Pathology*, *151*(2), 531–538.

Lancaster, M. A., Renner, M., Martin, C., Wenzel, D., Bicknell, S., Hurles, M. E., Homfray, T., Penninger, J. M., & Andrew, P. (2013). Cerebral organoids model human brain development and microcephaly. *Nature.*, *501*(7467). https://doi.org/10.1038/nature12517.

Landry, J., Freyer, J. P., & Sutherland, R. M. (1981). Shedding of mitotic cells from the surface of multicell spheroids during growth. *Journal of Cellular Physiology*, *106*(1), 23–32. https://doi.org/10.1002/jcp.1041060104

Laouari, D., Burtin, M., Martino, C., Pillebout, E., Montagutelli, X., Friedlander, G., & Terzi, F. (2011). TGF- a Mediates Genetic Susceptibility to Chronic Kidney Disease. *J Am Soc Nephrol*, *22*, 327–335. https://doi.org/10.1681/ASN.2010040356

Lasagni, L., Lazzeri, E., Shankland, S. J., Anders, H., & Romagnani, P. (2013). Podocyte Mitosis – A Catastrophe. *Current Molecular Medicine*, *13*, 13–23.

Lassé, M., El Saghir, J., Berthier, C. C., Eddy, S., Fischer, M., Laufer, S. D., Kylies, D., Hutzfeldt,

A., Bonin, L. L., Dumoulin, B., Menon, R., Vega-Warner, V., Eichinger, F., Alakwaa, F., Fermin, D., Billing, A. M., Minakawa, A., McCown, P. J., Rose, M. P., … Rinschen, M. M. (2023). An integrated organoid omics map extends modeling potential of kidney disease. *Nature Communications*, *14*(1), 8–13. https://doi.org/10.1038/s41467-023-39740-7

Lazareth, H. (2020). *Implication des facteurs locaux (CD9, HB-EGF, PDGF-BB) au sein des cellules épithéliales pariétales glomérulaires au cours de la glomérulonéphrite extracapillaire et de la hyalinose segmentaire et focale : Études in vitro et in vivo* [Université Paris-Saclay]. https://doi.org/tel-02614329

Lazareth, H., Henique, C., Lenoir, O., Puelles, V. G., Flamant, M., Bollée, G., Fligny, C., Camus, M., Guyonnet, L., Millien, C., Gaillard, F., Chipont, A., Robin, B., Fabrega, S., Dhaun, N., Camerer, E., Kretz, O., Grahammer, F., Braun, F., … Tharaux, P. L. (2019). The tetraspanin CD9 controls migration and proliferation of parietal epithelial cells and glomerular disease progression. *Nature Communications*, *10*(1). https://doi.org/10.1038/s41467-019-11013-2

Leclech, C., Natale, C. F., & Barakat, A. I. (2021). The basement membrane as a structured surface – role in vascular health and disease. *Journal of Cell Science*, *133*(18). https://doi.org/10.1242/jcs.239889

Lee, M., Rizzo, R., Surman, F., & Zenobi-Wong, M. (2020). Guiding Lights: Tissue Bioprinting Using Photoactivated Materials. *Chemical Reviews*, *120*(19), 10950–11027. https://doi.org/10.1021/acs.chemrev.0c00077

Lehtonen, S., Ryan, J. J., Kudlicka, K., Iino, N., Zhou, H., & Farquhar, M. G. (2005). Cell junction-associated proteins IQGAP1, MAGI-2, CASK, spectrins, and α-actinin are components of the nephrin multiprotein complex. *PNAS*, *102*(28), 9814–9819. https://doi.org/10.1073/pnas.0504166102

Lennon, R., Byron, A., Humphries, J. D., Randles, M. J., Carisey, A., Murphy, S., Knight, D., Brenchley, P. E., Zent, R., & Humphries, M. J. (2014). Global Analysis Reveals the Complexity of the Human Glomerular Extracellular Matrix. *J Am Soc Nephrol*, *25*, 939–951. https://doi.org/10.1681/ASN.2013030233

Lerner, R. A., J-, G. R., & Dixon, F. J. (1967). The role of anti-glomerular basement membrane antibody in the pathogenesis of human glomerulonephritis*. *J Exp Med*, *126*(6), 989–1004. https://doi.org/10.1084/jem.126.6.989.

Levet, F., Hosy, E., Kechkar, A., Butler, C., Beghin, A., Choquet, D., & Sibarita, J. B. (2015). SR-Tesseler: A method to segment and quantify localization-based super-resolution microscopy data. *Nature Methods*, *12*(11), 1065–1071. https://doi.org/10.1038/nmeth.3579

Levet, F., Julien, G., Galland, R., Butler, C., Beghin, A., Chazeau, A., Hoess, P., Ries, J., Giannone, G., & Sibarita, J.-B. (2019). A tessellation-based colocalization analysis approach for single-molecule localization microscopy. *Nature Communications*, *10*(1). https://doi.org/10.1038/s41467-019-10007-4ï

Levet, F., Julien, G., Galland, R., Butler, C., Beghin, A., Chazeau, A., Ries, J., Giannone, G., & Sibarita, J. (2019). A tessellation-based colocalization analysis approach for single-molecule localization microscopy. *Nature Communications*, 1–12. https://doi.org/10.1038/s41467-019-10007-4

Levick, J. R., & Smaje, L. H. (1987). An analysis of the permeability of a fenestra. *Microvascular Research*, *33*(2), 233–256. https://doi.org/10.1016/0026-2862(87)90020-3

Lewis, E. J., Schwartz, M. M., Pauli, B. U., & Sharon, Z. (1978). Endocytosis : A Property of the Glomerular Visceral Epithelial Cell. *Nephron*, *22*, 91–96.

Li Jeon, N., Baskaran, H., Dertinger, S. K. W., Whitesides, G. M., De Water, L. Van, & Toner, M.

(2002). Neutrophil chemotaxis in linear and complex gradients of interleukin-8 formed in a microfabricated device. *Nature Biotechnology*, *20*(8), 826–830. https://doi.org/10.1038/nbt712

Li, M., Alfieri, C. M., Morello, W., Cellesi, F., Armelloni, S., Mattinzoli, D., Montini, G., & Messa, P. (2020). Assessment of increased glomerular permeability associated with recurrent focal segmental glomerulosclerosis using an in vitro model of the glomerular filtration barrier. *Journal of Nephrology*, *33*(4), 747–755. https://doi.org/10.1007/s40620-019-00683-2

Li, W., Khan, M., Mao, S., Feng, S., & Lin, J. M. (2018). Advances in tumor-endothelial cells co-culture and interaction on microfluidics. *Journal of Pharmaceutical Analysis*, *8*(4), 210–218. https://doi.org/10.1016/j.jpha.2018.07.005

Linde, S. Van De, Löschberger, A., Klein, T., Heidbreder, M., Wolter, S., Heilemann, M., & Sauer, M. (2011). Direct stochastic optical reconstruction microscopy with standard fluorescent probes. *Nature Protocols*, *6*(7), 991–1009. https://doi.org/10.1038/nprot.2011.336

Lippert, A. R., VAn de Bittner, G. C., & Chang, C. J. (2011). Boronate Oxidation as a Bioorthogonal Reaction Approach for Studying the Chemistry of Hydrogen Peroxide in Living Systems. *Accounts of Chemical Research*, *44*(9), 793–804. https://doi.org/10.1021/ar200126t

Lochovsky, C., Yasotharan, S., & Günther, A. (2012). Bubbles no more: In-plane trapping and removal of bubbles in microfluidic devices. *Lab on a Chip*, *12*(3), 595–601. https://doi.org/10.1039/c1lc20817a

Lote, C. J. (1994). Principles of Renal Physiology. In *Principles of Renal Physiology*. https://doi.org/10.1007/978-94-011-6470-2

Low, J. H., Li, P., Chew, E. G. Y., Zhou, B., Suzuki, K., Zhang, T., Lian, M. M., Liu, M., Aizawa, E., Rodriguez Esteban, C., Yong, K. S. M., Chen, Q., Campistol, J. M., Fang, M., Khor, C. C., Foo, J. N., Izpisua Belmonte, J. C., & Xia, Y. (2019). Generation of Human PSC-Derived Kidney Organoids with Patterned Nephron Segments and a De Novo Vascular Network. *Cell Stem Cell*, *25*(3), 373-387.e9. https://doi.org/10.1016/j.stem.2019.06.009

Low, L. A., Mummery, C., Berridge, B. R., Austin, C. P., & Tagle, D. A. (2021). Organs-on-chips: into the next decade. *Nature Reviews Drug Discovery*, *20*(345). https://doi.org/10.1038/s41573-020-0079-3

Lozahic, S., Christiansen, D., Mani, S., Gerlier, D., Billard, M., Boucheix, C., & Rubinstein, E. (2000). CD46 (membrane cofactor protein) associates with multiple β1 integrins and tetraspans. *Eur. J. Immunol*, *30*, 900–907.

Lu, S. M., & Fairn, G. D. (2018). Mesoscale organization of domains in the plasma membrane – beyond the lipid raft. *Critical Reviews in Biochemistry and Molecular Biology*. https://doi.org/10.1080/10409238.2018.1436515

Ludvikova, L., Simon, E., Deygas, M., Panier, T., Plamont, M.-A., Ollion, J., Tebo, A., Piel, M., Jullien, L., Robert, L., Le Saux, T., & Espagne, A. (2023). Near-infrared co-illumination of fluorescent proteins reduces photobleaching and phototoxicity. *Nature Biotechnology*. https://doi.org/10.1038/s41587-023-01893-7

Lund, U., Rippe, A., Venturoli, D., Tenstad, O., Grubb, A., Rippe, B., Rippe, A., Venturoli, D., Grubb, A., & Rippe, B. (2003). Glomerular filtration rate dependence of sieving of albumin and some neutral proteins in rat kidneys. *Am J Physiol Renal Physiol*, *284*, 1226–1234. https://doi.org/10.1152/ajprenal.00316.2002

Maciag, T., Kadish, J., Wllkins, L., Stemerman, M. B., & Weinstein, R. (1982). Organizational behavior of human umbilical vein endothelial cells. *Journal of Cell Biology*, *94*(3), 511–520. https://doi.org/10.1083/jcb.94.3.511

Madshus, I. H., & Stang, E. (2009). Internalization and intracellular sorting of the EGF receptor: A model for understanding the mechanisms of receptor trafficking. *Journal of Cell Science*, *122*(19), 3433–3439. https://doi.org/10.1242/jcs.050260

Malpighi, M. (1687). De renibus. *Opera Omnia Seu Thesaurus Locupletissimus Botanico-Medico-Anatomicus, tomus secu*.

Mangeat, T., Labouesse, S., Allain, M., Negash, A., Martin, E., Guénolé, A., Poincloux, R., Estibal, C., Bouissou, A., Cantaloube, S., Vega, E., Li, T., Rouvière, C., Allart, S., Keller, D., Debarnot, V., Wang, X. B., Michaux, G., Pinot, M., … Sentenac, A. (2021). Super-resolved live-cell imaging using random illumination microscopy. *Cell Reports Methods*, *1*(1). https://doi.org/10.1016/j.crmeth.2021.100009

Marsh, R. J., Pfisterer, K., Bennett, P., Hirvonen, L. M., Gautel, M., Jones, G. E., & Cox, S. (2018). Artifact-free high-density localization microscopy analysis. *Nature Methods*, *15*(9), 689–692. https://doi.org/10.1038/s41592-018-0072-5

Mastrangeli, M., Millet, S., Mummery, C., Loskill, P., Braeken, D., Eberle, W., Cipriano, M., Fernandez, L., Graef, M., Gidrol, X., Picollet-D'Hahan, N., Van Meer, B., Ochoa, I., Schutte, M., & Van den Eijnden-van Raaij, J. (2019). Building blocks for a European Organ-on-Chip roadmap. *Altex*, *36*(3), 481–492. https://doi.org/10.14573/altex.1905221

Mattheyses, A. L., Simon, S. M., & Rappoport, J. Z. (2010). Imaging with total internal reflection fluorescence microscopy for the cell biologist. *Journal of Cell Science*, *123*(21), 3621–3628. https://doi.org/10.1242/jcs.056218

McAdoo, S. P., & Pusey, C. D. (2017). Anti-glomerular basement membrane disease. *CJASN*, *12*, 1162–1172. https://doi.org/10.53738/REVMED.2023.19.821.680

McGrogan, A., Franssen, C. F. M., & De Vries, C. S. (2011). The incidence of primary glomerulonephritis worldwide: A systematic review of the literature. *Nephrology Dialysis Transplantation*, *26*(2), 414–430. https://doi.org/10.1093/ndt/gfq665

Meer, G. Van, Voelker, D. R., & Feigenson, G. W. (2008). Membrane lipids : where they are and how they behave. *Nature Reviews Molecular Cell Biology*, *9*(February), 112–124. https://doi.org/10.1038/nrm2330

Meuwese, M. C., Broekhuizen, L. N., Kuikhoven, M., Heeneman, S., Lutgens, E., Gijbels, M. J. J., Nieuwdorp, M., Peutz, C. J., Stroes, E. S. G., Vink, H., & van den Berg, B. M. (2010). Endothelial surface layer degradation by chronic hyaluronidase infusion induces proteinuria in apolipoprotein E-deficient mice. *PLoS ONE*, *5*(12), 1–7. https://doi.org/10.1371/journal.pone.0014262

Meyer, A. J., & Dick, T. P. (2010). Fluorescent Protein-Based Redox Probes. *Antioxidants & Redox Signaling*, *13*(5). https://doi.org/10.1089=ars.2009.2948

Miesen, L., Bándi, P., Willemsen, B., Mooren, F., Strieder, T., Boldrini, E., Drenic, V., Eymael, J., Wetzels, R., Lotz, J., Weiss, N., Steenbergen, E., van Kuppevelt, T. H., van Erp, M., van der Laak, J., Endlich, N., Moeller, M. J., Wetzels, J. F. M., Jansen, J., & Smeets, B. (2022). Parietal epithelial cells maintain the epithelial cell continuum forming Bowman's space in focal segmental glomerulosclerosis. *DMM Disease Models and Mechanisms*, *15*(3). https://doi.org/10.1242/dmm.046342

Miner, J. H. (2012). The glomerular basement membrane. *Experimental Cell Research*, *318*(9), 973–978. https://doi.org/10.1016/j.yexcr.2012.02.031

Miner, J. H., & Sanes, J. R. (1994). Collagen IV α3, α4, and α5 Chains in Rodent Basal Laminae: Sequence, Distribution, Association with Laminins, and Developmental Switches. *The Journal of Cell Biology*, *127*(3), 879–891. https://doi.org/http:// dx.doi.org/10.1083/jcb.127.3.879

Mitamura, T., Iwamoto, R., Umata, T., Yomo, T., Urabe, I., TsuneokaMekada, M., & Mekada, E. (1992). The 27-kD Diphtheria Toxin Receptor-associated Protein (DRAP27) from Vero Cells Is the Monkey Homologue of Human CD9 Antigen : Expression of DRAP27 Elevates the Number of Diphtheria Toxin Receptors on Toxin-sensitive Cells. *The Journal of Cell Biology*, *118*(6), 1389–1399.

Moeller, M. J., & Smeets, B. (2014). Role of parietal epithelial cells in kidney injury: The case of rapidly progressing glomerulonephritis and focal and segmental glomerulosclerosis. *Nephron - Experimental Nephrology*, *126*(2), 97–100. https://doi.org/10.1159/000360677

Moeller, M. J., Soofi, A., Hartmann, I., Le Hir, M., Wiggins, R., Kriz, W., & Holzman, L. B. (2004). Podocytes Populate Cellular Crescents in a Murine Model of Inflammatory Glomerulonephritis. *Journal of the American Society of Nephrology*, *15*(1). https://journals.lww.com/jasn/fulltext/2004/01000/podocytes_populate_cellular_crescents_in_a_murine.7.aspx

Moeller, M. J., & Tenten, V. (2013). Renal albumin filtration : alternative models to the standard physical barriers. *Nat. Rev. Nephrol*, *9*(5), 266–277. https://doi.org/10.1038/nrneph.2013.58

Moiseev, S., Novikov, P., Jayne, D., & Mukhin, N. (2017). End-stage renal disease in ANCA-associated vasculitis. *Nephrology Dialysis Transplantation*, *32*(2), 248–253. https://doi.org/10.1093/ndt/gfw046

Mondrinos, M. J., Yi, Y. S., Wu, N. K., Ding, X., & Huh, D. (2017a). Native extracellular matrix-derived semipermeable, optically transparent, and inexpensive membrane inserts for microfluidic cell culture. *Lab on a Chip*, *17*(18), 3146–3158. https://doi.org/10.1039/c7lc00317j

Mondrinos, M. J., Yi, Y. S., Wu, N. K., Ding, X., & Huh, D. (2017b). Native extracellular matrix-derived semipermeable, optically transparent, and inexpensive membrane inserts for microfluidic cell culture. *Lab on a Chip*, *17*(18), 3146–3158. https://doi.org/10.1039/c7lc00317j

Morrison, A. A., Viney, R. L., Saleem, M. A., & Ladomery, M. R. (2008). New insights into the function of the Wilms tumor suppressor gene WT1 in podocytes. *American Journal of Physiology - Renal Physiology*, *295*(1), 12–17. https://doi.org/10.1152/ajprenal.00597.2007

Mubaid, F., & Brown, C. M. (2017). Less is More: Longer Exposure Times with Low Light Intensity is Less Photo-Toxic. *Microscopy Today*, *25*(6), 26–35. https://doi.org/10.1017/s1551929517000980

Mukaka, M. M. (2012). Statistics corner: A guide to appropriate use of correlation coefficient in medical research. *Malawi Medical Journal*, *24*(3), 69–71. https://doi.org/10.1016/j.cmpb.2016.01.020

Murayama, Y., Shinomura, Y., Oritani, K., Miyagawa, J., Yoshida, H., Nishida, M., Katsube, F., Shiraga, M., Miyazaki, T., Nakamoto, T., Tsutsui, S., Tamura, S., Higashiyama, S., Shimomura, I., & Hayashi, N. (2007). The Tetraspanin CD9 Modulates Epidermal Growth Factor Receptor Signaling in Cancer Cells. *Journal of Cellular Physiology*, *March*, 135–143. https://doi.org/10.1002/jcp.21384

Musah, S., Mammoto, A., Ferrante, T. C., Jeanty, S. S. F., Hirano-Kobayashi, M., Mammoto, T., Roberts, K., Chung, S., Novak, R., Ingram, M., Fatanat-Didar, T., Koshy, S., Weaver, J. C., Church, G. M., & Ingber, D. E. (2017). Mature induced-pluripotent-stem-cell-derived human podocytes reconstitute kidney glomerular-capillary-wall function on a chip. *Nature Biomedical Engineering*, *1*(5). https://doi.org/10.1038/s41551-017-0069

Nadasdy, T., Laszik, Z., Buck, K. E., Johnson, L. D., & SiIva, F. G. (1994). Proliferative Activity of Intrinsic Normal Human Kidney. *J. Am. Soc. Nephrol.*, *4*, 2032–2039.

Nagata, M., Horita, S., Shu, Y., Shibata, S., Hattori, M., Ito, K., & Watanabe, T. (2000). Phenotypic Characteristics and Cyclin-Dependent Kinase Inhibitors Repression in Hyperplastic Epithelial Pathology in Idiopathic Focal Segmental Glomerulosclerosis. *Laboratory Investigation*, *80*(6), 869–880. https://doi.org/10.1038/labinvest.3780091

Nakagawa, T., Higashiyama, S., Mitamura, T., Mekada, E., & Taniguchi, N. (1996). Amino-terminal Processing of Cell Surface Heparin-binding Epidermal Growth Factor-like Growth Factor Up-regulates Its Juxtacrine but Not Its Paracrine Growth Factor Activity*. *Journal of Biological Chemistry*, *271*(48), 30858–30863. https://doi.org/10.1074/jbc.271.48.30858

Nakopoulou, L., Stefanaki, K., Boletis, J., Papadakis, J., Kostakis, A., Vosnides, G., & Zeis, P. M. (1994). Nephroloqy Dialysis Transplantation Immunohistochemical study of epidermal growth factor receptor (EGFR) in various types of renal injury. *Nephrol Dial Transplant*, *9*, 764–769.

Nanba, D., Mammoto, A., Hashimoto, K., & Higashiyama, S. (2003). Proteolytic release of the carboxy-terminal fragment of proHB-EGF causes nuclear export of PLZF. *The Journal of Cell Biology*, *163*(3), 489–502. https://doi.org/10.1083/jcb.200303017

Nashimoto, Y., Hayashi, T., Kunita, I., Nakamasu, A., Torisawa, Y. S., Nakayama, M., Takigawa-Imamura, H., Kotera, H., Nishiyama, K., Miura, T., & Yokokawa, R. (2017). Integrating perfusable vascular networks with a three-dimensional tissue in a microfluidic device. *Integrative Biology (United Kingdom)*, *9*(6), 506–518. https://doi.org/10.1039/c7ib00024c

Ng, Y., Fan, J., Mu, W., Nikolic-paterson, D. J., Yang, W., Huang, T., Atkins, R. C., & Lan, H. Y. (1999). Nephrology Dialysis Transplantation Glomerular epithelial – myofibroblast transdifferentiation in the evolution of glomerular crescent formation. *Nephrol Dial Transplant*, *14*, 2860–2872.

Ogien, J., Levecq, O., Azimani, H., & Dubois, A. (2020). Dual-mode line-field confocal optical coherence tomography for ultrahigh-resolution vertical and horizontal section imaging of human skin in vivo. *Biomedical Optics Express*, *11*(3), 1327. https://doi.org/10.1364/boe.385303

Ohse, T., Chang, A. M., Pippin, J. W., Jarad, G., Hudkins, K. L., Alpers, C. E., Miner, J. H., & Shankland, S. J. (2009). A new function for parietal epithelial cells: a second glomerular barrier. *Am J Physiol Renal Physiol*, *297*, 1566–1574. https://doi.org/10.1152/ajprenal.00214.2009.

Ohse, T., Pippin, J. W., Chang, A. M., Krofft, R. D., Miner, J. H., Vaughan, M. R., & Shankland, S. J. (2009). The enigmatic parietal epithelial cell is finally getting noticed : a review. *Kidney International*, *76*(12), 1225–1238. https://doi.org/10.1038/ki.2009.386

Okada, C. Y., & Rechsteiner, M. (1982). Introduction of macromolecules into cultured mammalian cells by osmotic lysis of pinocytic vesicles. *Cell*, *29*(1), 33–41. https://doi.org/10.1016/0092-8674(82)90087-3

Ostendorf, T., Roeyen, C. R. C. V. A. N., Peterson, J. D., Kunter, U. T. A., Eitner, F., Hamad, A. J., Chan, G., Jia, X., Macaluso, J., Gazit-bornstein, G., Keyt, B. A., Lichenstein, H. S., Larochelle, W. J., & Floege, R. (2003). A Fully Human Monoclonal Antibody (CR002) Identifies PDGF-D as a Novel Mediator of Mesangioproliferative Glomerulonephritis. *J Am Soc Nephrol*, *14*, 2237–2247. https://doi.org/10.1097/01.ASN.0000083393.00959.02

Ozeki, K., Tanida1, S., Morimoto, C., Inoue, Y., Mizoshita, T., Tsukamoto, H., Shimura, T., Kataoka, H., Kamiya, T., Nishiwaki, E., Ishiguro, H., Higashiyama, S., & Joh, T. (2013). Telmisartan Inhibits Cell Proliferation by Blocking Nuclear Translocation of ProHB-EGF C-Terminal Fragment in Colon Cancer Cells. *PLoS ONE*, *8*(2). https://doi.org/10.1371/journal.pone.0056770

Pabst, R., & Sterzel, R. B. (1983). Cell renewal of glomerular cell types in normal rats. An autoradiographic analysis. *Kidney International*, *24*, 626–631. https://doi.org/10.1038/ki.1983.203

Pageon, S. V., Nicovich, P. R., Mollazade, M., Tabarin, T., & Gaus, K. (2016). Clus-DoC: a combined cluster detection and colocalization analysis for single-molecule localization microscopy data. *Molecular Biology of the Cell*, *27*(22), 3627–3636. https://doi.org/10.1091/mbc.E16-07-0478

Paizis, K., Kirkland, G., Khong, T., Kasterelos, M., Fraser, S., Kanellis, J., & Power, D. A. (1999). Heparin-binding epidermal growth factor-like growth factor is expressed in the adhesive lesions of experimental focal glomerular sclerosis. *Kidney International*, *55*, 2310–2321. https://doi.org/10.1046/j.1523-1755.1999.00469.x

Pan, T., & Wang, W. (2011). From cleanroom to desktop: Emerging micro-nanofabrication technology for biomedical applications. *Annals of Biomedical Engineering*, *39*(2), 600–620. https://doi.org/10.1007/s10439-010-0218-9

Pavenstädt, H., Kriz, W., & Kretzler, M. (2003). Cell biology of the glomerular podocyte. In *Physiological Reviews* (Vol. 83, Issue 1, pp. 253–307). American Physiological Society. https://doi.org/10.1152/physrev.00020.2002

Pavliček, P., & Mikeska, E. (2020). White-light interferometer without mechanical scanning. *Optics and Lasers in Engineering*, *124*(May 2019), 105800. https://doi.org/10.1016/j.optlaseng.2019.105800

Petrosyan, A., Cravedi, P., Villani, V., Angeletti, A., Manrique, J., Renieri, A., De Filippo, R. E., Perin, L., & Da Sacco, S. (2019). A glomerulus-on-a-chip to recapitulate the human glomerular filtration barrier. *Nature Communications*, *10*(1). https://doi.org/10.1038/s41467-019-11577-z

Phelps, R. G., & Turner, A. N. (2010). Antiglomerular Basement Membrane Disease and Goodpasture's Disease. In *Comprehensive Clinical Nephrology: Fourth Edition* (Fourth Edi). Elsevier Inc. https://doi.org/10.1016/B978-0-323-05876-6.00023-X

Plotnikov, S. V., Sabass, B., Schwarz, U. S., & Waterman, C. M. (2014). High-Resolution Traction Force Microscopy. In *Methods in Cell Biology* (1st ed., Vol. 123). Elsevier Inc. https://doi.org/10.1016/B978-0-12-420138-5.00020-3

Pouvreau, S. (2014). Genetically encoded reactive oxygen species (ROS) and redox indicators. *Biotechnology Journal*, *9*(2), 282–293. https://doi.org/10.1002/biot.201300199

Puelles, V. G., Cullen-mcewen, L. A., Taylor, G. E., Li, J., Hughson, M. D., Kerr, P. G., Hoy, X. W. E., Bertram, J. F., Pg, K., We, H., & Jf, B. (2016). Human podocyte depletion in association with older age and hypertension. *Am J Physiol Renal Physiol*, *310*, 656–668. https://doi.org/10.1152/ajprenal.00497.2015

Puelles, V. G., Fleck, D., Ortz, L., Papadouri, S., Strieder, T., Böhner, A. M. C., van der Wolde, J. W., Vogt, M., Saritas, T., Kuppe, C., Fuss, A., Menzel, S., Klinkhammer, B. M., Müller-Newen, G., Heymann, F., Decker, L., Braun, F., Kretz, O., Huber, T. B., … Moeller, M. J. (2019). Novel 3D analysis using optical tissue clearing documents the evolution of murine rapidly progressive glomerulonephritis. *Kidney International*, *96*(2), 505–516. https://doi.org/10.1016/j.kint.2019.02.034

Puelles, V. G., Hoy, W. E., Hughson, M. D., Diouf, B., Douglas-Denton, R. N., & Bertram, J. F. (2011). Glomerular number and size variability and risk for kidney disease. *Current Opinion in Nephrology and Hypertension*, *20*(1), 7–15. https://doi.org/10.1097/MNH.0b013e3283410a7d

Puelles, V. G., & Moeller, M. J. (2018). Postnatal podocyte gain : Is the jury still out ? *Seminars in Cell and Developmental Biology*. https://doi.org/10.1016/j.semcdb.2018.07.007

Puschhof, J., Pleguezuelos-Manzano, C., & Clevers, H. (2021). Organoids and organs-on-chips: Insights into human gut-microbe interactions. *Cell Host and Microbe*, *29*(6), 867–878. https://doi.org/10.1016/j.chom.2021.04.002

Raikwar, S. P., Kim, E. M., Sivitz, W. I., Allamargot, C., Thedens, D. R., & Zavazava, N. (2015). Human iPS cell-derived insulin producing cells form vascularized organoids under the kidney capsules of diabetic mice. *PLoS ONE*, *10*(1), 1–15. https://doi.org/10.1371/journal.pone.0116582

Reigstad, L. J., Varhaug, J. E., & Lillehaug, J. R. (2005). Structural and functional specificities of PDGF-C and PDGF-D , the novel members of the platelet-derived growth factors family. *FEBS Journal*, *272*, 5723–5741. https://doi.org/10.1111/j.1742-4658.2005.04989.x

Remuzzi, A., Brenner, B. M., Pata, V., Tebaldi, G., Mariano, R., Belloro, A., & Remuzzi, G. (1992). Three-dimensional reconstructed glomerular capillary network: Blood flow distribution and local filtration. *American Journal of Physiology - Renal Fluid and Electrolyte Physiology*, *263*(3 32-3). https://doi.org/10.1152/ajprenal.1992.263.3.f562

Rennke, H. G., Cotran, R. S., & Venkatachalam, M. A. (1975). Role of molecular charge in glomerular permeability. *The Journal of Cell Biology*, *67*, 638–646. https://doi.org/10.1083/jcb.67.3.638

Rennke, H. G., & Venkatachalam, M. A. (1977). Glomerular permeability : In vivo tracer studies with polyanionic and polycationic ferritins. *Kidney International*, *11*(1), 44–53. https://doi.org/10.1038/ki.1977.6

Rezakhaniha, R., Agianniotis, A., Schrauwen, J. T. C., Griffa, A., Sage, D., Bouten, C. V. C., Van De Vosse, F. N., Unser, M., & Stergiopulos, N. (2012). Experimental investigation of collagen waviness and orientation in the arterial adventitia using confocal laser scanning microscopy. *Biomechanics and Modeling in Mechanobiology*, *11*(3–4), 461–473. https://doi.org/10.1007/s10237-011-0325-z

Rhee, S. G. (2006). H2O2, a necessary evil for cell signaling. *Science*, *312*(5782), 1882–1883. https://doi.org/10.1126/science.1130481

Rheinwald, J. G., & Green, H. (1975). Serial cultivation of strains of human epidermal keratinocytes in defined clonal and serum-free culture. *Cell*, *6*, 331–344.

Ribou, A.-C. (2016). Synthetic sensors for ROS detection and quantification: a critical review of current methods. *Antioxidants & Redox Signaling*, *33*(514), 1–37. https://doi.org/10.1089/ars.2016.6741

Richly, M. U. (2015). *Investigation des Interactions Toxine-Cellule et du Confinement des Récepteurs dans la Membrane Cellulaire* [Ecole Doctorale Polytechnique]. https://doi.org/tel-01179545

Rintala, J. M., Savikko, J., Rintala, S. E., Palin, N., & Koskinen, P. K. (2015). Epidermal growth factor receptor inhibition with erlotinib ameliorates anti-Thy 1.1-induced experimental glomerulonephritis. *Journal of Nephrology*. https://doi.org/10.1007/s40620-015-0233-x

Ripley, B. D. (1977). Modelling Spatial Patterns. *Journal of the Royal Statistical Society: Series B (Methodological)*, *39*(2), 172–192. https://doi.org/10.1111/j.2517-6161.1977.tb01615.x

Robert, B., Zhao, X., & Abrahamson, D. R. (2000). Coexpression of neuropilin-1, Flk1, and VEGF164 in developing and mature mouse kidney glomeruli. *Am J Physiol Renal Physiol*, *279*, 275–282.

Robinson, S. P., & Craig Jordan, V. (1989). The paracrine stimulation of MCF-7 cells by MDA-MB-231 cells: Possible role in antiestrogen failure. *European Journal of Cancer and Clinical Oncology*, *25*(3), 493–497. https://doi.org/10.1016/0277-5379(89)90262-9

Robles-Flores, M. (2021). Cancer Cell Signaling. In *Cancer Cell Signaling, Methods in Molecular Biology*. https://doi.org/10.1385/1592593569

Roeyen, C. R. C. Van, Eitner, F., Boor, P., Moeller, M. J., Raffetseder, U., Villa, L., Banas, M. C.,

Hudkins, K. L., Alpers, C. E., Hanssen, L., Bucher1, E., Villa, L., Banas, M. C., Hudkins, K. L., Alpers, C. E., Ostendorf, T., & Floege, J. (2011). Induction of progressive glomerulonephritis by podocyte-specific overexpression of platelet-derived growth factor-D. *Kidney International (2011)*, *80*, 1292–1305. https://doi.org/10.1038/ki.2011.278

Rogers, J. A., & Nuzzo, R. G. (2005). Recent progress in soft lithography. *Materials Today*, *8*(2), 50–56. https://doi.org/10.1016/S1369-7021(05)00702-9

Ronconi, E., Sagrinati, C., Angelotti, M. L., Lazzeri, E., Mazzinghi, B., Ballerini, L., Parente, E., Becherucci, F., Gacci, M., Carini, M., Maggi, E., Serio, M., Vannelli, G. B., Lasagni, L., Romagnani, S., & Romagnani, P. (2009). Regeneration of Glomerular Podocytes by Human Renal Progenitors. *J Am Soc Nephrol*, *20*, 322–332. https://doi.org/10.1681/ASN.2008070709

Rosenkranz, S., & Kazlauskas, A. (1998). Evidence for Distinct Signaling Properties and Biological a and B Subtypes. *Growth Factors*, *16*, 201–216.

Ross, R., Glomsett, J., Kariya, B., & Harkert, L. (1974). A Platelet-Dependent, Serum Factor That Stimulates the Proliferation of Arterial Smooth Muscle Cells In Vitro. *Proc. Nat. Acad. Sci. USA*, *71*(4), 1207–1210. https://doi.org/10.1073/pnas.71.4.1207

Rossi, M., Morita, H., Sormunen, R., Airenne, S., Kreivi, M., Wang, L., Fukai, N., Olsen, B. R., Tryggvason, K., & Soininen, R. (2003). Heparan sulfate chains of perlecan are indispensable in the lens capsule but not in the kidney. *The EMBO Journal*, *22*(2), 236±245. https://doi.org/10.1093/emboj/cdg019

Rostgaard, J., & Qvortrup, K. (2001). Sieve plugs in fenestrae of glomerular capillaries - Site of the filtration barrier? *Cells Tissues Organs*, *170*(2–3), 132–138. https://doi.org/10.1159/000046186

Roye, Y., Bhattacharya, R., Mou, X., Zhou, Y., Burt, M. A., & Musah, S. (2021). A personalized glomerulus chip engineered from stem cell-derived epithelium and vascular endothelium. *Micromachines*, *12*(8), 1–16. https://doi.org/10.3390/mi12080967

Ruotsalainen, V., LJungberg, P., Wartiovaara, J., Lenkkeri, U., Kestila, M., Jalanko, H., Holmberg, C., & Tryggvason, K. (1999). Nephrin is specifically located at the slit diaphragm of glomerular podocytes. *Proc. Natl. Acad. Sci. USA*, *96*(July), 7962–7967. https://doi.org/10.1073/pnas.96.14.7962

Russo, L. M., Sandoval, R. M., McKee, M., Osicka, T. M., Collins, A. B., Brown, D., Molitoris, B. A., & Comper, W. D. (2007). The normal kidney filters nephrotic levels of albumin retrieved by proximal tubule cells: Retrieval is disrupted in nephrotic states. *Kidney International*, *71*(6), 504–513. https://doi.org/10.1038/sj.ki.5002041

Rust, M. J., Bates, M., & Zhuang, X. (2006). Sub-diffraction-limit imaging by stochastic optical reconstruction microscopy (STORM). *Nature Methods*, *3*(10), 793–795. https://doi.org/10.1038/nmeth929

Ryan, G. B., & Karnovsky, M. J. (1976). Distribution of endogenous albumin in the rat glomerulus : Role of hemodynamic factors in glomerular barrier function. *Kidney International*, *9*(1), 36–45. https://doi.org/10.1038/ki.1976.5

Sadegh, S., Higgins, J. L., Mannion, P. C., Tamkun, M. M., & Krapf, D. (2017). Plasma Membrane is Compartmentalized by a Self-Similar Cortical Actin Meshwork. *Physical Review*, *7*, 1–10. https://doi.org/10.1103/PhysRevX.7.011031

Sagrinati, C., Netti, G. S., Mazzinghi, B., Lazzeri, E., Liotta, F., Frosali, F., Ronconi, E., Meini, C., Gacci, M., Squecco, R., Carini, M., Gesualdo, L., Francini, F., Maggi, E., Annunziato, F., Lasagni, L., Serio, M., Romagnani, S., & Romagnani, P. (2006). Isolation and Characterization of Multipotent Progenitor Cells from the Bowman's Capsule of Adult Human Kidneys. *J Am*

Soc Nephrol, 2443–2456. https://doi.org/10.1681/ASN.2006010089

Saha, D., Schmidt, U., Zhang, Q., Barbotin, A., Hu, Q., Ji, N., Booth, M. J., Weigert, M., & Myers, E. W. (2020). Practical sensorless aberration estimation for 3D microscopy with deep learning. *Optics Express*, *28*(20), 29044. https://doi.org/10.1364/oe.401933

Sahin, U., Weskamp, G., Kelly, K., Zhou, H., Higashiyama, S., Peschon, J., Hartmann, D., Saftig, P., & Blobel, C. P. (2004). Distinct roles for ADAM10 and ADAM17 in ectodomain shedding of six EGFR ligands. *The Journal of Cell Biology*, *164*(5), 769–779. https://doi.org/10.1083/jcb.200307137

Saleem, M. A., Ni, L., Witherden, I., Tryggvason, K., Ruotsalainen, V., Mundel, P., & Mathieson, P. W. (2002). Co-localization of nephrin, podocin, and the actin cytoskeleton: Evidence for a role in podocyte foot process formation. *American Journal of Pathology*, *161*(4), 1459–1466. https://doi.org/10.1016/S0002-9440(10)64421-5

Saleem, M. A., O'Hare, M. J., Reiser, J., Coward, R. J., Inward, C. D., Farren, T., Chang, Y. X., Ni, L., Mathieson, P. W., & Mundel, P. (2002). A conditionally immortalized human podocyte cell line demonstrating nephrin and podocin expression. *Journal of the American Society of Nephrology*, *13*(3), 630–638. https://doi.org/10.1681/asn.v133630

Salmon, A. H. J., Ferguson, J. K., Burford, J. L., Gevorgyan, H., Nakano, D., Harper, S. J., Bates, D. O., & Peti-Peterd, J. (2012). Loss of the endothelial glycocalyx links albuminuria and vascular dysfunction. *Journal of the American Society of Nephrology*, *23*(8), 1339–1350. https://doi.org/10.1681/ASN.2012010017

Salmon, A. H., & Satchell, S. C. (2012). Endothelial glycocalyx dysfunction in disease: Albuminuria and increased microvascular permeability. *Journal of Pathology*, *226*(4), 562–574. https://doi.org/10.1002/path.3964

Saran, R., Robinson, B., Abbott, K. C., Agodoa, L. Y. C., Bragg-Gresham, J., Balkrishnan, R., Bhave, N., Dietrich, X., Ding, Z., Eggers, P. W., Gaipov, A., Gillen, D., Gipson, D., Gu, H., Guro, P., Haggerty, D., Han, Y., He, K., Herman, W., … Shahinian, V. (2019). US Renal Data System 2018 Annual Data Report: Epidemiology of Kidney Disease in the United States. *American Journal of Kidney Diseases*, *73*(3), A7–A8. https://doi.org/10.1053/j.ajkd.2019.01.001

Satchell, S. C., & Braet, F. (2009). Glomerular endothelial cell fenestrations: An integral component of the glomerular filtration barrier. *American Journal of Physiology - Renal Physiology*, *296*(5). https://doi.org/10.1152/ajprenal.90601.2008

Satchell, S. C., Tasman, C. H., Singh, A., Ni, L., Geelen, J., Von Ruhland, C. J., O'Hare, M. J., Saleem, M. A., Van Den Heuvel, L. P., & Mathieson, P. W. (2006). Conditionally immortalized human glomerular endothelial cells expressing fenestrations in response to VEGF. *Kidney International*, *69*(9), 1633–1640. https://doi.org/10.1038/sj.ki.5000277

Schwarz, K., Simons, M., Reiser, J., Saleem, M. A., Faul, C., Kriz, W., Shaw, A. S., Holzman, L. B., & Mundel, P. (2001). Podocin, a raft-associated component of the glomerular slit diaphragm, interacts with CD2AP and nephrin. *Journal of Clinical Investigation*, *108*(11), 1621–1629. https://doi.org/10.1172/jci12849

Scott, R. P., & Quaggin, S. E. (2015). The cell biology of renal filtration. *Journal of Cell Biology*, *209*(2), 199–210. https://doi.org/10.1083/jcb.201410017

Seger, R., & Krebs, E. C. (1995). The MAPK signaling cascade. *The FASEB*, *9*, 726–735.

Sezgin, E., Levental, I., Mayor, S., & Eggeling, C. (2017). The mystery of membrane organization: Composition, regulation and roles of lipid rafts. *Nature Reviews Molecular Cell Biology*, *18*(6), 361–374. https://doi.org/10.1038/nrm.2017.16

Shankland, S. J., Smeets, B., Pippin, J. W., & Moeller, M. J. (2014). The emergence of the glomerular

parietal epithelial cell. *Nature Reviews Nephrology*, *10*(3), 158–173. https://doi.org/10.1038/nrneph.2014.1

Sherlock, B. E., Harvestine, J. N., Mitra, D., Haudenschild, A., Hu, J., Athanasiou, K. A., Leach, J. K., & Marcu, L. (2018). Nondestructive assessment of collagen hydrogel cross-linking using time-resolved autofluorescence imaging. *Journal of Biomedical Optics*, *23*(03), 1. https://doi.org/10.1117/1.jbo.23.3.036004

Shi, W., Fan, H., Shum, L., & Derynck, R. (2000). The Tetraspanin CD9 Associates with Transmembrane TGF-α and Regulates TGF- α– induced EGF Receptor Activation and Cell Proliferation. *The Journal of Cell Biology*, *148*(3), 591–601.

Shimizu, A., Masuda, Y., Kitamura, H., Ishizaki, M., Sugisaki, Y., & Yamanaka, N. (1996). Apoptosis in progressive crescentic glomerulonephritis. *Laboratory Investigation; a Journal of Technical Methods and Pathology*, *74*(5), 941–951.

Shimizu, M., Kondo, S., Urushihara, M., Takamatsu, M., Kanemoto, K., Nagata, M., & Kagami, S. (2006). Role of integrin-linked kinase in epithelial – mesenchymal transition in crescent formation of experimental glomerulonephritis. *Nephrol Dial Transplant*, *21*(May), 2380–2390. https://doi.org/10.1093/ndt/gfl243

Shirato, I., Tomino, Y., Koide, H., & Sakai, T. (1991). Fine structure of the glomerular basement membrane of the rat kidney visualized by high-resolution scanning electron microscopy. *Cell and Tissue Research*, *266*(1), 1–10. https://doi.org/10.1007/BF00678705

Siegerist, F., Hay, E., Dikou, J. S., Pollheimer, | Marion, Büscher, A., Oh, J., Ribback, S., Zimmermann, U., Jan, |, Bräsen, H., Lenoir, O., Drenic, V., Eller, K., Tharaux, P.-L., & Endlich, N. (2022). ScoMorphoFISH: A deep learning enabled toolbox for single-cell single-mRNA quantification and correlative (ultra-) morphometry. *J Cell Mol Med*, *26*, 3513–3526. https://doi.org/10.1111/jcmm.17392

Simons, K., & Ikonen, E. (1997). Functional rafts in cell membranes. *Nature*, *Vol. 387*(June), 569–572.

Singer, S. J., & Nicolson, G. L. (1972). The fluid mosaic model of the structure of cell membranes. *Science*, *175*((4023)), 720–731.

Singh, A., Ramnath, R. D., Foster, R. R., Wylie, E. C., Fridén, V., Dasgupta, I., Haraldsson, B., Welsh, G. I., Mathieson, P. W., & Satchell, S. C. (2013). Reactive Oxygen Species Modulate the Barrier Function of the Human Glomerular Endothelial Glycocalyx. *PLoS ONE*, *8*(2). https://doi.org/10.1371/journal.pone.0055852

Singh, A., Satchell, S. C., Neal, C. R., McKenzie, E. A., Tooke, J. E., & Mathieson, P. W. (2007). Glomerular endothelial glycocalyx constitutes a barrier to protein permeability. *Journal of the American Society of Nephrology*, *18*(11), 2885–2893. https://doi.org/10.1681/ASN.2007010119

Sison, K., Eremina, V., Baelde, H., Min, W., Hirashima, M., Fantus, I. G., & Quaggin, S. E. (2010). Glomerular Structure and Function Require Paracrine , Not Autocrine , VEGF – VEGFR-2 Signaling. *J Am Soc Nephrol*, *21*, 1691–1701. https://doi.org/10.1681/ASN.2010030295

Smeets, B., Stucker, F., Wetzels, J., Brocheriou, I., Ronco, P., Gröne, H. J., D'Agati, V., Fogo, A. B., Van Kuppevelt, T. H., Fischer, H. P., Boor, P., Floege, J., Ostendorf, T., & Moeller, M. J. (2014). Detection of activated parietal epithelial cells on the glomerular tuft distinguishes early focal segmental glomerulosclerosis from minimal change disease. *American Journal of Pathology*, *184*(12), 3239–3248. https://doi.org/10.1016/j.ajpath.2014.08.007

Smeets, B., Uhlig, S., Fuss, A., Mooren, F., Wetzels, J. F. M., Floege, J., & Moeller, M. J. (2009). Tracing the origin of glomerular extracapillary lesions from parietal epithelial cells. *Journal of*

the American Society of Nephrology, *20*(12), 2604–2615. https://doi.org/10.1681/ASN.2009010122

Sneddon, L. U., Halsey, L. G., & Bury, N. R. (2017). Considering aspects of the 3Rs principles within experimental animal biology. *Journal of Experimental Biology*, *220*(17), 3007–3016. https://doi.org/10.1242/jeb.147058

Srinivasan, B., Kolli, A. R., Esch, M. B., Abaci, H. E., Shuler, M. L., & Hickman, J. J. (2015). TEER Measurement Techniques for In Vitro Barrier Model Systems. *Journal of Laboratory Automation*, *20*(2), 107–126. https://doi.org/10.1177/2211068214561025

Steck, T. L. (1974). The organization of proteins in the human red blood cell membrane. *The Journal of Cell Biology*, *62*, 1–19.

Stein, J. H., & Fadem, S. Z. (1978). The renal circulation. *JAMA*, *239*(13), 1308–13012.

Stipp, C. S., Kolesnikova, T. V, & Hemler, M. E. (2003). Functional domains in tetraspanin proteins. *TRENDS in Biochemical Sciences*, *28*(2), 23–25.

Stylianou, A. (2022). Assessing Collagen D-Band Periodicity with Atomic Force Microscopy. *Materials*, *15*(1608). https://doi.org/https://doi.org/10.3390/ma15041608

Suarez-Arnedo, A., Figueroa, F. T., Clavijo, C., Arbeláez, P., Cruz, J. C., & Muñoz-Camargo, C. (2020). An image J plugin for the high throughput image analysis of in vitro scratch wound healing assays. *PLoS ONE*, *15*(7 July), 1–14. https://doi.org/10.1371/journal.pone.0232565

Sugio, S., Kashima, A., Mochizuki, S., Noda, M., & Kobayashi, K. (1999). Crystal structure of human serum albumin at 2.5 Å resolution. *Protein Engineering*, *12*(6), 439–446. https://doi.org/10.1093/protein/12.6.439

Suleiman, H., Zhang, L., Roth, R., Heuser, J. E., Miner, J. H., Shaw, A. S., & Dani, A. (2013). Nanoscale protein architecture of the kidney glomerular basement membrane. *ELife*, *2*(Iv), 1–18. https://doi.org/10.7554/elife.01149

Sunnarborg, S. W., Hinkle, C. L., Stevenson, M., Russell, W. E., Raska, C. S., Peschon, J. J., Castner, B. J., Gerhart, M. J., Paxton, R. J., Black, R. A., & Lee, D. C. (2002). Tumor Necrosis Factor- α Converting Enzyme (TACE) Regulates Epidermal Growth Factor Receptor Ligand Availability. *Journal of Biological Chemistry*, *277*(15), 12838–12845. https://doi.org/10.1074/jbc.M112050200

Swetha, G., Chandra, V., Phadnis, S., & Bhonde, R. (2011). Glomerular parietal epithelial cells of adult murine kidney undergo EMT to generate cells with traits of renal progenitors. *J. Cell. Mol. Med*, *15*(2), 396–413. https://doi.org/10.1111/j.1582-4934.2009.00937.x

Tabeling, P. (2014). Recent progress in the physics of microfluidics and related biotechnological applications. *Current Opinion in Biotechnology*, *25*, 129–134. https://doi.org/10.1016/j.copbio.2013.11.009

Takasato, M., Er, P. X., Chiu, H. S., Maier, B., Baillie, G. J., Ferguson, C., Parton, R. G., Wolvetang, E. J., Roost, M. S., De Sousa Lopes, S. M. C., & Little, M. H. (2015). Kidney organoids from human iPS cells contain multiple lineages and model human nephrogenesis. *Nature*, *526*(7574), 564–568. https://doi.org/10.1038/nature15695

Takemura, T., Hino, S., Murata, Y., Yanagida, H., Okada, M., Yoshioka, K., & Harris, R. C. (1999). Coexpression of CD9 augments the ability of membrane- bound heparin-binding epidermal growth factor-like growth factor (proHB-EGF) to preserve renal epithelial cell viability. *Kidney International*, *55*, 71–81. https://doi.org/10.1046/j.1523-1755.1999.00259.x

Tassin, M., Beziau, A., Gubler, M., & Boyer, B. (1994). Spatiotemporal expression of molecules associated with junctional complexes during the in vivo maturation of renal podocytes. *Inl..I.*

Dev. BioI, *38*, 45–54.

Taylor, S. R., Markesbery, M. G., & Harding, P. A. (2014). Heparin-binding epidermal growth factor-like growth factor (HB-EGF) and proteolytic processing by a disintegrin and metalloproteinases (ADAM): A regulator of several pathways. *Seminars in Cell and Developmental Biology*. https://doi.org/10.1016/j.semcdb.2014.03.004

Théry, M., Racine, V., Pépin, A., Piel, M., Chen, Y., Sibarita, J. B., & Bornens, M. (2005). The extracellular matrix guides the orientation of the cell division axis. *Nature Cell Biology*, *7*(10), 947–953. https://doi.org/10.1038/ncb1307

Thiery, J. P., & Sleeman, J. P. (2006). Complex networks orchestrate epithelial – mesenchymal transitions. *Nature Reviews Molecular Cell Biology*, *7*(February), 131–142. https://doi.org/10.1038/nrm1835

Thompson, S. A., Higashiyamanll, S., Wood, K., Pollitts, N. S., Damms, D., Mcenroes, G., Garrick, B., Ashton, N., Laus, K., Hamock, N., Klagsbrunll, M., & Abraham, J. A. (1994). Characterization of Sequences within Heparin-binding EGF-like Growth Factor That Mediate Interaction with Heparin*. *THE JOURNAL OF BIOLOGICAL CHEMISTRY*, *269*(4), 2541–2543. https://doi.org/10.1016/S0021-9258(17)41979-X

Tidu, A., Ghoubay-Benallaoua, D., Teulon, C., Asnacios, S., Grieve, K., Portier, F., Schanne-Klein, M. C., Borderie, V., & Mosser, G. (2018). Highly concentrated collagen solutions leading to transparent scaffolds of controlled three-dimensional organizations for corneal epithelial cell colonization. *Biomaterials Science*, *6*(6), 1492–1502. https://doi.org/10.1039/c7bm01163f

Tinevez, J. Y., Perry, N., Schindelin, J., Hoopes, G. M., Reynolds, G. D., Laplantine, E., Bednarek, S. Y., Shorte, S. L., & Eliceiri, K. W. (2017). TrackMate: An open and extensible platform for single-particle tracking. *Methods*, *115*(2017), 80–90. https://doi.org/10.1016/j.ymeth.2016.09.016

Tipping, P. G., & Timoshanko, J. (2005). Contributions of Intrinsic Renal Cells to Crescentic Glomerulonephritis. *Nephron Exp Nephrol*, *101*, 173–178. https://doi.org/10.1159/000088165

Tjorve, K. M. C., & Tjorve, E. (2017). The use of Gompertz models in growth analyses , and new Gompertz-model approach : An addition to the Unified-Richards family. *PLoS ONE*, 1–17. https://doi.org/10.1371/journal.pone.0178691

Tlili, A., Dupré-Crochet, S., Erard, M., & Nüße, O. (2011). Kinetic analysis of phagosomal production of reactive oxygen species. *Free Radical Biology and Medicine*, *50*(3), 438–447. https://doi.org/10.1016/j.freeradbiomed.2010.11.024

Tojo, A., & Endou, H. (1992). Intrarenal handling of proteins in rats using fractional micropuncture technique. *American Journal of Physiology - Renal Fluid and Electrolyte Physiology*, *263*(4 32-4), 601–606. https://doi.org/10.1152/ajprenal.1992.263.4.f601

Tosheva, K. L., Yuan, Y., Matos Pereira, P., Culley, S. n., & Henriques, R. (2020). Between life and death: Strategies to reduce phototoxicity in super-resolution microscopy. *Journal of Physics D: Applied Physics*, *53*(16). https://doi.org/10.1088/1361-6463/ab6b95

Toyoda, M., Najafian, B., Kim, Y., Caramori, M. L., & Mauer, M. (2007). Podocyte Detachment and Reduced Glomerular Capillary Endothelial Fenestration in Human Type 1 Diabetic Nephropathy. *Diabetes*, *56*(August), 2155–2160. https://doi.org/10.2337/db07-0019.This

Tuffin, J., Chesor, M., Kuzmuk, V., Johnson, T., Satchell, S. C., Welsh, G. I., & Saleem, M. A. (2021). GlomSpheres as a 3D co-culture spheroid model of the kidney glomerulus for rapid drug-screening. *Communications Biology*, *4*(1). https://doi.org/10.1038/s42003-021-02868-7

Türkcan, S., Richly, M. U., Bouzigues, C. I., Allain, J. M., & Alexandrou, A. (2013). Receptor

displacement in the cell membrane by hydrodynamic force amplification through nanoparticles. *Biophysical Journal*, *105*(1), 116–126. https://doi.org/10.1016/j.bpj.2013.05.045

Umeda, R., Satouh, Y., Takemoto, M., Nakada-nakura, Y., Liu, K., Yokoyama, T., Shirouzu, M., Iwata, S., Nomura, N., Sato, K., Ikawa, M., Nishizawa, T., & Nureki, O. (2020). Structural insights into tetraspanin CD9 function. *Nature Communications*, *11*(1606), 1–7. https://doi.org/10.1038/s41467-020-15459-7

Uusitalo, L. M., & Hempel, N. (2012). Recent advances in intracellular and in vivo ROS sensing: Focus on nanoparticle and nanotube applications. *International Journal of Molecular Sciences*, *13*(9), 10660–10679. https://doi.org/10.3390/ijms130910660

Van Den Hoven, M. J., Wijnhoven, T. J., Li, J., Zcharia, E., Dijkman, H. B., Wismans, R. G., & Rops, A. L. (2008). Reduction of anionic sites in the glomerular basement membrane by heparanase does not lead to proteinuria. *Kidney International*, *73*, 278–287. https://doi.org/10.1038/sj.ki.5002706

Van Der Woude, F. J., Lobatto, S., Permin, H., Van Der Giessen, M., Rasmussen, N., Wiik, A., Van Es, L. A., Van Der Hem, G. K., & The, T. H. (1985). Autoantibodies Against Neutrophils and Monocytes: Tool for Diagnosis and Marker of Disease Activity in Wegener'S Granulomatosis. *The Lancet*, *325*(8426), 425–429. https://doi.org/10.1016/S0140-6736(85)91147-X

Vimtrup, B. (1928). On the number, shape, structure, and surface area of the glomeruli in the kidneys of man and mammals. *Am. J. Anat.*, *41*, 123–151.

Viola, A., & Gupta, N. (2007). Tether and trap : regulation of membrane-raft dynamics by actin-binding proteins. *Nature Reviews Immunology*, *7*(november). https://doi.org/10.1038/nri2193

Vunjak-Novakovic, G., Ronaldson-Bouchard, K., & Radisic, M. (2021). Organs-on-a-chip models for biological research. *Cell*, *184*(18), 4597–4611. https://doi.org/10.1016/j.cell.2021.08.005

W. F. Scherer, J. T. Sylverton, G., & Gey, O. (1953). Viral multiplication in a stable strain of human malignant epithelial cells (strain HeLa) derived from an epidermoid carcinoma of the cervix. *J Exp Med*, *97*(5), 695–710.

Waldherr, R., Noronha, I. L., Niemir, Z., Kriiger, C., Stein, H., & Stumm, G. (1993). Expression of cytokines and growth factors in human glomerulonephritides. *Pedialr Nephrol*, *7*, 471–478.

Walrand, S., Valeix, S., Rodriguez, C., Ligot, P., Chassagne, J., & Vasson, M. P. (2003). Flow cytometry study of polymorphonuclear neutrophil oxidative burst: A comparison of three fluorescent probes. *Clinica Chimica Acta*, *331*(1–2), 103–110. https://doi.org/10.1016/S0009-8981(03)00086-X

Wang, L., Tao, T., Su, W., Yu, H., Yu, Y., & Qin, J. (2017). A disease model of diabetic nephropathy in a glomerulus-on-a-chip microdevice. *Lab on a Chip*, *17*(10), 1749–1760. https://doi.org/10.1039/c7lc00134g

Wang, S. J., Saadi, W., Lin, F., Minh-Canh Nguyen, C., & Li Jeon, N. (2004). Differential effects of EGF gradient profiles on MDA-MB-231 breast cancer cell chemotaxis. *Experimental Cell Research*, *300*(1), 180–189. https://doi.org/10.1016/j.yexcr.2004.06.030

Wang, X., Fang, H., Huang, Z., Shang, W., Hou, T., Cheng, A., & Cheng, H. (2013a). Imaging ROS signaling in cells and animals. In *Journal of Molecular Medicine* (Vol. 91, Issue 8, pp. 917–927). https://doi.org/10.1007/s00109-013-1067-4

Wang, X., Fang, H., Huang, Z., Shang, W., Hou, T., Cheng, A., & Cheng, H. (2013b). Imaging ROS signaling in cells and animals. *Journal of Molecular Medicine*, *91*(8), 917–927. https://doi.org/10.1007/s00109-013-1067-4

Wang, Y. I., Carmona, C., Hickman, J. J., & Shuler, M. L. (2018). Multiorgan Microphysiological

Systems for Drug Development: Strategies, Advances, and Challenges. *Advanced Healthcare Materials*, *7*(2). https://doi.org/10.1002/adhm.201701000

Wang, Y., Schnitzbauer, J., Hu, Z., Li, X., Cheng, Y., Huang, Z.-L., & Huang, B. (2014). Localization events-based sample drift correction for localization microscopy with redundant cross-correlation algorithm. *Optics Express*, *22*(13), 15982. https://doi.org/10.1364/OE.22.015982

Wartiovaara, J., Öfverstedt, L. G., Khoshnoodi, J., Zhang, J., Mäkelä, E., Sandin, S., Ruotsalainen, V., Cheng, R. H., Jalanko, H., Skoglund, U., & Tryggvason, K. (2004). Nephrin strands contribute to a porous slit diaphragm scaffold as revealed by electron tomography. *Journal of Clinical Investigation*, *114*(10), 1475–1483. https://doi.org/10.1172/JCI22562

Watt, F. M., Jordan, P. W., & O'Neill, C. H. (1988). Cell shape controls terminal differentiation of human epidermal keratinocytes. *Proc. Nat. Acad. Sci. USA*, *85*(15), 5576–5580. https://doi.org/10.1073/pnas.85.15.5576

Weil, E. J., Lemley, K. V, Mason, C. C., Yee, B., Jones, L. I., Blouch, K., Lovato, T., Richardson, M., Myers, B. D., & Nelson, R. G. (2012). Podocyte detachment and reduced glomerular capillary endothelial fenestration promote kidney disease in type 2 diabetic nephropathy. *Kidney International*, *82*(9), 1010–1017. https://doi.org/10.1038/ki.2012.234

Willig, K. I., Kellner, R. R., Medda, R., Hein, B., Jakobs, S., & Hell, S. W. (2006). Nanoscale resolution in GFP-based microscopy. *Nature Methods*, *3*(9), 721–723. https://doi.org/10.1038/nmeth922

Winder, S. J., Kathryn, R., Winder, S. J., & Ayscough, K. R. (2005). Actin-binding proteins. *Journal of Cell Science*, *118*, 651–654. https://doi.org/10.1242/jcs.01670

Wong, M. N., Tharaux, P. L., Grahammer, F., & Puelles, V. G. (2021). Parietal epithelial cell dysfunction in crescentic glomerulonephritis. *Cell and Tissue Research*, *385*(2), 345–354. https://doi.org/10.1007/s00441-021-03513-9

Wrede, C., Hegermann, J., & Mühlfeld, C. (2020). Novel cell contact between podocyte microprojections and parietal epithelial cells analyzed by volume electron microscopy. *American Journal of Physiology - Renal Physiology*, *318*(5), F1246–F1251. https://doi.org/10.1152/ajprenal.00097.2020

Würth, C., Grabolle, M., Pauli, J., Spieles, M., & Resch-Genger, U. (2013). Relative and absolute determination of fluorescence quantum yields of transparent samples. *Nature Protocols*, *8*(8), 1535–1550. https://doi.org/10.1038/nprot.2013.087

Xie, R., Xie, R., Korolj, A., Korolj, A., Liu, C., Song, X., Lu, R. X. Z., Zhang, B., Ramachandran, A., Liang, Q., & Radisic, M. (2020). H-FIBER: Microfluidic Topographical Hollow Fiber for Studies of Glomerular Filtration Barrier. *ACS Central Science*, *6*(6), 903–912. https://doi.org/10.1021/acscentsci.9b01097

Yan, Y., Shirakabe, K., & Werb, Z. (2002). The metalloprotease Kuzbanian (ADAM10) mediates the transactivation of EGF receptor by G protein–coupled receptors. *The Journal of Cell Biology*, *158*(2), 221–226. https://doi.org/10.1083/jcb.200112026

Yanez-Mo, M., Barreiro, O., Gordon-Alonso, M., Sala-Valdes, M., & Sanchez-Madrid, F. (2009). Tetraspanin-enriched microdomains : a functional unit in cell plasma membranes. *Trends in Cell Biology*, *Vol. 19*(No. 9), 434–446. https://doi.org/10.1016/j.tcb.2009.06.004

Yáñez-mó, M., Tejedor, R., Rousselle, P., & Sánchez-madrid, F. (2000). Tetraspanins in intercellular adhesion of polarized epithelial cells : spatial and functional relationship to integrins and cadherins. *Journal of Cell Science*, *114*, 577–587.

Yang, J. A., Phan, H. T., Vaidya, S., & Murphy, C. J. (2013). Nano-vacuums : Nanoparticle Uptake

and Differential Cellular Migration on a Carpet of Nanoparticles. *Nano Letters*. https://doi.org/10.1021/nl400972r

Yang, S. H., Choi, J. W., Huh, D., Jo, H. A., Kim, S., Lim, C. S., Lee, J. C., Kim, H. C., Kwon, H. M., Jeong, C. W., Kwak, C., Joo, K. W., Kim, Y. S., & Kim, D. K. (2017). Roles of fluid shear stress and retinoic acid in the differentiation of primary cultured human podocytes. *Experimental Cell Research*, *354*(1), 48–56. https://doi.org/10.1016/j.yexcr.2017.03.026

Yang, X., Claas, C., Kraeft, S., Chen, L. B., Wang, Z., Kreidberg, J. A., & Hemler, M. E. (2002). Palmitoylation of Tetraspanin Proteins: Modulation of CD151 Lateral Interactions, Subcellular Distribution, and Integrin-dependent Cell Morphology. *Molecular Biology of the Cell*, *13*(March), 767–781. https://doi.org/10.1091/mbc.01–05–0275.

Yarden, Y., & Shilo, B. Z. (2007). SnapShot: EGFR Signaling Pathway. *Cell*, *131*(5), 11–12. https://doi.org/10.1016/j.cell.2007.11.013

Yuan, J., Li, X., & Yu, S. (2023). Advances in tumor-endothelial cells co-culture and interaction on microfluidics. *Frontiers in Immunology*, *13*(January). https://doi.org/10.3389/fimmu.2022.1061388

Zeng, F., Kloepfer, L. A., Finney, C., Diedrich, A., & Harris, R. C. (2016). Specific endothelial heparin-binding EGF-like growth factor deletion ameliorates renal injury induced by chronic angiotensin II infusion. *Am J Physiol Renal Physiol*, *311*, 695–707. https://doi.org/10.1152/ajprenal.00377.2015

Zhang, J., Wang, X., Vikash, V., Ye, Q., Wu, D., Liu, Y., & Dong, W. (2016). ROS and ROS-Mediated Cellular Signaling. *Oxidative Medicine and Cellular Longevity*, *2016*(Figure 1). https://doi.org/10.1155/2016/4350965

Zhang, X. A., & Huang, C. (2012). Tetraspanins and cell membrane tubular structures. *Cell. Mol. Life Sci.*, *69*, 2843–2852. https://doi.org/10.1007/s00018-012-0954-0

Zhang, Y. S., Aleman, J., Shin, S. R., Kilic, T., Kim, D., Shaegh, S. A. M., Massa, S., Riahi, R., Chae, S., Hu, N., Avci, H., Zhang, W., Silvestri, A., Nezhad, A. S., Manbohi, A., De Ferrari, F., Polini, A., Calzone, G., Shaikh, N., … Khademhosseini, A. (2017). Multisensor-integrated organs-on-chips platform for automated and continual in situ monitoring of organoid behaviors. *Proceedings of the National Academy of Sciences of the United States of America*, *114*(12), E2293–E2302. https://doi.org/10.1073/pnas.1612906114

Zheng, W., Wang, Z., Zhang, W., & Jiang, X. (2010). A simple PDMS-based microfluidic channel design that removes bubbles for long-term on-chip culture of mammalian cells. *Lab on a Chip*, *10*(21), 2906–2910. https://doi.org/10.1039/c005274d

Zhou, A., Ueno, H., Shimomura, M., Tanaka, R., Shirakawa, T., Nakamura, H., Matsuo, M., & Iijima, K. (2003). Blockade of TGF-B action ameliorates renal dysfunction and histologic progression in anti-GBM nephritis. *Kidney International*, *64*, 92–101. https://doi.org/10.1046/j.1523-1755.2003.00045.x

Zhou, M., Zhang, X., Wen, X., Wu, T., Wang, W., Yang, M., Wang, J., Fang, M., Lin, B., & Lin, H. (2016a). Development of a Functional Glomerulus at the Organ Level on a Chip to Mimic Hypertensive Nephropathy. *Scientific Reports*, *6*(457), 1–13. https://doi.org/10.1038/srep31771

Zhou, M., Zhang, X., Wen, X., Wu, T., Wang, W., Yang, M., Wang, J., Fang, M., Lin, B., & Lin, H. (2016b). Development of a Functional Glomerulus at the Organ Level on a Chip to Mimic Hypertensive Nephropathy. *Scientific Reports*, *6*. https://doi.org/10.1038/srep31771

Zhou, Z., & Harding, P. A. (2007). Amino-terminal deletion of heparin-binding epidermal growth factor-like growth factor 4−127 stimulates cell proliferation but lacks insulin-like activity. *Cell Prolif*, *40*, 213–230.

Zimmermann, M., Bonn, S., Puelles, V. G., Zimmermann, M., Klaus, M., Wong, M. N., Thebille, A., Gernhold, L., Kuppe, C., Halder, M., Kranz, J., Wanner, N., Braun, F., Wulf, S., Wiech, T., Panzer, U., Krebs, C. F., Hoxha, E., & Kramann, R. (2021). Deep learning – based molecular morphometrics for kidney biopsies Deep learning – based molecular morphometrics for kidney biopsies. *JCI Insight*, *6*(7). https://doi.org/https://doi.org/10.1172/jci.insight.144779.

Zuidscherwoude, M., Göttfert, F., Dunlock, V. M. E., & Figdor, C. G. (2015). The tetraspanin web revisited by super-resolution microscopy. *Scientific Reports*, *5*(12201), 1–18. https://doi.org/10.1038/srep12201

Résumé en Français

La thèse est intitulée "Développement d'un système opto-microfluidique pour sonder la fonction et la signalisation d'un glomérule rénal sur puce" et présente une étude complète de la fonction du glomérule rénal ainsi que le développement de nouvelles méthodologies pour l'étudier. Le contenu est organisé ainsi :

- L'introduction générale donne un aperçu de l'importance de la compréhension des processus physio-pathologiques, en particulier dans des maladies complexes telles que la glomérulonéphrite à progression rapide et la hyalinose segmentaire focale. Elle met notamment l'accent sur la nécessité de disposer de technologies permettant de concevoir des systèmes modèles physiologiquement pertinents et de développer des techniques quantitatives permettant de sonder les processus biologiques à des résolutions spatiales et temporelles élevées à diverses échelles.
- Le chapitre 1, intitulé « Physiopathologie glomérulaire », traite de l'anatomie et de la fonction du rein, en décrivant finement la physiopathologie glomérulaire. Il explore le rôle des différents composants cellulaires du glomérule, notamment les cellules endothéliales, les podocytes et les cellules épithéliales pariétales, à la fois dans les états sains et pathologiques.
- Le chapitre 2, intitulé « Développement d'un glomérule sur puce », décrit la conception d'un microsystème optiquement accessible qui récapitule la complexité du glomérule humain en utilisant la technique de "l'organe sur puce". Il s'agit notamment de reproduire la barrière de filtration glomérulaire et d'étudier les processus cellulaires et à l'échelle du pseudo organe en réponse aux stimulations par le Facteur de Croissance Epidermique (EGF).
- Le chapitre 3, intitulé « Imagerie de molécules individuelles » se concentre sur les essais moléculaires et cellulaires pour étudier le comportement des récepteurs de l'EGF et leurs interactions avec la tétraspanine CD9 lors de la stimulation par l'EGF de cellules pariétales épithéliales. Il explore également l'utilisation de nanoparticules dopées à l'europium pour mesurer la réponse oxydante cellulaire (Espèces Réactives de l'Oxygène, ROS) et l'intégration de surfaces sensibles aux ROS dans les systèmes "Organe sur puce".
- La conclusion générale résume les principaux résultats et contributions de la thèse, en mettant l'accent sur le développement d'outils puissants pour comprendre la signalisation moléculaire dans des situations normales et pathologiques.

Introduction

Il est crucial d'identifier les voies de signalisation pour comprendre et traiter les maladies complexes, en particulier dans les cas où les approches traditionnelles sont insuffisantes. Dans des maladies telles que la glomérulonéphrite et la hyalinose segmentaire et focale, qui causent une insuffisance rénale terminale due à la désorganisation du glomérule, il est crucial de comprendre les interactions moléculaires complexes. Des régulateurs clés tels que HB-EGF, PDGF et CD9 sont impliqués, et le rôle des Espèces Réactives de l'Oxygène (ROS) en tant que régulateur central dans ces maladies est supposé.

Le manque de tests quantitatifs efficaces pour la réponse cellulaire et la détection des ROS dans les environnements multicellulaires a entravé la compréhension de ces maladies. Pour y remédier, nous avons développé un essai biomimétique opto-microfluidique. Cette technologie innovante combine la reconstitution du glomérule sur puce et des méthodes d'imagerie quantitative avancées, y compris des nanoparticules luminescentes à base de lanthanides pour une détection rapide des ROS. Cela permet une évaluation quantitative des réponses cellulaires et de la production de ROS sous des stimuli contrôlés, comblant ainsi le fossé entre les études *in vitro* et *in vivo*.

L'objectif principal de ce travail est de mieux comprendre la signalisation moléculaire dans des conditions normales et pathologiques et de développer des stratégies pour profiler de manière non invasive et quantitative des pathologies complexes telles que les tumeurs et les maladies auto-immunes. Ceci est crucial pour le développement de traitements personnalisés et de stratégies thérapeutiques moléculaires efficaces.

Chapitre 1 : Physiopathologie glomérulaire

Le glomérule est un élément clé du système de filtration rénal. Structurellement le glomérule est situé entre deux artérioles et comprend quatre types de cellules distincts : les cellules endothéliales glomérulaires (GEnCs) qui forment un endothélium fenestré pour la filtration du plasma, les podocytes, des péricytes différenciés du côté urinaire qui ont des prolongements appelés pieds étroitement enroulés autour des capillaires, les cellules épithéliales pariétales (PECs) qui forment la capsule de Bowman étanche, et les cellules mésangiales qui fournissent un soutien structurel aux vaisseaux glomérulaires (Schéma bilan 1). La Barrière de Filtration Glomérulaire (BFG) est composée de GEnCs, de podocytes et de la membrane basale glomérulaire (MBG). Cette barrière agit comme un tamis, filtrant le sang pour créer un filtrat urinaire primaire, principalement dépourvu de protéines.

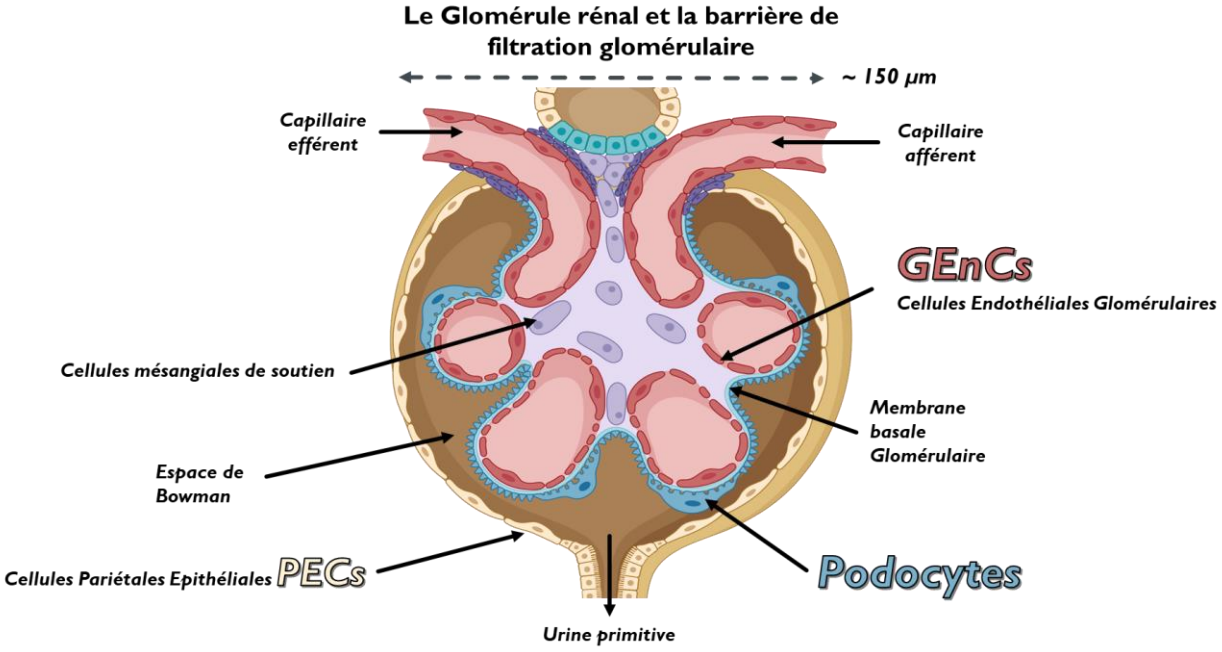

Schéma bilan 1 : Structure du Glomérule rénal et organisation cellulaire

La glomérulonéphrite et la hyalinose segmentaire et focale sont des affections qui sont dues à des dommages au glomérule, menant à une insuffisance rénale terminale. Elles impliquent l'activation

des cellules glomérulaires (podocytes, PECs), entraînant prolifération et migration, mais les mécanismes moléculaires précis ne sont pas entièrement compris. La glomérulonéphrite se caractérisée par une prolifération cellulaire en forme de croissant dans l'espace urinaire, elle résulte de l'infiltration de leucocytes et de la prolifération des podocytes et des PECs. La hyalinose segmentaire et focale implique l'effondrement des capillaires glomérulaires et la sclérose avec des dépôts de matrice extracellulaire. C'est une cause majeure de maladie rénale chronique et de maladie rénale en phase terminale.

Des facteurs tels que la tétraspanine CD9, le Facteur de Croissance Dérivé des Plaquettes (PDGF) et EGF sont impliqués dans la réponse des PECs aux lésions rénales. Nous avons étudié l'implication de ces différents facteurs à différentes échelles : moléculaires, cellulaires, jusqu'à celle du pseudo-organe grâce à différentes techniques détaillées dans les chapitres expérimentaux du manuscrit.

Chapitre 2 : Développement d'un glomérule sur puce

L'objectif était tout d'abord de développer un microsystème permettant de combiner une approche systématique d'organe sur puce avec des méthodes de mesure quantitatives non invasives avancées, pour identifier les mécanismes conduisant à des réponses pathophysiologiques, à l'échelle cellulaire et de l'organe.

À cette fin, nous avons conçu des systèmes microfluidiques biocompatibles aux dimensions adaptées pour imiter à la fois les dimensions d'un glomérule réel et permettre de bonnes capacités d'imagerie. Les dispositifs sont construits en utilisant des techniques de microfabrication classiques permettant un bon contrôle global des dimensions des systèmes et la répétabilité de la fabrication. Les systèmes sont composés de deux petits compartiments imitant l'espace vasculaire et urinaire d'un glomérule et sont séparés par une membrane (Schéma bilan 2).

Les systèmes ont été caractérisés pour des membranes synthétiques et bioartificielles (membranes à base de PET ou de collagène) qui ont fourni un support pour la co-culture de cellules endothéliales glomérulaires conditionnellement immortalisées (GEnCs) et de podocytes (Podocytes) qui reproduisent la barrière de filtration glomérulaire. L'espace de Bowman dans de tels systèmes est délimité par une troisième couche de cellules épithéliales pariétales (PECs) alignées directement au fond du dispositif qui se trouve être optiquement accessible, offrant une fenêtre optique pour observer les systèmes avec pratiquement n'importe quel microscope. Lorsque les cellules sont co-cultivées dans de tels dispositifs, un renouvellement continu du milieu de culture et un stress de cisaillement contrôlé sont fournis par une approche de perfusion entraînée par gravité qui permet une culture soutenue pendant plusieurs semaines.

Après 2 semaines de co-culture et de différenciation sur puce, les 3 types de cellules utilisés pour reproduire l'organisation glomérulaire ont tous montré des marqueurs spécifiques trouvés *in vivo*. Les cellules ont formé des monocouches confluentes sur toute la surface du système. Les cellules ont également sécrété des quantités pertinentes de protéines spécifiques de la membrane basale de la matrice extra-cellulaire (MEC) et ont montré une réponse au stress de cisaillement en s'alignant avec le flux dans le dispositif (Schéma bilan 2).

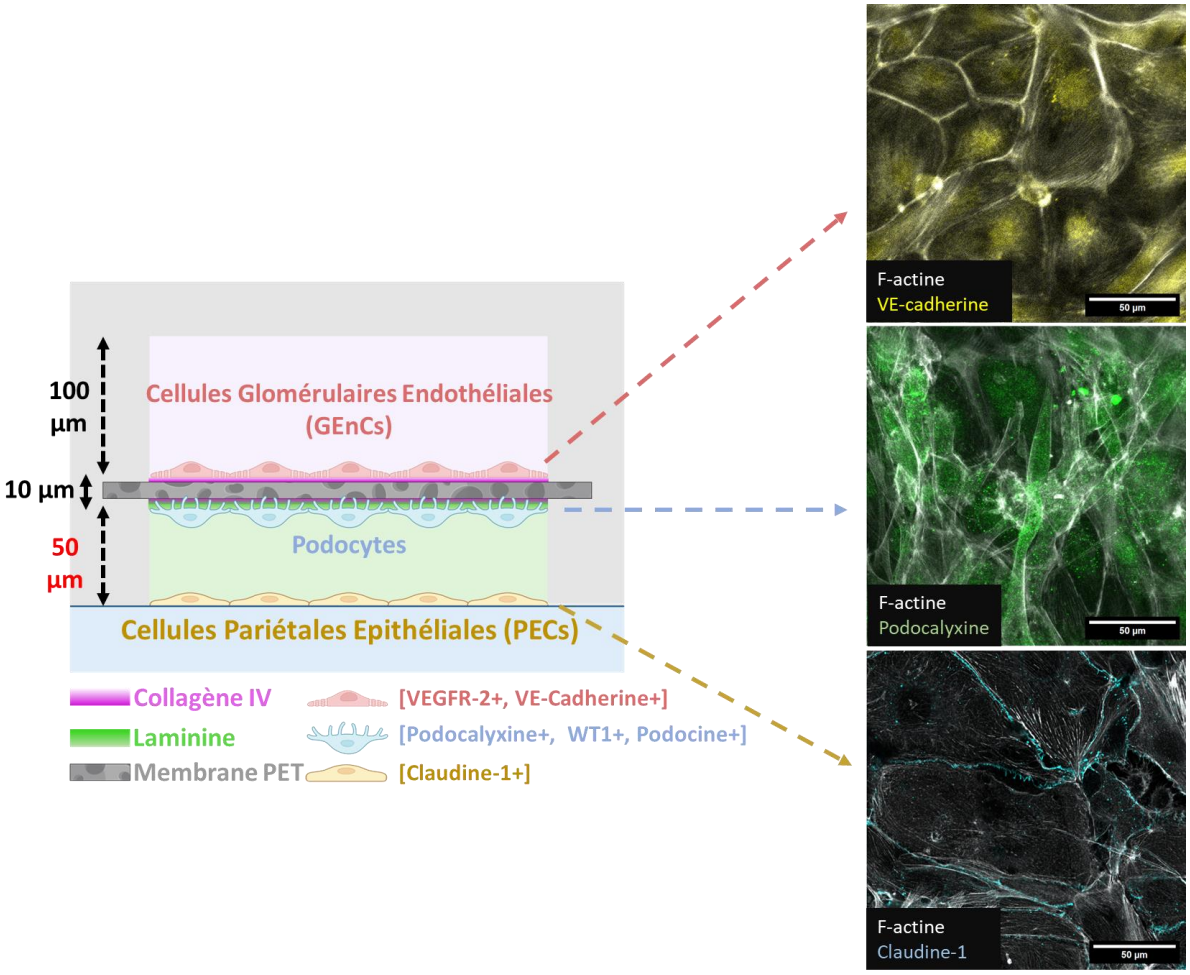

Schéma bilan 2 : Récapitulation de l'organisation d'un glomérule renal sur puce.

Un test fonctionnel a montré que les systèmes présentaient des propriétés de filtration similaires à ce qui est attendu d'un glomérule réel. De plus, la filtration d'albumine (ou coefficient de tamisage) a également été mesurée à des valeurs proches des valeurs *in vivo*. Cela a confirmé que notre système se comportait fonctionnellement comme un glomérule réel.

Nous avons ensuite étudié la réponse du système à l'EGF en stimulant artificiellement les systèmes avec de l'EGF pendant plusieurs semaines. Les systèmes stimulés par EGF ont montré une capacité de filtration réduite à la fois pour l'albumine et les petites molécules. L'EGF a également induit une forte prolifération des PECs conduisant finalement à l'invasion de la chambre urinaire et à la déstabilisation de la couche de Podocytes. Ce sont également des marqueurs de la progression de la glomérulonéphrite et de la hyalinose segmentaire et focale observés *in vivo* (Kuppe et al., 2019 ; Lazareth et al., 2019 ; Moeller & Smeets, 2014).

Dans l'ensemble, nous avons récapitulé une organisation et une fonction glomérulaire sur puce en quelques semaines en utilisant des cellules résidentes du glomérule, tout en étant capables de déclencher un phénotype semblable à une maladie par stimulation par EGF conduisant à l'activation des PECs (migration et prolifération) et à l'invasion de la chambre urinaire.

En étudiant ces phénomènes (filtration, migration, prolifération, différenciation) à différents niveaux de complexité, ces dispositifs biomimétiques à l'échelle 'méso' sont capables de créer un

environnement plus pertinent pour déchiffrer des voies de signalisation complexes et éventuellement élaborer des stratégies de contrôle, dans une perspective thérapeutique future.

Chapitre 3 : Imagerie de molécules individuelles

Des recherches antérieures (Hoang, 2022) ont montré que le retrait des protéines CD9 dans les cellules épithéliales pariétales (PECs) entraîne des modifications notables par rapport aux PECs sauvages. Des images de microscopie de super-résolution (dSTORM) montrent que les domaines membranaires nanométriques des récepteurs à l'EGF sont plus grands en surface et en diamètre dans les PECs déficientes en CD9 (CD9-KO). Cela est confirmé par le suivi de récepteurs individuels, qui révèlent des domaines de confinement plus grands pour les récepteurs à l'EGF dans les PECs déficientes en CD9. De plus, les domaines enrichis en CD9 et les domaines des récepteurs à l'EGF, co-localisent au moins partiellement.

Nous avons donc cherché à comprendre comment les EGFRs et CD9 réagissent aux stimulations par HB-EGF, en se concentrant sur leur organisation au sein des nanodomaines qu'ils forment. Nous avons révélé, grâce à l'imagerie dSTORM, qu'avec la stimulation par HB-EGF, le nombre de nano-domaines membranaires des EGFRs et CD9 diminuait. La taille des domaines à EGFR diminuait avec la stimulation par HB-EGF, tandis que les domaines CD9 ne changent pas de dimension. La stimulation par HB-EGF entraîne un regroupement plus dense des molécules d'EGFR au sein de leur nano-domaines membranaires.

Une observation intéressante est que la taille et la densité de molécules des deux types de domaines converge après la stimulation, soulignant l’interaction potentielle entre EGFR et CD9. De plus, une analyse avancée des localisation des deux types molécules par dSTORM indique une co-localisation accrue entre les domaines EGFR et CD9 après la stimulation par HB-EGF. Les EGFRs peuvent être transloqués vers des zones riches en CD9 sur la membrane cellulaire, conduisant à une dimérisation potentiellement favorisée. La suppression de CD9 a donc potentiellement des implications dans la signalisation en aval dans les PECs.

Pour suivre la réponse cellulaire à un stimulation à l’HB-EGF, nous avons utilisé des nanoparticules dopées à l'Europium permettant mesurer les niveaux d'eau oxygénée intracellulaire (H_2O_2) dans les PECs de type sauvage et déficientes en CD9.

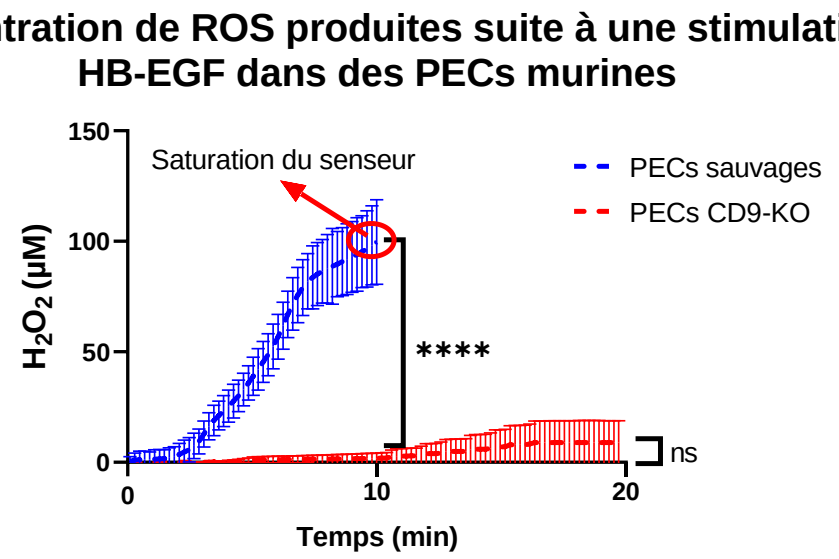

Schéma bilan 3 : Production de H_2O_2 médiée par la stimulations de PECs par l'HB-EGF suivie par l'imagerie de nanoparticules dopées à l'Europium.

Lors de l'évaluation de la concentration intracellulaire en H_2O_2 en réponse à HB-EGF dans les PECs de type sauvage, les niveaux ont rapidement dépassé le seuil de calibration du capteur de 100 µM. Cependant, une analyse comparative entre les PECs sauvages et les PECs déficientes en CD9 pendant les 10 premières minutes après la stimulation par HB-EGF a révélé une réduction marquée de la production de H_2O_2 dans les PECs CD9-KO (Schéma bilan 3).

Dans l'ensemble, ces résultats soutiennent l'hypothèse et les découvertes précédentes suggérant que dans les PECs, CD9 organise au moins partiellement le confinement des EGFRs dans des nanodomaines et régule leur signalisation. Étant donné que l'épuisement de CD9 a montré un phénotype protecteur pour la progression de la RPGN et de la FSGS (Lazareth et al., 2019), et que l'EGF est absent dans l'espace de Bowman, cela fournit une base moléculaire sur la régulation de la transition pathologique dépendante de l'EGF.

Une dernière partie traite de l'intégration de surfaces innovantes pour la détection des ROS dans la plateforme de glomérule sur puce qui permettra à terme des mesures *in situ* dans ce modèle complexe. Cela permet une enquête directe sur la signalisation des ROS dans les PECs au sein du glomérule sur puce, la comparant avec une monoculture simple de PECs, ce qui pourrait aider à comprendre les transitions pathologiques dans la RPGN et la FSGS.

Conclusion

Ce travail traite des défis liés à l'étude de la glomérulonéphrite et de la hyalinose segmentaire et focale, des maladies causant des dommages aigus ou chroniques au glomérule et menant à l'insuffisance rénale. L'activation des cellules glomérulaires (podocytes, cellules épithéliales pariétales) et leurs changements phénotypiques (prolifération, migration) sont centrales dans ces maladies, avec différents facteurs impliqués tels que CD9, EGF et PDGF jouant un rôle, bien qu'ils ne soient pas entièrement compris.

Les méthodes de recherche traditionnelles telles que les cultures cellulaires, les modèles animaux ou les observations cliniques ont des limites pour démêler ces mécanismes complexes. Nous

proposons d'utiliser une approche d’organe sur puce pour modéliser l'environnement glomérulaire et étudier les réponses pathophysiologiques tant au niveau cellulaire que celui de l’organe.

Dans cet objectif nous avons développé un système microfluidique mimant le glomérule et intégrant des capacités d'imagerie avancées et permettant d’étudier les effets de l'EGF sur les cellules épithéliales pariétales (PECs). Ce système permettra à terme l’utilisation de l'imagerie de super-résolution pour étudier *in situ* les mécanismes moléculaires de l’activation des PECs.

Ce cadre microfluidique biomimétique vise à combler le fossé entre les études *in vitro* et *in vivo* en introduisant une complexité pertinente (par exemple, un microenvironnement 3D, des co-cultures contrôlées) et en abordant des questions biologiques au niveau de la construction tissulaire. La technologie pourrait limiter l'utilisation de modèles animaux pour des raisons éthiques et économiques et pourrait fournir des données précieuses pour le criblage de médicaments et la compréhension des pathologies complexes. Étant donné que la RPGN et la FSGS n'ont actuellement aucun traitement efficace autre que la transplantation, ce travail pourrait avoir d'importantes implications médicales et éthiques.

ECOLE DOCTORALE

Titre : Suivi quantitatif de processus biologiques complexes dans des microsystèmes par l'imagerie de nanoparticules

Mots clés : Glomérulonéphrites, Glomérule-sur-puce, EGFR/HB-EGF, CD9, PECs, Podocytes, GEnCs, nanoparticules luminescentes, ROS, dSTORM

Résumé : La glomérulonéphrite et la hyalinose segmentaire et focale sont des maladies résultant d'une atteinte au glomérule, entraînant l'activation des cellules spécialisées telles que les cellules épithéliales pariétales glomérulaires (PECs), et pouvant conduire à une insuffisance rénale terminale. Nous avons développé un système microfluidique (organe-sur-puce) qui reproduit la structure du glomérule et permet la co-culture contrôlée des types de cellules glomérulaire (cellules endothéliales glomérulaires GEnCs, podocytes et PECs), et conserve les fonctions de filtration d'un glomérule réel. L'exposition à l'EGF a provoqué une augmentation de la prolifération des PECs et une réduction des capacités de filtration glomérulaire. Les caractéristiques observées sur notre puce reflètent étroitement celles des PECs lors de la progression des glomérulonéphrites *in vivo*.

Par super-résolution (dSTORM), nous avons découvert que les nano-domaines riches en CD9 sont les sites principaux pour l'activation des EGFRs suite aux stimulations par HB-EGF chez les PECs. De plus, chez les PECs CD9-KO, la production de ROS induite par l'activation des EGFRs par HB-EGF, suivie quantitativement à l'aide de nanoparticules luminescentes, était nettement réduite. Ainsi, le CD9 organise les EGFRs et régule leur signalisation.

En combinant des techniques d'imagerie de molécules uniques et un organe-sur-puce, notre technologie crée un lien entre les études *in vitro* et *in vivo*, réduisant potentiellement le besoin d'expérimentation animale.

Title : Development of an opto-microfluidic assay, to probe kidney glomerulus function and signaling on-chip

Keywords : RPGN, FSGS, Glomerulus-on-chip, EGFR/HB-EGF, CD9, PECs, Podocytes, GEnCs, luminescent nanoparticles, ROS, dSTORM

Abstract : Glomerulonephritis (RPGN) and glomerulosclerosis (FSGS) are diseases resulting from damage to the glomerulus, causing activation of specialized cells, such as glomerular parietal epithelial cells (PECs), which can lead ultimately to fatal renal insufficiency. We developed an organ-on-chip microfluidic system that emulates the structure and cell types of the glomerulus. This system allows for the controlled co-culture of three cell types mimicking the glomerular organization (glomerular endothelial cells GEnCs, podocytes, and PECs), and retained filtration functions of an actual glomerulus. EGF exposure led to an increased PECs proliferation and decreased glomerular filtration capabilities. The characteristics observed in our chip closely mirror those of PECs in RPGN and FSGS progression *in vivo*.

We found through super-resolution imaging (dSTORM) that CD9-rich nanodomains are primary sites for EGFR activation upon HB-EGF stimulations in PECs. Furthermore, in CD9-KO PECs, the ROS production induced by EGFR activation by HB-EGF, quantitatively tracked using luminescent nanoparticles, was significantly reduced. CD9 thus organizes EGFR and regulates its signaling.

By combining single molecule imaging techniques and an organ-on-chip, our technology offers a bridge between *in vitro* and *in vivo* studies, potentially limiting the need for animal testing.

Institut Polytechnique de Paris

91120 Palaiseau, France